Synthesis and evaluation of PET radioligands for the autonomic nervous system and vascular inflammation

By

Uzair Sayani

uOttawa

Department of Biochemistry, Microbiology, and Immunology.
Faculty of Medicine
University of Ottawa

Thesis submitted to the Faculty of Medicine as a partial fulfillment of the requirements for the PhD degree in Biochemistry, Immunology, and Microbiology.

ABSTRACT

Recently discovered methods for both diagnosis and treatment management of heart failure (HF) and other cardiovascular diseases include the use of molecular imaging modalities such as positron emission tomography (PET). As such, PET radiotracers have been developed and show strong evidence for quantifiable sympathetic nervous system (SNS) imaging in animals and humans using radioligands that target the norepinephrine transporter (NET). In this study, the cardiac sympathetic nervous system imaging probe [^{18}F]*meta*-fluorobenzylguanidine ([^{18}F]mFBG) was evaluated in Sprague Dawley (SD) rats and hypothesized to i) have measurable NET-dependent uptake kinetics; ii) possess measurable NET reuptake, iii) be stored into vesicles, and remain metabolically stable within the myocardium, iv) be sensitive to changes in sympathetic tone, and v) discriminate between healthy and diseased animals. Using the selective NET inhibitor desipramine (DMI) and nonselective extraneural and neural uptake inhibitor phenoxybenzamine (PBZ) we observed 30-35% and ~70% reduced uptake in the myocardium, respectively. Neuronal ablation with 6-hydroxydopamine (6-OHDA) resulted in a 36% loss of myocardial retention. DMI and PBZ chase dosing revealed no change in myocardial washout by PET, suggesting minimal reuptake of the tracer and preferential clearance into blood. Pretreatment with the vesicular monoamine transporter (VMAT) inhibitor reserpine (RSP) reduced myocardial retention by 34% within 5 minutes in comparison to baseline, providing evidence for intraneural vesicular retention. Dahl salt-sensitive (DSS) rats were induced with HF via high salt (HS, 8%) diet. After 16 weeks, rats kept on HS diet showed ~32% reduced myocardial uptake in comparison to low salt (LS) controls. Non-invasive PET imaging of HF is therefore sensitive to the expected changes in myocardial uptake in small animal imaging.

The myocardial cholinergic system was evaluated using the vesicular acetylcholine transporter (VAChT) ligand [^{18}F]fluoroethoxybenzylvesamicol ([^{18}F]FEOBV) in CD-1 mice. We hypothesized that i) [^{18}F]FEOBV uptake in the myocardium is VAChT dependent; and more specific in the absence of isoflurane anesthesia. Baseline uptake was observed in the ventricles. However, pretreatment with vesamicol in the presence and absence of isoflurane did not reduce myocardial activity. Analysis of PET images in mice with differential cardiac VAChT expression showed minimal changes in blood and cardiac activity. These studies have demonstrated a lack of specific binding of [^{18}F]FEOBV in the myocardium of mice, rendering this imaging probe unfit in interpreting cholinergic function in small animals.

The second half of the thesis is focused on the development of a radiolabeling technique using novel iminophosphorane precursors, and their subsequent reactivity and application using the naturally abundant (99% carbon-12) and positron emission tomography (PET) imaging isotope (carbon-11). We hypothesized that the reaction of iminophosphorane precursors with [^{11}C]CO_2 with allow us to i) synthesize a myriad of labelled isocyanate derived functional groups ii) apply this chemistry to label relevant radiopharmaceuticals in high yield and molar activity. Optimization of reaction conditions was performed, and a substrate scope was developed. Using the naturally abundant carbon isotope, we synthesized isocyanate derived functional groups such as carbamates, thiocarbamates, ureas, and amides in 63-94% yield. Pharmaceuticals such as regorafenib, URB694, and melatonin were synthesized in 60-72% yield. When applied to carbon-11 radiochemistry, labelled products were produced in 32-84% radiochemical yield (RCY). Radiopharmaceuticals such as [^{11}C]URB694 and [^{11}C]glibenclamide were synthesized in high yield and molar activity suitable for preclinical evaluation. We have demonstrated the utility of

iminophosphorane precursors in synthesizing labelled functional groups and relevant radiopharmaceuticals in high yields, enabling their use for future preclinical or clinical studies.

The recent development of the potent and selective nod-like receptor protein-3 (NLRP3) inhibitor MCC950 has demonstrated remarkable application as a therapeutic in reducing macrophage infiltration and aortic lesion area, but has yet to be applied to PET imaging due to poor synthesis yields. We hypothesized that i) using our previously established iminophosphorane chemistry we can synthesize [^{11}C]MCC950, and ii) selective uptake of [^{11}C]MCC950 occurs in aortic atherosclerotic lesions. We successfully radiolabeled [^{11}C]MCC950 in 45 ± 4 % RCY (27 ± 2 GBq/μmol). Plasma metabolite analysis revealed 94% intact tracer after 15 minutes, and *ex vivo* autoradiography on excised aortas showed heterogeneous uptake in atherosclerotic plaques of ApoE$^{-/-}$ mice. Pretreatment with nonradioactive MCC950 resulted in significantly increased uptake in aortic lesions (48 ± 17 %ID/m^2 vs 104 ± 15 %ID/m^2), without significantly increasing plasma free fraction (1.3 ± 0.4% vs 1.7 ± 0.8%). The data suggests increased specific binding following blockade which may be due to biochemical mechanisms such as disaggregation of NLRP3 oligomers, artificially increasing the available number of binding sites. Thus, the data suggest [^{11}C]MCC950 uptake demonstrates specific binding and may therefore prove useful as an *in vivo* imaging probe to detect NLRP3-mediated inflammation in atherosclerosis.

ACKNOWLEDGEMENTS

The projects completed in this doctoral thesis would not have been possible without the cooperation of several researchers, technicians, and students. To my supervisor, Dr. Benjamin Rotstein, I am very fortunate to have received training in this field with your guidance. Throughout the course of my graduate studies, you have created a positive atmosphere in the lab and have been very supportive in any decision that I have made. Your ability to connect with your students and listen to our comments, concerns, or improvements regarding research projects are unmatched. Designing and performing experiments on projects we are both passionate about really drove the research that we completed, and I am happy to have had such a positive experience.

To my thesis committee members, Dr. Adam Shuhendler, Dr. Emilio Alarcon, and Dr. Lauri Tuominen, I am grateful for all your support throughout the years. The positive feedback that was provided to me was indispensable. Furthermore, the discussions and constructive criticism helped me develop into a more mature researcher and aided in my ability to think outside of the box.

To my lab members, who have been an incredible source of inspiration and motivation. First, Maxime Munch & Braeden Mair, who aided in the completion of carbon-11 projects in my absence, thank you for all your support and hard work. The completion of those projects would not have been possible without your assistance. Ariel Buchler, who taught me several technical skills and aided in the completion of all radiotracer imaging projects, your contribution and support will always be remembered. To all of you, we spent half a decade together and made lasting memories in that time, I cannot express how grateful I am to have completed my PhD with all of you around. To all the students in the lab, Myriam Adi, Jadde de Carvalho Tso, Faduma Abdirahman, Hala Almeneim, Talia Knuth, your kindness and ability to lift my spirits up will always be remembered.

To my family, thank you for your continued support during my studies and for holding down the fort in my absence.

TABLE OF CONTENTS

LISTS OF FIGURES, TABLES, AND SCHEMES

Chapter 1

Chapter 2

Chapter 3

Chapter 4

Chapter 5

Chapter 6

Chapter 7

LIST OF ABBREVIATIONS

^{18}F	Fluorine-18
^{18}O	Oxygen-18
^{11}C	Carbon-11
[^{18}F]mFBG	[^{18}F]*meta*-fluorobenzylguanidine
[^{18}F]FEOBV	[^{18}F]fluoroethoxybenzylvesamicol
[^{123}I]mIBG	[^{123}I]*meta*-iodobenzylguanidine
[^{11}C]HED	[^{11}C]hydroxyephedrine
[^{18}F]FBBG	[^{18}F]Flubrobenguan
[^{18}F]4F-MHPG	4-[^{18}F]fluoro-*m*-hydroxyphenethylguanidine
[^{18}F]3F-PHPG	3-[^{18}F]fluoro-*p*-hydroxyphenethylguanidine
[^{18}F]FDG	2-deoxy-2-[^{18}F]fluoro-D-glucose
[^{11}C]MQNB	[^{11}C]methquinuclidnyl benzilate
[^{11}C]CH_3I	[^{11}C]methyl iodide
[^{11}C]CH_3OTf	[^{11}C]methyl triflate
[^{11}C]CH_4	[^{11}C]methane
[^{11}C]HCN	[^{11}C]hydrogen cyanide
[^{11}C]CO_2	[^{11}C]Carbon Dioxide
PET	Positron Emission Tomography
ANS	Autonomic Nervous System
CNS	Central Nervous system
SNS	Sympathetic Nervous System
PNS	Parasympathetic Nervous System

ENS	Enteric Nervous System
NE	Norepinephrine
EPI	Epinephrine
Acetylcholine	ACh
NNCS	Non-Neuronal Cholinergic System
HF	Heart Failure
NET (uptake-1)	Norepinephrine Transporter
VMAT2	Vesicular monoamine transporter 2
GPCR	G protein-coupled receptor
α_1R	Alpha-1 receptor
α_2R	Alpha-2 receptor
β_2AR	Beta-2 Adrenergic receptor
β_1AR	Beta-1 Adrenergic receptor
PIP2	Phosphatidylinositol-4,5-biphosphate 2
PLC	Phospholipase C
IP3	Inositol 1,4,5-triphosphate
DAG	2-diacylglycerol
ER	Endoplasmic Reticulum
PKC	Protein Kinase C
PKA	Protein Kinase A
G_s	G stimulatory
cAMP	Cyclic Adenosine Monophosphate
COMT	Catecholamine-O-methyl transferase

MAO	Monoamine oxidase
OCT3	Organic cation transporter 3
SD	Sprague Dawley
CAD	Coronary Artery Disease
CAL	Coronary Artery Ligation
AB	Supracoronary aortic banding
GRK	G-protein receptor kinases
HFpEF	Heart failure with preserved ejection fraction
HFmrEF	Heart failure with mid-range ejection fraction
HFrEF	Heart Failure with reduced ejection fraction
DSS	Dahl salt-sensitive
HS	High salt
LS	Low salt
LV	Left ventricle
EDV	End diastolic volume
EDVPR	End diastolic pressure-volume relationship
ESPVR	End systolic pressure volume relationship
EF	Ejection fraction
SV	Stroke volume
EDP	End diastolic pressure
NYHA	New York Heart Association
ACC	College of Cardiology/American Heart Association
BNP	Brain natriuretic peptide

NT-proBNP	N-terminal pro brain natriuretic peptide
ANP	Atrial natriuretic peptide
Oxphos	Oxidative phosphorylation
ATP	Adenosine triphosphate
CK	Creatine kinase
FA	Fatty acids
AChE	Acetylcholine esterase
VAChT	Vesicular acetylcholine transporter
NHP	Nonhuman primate
H/M	Heart to mediastinum ratio
WR	Washout rate
ADMIRE-HF	AdreView Myocardial Imaging for Risk Evaluation in Heart Failure
PAREPET	Prediction of Arrhythmic Events with Positron Emission Tomography
LVEF	Left ventricular ejection fraction
SCA	Sudden cardiac arrest
ICD	Implantable cardiac defibrillator
DMI	Desipramine
PBZ	Phenoxybenzamine
TH	Tyrosine hydroxylase
SEC	subepicardium
SENC	subendocardium
NB	Neuroblastoma
EWG	Electron withdrawing group

EDG	Electron donating group
BEMP	2-tert-butylimino-2-diethylamino-1,3-dimethylperhydro-1,3,2-diazaphosphorine
DBU	1,8-diazabycyclo[5.4.0]undec-7-ene
DBAD	di-tert-butyl azodicarboxylate
PBu_3	tributylphosphine
$POCl_3$	Phosphorous (V) oxychloride
$scCO_2$	Supercritical carbon dioxide
NLRP3	Nucleotide Oligomerization Domain like Receptor Protein-3
PRR	Pattern recognition receptors
DAMP	Danger associated molecular patterns
PAMP	Pathogen associated molecular pattern
TLR	Toll-like receptor
RLR	retinoic acid-inducible gene-I-like receptors
CLR	C-type lectin receptors
ASC	Adaptor molecule apoptosis-associated speck-like protein
CPC1	cysteine protease caspase-1
ROS	Reactive oxygen species
NEK7	NIMA-related kinase 7
DARTS	Drug affinity responsive target stability
PEV	Platelet-derived extracellular vesicles
BMI	Body mass index

Chapter 1: Introduction

1. Introduction

1.1. Autonomic nervous system (ANS)

The ANS is responsible for regulating involuntary functions and maintaining homeostatic mechanisms including heart rate, blood pressure, and respiration. The ANS is composed of three functionally distinct divisions: sympathetic, parasympathetic, and enteric.[1–3] At rest, the myocardium is primarily under parasympathetic control by the vagus nerve.[1–3] However, upon activation by an external stimulus, the sympathetic nerve system activates systemic fight-or-flight responses that alter cardiac inotropy and chronotropy.[2,4] The sympathetic and parasympathetic nervous systems (SNS, PNS) both contain afferent and efferent nerve fibers critical for providing sensory input and motor output, respectively, to the central nervous system (CNS).[1,3] Organizationally, the SNS and PNS motor pathways consist of preganglionic neurons with cell bodies originating in the CNS, and postganglionic neurons in the periphery that innervate target tissues.[1–3,5] On the other hand, the enteric nervous system (ENS) is a quasi-autonomous part of the nervous system equipped with intrinsic micro circuits that orchestrate gastrointestinal behavior independent of the CNS.[3]

A three-level hierarchical network is used to control the heart: (1) central nervous system neurons, (2) extracardiac-intrathoracic neurons, and (3) the intrinsic cardiac nervous system.[6,7] To ensure that cardiac output fulfils blood flow requirements, these network components function in tandem with one another. In fact, alterations in cardiovascular afferent inputs are influenced by both central and peripheral reflexes in response to common physiological stressors including dynamic exercise and orthostatic stress, which in turn govern motor outputs to meet bodily needs.[4,6,8] As a result, this system ensures that the sympathetic-parasympathetic balance in the heart is precisely controlled.

1.1.1. Parasympathetic myocardial innervation

The PNS emerges from medial medullary sites in the brain (nucleus ambiguous, tractus solitarius, dorsal motor nucleus) and is regulated by the hypothalamus.[3,9,10] Vagal efferents extend from the medulla to postganglionic nerves that innervate the atria via ganglia situated in cardiac fat pads, with neurotransmission mechanisms modulated by nicotinic receptors.[3,4,10] Cholinergic postganglionic parasympathetic and sympathetic nerves then affect cardiac muscarinic receptors.[8,11,12] Peripheral vagus nerve afferent activation can influence central and baroreceptor-level efferent sympathetic and parasympathetic function.[10,13] Efferent vagus activation has tonic and basal effects that function to inhibit sympathetic activation and reduce release of norepinephrine (NE) in the presynaptic neuron.[5,10,14] Release of acetylcholine (ACh) from parasympathetic neurons activates ganglionic nicotinic receptors, further activating muscarinic receptors to reduce heart rate and cause direct hyperpolarization of sinoatrial node cells.[14] In addition, muscarinic receptors present on blood vessels induce vasorelaxation via nitric oxide (NO)-dependent pathways.[14]

The SNS and PNS are classically referred to as having opposing functions. However, the dynamic interaction that occurs between the two systems is complex. At rest, tonic parasympathetic activation (vagal tone) predominates over sympathetic tone.[14,15] However, sudden PNS stimulation will inhibit sympathetic activation (tonic) during rest and exercise.[3,14,15] This phenomenon has been termed accentuated antagonism.[3,14,15] In a static or dynamic state, elevated sympathetic tone is overridden by excessive vagus nerve discharge.

In the PNS, most parasympathetic fibers (75%) are carried by the vagus nerve, which regulates internal organ functions such as digestion, heart rate, respiratory rate, vasomotor activity,

among others.[3] In the myocardium, the intrinsic conduction of action potentials originates from the sinoatrial node (SA node), located in the right atrium.[14,16] All components of this conduction system are composed of autorhythmic cells that spontaneously depolarize to maintain basal cardiac function under resting conditions.[3] However, depending on the body's nutrient and oxygen deprivation status, heart rate and cardiac output must undergo rapid changes that are regulated by the autonomic nervous system (ANS) and hormones, among other factors.[14,16]

Mechanistically, ACh transmission has been hypothesized to begin with the synthesis of ACh by choline acetyltransferase (ChAT) in the cytoplasm of presynaptic cholinergic neurons (figure 1).[17,18] The storage of ACh is mediated by vesicular ACh transporter (VAChT) via the exchange of two vesicular protons released upon stimulation.[17,18] The rate determining step in the synthesis of ACh is dependent on choline transporter (CHT1), responsible for reuptake of extracellular free choline into the pre-synaptic neuron for synthesis.[17,18] Lastly, termination of the effects of ACh is dependent on acetylcholine esterase (AChE), responsible for the enzymatic degradation of ACh.[17,18] Dysfunction of these transporters and enzymes can result in a variety of pathological conditions. For example, aberrant signaling via muscarinic receptors has been correlated with diseases such as Parkinson's disease, Alzheimer's disease, epilepsy, and schizophrenia.[14,19–21]

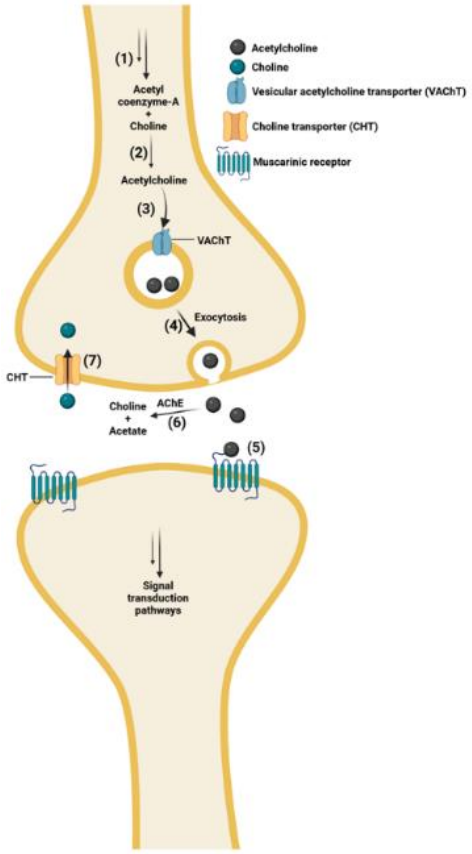

1.1.1.1. **Figure 1. Acetylcholine neurotransmission**. (1) Synthesis and transport of acetyl coenzyme-A via glycolysis. (2) Choline derived from choline transporter (CHT1) combines with acetyl coenzyme-A via choline acetyltransferase (CHAT) to yield acetylcholine. (3) Acetylcholine is stored in vesicles by vesicular acetylcholine transporter (VAChT) and (4) is stimulated to be released into the synaptic cleft via calcium-dependent exocytosis. (5) Synaptic ACh binds post-synaptic muscarinic receptors on neurons or effector organs to stimulate signal transduction pathways. (6) Signal transmission is terminated by the degradation of ACh by synaptic acetylcholine esterase (AChE) into choline and transported back into the presynaptic membrane by CHT1.

Muscarinic ACh receptors are highly expressed in the atrium and conduction system such as the SA node and atrioventricular (AV) node, whereas its expression is observed to be low in the ventricle in comparison.[9,11,14] To date, a large body of literature has reported on reduced ACh secretion as a result of decreased cholinergic activity to be associated with cardiovascular diseases such as hypertension, arrhythmias, myocardial infarctions, and heart failure.[12,22–27] Interestingly, increased ACh secretion as a result of vagal stimulation is observed to have protective features by attenuating positive inotropic responses in the left ventricle, suppressing reactive oxygen species (ROS) injury, preventing ischemia-reperfusion injury, and improving the survival rates in chronic HF animal models.[18,28] The therapeutic benefits of modulating ACh secretion is under investigation for cardiovascular diseases. However, little is known about the regulation of ACh in ventricles due to its extremely sparse cholinergic innervation.[9,18]

1.1.1.2. Non-neuronal cholinergic system (NNCS)

Several studies have been published that provide evidence for the capability of the left ventricle to possess an intrinsic cholinergic system, now termed as the non-neuronal cholinergic system (NNCS).[18,29–31] Initial evidence for the NNCS was determined by the localization of ChAT, CHT1, VAChT, and AChE in isolated primary mouse and rat cardiomyocytes, where contamination from neuronal cholinergic neurons is not observed.[32–34] In addition, the presence of vesicle-like structures was observed to be VAChT positive using immunoreactivity assays, indicating ACh storage and release by intracellular vesicles.[32,34] In addition, the use of ChAT inhibitors such as bromoacetylcholine was observed to reduce ACh secretion in comparison to controls.[33]

These findings precipitated further research into the role of acetylcholine signaling in cardiomyocytes. Recent work suggests a critical role of the NNCS in the maintenance of glucose

and cellular homeosis, and in promoting angiogenesis.[30,32,35] Furthermore, dysfunctional NNCS signaling has been shown to lead to the development of diabetic heart disease.[31] As evidence accumulates towards deciphering the role of aberrant NNCS signaling in disease development, novel therapeutic strategies can be developed for symptom management.

1.1.2. Sympathetic myocardial innervation

Sympathetic neuronal cell bodies originate in the intermediolateral column (lateral horns) of the spinal cord. Presynaptic fibers exit the CNS through anterior roots to the anterior rami of T1-L2 spinal nerves, then onto sympathetic trunks via white rami communicantes.[5,9] Nerve fibers can descend or ascend the sympathetic trunk to the inferior or superior paravertebral ganglion, respectively, pass to adjacent anterior spinal nerve, or cross the trunk and continue through the abdominopelvic splanchnic nerve to reach the prevertebral ganglia.[5] Due to the central location of the sympathetic ganglia, the presynaptic nerve fibers are observed to be shorter than their postsynaptic counterparts.[5,8,9] Cardiac sympathetic preganglionic fibers originate in the brainstem and can be modulated by centers such as the subthalamic and periaqueductal grey, and rostral ventrolateral medulla.[5] The preganglionic fibers exit the spinal cord at T1-T4 and synapse at the left and right stellate ganglia, T2-T4 thoracic, and middle cervical ganglia.[5,9,36] Postganglionic fibers relay from the stellate and upper thoracic sympathetic ganglia to the epicardial vascular structures including the coronary veins and then arteries.[5,9,10,36] These fibers provide input to several ganglionated subplexuses interspersed throughout the ventricles and bilateral atria.[5] Increased density of sympathetic innervation is the myocardium is observed at the sinus node and coronary sinus, with decreasing density from the base of the ventricle to the apex.[4,5] Most post-ganglionic sympathetic nerve fibers synapse directly onto the myocardium.

Terminal release of neurotransmitters occurs from the terminal axons of sympathetic nerves, termed as varicosities or boutons, which form neuroeffector junctions with cardiomyocytes (figure 2).[1,4,37]

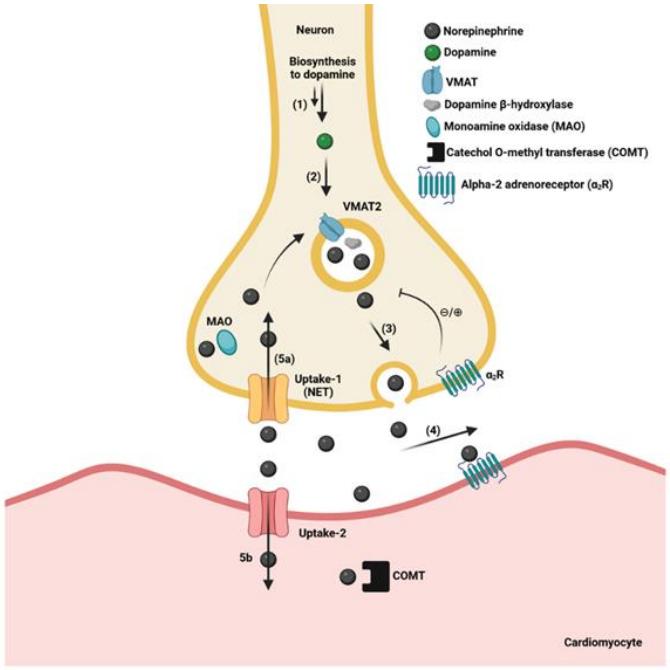

1.1.2.1. Figure 2. Cardiac NE neurotransmission. (1) Biosynthesis of NE begins from L-tyrosine and eventually results in the production of dopamine. (2) Dopamine is transported into the neuronal vesicle by vesicular monoamine transporter 2 (VMAT) and is converted into NE by dopamine β-hydroxylase present in the vesicle. (3) Calcium mediated exocytosis causes release of NE into the synaptic cleft. (4) Binding of NE to postsynaptic alpha and beta receptors induces signal transduction pathways. (5a) NE is transported back into the neuron by norepinephrine transporter (NET) to be recycled and repackaged into vesicles by VMAT or degraded by monoamine oxidase. (5b) NE enters the cardiomyocyte via uptake-2 transport [organic cation transporter 3] and is degraded by catechol-O-methyltransferase (COMT). Presynaptic alpha-2 receptors present on the neuron can induce negative feedback via agonism by excess NE, subsequently resulting in reduced action potential firing rate and diminished active release of neurotransmitters

1.1.3. Adrenoreceptor downstream signaling

NE in the neuroeffector junction predominantly exerts its physiological effects by agonizing post-synaptic α_1 and β_1 receptors to initiate downstream signaling pathways.[49,55] Under physiological conditions, homeostatic mechanisms dictate the degree of activation of each of the receptors.[46] However, during a flight-or-fight response, increased secretion of NE into the synaptic space causes activation above basal levels.[37] The α_1R is coupled to the $G_{q/11}$ family of GPCRs, where agonism results in the dissociation of the α, β, γ subunits and stimulates phospholipase C (PLC) to cleave membrane bound phosphatidylinositol-4,5-biphosphate 2 (PIP2) into inositol 1,4,5-triphosphate (IP3) and 2-diacylglycerol (DAG).[56,57] DAG remains in the plasma membrane, whereas IP3 is released into the cytosol and binds to transmembrane IP3 gated calcium channels in the endoplasmic reticulum (ER).[56,57] Stimulation of this receptor causes release of sequestered calcium into the cytosol, activating protein kinase C (PKC) with the aid of DAG.[56,57] PKC catalyzes the phosphorylation of cellular proteins that mediate the observed biological changes such as increased heart rate, blood pressure, and smooth muscle contractions.[49,56,57] In parallel, activation of β_1 receptors by NE triggers G_s dependent adenylate cyclase activity, increasing the product of secondary messenger cyclic adenosine monophosphate (cAMP).[52] Increased intracellular concentrations of cAMP leads to activation of protein kinase A (PKA) causing a phosphorylation cascade, activating a variety of proteins that increase the rate and force of cardiac contraction.[50,53,58,59] For instance, phosphorylation of L-type calcium channels increases the permeability of calcium entry into cytosol of cardiomyocytes, leading to increased contractility.[60,61]

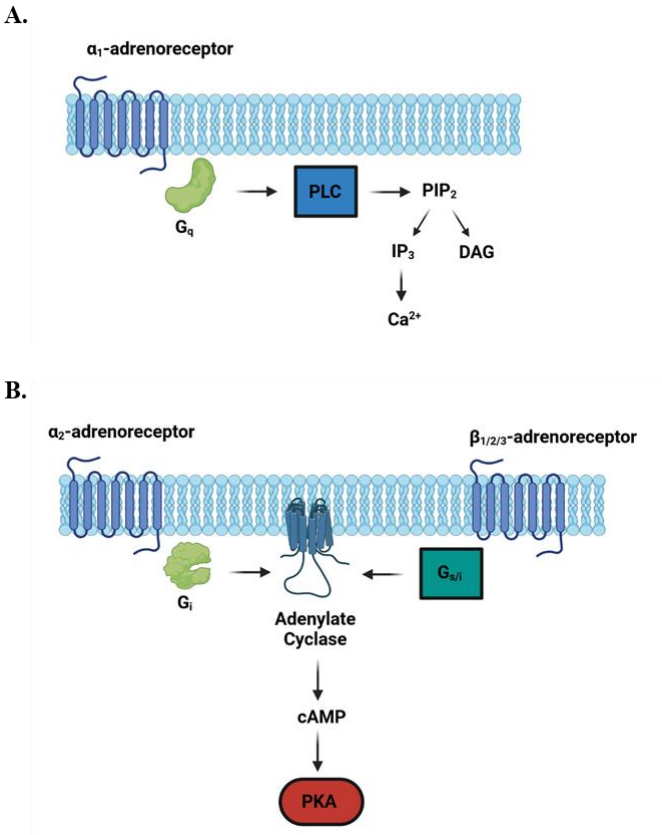

1.1.3.1. Figure 3. Adrenoreceptor downstream signaling mechanism. (A) Catecholamine bound α_1R activates G_q alpha subunit which activates PLC and increases IP3 and intracellular calcium concentrations. (B) Catecholamine bound α_2R are G_i-coupled and inhibit adenylate cyclase (AC) activation. $\beta_{1\text{-}3}$ Adrenergic receptors couple to G_s and activate AC to promote the synthesis of cyclic adenosine monophosphate (cAMP). cAMP activates PKA, regulating the activity of multiple cellular proteins

In addition to activating α_1R, NE can regulate the rate of neurotransmitter release by binding to α_2R, predominantly located on the pre-synaptic nerve terminal to provide negative feedback.[62,63] Agonism of this receptor activates the G_i-coupled GPCR pathway, inducing inhibition of adenylate cyclase and reducing the concentration of intracellular cAMP.[63] As cAMP is inhibited, potassium efflux through activated calcium channels prevents transport of calcium ions into the nerve terminal, reducing the rate at which action potentials are fired.[63] Consequently, the rate of vesicular fusion and release of neurotransmitters into the synapse is diminished and can produce reductions in heart rate, blood pressure, and an attenuated sympathetic stress response.[62,63]

1.1.4. Norepinephrine reuptake

Approximately 90% of the NE released by the presynaptic terminal is transported back into the neuron via NET also called the "uptake-1 transporter".[64] However, a small fraction of synaptic NE is metabolized into noremetanephrine via soluble catecholamine-*O*-methyl transferase (COMT).[45] NET is a member of the superfamily of monoamine transporters composed of twelve transmembrane domains, primarily located on the presynaptic nerve terminal.[65] NET functions to clear and recycle synaptic NE to maintain sympathetic homeostasis. NET is a secondary active transporter, coupling the influx of sodium and chloride ions (Na^+/Cl^-) ions to drive the transport of NE.[65–67] The ion gradient is regenerated by a Na+/K+-ATPase which transports three Na^+ ions out and two K^+ ions into the cell.[65–67] NE present in the axoplasm is subject to two fates: metabolism by monoamine oxidase (MAO), or storage into neuronal vesicles.[45,67,68] MAO is predominantly expressed in the terminal axons where it functions to break down NE into dihydroxphenethyleneglycol, which is eventually metabolized to vanillyl mandelic acid via a series of biochemical transformations.[45,68] As such, inhibition of MAO in the CNS and periphery causes a dose-dependent elevation in NE content.[69] Furthermore, novel MAOA/B knockout mice

have been characterized to have increased levels of NE and other neurotransmitters in the CNS, exemplifying the critical role of MAO in regulating NE content.[70,71] In addition to neuronal reuptake in the cardiac sympathetic nerves, NE can be transported into neighboring cardiomyocytes by the "uptake-2 transporter", identified as the organic cation transporter 3 (OCT3).[72–75] Extraneuronal NE is subsequently metabolized by COMT present in the cardiomyocyte.[76] The relative contribution of uptake-1 vs uptake-2 mediated recycling has been shown to be species dependent. In humans, a small (≤5%) contribution of NE turnover is attributed to extraneural transport in the cardiomyocyte, whereas in rodents extraneural transport has been observed to be the dominant mechanism of catecholamine handling.[77]

1.1.5. SNS dysfunction and HF

HF is defined as the inability of the myocardium to sufficiently supply organs with oxygenated blood.[78] HF generally develops in response to a cardiac injury that causes a decline in pumping capacity (contractile function) of the heart.[78] This condition is marked by the complex interplay between the underlying myocardial dysfunction and compensatory neurohumoral mechanisms that are activated to maintain cardiac output in the face of decompensating function.[78,79] Among these mechanisms are overstimulation of the SNS, cardiac remodelling, and reduced contractility.[78,79] Elevated SNS outflow can be determined by calculating the concentration of plasma NE entering the heart and the amount of NE exiting the heart. Indeed, various processes may contribute to increased spillover such as catechol release, reuptake, and metabolism.[78] Thus, the dynamic nature of correlating plasma NE concentrations to disease progression or survival limits the utility of this measurement to a parameter of SNS activity.[78,80,81] The spillover of NE is typically estimated and used clinically as a measure of sympathetic nerve activity in the heart. Studies conducted in ovine found pacing-induced HF to be associated with

significantly higher total and cardiac NE spillover.[82] Indeed, similar results were obtained in coronary artery ligation models (CAL) of HF in rats, in addition to enhanced renal SNS activity.[83] Consequently, the likelihood that HF can alter sympathetic outflow regionally in the kidney presents the possibility of dysregulated cortical and medullary mechanisms that can impact hemodynamic measurements and alter excretion from blood. In humans and animals with experimentally induced heart failure, decreased tissue NE and NE storage capacity are observed in hypertrophic hearts, whereas turnover is unaltered or moderately higher in pressure overload hypertrophy.[84] Failing hearts are also observed to have reduced expression of tyrosine hydroxylase, consequently limiting NE biosynthesis.[85] In failing hearts of rat models with streptozotocin-induced diabetes mellitus, NE content and turnover are accelerated.[86] In a separate study, rat models of CAL displayed an accelerated rate of disappearance that was attributed to increased NE turnover.[83] In clinical studies, increased NE secretions, decreased efficiency of reuptake, and reduced NE stores due to chronic noradrenergic stimulation all synergistically contribute to increased turnover in humans with congestive HF.[78]

1.1.6. NET in HF

Due to the central role NET has in regulating NE turnover in the CNS and periphery, minor alterations in NET function have significant impacts, especially the cardiovascular system. Given that NET transport is an energy-dependent mechanism, poor tissue oxygenation and substrate supply promote myocardial adrenergic dysfunction.[87] In addition to excess sympathetic drive, NET dysfunction limits the ability of the neurons to maintain neurohumoral homeostasis.[88] Cardiac radiotracers applied in clinical imaging such as [^{123}I]*meta*-iodobenzylguanidine [^{123}I]mIBG, [^{18}F]fluorodopamine, [^{11}C]hydroxyephedrine (HED), and [^{3}H]NE display myocardial adrenergic uptake dependent on NET.[89,90] Reduced tracer accumulation has been noted with these NET

substrates in patients with ischemic cardiomyopathy and congestive HF.[91,92] In patients with ventricular arrhythmias, often a mechanistic precursor to HF, NET gene expression was significantly downregulated in the septal wall of the right ventricular outflow tract.[93–95] Decreased neuronal retention of these radiotracers have been associated with poor prognosis in patients with dilated or hypertrophic cardiomyopathy, as well as ischemic heart disease.[96,97] Increased cardiac NE release in HF is associated with either downregulated NET or decreased NET efficiency.[78,87,98] This was noted in human cardiac tissue samples obtained during transplantation, where NET expression and reuptake were reduced.[87,98,99]

In rabbit models of heart failure, NET downregulation was prevented by adenoviral transfer of NET gene, consequently increasing cardiac NE content, and improving cardiac function.[100] Studies in Wistar rats induced with HF by supracoronary aortic banding (AB) resulted in biventricular myocardial hypertrophy and overt heart failure with elevated left ventricular end diastolic pressure and pulmonary congestion.[80] Moreover, NET density following myocardial hypertrophy was not observed to be reduced, likely due to a proportional increase in neuronal growth to cardiac mass in AB rats.[80] However, reduced NET density per neuron was observed as a primary contributor for adrenergic dysfunction.[80]

1.1.7. β-blockers for HF therapy

Left ventricular systolic dysfunction such as decreased ejection fraction is a mechanical defect that manifests hemodynamic and physiologic aberrations such as poor cardiac output to tissues, increased pulmonary capillary wedge pressure, and reduced exercise tolerance.[87,101,102] Elevated plasma neurohormones result in fibrosis, necrosis, and apoptosis within the myocardium.[87,101,102] Consequently, progression of HF can be halted by blocking the overactivated

postsynaptic receptors of NE on myocytes. Clinical trials have provided adequate evidence for the role of beta-blocking (β_1, primarily located on myocytes) agents to reduce the ability of NE to stimulate beta receptors on the myocyte and slow disease progression.[103,104] As a result, negative chronotropic, inotropic and lusitropic agents have been studied extensively in clinical trials and remain the first line of therapy in controlling HF. Molecular changes in the density of β_1 receptors are noted due to chronic stimulation, producing blunted responses that reduce the efficiency of downstream signaling pathways due to a shift in G_i protein subtype expression (figure 4).[105–108]

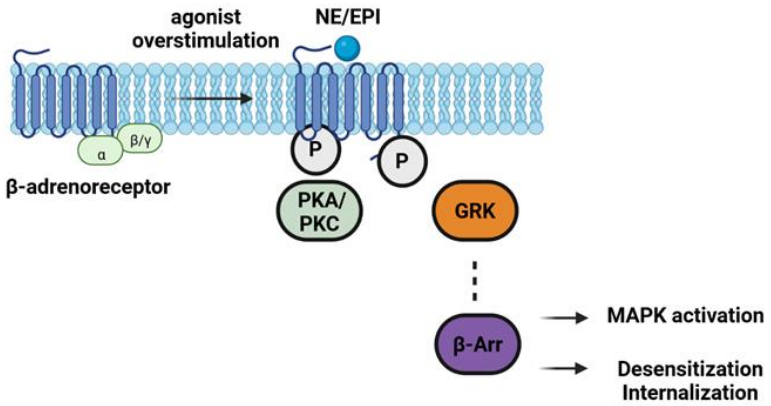

1.1.7.1. Figure 4. Regulation of β-adrenoreceptors. Overactivation of β-adrenoreceptors results in their phosphorylation by PKA/PKC and GRK leading to β-arrestin recruitment. B-Arrestin prevents activation of G proteins and promotes desensitization and internalization of β-adrenoreceptors.

Rapid uncoupling of the receptors from the membrane is observed due to PKA mediated phosphorylation of β_1 receptors (absence of agonist) as well as G-protein receptor kinases (GRK, agonist occupied).[105,109] Phosphorylated β_1 receptor interactions with cytosolic β-arrestin inhibits G_s stimulatory pathways and facilitates internalization via a clathrin-mediated endocytic pathway.[109] Resensitization of β_1-AR remains a possibility, with evidence of receptor

dephosphorylation in endosomal vesicles following beta-blocker therapy.[109] In the absence of therapeutics, degradation of β_1-AR and decreased β_1 mRNA expression is evident and has been observed in left ventricle samples of patients with end-stage HF.[87,105] Reduced expression is hypothesized to be an adaptive mechanism to protect the myocardium from further insult.

1.1.8. Animal models for HF

Given the high mortality rate (50% within 5 years of initial diagnosis) and increasing prevalence of HF, increasing research output has become critical in understanding HF and its underlying mechanisms to develop novel therapeutic strategies.[110] HF is categorized as either HF with preserved ejection fraction (HFpEF, LVEF ≥ 50%), HF with reduced ejection fraction (HFrEF, LVEF <40%), or HF with mid-range ejection fraction (HFmrEF, LVEF 40-49%).[111–113,113–115] Approximately fifty percent of patients are diagnosed with HFpEF with impaired cardiac contractility and compliance.[114] In comparison, HFrEF is commonly associated with a reduction in cardiomyocytes due to myocardial insult (such as MI) with increased myocardial wall stress.[111,112] It was previously advocated that HFpEF is due to diastolic dysfunction (reduced chamber capacity in the absence of systolic dysfunction) and was once termed “diastolic heart failure (DHF)”.[116] However, newer research has identified HFpEF can also occur in the absence of diastolic dysfunction.[116] In the setting of idiopathic hypertrophic cardiomyopathy and infiltrative cardiac diseases, diastolic dysfunction however does result in HFpEF.[117]

The high degree of homology with the human genome has prompted the use of mice and rats to study HF.[118,119] In addition to their low breeding cost and housing, researchers can utilize genetic modifications, and pharmacological and surgical models to induce symptoms. One disadvantage of this is the multifactorial pathogenesis of HFpEF and HFrEF in humans which can

instigate disease development. Therefore, close attention must be paid to the model of HF chosen and the broad applicability of the experimental findings. Regardless, rodent HF models provide the opportunity to investigate specific risk factors without confounding comorbidities. Numerous surgical methods exist to induce pressure overload in rats. The most common method to accomplish this is aortic banding, in which a stricture is fixed around the ascending aorta of 3–4-week-old rats.[118,119] As the rats mature, aortic outflow is increasingly constricted, and hypertension gradually manifests.[118,119] Researchers that developed this surgical model showed evidence of LV compensatory hypertrophy and increased left atrial pressure via doppler echocardiography after 8 weeks post-banding.[118,119] At 18 weeks, tachypnea, edema, pleural effusion, and ascites were evident and are associated with systolic dysfunction and LV dilation.[118,119] Advantages of this model include gradual onset of HF and progression from compensated hypertrophy to decompensated HF, providing a clinically accurate time-course in the development of HF.[118,119]

Genetic models for inducing hypertension and HF have also been used extensively by researchers. Notably, Dahl salt-sensitive (DSS) rats have been used in research for over 50 years. Genetic analysis of rat crosses has overcome challenges faced in human studies such as complex genetic traits influenced by several genes, moderate gene penetrance, environmental factors, and genetic heterogeneity (different alleles within the same genes, or different gene combinations resulting in the same phenotype). Hereditary hypertension in rats is due to naturally occurring allele variants captured during the selection and inbreeding process.[120] Using inbred rats diminishes the problem of heterogeneity and may identify disease genes in humans given the 90% sequence similarity to the human genome.[119,120] Using an inbred cross of DSS rats and Brown Norway rats, cosegregation analysis was performed using an F2 intercross.[121] A genome wide scan

for 265 polymorphic simple sequence length polymorphism (SSLP) markers for 247 traits identified seven arterial pressure phenotypes mapped to the same region of chromosome 18 in the rat.[121] Notably, the salt sensitivity trait was influenced by the presence of SS alleles in a specific locus of chromosome 18.[121] Consequently, rats homozygous for SS/SS displayed significantly greater reductions in mean arterial pressure after sodium depletion in comparison to homozygous BN/BN or heterozygous rats.[121] This region of chromosome 18 in rats corresponds to the long arm of human chromosome 5 and a region of human chromosome 18 linked to hypertension in humans.[121] DSS rats gradually develop hypertension leading to progressive hypertrophy and HF.

DSS Rats fed high salt (HS) diet for 12 weeks are characterized to have normal ejection fraction, with reductions in end diastolic volume (EDV) and an upward shift of the end-diastolic pressure-volume relationship (EDVPR).[122] These early physiological alterations are passive indications of diastolic dysfunction.[122] At 16 weeks, LV hypertrophy continually develops. However, dilation of the heart results in an indistinguishable EDPVR in comparison to age matched controls.[122] As the rats continue on diet, ejection fraction (EF) and stroke volume (SV) are reduced, and end diastolic pressure (EDP) and wet lung weight increase, and aberrations in diastolic filling are identified by Doppler echocardiography.[122] HF (fluid accumulation, high filling pressure, reduced SV) becomes increasingly more severe in the absence of diastolic dysfunction.[122] Initially, systolic and diastolic properties yield upward shifts at 12 weeks in rats. By 20 weeks, the ESPVRs, EDPVRs, and pump function curves of high salt fed and control animals are nearly identical.[122] As such, researchers propose the development of HF as a result of fluid accumulation. As such, this genetic model of HF displays HF in the absence of late stage diastolic, systolic and pump dysfunction, but parallels deterioration of renal function.[118,119,122] The researchers note the careful distinction of pump dysfunction and myocardial dysfunction, as myocardial and muscle

cells isolated from DSS rats show abnormal contractile forces, endocardial shortening, and midwall shortening fraction by 30% at 20 weeks on HS diet.[122] However, due to insignificant changes in the myocardial stiffness constant, pump function was conserved.

1.1.9. Current methods of diagnosis & disease management

The New York Heart Association (NHYA) provides functional classification definitions for the four stages of heart failure.[123] In each stage, the limitations to physical activity, patient comfort, and symptoms after exercise gradually worsen, with class IV HF patients being uncomfortable at rest, and unable to perform physical activity without symptoms.[123] The American College of Cardiology/American Heart Association (ACC/AHA) classification attempts to capture the evolution and progression of HF within four stages (A-D).[124] In stage A, patients are classified to be at high risk of heart failure with no structural heart disease or symptoms of HF.[124] In stage B, structural heart disease is present in the absence of symptoms.[124] Whereas in stage C symptoms are present.[124] Stage D HF is defined as refractory HF requiring special interventions.[124] Patients with HF often present with shortness of breath, fatigue and weakness, edema, and abdominal distention.[125] Unfortunately, due to compensatory mechanisms, the early stages of HF lack specific signs of disease.[125] Whereas late-stage HF patients demonstrate significant tachycardia, pedal edema, increased jugular venous pressure, including other signs and symptoms.[125]

Diagnosis is performed by investigating a variety of parameters including complete blood count, uranalysis, metabolic profile, blood urea nitrogen, lipid profile, among others.[125] HF-specific laboratory tests (patients at risk for HF) include brain natriuretic peptide (BNP), displaying 90% sensitivity and 73% specificity.[126] In addition, N-terminal proBNP (NT-proBNP) has showed 99% sensitivity and 85% specificity and is recommended in outpatient and hospital settings.[127–129] The

neuro-hormone BNP is an activated form of proBNP, stored in secretory vesicles in both ventricles and to a lesser extent in the atria.[129] In response to pressure overload and volume expansion, proBNP is secreted and cleaved into NT-proBNP and BNP.[127,129] Both peptide fragments are diagnostic and prognostic markers in HF management, with patients presenting with acute dyspnea having <100 pg/mL having a 90% negative predictive value, whereas values greater than 500 pg/mL have 81% positive predictive value.[126] Furthermore, BNP concentrations are strong predictors of cardiovascular events and risk of death for individuals previously diagnosed with HF or cardiac dysfunction.[126] However, elevated BNP is also associated with pulmonary embolism, renal failure, pulmonary hypertension, and chronic hypoxia.[126,127] No significant difference has been noted between BNP and NT-proBNP in terms of diagnostic and prognostic value and cut off values have been established in clinical settings to aid in risk stratification for HF patients.[126,127,129] Atrial natriuretic peptide (ANP), produced by muscle cells in the atrial wall as a result of stretch has also been assessed, although its predictive value has not shown to be significantly higher than BNP.[126,127,130]

1.1.9.1. Table 1. Biomarkers in Heart failure

Class	Biomarker
Myocardial Injury	Troponin, creatine kinase, H-type fatty acid binding protein
Renal injury	Creatinine, cystatin C, electrolytes, neutrophil gelatinase associated lipocalin
Fibrosis, matrix remodeling	Suppression of tumourigenicity-2, Galectin 2, matrix metalloproteinase
Inflammation	High sensitivity C-reactive protein, interleukin-6, tumor necrosis factor-α, procalcitonin
Chamber dilation/myocardial stretch	B-type natriuretic peptide, proBNP, atrial natriuretic peptide
Neuroendocrine	Mid-regional pro adrenomedullin, copeptin, endothelin 1
Oxidative stress	Uric acid, myeloperoxidase

Multiple other biomarkers have been classified in the research setting, but none have shown enough utility to be introduced into the clinical practice (**Table 1**).[127,130] Diagnostic imaging tests are also routinely performed in the clinic for HF patients including chest X-ray and transthoracic echocardiography. Chest x-rays are used to determine heart size, pulmonary congestion, and other cardiopulmonary diseases which may contribute to patients' symptoms.[131] 2D echocardiography with Doppler is the recommended evaluation for patients suspected to have HF to assess ventricular function and size, wall thickness, wall motion, and valve function.[132] Transthoracic echo also provides measurements of ejection fraction, critical for establishing diagnosis and subsequent patient management.[132]

Indeed, there is a growing need for a reliable method to assess disease severity especially in the early stages of HF. This can be exemplified in the population of HF individuals that present with chronic obstructive airway disease (30%), where diagnosis can be difficult and nonspecific.[133] The Breathing Not Properly trial reported clinical confusion among patients presenting breathlessness in emergency.[133] While echocardiography detects aberrant LV function, breathlessness is shown to be asymptomatic in 50% of cases.[133] In addition to diagnosis, current clinical methods are inadequate for monitoring patients receiving treatment for HF. Since physiological changes in the absence of symptomatic presentation often precede clinical deterioration, invasive monitoring via pacemaker devices can be used.[134] Thus, a growing need for non-invasive methods of monitoring disease progression are needed.

1.2. Positron Emission Tomography (PET)

PET is a noninvasive molecular imaging technology capable of static or dynamic imaging protocols. Dynamic imaging provides visualization of the distribution of a radiolabeled biological ligand over the duration of the scan within the body.[135,136] Radiolabeled isotopes are produced using a medical cyclotron, accelerating a positively charged hydrogen nucleus (proton) by magnetic centripetal acceleration and bombarding a target material.[137,138] For instance, fluorine-18 is produced by irradiating heavy oxygen-18 enriched water ($[^{18}O]H_2O$) with protons.[139] The resulting nuclear $^{18}O(p,n)^{18}F$ reaction substitutes a proton for a neutron and generates the positron emitting isotope fluorine-18.[139] This radioisotope is then incorporated into a molecule of interest (ligand, protein, antibody, etc) and subsequently purified to yield a radiotracer.

Radiotracers injected into live animals or humans enable molecular imaging due to the radioactive isotope undergoing β-decay to release a positron, a positively charged subatomic particle with the same mass as an electron.[136,138] The positron annihilates with an electron from ionized tissue and generates two approximately antiparallel (~180°) gamma photons of 511 keV.[138] The imaging subject is placed in a PET camera comprised of a ring of detectors with the capability to detect coincident photons.[138] With the use of automated iterative and non-interactive reconstruction algorithms, a map of radioactivity distribution is generated within the field of view over time producing a dynamic image, allowing quantitative extrapolation of tissue activity data from the subject.[138] The development of this technology has instigated preclinical studies on a variety of organisms most typically rodents, rabbits, and nonhuman primates. Continual improvements in camera and detection technology in addition to the ability of multimodal imaging using CT and MR has enabled quantification of anatomically small structures (<1 mm).[140] Furthermore, PET imaging can be used to perform serial noninvasive measurements in the preclinical and clinical settings and is commonly used to evaluate novel tracers in healthy and transgenic mice/rats. Indeed, cardiac PET has a profound application in the clinic and is utilized on a routine basis.[135]

1.2.1. Metabolic imaging

Cardiac metabolism is defined as the supply of substrate, utilization, downstream oxidative phosphorylation (oxphos), and production of high energy molecules such as adenosine triphosphate (ATP).[141] In the healthy myocardium, ATP production is achieved in a 3:1 ratio by β-oxidation of fatty acids (FA) and oxphos.[141,142] ATP is transferred in the creatine kinase (CK) energy shuttle for ATP utilization in the heart.[141,142] The wavering aerobic demands are met by changes in myocardial perfusion to maintain homeostasis.[143] In disease states, myocardial

metabolism can often be altered. For example, the failing heart is observed to have changes in FA and glucose metabolism that is dependent on the stage of HF, animal species, and type of HF.[141,142] However, in general a downregulation of myocardial FA oxidation and accelerated glucose oxidation is typically observed.[141,142] The most widely used PET imaging tracer is 2-deoxy-2-[^{18}F]fluoro-D-glucose ([^{18}F]FDG), which displays excellent retention in organs with high metabolic demand, such as the myocardium.[144] The uptake mechanism into the myocardium is irreversible, as [^{18}F]FDG becomes trapped within tissues via phosphorylation to yield [^{18}F]FDG-6-phosphate and cannot be metabolized further.[144] The irreversible accumulation of the tracer can be quantified at a given timepoint and provide insight of myocardial metabolic flux and correlate with glucose metabolism in healthy and diseased hearts.[145]

1.2.2. Perfusion imaging

Myocardial blood flow of patients is frequently evaluated in cardiac PET centers. Radiotracers used for imaging perfusion such as ^{82}Rb or ammonia ([^{13}N]NH_3) identify regional defects in blood flow at rest or under stress, indicative of ischemic or scarred tissue.[146] The uptake rate into the LV can be quantified by flow imaging. However, high positron energy (particularly for ^{82}Rb) and low acquisition times can limit the use of these two tracers in small animals due to blurring.[146]

1.2.3. PNS Imaging

PET imaging of the PNS has been a topic of research for decades. Indeed, radioligands that bind muscarinic receptors such as [^{11}C]methquinuclidnyl benzilate ([^{11}C]MQNB, muscarinic) have been studied, but none have achieved clinical validation to image the myocardial PNS.[147,148] Efforts to synthesize radiolabeled AChE inhibitors such as [^{11}C]donepezil have been a topic of

interest mainly in the area of CNS imaging, with limited evaluation of myocardial uptake.[149–151] One radiotracer that has demonstrated reliability for imaging cholinergic synapses is the VAChT substrate [^{18}F]fluoroethoxybenzovesamicol ([^{18}F]FEOBV). This radiotracer was first evaluated in 1998 by Mulholland et al, and found to have high brain extraction, favorable metabolism, and a good localization pattern of AChE in the brain.[152] Currently, [^{18}F]FEOBV is under clinical investigation as a diagnostic tool to determine the severity of neurodegenerative diseases such as Alzheimer's disease and Parkinson's disease.[153,154]

[^{18}F]FEOBV myocardial uptake was first evaluated in the early 1990s by Degrado et al.[155] Isolated rat hearts were used to determine the extent of specific binding. Degrado noted high [^{18}F]FEOBV uptake as an index of high lipophilicity rather than receptor-mediated binding.[155] Furthermore, extensive clearance in the washout phase (90%+) is indicative of the tracer being freely diffusible.[155] This hypothesis was further tested by blocking the VAChT receptor with (-)-vesamicol prior to injecting [^{18}F]FEOBV. Pharmacological challenge yielded similar peak uptake of the tracer in the myocardium, but faster tracer washout. Increased washout is indicative of clearance of the tracer from nonspecific targets to specific targets during this phase. The authors surmised [^{18}F]FEOBV myocardial uptake is due to nonspecific binding and myocardial perfusion, providing inadequate contrast of innervated tissues and thus not a suitable molecular imaging agent for the myocardial PNS. These findings deterred any future research for the application of [^{18}F]FEOBV in myocardial PNS imaging.

Recently, evaluation of [^{18}F]FEOBV in the myocardium of four healthy participants noted high uptake of the radiotracer in the LV within 4-5 minutes followed by slow monophasic washout.[156] The distribution volume (DV) was observed to be similar using Logan graphical analysis and tissue compartmental models (1-TCM, 2-TCM). The authors noted favorable uptake

and washout properties of the radiotracer in the myocardium, which may be attributed to non-neuronal cholinergic handling in humans. Unfortunately, due to the toxicity of vesamicol and its derivatives (FEOBV) blocking studies were not performed. Whole body PET imaging with [^{18}F]FEOBV in humans was also performed in a separate study and noted significantly higher uptake in older individuals when using similar methods of quantification with uptake parameters such as SUV or volume of distribution (V_d).[157] The authors note a negative correlation between age and the rate parameter k_2, which describes the rate of [^{18}F]FEOBV being transported from the myocardium back to the blood, indicative of a higher specific binding fraction in older individuals.[157]

1.2.4. Neurohormonal Imaging

The development of radiotracers for cardiac SNS imaging is a competitive field with emphasis placed on designing radioligands that mimic endogenous NE uptake and release pathways, targeting NET/uptake-1.[158] These ligands have quantifiable parameters such as tracer retention, used as a proxy for cardiac sympathetic innervation and NET expression, whereas washout is reflective of sympathetic tone.[91,92,159] Given the unique role of β-AR in sympathetic tone, radiolabeled ligands have been developed to noninvasively assess β-AR density during disease.[160] Initial efforts geared towards isotopic labeling of β-blockers using carbon-11 yielded variable results due to subpar lipophilicity and binding affinity.[160] The most recognized radioligand for assessing cardiac β-AR density is [^{11}C](*S*)-CGP12177. Myocardial uptake has been shown to be specific via pretreatment with selective β-AR ligands, and treatment with isoproterenol over a two-week period reduced ^{3}H-CGP12177 uptake in *ex vivo* biodistribution experiments, indicative of reduced uptake following overstimulation of the receptor (internalization).[161,162] Furthermore, PET imaging in human subjects provided high contrast

imaging of the myocardium with minimal metabolism.[163,164] Determination of β-AR density (B_{max}, pmol/g) was performed by graphical analysis and requires two injections of [^{11}C](*S*)-CGP12177, one with high molar activity (>1 Ci/μmol) followed by low molar activity.[164] In patients with scar tissue following MI, myocardial β-AR density was reduced and correlated with LV dilation.[164] Researchers measured β-AR density early after MI and found significantly reduced density (1 pmol/g) in association with a three-fold increased risk of developing congestive HF in patients.[164]

1.3. Radiotracers targeting myocardial presynaptic nerves

Radiotracers targeting presynaptic neurons are developed with the intent to mimic the kinetics of endogenous neurotransmitters. The first use of the radiolabeled catecholamine analogue [^{123}I]mIBG was first reported almost 40 years ago and has since then found good clinical utility using lower resolution planar scintigraphy and single photon emission tomography (SPECT) imaging.[165] In PET, the predominant tracers are [^{11}C]HED and [^{18}F]LMI1195/[^{18}F]FBBG, the latter of which has shown favorable utility due to the longer half-life of fluorine-18.[91] Of note, the radiofluorinated phenethylguanidine tracers 4-[^{18}F]fluoro-*m*-hydroxyphenethylguanidine ([^{18}F]4F-MHPG) and 3-[^{18}F]fluoro-*p*-hydroxyphenethylguanidine ([^{18}F]3F-PHPG) have shown unique myocardial kinetics in NHPs and are currently being evaluated in clinical trials.[166,167]

1.3.1. [^{123}I]mIBG

Planar scintigraphy was a dominant form of nuclear imaging prior to the advent of PET. However, due to increasing costs, scarce supply of radiolabeled iodine, the use of this imaging modality is losing pace. [^{123}I]mIBG, initially synthesized for imaging presynaptic neurons in adrenal glands, has found profound applications in the field of cardiac imaging, in addition to imaging pheochromocytomas and neuroblastomas.[165] As a NE analogue, [^{123}I]mIBG is a substrate

for NET and is readily packaged into vesicles within the nerve terminal by VMAT2.[90] Gradually, [^{123}I]mIBG exhibits washout from the myocardium which is hypothesized to reflect sympathetic tone/rate of release from the presynaptic neuron.[159,168,169] [^{123}I]mIBG is semi-quantified by calculating the heart-to-mediastinum ratio (H/M), providing a reproducible method of gauging cardiac sympathetic activity.[165,170] Using two imaging acquisitions, early and late retention of the tracer can provide a washout rate (WR), reflecting the turnover of catecholamines and sympathetic tone.[170] WR is increased in patients with HF and correlated to an increase in cardiac death or hospital admission.[165,168,170,171]

One of the pivotal studies in the field of cardiac molecular imaging was the AdreView Myocardial Imaging for Risk Evaluation in Heart Failure (ADMIRE-HF) clinical trial, using [^{123}I]mIBG. This imaging agent was evaluated to predict the prognosis of significant cardiac events by assessing the H/M ratio for patients with HF and significant left ventricular dysfunction.[172] A significant relationship between HF-related events and reduced H/M ratio was observed independent of factors such as left ventricular ejection fraction (LVEF), BNP, and demographic parameters.[172] Preserved neuronal uptake of [^{123}I]mIBG identified a low-risk HF population with a late H/M ≥1.60 (21% of trial subjects) associated with <1%/year incidence of cardiac death. In contrast, 10% of the subjects, characterized by H/M <1.20, had a ten-fold higher annual rate of cardiac mortality (9.6%).[172] Thus, [^{123}I]mIBG nuclear imaging discriminated populations of HF patients at risk for near-term mortality from those at low risk at the current level of therapy. Overall, [^{123}I]mIBG has shown a unique application in determining cardiac sympathetic function, and has the potential to improve treatment management for HF patients. Mechanistic studies in human population are ongoing with this radioligand to determine [^{123}I]mIBG scintigraphy's correlation with myocardial remodeling and cardiopulmonary exercise, diagnosis and symptom

severity of Parkinson's Disease (PD), and autonomic dysfunction in type 2 diabetes mellitus.[169,173,174]

1.3.2. [^{11}C]HED

Advancements in the field of molecular imaging have led to the production of cardiac neuronal imaging agents that provide higher resolution and are more easily quantifiable using PET. Fluorine-18 and carbon-11 are the most common PET radionuclides due to a highly selective decay process with ≥ 97% positron (β+) emissions.[175] The attractive features of fluorine-18 over other PET radionuclides include its longer half-life ($t_{1/2}$ =109.77 min), enabling radiotracer transport in addition to longer PET acquisition times and same-day multi-patient imaging. In contrast, carbon-11 is prized for isotopic labelling of relevant biomolecules, thereby conserving the biochemical properties of the native ligand.

The most widely studied SNS tracer for PET is [^{11}C]HED, a derivative of sympathomimetic amine metaraminol (MR, 1R,2S).[176] MR is structurally similar to NE but lacks catechol functionality to restrict tracer metabolism by MAO.[176,177] [^{11}C]HED has high binding affinity for myocardial NET (K_i = 20.9 nM), and has shown utility for predicting lethal arrhythmias, sudden cardiac death, and all-cause mortality in heart failure patients with reduced ejection fraction.[177] Furthermore, [^{11}C]HED PET imaging studies have elucidated the relationship between impaired SNS innervation and severity of diastolic dysfunction in HF patients.[178,179] The Prediction of Arrhythmic Events with Positron Emission Tomography (PAREPET) study tested the application of [^{11}C]HED in identifying patients at high risk for sudden cardiac arrest (SCA) who benefit from an implantable cardiac defibrillator (ICD) by quantifying inhomogeneities in LV retention.[180] Data collected from 204 individuals determined [^{11}C]HED PET in predicting cause-

specific mortality from SCA independently from LVEF and infarct size.[180] The PARAPET II trial is currently ongoing with further applications towards selecting patients suitable for ICD.

1.3.3. [^{18}F]FBBG/[^{18}F]LMI1195

To date, the most successful radiofluorinated PET analogue of [^{123}I]mIBG is N-3[3-bromo-4-(3-^{18}F-fluoro-propoxy)-benzyl]-guanidine ([^{18}F]LMI1195/flubrobenguane), a benzylguanidine class of radiotracers for presynaptic nerve imaging. [^{18}F]Flubrobenguane displays excellent contrast of the myocardium and desipramine (selective NET inhibition) sensitivity in both rabbits and NHP, with a favorable heart-to-liver ratio in comparison to [^{123}I]mIBG.[90,181–183] Indeed, the phase I first-in-human multicenter trial for flubrobenguane displayed rapid cardiac extraction and excellent contrast of the myocardium.[184] Research conducted at the University of Ottawa Heart Institute compared the regional distribution of [^{11}C]HED and [^{18}F]flubrobenguane for imaging sympathetic innervation.[91] Dynamic PET was performed on patients with and without ischemic cardiomyopathy, and regional denervation, distribution volume and retention index were used to quantify presynaptic sympathetic innervation.[91] The results of the study yielded equivocal distributions in both patient cohorts. Thus far, [^{18}F]flubrobenguane is a promising radiofluorinated candidate for presynaptic imaging and necessitates further clinical studies to enable its widescale distribution.

1.3.4. [^{18}F]Phenethylguanidines (PHEG)

The third class of NE mimics for presynaptic imaging include phenethylguanidine (PHEG) radiotracers [^{18}F]4F-MHPG and [^{18}F]3F-PHPG, developed in Michigan. Preclinical studies in NHPs showed NET-dependent uptake for both radiotracers, with excellent contrast of the myocardium.[166,167,185] Both tracers exhibited poor metabolic stability 10 minutes after intravenous

injection (<25% parent intact).[167] The advantages of PHEGs however arise from their slower neuronal uptake rates, where uptake of the tracer by NET becomes the rate determining step, and is likely to aid in the sensitivity of detecting small changes in NET expression or neuronal density. Human studies conducted with both tracers yielded marginally better metabolism (~25% parent intact) at 10 minutes.[186] Patlak graphical analysis performed to quantify presynaptic nerve density yielded similar results for both tracers. Faster clearance from the liver was observed from [^{18}F]4F-MHPG, improving image interpretation and reducing spillover into the LV.[186] Conversely, [^{18}F]3F-PHPG displayed prolonged accumulation into presynaptic neurons and might be more accurate in detecting changes in neuronal density.[186]

1.3.5. Pharmacological characterization of SNS radiotracers

Most mechanistic studies performed with [^{123}I]mIBG are restricted to cell lines, tumor studies, and canines. Within the last 20 years, presynaptic tracer evaluations have predominated in rodents such as rats. As a result, significant differences in species-dependent myocardial uptake mechanisms are observed.[77] Tracer kinetics and tissue distribution vary among the classes of currently available PET radiotracers, and pre-clinical studies help to determine which tracers are best suited for clinical translation.

The evaluation [^{11}C]HED in SD rats showed strong baseline myocardial uptake, and preferential retention in organs with rich adrenergic innervation.[187] Organs such as the heart, spleen, and adrenals showed tracer retention values of 3.46, 1.42, and 1.30 %ID/g (percent injected dose per g), respectively at five minutes.[187] After thirty minutes, the myocardial activity reduced to 2.69 %ID/g, with heart to blood (H/B) ratios of 26 and 35 at 5- and 30-minutes post injection (p.i.), respectively.[187] Mechanistic studies were performed to assess tracer localization using the

selective and potent NET inhibitor desipramine (DMI, 10 mg/kg, intraperitoneal [i.p]), which displayed a 92% reduction of tracer uptake in the ventricles, suggesting high neuronal occupancy of [^{11}C]HED.[187] In contrast, DMI pre-treatment was not found to have a significant reduction in myocardial tracer retention for [^{123}I]mIBG, whereas pretreatment with the nonselective NET and extraneural uptake inhibitor phenoxybenzamine (PBZ, 50 mg/kg, iv, uptake-1 and uptake-2 inhibitor) reduced myocardial uptake by 90%.[188] These results provide strong evidence that [^{123}I]mIBG myocardial uptake is solely dependent on extraneuronal uptake-2 mediated transport in SD rats, whereas [^{11}C]HED accumulates within myocardial neurons and is NET dependent.

Rischpler et al. further investigated this phenomenon in rats with chronic infarction by transient coronary occlusion and reperfusion (CI) and healthy controls, followed by injection of [^{11}C]HED and [$^{123/131}$I]mIBG.[188] An autoradiography study revealed the local distribution pattern of [^{11}C]HED to have a decreasing gradient from the subepicardium (SEC) to the subendocardium (SENC) in healthy rat hearts.[188] This transmural pattern of sympathetic nerve distribution has been previously reported in mouse hearts and was assessed by tyrosine hydroxylase (TH) immunofluorescence, revealing a similar gradient of innervation (1:0.29, ratio of nerve density between SEC and SENC).[189] It was concluded that the tracer distribution pattern may reflect physiological sympathetic innervation in rat hearts. In contrast, autoradiography studies with [^{131}I]mIBG showed an even distribution of radioactivity in the myocardium, consistent with non-neural uptake-2 mediated tracer accumulation.[188] Radiotracer distribution and kinetics vary in rats in comparison to rabbits and higher species, and has been attributed to a higher contribution of catecholamine handling by uptake-2 mediated transport, rendering NET blockade by DMI less significant.[77,90] Consequently, SNS tracer distribution studies are often advanced to higher species

such as rabbits and non-human primates, where catecholamine handling occurs predominantly by NET, similar to humans.

Mechanistically, both [^{11}C]HED and [^{18}F]FBBG are localized in the neurons of higher species, however, the former displays *apparent* irreversibility by NET (fast transport in and out of the neuron), whereas the latter is shown to accumulate irreversibly in neuronal storage vesicles (figure 5).[90,190] This was exemplified in rabbits using DMI "chase" dosing, where DMI is administered following peak radiotracer uptake.[90] While both [^{18}F]FBBG and [^{11}C]HED are sensitive to DMI pre-treatment in rabbits, chase dosing was observed to have no effect on the myocardial retention of [^{18}F]FBBG, but markedly reduced the uptake of [^{11}C]HED.

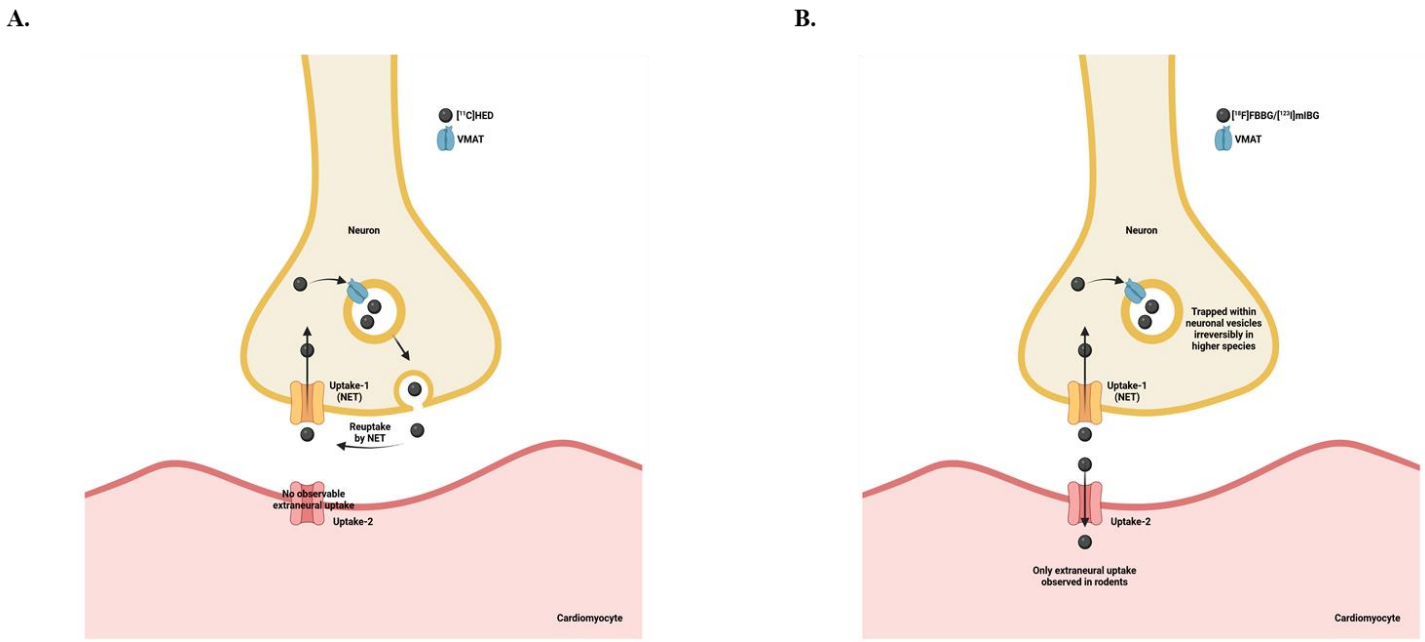

1.3.5.1. Figure 5. Myocardial kinetics of [^{11}C]HED, [^{18}F]FBBG, and [^{123}I]mIBG. (A) [^{11}C]HED is transported by NET into the presynaptic neuron and contains VMAT2 affinity resulting in translocation within neuronal storage vesicles. Exocytosis results in release of [^{11}C]HED into the synaptic cleft, followed by reuptake by NET back into the presynaptic neuron. (B) Benzylguanidines [^{18}F]FBBG and [^{123}I]mIBG are transported into the presynaptic neuron by NET and retained in storage vesicles where they remain irreversibly trapped.

Using comparable assay methodology for human and rat left ventricle samples, the measured NET B_{max} values in the human heart are ~15 times higher than in rat hearts.[191] Indeed, each ligand possesses a unique combination of transport parameters that may be advantageous or limit accurate quantification.[77,90] For [^{11}C]HED, rapid NET transport compared to the rate of clearance back into the plasma may lead to neuronal uptake of this tracer being rate limited by

delivery from the plasma into the insterstitium rather than by NET transport. For [^{18}F]FBBG, rapid uptake may also be influenced by perfusion rather than NET transport. However, [^{18}F]FBBG does not undergo continuous recycling and remains trapped within the presynaptic neuron, and thus may be advantageous in identifying dysfunctional vesicular storage mechanisms in addition to reduced NET density.

1.4. [^{18}F]mFBG

1.4.1. Chemistry

Historically, the radiosynthesis of [^{18}F]mFBG has posed challenges to its routine development. The tracer was initially synthesized using fluoro-for-nitro exchange reactions with 3-nitrobenzonitrile, obtained in 16 ± 4% RCY.[192] Similar yields were reported using a quaternary ammonium perchlorate exchange reaction with *meta*-nitro aryltrimethylammonium perchlorate as a precursor.[193] Challenges in the purification of volatile radiofluorinated intermediates using these methods yielded losses in radioactivity and were abandoned. Shortly thereafter, multistep synthesis from benzonitrile precursors was attempted, requiring the use of lithium aluminium hydride reduction, consequently hindering radiotracer automation.[192] The most successful synthesis reported the use of a protected diaryliodonium salt precursor, achieving high yields (31%) and molar activity (> 1 Ci/μmol) in two steps.[194] However, multi-step precursor synthesis including challenging purification and poor solubility of the diaryliodonium salt were notable drawbacks of this method. Furthermore, the purification of [^{18}F]mFBG was limited to the use of biocompatible HPLC eluent, resulting in dilute formulations, consequently hindering the ability for its widespread distribution for multi-center imaging. With the advent of spirocyclic iodonium ylide (SCIDY) radiofluorination technology, many of the mentioned limitations have been overcome.[195,196] The SCIDY precursor for [^{18}F]mFBG radiofluorination is prepared using three synthetic steps from

inexpensive starting materials, enabling the synthesis and purification of [^{18}F]mFBG using an automated radiosynthetic method.[196]

1.4.2. Application in clinic

mFBG is currently used for PET imaging of neuroblastomas (NB) and neuroendocrine tumors as an alternative to SPECT imaging by [^{123}I]MIBG.[197] Ten patients, half of which were diagnosed with NB, and the other half diagnosed with paraganglioma/pheochromocytoma, were imaged using [^{18}F]mFBG to visualize the lesions. Biodistribution revealed biexponential clearance from the blood pool with $t_{1/2\ early}$ = 18 min and $t_{1/2\ late}$ = 6 h, in comparison to monophasic 2-15 h clearance with [^{123}I]mIBG.[197] Liver activity is high in early stages of the scan ($t_{1/2}$ = 80 min) and decreases over time with lesions detectable at 1 h after injection with excellent contrast.[197] Prominent activity was noted in the left ventricle (LV), with biphasic washout over the duration of the scan (240 min).[197] Parent tracer metabolism was determined by venous blood sampling followed by HPLC analysis and revealed 90-92% of the parent intact after 2 h, representing excellent *in vivo* stability in humans.[197] [^{18}F]mFBG provided both superior metabolism, kinetics, and diagnostic imaging (122 vs 63 lesions detected) in comparison to [^{123}I]mIBG and is particularly appealing in pediatric patients, enabling the use of PET/MR to reduce radiation exposure.[197] Further analysis of radiotracer kinetics in the LV of patient cohorts enabled the absolute quantification using a 2-tissue-4-compartmental (2T4K) to calculate the volume of distribution (V_T).[198] Human imaging revealed reversible kinetics of [^{18}F]mFBG, hypothesized to be a function of sympathetic nerve tone.[198]

1.4.3. Physicochemical properties & preclinical imaging

Affinity studies performed with C6-hNET cells using [^{123}I]mIBG and various concentrations of MIBG, PIBG, PFBG, and MFBG provided IC_{50} values of 1.72, 7.2, 9.8, and 4.86 µM, respectively.[199] While [^{18}F]mFBG results in a 2.8-fold loss in competitive affinity in comparison to MIBG, its potency has been well demonstrated in cell-lines and tumour imaging.[199,200] [^{18}F]mFBG imaging is also appealing as data have revealed greater hydrophilicity compared to [^{123}I]mIBG (logD of -0.52 vs. 0.42), with 70% less plasma protein binding, resulting in faster washout in most organs.[199] Furthermore, the higher IC_{50} of [^{18}F]mFBG (4.9 µM), in comparison to [^{123}I]mIBG (1.7 µM) and [^{18}F]FBBG (0.90 µM) is likely to result in slower NET mediated neuronal uptake and reversible kinetics. Biodistribution studies in rats with C6 wild-type rat glioma cells (C6-WT) and human NET gene stably transduced C6 cell (C6-hNET) xenografts revealed strong cardiac uptake after 4 h post injection (p.i).[199] In rats with C6-hNET xenografts, a more rapid clearance of [^{18}F]mFBG from both target and non-target organs was also observed in comparison to [^{123}I]mIBG, with higher urinary excretion.[199]

1.4.4. Image quantification

PET image quantification is commonly performed in units of standardized uptake value (SUV), representing the activity concentration of summed frames normalized to injected dose and body weight of the subject. This normalization is important when imaging subjects of variable sizes using a consistent dose. SUV is calculated as:

Equation 1 $$SUV = \frac{A_c}{ID/W_b}$$

Where A_c is the activity concentration in the organ in nCi/cc, ID is the total injected dose in nCi, and W_b is the subject bodyweight in grams. SUV is a unitless ratio. SUV can also be calculated for *ex vivo* tissue counting experiments by dividing A_c by tissue weight to further normalize the dataset. In the scenario where *ex vivo* biodistribution was performed at a given timepoint where animal mass is consistent, %ID/g is most appropriate and is calculated as

$$\text{Equation 2} \qquad \%ID = \frac{ID}{W_m} * 100$$

Where W_m is the mass of tissue in grams.

1.4.5. Exponential modeling of time-activity curves

The clearance of [^{18}F]mFBG in the myocardium of rats follows monoexponential kinetics, providing constants A_{mono}/A_0 and k_{mono}.[201] A_0 reflects the extrapolated y-intercept of the fitted function and is therefore expressed in units of SUV. Whereas k_{mono} is indicative of the washout rate and is expressed as min^{-1}. With respect to sympathetic nerve imaging, A_0 is a measure of functional nerve terminal density/concentration, and k_{mono} describes the clearance of the tracer from the myocardium. The measurements are performed using organ TACs in the absence of a blood input function (blood activity not corrected for metabolites).

1.4.6. Significance

Small animal imaging using [^{18}F]mFBG to evaluate its use for imaging cardiac sympathetic nerves was not performed prior to our published work. The previous evaluation of structurally similar benzylguanidine analogs has informed human imaging with this tracer. However, the lack of mechanistic details raises concerns for the accurate interpretation of human cardiac imaging data. As such, this project aimed to investigate myocardial uptake and washout mechanisms in rats

to provide a foundation for explaining the kinetics of the tracer in the myocardium. To date, available neurohormonal imaging tracers are quantified using irreversible kinetic models. [^{18}F]mFBG displays reversible kinetics, and may therefore prove useful in imaging both NET density and intraneuronal dysfunction.

1.5. Carbon-11 radiochemistry

Carbon-11 ($t_{1/2}$ = 20.4min, β^+ emission = 99.8%) is one of the most used short-lived isotopes incorporated into biomolecules for PET imaging.[136] The cyclotron generated radionuclide is prized for its isotopic labeling, enabling the use of well-established native pharmaceuticals as molecular imaging agents. [^{11}C]CO_2 is produced from the bombardment of target gas composed of N_2 + 0.1-1% O_2 via an $^{14}N(p,a)^{11}C$ nuclear reaction resulting in a substitution of a proton for an alpha particle.[138] This method of production is known as no-carrier-added (NCA, absence of deliberately added stable isotope), important in retaining high molar activity (GBq/μmol). In comparison, carrier added PET isotopes can be produced such as in the case of [^{18}F]fluorine (^{18}F-^{19}F), resulting in low molar activity.[136] The ratio of radioactive to non-radioactive isotopes in NCA is preferred especially when synthesizing tracers that bind to low-density targets to avoid protein saturation to the point of competitive inhibition (labelled molecule vs unlabelled molecule).[202] Molar activity values are dependent on the half-life of the isotope in question. In the case of carbon-11, molar activity values are reduced by ½ approximately every 20 minutes, necessitating rapid chemical synthesis, purification, formulation, and injection into animals or patients.

1.5.1. ^{11}C-Methylation

The most inexpensive and available form of carbon-11 is [^{11}C]CO_2, considered to be a primary carbon-11 precursor (Scheme 1).[203] Often times, [^{11}C]methane ([^{11}C]CH_4) is directly

generated and converted into secondary precursors such as [^{11}C]iodomethane ([^{11}C]CH_3I), [^{11}C]methyl triflate ([^{11}C]CH_3OTf), or more rarely [^{11}C]hydrogen cyanide ([^{11}C]HCN).[203,204]

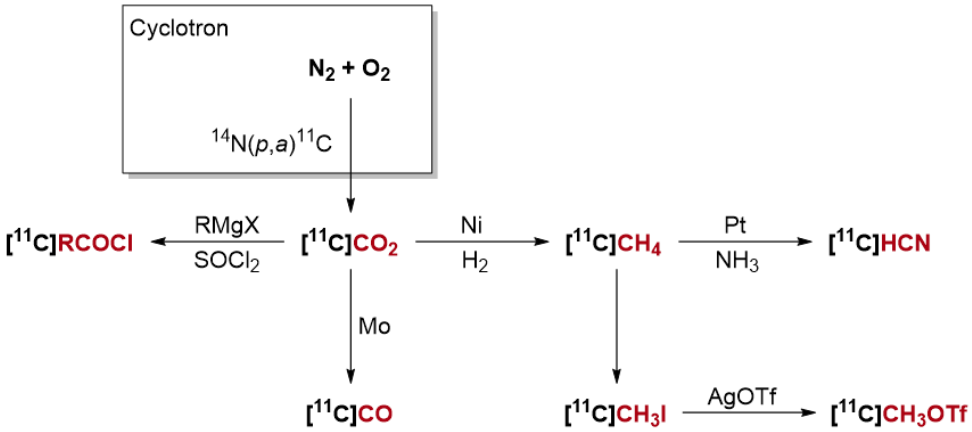

1.5.1.1. Scheme 1. Summary of secondary precursors prepared from [^{11}C]CO_2

The most common method to incorporate carbon-11 into molecules is the use of methylating agents [^{11}C]CH_3I or [^{11}C]CH_3OTf.[204,205] However, the reactivity of [^{11}C]CH_3I towards arylamines, especially those that are deactivated (containing electron withdrawing groups, EWG) is poor, but may be marginally improved upon by using the more reactive electrophile, [^{11}C]CH_3OTf.[203] Methods developed to use [^{11}C]CO_2 as a C_1 building block to methylate amines is a topic of interest, but not implemented on a wide-scale as of yet. For example, the use of catalytic substrates $ZnCl_2$/IPr and $PhSiH_3$ with [^{11}C]CO_2 to prepare the corresponding methylamine.[203] Rather, efforts are generally focused on the development of novel reactions for ^{11}C-labeling of radiopharmaceuticals using ^{11}C-methylation.[203,206] For example, the use of transition-metal-mediated carbon-carbon bond forming reactions using Pd has shown utility for labelling novel radioligands for the serotonin and nicotinic acetylcholine receptor, [*p-methyl-*

[11C]MADAM and [11C]5-methyl-5-nitroquipazine, respectively.[203,204,207,208] Common cross-coupling reactions such as the Suzuki and Stille reaction are plentiful in the field, relying on the reactivity of organoborane and organotin precursors, respectively, with [11C]CH_3I.[203] Methylation of α-carbons with [11C]CH_3I is also an effective strategy to radiolabel, but requires the use of strong alkyl lithium bases limiting substrate versatility.[203,204]

1.5.2. $^{11}CO_2$-fixation

Carbonyl groups are abundantly found throughout a large array of biomolecules and are utilized by medicinal chemists during the development of pharmaceuticals. Previous library analyses of drug candidates from AstraZeneca reveal that less than 35% of compounds could be labeled by 11C-methylation, compared to a 75% success rate for compounds that can be labeled by 11C-carbonylation.[205] Therefore, [11C]CO_2 serves as an important labelling strategy for carbon-11 radiotracer development.

The production of [11C]CO_2 is generated by proton bombardment of nitrogen gas ($^{14}N(p,\alpha)^{11}C$) in the presence of 0.5% oxygen.[138] The [11C]CO_2 generated from the cyclotron can be directly used through trap-and-release purification and concentration steps to remove excess oxygen and nitrous oxides, and to control the delivery rate of the gaseous reagent.[205] The two methods for this process are cryogenic purification and immobilized supports. Cryogenic purification requires condensing [11C]CO_2 in a small vessel cooled by liquid nitrogen, and the removal of condensable impurities by in-line chemical traps.[205] In contrast, [11C]CO_2 can be immobilized onto solid supports such as molecule sieves, and delivered into the reactor upon heating.[205] Due to the low solubility of [11C]CO_2 in polar organic solvents, bases that trap [11C]CO_2 are frequently used. Such bases are 2-tert-butylimino-2-diethylamino-1,3-dimethylperhydro-

1,3,2-diazaphosphorine (BEMP), or 1,8-diazabycyclo[5.4.0]undec-7-ene (DBU) in dimethylformamide (DMF) or other polar organic solvents.[136,203,205,209,210] This dramatically improves yields due to an increase in [^{11}C]CO_2 trapping efficiency.

Due to the poor electrophilicity of [^{11}C]CO_2, the development of chemical technologies directly utilizing this primary precursor are limited (scheme 2).[209]

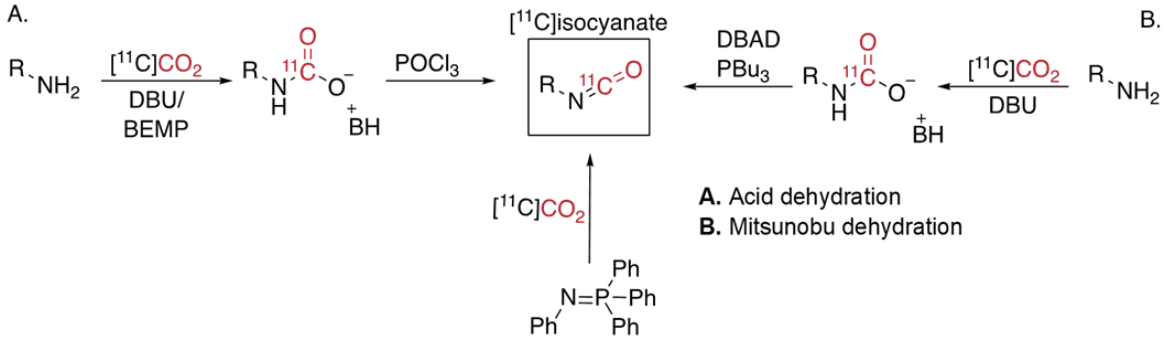

1.5.2.1. **Scheme 2.** Radiosynthetic methods to synthesize ^{11}C-isocyanates

Regardless, efforts have been made to produce diverse sets of molecules to facilitate the development of PET radioligands. Initial efforts focused on the synthesis of high value intermediates such as ^{11}C-isocyanates from [^{11}C]phosgene ([^{11}C]COCl) and enabled the accessibility of key functional groups such as ^{11}C-imidazolones and oxazolidindiones.[205,211] However, the use of [^{11}C]phosgene has been discontinued in the vast majority of facilities due to a complex production requiring specialized apparatus and extensive upkeep prior to each use.[205,209,211] Instead, radiochemical strategies to produce isocyanate equivalents have provided an adequate means to synthesize ^{11}C-isocyanates under milder conditions with increased substrate versatility. Early attempts to prepare structurally complex ^{11}C-ureas utilized the carboxylation of

amines by [^{11}C]CO_2 in the presence of triethylamine or BEMP to form a carbamate intermediate, followed by the addition of a dehydrating agent $POCl_3$ to facilitate the formation of ^{11}C-isocyanates (scheme 2).[212,213] Under these conditions, isocyanates react with excess amine to produce symmetrical ureas and ^{11}C-carbodiimides.[213] However, the inherent challenge of this method is the synthesis of asymmetrical products, supressed with the use of excess $POCl_3$ and high concentrations of the secondary amine to reach the desired selectivity within 2 minutes in high radiochemical yields.[205,212,213] This is currently one of the most used strategies to reliably produce labelled isocyanates directly from [^{11}C]CO_2, but still suffers with poor reactivity towards anilines, and releases HCl as a by-product, creating highly acidic conditions that can limit [^{11}C]CO_2 trapping efficiencies and substrate selectivity. The second popular strategy to produce ^{11}C-isocyanates is using Mitsunobu chemistry, replacing the use of the acidic dehydrating reagent $POCl_3$ with di-tert-butyl azodicarboxylate (DBAD) and tributylphosphine (PBu_3) following stepwise trapping with an amine and DBU (scheme 2).[214] This technology led to high yielding synthesis of both symmetrical and asymmetrical ureas including electron deficient anilines. Advancements in this technology also led to the production of ^{11}C-amides using Grignards, and organozinc coupling reactions following isocyanate formation.[215,216] The third strategy used to expand the feedstock of ^{11}C-isocyanate synthons is the use of phosphinimine precursors, prepared by azides or amines, and have shown utility in synthesizing a small scope of asymmetrical ureas in moderate yields (scheme 2).[217,218]

1.5.3. Iminophosphorane structure and reactivity

Iminophosphoranes (phosphinimines, phosphoranimines, phosphazenes) are nitrogen organophosphorous compounds with the chemical structure $R_3P{=}NR$. The structure of these nitrogen-phosphorous ylides was demonstrated in 1919 by Staudinger and Meyer, and their

reactivity has been extensively explored since then.[219] This functional group is commonly installed in intermediates for multi-step synthesis, have shown utility as superbases (ketimine nitro-Mannich reaction), are building blocks for P-N containing polymers, and are commonly employed in transitional metal chemistry.[220,220–224] The two most common methods to prepare iminophosphoranes are the Staudinger and Kirsanov reaction. In the former reaction, oxidation of an organic azide is required with the use of a phosphine ligand (PR_3), most commonly triphenylphosphine.[221] In the latter reaction, a phosphine-dibromide (P[V]) reagent such as triphenylphosphine dibromide is used in conjunction with a primary amine and base such as triethylamine or pyridine.[225] The highly polarized P=N bond of the iminophosphorane is commonly described as resonance hybrids of the two canonical forms, one in which the nitrogen and phosphorous share a covalent double bond (A), and the other which places a positive charge on the phosphorous and negative charge on the nitrogen (B).[226]

As aza-ylides, iminophosphoranes react both at the nitrogen (nucleophilic) and phosphorous (vacant 3d-orbitals) atoms, allowing the preparation of a wide variety of derivatives with ease. The most widely explored use of iminophosphoranes surrounds its application in heterocycle synthesis via intramolecular *aza*-Wittig reactions. The reactivity towards cyclization is shown to be controlled by a variety of factors such as a) chain length (ring size/strain), b) reactivity of the carbonyl group, and substituents on the iminophosphorane.[226] In general, this class of compounds is efficient in generating 5-7 member rings but not 3-4 member rings due to excessive strain of the oxazaphosphetane intermediate.[226,226] In terms of carbonyl reactivity, aldehydes and ketones are the most reactive, but esters, amides, and imide carbonyls have all been employed in the synthesis of heterocycles.[226,227] Substituent groups on the N and P atom are also of paramount importance. Electron poor R groups of the nitrogen will consequently reduce

nucleophilicity, whereas reducing steric bulk (triphenylphosphine vs trimethylphosphine) or adding EWG will increase the electrophilicity of the phosphorous.[226,227] Useful synthetic reactions of iminophosphoranes are summarized in **Scheme 3** but do not encompass the total diversity of synthesizable functional groups using this chemistry. In addition to intramolecular *aza*-Wittig reactions, the intermolecular variant has also been explored, albeit to a lesser extent. It is known that iminophosphoranes are particularly reactive with carbon dioxide, carbon disulfide, isocyanates, ketenes, and sulfur dioxide in intermolecular reactions and can function as robust dehydrating agents to yield reactive intermediates.[226,228,229]

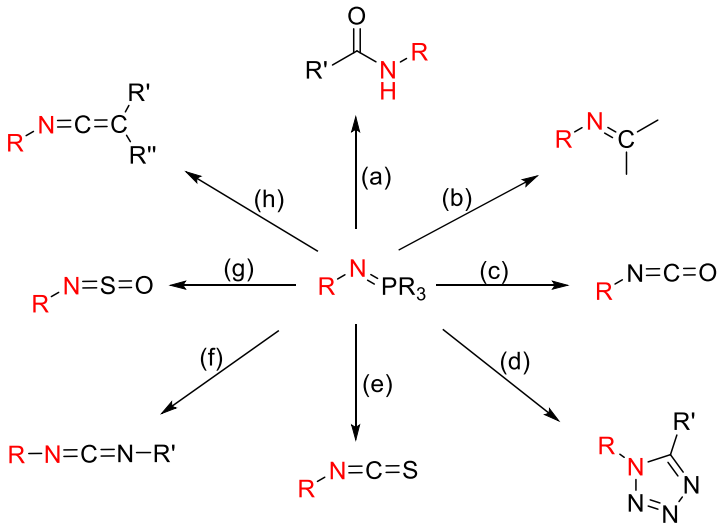

1.5.3.1. **Scheme 3.** Reactions of iminophosphoranes. (a) R'COOH, (b) Me_2CO, (c) CO_2, (d) R'COCl, NaN_3, (e) CS_2, (f) R'NCO, (g) SO_2, (h)$R_2C=C=O$

1.5.4. Iminophosphoranes and supercritical CO_2 ($scCO_2$)

Marsura and co-workers discovered the inherent intermolecular reactivity of iminophosphoranes with supercritical carbon dioxide ($scCO_2$), yielding an isocyanate intermediate readily converted into a urea with the addition of an amine nucleophile.[230] The interest in this

chemical reaction for a synthetic point of view stems from a safe route to isocyanate synthesis that does not require the use of phosgene or acid chlorides, benefiting both research and industrial markets. In addition, $scCO_2$ chemistry is applicable in the context of Green Chemistry as in this state CO_2 functions as both a solvent and reactant. This reaction has been well documented in the literature; however, the chemical mechanism was only probed recently. From an electronic standpoint, iminophosphoranes have high proton affinity and are organic neutral, low-nucleophilic superbases, owing to their zwitterionic nature.[222] As such, the electron density on the nitrogen atom is large, with pK_{BH^+} values of 23-25 for triaryliminophosphoranes in acetonitrile, comparable to guanidines (~24).[222] In contrast, CO_2 behaves as an electron acceptor or Lewis acid (LA), exemplified by the interaction of compounds containing carbonyl groups or fluorine atoms having Lewis acid – Lewis base (LA-LB) interactions with CO_2.[231,232] However, CO_2 typically acts as an electron donor/LB. *Ab initio* calculations describe competitive donor-acceptor interactions of CO_2 and π-systems that are significantly stronger than LA-LB interactions.[222] Calculations performed with a methylene iminophosphorane $CH_3N{=}PR_3$ containing PPh_3 and PH_3 functionalized phosphines show the nucleophilicity and basicity is highly dependent on the substitution of the phosphine.[222] For instance, replacing H by Ph on the phosphorous atom resulted in a 22 kcal/mol increase in gas-phase basicity, but lowers the nucleophilicity of the iminophosphorane, exemplified by a -6.42 to -5.18 kcal/mol difference in the interaction energy of iminophosphorane-CO_2, explained by an increase in steric hinderance[222].

1.5.5. Reactivity with gaseous CO_2

While applications of iminophosphorane reactivity with $scCO_2$ are apparent, access to specialized vessels to form $scCO_2$ can limit its use in traditional organic synthesis and radiochemistry. Attempts to react normal phase CO_2 with cyclohexyliminotriphenylphosphorane

report reduced selectivity, producing the corresponding cyclohexyl isocyanate in 24% yield and the symmetrical cyclohexyl carbodiimide in 53% yield.[233] Molina *et al* described the carbodiimide free synthesis of isocyanates using triaryl and trialkyl iminophosphoranes in yields of 73-97%, paving the way for further research into intermolecular reactions of isocyanates under mild conditions.[228]

1.5.6. Iminophosphoranes in ^{11}C-radiochemisty

Van Tilburg *et al* replicated the chemistry by Molina *et* al using carbon-11 radiochemistry using a stepwise approach of bubbling and trapping [^{11}C]CO_2 into a reaction vessel at low temperatures in THF with the commercially available *N*-(triphenylphosphoranylidene)aniline.[218] Following [^{11}C]CO_2 trapping, the reactor was heated at 90 °C for 6 minutes, and subsequent addition of an amine nucleophile heated at 35 °C for 3 minutes to obtain an asymmetrical urea in 33% yield.[218] The authors noted improved yields and trapping efficiencies when the nucleophilic amine was present with the iminophosphorane in the vessel and heating the vessel to 90 °C following [^{11}C]CO_2 trapping. Using this method, 4 asymmetrical ureas were formed from 8-46% radiochemical yield.[218]

The most popular methods for utilizing iminophosphorane-CO_2 reactivity circumvents the isolation and synthesis of iminophosphorane precursors. Rather, reactions are typically performed *in situ* in the presence of phosphine, amines, or azides. An *in* situ Kirsanov reaction demonstrated good application for the synthesis of three carbon-11 labelled hydratoins using trimethylphosphine diiodide and the corresponding amine to yield the corresponding iminophosphorane, followed by the addition of [^{11}C]CO_2.[234] Del Vecchio *et al* utilized a similar strategy of intramolecular ring closure to form cyclic ureas using a Staudinger *aza*-Wittig (SAW) approach with *o*-azidoanilines

and dimethylphenylphosphine.[217] The technique resulted in the successful synthesis of pharmaceutically relevant cyclic ureas such as [^{11}C]oxatomide, [^{11}C]domperidone, [^{11}C]flibanserin, and [^{11}C]CGP12177A. This technology was further expanded to produce cyclic carbamates such as [^{11}C]chlorzoxazone, [^{11}C]metaxalone, and [^{11}C]fenspiride.[217] One attempt was made to synthesize a linear acyclic carbamate under harsh conditions, resulting in a low 4% radiochemical yield.[235]

1.5.7. Significance

Developing a radiolabeling technique using iminophosphorane precursors obviates the use of explosive azide precursors, toxic phosphines, and high mass loading of reagents that can hinder radiotracer purification and limit functional group tolerance. Developing a straightforward strategy to isolate stable iminophosphorane precursors reduces the complexity of the sample matrix allowing a more robust reactivity profile and increases the practicality of this labelling method for good manufacturing practices (GMP) environments.

1.6. Atherosclerosis and cardiovascular disease

Coronary artery disease (CAD) is the leading cause of mortality worldwide, responsible for one in every five deaths.[236] CAD is a condition caused by atherosclerosis, the obstruction or narrowing of arteries due to a buildup of plaque within the vessel walls. The early lesions of atherosclerosis are composed of subendothelial accumulations of macrophages engorged with cholesterol, also known as foam cells.[237] These lesions are typically found in the aorta, and are described as fatty streaks found within the first decade of life in humans. Fatty streaks are not clinically significant but are prone to develop into advanced lesions characterized by lipid-rich necrotic debris and smooth muscle cells (SMCs).[238] Pathological studies have shown a series of

changes in the endothelium during atherogenesis, especially with increased monocyte/macrophage content. Current evidence suggests a central role of macrophages in disease initiation and progression, as the accumulation of oxidized low-density lipoprotein (LDL) in the vascular intima has a significant contribution to macrophage recruitment and foam cell formation.[239]

1.6.1. NLRP3 mediated vascular inflammation

The recruitment of macrophages and other cells of the innate immune system is recognized by chemical signals released by pathogens or injured cells and tissues by pattern recognition receptors (PRR).[239,240] PRRs are expressed in innate immune cells and can distinguish between two types of molecular patterns: danger associated molecular patterns (DAMPs) and pathogen-associated molecular patterns (PAMPs).[240] Several different PRRs are responsible for recognizing distinct PAMPs and DAMPs and are generally classified into four groups: Toll-like receptors (TLR), nucleotide-binding oligomerization domain-like receptors (NLRs), retinoic acid-inducible gene-I-like receptors (RLRs) and C-type lectin receptors (CLRs).[240,241] Importantly, NLRP3, a member of the NLR family, can recognize various DAMPs and form a molecular complex known as the NLRP3 inflammasome. In general, the NLRP3 inflammasomes are composed of an apoptosis-associated speck-like protein containing a caspase recruitment domain (ASC), and a cysteine protease caspase-1 (CPC1), responsible for activating proinflammatory cytokines such as prointerleukin-1β and prointerleukin-18 into its active form.[241] NLRP3 inflammasome activation is thought to occur in two steps: 1) priming by transcriptional upregulation of pro-interleukins and NLRP3, and 2) the presence of activation signals causing inflammasome assembly, leading to proteolytic processing of interleukins into its mature form by activated caspase-1.[242] In order to activate NLRP3, macrophages must first be exposed to stimuli such as ligands for the TLR, NLRs, or cytokine receptors which activate the widely known transcription factor NF-κB.[242] NF-κB is

responsible for upregulating the expression of NLRP3 and pro-interleukins which are currently known to exist in concentrations that are inadequate for inducing inflammasome activation under normal conditions.[242] Following the priming step, NLRP3 inflammasome assembly can be activated by ATP, potassium ionophores, heme, particular matter, reactive oxygen species (ROS), among other signals.[241,242]

Experimental and clinical studies have described a crucial role of IL-1β in the progression of atherosclerosis and characterized this cytokine as proatherogenic. In 2012, Duewell et al used atherosclerotic-prone low-density lipoprotein receptor-deficient LDLR-/- chimeric mice whose bone marrows (BM) were transplanted with inflammasome-related molecules NLRP3-/-, ASC-/-, or IL-1α/β-/-, and show reduced atherosclerotic lesion development.[243] This research also highlighted the presence of cholesterol crystals, found in all stages of atherosclerosis as a DAMP candidate that strongly activated NLRP3 inflammasomes in macrophages. Since vascular wall macrophage infiltration is the hallmark of atherosclerosis, most studies have focused on the role of NLRP3 activation in macrophages. In the earliest stages of fatty streak development, it was noted that cholesterol crystals are phagocytosed by macrophages, but induced phagolysosomal destabilization and rupture due the inability to efficiently phagocytize cholesterol crystals.[244] This process is now known as frustrated phagocytosis. The inefficient processing of cholesterol crystals further causes lysosomal rupture, inducing leakage of the lysosomal enzyme cathepsin B, resulting in NLRP3 inflammasome activation.[244,245] Similarly, calcium phosphate crystals including hydroxyl apatite and tricalcium phosphate are shown to accumulate in atherosclerotic lesions and activate NLRP3 inflammasomes though the same mechanism.[244,245]

1.6.2. MCC950 as a small molecule inhibitor

The evaluation of MCC950 as a small molecule IL-1β processing inhibitor occurred as recently as 2015.[246] The mechanism for NLRP3 inhibition is still currently under investigation, and evidence as recent as 2022 continues to provide additional insight into the exact inhibition mechanism. Current evidence suggests that this inhibitor has not been shown to inhibit TLR signaling, or any proteins in the priming/transcriptional upregulation stage of NLRP3 activation.[246] Furthermore, calcium signaling, potassium efflux, NLRP3-ASC interactions are not shown to be inhibited. While some groups have postulated MCC950 as a substrate for NIMA-related kinase 7 (NEK7), a regulatory protein that inhibits NLRP3 activation, a drug affinity responsive target stability (DARTS) approach has demonstrated that MCC950 binds directly to NLRP3 itself.[247] Using bone marrow-derived macrophages and a broad specificity protease mix (pronase), an assay was performed to induce the degradation of NLRP3. Increasing doses of MCC950 was shown to protect NLRP3 from pronase-mediated degradation, evident from changes in the digestion pattern detected using antibodies against the NACHT or PYD domains of NLRP3.[247] MCC950 was shown to be selective and did not alter the digestion pattern of NEK7. In primed and unprimed BM derived macrophage stimulated cells, MCC950 exposure was shown to protect NLRP3, which suggests that it binds to both the active and inactive conformation of NLRP3.[247] With the production of mutant NLRP3 proteins, the binding site domain was identified to be the NLRP3 NACHT domain.[247] Further evaluation demonstrated that MCC950 binds non-covalently to the Walker B motif to block NLRP3 ATPase activity, critical for NLRP3 assembly and function.[247]

In a separate study by Tapia-Abellán *et al*, a bioluminescence resonance energy transfer (BRET) assay was employed to study the open and closed conformations of NLRP3.[248] Analysis in cells of the disease relevant mutant NLRP3 p.D305N revealed an enhanced propensity of

oligomerization. Treatment with MCC950 was found to cause almost complete disaggregation of all p.D305N oligomers presumably into closed monomeric NLRP3 monomers.[248] MCC950 is now being evaluated as a therapeutic in a multitude of chronic inflammatory conditions such as rheumatoid arthritis, Alzheimer's disease, aortic aneurysms, myocardial infarctions, ulcerative colitis, among others.[249]

1.6.3. MCC950 and atherosclerosis

NLRP3 inflammasome inhibition in atherosclerotic ApoE$^{-/-}$ mouse models have demonstrated profound therapeutic benefit. Insulin-deficient type 1 diabetes ApoE$^{-/-}$ mice generated by intraperitoneal injections of streptozotocin (100 mg/kg/day) had increased atherosclerotic total plaque area by fourfold in arch, thoracic, and abdominal aortic regions.[250] MCC950 treatment significantly attenuated atherosclerotic lesions in diabetic ApoE$^{-/-}$ mice by ~40%, reduced systemic oxidative stress, and reduced the expression of proatherogenic mediators TNF-α, ICAM-1, and MCP-1, and IL1β after a five-week treatment cycle.[250] In aortic sinus plaques, reduced macrophage infiltration was noted in the treatment group. Furthermore, MCC950 reduced the necrotic core of diabetic plaques without altering α-smooth muscle actin (α-SMA) or collagen content.[250] Improved delivery methods of MCC950 to atherosclerotic plaques to increase the therapeutic effect were demonstrated by packaging MCC950 into platelet-derived extracellular vesicles (PEVs) followed by intravenous injection.[251] Immune cell populations, plaque size, and proinflammatory cytokines such as IL-1β and IL-6 were significantly reduced in the aortic arch of animals treated with MCC950-PEVs in compared to the control group, enabling improved drug delivery to minimize the risk of side effects and increase its therapeutic action.[251]

1.6.4. Clinical significance

Patients with coronary atherosclerosis have demonstrated high expression of NLRP3 in the aorta correlated to the severity of stenosis. Patients with high level risk factors such as hypertension, smoking, diabetes, and blood lipid chemistry also correlates with increased NLRP3 expression levels in the aorta of patients with CAD.[252,253] Studies comparing carotid atherosclerotic lesions with normal iliac or mesenteric arteries show high levels of mRNA and protein levels of inflammasome components such as ASC, NLRP3, caspase-1, and consequently IL-1β and IL-18.[253] Within plaques, co-staining revealed increased CD68 positive macrophage population. In addition, increased NLRP3 expression in subcutaneous adipose tissue was observed to be positively correlated with lifestyle-related indexes that impact the development of CAD such as body mass index (BMI) and uric acid serum levels.[253] Genetic polymorphisms are also hypothesized to contribute to aberrant NLRP3 inflammasome activation, but have not yet been extensively identified in patient populations. Given the extensive role of NLRP3 in mediating inflammation, efforts to synthesize safe potent inhibitors with the goal of treatment are underway. In addition, high expression of NLRP3 in inflammatory conditions has generated interest in performing non-invasive *in* vivo PET imaging using an NLRP3-specific probe to enable the visualization of NLRP3-dependent inflammation.

1.6.5. Rationale

The use of MCC950 as a PET radiotracer candidate for neuroimaging applications was first evaluated by Hill *et al.*[254] The radiotracer was synthesized using traditional Mitsunobu radiochemistry and acquired in 1% yield in low molar activity.[254] [^{11}C]MCC950 brain uptake was absent, and is hypothesized to lack the chemical properties required for BBB penetration. Recently,

efforts have been made to synthesize derivative radiotracers that retain the potency of MCC950 but are easier to label and evaluate.[255] With the completion of our recent project, we have shown the use of iminophosphorane chemistry to be a more reliable strategy for obtaining ^{11}C-sulfonylureas in high yields suitable for the preclinical evaluation of radiotracers.[256] We were interested in evaluating [^{11}C]MCC950 in detecting NLRP3-mediated inflammation in atherosclerotic plaques, with the eventual goal of *in vivo* PET imaging, as this imaging probe may provide useful information about NLRP3 expression and provide molecular information regarding plaque stability.

1.7. Hypotheses and research aims

Project 1: Cardiac SNS imaging using [^{18}F]mFBG (chapters II-III)

The hypotheses for this research project are:

1. [^{18}F]mFBG possesses measurable NET-dependent uptake kinetics
2. [^{18}F]mFBG reuptake occurs, and tracer retention is not complicated by additional kinetics compartments and radiolabeled metabolites
3. [^{18}F]mFBG washout is sensitive to changes in sympathetic tone
4. [^{18}F]mFBG PET imaging can discriminate between healthy and diseases animals

These hypotheses are addressed by completing the following aims:

1. Determining baseline uptake and assessing tracer specificity towards NET using neuronal and extraneuronal uptake inhibitors
2. *In vivo* studies of intraneural tracer kinetics, and determination of radiolabeled metabolites
3. Pharmacological challenge (chase dosing) of α_2 receptors

4. Determining whether quantifiable differences in [^{18}F]mFBG myocardial kinetics accurately reflect neuropathology in an animal model of HF (control vs Dahl salt-sensitive rats)

Project 2: PNS imaging using [^{18}F]FEOBV (chapter IV)

The hypothesis for this research project is:

1. [^{18}F]FEOBV uptake in the myocardium is VAChT dependent; and more specific in the absence of isoflurane anesthesia

We will address these hypotheses by completing the following aims:

1. Perform baseline uptake and pharmacological challenge experiments in mice with and without isoflurane anesthesia
2. Assess myocardial uptake in mouse models containing differential expression of VAChT

Project 3: Interrupted aza-Wittig reaction using iminophosphoranes (chapter V)

The hypotheses for this research project are:

1. Iminophosphorane precursors can react with stable CO_2 and [^{11}C]CO_2 to yield isocyanate derived products with application to pharmaceutically relevant drugs and in-demand ^{11}C-radiotracers

This hypothesis is addressed by completing the following aims:

1. Investigating reaction selectivity towards a substrate of choice and optimizing reaction conditions
2. Synthesis of multiple isocyanate derived functional groups with the naturally abundant carbon isotope and carbon-11 by utilizing unique iminophosphorane precursors

Project 4: Synthesis and evaluation of [^{11}C]MCC950 for imaging atherosclerotic plaques (chapter VI)

The hypotheses for this research are:

1. [^{11}C]MCC950 can be radiolabeled using iminophosphorane chemistry in yields suitable for its evaluation
2. Selective [^{11}C]MCC950 uptake occurs in aortic atherosclerotic lesions

These hypotheses are addressed by completing the following aims:

1. Developing suitable automated reaction conditions for labeling [^{11}C]MCC950
2. Assessing baseline biodistribution and aortic plaque accumulation of [^{11}C]MCC950 in ApoE$^{-/-}$ and C57BL/6 mice.
3. Performing homologous blockade to determine specific binding

1.8. References

(1) Gabella, G. Autonomic Nervous System. In *eLS*; John Wiley & Sons, Ltd, 2001. https://doi.org/10.1038/npg.els.0000081.

(2) Gibbons, C. H. Chapter 27 - Basics of Autonomic Nervous System Function. In *Handbook of Clinical Neurology*; Levin, K. H., Chauvel, P., Eds.; Clinical Neurophysiology: Basis and Technical Aspects; Elsevier, 2019; Vol. 160, pp 407–418. https://doi.org/10.1016/B978-0-444-64032-1.00027-8.

(3) McCorry, L. K. Physiology of the Autonomic Nervous System. *Am. J. Pharm. Educ.* **2007**, *71* (4), 78.

(4) Jamali, H. K.; Waqar, F.; Gerson, M. C. Cardiac Autonomic Innervation. *J. Nucl. Cardiol.* **2017**, *24* (5), 1558–1570. https://doi.org/10.1007/s12350-016-0725-7.

(5) Waxenbaum, J. A.; Reddy, V.; Varacallo, M. Anatomy, Autonomic Nervous System. In *StatPearls*; StatPearls Publishing: Treasure Island (FL), 2022.

(6) Fedele, L.; Brand, T. The Intrinsic Cardiac Nervous System and Its Role in Cardiac Pacemaking and Conduction. *J. Cardiovasc. Dev. Dis.* **2020**, *7* (4), 54. https://doi.org/10.3390/jcdd7040054.

(7) Pascale, A.; Govoni, S. Brain-Heart Communication. In *Brain and Heart Dynamics*; Govoni, S., Politi, P., Vanoli, E., Eds.; Springer International Publishing: Cham, 2020; pp 25–41. https://doi.org/10.1007/978-3-030-28008-6_4.

(8) Karemaker, J. M. An Introduction into Autonomic Nervous Function. *Physiol. Meas.* **2017**, *38* (5), R89. https://doi.org/10.1088/1361-6579/aa6782.

(9) Phillips, C.; Ower, K. Anatomy of the Sympathetic and Parasympathetic Nervous System. In *Pain: A Review Guide*; Abd-Elsayed, A., Ed.; Springer International Publishing: Cham, 2019; pp 9–14. https://doi.org/10.1007/978-3-319-99124-5_2.

(10) Tindle, J.; Tadi, P. Neuroanatomy, Parasympathetic Nervous System. In *StatPearls*; StatPearls Publishing: Treasure Island (FL), 2022.

(11) Gordan, R.; Gwathmey, J. K.; Xie, L.-H. Autonomic and Endocrine Control of Cardiovascular Function. *World J. Cardiol.* **2015**, *7* (4), 204–214. https://doi.org/10.4330/wjc.v7.i4.204.

(12) Vaseghi, M.; Shivkumar, K. The Role of the Autonomic Nervous System in Sudden Cardiac Death. *Prog. Cardiovasc. Dis.* **2008**, *50* (6), 404–419. https://doi.org/10.1016/j.pcad.2008.01.003.

(13) Thomas, G. D. Neural Control of the Circulation. *Adv. Physiol. Educ.* **2011**, *35* (1), 28–32. https://doi.org/10.1152/advan.00114.2010.

(14) Olshansky, B.; Sabbah, H. N.; Hauptman, P. J.; Colucci, W. S. Parasympathetic Nervous System and Heart Failure. *Circulation* **2008**, *118* (8), 863–871. https://doi.org/10.1161/CIRCULATIONAHA.107.760405.

(15) Uijtdehaage, S. H.; Thayer, J. F. Accentuated Antagonism in the Control of Human Heart Rate. *Clin. Auton. Res. Off. J. Clin. Auton. Res. Soc.* **2000**, *10* (3), 107–110. https://doi.org/10.1007/BF02278013.

(16) Ziemssen, T.; Siepmann, T. The Investigation of the Cardiovascular and Sudomotor Autonomic Nervous System—A Review. *Front. Neurol.* **2019**, *10*.

(17) Chen, Z.-R.; Huang, J.-B.; Yang, S.-L.; Hong, F.-F. Role of Cholinergic Signaling in Alzheimer's Disease. *Molecules* **2022**, *27* (6), 1816. https://doi.org/10.3390/molecules27061816.

(18) The Non-Neuronal Cholinergic System in the Heart: A Comprehensive Review. *J. Mol. Cell. Cardiol.* **2018**, *125*, 129–139. https://doi.org/10.1016/j.yjmcc.2018.10.013.

(19) Jiang, S.; Li, Y.; Zhang, C.; Zhao, Y.; Bu, G.; Xu, H.; Zhang, Y.-W. M1 Muscarinic Acetylcholine Receptor in Alzheimer's Disease. *Neurosci. Bull.* **2014**, *30* (2), 295–307. https://doi.org/10.1007/s12264-013-1406-z.

(20) Moran, S. P.; Maksymetz, J.; Conn, P. J. Targeting Muscarinic Acetylcholine Receptors for the Treatment of Psychiatric and Neurological Disorders. *Trends Pharmacol. Sci.* **2019**, *40* (12), 1006–1020. https://doi.org/10.1016/j.tips.2019.10.007.

(21) Marcé-Grau, A.; Elorza-Vidal, X.; Pérez-Rius, C.; Ruiz-Nel·lo, A.; Sala-Coromina, J.; Gabau, E.; Estévez, R.; Macaya, A. Muscarinic Acetylcholine Receptor M1 Mutations Causing Neurodevelopmental Disorder and Epilepsy. *Hum. Mutat.* **2021**, *42* (10), 1215–1220. https://doi.org/10.1002/humu.24252.

(22) Edwards, K. M.; Wilson, K. L.; Sadja, J.; Ziegler, M. G.; Mills, P. J. Effects on Blood Pressure and Autonomic Nervous System Function of a 12-Week Exercise or Exercise plus DASH-Diet Intervention in Individuals with Elevated Blood Pressure. *Acta Physiol. Oxf. Engl.* **2011**, *203* (3), 343–350. https://doi.org/10.1111/j.1748-1716.2011.02329.x.

(23) Brook, R. D.; Julius, S. Autonomic Imbalance, Hypertension, and Cardiovascular Risk. *Am. J. Hypertens.* **2000**, *13* (S4), 112S-122S. https://doi.org/10.1016/S0895-7061(00)00228-4.

(24) Shanks, J.; Ramchandra, R. Angiotensin II and the Cardiac Parasympathetic Nervous System in Hypertension. *Int. J. Mol. Sci.* **2021**, *22* (22), 12305. https://doi.org/10.3390/ijms222212305.

(25) Franciosi, S.; Perry, F. K. G.; Roston, T. M.; Armstrong, K. R.; Claydon, V. E.; Sanatani, S. The Role of the Autonomic Nervous System in Arrhythmias and Sudden Cardiac Death. *Auton. Neurosci.* **2017**, *205*, 1–11. https://doi.org/10.1016/j.autneu.2017.03.005.

(26) Herring, N.; Kalla, M.; Paterson, D. J. The Autonomic Nervous System and Cardiac Arrhythmias: Current Concepts and Emerging Therapies. *Nat. Rev. Cardiol.* **2019**, *16* (12), 707–726. https://doi.org/10.1038/s41569-019-0221-2.

(27) Vaseghi, M.; Salavatian, S.; Rajendran, P. S.; Yagishita, D.; Woodward, W. R.; Hamon, D.; Yamakawa, K.; Irie, T.; Habecker, B. A.; Shivkumar, K. Parasympathetic Dysfunction and Antiarrhythmic Effect of Vagal Nerve Stimulation Following Myocardial Infarction. *JCI Insight 2* (16), e86715. https://doi.org/10.1172/jci.insight.86715.

(28) Kong, S.-S.; Liu, J.-J.; Yu, X.-J.; Lu, Y.; Zang, W.-J. Protection against Ischemia-Induced Oxidative Stress Conferred by Vagal Stimulation in the Rat Heart: Involvement of the AMPK-PKC Pathway. *Int. J. Mol. Sci.* **2012**, *13* (11), 14311–14325. https://doi.org/10.3390/ijms131114311.

(29) Beckmann, J.; Lips, K. S. The Non-Neuronal Cholinergic System in Health and Disease. *Pharmacology* **2013**, *92* (5–6), 286–302. https://doi.org/10.1159/000355835.

(30) Kakinuma, Y.; Akiyama, T.; Okazaki, K.; Arikawa, M.; Noguchi, T.; Sato, T. A Non-Neuronal Cardiac Cholinergic System Plays a Protective Role in Myocardium Salvage during Ischemic Insults. *PLOS ONE* **2012**, *7* (11), e50761. https://doi.org/10.1371/journal.pone.0050761.

(31) Saw, E. L.; Pearson, J. T.; Schwenke, D. O.; Munasinghe, P. E.; Tsuchimochi, H.; Rawal, S.; Coffey, S.; Davis, P.; Bunton, R.; Van Hout, I.; Kai, Y.; Williams, M. J. A.; Kakinuma, Y.; Fronius, M.; Katare, R. Activation of the Cardiac Non-Neuronal Cholinergic System Prevents the Development of Diabetes-Associated Cardiovascular Complications. *Cardiovasc. Diabetol.* **2021**, *20* (1), 50. https://doi.org/10.1186/s12933-021-01231-8.

(32) Kakinuma, Y.; Akiyama, T.; Sato, T. Cholinoceptive and Cholinergic Properties of Cardiomyocytes Involving an Amplification Mechanism for Vagal Efferent Effects in Sparsely Innervated Ventricular Myocardium. *FEBS J.* **2009**, *276* (18), 5111–5125. https://doi.org/10.1111/j.1742-4658.2009.07208.x.

(33) Rana, O. R.; Schauerte, P.; Kluttig, R.; Schröder, J. W.; Koenen, R. R.; Weber, C.; Nolte, K. W.; Weis, J.; Hoffmann, R.; Marx, N.; Saygili, E. Acetylcholine as an Age-Dependent Non-Neuronal Source in the Heart. *Auton. Neurosci.* **2010**, *156* (1), 82–89. https://doi.org/10.1016/j.autneu.2010.04.011.

(34) Rocha-Resende, C.; Roy, A.; Resende, R.; Ladeira, M. S.; Lara, A.; de Morais Gomes, E. R.; Prado, V. F.; Gros, R.; Guatimosim, C.; Prado, M. A. M.; Guatimosim, S. Non-Neuronal Cholinergic Machinery Present in Cardiomyocytes Offsets Hypertrophic Signals. *J. Mol. Cell. Cardiol.* **2012**, *53* (2), 206–216. https://doi.org/10.1016/j.yjmcc.2012.05.003.

(35) Oikawa, S.; Iketani, M.; Kakinuma, Y. A Non-Neuronal Cholinergic System Regulates Cellular ATP Levels to Maintain Cell Viability. *Cell. Physiol. Biochem.* **2014**, *34* (3), 781–789. https://doi.org/10.1159/000363042.

(36) Kattar, N.; Flowers, T. Anatomy, Head and Neck, Sympathetic Chain. In *StatPearls*; StatPearls Publishing: Treasure Island (FL), 2022.

(37) Burnstock, G. Autonomic Neurotransmission: 60 Years Since Sir Henry Dale. *Annu. Rev. Pharmacol. Toxicol.* **2009**, *49* (1), 1–30. https://doi.org/10.1146/annurev.pharmtox.052808.102215.

(38) Daubner, S. C.; Le, T.; Wang, S. Tyrosine Hydroxylase and Regulation of Dopamine Synthesis. *Arch. Biochem. Biophys.* **2011**, *508* (1), 1–12. https://doi.org/10.1016/j.abb.2010.12.017.

(39) Fernstrom, J. D.; Fernstrom, M. H. Tyrosine, Phenylalanine, and Catecholamine Synthesis and Function in the Brain. *J. Nutr.* **2007**, *137* (6), 1539S-1547S. https://doi.org/10.1093/jn/137.6.1539S.

(40) Rios, M.; Habecker, B.; Sasaoka, T.; Eisenhofer, G.; Tian, H.; Landis, S.; Chikaraishi, D.; Roffler-Tarlov, S. Catecholamine Synthesis Is Mediated by Tyrosinase in the Absence of Tyrosine Hydroxylase. *J. Neurosci.* **1999**, *19* (9), 3519–3526. https://doi.org/10.1523/JNEUROSCI.19-09-03519.1999.

(41) Bernstein, A. I.; Stout, K. A.; Miller, G. W. The Vesicular Monoamine Transporter 2: An Underexplored Pharmacological Target. *Neurochem. Int.* **2014**, *73*, 89–97. https://doi.org/10.1016/j.neuint.2013.12.003.

(42) Nickell, J. R.; Siripurapu, K. B.; Vartak, A.; Crooks, P. A.; Dwoskin, L. P. The Vesicular Monoamine Transporter-2: An Important Pharmacological Target for the Discovery of Novel Therapeutics to Treat Methamphetamine Abuse. *Adv. Pharmacol. San Diego Calif* **2014**, *69*, 71–106. https://doi.org/10.1016/B978-0-12-420118-7.00002-0.

(43) Madrigal Verdú, M. P.; Portalés, A.; SanJuan, M. P.; Jurado, S. Postsynaptic SNARE Proteins: Role in Synaptic Transmission and Plasticity. *Neuroscience* **2019**, *420*, 12–21. https://doi.org/10.1016/j.neuroscience.2018.11.012.

(44) Cohen, R. S. Cell Biology of the Synapse. In *Neuroscience in the 21st Century: From Basic to Clinical*; Pfaff, D. W., Ed.; Springer: New York, NY, 2013; pp 309–349. https://doi.org/10.1007/978-1-4614-1997-6_15.

(45) Hussain, L. S.; Reddy, V.; Maani, C. V. Physiology, Noradrenergic Synapse. In *StatPearls*; StatPearls Publishing: Treasure Island (FL), 2022.

(46) Zhang, J.; Simpson, P. C.; Jensen, B. C. Cardiac A1A-Adrenergic Receptors: Emerging Protective Roles in Cardiovascular Diseases. *Am. J. Physiol.-Heart Circ. Physiol.* **2021**, *320* (2), H725–H733. https://doi.org/10.1152/ajpheart.00621.2020.

(47) Bers, D. M. Adrenergic Fight-or-Flight. *Circ. Res.* **2015**, *117* (9), 747–749. https://doi.org/10.1161/CIRCRESAHA.115.307397.

(48) Perez, D. M. A1-Adrenergic Receptors in Neurotransmission, Synaptic Plasticity, and Cognition. *Front. Pharmacol.* **2020**, *11*.

(49) Mitrano, D. A.; Schroeder, J. P.; Smith, Y.; Cortright, J. J.; Bubula, N.; Vezina, P.; Weinshenker, D. Alpha-1 Adrenergic Receptors Are Localized on Presynaptic Elements in the Nucleus Accumbens and Regulate Mesolimbic Dopamine Transmission. *Neuropsychopharmacology* **2012**, *37* (9), 2161–2172. https://doi.org/10.1038/npp.2012.68.

(50) Ladage, D.; Schwinger, R. H. G.; Brixius, K. Cardio-Selective Beta-Blocker: Pharmacological Evidence and Their Influence on Exercise Capacity. *Cardiovasc. Ther.* **2013**, *31* (2), 76–83. https://doi.org/10.1111/j.1755-5922.2011.00306.x.

(51) Lynch, G. S.; Ryall, J. G. Role of β-Adrenoceptor Signaling in Skeletal Muscle: Implications for Muscle Wasting and Disease. *Physiol. Rev.* **2008**, *88* (2), 729–767. https://doi.org/10.1152/physrev.00028.2007.

(52) Woo, A. Y. H.; Xiao, R. β-Adrenergic Receptor Subtype Signaling in Heart: From Bench to Bedside. *Acta Pharmacol. Sin.* **2012**, *33* (3), 335–341. https://doi.org/10.1038/aps.2011.201.

(53) Masuo, K. Roles of Beta2- and Beta3-Adrenoceptor Polymorphisms in Hypertension and Metabolic Syndrome. *Int. J. Hypertens.* **2010**, *2010*, 832821. https://doi.org/10.4061/2010/832821.

(54) Schena, G.; Caplan, M. J. Everything You Always Wanted to Know about B3-AR * (* But Were Afraid to Ask). *Cells* **2019**, *8* (4), 357. https://doi.org/10.3390/cells8040357.

(55) Woodcock, E. A.; Du, X.-J.; Reichelt, M. E.; Graham, R. M. Cardiac A1-Adrenergic Drive in Pathological Remodelling. *Cardiovasc. Res.* **2008**, *77* (3), 452–462. https://doi.org/10.1093/cvr/cvm078.

(56) Weis, W. I.; Kobilka, B. K. The Molecular Basis of G Protein–Coupled Receptor Activation. *Annu. Rev. Biochem.* **2018**, *87*, 897–919. https://doi.org/10.1146/annurev-biochem-060614-033910.

(57) O'Connell, T. D.; Jensen, B. C.; Baker, A. J.; Simpson, P. C. Cardiac Alpha1-Adrenergic Receptors: Novel Aspects of Expression, Signaling Mechanisms, Physiologic Function, and Clinical Importance. *Pharmacol. Rev.* **2014**, *66* (1), 308–333. https://doi.org/10.1124/pr.112.007203.

(58) Wachter, S. B.; Gilbert, E. M. Beta-Adrenergic Receptors, from Their Discovery and Characterization through Their Manipulation to Beneficial Clinical Application. *Cardiology* **2012**, *122* (2), 104–112. https://doi.org/10.1159/000339271.

(59) Lucia, C. de; Eguchi, A.; Koch, W. J. New Insights in Cardiac β-Adrenergic Signaling During Heart Failure and Aging. *Front. Pharmacol.* **2018**, *9*.

(60) Striessnig, J.; Pinggera, A.; Kaur, G.; Bock, G.; Tuluc, P. L-Type Ca2+ Channels in Heart and Brain. *Wiley Interdiscip. Rev. Membr. Transp. Signal.* **2014**, *3* (2), 15–38. https://doi.org/10.1002/wmts.102.

(61) Kamp, T. J.; Hell, J. W. Regulation of Cardiac L-Type Calcium Channels by Protein Kinase A and Protein Kinase C. *Circ. Res.* **2000**, *87* (12), 1095–1102. https://doi.org/10.1161/01.RES.87.12.1095.

(62) Miyamoto, T.; Kawada, T.; Yanagiya, Y.; Akiyama, T.; Kamiya, A.; Mizuno, M.; Takaki, H.; Sunagawa, K.; Sugimachi, M. Contrasting Effects of Presynaptic A2-Adrenergic Autoinhibition and Pharmacologic Augmentation of Presynaptic Inhibition on Sympathetic Heart Rate Control. *Am. J. Physiol.-Heart Circ. Physiol.* **2008**, *295* (5), H1855–H1866. https://doi.org/10.1152/ajpheart.522.2008.

(63) Giovannitti, J. A.; Thoms, S. M.; Crawford, J. J. Alpha-2 Adrenergic Receptor Agonists: A Review of Current Clinical Applications. *Anesth. Prog.* **2015**, *62* (1), 31–38. https://doi.org/10.2344/0003-3006-62.1.31.

(64) Charkoudian, N.; Rabbitts, J. A. Sympathetic Neural Mechanisms in Human Cardiovascular Health and Disease. *Mayo Clin. Proc.* **2009**, *84* (9), 822–830.

(65) Schwartz, J. W.; Blakely, R. D.; DeFelice, L. J. Binding and Transport in Norepinephrine Transporters: REAL-TIME, SPATIALLY RESOLVED ANALYSIS IN SINGLE CELLS USING A FLUORESCENT SUBSTRATE *. *J. Biol. Chem.* **2003**, *278* (11), 9768–9777. https://doi.org/10.1074/jbc.M209824200.

(66) Bönisch, H.; Brüss, M. The Norepinephrine Transporter in Physiology and Disease. In *Neurotransmitter Transporters*; Sitte, H. H., Freissmuth, M., Eds.; Handbook of Experimental Pharmacology; Springer: Berlin, Heidelberg, 2006; pp 485–524. https://doi.org/10.1007/3-540-29784-7_20.

(67) Mandela, P.; Ordway, G. A. The Norepinephrine Transporter and Its Regulation. *J. Neurochem.* **2006**, *97* (2), 310–333. https://doi.org/10.1111/j.1471-4159.2006.03717.x.

(68) Joers, V.; Emborg, M. E. Modeling and Imaging Cardiac Sympathetic Neurodegeneration in Parkinson's Disease. *Am. J. Nucl. Med. Mol. Imaging* **2014**, *4* (2), 125–159.

(69) Sved, A. F. Effect of Monoamine Oxidase Inhibition on Catecholamine Levels: Evidence for Synthesis but Not Storage of Epinephrine in Rat Spinal Cord. *Brain Res.* **1990**, *512* (2), 253–258. https://doi.org/10.1016/0006-8993(90)90634-N.

(70) Bortolato, M.; Godar, S. C.; Alzghoul, L.; Zhang, J.; Darling, R. D.; Simpson, K. L.; Bini, V.; Chen, K.; Wellman, C. L.; Lin, R. C. S.; Shih, J. C. Monoamine Oxidase A and A/B Knockout Mice Display Autistic-like Features. *Int. J. Neuropsychopharmacol. Off. Sci. J. Coll. Int. Neuropsychopharmacol. CINP* **2013**, *16* (4), 869–888. https://doi.org/10.1017/S1461145712000715.

(71) Chen, K.; Holschneider, D. P.; Wu, W.; Rebrin, I.; Shih, J. C. A Spontaneous Point Mutation Produces Monoamine Oxidase A/B Knock-out Mice with Greatly Elevated Monoamines and Anxiety-like Behavior*♦. *J. Biol. Chem.* **2004**, *279* (38), 39645–39652. https://doi.org/10.1074/jbc.M405550200.

(72) Bell, C.; Kushinsky, R. Involvement of Uptake1 and Uptake2 in Terminating the Cardiovascular Activity of Noradrenaline in Normotensive and Genetically Hypertensive Rats. *J. Physiol.* **1978**, *283* (1), 41–51. https://doi.org/10.1113/jphysiol.1978.sp012487.

(73) Gasser, P. J. Roles for the Uptake2 Transporter OCT3 in Regulation of Dopaminergic Neurotransmission and Behavior. *Neurochem. Int.* **2019**, *123*, 46–49. https://doi.org/10.1016/j.neuint.2018.07.008.

(74) Grube, M.; Ameling, S.; Noutsias, M.; Köck, K.; Triebel, I.; Bonitz, K.; Meissner, K.; Jedlitschky, G.; Herda, L. R.; Reinthaler, M.; Rohde, M.; Hoffmann, W.; Kühl, U.; Schultheiss, H.-P.; Völker, U.; Felix, S. B.; Klingel, K.; Kandolf, R.; Kroemer, H. K. Selective Regulation of Cardiac Organic Cation Transporter Novel Type 2 (OCTN2) in

Dilated Cardiomyopathy. *Am. J. Pathol.* **2011**, *178* (6), 2547–2559. https://doi.org/10.1016/j.ajpath.2011.02.020.

(75) Iversen, L. l. The Uptake of Catechol Amines at High Perfusion Concentrations in the Rat Isolated Heart: A Novel Catechol Amine Uptake Process. *Br. J. Pharmacol.* **1997**, *120* (S1), 264–266. https://doi.org/10.1111/j.1476-5381.1997.tb06806.x.

(76) Magaribuchi, T.; Hama, T.; Kurahashi, K.; Fujiwara, M. Effects of Extraneuronal Uptake Inhibitors on the Positive Chronotropic Response to Isoprenaline and on the Accumulation of Isoprenaline in Perfused Rat Heart after Inhibition of Catechol-O-Methyl Transferase. *Naunyn. Schmiedebergs Arch. Pharmacol.* **1987**, *335* (2), 123–128. https://doi.org/10.1007/BF00177712.

(77) Yu, M.; Bozek, J.; Kagan, M.; Guaraldi, M.; Silva, P.; Azure, M.; Onthank, D.; Robinson, S. P. Cardiac Retention of PET Neuronal Imaging Agent LMI1195 in Different Species: Impact of Norepinephrine Uptake-1 and -2 Transporters. *Nucl. Med. Biol.* **2013**, *40* (5), 682–688. https://doi.org/10.1016/j.nucmedbio.2013.03.003.

(78) Borovac, J. A.; D'Amario, D.; Bozic, J.; Glavas, D. Sympathetic Nervous System Activation and Heart Failure: Current State of Evidence and the Pathophysiology in the Light of Novel Biomarkers. *World J. Cardiol.* **2020**, *12* (8), 373–408. https://doi.org/10.4330/wjc.v12.i8.373.

(79) Zhang, D. Y.; Anderson, A. S. The Sympathetic Nervous System and Heart Failure. *Cardiol. Clin.* **2014**, *32* (1), 33–vii. https://doi.org/10.1016/j.ccl.2013.09.010.

(80) Backs, J.; Haunstetter, A.; Gerber, S. H.; Metz, J.; Borst, M. M.; Strasser, R. H.; Kübler, W.; Haass, M. The Neuronal Norepinephrine Transporter in Experimental Heart Failure:

Evidence for a Posttranscriptional Downregulation. *J. Mol. Cell. Cardiol.* **2001**, *33* (3), 461–472. https://doi.org/10.1006/jmcc.2000.1319.

(81) Leclerc, K. M.; Levy, W. C. The Role of Norepinephrine in Exercise Impairment in Congestive Heart Failure. *Congest. Heart Fail.* **2003**, *9* (1), 25–28. https://doi.org/10.1111/j.1527-5299.2002.00948.x.

(82) Watson, A. M. D.; Hood, S. G.; Ramchandra, R.; McAllen, R. M.; May, C. N. INCREASED CARDIAC SYMPATHETIC NERVE ACTIVITY IN HEART FAILURE IS NOT DUE TO DESENSITIZATION OF THE ARTERIAL BAROREFLEX. *Am. J. Physiol. Heart Circ. Physiol.* **2007**, *293* (1), H798–H804. https://doi.org/10.1152/ajpheart.00147.2007.

(83) Patel, K. P.; Zhang, K.; Carmines, P. K. Norepinephrine Turnover in Peripheral Tissues of Rats with Heart Failure. *Am. J. Physiol.-Regul. Integr. Comp. Physiol.* **2000**, *278* (3), R556–R562. https://doi.org/10.1152/ajpregu.2000.278.3.R556.

(84) Böhm, M.; Castellano, M.; Flesch, M.; Maack, C.; Moll, M.; Paul, M.; Schiffer, F.; Zolk, O. Chamber-Specific Alterations of Norepinephrine Uptake Sites in Cardiac Hypertrophy. *Hypertension* **1998**, *32* (5), 831–837. https://doi.org/10.1161/01.HYP.32.5.831.

(85) Parrish, D. C.; Alston, E. N.; Rohrer, H.; Nkadi, P.; Woodward, W. R.; Schütz, G.; Habecker, B. A. Infarction-Induced Cytokines Cause Local Depletion of Tyrosine Hydroxylase in Cardiac Sympathetic Nerves. *Exp. Physiol.* **2010**, *95* (2), 304–314. https://doi.org/10.1113/expphysiol.2009.049965.

(86) Ganguly, P. K.; Dhalla, K. S.; Innes, I. R.; Beamish, R. E.; Dhalla, N. S. Altered Norepinephrine Turnover and Metabolism in Diabetic Cardiomyopathy. *Circ. Res.* **1986**, *59* (6), 684–693. https://doi.org/10.1161/01.RES.59.6.684.

(87) Lymperopoulos, A.; Rengo, G.; Koch, W. J. The Adrenergic Nervous System in Heart Failure: Pathophysiology and Therapy. *Circ. Res.* **2013**, *113* (6). https://doi.org/10.1161/CIRCRESAHA.113.300308.

(88) Goldberger, J. J.; Arora, R.; Buckley, U.; Shivkumar, K. Autonomic Nervous System Dysfunction. *J. Am. Coll. Cardiol.* **2019**, *73* (10), 1189–1206. https://doi.org/10.1016/j.jacc.2018.12.064.

(89) Zhou, J. Norepinephrine Transporter Inhibitors and Their Therapeutic Potential. *Drugs Future* **2004**, *29* (12), 1235–1244.

(90) Werner, R. A.; Rischpler, C.; Onthank, D.; Lapa, C.; Robinson, S.; Samnick, S.; Javadi, M.; Schwaiger, M.; Nekolla, S. G.; Higuchi, T. Retention Kinetics of the 18F-Labeled Sympathetic Nerve PET Tracer LMI1195: Comparison with 11C-Hydroxyephedrine and 123I-MIBG. *J. Nucl. Med. Off. Publ. Soc. Nucl. Med.* **2015**, *56* (9), 1429–1433. https://doi.org/10.2967/jnumed.115.158493.

(91) Zelt, J.; Renaud, J.; Mielniczuk, L.; Garrard, L.; Orlandi, C.; Robinson, S.; Beanlands, R.; DeKemp, R. Equivalent Regional Distribution of Fluorine-18 Flurobenguan and Carbon-11 Hydroxyephedrine for PET Imaging of Sympathetic Innervation. *J. Nucl. Med.* **2019**, *60* (supplement 1), 32–32.

(92) Dimitriu-Leen, A. C.; Scholte, A. J. H. A.; Jacobson, A. F. 123I-MIBG SPECT for Evaluation of Patients with Heart Failure. *J. Nucl. Med.* **2015**, *56* (Supplement 4), 25S-30S. https://doi.org/10.2967/jnumed.115.157503.

(93) Hasdemir, C.; Aydin, H. H.; Celik, H. A.; Simsek, E.; Payzin, S.; Kayikcioglu, M.; Aydin, M.; Kultursay, H.; Can, L. H. Transcriptional Profiling of Septal Wall of the Right

Ventricular Outflow Tract in Patients with Idiopathic Ventricular Arrhythmias. *Pacing Clin. Electrophysiol.* **2010**, *33* (2), 159–167. https://doi.org/10.1111/j.1540-8159.2009.02606.x.

(94) Sch, äfers M.; Lerch, H.; Wichter, T.; Rhodes, C. G.; Lammertsma, A. A.; Borggrefe, M.; Hermansen, F.; Schober, O.; Breithardt, G.; Camici, P. G. Cardiac Sympathetic Innervation in Patients with Idiopathic Right Ventricular Outflow Tract Tachycardia. *J. Am. Coll. Cardiol.* **1998**, *32* (1), 181–186. https://doi.org/10.1016/S0735-1097(98)00213-7.

(95) Haddad, F.; Doyle, R.; Murphy, D. J.; Hunt, S. A. Right Ventricular Function in Cardiovascular Disease, Part II. *Circulation* **2008**, *117* (13), 1717–1731. https://doi.org/10.1161/CIRCULATIONAHA.107.653584.

(96) Manabe, O.; Kikuchi, T.; Scholte, A. J. H. A.; El Mahdiui, M.; Nishii, R.; Zhang, M.-R.; Suzuki, E.; Yoshinaga, K. Radiopharmaceutical Tracers for Cardiac Imaging. *J. Nucl. Cardiol.* **2018**, *25* (4), 1204–1236. https://doi.org/10.1007/s12350-017-1131-5.

(97) Fesas, A.; Giannoula, E.; Vrachimis, A.; Doumas, A.; Wenning, C.; Didagelos, M.; Iakovou, I. Cardiac Autonomic Nervous System and Ventricular Arrhythmias: The Role of Radionuclide Molecular Imaging. *Diagnostics* **2021**, *11* (7), 1273. https://doi.org/10.3390/diagnostics11071273.

(98) Schroeder, C.; Jordan, J. Norepinephrine Transporter Function and Human Cardiovascular Disease. *Am. J. Physiol.-Heart Circ. Physiol.* **2012**, *303* (11), H1273–H1282. https://doi.org/10.1152/ajpheart.00492.2012.

(99) Grupper, A.; Gewirtz, H.; Kushwaha, S. Reinnervation Post-Heart Transplantation. *Eur. Heart J.* **2018**, *39* (20), 1799–1806. https://doi.org/10.1093/eurheartj/ehw604.

(100) Münch, G.; Rosport, K.; Bültmann, A.; Baumgartner, C.; Li, Z.; Laacke, L.; Ungerer, M. Cardiac Overexpression of the Norepinephrine Transporter Uptake-1 Results in Marked

Improvement of Heart Failure. *Circ. Res.* **2005**, *97* (9), 928–936. https://doi.org/10.1161/01.RES.0000186685.46829.E5.

(101) Cleland, J. G. F.; Torabi, A.; Khan, N. K. Epidemiology and Management of Heart Failure and Left Ventricular Systolic Dysfunction in the Aftermath of a Myocardial Infarction. *Heart* **2005**, *91* (suppl 2), ii7–ii13. https://doi.org/10.1136/hrt.2005.062026.

(102) McMurray, J. J. V.; Ezekowitz, J. A.; Lewis, B. S.; Gersh, B. J.; van Diepen, S.; Amerena, J.; Bartunek, J.; Commerford, P.; Oh, B.-H.; Harjola, V.-P.; Al-Khatib, S. M.; Hanna, M.; Alexander, J. H.; Lopes, R. D.; Wojdyla, D. M.; Wallentin, L.; Granger, C. B.; null, null. Left Ventricular Systolic Dysfunction, Heart Failure, and the Risk of Stroke and Systemic Embolism in Patients With Atrial Fibrillation. *Circ. Heart Fail.* **2013**, *6* (3), 451–460. https://doi.org/10.1161/CIRCHEARTFAILURE.112.000143.

(103) Foody, J. M.; Farrell, M. H.; Krumholz, H. M. β-Blocker Therapy in Heart FailureScientific Review. *JAMA* **2002**, *287* (7), 883–889. https://doi.org/10.1001/jama.287.7.883.

(104) Domanski, M. J.; Krause-Steinrauf, H.; Massie, B. M.; Deedwania, P.; Follmann, D.; Kovar, D.; Murray, D.; Oren, R.; Rosenberg, Y.; Young, J.; Zile, M.; Eichhorn, E.; for the Best Investigators. A Comparative Analysis of the Results from 4 Trials of β-Blocker Therapy for Heart Failure: BEST, CIBIS-II, MERIT-HF, and COPERNICUS. *J. Card. Fail.* **2003**, *9* (5), 354–363. https://doi.org/10.1054/S1071-9164(03)00133-7.

(105) Ho, D.; Yan, L.; Iwatsubo, K.; Vatner, D. E.; Vatner, S. F. Modulation of β-Adrenergic Receptor Signaling in Heart Failure and Longevity: Targeting Adenylyl Cyclase Type 5. *Heart Fail. Rev.* **2010**, *15* (5), 495–512. https://doi.org/10.1007/s10741-010-9183-5.

(106) Plouffe, B.; Thomsen, A. R. B.; Irannejad, R. Emerging Role of Compartmentalized G Protein-Coupled Receptor Signaling in the Cardiovascular Field. *ACS Pharmacol. Transl. Sci.* **2020**, *3* (2), 221–236. https://doi.org/10.1021/acsptsci.0c00006.

(107) Smrcka, A. V. G Protein Bγ Subunits: Central Mediators of G Protein-Coupled Receptor Signaling. *Cell. Mol. Life Sci. CMLS* **2008**, *65* (14), 2191–2214. https://doi.org/10.1007/s00018-008-8006-5.

(108) He, J.-Q.; Balijepalli, R. C.; Haworth, R. A.; Kamp, T. J. Crosstalk of β-Adrenergic Receptor Subtypes Through Gi Blunts β-Adrenergic Stimulation of L-Type Ca2+ Channels in Canine Heart Failure. *Circ. Res.* **2005**, *97* (6), 566–573. https://doi.org/10.1161/01.RES.0000181160.31851.05.

(109) Vasudevan, N. T.; Mohan, M. L.; Goswami, S. K.; Naga Prasad, S. V. Regulation of β-Adrenergic Receptor Function. *Cell Cycle* **2011**, *10* (21), 3684–3691. https://doi.org/10.4161/cc.10.21.18042.

(110) Taylor, C. J.; Ryan, R.; Nichols, L.; Gale, N.; Hobbs, F. R.; Marshall, T. Survival Following a Diagnosis of Heart Failure in Primary Care. *Fam. Pract.* **2017**, *34* (2), 161–168. https://doi.org/10.1093/fampra/cmw145.

(111) Bloom, M. W.; Greenberg, B.; Jaarsma, T.; Januzzi, J. L.; Lam, C. S. P.; Maggioni, A. P.; Trochu, J.-N.; Butler, J. Heart Failure with Reduced Ejection Fraction. *Nat. Rev. Dis. Primer* **2017**, *3* (1), 1–19. https://doi.org/10.1038/nrdp.2017.58.

(112) Murphy, S. P.; Ibrahim, N. E.; Januzzi, J. L., Jr. Heart Failure With Reduced Ejection Fraction: A Review. *JAMA* **2020**, *324* (5), 488–504. https://doi.org/10.1001/jama.2020.10262.

(113) Savarese, G.; Stolfo, D.; Sinagra, G.; Lund, L. H. Heart Failure with Mid-Range or Mildly Reduced Ejection Fraction. *Nat. Rev. Cardiol.* **2022**, *19* (2), 100–116. https://doi.org/10.1038/s41569-021-00605-5.

(114) Borlaug, B. A.; Paulus, W. J. Heart Failure with Preserved Ejection Fraction: Pathophysiology, Diagnosis, and Treatment. *Eur. Heart J.* **2011**, *32* (6), 670–679. https://doi.org/10.1093/eurheartj/ehq426.

(115) ANDRONIC, A. A.; MIHAILA, S.; CINTEZA, M. Heart Failure with Mid-Range Ejection Fraction – a New Category of Heart Failure or Still a Gray Zone. *Mædica* **2016**, *11* (4), 320–324.

(116) Aziz, F.; TK, L.-A.; Enweluzo, C.; Dutta, S.; Zaeem, M. Diastolic Heart Failure: A Concise Review. *J. Clin. Med. Res.* **2013**, *5* (5), 327–334. https://doi.org/10.4021/jocmr1532w.

(117) Buono, M. G. D.; Buckley, L.; Abbate, A. Primary and Secondary Diastolic Dysfunction in Heart Failure With Preserved Ejection Fraction. *Am. J. Cardiol.* **2018**, *122* (9), 1578–1587. https://doi.org/10.1016/j.amjcard.2018.07.012.

(118) Patten, R. D.; Hall-Porter, M. R. Small Animal Models of Heart Failure. *Circ. Heart Fail.* **2009**, *2* (2), 138–144. https://doi.org/10.1161/CIRCHEARTFAILURE.108.839761.

(119) Riehle, C.; Bauersachs, J. Small Animal Models of Heart Failure. *Cardiovasc. Res.* **2019**, *115* (13), 1838–1849. https://doi.org/10.1093/cvr/cvz161.

(120) Rapp, J. P.; Garrett, M. R. Will the Real Dahl S Rat Please Stand Up? *Am. J. Physiol. - Ren. Physiol.* **2019**, *317* (5), F1231–F1240. https://doi.org/10.1152/ajprenal.00359.2019.

(121) Cowley, A. W.; Stoll, M.; Greene, A. S.; Kaldunski, M. L.; Roman, R. J.; Tonellato, P. J.; Schork, N. J.; Dumas, P.; Jacob, H. J. Genetically Defined Risk of Salt Sensitivity in an

Intercross of Brown Norway and Dahl S Rats. *Physiol. Genomics* **2000**, *2* (3), 107–115. https://doi.org/10.1152/physiolgenomics.2000.2.3.107.

(122) Klotz, S.; Hay, I.; Zhang, G.; Maurer, M.; Wang, J.; Burkhoff, D. Development of Heart Failure in Chronic Hypertensive Dahl Rats. *Hypertension* **2006**, *47* (5), 901–911. https://doi.org/10.1161/01.HYP.0000215579.81408.8e.

(123) Holland, R.; Rechel, B.; Stepien, K.; Harvey, I.; Brooksby, I. Patients' Self-Assessed Functional Status in Heart Failure by New York Heart Association Class: A Prognostic Predictor of Hospitalizations, Quality of Life and Death. *J. Card. Fail.* **2010**, *16* (2), 150–156. https://doi.org/10.1016/j.cardfail.2009.08.010.

(124) Bonow, R. O.; Bennett, S.; Casey, D. E.; Ganiats, T. G.; Hlatky, M. A.; Konstam, M. A.; Lambrew, C. T.; Normand, S.-L. T.; Pi, ña I. L.; Radford, M. J.; Smith, A. L.; Stevenson, L. W.; Bonow, R. O.; Bennett, S. J.; Burke, G.; Eagle, K. A.; Krumholz, H. M.; Lambrew, C. T.; Linderbaum, J.; Masoudi, F. A.; Normand, S.-L. T.; Ritchie, J. L.; Rumsfeld, J. S.; Spertus, J. A. ACC/AHA Clinical Performance Measures for Adults With Chronic Heart Failure. *J. Am. Coll. Cardiol.* **2005**, *46* (6), 1144–1178. https://doi.org/10.1016/j.jacc.2005.07.012.

(125) Inamdar, A. A.; Inamdar, A. C. Heart Failure: Diagnosis, Management and Utilization. *J. Clin. Med.* **2016**, *5* (7), 62. https://doi.org/10.3390/jcm5070062.

(126) McCullough, P. A.; Nowak, R. M.; McCord, J.; Hollander, J. E.; Herrmann, H. C.; Steg, P. G.; Duc, P.; Westheim, A.; Omland, T.; Knudsen, C. W.; Storrow, A. B.; Abraham, W. T.; Lamba, S.; Wu, A. H. B.; Perez, A.; Clopton, P.; Krishnaswamy, P.; Kazanegra, R.; Maisel, A. S. B-Type Natriuretic Peptide and Clinical Judgment in Emergency Diagnosis of Heart

Failure. *Circulation* **2002**, *106* (4), 416–422. https://doi.org/10.1161/01.CIR.0000025242.79963.4C.

(127) Braunwald, E. Biomarkers in Heart Failure. *N. Engl. J. Med.* **2008**, *358* (20), 2148–2159. https://doi.org/10.1056/NEJMra0800239.

(128) Ozturk, T. C.; Unluer, E.; Denizbasi, A.; Guneysel, O.; Onur, O. Can NT-ProBNP Be Used as a Criterion for Heart Failure Hospitalization in Emergency Room? *J. Res. Med. Sci. Off. J. Isfahan Univ. Med. Sci.* **2011**, *16* (12), 1564–1571.

(129) Cao, Z.; Jia, Y.; Zhu, B. BNP and NT-ProBNP as Diagnostic Biomarkers for Cardiac Dysfunction in Both Clinical and Forensic Medicine. *Int. J. Mol. Sci.* **2019**, *20* (8), 1820. https://doi.org/10.3390/ijms20081820.

(130) Gaggin, H. K.; Januzzi, J. L. Biomarkers and Diagnostics in Heart Failure. *Biochim. Biophys. Acta BBA - Mol. Basis Dis.* **2013**, *1832* (12), 2442–2450. https://doi.org/10.1016/j.bbadis.2012.12.014.

(131) Mueller-Lenke, N.; Rudez, J.; Staub, D.; Laule-Kilian, K.; Klima, T.; Perruchoud, A. P.; Mueller, C. Use of Chest Radiography in the Emergency Diagnosis of Acute Congestive Heart Failure. *Heart* **2006**, *92* (5), 695–696. https://doi.org/10.1136/hrt.2005.074583.

(132) Oh, J. K. Echocardiography in Heart Failure: Beyond Diagnosis. *Eur. J. Echocardiogr.* **2007**, *8* (1), 4–14. https://doi.org/10.1016/j.euje.2006.09.002.

(133) Hawkins, N. M.; Petrie, M. C.; Jhund, P. S.; Chalmers, G. W.; Dunn, F. G.; McMurray, J. J. V. Heart Failure and Chronic Obstructive Pulmonary Disease: Diagnostic Pitfalls and Epidemiology. *Eur. J. Heart Fail.* **2009**, *11* (2), 130–139. https://doi.org/10.1093/eurjhf/hfn013.

(134) Mohebali, D.; Kittleson, M. M. Remote Monitoring in Heart Failure: Current and Emerging Technologies in the Context of the Pandemic. *Heart* **2021**, *107* (5), 366–372. https://doi.org/10.1136/heartjnl-2020-318062.

(135) Li, Y.; Zhang, W.; Wu, H.; Liu, G. Advanced Tracers in PET Imaging of Cardiovascular Disease. *BioMed Res. Int.* **2014**, *2014*. https://doi.org/10.1155/2014/504532.

(136) Dollé, F. Carbon-11 and Fluorine-18 Chemistry Devoted to Molecular Probes for Imaging the Brain with Positron Emission Tomography. *J. Label. Compd. Radiopharm.* **2013**, *56* (3–4), 65–67. https://doi.org/10.1002/jlcr.3037.

(137) Schmor, P. Review of Cyclotrons for the Production of Radioactive Isotopes for Medical and Industrial Applications. In *Reviews of Accelerator Science and Technology*; WORLD SCIENTIFIC, 2012; pp 103–116. https://doi.org/10.1142/9789814383998_0005.

(138) Conti, M.; Eriksson, L. Physics of Pure and Non-Pure Positron Emitters for PET: A Review and a Discussion. *EJNMMI Phys.* **2016**, *3* (1), 8. https://doi.org/10.1186/s40658-016-0144-5.

(139) Le Bars, D. Fluorine-18 and Medical Imaging: Radiopharmaceuticals for Positron Emission Tomography. *J. Fluor. Chem.* **2006**, *127* (11), 1488–1493. https://doi.org/10.1016/j.jfluchem.2006.09.015.

(140) Vermeulen, I.; Isin, E. M.; Barton, P.; Cillero-Pastor, B.; Heeren, R. M. A. Multimodal Molecular Imaging in Drug Discovery and Development. *Drug Discov. Today* **2022**, *27* (8), 2086–2099. https://doi.org/10.1016/j.drudis.2022.04.009.

(141) Ingwall, J. S. Energy Metabolism in Heart Failure and Remodelling. *Cardiovasc. Res.* **2009**, *81* (3), 412–419. https://doi.org/10.1093/cvr/cvn301.

(142) Tran, D. H.; Wang, Z. V. Glucose Metabolism in Cardiac Hypertrophy and Heart Failure. *J. Am. Heart Assoc.* **2019**, *8* (12), e012673. https://doi.org/10.1161/JAHA.119.012673.

(143) Taegtmeyer, H. Tracing Cardiac Metabolism In Vivo: One Substrate at a Time. *J. Nucl. Med.* **2010**, *51* (Supplement 1), 80S-87S. https://doi.org/10.2967/jnumed.109.068205.

(144) Barrio, J. R.; Huang, S.-C.; Satyamurthy, N.; Scafoglio, C. S.; Yu, A. S.; Alavi, A.; Krohn, K. A. Does 2-FDG PET Accurately Reflect Quantitative In Vivo Glucose Utilization? *J. Nucl. Med.* **2020**, *61* (6), 931–937. https://doi.org/10.2967/jnumed.119.237446.

(145) Minamimoto, R. Series of Myocardial FDG Uptake Requiring Considerations of Myocardial Abnormalities in FDG-PET/CT. *Jpn. J. Radiol.* **2021**, *39* (6), 540–557. https://doi.org/10.1007/s11604-021-01097-6.

(146) Driessen, R. S.; Raijmakers, P. G.; Stuijfzand, W. J.; Knaapen, P. Myocardial Perfusion Imaging with PET. *Int. J. Cardiovasc. Imaging* **2017**, *33* (7), 1021–1031. https://doi.org/10.1007/s10554-017-1084-4.

(147) Chen, X.; Werner, R. A.; Javadi, M. S.; Maya, Y.; Decker, M.; Lapa, C.; Herrmann, K.; Higuchi, T. Radionuclide Imaging of Neurohormonal System of the Heart. *Theranostics* **2015**, *5* (6), 545–558. https://doi.org/10.7150/thno.10900.

(148) Le Guludec, D.; Delforge, J.; Dollé, F. Imaging the Parasympathetic Cardiac Innervation with PET. In *Autonomic Innervation of the Heart: Role of Molecular Imaging*; Slart, R. H. J. A., Tio, R. A., Elsinga, P. H., Schwaiger, M., Eds.; Springer: Berlin, Heidelberg, 2015; pp 111–135. https://doi.org/10.1007/978-3-662-45074-1_6.

(149) Gjerløff, T.; Jakobsen, S.; Nahimi, A.; Munk, O. L.; Bender, D.; Alstrup, A. K. O.; Vase, K. H.; Hansen, S. B.; Brooks, D. J.; Borghammer, P. In Vivo Imaging of Human Acetylcholinesterase Density in Peripheral Organs Using 11C-Donepezil: Dosimetry,

Biodistribution, and Kinetic Analyses. *J. Nucl. Med.* **2014**, *55* (11), 1818–1824. https://doi.org/10.2967/jnumed.114.143859.

(150) Kikuchi, T.; Okamura, T.; Zhang, M.-R.; Irie, T. PET Probes for Imaging Brain Acetylcholinesterase. *J. Label. Compd. Radiopharm.* **2013**, *56* (3–4), 172–179. https://doi.org/10.1002/jlcr.3002.

(151) Smart, K.; Naganawa, M.; Baldassarri, S. R.; Nabulsi, N.; Ropchan, J.; Najafzadeh, S.; Gao, H.; Navarro, A.; Barth, V.; Esterlis, I.; Cosgrove, K. P.; Huang, Y.; Carson, R. E.; Hillmer, A. T. PET Imaging Estimates of Regional Acetylcholine Concentration Variation in Living Human Brain. *Cereb. Cortex* **2021**, *31* (6), 2787–2798. https://doi.org/10.1093/cercor/bhaa387.

(152) Mulholland, G. K.; Wieland, D. M.; Kilbourn, M. R.; Frey, K. A.; Sherman, P. S.; Carey, J. E.; Kuhl, D. E. [18F]Fluoroethoxy-Benzovesamicol, a PET Radiotracer for the Vesicular Acetylcholine Transporter and Cholinergic Synapses. *Synapse* **1998**, *30* (3), 263–274. https://doi.org/10.1002/(SICI)1098-2396(199811)30:3<263::AID-SYN4>3.0.CO;2-9.

(153) Aghourian, M.; Legault-Denis, C.; Soucy, J.-P.; Rosa-Neto, P.; Gauthier, S.; Kostikov, A.; Gravel, P.; Bédard, M.-A. Quantification of Brain Cholinergic Denervation in Alzheimer's Disease Using PET Imaging with [18F]-FEOBV. *Mol. Psychiatry* **2017**, *22* (11), 1531–1538. https://doi.org/10.1038/mp.2017.183.

(154) Nejad-Davarani, S.; Koeppe, R. A.; Albin, R. L.; Frey, K. A.; Müller, M. L. T. M.; Bohnen, N. I. Quantification of Brain Cholinergic Denervation in Dementia with Lewy Bodies Using PET Imaging with [18F]-FEOBV. *Mol. Psychiatry* **2019**, *24* (3), 322–327. https://doi.org/10.1038/s41380-018-0130-5.

(155) Evaluation of (−)[18F]Fluoroethoxybenzovesamicol as a New PET Tracer of Cholinergic Neurons of the Heart. *Nucl. Med. Biol.* **1994**, *21* (2), 189–195. https://doi.org/10.1016/0969-8051(94)90008-6.

(156) Saint-Georges, Z.; Zayed, V. K.; Dinelle, K.; Cassidy, C.; Soucy, J.-P.; Massarweh, G.; Rotstein, B.; Nery, P. B.; Guimond, S.; deKemp, R.; Tuominen, L. First-in-Human Imaging and Kinetic Analysis of Vesicular Acetylcholine Transporter Density in the Heart Using [18F]FEOBV PET. *J. Nucl. Cardiol.* **2021**, *28* (1), 50–54. https://doi.org/10.1007/s12350-020-02323-w.

(157) Horsager, J.; Okkels, N.; Van Den Berge, N.; Jacobsen, J.; Schact, A.; Munk, O. L.; Vang, K.; Bender, D.; Brooks, D. J.; Borghammer, P. In Vivo Vesicular Acetylcholine Transporter Density in Human Peripheral Organs: An [18F]FEOBV PET/CT Study. *EJNMMI Res.* **2022**, *12* (1), 17. https://doi.org/10.1186/s13550-022-00889-9.

(158) van der Bijl, P.; Knuuti, J.; Delgado, V.; Bax, J. J. Cardiac Sympathetic Innervation Imaging with PET Radiotracers. *Curr. Cardiol. Rep.* **2021**, *23* (1), 4. https://doi.org/10.1007/s11886-020-01432-9.

(159) Takatsu, H.; Noda, T.; Arai, M.; Kunishima, A.; Inoue, M.; Tazawa, S.; Kurosawa, H.; Nishigaki, K.; Fujiwara, H. Washout of I-123 Meta-Iodobenzylguanidine for Assessing Cardiac Sympathetic Activity with Progression of Hypertension in Dahl Salt-Sensitive Rats. *J. Nucl. Cardiol.* **1999**, *6* (2), 204–210. https://doi.org/10.1016/S1071-3581(99)90081-8.

(160) Alluri, S. R.; Kim, S. W.; Volkow, N. D.; Kil, K.-E. PET Radiotracers for CNS-Adrenergic Receptors: Developments and Perspectives. *Molecules* **2020**, *25* (17), 4017. https://doi.org/10.3390/molecules25174017.

(161) Baker, J. G.; Hall, I. P.; Hill, S. J. Pharmacological Characterization of CGP 12177 at the Human B2-Adrenoceptor. *Br. J. Pharmacol.* **2002**, *137* (3), 400–408. https://doi.org/10.1038/sj.bjp.0704855.

(162) Staehelin, M.; Simons, P.; Jaeggi, K.; Wigger, N. CGP-12177. A Hydrophilic Beta-Adrenergic Receptor Radioligand Reveals High Affinity Binding of Agonists to Intact Cells. *J. Biol. Chem.* **1983**, *258* (6), 3496–3502.

(163) Merlet, P.; Delforge, J.; Syrota, A.; Angevin, E.; Mazière, B.; Crouzel, C.; Valette, H.; Loisance, D.; Castaigne, A.; Randé, J. L. Positron Emission Tomography with 11C CGP-12177 to Assess Beta-Adrenergic Receptor Concentration in Idiopathic Dilated Cardiomyopathy. *Circulation* **1993**, *87* (4), 1169–1178. https://doi.org/10.1161/01.CIR.87.4.1169.

(164) Naya, M.; Tsukamoto, T.; Morita, K.; Katoh, C.; Nishijima, K.; Komatsu, H.; Yamada, S.; Kuge, Y.; Tamaki, N.; Tsutsui, H. Myocardial β-Adrenergic Receptor Density Assessed by 11C-CGP12177 PET Predicts Improvement of Cardiac Function After Carvedilol Treatment in Patients with Idiopathic Dilated Cardiomyopathy. *J. Nucl. Med.* **2009**, *50* (2), 220–225. https://doi.org/10.2967/jnumed.108.056341.

(165) Verschure, D. O.; Nakajima, K.; Jacobson, A. F.; Verberne, H. J. 40 Years Anniversary of Cardiac 123I-MIBG Imaging: State of the Heart. *Curr. Cardiovasc. Imaging Rep.* **2021**, *14* (5), 5. https://doi.org/10.1007/s12410-021-09555-5.

(166) Jang, K. S.; Jung, Y.-W.; Sherman, P. S.; Quesada, C. A.; Gu, G.; Raffel, D. M. Synthesis and Bioevaluation of [18F]4-Fluoro-m-Hydroxyphenethylguanidine ([18F]4F-MHPG): A Novel Radiotracer for Quantitative PET Studies of Cardiac Sympathetic Innervation.

Bioorg. Med. Chem. Lett. **2013**, *23* (6), 1612–1616. https://doi.org/10.1016/j.bmcl.2013.01.106.

(167) Jung, Y.-W.; Jang, K. S.; Gu, G.; Koeppe, R. A.; Sherman, P. S.; Quesada, C. A.; Raffel, D. M. [18F]Fluoro-Hydroxyphenethylguanidines: Efficient Synthesis and Comparison of Two Structural Isomers as Radiotracers of Cardiac Sympathetic Innervation. *ACS Chem. Neurosci.* **2017**, *8* (7), 1530–1542. https://doi.org/10.1021/acschemneuro.7b00051.

(168) Henderson E B; Kahn J K; Corbett J R; Jansen D E; Pippin J J; Kulkarni P; Ugolini V; Akers M S; Hansen C; Buja L M. Abnormal I-123 Metaiodobenzylguanidine Myocardial Washout and Distribution May Reflect Myocardial Adrenergic Derangement in Patients with Congestive Cardiomyopathy. *Circulation* **1988**, *78* (5), 1192–1199. https://doi.org/10.1161/01.CIR.78.5.1192.

(169) Jeong, Y. J.; Jeong, J.-E.; Cheon, S.-M.; Yoon, B.-A.; Kim, J. W.; Kang, D.-Y. Relationship between the Washout Rate of I-123 MIBG Scans and Autonomic Function in Parkinson's Disease. *PLOS ONE* **2020**, *15* (3), e0229860. https://doi.org/10.1371/journal.pone.0229860.

(170) Travin, M. I. Cardiac Autonomic Imaging with SPECT Tracers. *J. Nucl. Cardiol.* **2013**, *20* (1), 128–143. https://doi.org/10.1007/s12350-012-9655-1.

(171) van der Veen, B. J.; Younis, I. A.; de Roos, A.; Stokkel, M. P. M. Assessment of Global Cardiac I-123 MIBG Uptake and Washout Using Volumetric Quantification of SPECT Acquisitions. *J. Nucl. Cardiol.* **2012**, *19* (4), 752–762. https://doi.org/10.1007/s12350-012-9539-4.

(172) Jacobson, A. F.; Senior, R.; Cerqueira, M. D.; Wong, N. D.; Thomas, G. S.; Lopez, V. A.; Agostini, D.; Weiland, F.; Chandna, H.; Narula, J.; ADMIRE-HF Investigators. Myocardial Iodine-123 Meta-Iodobenzylguanidine Imaging and Cardiac Events in Heart Failure.

Results of the Prospective ADMIRE-HF (AdreView Myocardial Imaging for Risk Evaluation in Heart Failure) Study. *J. Am. Coll. Cardiol.* **2010**, *55* (20), 2212–2221. https://doi.org/10.1016/j.jacc.2010.01.014.

(173) Verschure, D. O.; Nakajima, K.; Verberne, H. J. Cardiac 123I-MIBG Imaging in Heart Failure. *Pharmaceuticals* **2022**, *15* (6), 656. https://doi.org/10.3390/ph15060656.

(174) Pontico, M.; Brunotti, G.; Conte, M.; Corica, F.; Cosma, L.; De Angelis, C.; De Feo, M. S.; Lazri, J.; Matto, A.; Montebello, M.; Di Rocco, A.; Frantellizzi, V.; Farcomeni, A.; De Vincentis, G. The Prognostic Value of 123I-MIBG SPECT Cardiac Imaging in Heart Failure Patients: A Systematic Review. *J. Nucl. Cardiol.* **2021**. https://doi.org/10.1007/s12350-020-02501-w.

(175) Muehllehner, G.; Karp, J. S. Positron Emission Tomography. *Phys. Med. Biol.* **2006**, *51* (13), R117-137. https://doi.org/10.1088/0031-9155/51/13/R08.

(176) Langer, O.; Halldin, C. PET and SPET Tracers for Mapping the Cardiac Nervous System. *Eur. J. Nucl. Med. Mol. Imaging* **2002**, *29* (3), 416–434. https://doi.org/10.1007/s002590100640.

(177) Boutagy, N. E.; Sinusas, A. J. Recent Advances and Clinical Applications of PET Cardiac Autonomic Nervous System Imaging. *Curr. Cardiol. Rep.* **2017**, *19* (4), 33. https://doi.org/10.1007/s11886-017-0843-0.

(178) Franzius, C.; Hermann, K.; Weckesser, M.; Kopka, K.; Juergens, K. U.; Vormoor, J.; Schober, O. Whole-Body PET/CT with 11C-Meta-Hydroxyephedrine in Tumors of the Sympathetic Nervous System: Feasibility Study and Comparison with 123I-MIBG SPECT/CT. *J. Nucl. Med.* **2006**, *47* (10), 1635–1642.

(179) Tipre, D. N.; Fox, J. J.; Holt, D. P.; Green, G.; Yu, J.; Pomper, M.; Dannals, R. F.; Bengel, F. M. In Vivo PET Imaging of Cardiac Presynaptic Sympathoneuronal Mechanisms in the Rat. *J. Nucl. Med.* **2008**, *49* (7), 1189–1195. https://doi.org/10.2967/jnumed.107.050252.

(180) Fallavollita, J. A.; Heavey, B. M.; Luisi, A. J.; Michalek, S. M.; Baldwa, S.; Mashtare, T. L.; Hutson, A. D.; Dekemp, R. A.; Haka, M. S.; Sajjad, M.; Cimato, T. R.; Curtis, A. B.; Cain, M. E.; Canty, J. M. Regional Myocardial Sympathetic Denervation Predicts the Risk of Sudden Cardiac Arrest in Ischemic Cardiomyopathy. *J. Am. Coll. Cardiol.* **2014**, *63* (2), 141–149. https://doi.org/10.1016/j.jacc.2013.07.096.

(181) Higuchi, T.; Yousefi, B. H.; Kaiser, F.; Gärtner, F.; Rischpler, C.; Reder, S.; Yu, M.; Robinson, S.; Schwaiger, M.; Nekolla, S. G. Assessment of the 18F-Labeled PET Tracer LMI1195 for Imaging Norepinephrine Handling in Rat Hearts. *J. Nucl. Med. Off. Publ. Soc. Nucl. Med.* **2013**, *54* (7), 1142–1146. https://doi.org/10.2967/jnumed.112.104232.

(182) Yu, M.; Bozek, J.; Lamoy, M.; Kagan, M.; Benites, P.; Onthank, D.; Robinson, S. P. LMI1195 PET Imaging in Evaluation of Regional Cardiac Sympathetic Denervation and Its Potential Role in Antiarrhythmic Drug Treatment. *Eur. J. Nucl. Med. Mol. Imaging* **2012**, *39* (12), 1910–1919. https://doi.org/10.1007/s00259-012-2204-y.

(183) Yu Ming; Bozek Jody; Lamoy Melanie; Guaraldi Mary; Silva Paula; Kagan Mikhail; Yalamanchili Padmaja; Onthank David; Mistry Mahesh; Lazewatsky Joel; Broekema Matthias; Radeke Heike; Purohit Ajay; Cdebaca Michael; Azure Michael; Cesati Richard; Casebier David; Robinson Simon P. Evaluation of LMI1195, a Novel 18F-Labeled Cardiac Neuronal PET Imaging Agent, in Cells and Animal Models. *Circ. Cardiovasc. Imaging* **2011**, *4* (4), 435–443. https://doi.org/10.1161/CIRCIMAGING.110.962126.

(184) Sinusas, A. J.; Lazewatsky, J.; Brunetti, J.; Heller, G.; Srivastava, A.; Liu, Y.-H.; Sparks, R.; Puretskiy, A.; Lin, S.; Crane, P.; Carson, R. E.; Lee, L. V. Biodistribution and Radiation Dosimetry of LMI1195: First-in-Human Study of a Novel 18F-Labeled Tracer for Imaging Myocardial Innervation. *J. Nucl. Med.* **2014**, *55* (9), 1445–1451. https://doi.org/10.2967/jnumed.114.140137.

(185) Raffel, D. M.; Jung, Y.-W.; Gildersleeve, D. L.; Sherman, P. S.; Moskwa, J. J.; Tluczek, L. J.; Chen, W. Radiolabeled Phenethylguanidines: Novel Imaging Agents for Cardiac Sympathetic Neurons and Adrenergic Tumors. *J. Med. Chem.* **2007**, *50* (9), 2078–2088. https://doi.org/10.1021/jm061398y.

(186) Raffel David M.; Jung Yong-Woon; Koeppe Robert A.; Jang Keun Sam; Gu Guie; Scott Peter J.H.; Murthy Venkatesh L.; Rothley Jill; Frey Kirk A. First-in-Human Studies of [18F] Fluorohydroxyphenethylguanidines. *Circ. Cardiovasc. Imaging* **2018**, *11* (12), e007965. https://doi.org/10.1161/CIRCIMAGING.118.007965.

(187) Rosenspire, K. C.; Haka, M. S.; Dort, M. E. V.; Jewett, D. M.; Gildersleeve, D. L.; Schwaiger, M.; Wieland, D. M. Synthesis and Preliminary Evaluation of Carbon-11-Meta-Hydroxyephedrine: A False Transmitter Agent for Heart Neuronal Imaging. *J. Nucl. Med.* **1990**, *31* (8), 1328–1334.

(188) Rischpler, C.; Fukushima, K.; Isoda, T.; Javadi, M. S.; Dannals, R. F.; Abraham, R.; Wahl, R.; Bengel, F. M.; Higuchi, T. Discrepant Uptake of the Radiolabeled Norepinephrine Analogues Hydroxyephedrine (HED) and Metaiodobenzylguanidine (MIBG) in Rat Hearts. *Eur. J. Nucl. Med. Mol. Imaging* **2013**, *40* (7), 1077–1083. https://doi.org/10.1007/s00259-013-2393-z.

(189) Ieda, M.; Kanazawa, H.; Kimura, K.; Hattori, F.; Ieda, Y.; Taniguchi, M.; Lee, J.-K.; Matsumura, K.; Tomita, Y.; Miyoshi, S.; Shimoda, K.; Makino, S.; Sano, M.; Kodama, I.; Ogawa, S.; Fukuda, K. Sema3a Maintains Normal Heart Rhythm through Sympathetic Innervation Patterning. *Nat. Med.* **2007**, *13* (5), 604–612. https://doi.org/10.1038/nm1570.

(190) Chen, X.; Werner, R. A.; Lapa, C.; Nose, N.; Hirano, M.; Javadi, M. S.; Robinson, S.; Higuchi, T. Subcellular Storage and Release Mode of the Novel 18F-Labeled Sympathetic Nerve PET Tracer LMI1195. *EJNMMI Res.* **2018**, *8* (1), 12. https://doi.org/10.1186/s13550-018-0365-9.

(191) Raffel, D. M.; Chen, W.; Sherman, P. S.; Gildersleeve, D. L.; Jung, Y.-W. Dependence of Cardiac 11C-Meta-Hydroxyephedrine Retention on Norepinephrine Transporter Density. *J. Nucl. Med.* **2006**, *47* (9), 1490–1496.

(192) Synthesis and Preliminary Evaluation of Para- and Meta-[18F]Fluorobenzylguanidine. *Nucl. Med. Biol.* **1994**, *21* (1), 97–103. https://doi.org/10.1016/0969-8051(94)90135-X.

(193) Angelini, G.; Speranza, M.; Wolf, A. P.; Shiue, C.-Y. Nucleophilic Aromatic Substitution of Activated Cationic Groups by 18F-Labeled Fluoride. A Useful Route to No-Carrier-Added (NCA) 18F-Labeled Aryl Fluorides. *J. Fluor. Chem.* **1985**, *27* (2), 177–191. https://doi.org/10.1016/S0022-1139(00)84987-8.

(194) Hu, B.; Vāvere, A. L.; Neumann, K. D.; Shulkin, B. L.; DiMagno, S. G.; Snyder, S. E. A Practical, Automated Synthesis of Meta-[18F]Fluorobenzylguanidine for Clinical Use. *ACS Chem. Neurosci.* **2015**, *6* (11), 1870–1879. https://doi.org/10.1021/acschemneuro.5b00202.

(195) Rotstein, B. H.; Stephenson, N. A.; Vasdev, N.; Liang, S. H. Spirocyclic Hypervalent Iodine(III)-Mediated Radiofluorination of Non-Activated and Hindered Aromatics. *Nat. Commun.* **2014**, *5* (1), 4365. https://doi.org/10.1038/ncomms5365.

(196) H. Rotstein, B.; Wang, L.; Y. Liu, R.; Patteson, J.; E. Kwan, E.; Vasdev, N.; H. Liang, S. Mechanistic Studies and Radiofluorination of Structurally Diverse Pharmaceuticals with Spirocyclic Iodonium(Iii) Ylides. *Chem. Sci.* **2016**, *7* (7), 4407–4417. https://doi.org/10.1039/C6SC00197A.

(197) Pandit-Taskar, N.; Zanzonico, P. B.; Staton, K. D.; Carrasquillo, J. A.; Reidy-Lagunes, D.; Lyashchenko, S. K.; Burnazi, E.; Zhang, H.; Lewis, J. S.; Blasberg, R.; Larson, S. M.; Weber, W. A.; Modak, S. Biodistribution and Dosimetry of 18F-Meta Fluorobenzyl Guanidine (MFBG): A First-in-Human PET-CT Imaging Study of Patients with Neuroendocrine Malignancies. *J. Nucl. Med.* **2017**. https://doi.org/10.2967/jnumed.117.193169.

(198) Grkovski, M.; Zanzonico, P. B.; Modak, S.; Humm, J. L.; Narula, J.; Pandit-Taskar, N. F-18 Meta-Fluorobenzylguanidine PET Imaging of Myocardial Sympathetic Innervation. *J. Nucl. Cardiol.* **2022**. https://doi.org/10.1007/s12350-021-02813-5.

(199) Zhang, H.; Huang, R.; Pillarsetty, N.; Thorek, D. L. J.; Vaidyanathan, G.; Serganova, I.; Blasberg, R. G.; Lewis, J. S. Synthesis and Evaluation of 18F-Labeled Benzylguanidine Analogs for Targeting the Human Norepinephrine Transporter. *Eur. J. Nucl. Med. Mol. Imaging* **2014**, *41* (2), 322–332. https://doi.org/10.1007/s00259-013-2558-9.

(200) Turnock, S.; Turton, D. R.; Martins, C. D.; Chesler, L.; Wilson, T. C.; Gouverneur, V.; Smith, G.; Kramer-Marek, G. 18 F-Meta-Fluorobenzylguanidine (18 F-MFBG) to Monitor Changes in Norepinephrine Transporter Expression in Response to Therapeutic Intervention in Neuroblastoma Models. *Sci. Rep.* **2020**, *10* (1), 20918. https://doi.org/10.1038/s41598-020-77788-3.

(201) Ismailani, U. S.; Buchler, A.; Farber, G.; Pekošak, A.; Farber, E.; MacMullin, N.; Suuronen, E. J.; Vasdev, N.; Beanlands, R. S. B.; de Kemp, R. A.; Rotstein, B. H. Cardiac Sympathetic Positron Emission Tomography Imaging with Meta-[18F]Fluorobenzylguanidine Is Sensitive to Uptake-1 in Rats. *ACS Chem. Neurosci.* **2021**. https://doi.org/10.1021/acschemneuro.1c00575.

(202) Pike, V. W. Considerations in the Development of Reversibly Binding PET Radioligands for Brain Imaging. *Curr. Med. Chem.* **2016**, *23* (18), 1818–1869.

(203) Dahl, K.; Halldin, C.; Schou, M. New Methodologies for the Preparation of Carbon-11 Labeled Radiopharmaceuticals. *Clin. Transl. Imaging* **2017**, *5* (3), 275–289. https://doi.org/10.1007/s40336-017-0223-1.

(204) Wuest, F.; Berndt, M.; Kniess, T. Carbon-11 Labeling Chemistry Based upon [11C]Methyl Iodide. In *PET Chemistry*; Schubiger, P. A., Lehmann, L., Friebe, M., Eds.; Ernst Schering Research Foundation Workshop; Springer: Berlin, Heidelberg, 2007; pp 183–213. https://doi.org/10.1007/978-3-540-49527-7_7.

(205) Rotstein, B. H.; Liang, S. H.; Placzek, M. S.; Hooker, J. M.; Gee, A. D.; Dollé, F.; Wilson, A. A.; Vasdev, N. 11CO Bonds Made Easily for Positron Emission Tomography Radiopharmaceuticals. *Chem. Soc. Rev.* **2016**, *45* (17), 4708–4726. https://doi.org/10.1039/C6CS00310A.

(206) Pipal, R. W.; Stout, K. T.; Musacchio, P. Z.; Ren, S.; Graham, T. J. A.; Verhoog, S.; Gantert, L.; Lohith, T. G.; Schmitz, A.; Lee, H. S.; Hesk, D.; Hostetler, E. D.; Davies, I. W.; MacMillan, D. W. C. Metallaphotoredox Aryl and Alkyl Radiomethylation for PET Ligand Discovery. *Nature* **2021**, *589* (7843), 542–547. https://doi.org/10.1038/s41586-020-3015-0.

(207) Sandell, J.; Halldin, C.; Sovago, J.; Chou, Y.-H.; Gulyás, B.; Yu, M.; Emond, P.; Någren, K.; Guilloteau, D.; Farde, L. PET Examination of [11C]5-Methyl-6-Nitroquipazine, a Radioligand for Visualization of the Serotonin Transporter. *Nucl. Med. Biol.* **2002**, *29* (6), 651–656. https://doi.org/10.1016/S0969-8051(02)00318-9.

(208) Tarkiainen, J.; Vercouillie, J.; Emond, P.; Sandell, J.; Hiltunen, J.; Frangin, Y.; Guilloteau, D.; Halldin, C. Carbon-11 Labelling of MADAM in Two Different Positions: A Highly Selective PET Radioligand for the Serotonin Transporter. *J. Label. Compd. Radiopharm.* **2001**, *44* (14), 1013–1023. https://doi.org/10.1002/jlcr.523.

(209) Thompson, S.; Kealey, S.; Sephton, S. M.; Aigbirhio, F. I. Radiochemistry with Carbon-11. In *Handbook of Radiopharmaceuticals*; John Wiley & Sons, Ltd, 2020; pp 143–249. https://doi.org/10.1002/9781119500575.ch7.

(210) Goud, N. S.; Bhattacharya, A.; Joshi, R. K.; Nagaraj, C.; Bharath, R. D.; Kumar, P. Carbon-11: Radiochemistry and Target-Based PET Molecular Imaging Applications in Oncology, Cardiology, and Neurology. *J. Med. Chem.* **2021**, *64* (3), 1223–1259. https://doi.org/10.1021/acs.jmedchem.0c01053.

(211) Fukumura, T.; Mori, W.; Ogawa, M.; Fujinaga, M.; Zhang, M.-R. [11C]Phosgene: Synthesis and Application for Development of PET Radiotracers. *Nucl. Med. Biol.* **2021**, *92*, 138–148. https://doi.org/10.1016/j.nucmedbio.2020.04.007.

(212) Deng, X.; Rong, J.; Wang, L.; Vasdev, N.; Zhang, L.; Josephson, L.; Liang, S. H. Chemistry for Positron Emission Tomography: Recent Advances in 11C-, 18F-, 13N-, and 15O-Labeling Reactions. *Angew. Chem. Int. Ed.* **2019**, *58* (9), 2580–2605. https://doi.org/10.1002/anie.201805501.

(213) Wilson, A. A.; Garcia, A.; Houle, S.; Sadovski, O.; Vasdev, N. Synthesis and Application of Isocyanates Radiolabeled with Carbon-11. *Chem. – Eur. J.* **2011**, *17* (1), 259–264. https://doi.org/10.1002/chem.201002345.

(214) Dheere, A. K. H.; Yusuf, N.; Gee, A. Rapid and Efficient Synthesis of [11C]Ureas via the Incorporation of [11C]CO2 into Aliphatic and Aromatic Amines. *Chem. Commun.* **2013**, *49* (74), 8193–8195. https://doi.org/10.1039/C3CC44046J.

(215) Bongarzone, S.; Runser, A.; Taddei, C.; Dheere, A. K. H.; Gee, A. D. From [11C]CO2 to [11C]Amides: A Rapid One-Pot Synthesis via the Mitsunobu Reaction. *Chem. Commun.* **2017**, *53* (38), 5334–5337. https://doi.org/10.1039/C7CC01407D.

(216) Mair, B. A.; Fouad, M. H.; Ismailani, U. S.; Munch, M.; Rotstein, B. H. Rhodium-Catalyzed Addition of Organozinc Iodides to Carbon-11 Isocyanates. *Org. Lett.* **2020**, *22* (7), 2746–2750. https://doi.org/10.1021/acs.orglett.0c00729.

(217) Vecchio, A. D.; Talbot, A.; Caillé, F.; Chevalier, A.; Sallustrau, A.; Loreau, O.; Destro, G.; Taran, F.; Audisio, D. Carbon Isotope Labeling of Carbamates by Late-Stage [11C], [13C] and [14C]Carbon Dioxide Incorporation. *Chem. Commun.* **2020**, *56* (78), 11677–11680. https://doi.org/10.1039/D0CC05031H.

(218) van Tilburg, E. W.; Windhorst, A. D.; van der Mey, M.; Herscheid, J. D. M. One-Pot Synthesis of [11C]Ureas via Triphenylphosphinimines. *J. Label. Compd. Radiopharm.* **2006**, *49* (4), 321–330. https://doi.org/10.1002/jlcr.1052.

(219) Staudinger, H.; Meyer, J. Über Neue Organische Phosphorverbindungen III. Phosphinmethylenderivate Und Phosphinimine. *Helv. Chim. Acta* **1919**, *2* (1), 635–646. https://doi.org/10.1002/hlca.19190020164.

(220) Bézier, D.; Daugulis, O.; Brookhart, M. Polymerization of Ethylene Catalyzed by Phosphine-Iminophosphorane Palladium Complexes. *Organometallics* **2017**, *36* (15), 2947–2951. https://doi.org/10.1021/acs.organomet.7b00391.

(221) García-Álvarez, J.; García-Garrido, S. E.; Cadierno, V. Iminophosphorane–Phosphines: Versatile Ligands for Homogeneous Catalysis. *J. Organomet. Chem.* **2014**, *751*, 792–808. https://doi.org/10.1016/j.jorganchem.2013.07.009.

(222) Ingrosso, F.; Ruiz-López, M. F. Electronic Interactions in Iminophosphorane Superbase Complexes with Carbon Dioxide. *J. Phys. Chem. A* **2018**, *122* (6), 1764–1770. https://doi.org/10.1021/acs.jpca.7b11853.

(223) Ding, M.-W.; Xu, S.-Z.; Zhao, J.-F. Application of Bis(Iminophosphorane) in Heterocyclic Synthesis: New Entries to Symmetrically or Unsymmetrically Substituted Thieno[2,3-d:5,4-d']Dipyrimidine-4,5(3H,6H)-Diones. *J. Org. Chem.* **2004**, *69* (24), 8366–8371. https://doi.org/10.1021/jo048691v.

(224) Smith, D. A.; Batsanov, A. S.; Miqueu, K.; Sotiropoulos, J.-M.; Apperley, D. C.; Howard, J. A. K.; Dyer, P. W. A Truly Multifunctional Heterocycle: Iminophosphorane, N,P Chelate, and Dihydropyridine. *Angew. Chem. Int. Ed.* **2008**, *47* (45), 8674–8677. https://doi.org/10.1002/anie.200803373.

(225) Rodima, T.; Mäemets, V.; Koppel, I. Synthesis of N-Aryl-Substituted Iminophosphoranes and NMR Spectroscopic Investigation of Their Acid–Base Properties in Acetonitrile. *J. Chem. Soc. Perkin 1* **2000**, No. 16, 2637–2644. https://doi.org/10.1039/B003575K.

(226) Starzewski, K. A. O.; Tom Dieck, H. Electronic Structure and Reactivity. 8. Iminophosphoranes - Simple Ylide Analogs? An Investigation of Quantitative and

Phenomenological Differences. *Inorg. Chem.* **1979**, *18* (12), 3307–3316. https://doi.org/10.1021/ic50202a005.

(227) 6 - Iminophosphoranes. In *Organic Chemistry*; Johnson, A. W., Ed.; Ylid Chemistry; Elsevier, 1966; Vol. 7, pp 217–247. https://doi.org/10.1016/B978-0-12-395778-8.50011-9.

(228) Molina, P.; Alajarin, M.; Arques, A. Convenient Improved Syntheses of Isocyanates or Isothiocyanates from Amines. *Synthesis* **1982**, *1982* (07), 596–597. https://doi.org/10.1055/s-1982-29877.

(229) Molina, P.; Alajarín, M.; López-Leonardo, C.; Alcántara, J. Reaction of Allyl Iminophosphoranes with Ketenes and Acyl Chlorides: One-Pot Preparation of 4-Pentenenitriles. *Tetrahedron* **1993**, *49* (23), 5153–5168. https://doi.org/10.1016/S0040-4020(01)81880-9.

(230) Robak, J. Triphenylphosphine/Carbon Dioxide. *Synlett* **2014**, *25* (15), 2231–2232. https://doi.org/10.1055/s-0034-1378584.

(231) Raveendran, P.; Wallen, S. L. Exploring CO2-Philicity: Effects of Stepwise Fluorination. *J. Phys. Chem. B* **2003**, *107* (6), 1473–1477. https://doi.org/10.1021/jp027026s.

(232) Nelson, M. R.; Borkman, R. F. Ab Initio Calculations on CO2 Binding to Carbonyl Groups. *J. Phys. Chem. A* **1998**, *102* (40), 7860–7863. https://doi.org/10.1021/jp981824u.

(233) Wadsworth, W. S.; Emmons, W. D. Phosphoramidate Anions: The Preparation of Carbodiimides, Ketenimines and Isothiocyanates. *J. Am. Chem. Soc.* **1962**, *84* (7), 1316–1317. https://doi.org/10.1021/ja00866a060.

(234) Bow, J.-P. J.; Adami, V.; Marasco, A.; Grønnevik, G.; Rivers, D. A.; Alvaro, G.; Riss, P. J. A Direct Fixation of CO2 for Isotopic Labelling of Hydantoins Using Iodine–Phosphine

Charge Transfer Complexes. *Chem. Commun.* **2022**, *58* (54), 7546–7549. https://doi.org/10.1039/D2CC01754G.

(235) Babin, V.; Sallustrau, A.; Loreau, O.; Caillé, F.; Goudet, A.; Cahuzac, H.; Vecchio, A. D.; Taran, F.; Audisio, D. A General Procedure for Carbon Isotope Labeling of Linear Urea Derivatives with Carbon Dioxide. *Chem. Commun.* **2021**, *57* (54), 6680–6683. https://doi.org/10.1039/D1CC02665H.

(236) Cassar, A.; Holmes, D. R.; Rihal, C. S.; Gersh, B. J. Chronic Coronary Artery Disease: Diagnosis and Management. *Mayo Clin. Proc.* **2009**, *84* (12), 1130–1146. https://doi.org/10.4065/mcp.2009.0391.

(237) Yu, X.-H.; Fu, Y.-C.; Zhang, D.-W.; Yin, K.; Tang, C.-K. Foam Cells in Atherosclerosis. *Clin. Chim. Acta Int. J. Clin. Chem.* **2013**, *424*, 245–252. https://doi.org/10.1016/j.cca.2013.06.006.

(238) Lusis, A. J. Atherosclerosis. *Nature* **2000**, *407* (6801), 233–241. https://doi.org/10.1038/35025203.

(239) Karasawa, T.; Takahashi, M. Role of NLRP3 Inflammasomes in Atherosclerosis. *J. Atheroscler. Thromb.* **2017**, *24* (5), 443–451. https://doi.org/10.5551/jat.RV17001.

(240) Bobryshev, Y. V.; Ivanova, E. A.; Chistiakov, D. A.; Nikiforov, N. G.; Orekhov, A. N. Macrophages and Their Role in Atherosclerosis: Pathophysiology and Transcriptome Analysis. *BioMed Res. Int.* **2016**, *2016*, 9582430. https://doi.org/10.1155/2016/9582430.

(241) Jo, E.-K.; Kim, J. K.; Shin, D.-M.; Sasakawa, C. Molecular Mechanisms Regulating NLRP3 Inflammasome Activation. *Cell. Mol. Immunol.* **2016**, *13* (2), 148–159. https://doi.org/10.1038/cmi.2015.95.

(242) Kelley, N.; Jeltema, D.; Duan, Y.; He, Y. The NLRP3 Inflammasome: An Overview of Mechanisms of Activation and Regulation. *Int. J. Mol. Sci.* **2019**, *20* (13). https://doi.org/10.3390/ijms20133328.

(243) Duewell, P.; Kono, H.; Rayner, K. J.; Sirois, C. M.; Vladimer, G.; Bauernfeind, F. G.; Abela, G. S.; Franchi, L.; Nuñez, G.; Schnurr, M.; Espevik, T.; Lien, E.; Fitzgerald, K. A.; Rock, K. L.; Moore, K. J.; Wright, S. D.; Hornung, V.; Latz, E. NLRP3 Inflammasomes Are Required for Atherogenesis and Activated by Cholesterol Crystals. *Nature* **2010**, *464* (7293), 1357–1361. https://doi.org/10.1038/nature08938.

(244) Rajamäki, K.; Lappalainen, J.; Öörni, K.; Välimäki, E.; Matikainen, S.; Kovanen, P. T.; Eklund, K. K. Cholesterol Crystals Activate the NLRP3 Inflammasome in Human Macrophages: A Novel Link between Cholesterol Metabolism and Inflammation. *PLoS ONE* **2010**, *5* (7). https://doi.org/10.1371/journal.pone.0011765.

(245) Baldrighi, M.; Mallat, Z.; Li, X. NLRP3 Inflammasome Pathways in Atherosclerosis. *Atherosclerosis* **2017**, *267*, 127–138. https://doi.org/10.1016/j.atherosclerosis.2017.10.027.

(246) Coll, R. C.; Robertson, A. A. B.; Chae, J. J.; Higgins, S. C.; Muñoz-Planillo, R.; Inserra, M. C.; Vetter, I.; Dungan, L. S.; Monks, B. G.; Stutz, A.; Croker, D. E.; Butler, M. S.; Haneklaus, M.; Sutton, C. E.; Núñez, G.; Latz, E.; Kastner, D. L.; Mills, K. H. G.; Masters, S. L.; Schroder, K.; Cooper, M. A.; O'Neill, L. A. J. A Small-Molecule Inhibitor of the NLRP3 Inflammasome for the Treatment of Inflammatory Diseases. *Nat. Med.* **2015**, *21* (3), 248–255. https://doi.org/10.1038/nm.3806.

(247) Coll, R. C.; Hill, J. R.; Day, C. J.; Zamoshnikova, A.; Boucher, D.; Massey, N. L.; Chitty, J. L.; Fraser, J. A.; Jennings, M. P.; Robertson, A. A. B.; Schroder, K. MCC950 Directly

Targets the NLRP3 ATP-Hydrolysis Motif for Inflammasome Inhibition. *Nat. Chem. Biol.* **2019**, *15* (6), 556–559. https://doi.org/10.1038/s41589-019-0277-7.

(248) Tapia-Abellán, A.; Angosto-Bazarra, D.; Martínez-Banaclocha, H.; de Torre-Minguela, C.; Cerón-Carrasco, J. P.; Pérez-Sánchez, H.; Arostegui, J. I.; Pelegrin, P. MCC950 Closes the Active Conformation of NLRP3 to an Inactive State. *Nat. Chem. Biol.* **2019**, *15* (6), 560–564. https://doi.org/10.1038/s41589-019-0278-6.

(249) Mangan, M. S. J.; Olhava, E. J.; Roush, W. R.; Seidel, H. M.; Glick, G. D.; Latz, E. Targeting the NLRP3 Inflammasome in Inflammatory Diseases. *Nat. Rev. Drug Discov.* **2018**, *17* (8), 588–606. https://doi.org/10.1038/nrd.2018.97.

(250) Sharma, A.; Choi, J. S. Y.; Stefanovic, N.; Al-Sharea, A.; Simpson, D. S.; Mukhamedova, N.; Jandeleit-Dahm, K.; Murphy, A. J.; Sviridov, D.; Vince, J. E.; Ritchie, R. H.; de Haan, J. B. Specific NLRP3 Inhibition Protects Against Diabetes-Associated Atherosclerosis. *Diabetes* **2020**, *70* (3), 772–787. https://doi.org/10.2337/db20-0357.

(251) Ma, Q.; Fan, Q.; Han, X.; Dong, Z.; Xu, J.; Bai, J.; Tao, W.; Sun, D.; Wang, C. Platelet-Derived Extracellular Vesicles to Target Plaque Inflammation for Effective Anti-Atherosclerotic Therapy. *J. Controlled Release* **2021**, *329*, 445–453. https://doi.org/10.1016/j.jconrel.2020.11.064.

(252) Zheng, F.; Xing, S.; Gong, Z.; Xing, Q. NLRP3 Inflammasomes Show High Expression in Aorta of Patients with Atherosclerosis. *Heart Lung Circ.* **2013**, *22* (9), 746–750. https://doi.org/10.1016/j.hlc.2013.01.012.

(253) Liu, Y.; Li, C.; Yin, H.; Zhang, X.; Li, Y. *NLRP3 Inflammasome: A Potential Alternative Therapy Target for Atherosclerosis*. Evidence-Based Complementary and Alternative Medicine. https://doi.org/10.1155/2020/1561342.

(254) Hill, J. R.; Shao, X.; Massey, N. L.; Stauff, J.; Sherman, P. S.; Robertson, A. A. B.; Scott, P. J. H. Synthesis and Evaluation of NLRP3-Inhibitory Sulfonylurea [11C]MCC950 in Healthy Animals. *Bioorg. Med. Chem. Lett.* **2020**, *30* (12), 127186. https://doi.org/10.1016/j.bmcl.2020.127186.

(255) Xu, Y.; Xu, Y.; Blevins, H.; Lan, Y.; Liu, Y.; Yuan, G.; Striar, R.; Zagaroli, J. S.; Tocci, D. R.; Langan, A. G.; Zhang, C.; Zhang, S.; Wang, C. Discovery of Carbon-11 Labeled Sulfonamide Derivative: A PET Tracer for Imaging Brain NLRP3 Inflammasome. *Bioorg. Med. Chem. Lett.* **2021**, *34*, 127777. https://doi.org/10.1016/j.bmcl.2021.127777.

(256) Ismailani, U. S.; Munch, M.; Mair, B. A.; Rotstein, B. H. Interrupted Aza-Wittig Reactions Using Iminophosphoranes to Synthesize ^{11} C–Carbonyls. *Chem. Commun.* **2021**, 10.1039.D1CC01016F. https://doi.org/10.1039/D1CC01016F.

2. Chapter II: Cardiac Sympathetic PET Imaging with *meta*-[^{18}F]Fluorobenzylguanidine is Sensitive to Uptake-1 in Rats

The manuscript can be accessed at: https://doi.org/10.1021/acschemneuro.1c00575

Uzair S. Ismailani,[1,2] Ariel Buchler,[2,3] Gedaliah Farber,[1,2] Aleksandra Pekošak,[4] Eadan Farber,[2] Nicole MacMullin,[2] Erik J. Suuronen,[2] Neil Vasdev,[5] Rob S.B. Beanlands,[2] Robert A. deKemp,[2] and Benjamin H. Rotstein[1,2,3]*

[1] *Department of Biochemistry, Microbiology and Immunology, University of Ottawa, Ottawa, Ontario, Canada*

[2] *University of Ottawa Heart Institute, Ottawa, Ontario, Canada*

[3] *Department of Chemistry and Biomolecular Sciences, University of Ottawa, Ottawa, Ontario, Canada*

[4] *VU Medical Centre, Amsterdam, North Holland, Netherlands*

[5] *Azrieli Centre for Neuro-Radiochemistry, Centre for Addiction and Mental Health, Toronto, Ontario, Canada*

Correspondence: Benjamin H. Rotstein, PhD
University of Ottawa Heart Institute
40 Ruskin Street, H-5219
Ottawa, Ontario, Canada
K1Y 4W7
Phone: 613-696-7324
Email: benjamin.rotstein@uottawa.ca

2.1. Statement of the manuscript

The manuscript "**Cardiac Sympathetic PET Imaging with *meta*-[^{18}F]Fluorobenzylguanidine is Sensitive to Uptake-1 in Rats**" was accepted into *ACS Chemical Neuroscience* and published on October 29th, 2021. In this chapter, I further developed the radiosynthesis by reperforming experiments relating to radiofluorination yields and concentration of base. Moreover, I developed the entirety of the reformulation conditions. Solvent, reaction times, and deprotection conditions, and regioisomers analysis were previously conducted by Dr. Benjamin Rotstein & Aleksandra Pekošak. I performed *ex vivo* and *in vivo* experiments with the aid of Ariel Buchler. Tissue sectioning and autoradiography was performed by Eadan Farber and Nicole MacMullin. All data analysis was performed by me, and data interpretation was a collaborative effort of myself, Dr. Benjamin Rotstein, and Ariel Buchler. The manuscript was written by me and edited by Dr. Benjamin Rotstein and Ariel Buchler. All authors approved the final version.

2.2. Abstract

Dysfunction of the cardiac sympathetic nervous system contributes to the development of cardiovascular diseases including ischemia, heart failure, and arrhythmias. Molecular imaging probes such as *meta*-[^{123}I]iodobenzylguanidine have demonstrated the utility of assessing neuronal integrity by targeting norepinephrine transporter (NET, uptake-1). However, current radiotracers can report only on innervation due to suboptimal kinetics and lack of sensitivity to NET in rodents, precluding mechanistic studies in these species. The objective of this work was to characterize myocardial sympathetic neuronal uptake mechanisms and kinetics of the positron emission tomography (PET) radiotracer *meta*-[^{18}F]fluorobenzylguanidine ([^{18}F]mFBG) in rats. Automated synthesis using spirocyclic iodonium(III) ylide radiofluorination produces [^{18}F]mFBG in 24% ± 1% isolated radiochemical yield and 30–95 GBq/μmol molar activity. PET imaging in healthy rats delineated the left ventricle, with mono-exponential washout kinetics (k_{mono} = 0.027 ± 0.0026 min^{-1}, A_{mono} = 3.08 ± 0.33 SUV). *Ex vivo* biodistribution studies revealed tracer retention in the myocardium, while pharmacological treatment with selective NET inhibitor desipramine, non-selective neuronal and extraneuronal uptake-2 inhibitor phenoxybenzamine, and neuronal ablation with neurotoxin 6-hydroxydopamine reduced myocardial retention by 33%, 76%, and 36%, respectively. Clearance of [^{18}F]mFBG from the myocardium was unaffected by treatment with uptake-1 and uptake-2 inhibitors following peak myocardial activity. These results suggest that myocardial distribution of [^{18}F]mFBG in rats is dependent on both NET and extraneuronal transporters and that limited reuptake to the myocardium occurs. [^{18}F]mFBG may therefore prove useful for imaging intraneuronal dysfunction in small animals.

Keywords: norepinephrine transporter; sympathetic nervous system; cardiac imaging; *meta*-[^{18}F]fluorobenzylguanidine; positron emission tomography; fluorine-18

2.3. Introduction

The autonomic nervous system (ANS) has a crucial role in governing cardiac homeostasis, and in regulating functions including heart rate, blood pressure, and contractility.[1] The sympathetic branch of the ANS supplies excitatory stimuli to increase such functions above basal levels through the release of norepinephrine (NE) as the major postganglionic neurotransmitter, whereas the parasympathetic branch produces opposing effects using acetylcholine (ACh).[1,2] Loss of autonomic regulation in favour of increased sympathetic activity and vagal withdrawal has been described in chronic heart failure, cardiac arrythmias, sudden cardiac death, and diabetes mellitus.[3–6] As such, sympathetic dysfunction is considered central to many pathologies, and molecular imaging is used clinically for both mechanistic investigations and risk stratification in cardiovascular disease.[2,7–11]

Currently available radiotracers used for nuclear imaging of cardiac sympathetic dysfunction predominantly target the norepinephrine transporter (NET) to detect defects in global and regional myocardial presynaptic nerve density.[12] Radiolabeled neurotransmitters such as [^{11}C]epinephrine, [^{11}C]norepinephrine, [^{11}C]phenylephrine, and fluorinated dopamine derivatives can be imaged by positron emission tomography (PET) and exhibit high selectivity and rapid uptake by NET, but are complicated by both peripheral and intraneuronal metabolism giving rise to multiple substrates with distinct kinetics and target affinities.[13] These challenges were overcome with the development of structural analogs lacking catechol functionality such as the substituted amphetamine derivative *meta*-[^{11}C]hydroxyephedrine ([^{11}C]HED), and benzylguanidines *meta*-

[^{123}I]iodobenzylguanidine ([^{123}I]mIBG, used for lower resolution single-photon emission computed tomography or planar scintigraphy) and [^{18}F]flubrobenguane ([^{18}F]FBBG, formerly [^{18}F]LMI1195, Figure 1).[14] While NET-mediated neuronal retention provides excellent cardiac imaging contrast for these analogues, rapid uptake kinetics hinder the accurate quantification of sympathetic nerve abnormalities and cannot report on neural tone, thus necessitating the continued development of sympathetic nervous system (SNS) radiotracers which are easily accessible and possess favourable myocardial kinetics.[15–18] To this end, another benzylguanidine, *meta*-(3-[^{18}F]fluoropropyl)benzylguanidine ([^{18}F]mFPBG), has been developed for more facile alkyl radiofluorination and has shown utility for neuroblastoma imaging and preclinical cardiac imaging.[19]

More recently, radiotracer candidates bearing a phenethylguanidine core (Figure 1) have exhibited slower neuronal uptake rates in human imaging while maintaining irreversible kinetics due to vesicular trapping mediated by vesicular monoamine transporter 2 (VMAT2).[20] Initial challenges associated with nucleophilic ^{18}F-fluorination of the electron-rich aromatic rings in 4-[^{18}F]fluoro-*meta*-hydroxyphenethylguanidine ([^{18}F]4F-MHPG) have since been overcome using spirocyclic iodonium ylide radiofluorination.[16,21,22] Nevertheless, [^{18}F]4F-MHPG and its isomer [^{18}F]3F-PHPG inspired the development of [^{18}F]AF78, which retains the phenethylguanidine core with an appended 3-fluoropropyl ether moiety for more facile radiolabeling.[23] Preliminary studies with [^{18}F]AF78 have demonstrated cardiac retention in rats likely due to extraneuronal uptake mechanisms. However, further *in vivo* evaluation of this tracer is required to assess NET-dependent uptake in rats and higher species.

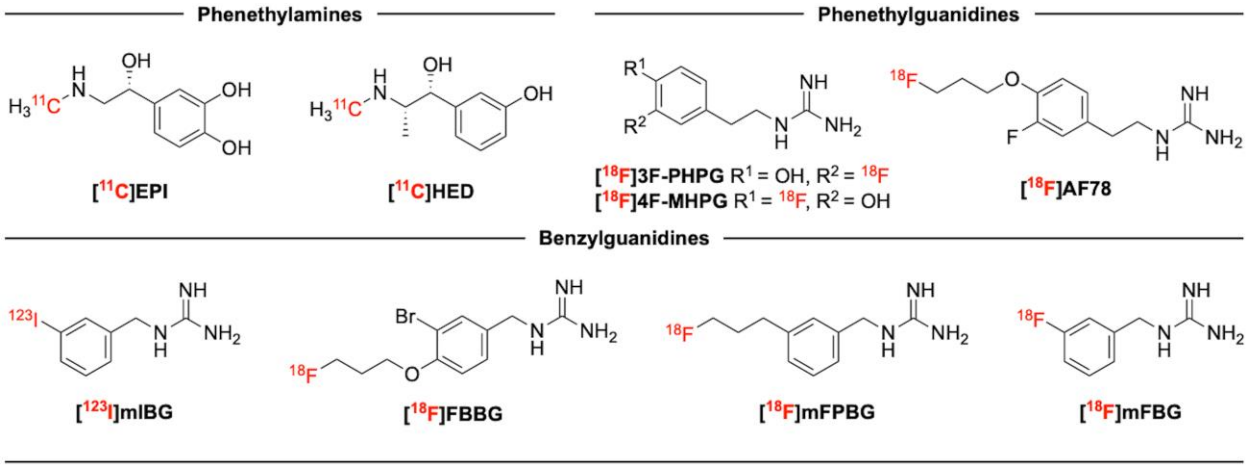

2.3.1. **Figure 1.** Chemical structures of NE radiotracer mimics used for SNS imaging

meta-[^{18}F]Fluorobenzylguanidine ([^{18}F]mFBG) is the closest structural analogue of [^{123}I]mIBG that can be used for imaging with fluorine-18 ($t_{1/2}$ = 109.7 min), the most convenient PET nuclide for labeling, transport, and dynamic imaging of small molecules. [^{18}F]mFBG was first reported in the 1990s but has not since been evaluated for cardiac SNS imaging.[24] While analogous to [^{123}I]mIBG, and to some extent [^{18}F]FBBG, available evidence suggests that [^{18}F]mFBG possesses lower affinity for NET, as well as reduced lipophilicity and serum protein binding.[25] Given these attributes, [^{18}F]mFBG may exhibit slower uptake into tissue, with distribution less dependent on tissue perfusion. This hypothesis is consistent with observable myocardial washout in [^{18}F]mFBG human imaging,[26] in contrast to the very slow washout kinetics that [^{123}I]mIBG displays,[27,28] and irreversible cardiac uptake of [^{11}C]HED and [^{18}F]FBBG.[29] We were further attracted to [^{18}F]mFBG by its potential for faster myocardial clearance and slower

reuptake as it may provide critical information on sympathetic tone and improvements in quantification of neuronal dysfunction.[29]

However, due to synthetic challenges associated with radiofluorination of deactivated arenes, the development of this compound has been gradual, with few recent reports demonstrating the utility of [^{18}F]mFBG for imaging neuroendocrine tumors.[26,30] New syntheses have been reported using either copper-mediated radiofluorination or diaryliodonium salt precursors, both of which are accompanied by technical challenges related to automation and access to precursors.[26,31–34] In addition, [^{18}F]mFBG is often obtained using biocompatible HPLC eluent, resulting in dilute activity concentrations that present an obstacle for routine production and small animal imaging studies. Using our previously reported methodology, we sought to develop an improved practical synthesis of [^{18}F]mFBG by spirocyclic iodonium ylide (SCIDY) radiofluorination.[35] The SCIDY precursor is prepared in three steps from commercially available reagents, radiolabeled, and subsequently reformulated using a carboxymethyl (CM) ion exchange resin to obtain the tracer in activity concentrations >370 MBq/mL, suitable for transport and imaging. The enhanced accessibility of this radiotracer prompted us to evaluate its pharmacokinetic properties and utility for cardiac SNS imaging in Sprague Dawley (SD) rats. Our *in vivo* and *ex vivo* evaluation includes PET imaging to assess tissue contrast and myocardial kinetics, metabolite analysis to gauge tracer stability, biodistribution to determine tracer localization, pharmacological blocking studies using desipramine (DMI) and phenoxybenzamine (PBZ), and chemical sympathectomy with 6-hydroxydopamine (6-OHDA) to study tracer uptake mechanisms.

2.4. Results and Discussion

Automated radiosynthesis of [^{18}F]mFBG in high activity yields. The synthetic route to obtain the precursor was first described by Rotstein *et al.*[35] Briefly, synthesis of the radiolabeling precursor began by guanylation of *meta*-iodobenzylamine to form the partially protected *meta*-iodobenzylguanidine **1** in 56% yield (Scheme 1). Following complete protection to afford compound **2** (92%), the intermediate was oxidized using Selectfluor and trimethylsilyl acetate,[36] followed by the addition of spiroadamantyl-1,3-dioxane-4,6-dione (SPIAd, **3**) to obtain the SCIDY precursor **4** in 54% yield (Scheme 1). Precursor stability studies conducted by NMR spectroscopy only revealed decomposition of the ylide after >6 months when stored at ambient temperature, but no apparent degradation upon long term storage at lower temperatures (<6 °C, Table S1).

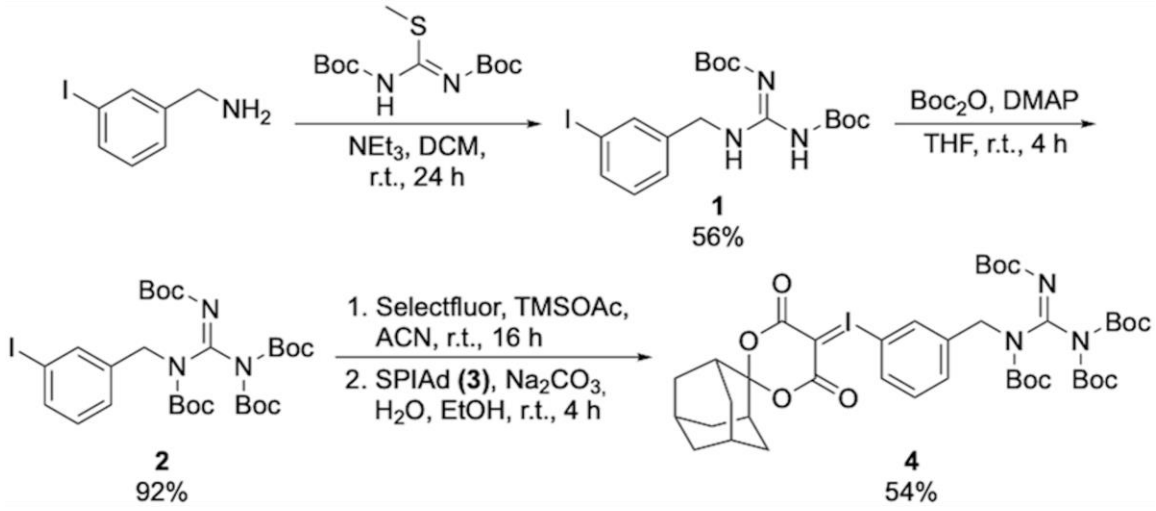

2.4.1. Scheme 1. Synthetic route to prepare SCIDY precursor

Further optimization of the previously reported radiolabeling conditions was carried out manually with low levels of starting radioactivity.[35] Radiochemical yields were determined by radioTLC integration of product peaks and unreacted [^{18}F]fluoride. This two-step radiosynthesis first

incorporates [^{18}F]fluoride by nucleophilic substitution, followed by acidic deprotection (Scheme 2). Radiofluorination of **4** in the presence of tetraethylammonium bicarbonate (TEAB) in DMF afforded the desired intermediate [^{18}F]**5** in 42 ± 11% yield after 5 minutes (Figure 2A). In line with previous studies on SCIDY radiofluorination, prolonged reaction times or elevated base concentrations above the optimal range of 4–6 equiv. had deleterious effects on precursor stability and radiochemical yield (RCY, Figure 2B).[22,35,37] Higher overall yields were observed in DMSO after 10 minutes (55 ± 9%) compared to DMF (Figure 2A), while replacing TEAB with potassium carbonate and Kryptofix® (K_2CO_3/$K_{2.2.2}$) led to markedly lower yields in either solvent (<7%, Table S2). Nearly quantitative disappearance of protected intermediate [^{18}F]**5** in the presence of 12 M HCl was observed after 5 minutes to form the desired product [^{18}F]**6** ([^{18}F]mFBG). Previously described radiofluorination reactions with iodonium ylides using Meldrum's acid as an auxiliary have suggested the formation of radiolabeled regioisomers as byproducts.[38] We prepared authentic standards of both *ortho*- and *para*-fluorobenzylguanidine and did not detect these radiochemical impurities from SCIDY radiofluorination (Figures S2-S3). In summary, [^{18}F]mFBG was formed with high selectivity, and synthesized in 53% RCY within 15 minutes.

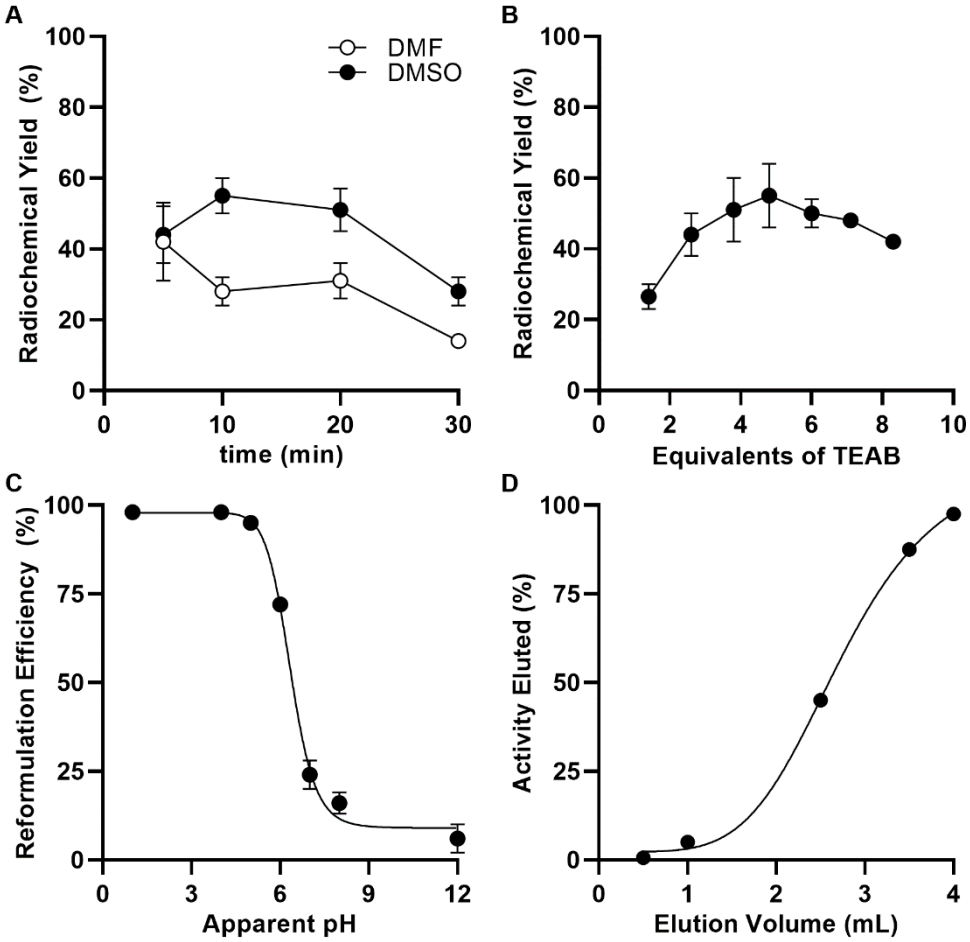

2.4.2. **Figure 2**. Optimization of [^{18}F]5 radiofluorination and [^{18}F]mFBG reformulation conditions. Dependence on (A) solvent (n = 1–4), and (B) base concentration (n = 2–4). Conditions: 20 mM precursor, 200 µL DMSO, 10 min, 120 °C. Radiochemical yield of [^{18}F]5 determined by radioTLC integration of product peaks and unreacted [^{18}F]fluoride. Product identity was confirmed by radioHPLC and co-injection of nonradioactive standard. (C) Dependence of [^{18}F]mFBG reformulation efficiency (RE) on influent pH (n = 6). RE is defined as the product of the trapping and elution efficiencies. (D) Volume of saline required for [^{18}F]mFBG elution (n = 6).

Using the optimized conditions, an automated two-step production of [^{18}F]mFBG was performed using the GE TRACERlab FX2N radiosynthesis module with in-line semi-preparative HPLC purification (Scheme 2, Figures S5-6). Following purification, we screened commercially available resins to concentrate the radiotracer. We observed no retention of [^{18}F]mFBG on commonly used C18 and HLB solid phase extraction cartridges. However, the weak ion-exchange CM resin showed greater promise for trap and release reformulation during initial screening, enabling the isolation of [^{18}F]mFBG in high activity concentrations. Unsurprisingly, we noted a dependency of activity retained by the CM resin on the pH of the influent solution collected from semi-preparative HPLC purification (Figure 2C). At pH >7, we noted poor REs (<25%), while a mildly acidic pH resulted in a steep increase to 48 ± 4%. Nearly quantitative retention (98 ± 1%) was achieved at pH ≤5, followed by complete elution of [^{18}F]mFBG in a maximum of 4 mL of physiological saline in activity concentrations >370 MBq/mL (Figure 2D). Satisfied with the quality of our reformulation, the entire production was then automated to reliably obtain the radiotracer in 55–65 minutes from the beginning of synthesis, in an isolated decay corrected yield of 24% ± 1% and in high molar activity (30–95 GBq/μmol), suitable for our preclinical evaluation (Scheme 2).

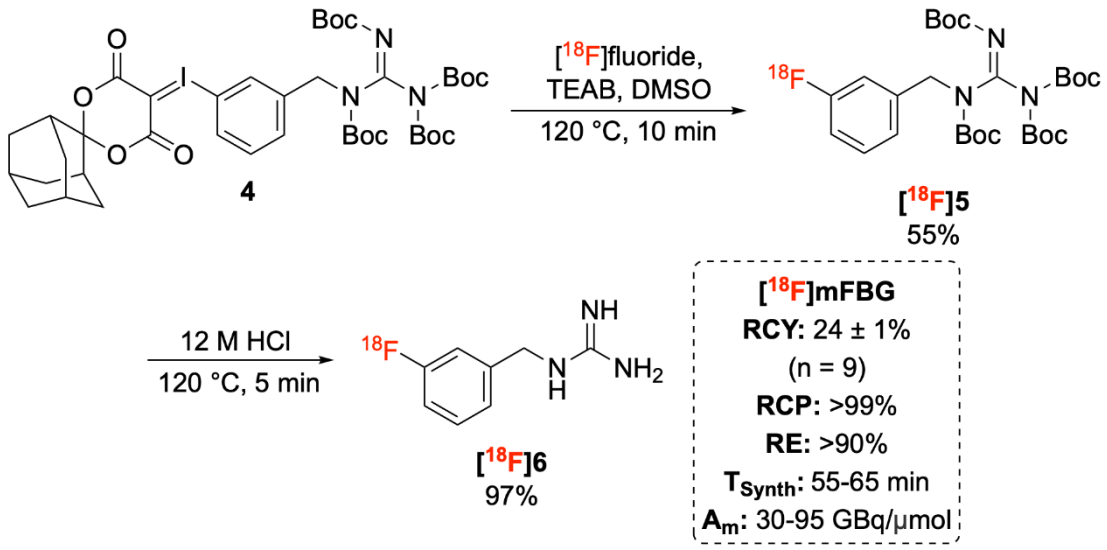

2.4.3. Scheme 2. Automated radiosynthesis of [^{18}F]mFBG

[^{18}F]mFBG exhibits cardiac uptake in SD rats. Dynamic PET scans were performed over 60 minutes to assess the cardiac imaging quality and myocardial kinetics of [^{18}F]mFBG in male SD rats following intravenous injection of the tracer in the lateral tail vein (Figure 3). The images show uniform uptake in the left ventricle (LV) that peaks at >3.0 SUV from 2.5–5 minutes. Minimal bone uptake was observed and did not interfere with quantification of LV activity (Figures S8-S9). While liver uptake remained constant after 30 minutes (2.69 ± 0.04 SUV), cardiac activity decreased monoexponentially after peak uptake (r^2 = 0.93, 5–55 min), with an observed k_{mono} = 0.027 ± 0.0026 min^{-1} and A_{mono} = 3.08 ± 0.33 SUV. Increased LV clearance of [^{18}F]mFBG is likely due to its reduced NET affinity (as measured *in vitro*) and lipophilicity in comparison to other benzylguanidine radiotracers,[25] since [^{123}I]mIBG and [^{18}F]FBBG display slow washout or irreversible uptake in rat myocardium.[39] Structure-activity relationships of benzylguanidines with respect to NET are complex, though it has been appreciated that *meta*-bromo or -iodo substitution and *para*-hydroxy or -alkoxy substituents are associated with NET-mediated uptake.[40] In this context, the observed faster clearance of [^{18}F]mFBG compared to [^{123}I]mIBG and other reported

analogues is in line with expectations and *in vitro* measurements. Considerable radiotracer washout from the myocardium over the course of a dynamic PET scan enables the use of readily available kinetic analyses such as k_{mono} and Logan plots for quantitative interpretation. Encouraged by the *in vivo* cardiac time-activity profiles, we next sought to better understand the mechanisms of [^{18}F]mFBG distribution.

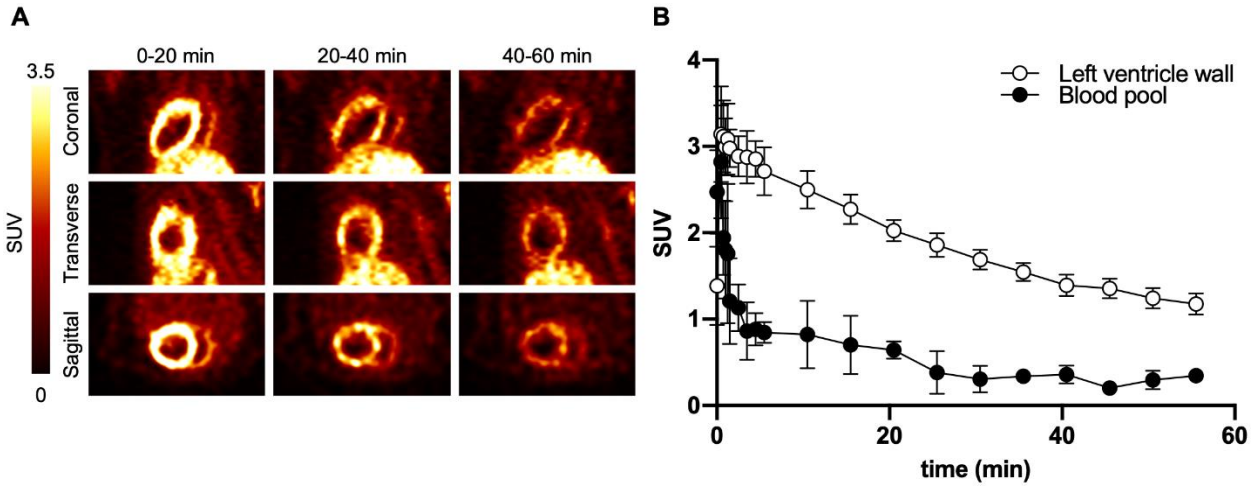

2.4.4. Figure 3. *in vivo* baseline PET imaging of the myocardium in SD rats. (A) Representative myocardial PET images and (B) corresponding time-activity curves (n = 5).

Ex vivo biodistribution studies were performed in male rats under baseline conditions at 30 minutes following intravenous radiotracer administration via the lateral tail vein, after blood pool activity stabilized (Table 2). As expected, high uptake in the myocardium was detected (3.12 ± 0.61 %ID/g) along with considerable distribution to other innervated organs such as the lung (1.12 ± 0.28 %ID/g), spleen (0.96 ± 0.22 %ID/g), adrenal gland (1.56 ± 0.36 %ID/g), and thyroid (1.25 ± 0.24 %ID/g). Renal retention (0.85 ± 0.03 %ID/g) predominated over hepatic retention (0.56 ± 0.27 %ID/g), and moderate bone uptake (0.85 ± 0.21 %ID/g) was observed in the femur, likely due to *in vivo* defluorination and consistent with previously reported findings on [^{18}F]mFBG and

related benzylguanidines.[32,39] The heart to blood (H:B) ratio was found to be 13.12, similar to [^{123}I]mIBG and [^{18}F]FBBG, despite lower NET affinity discussed above.[39] We conducted the same experiment on female rats (Table 1), and observed comparable retention in all organs except for the kidney (0.63 ± 0.09 %ID/g, $p = 0.035$).

2.4.5. Table 1. *Ex vivo* biodistribution in SD rats at 30 minutes.

	%ID/g				
Organ	**Baseline uptake**		**Uptake-1 blockade**		**Uptake 1 + uptake 2 blockade**
	Male	Female	Vehicle	DMI	PBZ
Heart	3.12 ± 0.61	3.08 ± 0.59	3.45 ± 0.69	2.40 ± 0.23 *	0.85 ± 0.12 *
Liver	0.56 ± 0.27	0.90 ± 0.46	0.54 ± 0.28	0.88 ± 0.33	0.64 ± 0.16
Kidney	0.85 ± 0.03	0.63 ± 0.09 *	0.87 ± 0.05	0.72 ± 0.18	5.05 ± 0.49 *
Lung	1.12 ± 0.28	1.26 ± 0.14	1.07 ± 0.35	0.75 ± 0.16	1.18 ± 0.15
Blood	0.24 ± 0.02	0.24 ± 0.08	0.26 ± 0.03	0.18 ± 0.07 *	0.27 ± 0.03
Spleen	0.96 ± 0.22	1.03 ± 0.21	0.99 ± 0.25	0.44 ± 0.11 *	0.74 ± 0.10
Adrenal	1.56 ± 0.36	1.50 ± 0.16	1.59 ± 0.43	0.58 ± 0.37 *	0.12 ± 0.02 *
Thyroid	1.25 ± 0.24	1.77 ± 0.68	1.29 ± 0.27	1.31 ± 0.36	1.37 ± 0.16
Bone	0.85 ± 0.21	0.77 ± 0.07	0.89 ± 0.24	0.59 ± 0.36	0.79 ± 0.16
H:B	13.12 ± 0.61	13.50 ± 3.48	13.27 ± 2.43	14.24 ± 1.50	3.40 ± 0.24 *
Animal weight (g)	111 ± 6	107 ± 3	125 ± 8	111 ± 10	100 ± 1

* Statistical significance ($p < 0.05$) reached by unpaired t-test comparing sexes (male and female, $n = 4$), and vehicle ($n = 5$) to uptake-1 blockade (DMI 1 mg/kg, $n = 5$), and uptake-1 + uptake-2 blockade (PBZ 27 ± 3 mg/kg, $n = 3$).

[^{18}F]mFBG is intact in SD rat myocardium. Next, we assessed the *in vivo* stability of [^{18}F]mFBG at the 30-minute time-point in myocardium and plasma samples (Figure 4A). Activity from the myocardium was extracted by homogenization, and metabolites were separated using reversed-phase HPLC. Fractions were collected every minute and radioactivity was quantified using a gamma counter. The parent compound accounted for 98 ± 1% and 97 ± 1% of myocardial uptake, with extraction efficiencies of 76 ± 3%, and 78 ± 2%, for males and females, respectively. These findings are consistent with previous reports on related NET radioligands and demonstrate selective uptake and limited myocardial metabolism of the radiotracer.[18,41,42] Concurrently,

[^{18}F]mFBG-associated activity was assessed in plasma following separation and protein precipitation of whole blood samples obtained via cardiac puncture. The parent fraction represented 22 ± 4 % and 20 ± 2% of total radioactivity with extraction efficiencies of 82 ± 2% and 81 ± 3% in males and females, respectively (Figure 4A). This is in marked contrast to the 90% parent fraction in plasma reported during human imaging experiments conducted by Pandit-Taskar *et al.*,[26] and likely arises from more aggressive peripheral metabolism in rodents. Lastly, we investigated the stability of [^{18}F]mFBG in human serum (Figure 4B), incubated at 37 °C and aliquoted samples for HPLC analysis at 0, 15, 60, and 120 minutes. Up to a 2-hour incubation, the tracer was found to remain 99% intact.

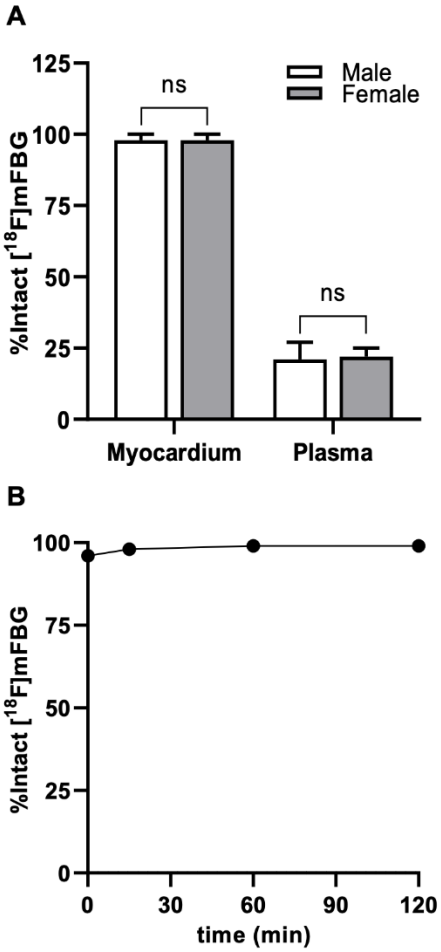

2.4.6. **Figure 4.** Percent intact [^{18}F]mFBG in (A) myocardium (n = 2), and plasma (n = 4) at 30 minutes *in vivo*, and (B) human serum *in vitro* (n =1).

[^{18}F]mFBG uptake is dependent on uptake-1 and uptake-2 transporters. To determine the uptake mechanisms of this tracer, animals were pre-treated with vehicle, desipramine (DMI, 1 mg/kg, iv), or phenoxybenzamine (PBZ, 27 ± 3 mg/kg, iv) 10 minutes prior to [^{18}F]mFBG administration and sacrificed at the 30-minute time-point (Table 1). DMI has been extensively evaluated in rodents and humans as a potent and selective NET inhibitor, while PBZ inhibits both neuronal and extraneuronal uptake non-selectively.[12,43–45] *Ex vivo* tissue counting experiments revealed 31% and 76% reductions in myocardial uptake with DMI (2.40 ± 0.23 %ID/g, p = 0.01), and PBZ (0.82 ± 0.12 %ID/g, p <0.0001), respectively, in comparison to vehicle (3.45 ± 0.69

%ID/g). *In* vivo PET imaging recapitulated these findings (Figure 5A), and time-activity curves revealed an increase in k_{mono} (accelerated washout) following DMI pre-treatment (0.058 min^{-1} vs 0.020 min^{-1}, $p = 0.044$). Uptake-1 and uptake-2 blockade also significantly reduced tracer retention in the blood pool and other innervated organs (Table 1).

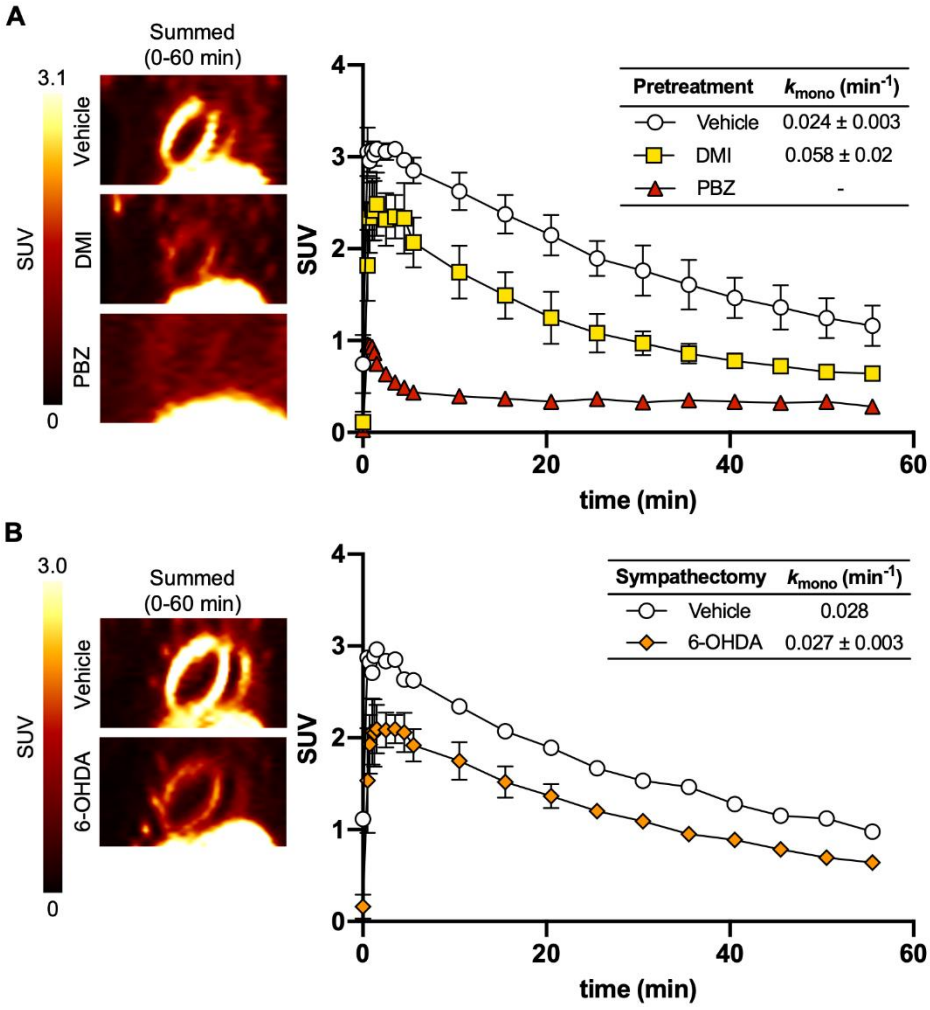

2.4.7. **Figure 5.** Representative *in vivo* myocardial PET imaging in SD rats following (A) pre-treatment (n =1-3), and (B) chemical sympathectomy (n = 1-3).

To provide additional evidence for tracer uptake in cardiac sympathetic neurons, chemical sympathetic denervation using 6-OHDA was performed on rats following an established treatment cycle.[46–48] [^{18}F]mFBG was administered one week after the last 6-OHDA treatment, and organ

uptake was measured *ex vivo* (Table 2). Myocardial tracer retention was reduced by 36% (1.32 ± 0.27 %ID/g, p = 0.02) relative to vehicle controls (2.04 ± 0.07 %ID/g). Notably, 6-OHDA treatment also reduced uptake in the spleen (0.30 ± 0.04, p <0.0001), and lowered the H:B ratio to 11.11 ± 2.21 compared to 17.20 ± 2.22 in vehicle treated rats (p = 0.01). The magnitude of the observed reduction of myocardial uptake with 6-OHDA treatment is consistent with the results obtained from DMI blocking experiments, indicating that [^{18}F]mFBG localizes within myocardial sympathetic neurons, mediated by NET. Representative PET images and time-activity curves for this treatment group further illustrate reduced LV myocardial uptake, with k_{mono} values remaining unaffected (Figure 5B).

We also performed autoradiography on mid-ventricular myocardial sections prepared from the same cohort of vehicle, PBZ, and 6-OHDA-treated rats (Figure 6). Comparable results were obtained by *ex vivo* autoradiography experiments, displaying high uptake of [^{18}F]mFBG throughout the LV (14.3 ±1.9 %ID×kg/m^2), in comparison to those pre-treated with PBZ (3.49 ± 0.99 %ID×kg/m^2, p = 0.02). Similarly, reduced uptake was observed in animals treated with 6-OHDA (8.07 ± 0.54 %ID×kg/m^2, p = 0.04) in comparison to vehicle controls (15.47 ± 2.10 %ID×kg/m^2). The uptake in the LV was observed to be homogenous in all samples. A reduction in myocardial uptake (Table 2) was also noted in rats treated with vehicle in comparison to our previously established baseline (Table 1) when measured in units of %ID/g. Myocardial sympathetic innervation is known to decrease in Wistar rats over one year in age,[49] and it is possible that a similar phenomenon could occur in young Sprague-Dawley animals. However, the apparent difference was resolved when expressing the dataset as standard uptake values (SUV, Table S3), suggesting that variations in animal bodyweight associated with the prolonged treatment cycle were responsible for this change.

2.4.8. Table 2. *Ex vivo* biodistribution in 6-OHDA treated SD rats at 30 minutes.

	%ID/g		
Organ	**Vehicle**	**6-OHDA**	
Heart	2.04 ± 0.07	1.32 ± 0.27	*
Liver	1.50 ± 0.23	1.49 ± 0.13	
Kidney	0.63 ± 0.13	0.73 ± 0.12	
Lung	1.30 ± 0.15	1.25 ± 0.29	
Blood	0.12 ± 0.02	0.12 ± 0.00	
Spleen	1.08 ± 0.10	0.30 ± 0.04	*
Adrenal	1.62 ± 0.29	1.41 ± 0.44	
Thyroid	1.56 ± 0.36	1.38 ± 0.35	
Bone	0.77 ± 0.25	1.01 ± 0.22	
H:B	17.20 ± 2.22	11.11 ± 2.21	*
Animal weight (g)	240 ± 12	235 ± 28	

* Statistical significance ($p < 0.05$) reached by unpaired t-test ($n = 4$).

NET blockade with DMI in rats has previously been shown to reduce radiotracer uptake in the myocardium using [^{11}C]HED and [^{18}F]mFPBG, but not [^{123}I]mIBG and [^{18}F]FBBG, due to a dominant contribution of extraneuronal uptake-2 dependent catecholamine handling of these latter molecules.[50–52] Consequently, NET-selective uptake with previously studied benzylguanidines is typically observed only in rabbits and higher species, where myocardial tracer retention is reduced by >60%.[53] Based on our findings, neuronal and extraneuronal uptake in the rat myocardium account for 31–36%, and 40–45% of [^{18}F]mFBG signal, respectively.

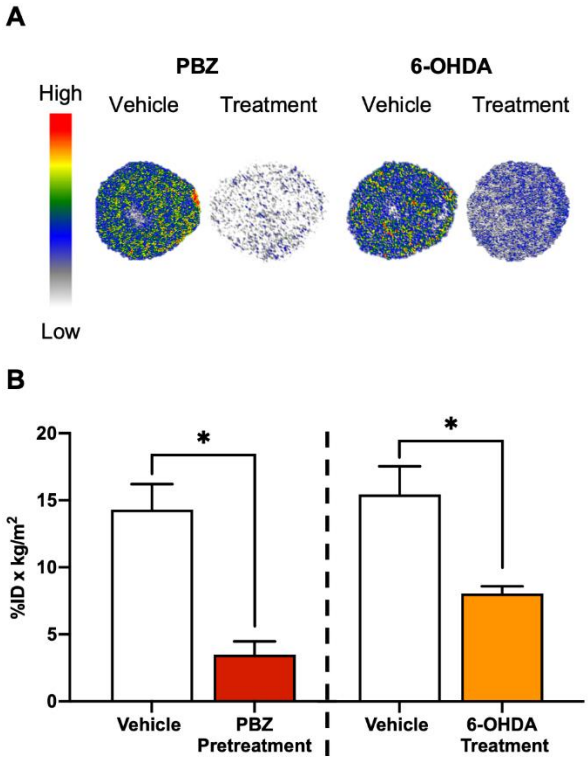

2.4.9. **Figure 6.** *Ex vivo* autoradiography of mid-ventricular short axis slices from SD rats at 30 minutes. (n = 2 animals per group). * Statistical significance reached by unpaired two-tailed t-test (p <0.05).

Clearance of myocardial [^{18}F]mFBG is independent of uptake-1 and uptake-2. Next, we were keen to determine the clearance mechanism of [^{18}F]mFBG in the myocardium and performed DMI- and PBZ-chase experiments with PET imaging (Figure 7). Each pharmacological treatment was administered after peak LV accumulation (10 minutes after tracer injection), and differences in tracer washout were quantified by k_{mono}. Animals treated with DMI chase (0.023 ± 0.004 min^{-1}), and PBZ chase (0.035 ± 0.008 min^{-1}) were not found to have significantly increased washout compared to animals administered vehicle chase treatment (0.027 ± 0.002 min^{-1}). DMI chase insensitivity suggests minimal activity reuptake by NET, consistent with the lower affinity of [^{18}F]mFBG for NET. Other benzylguanidine radiotracers have similarly shown insensitivity to

DMI-chase treatment in higher species, which is attributed to irreversible intraneuronal vesicular trapping.[53] PBZ chase insensitivity supports the notion of insignificant [^{18}F]mFBG reuptake through extraneuronal transporters. Based on our tracer stability results, the observed washout of radioactivity is unlikely to be the result of an excreted metabolite. Similarly, the high degree of myocardial washout over 60 minutes and good quality of monoexponential fits for these data suggest that selective clearance from myocytes along with neuronal retention is improbable. Importantly, human imaging studies, where uptake-2 contributes less to benzylguanidine uptake, have also revealed rapid washout uniquely for [^{18}F]mFBG.[26] Therefore, the absence of increased tracer washout from the myocardium upon inhibition of uptake-1 and uptake-2 mechanisms following peak activity accumulation suggests that [^{18}F]mFBG clearance to plasma predominates over reuptake by these transporters.

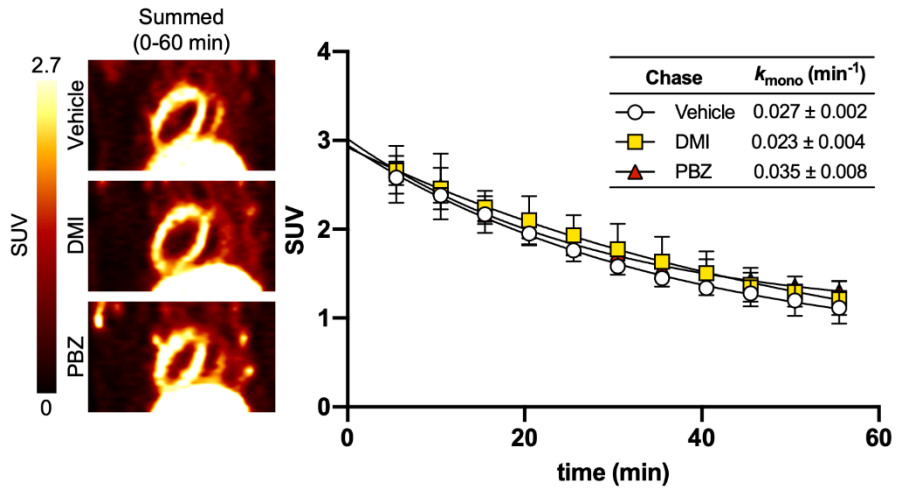

2.4.10. Figure 7. *in vivo* PET imaging of the myocardium in SD rats following chase dosing with vehicle, DMI, and PBZ at 10 minutes (n = 3 per group)

2.5. Conclusions

A reliable and efficient automated synthesis of [^{18}F]mFBG in high molar activity has been developed, enabling preclinical evaluation for cardiac sympathetic nerve imaging. Our *in vivo* investigation of [^{18}F]mFBG in Sprague Dawley rats showed clear delineation of the left ventricle with tracer washout following a monoexponential fit after 5 minutes. [^{18}F]mFBG stability studies revealed >97% of the parent tracer in the myocardium with moderate parent fraction in plasma at an equivalent time-point. No significant differences between sexes were identified for baseline myocardial uptake and parent fraction in tissue or plasma. [^{18}F]mFBG, in comparison to its benzylguanidine analogues [^{123}I]mIBG and [^{18}F]FBBG, possesses unique NET dependent neuronal uptake in rats evidenced by pre-treatment blockade with DMI and 6-OHDA sympathectomy. Extraneuronal uptake-2 dependent mechanisms also contribute significantly to radiotracer accumulation. These results were further supported by PET imaging and *ex vivo* autoradiography. Chase-dosing experiments with DMI and PBZ demonstrated insignificant radiotracer recycling in the myocardium through uptake-1 and uptake-2 transporters, which is distinct from the neurotransmitter analogue [^{11}C]HED. In summary, [^{18}F]mFBG is a promising radiotracer candidate that displays favourable imaging properties and unique myocardial clearance with the potential for accurate quantification of SNS dysfunction using PET imaging in rats and higher species.

2.6. Materials and Methods

Chemistry. The synthetic procedure for the preparation of the [^{18}F]mFBG precursor (**4**), including the synthesis of SPIAd (**3**) was performed as previously described.[35]

N′,*N*″-di(*tert*-butoxy)carbonyl-*meta*-iodobenzylguanidine (**1**). A solution of 1,3-bis(*tert*-butoxycarbonyl)-2-methyl-2-thiopseudourea (1.2 mmol) in DMF (0.5 mL) was added to a flask containing *meta*-iodobenzylamine hydrochloride (1 mmol) and triethylamine (3 mmol) dissolved in DMF (0.5 mL). The reaction was stirred at room temperature overnight, diluted with ethyl acetate, and washed with water (3×), then brine (3×). The organic layers were pooled and dried with magnesium sulfate, filtered, and concentrated under reduced pressure. The residue was purified by flash column chromatography (0–25% hexane/ethyl acetate) to yield the final product as a white solid (437 mg, 92%). ^{1}H NMR (600 MHz, $CDCl_3$): δ 11.53 (s, 1H), 8.58 (s, 1H), 7.67 (s, 1H), 7.61 (d, *J* = 7.8 Hz, 1H), 7.28 (d, *J* = 7.7 Hz, 1H), 7.08 (t, *J* =7.8 Hz, 1H), 4.57 (d, *J* = 5.4 Hz, 2H), 1.51 (s, 9H), 1.49 (s, 9H) ppm. ^{13}C NMR (151 MHz, $CDCl_3$): δ 163.5, 156.1, 153.2, 139.8, 136.9, 136.7, 130.4, 127.1, 94.5, 83.3, 79.5, 44.1, 28.3, 28.0, ppm.

N,*N*′,*N*′,*N*″-tetra(*tert*-butoxy)carbonyl-*meta*-iodobenzylguanidine (**2**). To a solution of **1** (0.92 mmol) in THF (6.12 mL) was added *N*,*N*-dimethylaminopyridine (4.6 mmol). The reaction was cooled to 0 °C and di-*tert*-butyl dicarbonate (3.45 mmol) was added over ten minutes. The reaction was then stirred at room temperature for two hours and concentrated under reduced pressure. The residue was resuspended in ethyl acetate, and the organic layer was washed with water (3×). The organic fractions were collected, dried with magnesium sulfate, filtered, concentrated under reduced pressure, and purified by flash chromatography (0–25% hexane/ethyl acetate) to yield the final product as a colorless oil (571 mg, 92%). ^{1}H NMR (400 MHz, $CDCl_3$): δ 7.71 (s, 1H), 7.55 (d, *J* = 7.9 Hz, 1H), 7.37 (d, *J* = 7.8 Hz, 1H), 7.01 (t, *J* = 7.7 Hz, 1H), 4.93 (s,

2H), 1.46 (s, 9H), 1.42 (s, 18H), 1.38 (s, 9H) ppm. ^{13}C NMR (101 MHz, $CDCl_3$): δ 157.2, 151.1, 147.2, 144.4, 139.8, 136.8, 136.3, 130.0, 127.2, 94.0, 84.0, 83.7, 82.0, 49.3, 28.0, 27.9, 27.8 ppm.

spiroadamantyl-1,3-dioxane-4,6-dione (**3**). Malonic acid (4.8 mmol), acetic anhydride (5.1 mmol, 0.5 mL), and H_2SO_4 (1 drop) were stirred at 60 °C for 15 minutes, then cooled to room temperature. 2-Adamantanone (4.8 mmol) was added dropwise over 0.5–1 hr, and the mixture was stirred at room temperature for an additional 1 hr. The reaction was concentrated under reduced pressure, reconstituted in dichloromethane (DCM) then washed with water (3×), dried with magnesium sulfate, and filtered. The crude was concentrated under reduced pressure and recrystallized using hexane and ethyl acetate to yield the final product as white crystals (680 mg, 60%).^{1}H NMR (600 MHz, $CDCl_3$) δ 3.60 (s, 2H), 2.18–2.10 (m, 6H), 1.89 (s, 2H), 1.79–1.73 (m, 6H). ^{13}C NMR (151 MHz, $CDCl_3$) δ 163.1, 109.6, 37.6, 36.7, 36.5, 33.5, 26.1 ppm.

N,*N*′,*N*′,*N*″-tetra(*tert*-butoxy)carbonyl-*meta*-(spiroadamantyl-1,3-dioxane-4,6-dione-5-ylidene)iodobenzylguanidine (**4**). Compound **2** (1.1 mmol) was dissolved in anhydrous acetonitrile (ACN, 6.8 mL) and TMSOAc (2.86 mmol) was added. Then, a slurry of Selectfluor (1.43 mmol) in ACN (6.8 mL) was added to the reaction and left to stir overnight. The crude mixture was then concentrated under pressure and resuspended in DCM (10 mL). The solution was filtered by gravity filtration, and the filtrate was collected, concentrated, and resuspended in EtOH (4.4 mL). A solution of **3** (1.1 mmol) dissolved in a 10% aqueous bicarbonate solution (3.7 mL) was then added dropwise to the reaction. After 6 hours, the contents of the flask were concentrated under reduced pressure and purified by column chromatography (0–100% hexane/ethyl acetate) to yield the final product as an off-white powder (415 mg, 41%). ^{1}H NMR (600 MHz, $CDCl_3$): δ 7.86 (s, 1H), 7.73 (d, *J* = 8.4 Hz, 1H), 7.64 (d, *J* = 7.8 Hz, 1H), 7.34 (t, *J* = 7.9 Hz, 1H), 5.00 (s, 2H), 2.41 (s, 2H), 2.16 (s, 2H), 2.14 (s, 2H), 1.84 (s, 2H), 1.69 (s, 4H), 1.67 (s, 2H), 1.48 (s, 9H), 1.45 (s,

18H), 1.40 (s, 9H) ppm. ^{13}C NMR (151 MHz, CDCl3): δ 163.4, 157.2, 150.9, 147.3, 144.5, 142.0, 132.4, 131.9, 131.7, 114.0, 107.5, 84.7, 84.1, 84.0, 82.4, 55.5, 49.5, 37.2, 35.6, 33.7, 33.5, 28.8, 28.0, 26.5 ppm.

meta-fluorobenzylguanidine hydrochloride (**6**). The non-radioactive standard (mFBG, **6**) was synthesized following the guanylation procedure outlined for the synthesis of compound **1** using *meta*-fluorobenzylamine (0.12 mmol). The partially Boc-protected intermediate (0.18 mmol, **5a**) was concentrated, and resuspended in dioxane, followed by the addition of excess 4.0 M HCl in dioxane. The reaction was left to stir for 15 min, and the residue was concentrated under reduced pressure. The product was precipitated (5×) using methanol and *tert*-butyl methyl ether to yield the final product as a white powder (27 mg, 88%). ^{1}H NMR (600 MHz, DMSO): δ = 8.25 (br, 1H), 7.90-6.90 (br, 3H), 7.46-7.40 (m, 1H), 7.18-7.12 (m, 3H), 4.42 (d, J = 6.0 Hz, 2H). ^{13}C NMR (151 MHz, DMSO): δ = 163.5 (d, J = 244.0 Hz), 157.6, 140.9 (d, J = 7.0 Hz), 131.1 (d, J = 8.3 Hz), 123.7 (d, J = 2.8 Hz), 114.8 (d, J = 21.0.8 Hz), 114.5 (d, J = 22.1 Hz), 43.8.^{19}F NMR (377 MHz, DMSO): δ = -113.1 (s, 1F). The product was characterized in accordance with the literature.[31]

Radiochemistry. Aqueous [^{18}F]fluoride (no-carrier-added) was produced by a Siemens CTI Eclipse HP/RD Hybrid Cyclotron (11 MeV) via an ^{18}O(p,n)^{18}F nuclear reaction and delivered to a hot cell. A solution of TEAB (4 mg in 1 mL of MeCN) was added to an aliquot of target water (≤ 1 mL) containing a suitable amount of [^{18}F]fluoride in a sealed conical vial equipped with a vent needle. The vial was placed in a heating block and dried under nitrogen flow (passed over a P_2O_5-Drieriete™ column) at 100 °C. Acetonitrile (1 mL) was added to the dried residue, and heating was resumed until the liquid was completely evaporated. This process was repeated three times. Subsequently, the contents of the vial were resolubilized in the desired solvent (0.3 mL) containing precursor **4** (6 mg) and then heated at the desired temperature for 5, 10, 15, or 20 min. An aliquot

of the crude reaction was spotted onto a silica plate developed in a chamber containing ethyl acetate, and crude yields were determined by radioTLC. Aqueous HCl (0.2 mL, 6 or 12 M) was then added to the vial and heated at the desired temperature (100 °C or 120 °C) for 5, 10, 15, or 20 min. Following completion, the reaction was partially neutralized with NaOH (0.2 mL, 8 M) and the mixture was sampled for radioTLC analysis. An additional sample was prepared to verify the yield by radioHPLC using a Waters 2695 Alliance HPLC equipped with a Phenomenex Luna 10 µm C18(2) (100 Å, 250 mm × 4.6 mm) column, a 996 Photodiode Array Detector (Waters), and a Carroll & Ramsey Associates 105-S high-sensitivity radiation detector. Gradient: 1/99 10 mM PBS/ACN for 1 min, linear gradient to 80/20 over 8 min, isocratic for 7 minutes, then linear gradient back to 1/99 over 3 minutes. Retention time: ~15 min, flow rate = 1 mL/min.

Automated radiosynthesis. A fully automated sequence was developed on a GE TRACERlab™ FX2N module to prepare [^{18}F]mFBG. The reagents were loaded as follows: TEAB (4 mg in 0.8 mL H_2O) in vial 1; HCl (0.6 mL, 12 M) in vial 2; precursor **4** (12 mg in 0.6 mL DMSO) in vial 3; ACN (1 mL) in vial 4; H_2O (0.6 mL) in vial 5; ACN/H_2O (30/70, 1.3 mL) in vial 6. A Sep-pak Carboxy Methyl (CM) ion exchange cartridge (preconditioned with 10 mL of EtOH and 10 mL of H_2O) was also installed. [^{18}F]Fluoride (~11 GBq) was captured from the [^{18}O]H_2O target solution using a Sep-pak Accel Plus QMA Plus Light cartridge (preconditioned using 10 mL of EtOH, 10 mL of H_2O, 10 mL of 0.1 M $NaHCO_3$, and 10 mL H_2O), and eluted into the reactor by unloading vial 1. After unloading vial 4, the reactor was heated to 80 °C for 5 minutes, and 120 °C for 3 minutes under a nitrogen stream to yield dried [^{18}F]TEAF. The reactor was then cooled to 40 °C using compressed air, before initiating the reaction by unloading vial 3. The radiofluorination reaction was performed at 120 °C for 10 minutes and subsequently cooled to 50 °C. Acidic deprotection was initiated by unloading vial 2 and heating the reactor to 120 °C

for 5 minutes. Following cooling with compressed air, the reaction was quenched with the contents of vial 5 and transferred to an adjacent vial. The reactor was further rinsed with the contents of vial 6 and collected in the same vial. The crude mixture was purified by reversed phase HPLC (Phenomenex Luna 10 µm C18(2), 250 x 10 mm, isocratic 30/70 ACN/H_2O + 0.1% TFA, flow rate of 5 mL/min). The product was collected from 13–15 min into a bulk vessel containing 20 mL of sterile water. The contents of this vessel were passed through the CM cartridge at a flow rate of 2.5 mL/min and rinsed with H_2O (10 mL). [^{18}F]mFBG was eluted with physiological saline (4 mL) and passed through a sterile filter into a crimped vial fitted with a vent needle. Radiochemical yield (RCY) was determined by decay correcting the amount of initial activity to the end of synthesis (EoS). Molar activity was determined by measurement of the UV absorbance of a known amount of radioactivity under identical HPLC conditions used to generate a calibration curve for the corresponding non-radioactive standard. The ratio of radioactivity (GBq) to moles (µmol) provided the molar activity (GBq/µmol), which was decay corrected to the end of synthesis (EoS).

Animal care. Male and female Sprague-Dawley rats (80–110 g) were purchased from Charles River Laboratories (Senneville, Quebec) and housed in environmentally enriched cages with free access to food and water. All housing, handling, and experimental procedures were in strict accordance with the guidelines of Canadian Council on Animal Care and with approval of the University of Ottawa Animal Care Committee. Animals used in this study were 4 weeks old unless specified otherwise.

PET imaging. Male and female Sprague-Dawley rats (4–8 weeks old, 80–270 g) were anesthetized with 2% isoflurane and placed in the PET scanner. Following a 10-minute transmission scan, the animals were injected with [^{18}F]mFBG as a bolus over 30 seconds via the lateral tail vein and maintained under isoflurane during the imaging protocol. Whole body PET

imaging was performed for 60 minutes (4 × 15 sec frames; 4 × 1 min frames; 10 × 5 min frames) using a Siemens DPET scanner. The collected emission data was corrected for attenuation and scatter and reconstructed using the 3D-OSEM/MAP algorithm. Volumes of interest (VOI) were drawn for the left ventricle and cardiac blood pool using FlowQuant™. Blood pool time-activity curves were created from mean values of three samples located in the left ventricle cavity, the left ventricle base, and the left atrium. Polar maps were also generated by FlowQuant™. Uptake values were obtained in nCi/cc and converted to SUV using the total injected dose and animal bodyweight, as shown in the time-activity curves.

***Ex vivo* pharmacological blocking studies.** Male and female Sprague Dawley rats were anesthetized using 2% isoflurane and received lateral tail-vein injections of 4–13 MBq of [^{18}F]mFBG in 0.15–0.3 mL of sterile saline (0.9% sodium chloride). For animals requiring pharmacological treatment, DMI (1 mg/kg), PBZ (27 ± 3 mg/kg), or saline was administered via the lateral tail vein 10 minutes prior to radiotracer injection. Baseline studies were conducted without pretreatment. Subsequently, anesthesia was stopped, and the animals were allowed to recover. After thirty minutes, the animals were sacrificed by CO_2 asphyxiation followed by cervical dislocation. All organs were harvested (blood collected by cardiac puncture), weighed, and counted for radioactivity in a gamma counter (Hidex Automatic Gamma Counter, Energy window: 480–558 keV). Counts per minute (CPM) were converted to activity using a set of calibration standards with known activities. Percentage injected dose (%ID) was calculated from dividing the organ activity by the injected dose (decay-corrected) and further normalized by sample mass to obtain the percentage injected dose per gram tissue (%ID/g).

Note: Due to the poor solubility of PBZ in physiological saline, a 20 mg/mL suspension of PBZ was prepared and filtered through a 0.45 μm filter. A known volume of the effluent was

sampled on a Waters Xevo TQD with an Acquity UPLC H-Class Plus system, and the concentration of the solution was determined using a calibration curve (Figure S11).

6-OHDA treatment. Male Sprague Dawley rats (80–110 g) were acclimatized for one week upon arrival, then given the previously reported treatment cycle (Figure S7).[46] Briefly, animals were treated with either vehicle (saline + 0.1% ascorbate) or 6-OHDA via the lateral tail vein as a bolus injection. Animals were dosed twice on day 1 (morning and afternoon, 50 mg/kg), and twice on day 7 (morning and afternoon, 100 mg/kg). On day 14, the animals were administered [^{18}F]mFBG, and organs were harvested, counted for radioactivity, and weighed. Alternatively, vehicle and 6-OHDA treated rats were subject to PET imaging, as previously described.

Parent Fraction in Plasma and Myocardium. Male and female Sprague Dawley rats (80–110 g) were injected with [^{18}F]mFBG. Blood samples (500–1200 µL) were obtained via cardiac puncture at the 30-minute time-point and placed in a heparinized tube. Samples were centrifuged at 4 °C for 7 minutes at 4000 rpm, and the plasma fraction was isolated. Protein free plasma (PFP) was obtained by the addition of an equal volume of ice-cold ACN, followed by centrifugation at 4 °C for 5 minutes at 4000 rpm. The myocardium was perfused with 15 mL of 1× PBS, cut into small pieces, and placed into separate tubes containing a 50/50 mixture of ACN/H_2O. The tubes were placed in an ice bath and homogenized using a Fisher Scientific PowerGen 125 (125 W, 115 V, 50/60 Hz) adapted with a sawtooth, 7 × 95 mm generator. Samples were then centrifuged at 4 °C for 5 minutes at 4000 rpm. For both plasma and myocardium preparations, additional extractions were performed until extraction efficiency was ≥70%, as measured on a gamma counter. The supernatants were then filtered through a 0.22 µm filter, spiked with non-radioactive standard (10 µL, 1 mg/mL), and injected onto the analytical radioHPLC. Fractions were collected every minute, for 20 minutes, and placed on the gamma counter to determine the total activity in each fraction.

Autoradiography. Sprague Dawley rats were administered vehicle or pharmacological treatment prior to receiving [^{18}F]mFBG, as described above. After 30 minutes, hearts were perfused with 15 mL of 1× PBS and harvested. Samples were embedded with OCT, flash frozen, sliced into 10 µm sections using a Thermofisher Science Microm HM 550 cryostat. Tissue sections from the apex to the base were obtained by slicing along the short axis of the heart. The sections were immediately exposed to a super-resolution Storage Phosphor Screen (BAS-IP SR 2025 E) in an Electrophoresis Systems Autoradiography Cassette (FBXC 810) overnight. The images were obtained using a Cyclone Plus Storage Phosphor System and images were analyzed using OptiQuant. ROIs were drawn for the whole myocardium and digital light units (DLU) were converted to activity using a using a set of calibration standards with known activities on the same screen. Percentage injected dose (%ID) was calculated by dividing the ROI activity by the injected dose (decay-corrected) and further normalized by area (m^2) and animal weight (kg) to obtain weight-normalized activity density (%ID×kg/m^2).

Statistical Analysis. Statistical analysis was performed using GraphPad Prism. Significance was set at the 0.05 level. The data are presented as mean ± standard deviation. Differences between two groups were tested using a 2-tailed unpaired Student's t-test.

2.7. Author information

Corresponding author* Molecular Imaging Probes and Radiochemistry Research Laboratory. University of Ottawa Heart Institute Ottawa K1Y 4W7, Canada. Department of Biochemistry, Microbiology and Immunology and Department of Chemistry and Biomolecular Sciences, University of Ottawa. E-mail: benjamin.rotstein@uottawa.ca

2.8. Acknowledgements

We thank the staff of the University of Ottawa Heart Institute PET Radiochemistry Laboratory and Biomedical Engineering for cyclotron and small animal PET scanner support. Financial support from the Heart & Stroke Foundation of Canada and CANet (PG-17-0736 to B.H.R.), CFI (JELF 36848 to B.H.R.), the Province of Ontario (ER17-13-119 to B.H.R.) and the University of Ottawa Heart Institute are gratefully acknowledged. Scholarship support was received from the Province of Ontario (A.B. & G.F.), CIHR (G.F.), and the IIE Fulbright Program (A.P.).

2.9. Abbreviations

[^{18}F]3F-PHPG, 3-[^{18}F]fluoro-*para*-hydroxyphenethylguanidine; [^{18}F]4F-MHPG, 4-[^{18}F]fluoro-*meta*-hydroxyphenethylguanidine; 6-OHDA, 6-hydroxydopamine; CM, carboxymethyl; DMI, desipramine; EoS, end of synthesis; [^{18}F]FBBG, [^{18}F]flubrobenguane; HLB, hydrophilic lipophilic balance; LV, left ventricle; [^{18}F]mFPBG, *meta*-(3-[^{18}F]fluoropropyl)benzylguanidine; [^{18}F]mFBG, *meta*-[^{18}F]fluorobenzylguanidine; [^{123}I]mIBG, *meta*-[^{123}I]iodobenzylguanidine; [^{11}C]HED, *meta*-[^{11}C]hydroxyephedrine; NET, norepinephrine transporter; PBZ, phenoxybenzamine; PET, positron emission tomography; QMA, quaternary methyl ammonium; RCY, radiochemical yield; RE, reformulation efficiency; SUV, standardized uptake value; SNS, sympathetic nervous system; VMAT, vesicular monoamine transporter;

2.10. References

(1) Jamali, H. K.; Waqar, F.; Gerson, M. C. Cardiac Autonomic Innervation. *J. Nucl. Cardiol.* **2017**, *24* (5), 1558–1570. https://doi.org/10.1007/s12350-016-0725-7.

(2) Zelt, J. G. E.; deKemp, R. A.; Rotstein, B. H.; Nair, G. M.; Narula, J.; Ahmadi, A.; Beanlands, R. S.; Mielniczuk, L. M. Nuclear Imaging of the Cardiac Sympathetic Nervous System: A Disease-Specific Interpretation in Heart Failure. *JACC Cardiovasc. Imaging* **2020**, *13* (4), 1036–1054. https://doi.org/10.1016/j.jcmg.2019.01.042.

(3) van der Bijl, P.; Knuuti, J.; Delgado, V.; Bax, J. J. Cardiac Sympathetic Innervation Imaging with PET Radiotracers. *Curr. Cardiol. Rep.* **2021**, *23* (1), 4. https://doi.org/10.1007/s11886-020-01432-9.

(4) Franciosi, S.; Perry, F. K. G.; Roston, T. M.; Armstrong, K. R.; Claydon, V. E.; Sanatani, S. The Role of the Autonomic Nervous System in Arrhythmias and Sudden Cardiac Death. *Auton. Neurosci.* **2017**, *205*, 1–11. https://doi.org/10.1016/j.autneu.2017.03.005.

(5) Jungen, C.; Scherschel, K.; Flenner, F.; Jee, H.; Rajendran, P.; De Jong, K. A.; Nikolaev, V.; Meyer, C.; Ardell, J. L.; Tompkins, J. D. Increased Arrhythmia Susceptibility in Type 2 Diabetic Mice Related to Dysregulation of Ventricular Sympathetic Innervation. *Am. J. Physiol.-Heart Circ. Physiol.* **2019**, *317* (6), H1328–H1341. https://doi.org/10.1152/ajpheart.00249.2019.

(6) Fisher, V. L.; Tahrani, A. A. Cardiac Autonomic Neuropathy in Patients with Diabetes Mellitus: Current Perspectives. *Diabetes Metab. Syndr. Obes. Targets Ther.* **2017**, *10*, 419–434. https://doi.org/10.2147/DMSO.S129797.

(7) Farber, G.; Boczar, K. E.; Wiefels, C. C.; Zelt, J. G. E.; Guler, E. C.; deKemp, R. A.; Beanlands, R. S.; Rotstein, B. H. The Future of Cardiac Molecular Imaging. *Semin. Nucl. Med.* **2020**, *50* (4), 367–385. https://doi.org/10.1053/j.semnuclmed.2020.02.005.

(8) Boutagy, N. E.; Sinusas, A. J. Recent Advances and Clinical Applications of PET Cardiac Autonomic Nervous System Imaging. *Curr. Cardiol. Rep.* **2017**, *19* (4), 33. https://doi.org/10.1007/s11886-017-0843-0.

(9) Thackeray, J. T.; Bengel, F. M. Assessment of Cardiac Autonomic Neuronal Function Using PET Imaging. *J. Nucl. Cardiol.* **2013**, *20* (1), 150–165. https://doi.org/10.1007/s12350-012-9644-4.

(10) Jacobson, A. F.; Senior, R.; Cerqueira, M. D.; Wong, N. D.; Thomas, G. S.; Lopez, V. A.; Agostini, D.; Weiland, F.; Chandna, H.; Narula, J.; ADMIRE-HF Investigators. Myocardial Iodine-123 Meta-Iodobenzylguanidine Imaging and Cardiac Events in Heart Failure. Results of the Prospective ADMIRE-HF (AdreView Myocardial Imaging for Risk Evaluation in Heart Failure) Study. *J. Am. Coll. Cardiol.* **2010**, *55* (20), 2212–2221. https://doi.org/10.1016/j.jacc.2010.01.014.

(11) Fallavollita, J. A.; Heavey, B. M.; Luisi, A. J.; Michalek, S. M.; Baldwa, S.; Mashtare, T. L.; Hutson, A. D.; Dekemp, R. A.; Haka, M. S.; Sajjad, M.; Cimato, T. R.; Curtis, A. B.; Cain, M. E.; Canty, J. M. Regional Myocardial Sympathetic Denervation Predicts the Risk of Sudden Cardiac Arrest in Ischemic Cardiomyopathy. *J. Am. Coll. Cardiol.* **2014**, *63* (2), 141–149. https://doi.org/10.1016/j.jacc.2013.07.096.

(12) Chen, X.; Kudo, T.; Lapa, C.; Buck, A.; Higuchi, T. Recent Advances in Radiotracers Targeting Norepinephrine Transporter: Structural Development and Radiolabeling Improvements. *J. Neural Transm.* **2020**, *127* (6), 851–873. https://doi.org/10.1007/s00702-020-02180-4.

(13) Langer, O.; Halldin, C. PET and SPET Tracers for Mapping the Cardiac Nervous System. *Eur. J. Nucl. Med. Mol. Imaging* **2002**, *29* (3), 416–434. https://doi.org/10.1007/s002590100640.

(14) Travin, M. I. Imaging of Cardiac Autonomic Innervation with SPECT and PET. *Curr. Cardiovasc. Imaging Rep.* **2013**, *7* (1), 9242. https://doi.org/10.1007/s12410-013-9242-0.

(15) Raffel, D. M.; Jung, Y.-W.; Gildersleeve, D. L.; Sherman, P. S.; Moskwa, J. J.; Tluczek, L. J.; Chen, W. Radiolabeled Phenethylguanidines: Novel Imaging Agents for Cardiac Sympathetic Neurons and Adrenergic Tumors. *J. Med. Chem.* **2007**, *50* (9), 2078–2088. https://doi.org/10.1021/jm061398y.

(16) Jang, K. S.; Jung, Y.-W.; Gu, G.; Koeppe, R. A.; Sherman, P. S.; Quesada, C. A.; Raffel, D. M. 4-[^{18}F]Fluoro-m-Hydroxyphenethylguanidine: A Radiopharmaceutical for Quantifying Regional Cardiac Sympathetic Nerve Density with Positron Emission Tomography. *J. Med. Chem.* **2013**, *56* (18), 7312–7323. https://doi.org/10.1021/jm400770g.

(17) Raffel, D. M.; Wieland, D. M. Assessment of Cardiac Sympathetic Nerve Integrity with Positron Emission Tomography. *Nucl. Med. Biol.* **2001**, *28* (5), 541–559. https://doi.org/10.1016/s0969-8051(01)00210-4.

(18) Bengel, F. M.; Schwaiger, M. Assessment of Cardiac Sympathetic Neuronal Function Using PET Imaging. *J. Nucl. Cardiol.* **2004**, *11* (5), 603–616. https://doi.org/10.1016/j.nuclcard.2004.06.133.

(19) Woo, S.-K.; Moon, B. S.; Kim, B. S.; Kim, M. H.; Lee, Y. J.; Jung, J. H.; Lee, K. C.; Seo, Y.; Kim, W.; Lim, S. M.; Lee, B. C.; Kim, S. E. Feasibility of Myocardial PET Imaging Using a Benzylguanidine Analog: Meta-(3-[^{18}F]Fluoropropyl)Benzylguanidine

([^{18}F]MFPBG). *Nucl. Med. Biol.* **2018**, *61*, 63–70. https://doi.org/10.1016/j.nucmedbio.2018.04.005.

(20) Raffel, D. M.; Jung, Y.-W.; Koeppe, R. A.; Jang, K S.; Gu, G.; Scott, P. J.H.; Murthy, V. L.; Rothley, J.; Frey, K. A. First-in-Human Studies of [^{18}F] Fluorohydroxyphenethylguanidines. *Circ. Cardiovasc. Imaging* **2018**, *11* (12), e007965. https://doi.org/10.1161/CIRCIMAGING.118.007965.

(21) Jung, Y.-W.; Jang, K. S.; Gu, G.; Koeppe, R. A.; Sherman, P. S.; Quesada, C. A.; Raffel, D. M. [^{18}F]Fluoro-Hydroxyphenethylguanidines: Efficient Synthesis and Comparison of Two Structural Isomers as Radiotracers of Cardiac Sympathetic Innervation. *ACS Chem. Neurosci.* **2017**, *8* (7), 1530–1542. https://doi.org/10.1021/acschemneuro.7b00051.

(22) Jung, Y.-W.; Gu, G.; Raffel, D. M. Improved Synthesis of 4-[^{18}F]Fluoro-m-Hydroxyphenethylguanidine Using an Iodonium Ylide Precursor. *J. Label. Compd. Radiopharm.* **2019**, *62* (12), 835–842. https://doi.org/10.1002/jlcr.3791.

(23) Chen, X.; Fritz, A.; Werner, R. A.; Nose, N.; Yagi, Y.; Kimura, H.; Rowe, S. P.; Koshino, K.; Decker, M.; Higuchi, T. Initial Evaluation of AF78: A Rationally Designed Fluorine-18-Labelled PET Radiotracer Targeting Norepinephrine Transporter. *Mol Imaging Biol* **2020**, *22* (3), 602–611. https://doi.org/10.1007/s11307-019-01407-5.

(24) Garg, P.K.; Garg, S.; Zalutsky, M.R. Synthesis and Preliminary Evaluation of *para*- and *meta*-[^{18}F]Fluorobenzylguanidine. *Nucl. Med. Biol.* **1994**, *21* (1), 97–103. https://doi.org/10.1016/0969-8051(94)90135-X.

(25) Zhang, H.; Huang, R.; Pillarsetty, N.; Thorek, D. L. J.; Vaidyanathan, G.; Serganova, I.; Blasberg, R. G.; Lewis, J. S. Synthesis and Evaluation of ^{18}F-Labeled Benzylguanidine

Analogs for Targeting the Human Norepinephrine Transporter. *Eur. J. Nucl. Med. Mol. Imaging* **2014**, *41* (2), 322–332. https://doi.org/10.1007/s00259-013-2558-9.

(26) Pandit-Taskar, N.; Zanzonico, P. B.; Staton, K. D.; Carrasquillo, J. A.; Reidy-Lagunes, D.; Lyashchenko, S. K.; Burnazi, E.; Zhang, H.; Lewis, J. S.; Blasberg, R.; Larson, S. M.; Weber, W. A.; Modak, S. Biodistribution and Dosimetry of ^{18}F-Meta Fluorobenzyl Guanidine (MFBG): A First-in-Human PET-CT Imaging Study of Patients with Neuroendocrine Malignancies. *J. Nucl. Med.* **2017**. https://doi.org/10.2967/jnumed.117.193169.

(27) Glowniak, J. V.; Turner, F. E.; Gray, L. L.; Palac, R. T.; Lagunas-Solar, M. C.; Woodward, W. R. Iodine-123 Metaiodobenzylguanidine Imaging of the Heart in Idiopathic Congestive Cardiomyopathy and Cardiac Transplants. *J. Nucl. Med.* **1989**, *30* (7), 1182–1191.

(28) Takatsu, H.; Noda, T.; Arai, M.; Kunishima, A.; Inoue, M.; Tazawa, S.; Kurosawa, H.; Nishigaki, K.; Fujiwara, H. Washout of I-123 Meta-Iodobenzylguanidine for Assessing Cardiac Sympathetic Activity with Progression of Hypertension in Dahl Salt-Sensitive Rats. *J. Nucl. Cardiol.* **1999**, *6* (2), 204–210. https://doi.org/10.1016/S1071-3581(99)90081-8.

(29) Zelt, J. G. E.; Britt, D.; Mair, B. A.; Rotstein, B. H.; Quigley, S.; Walter, O.; Garrard, L.; Robinson, S.; Mielniczuk, L. M.; deKemp, R. A.; Beanlands, R. S. Regional Distribution of Fluorine-18-Flubrobenguane and Carbon-11-Hydroxyephedrine for Cardiac PET Imaging of Sympathetic Innervation. *JACC Cardiovasc. Imaging* **2020**. https://doi.org/10.1016/j.jcmg.2020.09.026.

(30) Pauwels, E.; Celen, S.; Vandamme, M.; Leysen, W.; Baete, K.; Bechter, O.; Bex, M.; Serdons, K.; Van Laere, K.; Bormans, G.; Deroose, C. M. Improved Resolution and Sensitivity of [^{18}F]MFBG PET Compared with [^{123}I]MIBG SPECT in a Patient with a

Norepinephrine Transporter–Expressing Tumour. *Eur. J. Nucl. Med. Mol. Imaging* **2021**, *48* (1), 313–315. https://doi.org/10.1007/s00259-020-04830-x.

(31) Preshlock, S.; Calderwood, S.; Verhoog, S.; Tredwell, M.; Huiban, M.; Hienzsch, A.; Gruber, S.; Wilson, T. C.; Taylor, N. J.; Cailly, T.; Schedler, M.; Collier, T. L.; Passchier, J.; Smits, R.; Mollitor, J.; Hoepping, A.; Mueller, M.; Genicot, C.; Mercier, J.; Gouverneur, V. Enhanced Copper-Mediated ^{18}F-Fluorination of Aryl Boronic Esters Provides Eight Radiotracers for PET Applications. *Chem. Commun.* **2016**, *52* (54), 8361–8364. https://doi.org/10.1039/C6CC03295H.

(32) Turnock, S.; Turton, D. R.; Martins, C. D.; Chesler, L.; Wilson, T. C.; Gouverneur, V.; Smith, G.; Kramer-Marek, G. ^{18}F-Meta-Fluorobenzylguanidine (^{18}F-mFBG) to Monitor Changes in Norepinephrine Transporter Expression in Response to Therapeutic Intervention in Neuroblastoma Models. *Sci. Rep.* **2020**, *10* (1), 20918. https://doi.org/10.1038/s41598-020-77788-3.

(33) Zhang, H.; Huang, R.; Cheung, N.-K. V.; Guo, H.; Zanzonico, P. B.; Thaler, H. T.; Lewis, J. S.; Blasberg, R. G. Imaging the Norepinephrine Transporter in Neuroblastoma: A Comparison of [^{18}F]-MFBG and ^{123}I-MIBG. *Clin. Cancer Res.* **2014**, *20* (8), 2182–2191. https://doi.org/10.1158/1078-0432.CCR-13-1153.

(34) Hu, B.; Vāvere, A. L.; Neumann, K. D.; Shulkin, B. L.; DiMagno, S. G.; Snyder, S. E. A Practical, Automated Synthesis of *meta*-[^{18}F]Fluorobenzylguanidine for Clinical Use. *ACS Chem. Neurosci.* **2015**, *6* (11), 1870–1879. https://doi.org/10.1021/acschemneuro.5b00202.

(35) Rotstein, B. H.; Wang, L.; Liu, R. Y.; Patteson, J.; Kwan, E. E.; Vasdev, N.; Liang, S. H. Mechanistic Studies and Radiofluorination of Structurally Diverse Pharmaceuticals with

Spirocyclic Iodonium(III) Ylides. *Chem. Sci.* **2016**, *7* (7), 4407–4417. https://doi.org/10.1039/C6SC00197A.

(36) Qin, L.; Hu, B.; Neumann, K. D.; Linstad, E. J.; McCauley, K.; Veness, J.; Kempinger, J. J.; DiMagno, S. G. A Mild and General One-Pot Synthesis of Densely Functionalized Diaryliodonium Salts. *Eur. J. Org. Chem.* **2015**, *2015* (27), 5919–5924. https://doi.org/10.1002/ejoc.201500986.

(37) Rotstein, B. H.; Stephenson, N. A.; Vasdev, N.; Liang, S. H. Spirocyclic Hypervalent Iodine(III)-Mediated Radiofluorination of Non-Activated and Hindered Aromatics. *Nat. Commun.* **2014**, *5* (1), 4365. https://doi.org/10.1038/ncomms5365.

(38) Cardinale, J.; Ermert, J.; Humpert, S.; Coenen, H. H. Iodonium Ylides for One-Step, No-Carrier-Added Radiofluorination of Electron Rich Arenes, Exemplified with 4-(([^{18}F]Fluorophenoxy)-Phenylmethyl)Piperidine NET and SERT Ligands. *RSC Adv.* **2014**, *4* (33), 17293–17299. https://doi.org/10.1039/C4RA00674G.

(39) Yu, M.; Bozek, J.; Lamoy, M.; Guaraldi, M.; Silva, P.; Kagan, M.; Yalamanchili, P.; Onthank, D.; Mistry, M.; Lazewatsky, J.; Broekema, M.; Radeke, H.; Purohit, A.; Cdebaca, M.; Azure, M.; Cesati, R.; Casebier, D.; Robinson, S. P. Evaluation of LMI1195, a Novel ^{18}F-Labeled Cardiac Neuronal PET Imaging Agent, in Cells and Animal Models. *Circulation: Cardiovascular Imaging* **2011**, *4* (4), 435–443. https://doi.org/10.1161/CIRCIMAGING.110.962126.

(40) Vaidyanathan, G.; McDougald, D.; Koumarianou, E.; Choi, J.; Hens, M.; Zalutsky, M. R. Synthesis and Evaluation of 4-[^{18}F]Fluoropropoxy-3-Iodobenzylguanidine ([^{18}F]FPOIBG): A Novel 18F-Labeled Analogue of MIBG. *Nucl. Med. Biol.* **2015**, *42* (8), 673–684. https://doi.org/10.1016/j.nucmedbio.2015.04.005.

(41) Sinusas, A. J.; Lazewatsky, J.; Brunetti, J.; Heller, G.; Srivastava, A.; Liu, Y.-H.; Sparks, R.; Puretskiy, A.; Lin, S.; Crane, P.; Carson, R. E.; Lee, L. V. Biodistribution and Radiation Dosimetry of LMI1195: First-in-Human Study of a Novel ^{18}F-Labeled Tracer for Imaging Myocardial Innervation. *J. Nucl. Med.* **2014**, *55* (9), 1445–1451. https://doi.org/10.2967/jnumed.114.140137.

(42) Gebhard, C. Imaging of Cardiac Sympathetic Activity in Heart Failure: Not out of the Woods Yet. *J. Nucl. Cardiol.* **2018**, *25* (4), 1172–1177. https://doi.org/10.1007/s12350-017-0779-1.

(43) Zhou, Z.; Zhen, J.; Karpowich, N. K.; Goetz, R. M.; Law, C. J.; Reith, M. E. A.; Wang, D.-N. LeuT-Desipramine Structure Reveals How Antidepressants Block Neurotransmitter Reuptake. *Science* **2007**, *317* (5843), 1390–1393. https://doi.org/10.1126/science.1147614.

(44) Ordway, G. A.; Jia, W.; Li, J.; Zhu, M.-Y.; Mandela, P.; Pan, J. Norepinephrine Transporter Function and Desipramine: Residual Drug Effects versus Short-Term Regulation. *J. Neurosci. Methods* **2005**, *143* (2), 217–225. https://doi.org/10.1016/j.jneumeth.2004.11.006.

(45) Kreusser, M. M.; Lehmann, L. H.; Haass, M.; Buss, S. J.; Katus, H. A.; Lossnitzer, D. Depletion of Cardiac Catecholamine Stores Impairs Cardiac Norepinephrine Re-Uptake by Downregulation of the Norepinephrine Transporter. *PLOS ONE* **2017**, *12* (3), e0172070. https://doi.org/10.1371/journal.pone.0172070.

(46) Thoenen, H.; Tranzer, J. P. Chemical Sympathectomy by Selective Destruction of Adrenergic Nerve Endings with 6-Hydroxydopamine. *Naunyn-Schmiedebergs Arch. Für Pharmakol. Exp. Pathol.* **1968**, *261* (3), 271–288. https://doi.org/10.1007/BF00536990.

(47) Kostrzewa, R. M.; Jacobowitz, D. M. Pharmacological Actions of 6-Hydroxydopamine. *Pharmacol. Rev.* **1974**, *26* (3), 199–288.

(48) Sachs, C.; Jonsson, G. Mechanisms of Action of 6-Hydroxydopamine. *Biochem. Pharmacol.* **1975**, *24* (1), 1–8. https://doi.org/10.1016/0006-2952(75)90304-4.

(49) Werner, R. A.; Chen, X.; Maya, Y.; Eissler, C.; Hirano, M.; Nose, N.; Wakabayashi, H.; Lapa, C.; Javadi, M. S.; Higuchi, T. The Impact of Ageing on ^{11}C-Hydroxyephedrine Uptake in the Rat Heart. *Sci. Rep.* **2018**, *8* (1), 11120. https://doi.org/10.1038/s41598-018-29509-0.

(50) Rischpler, C.; Fukushima, K.; Isoda, T.; Javadi, M. S.; Dannals, R. F.; Abraham, R.; Wahl, R.; Bengel, F. M.; Higuchi, T. Discrepant Uptake of the Radiolabeled Norepinephrine Analogues Hydroxyephedrine (HED) and Metaiodobenzylguanidine (MIBG) in Rat Hearts. *Eur. J. Nucl. Med. Mol. Imaging* **2013**, *40* (7), 1077–1083. https://doi.org/10.1007/s00259-013-2393-z.

(51) Higuchi, T.; Yousefi, B. H.; Kaiser, F.; Gärtner, F.; Rischpler, C.; Reder, S.; Yu, M.; Robinson, S.; Schwaiger, M.; Nekolla, S. G. Assessment of the ^{18}F-Labeled PET Tracer LMI1195 for Imaging Norepinephrine Handling in Rat Hearts. *J. Nucl. Med.* **2013**, *54* (7), 1142–1146. https://doi.org/10.2967/jnumed.112.104232.

(52) Yu, M.; Bozek, J.; Kagan, M.; Guaraldi, M.; Silva, P.; Azure, M.; Onthank, D.; Robinson, S. P. Cardiac Retention of PET Neuronal Imaging Agent LMI1195 in Different Species: Impact of Norepinephrine Uptake-1 and -2 Transporters. *Nucl. Med. Biol.* **2013**, *40* (5), 682–688. https://doi.org/10.1016/j.nucmedbio.2013.03.003.

(53) Werner, R. A.; Rischpler, C.; Onthank, D.; Lapa, C.; Robinson, S.; Samnick, S.; Javadi, M.; Schwaiger, M.; Nekolla, S. G.; Higuchi, T. Retention Kinetics of the ^{18}F-Labeled

Sympathetic Nerve PET Tracer LMI1195: Comparison with ^{11}C-Hydroxyephedrine and ^{123}I-MIBG. *J. Nucl. Med.* **2015**, *56* (9), 1429–1433. https://doi.org/10.2967/jnumed.115.158493.

2.11. Supporting information

2.11.1. Section 1. General information

2.11.1.1. Chemistry

All commercial solvents and chemical reagents were utilized without further purification unless stated otherwise. All reactions were performed under inert (nitrogen or argon) atmosphere. All organic solvents were anhydrous. The characterization of reaction products was confirmed using ^{1}H-NMR, ^{13}C-NMR, and ^{19}F-NMR (when applicable). ^{1}H-NMR spectra were obtained using the Bruker AVANCE 600 MHz, 400 MHz, or 300 MHz spectrometers. Spectral data are reported in ppm using solvent as the reference ($CDCl_3$ at 7.26 ppm for ^{1}H NMR and DMSO at 2.50 ppm) and trimethylsilane as an internal standard ($\delta = 0$). ^{1}H NMR data were reported as: multiplicity, (s = singlet, d = doublet, dd = doublet of doublets, t = triplet, q = quartet, m = multiplet, br = broad), integration, and coupling constant(s) in Hz. Flash column chromatography was performed using a Biotage Isolera One system and preloaded biotage columns using high grade silica 40–63 µm.

2.11.1.2. Radiochemistry

No-carrier-added aqueous [^{18}F]fluoride was prepared on a Siemens CTI Eclipse HP/RD Hybrid Cyclotron (11 MeV) via the ^{18}O(p,n)^{18}F nuclear reaction. Radiofluorination methods were developed using GE TRACERlab FX2N software, and reactions were performed on a GE TRACERlab FX2N automation system equipped with in-line radioHPLC purification.

Radioactivity was quantified using a Biodex Atomlab 500 Dose Calibrator. TLC silica gel 60 plates (10 × 2 cm) were spotted with radioactivity on the baseline and developed in a chamber containing ethyl acetate until the solvent front reached 2 cm from the top of the plate. Analysis was performed using a Bioscan AR-2000 radio-TLC imaging scanner and WinScan software. Radiochemical identity and yield were determined by radioHPLC. UV and radiation detectors are connected in series.

2.11.2. Section 2. Synthetic procedures and characterization

2.11.2.1. N',N"-di(tert-butoxy)carbonyl-meta-iodobenzylguanidine (1)

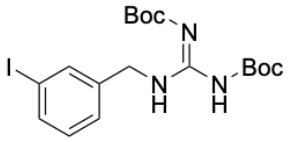

^{1}H NMR:

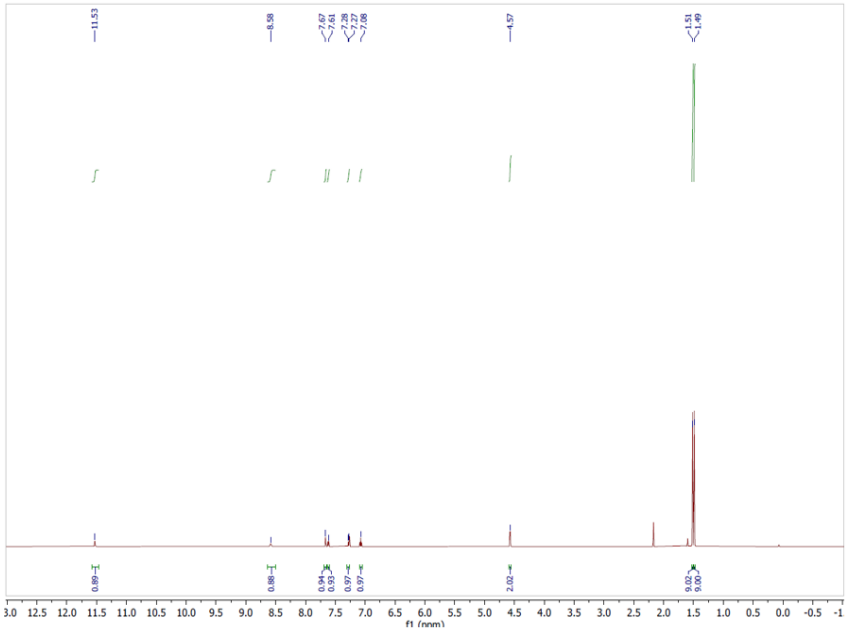

^{13}C NMR:

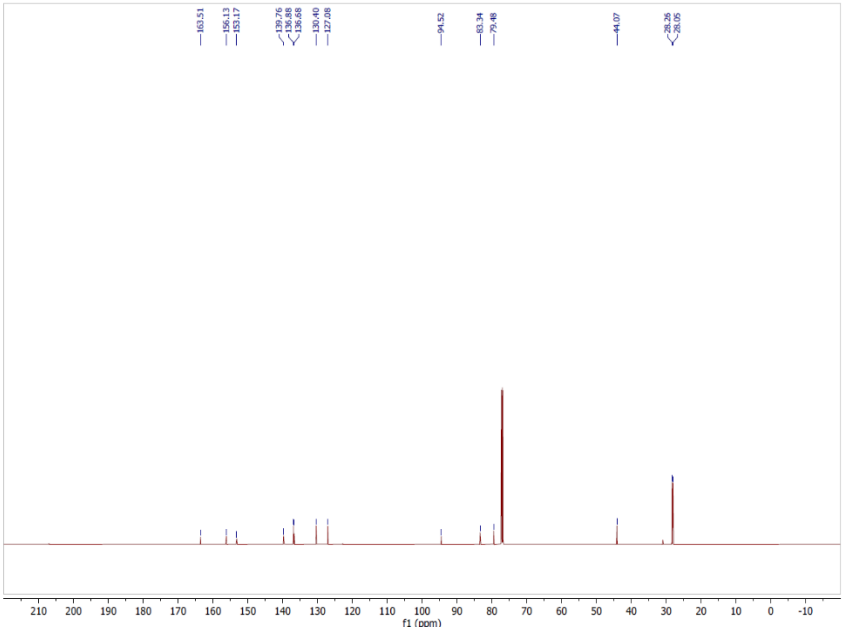

2.11.2.2. N,N′,N′,N″-tetra(tert-butoxy)carbonyl-meta-iodobenzylguanidine (2)

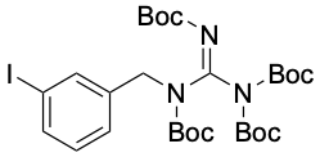

^{1}H NMR:

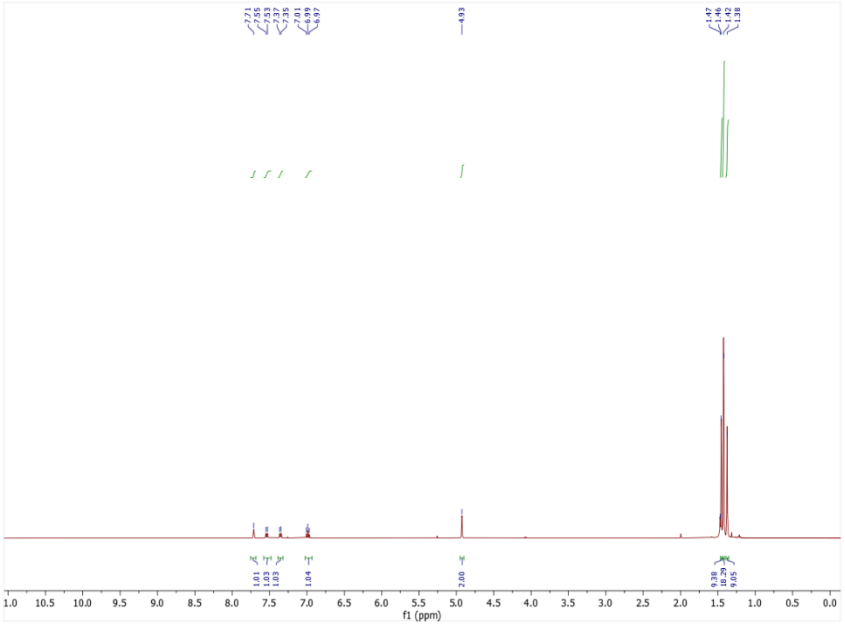

^{13}C NMR:

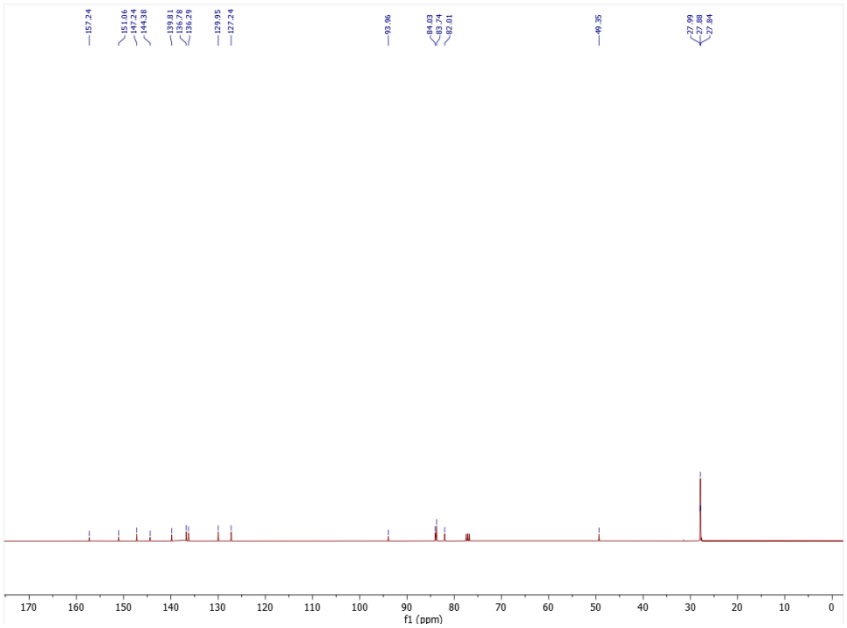

2.11.2.3. spiroadamantyl-1,3-dioxane-4,6-dione (3)

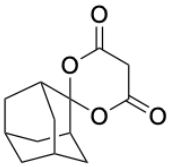

^{1}H NMR:

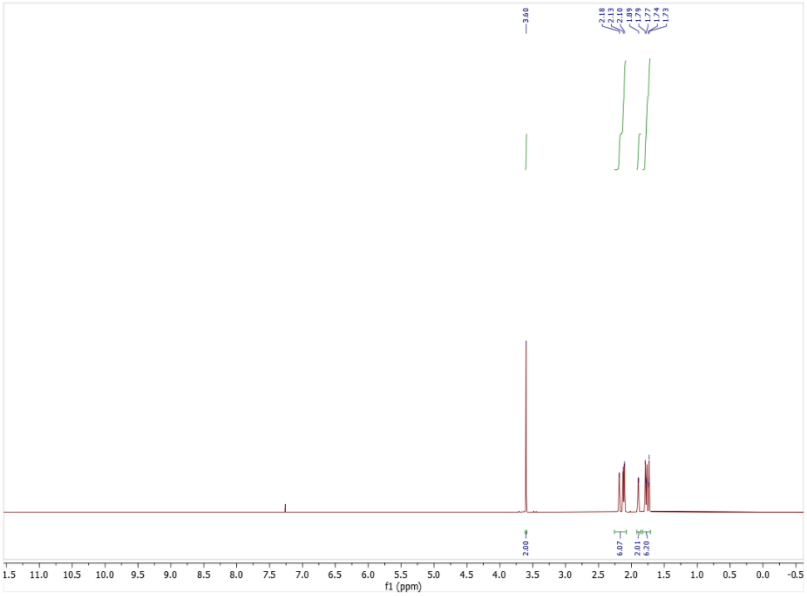

^{13}C NMR:

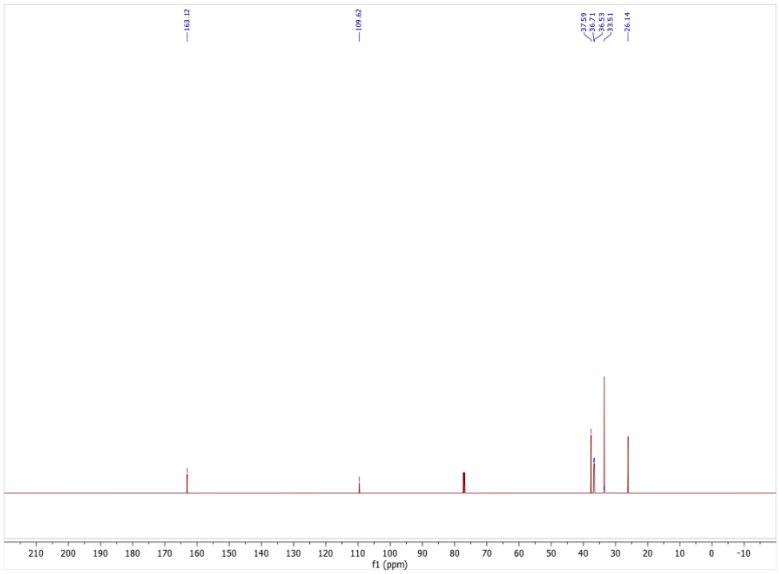

2.11.2.4. N,N′,N′,N″-tetra(tert-butoxy)carbonyl-meta-(spiroadamantyl-1,3-dioxane-4,6-dione-5-ylidene)iodobenzylguanidine (4)

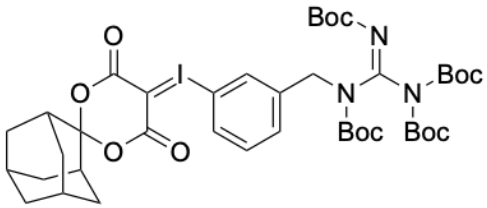

^{1}H NMR:

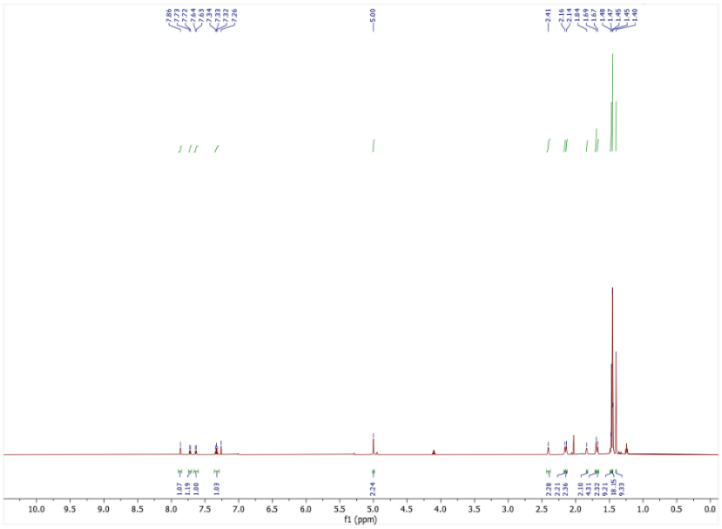

^{13}C NMR:

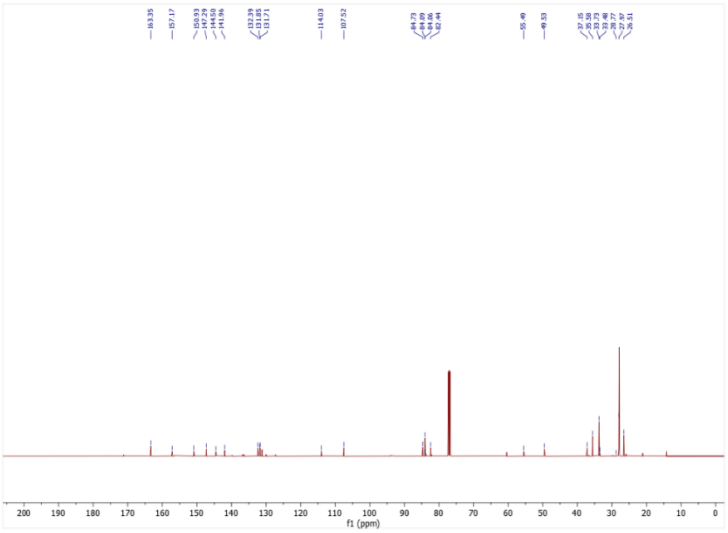

2.11.2.5. N′,N″-di(tert-butoxy)carbonyl-meta-fluorobenzylguanidine (5a)

Compound **5a** was synthesized according to the outlined procedure for compound **1** with *para*-fluorobenzylamine (1.0 mmol). The product was purified by flash chromatography (0-20 Hex/EtOAc) to yield a colourless solid (187 mg, 51%). The compound was characterized in accordance with the literature.[1] ^{1}H NMR (600 MHz, $CDCl_3$): δ = 11.54 (s, 1H), 8.62 (s, 1H), 7.33-7.27 (m, 1H), 7.10-7.06 (m, 1H), 7.04- 7.00 (m, 1H), 7.00-6.94 (m, 1H), 4.64 (d, *J* = 5.4 Hz, 2H), 1.51 (s, 9H), 1.49 (s, 9H); ^{13}C NMR (101 MHz, $CDCl_3$): δ = 163.8, 162.2 (d, *J* = 235 Hz), 156.2, 153.2, 139.9 (d, *J* = 16 Hz), 130.3 (d, *J* = 22 Hz), 123.3 (d, *J* = 7.6 Hz), 114.8 (d, *J* = 9 Hz), 114.6 (d, *J* = 9 Hz), 83.4, 79.5, 44.4 (d, *J* = 4.6 Hz), 28.3, 28.1; ^{19}F NMR (377 MHz, $CDCl_3$): δ = −112.7.

^{1}H NMR:

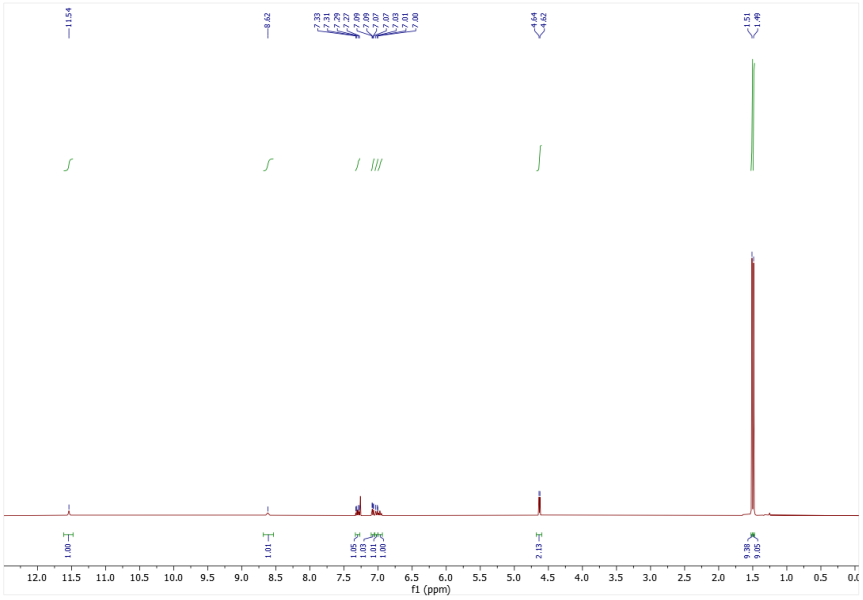

^{13}C NMR:

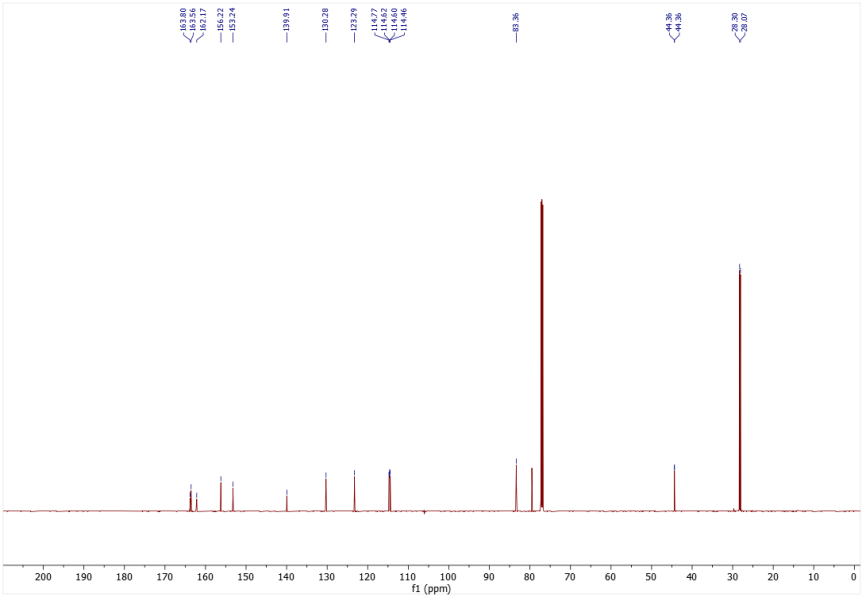

^{19}F NMR:

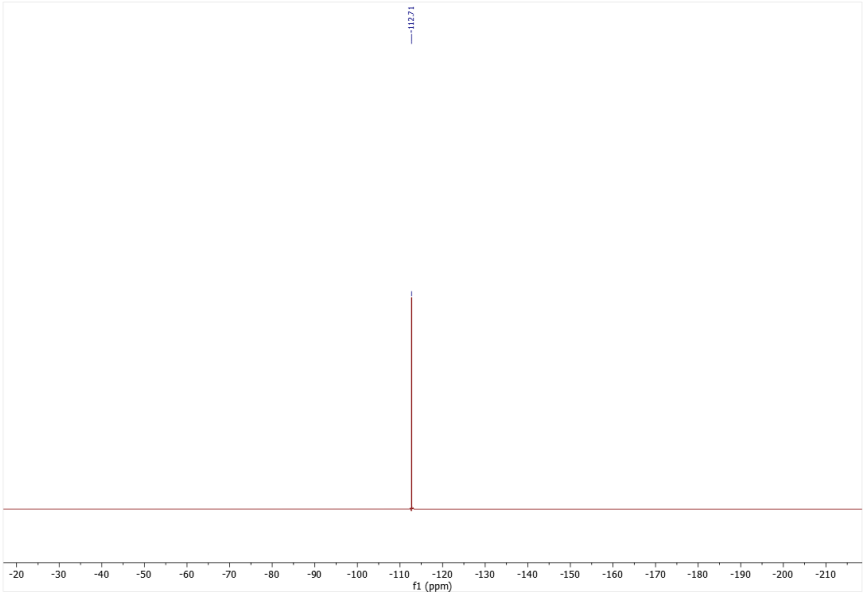

2.11.2.6. N′,N″-di(tert-butoxy)carbonyl-para-fluorobenzylguanidine (5b)

Compound **5b** was synthesized according to the outlined procedure for compound **1** with para-fluorobenzylamine (1.0 mmol). The product was purified by flash chromatography (0-20 Hex/EtOAc) to yield a colourless solid (326 mg, 88%). ^{1}H NMR (300 MHz, $CDCl_3$): δ 11.54 (s, 1H), 8.56 (s, 1H), 7.30 (m, 2H), 7.03 (t, *J* = 8.7 Hz, 2H), 4.59 (d, *J* = 5.2 Hz, 2H), 1.52 (s, 9H), 1.49 (s, 9H) ppm. ^{13}C NMR (75 MHz, $CDCl_3$): δ 163.7, 160.8, 156.2, 153.4, 133.2, 129.8, 129.7, 115.9, 115.6, 83.4, 79.6, 44.4, 28.4, 28.2 ppm. MS (m/z): calculated for $C_{18}H_{27}FN_3O_4$, 368.20; found 368.2 $[M+H]^+$; 168.1 $[M-2x\textit{t}Bu+H]^+$. The compound was characterized in accordance with the literature.[2]

^{1}H NMR:

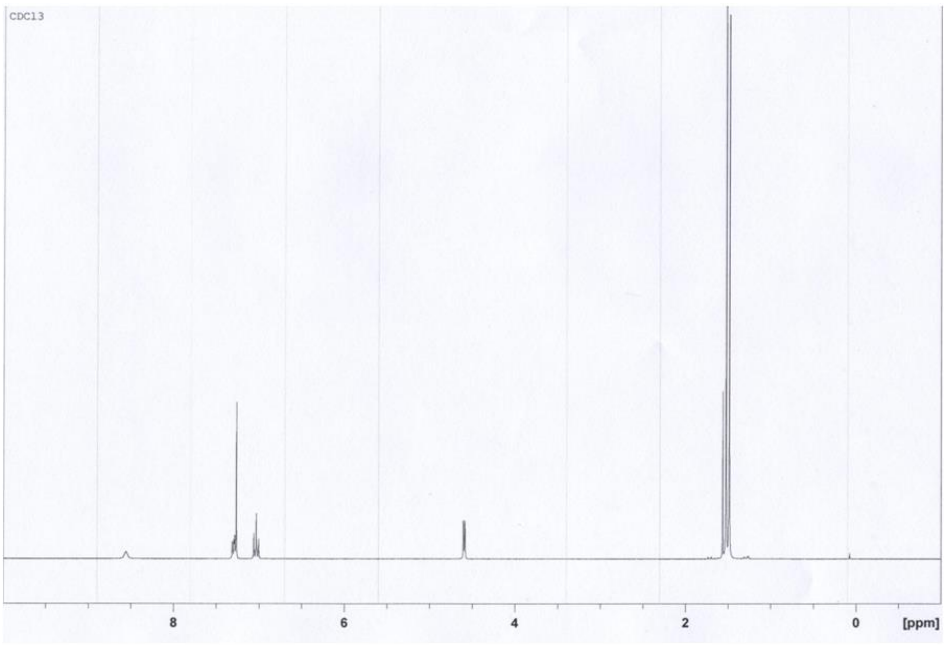

^{13}C NMR:

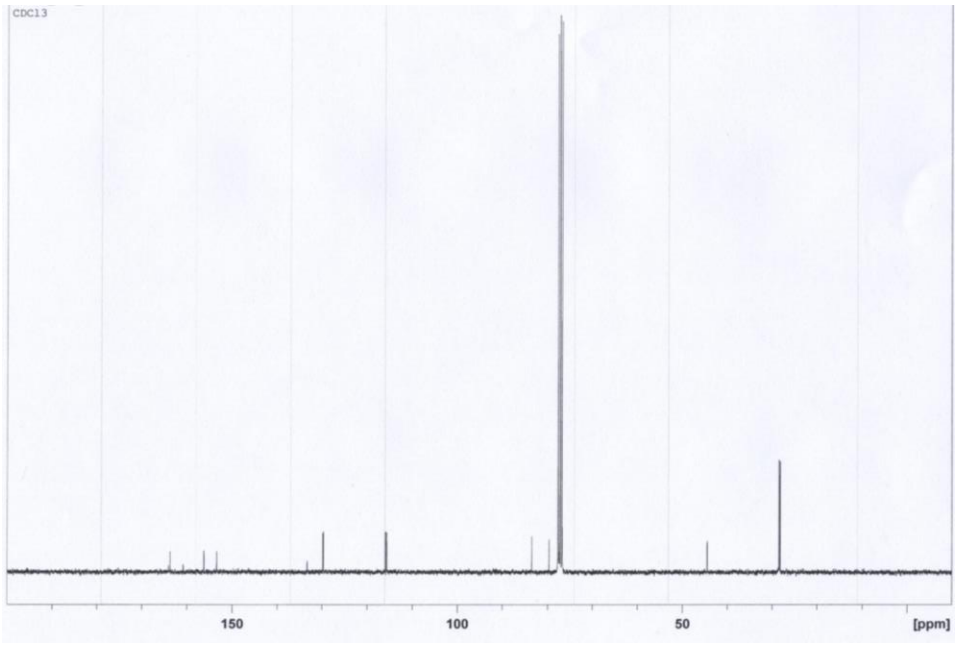

2.11.2.7. N′,N″-di(tert-butoxy)carbonyl-ortho-fluorobenzylguanidine (5c)

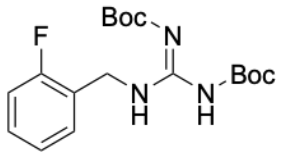

Compound **5c** was synthesized according to the outlined procedure for compound **1** with ortho-fluorobenzylamine (1.0 mmol). The product was purified by flash chromatography (0-20% Hex/EtOAc) to yield a white solid (355 mg, 97%). ^{1}H NMR (300 MHz, $CDCl_3$): δ 11.53 (s, 1H), 8.60 (s, 1H), 7.28 (m, 2H), 7.08 (m, 2H), 4.69 (d, *J* = 5.3 Hz, 2H), 1.52 (s, 9H), 1.49 (s, 9H) ppm. ^{13}C NMR (75 MHz, $CDCl_3$): δ 163.7, 162.8, 159.5, 156.3, 153.3, 130.2, 129.5, 124.4, 115.8, 115.5, 83.3, 79.5, 39.0, 28.4, 28.2 ppm. MS (m/z): calculated for $C_{18}H_{27}FN_3O_4$, 368.20; found 368.3 $[M+H]^+$; 267.1 $[M-t\text{Bu}]^+$; 167.1 $[M-2\times t\text{Bu}]^+$.

^{1}H NMR:

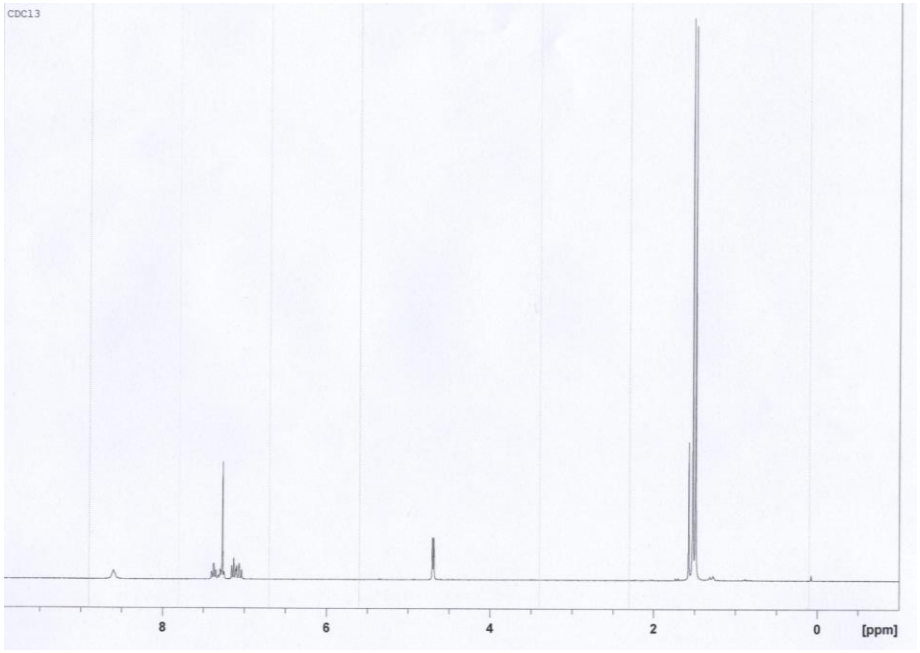

^{13}C NMR:

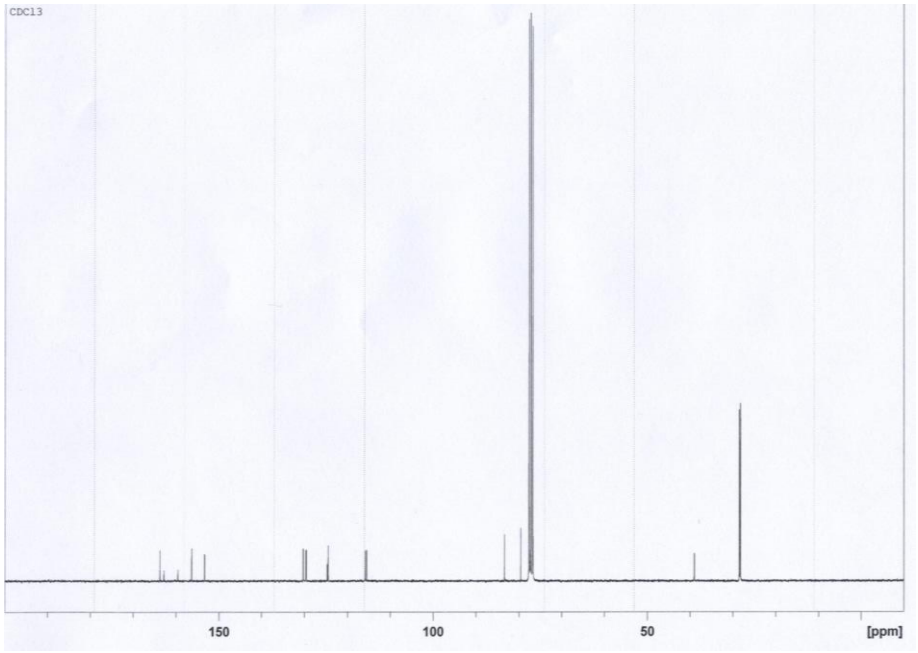

2.11.2.8. meta-fluorobenzylguanidine hydrochloride (6a)

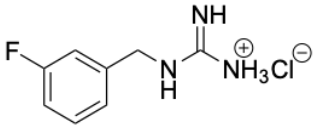

^{1}H NMR:

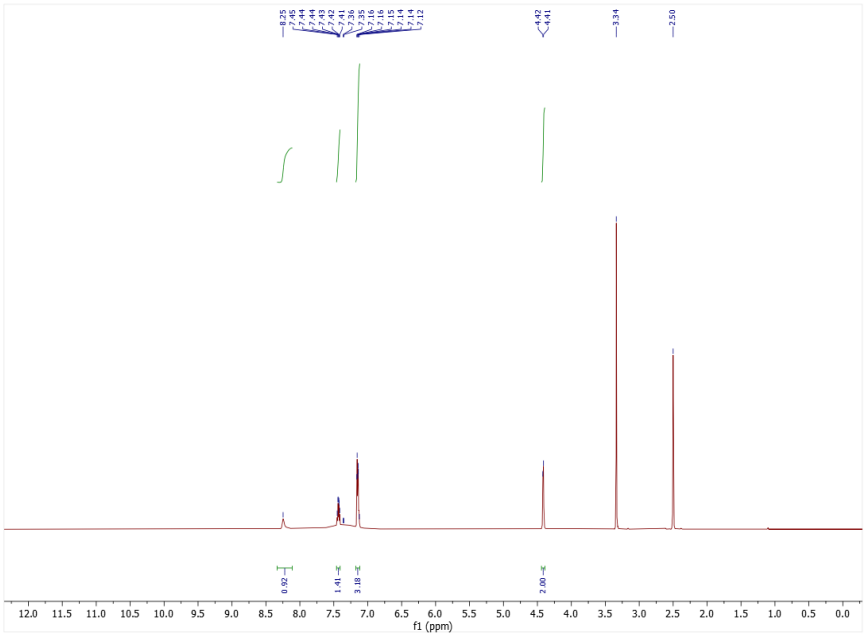

^{13}C NMR:

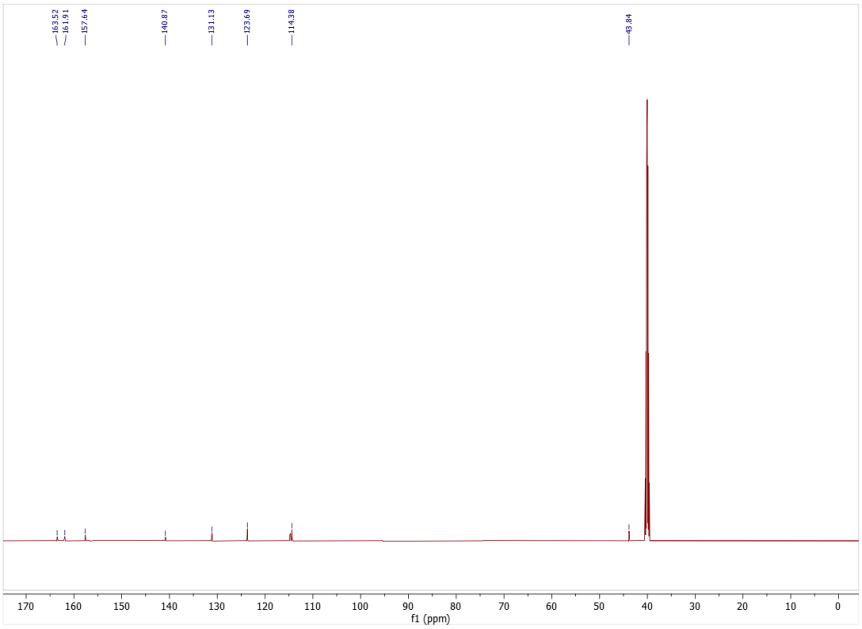

^{19}F NMR:

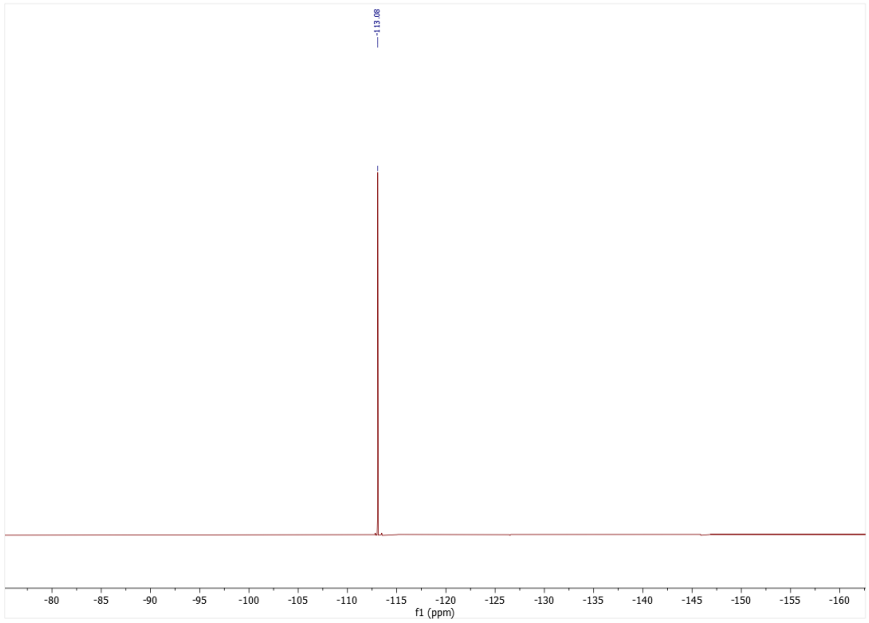
-113.08
-80
-85
-90
-95
-100
-105
-110
-115
-120
-125
-130
-135
-140
-145
-150
-155
-160
f1 (ppm)

2.11.2.9. para-fluorobenzylguanidine trifluoroacetate (6b)

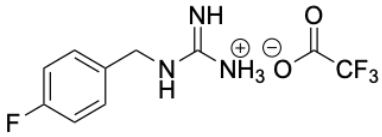

Compound **5b** (0.22 mmol) was dissolved in TFA/DCM (50/50, 0.8 mL) and stirred at room temperature for 15 min. The reaction mixture was then concentrated and dried with the addition of chloroform (3 x 5 mL) and diethyl ether (3 x 5 mL) to yield a white solid (**6b**, 36 mg, 0.21 mmol, 98%). ^{1}H NMR (300 MHz, $(CD_3)_2SO$): δ 7.95 (s, 1H), 7.34 (m, 2H), 7.22 (t, *J* = 8.9 Hz, 2H), 4.34 (d, *J* = 6.1 Hz, 2H) ppm. ^{13}C NMR (75 MHz, $(CD_3)_2SO$): δ 163.8, 160.5, 157.4, 134.0, 130.0, 116.1, 115.9, 43.9 ppm. The compound was characterized in accordance with the literature.[3] MS (m/z): calculated for $C_{18}H_{11}FN_3$, 168.09; found 168.0 $[M+H]^+$.

^{1}H NMR:

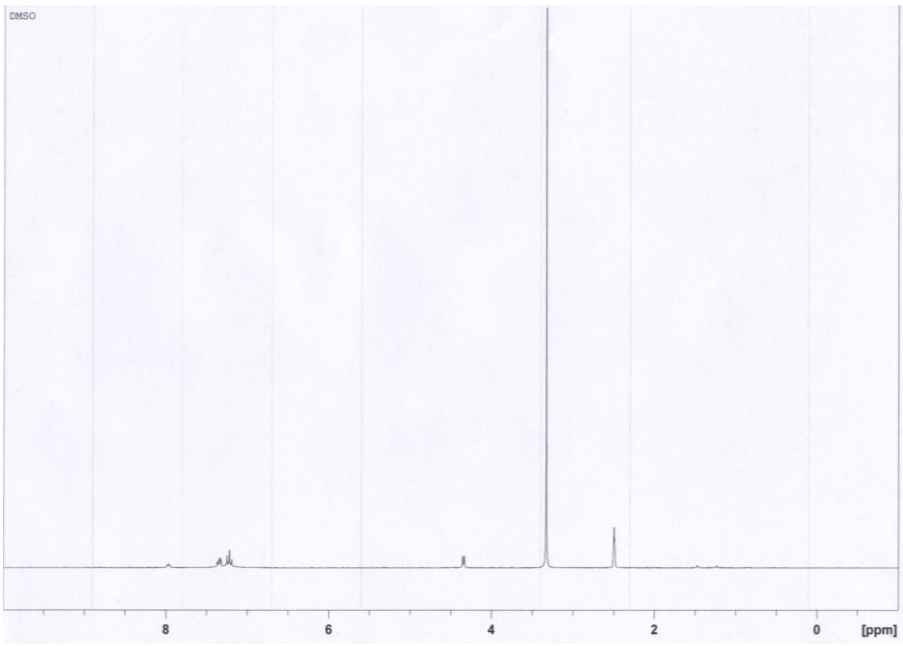

^{13}C NMR:

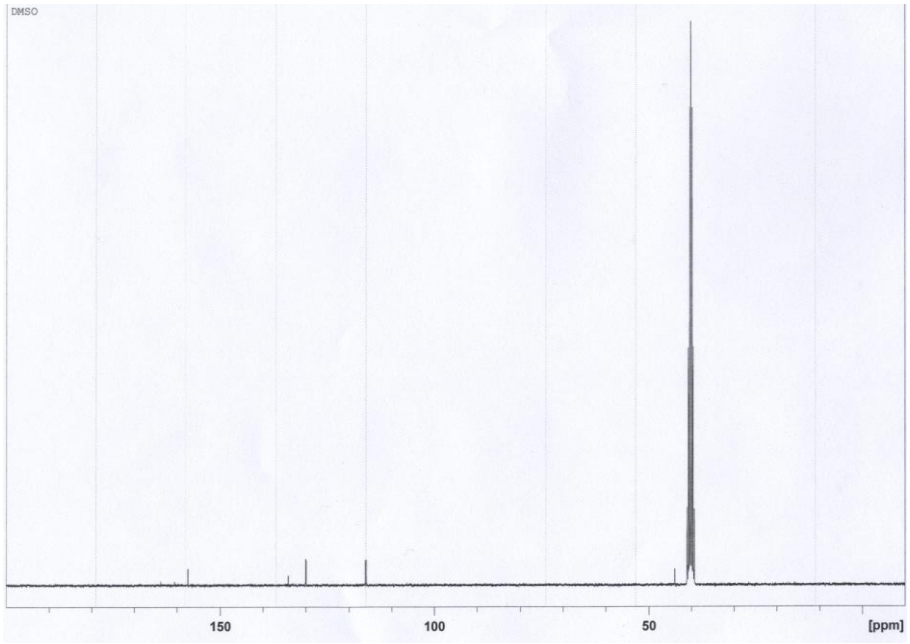

2.11.2.10. ortho-fluorobenzylguanidine trifluoroacetate (6c)

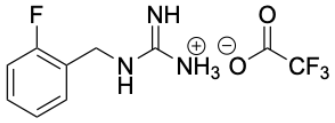

Compound **6c** was synthesized according to the outlined procedure for compound **6b** starting from compound **5c** (0.25 mmol). The product was obtained as a white solid (67 mg, 93%). ^{1}H NMR (300 MHz, $(CD_3)_2SO$): δ 7.92 (s, 1H), 7.37 (m, 2H), 7.22 (m, 2H), 4.43 (d, *J* = 4.1 Hz, 2H) ppm. ^{13}C NMR (75 MHz, $(CD_3)_2SO$): δ 162.4, 159.1, 157.5, 130.5, 129.8, 125.2, 124.7, 116.2, 115.9 ppm. MS (m/z): calculated for $C_{18}H_{11}FN_3$, 168.09; found 168.0 $[M+H]^+$.

^{1}H NMR

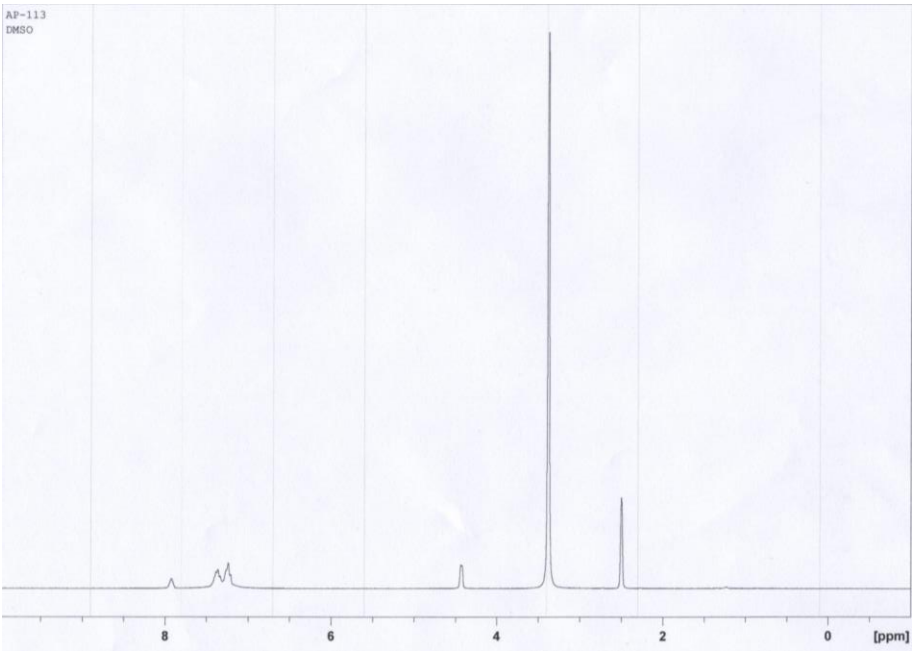

^{13}C NMR

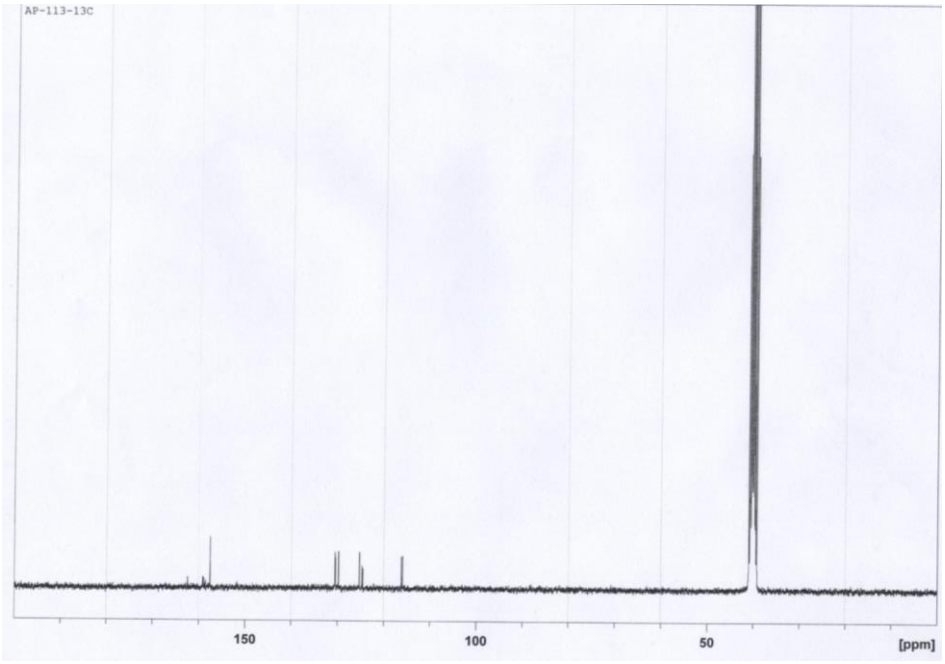

2.11.3. Section 3. Supplementary figures and tables

2.11.3.1. Scheme S1. Synthesis of SPIAd

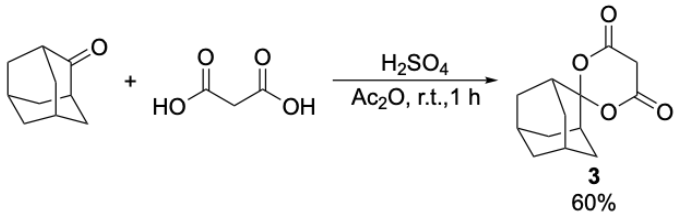

3
60%

2.11.3.2. Scheme S2. Synthesis of the fluorobenzylguanidine (FBG) regioisomers

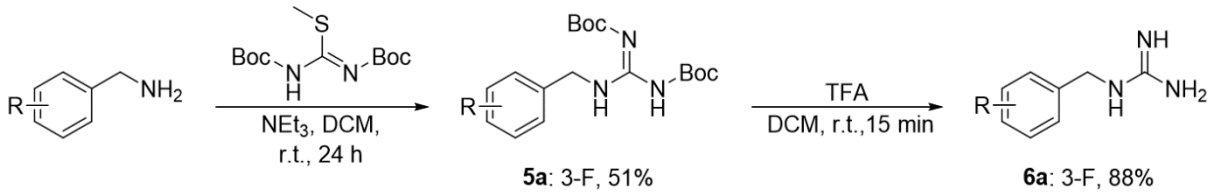

5a: 3-F, 51%
5b: 4-F, 88%
5c: 2-F, 97%

6a: 3-F, 88%
6b: 4-F, 98%
6c: 2-F, 93%

2.11.3.3. Table S1. Assessment of precursor stability

Storage Area	Temperature (°C)	Color at 0 months	Color at 7 months	NMR Characterization
Fumehood	ambient	white	yellow	decomposition
Fridge	2 – 6	white	white	stable
Freezer	-26 – -21	white	white	stable

^{1}H NMR after storage at ambient temperature:

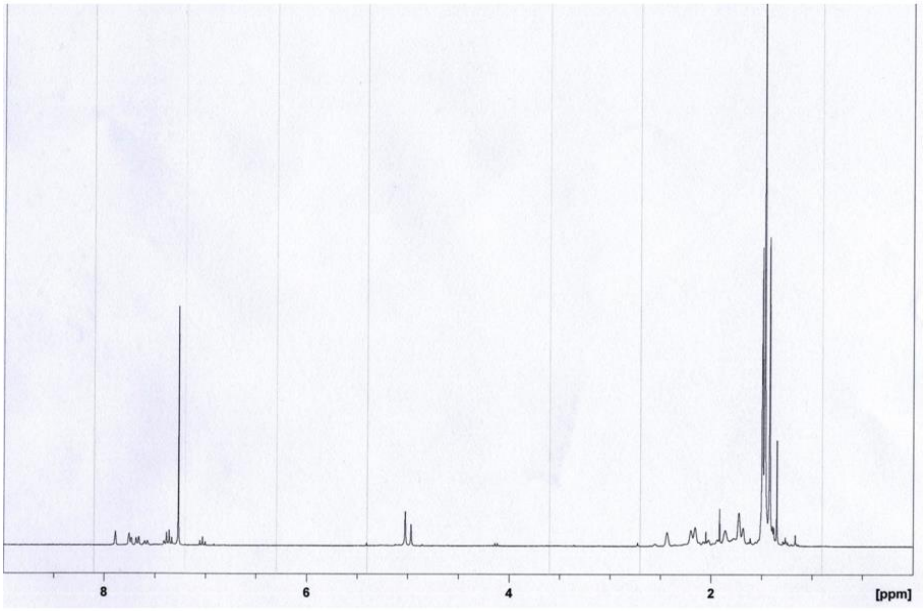

^{1}H NMR after storage in fridge:

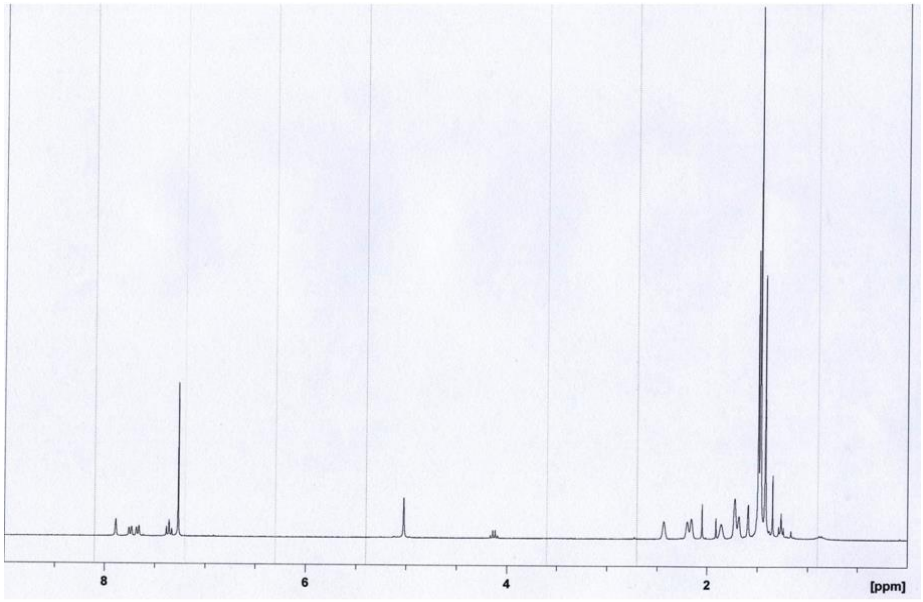

^{1}H NMR after storage in freezer:

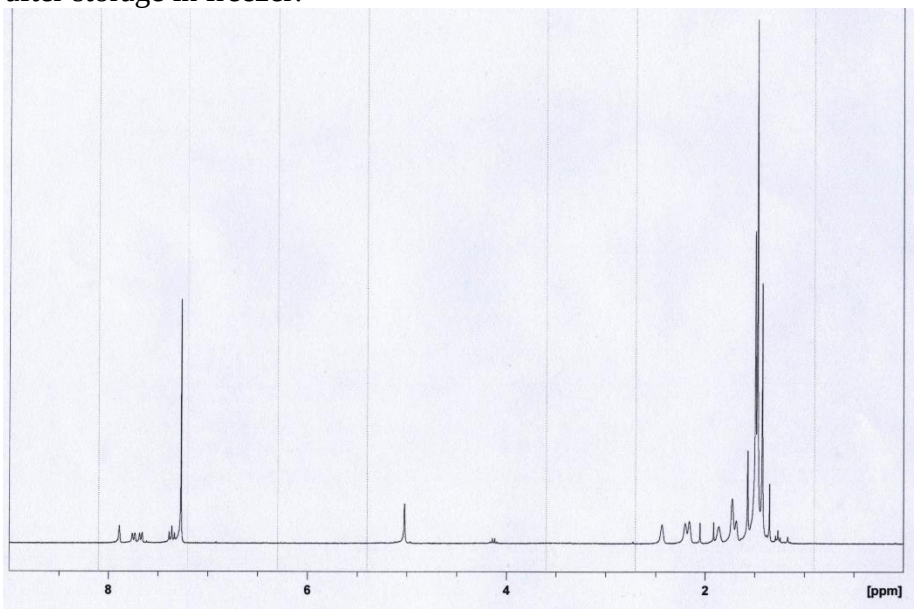

2.11.3.4. Table S2. Optimization of [^{18}F]mFBG radiosynthesis

Step 1: Nucleophilic radiofluorination				
Entry	Solvent	Equiv. base	Reaction time (min)	RCY (%)
1	DMF	4.8	5	42 ± 11 (n = 3)
2	DMF	4.8	10	28 ± 4 (n = 4)
3	DMF	4.8	20	31 ± 5 (n = 4)
4	DMF	4.8	30	14 (n = 1)
5	DMF	6.0	20	27 (n = 1)
6	DMF	7.1	20	22 (n = 1)
7	DMF	8.3	20	16 (n = 1)
8	DMSO	4.8	5	44 ± 8 (n = 3)
9	DMSO	4.8	10	55 ± 9 (n = 4)
10	DMSO	4.8	15	51 ± 6 (n = 3)
11	DMSO	4.8	20	58 ± 4 (n = 2)
12	DMSO	1.4	10	26 ± 4 (n = 2)
13	DMSO	2.6	10	44 ± 6 (n = 2)
14	DMSO	3.8	10	51 ± 9 (n = 2)
15	DMSO	6.0	10	50 ± 4 (n = 2)
16	DMSO	7.1	10	48 (n = 1)
17	DMSO	8.3	10	43 (n = 1)
18	DMSO	4.8[b]	10	<5 (n = 2)
19	DMSO	4.8[b]	20	<5 (n = 2)
20	DMF	4.8[b]	20	7 (n = 1)
Step 2: Deprotection				
Entry	[HCl] (M)	Temperature (°C)	Reaction time (min)	RCY (%)
21	6	100	10	89 ± 1 (n = 2)
22	6	120	10	93 ± 2 (n = 6)
23	12	120	5	97 ± 2 (n = 4)
24	12	120	10	95 ± 3 (n = 6)

[a] 0.02 M precursor, 200 µL solvent, TEAB, 120 °C. [b] K_2CO_3/K_{222}

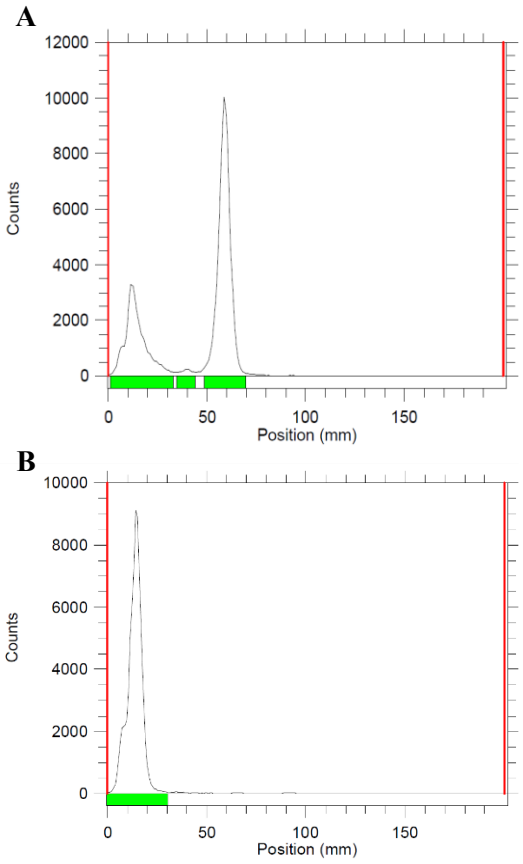

2.11.3.5. **Figure S1.** Representative radio-TLC chromatograms for (A) radiofluorination (B) deprotection. Mobile phase = 100% EtOAc

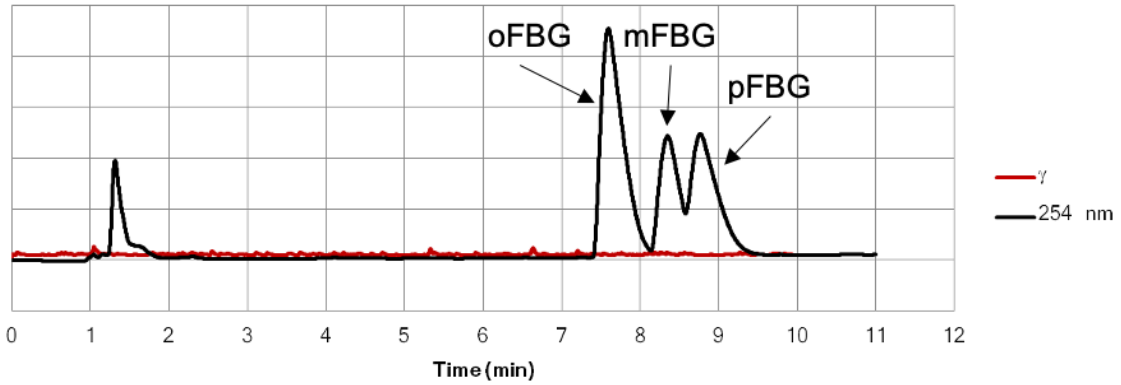

2.11.3.6. **Figure S2.** UV HPLC chromatogram of the FBG regioisomers. An Xbridge phenyl column (100 × 4.6 mm, 3.5 µm) was utilized with the following mobile phase: 3% ACN, 10 mM phosphate buffer (pH 7–8), 1 mL·min-1, 1 min; linear gradient to 20% ACN, 11 min; 20% ACN, 2 min.

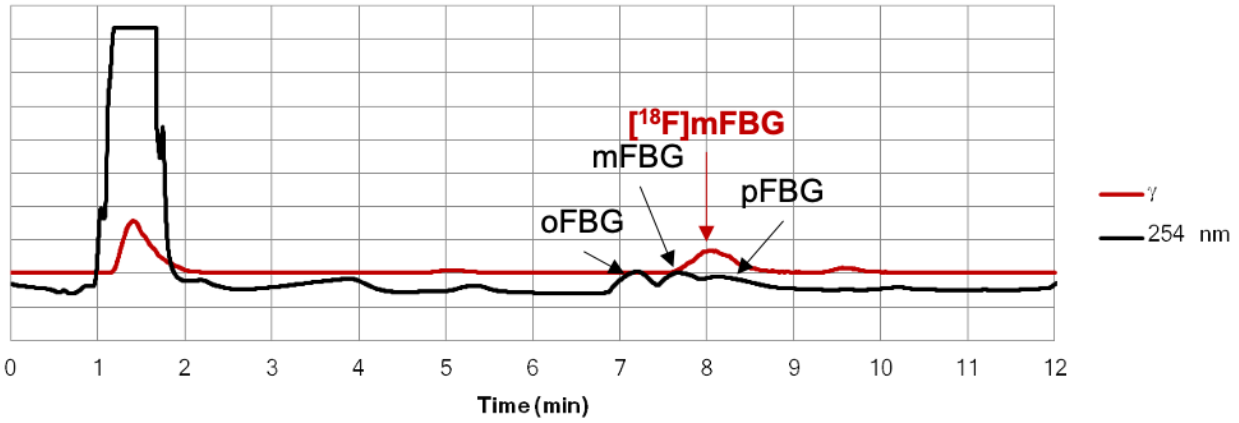

2.11.3.7. **Figure S3.** Crude radio-HPLC chromatogram co-injected with FBG regioisomers. Crude radio-HPLC chromatogram co-injected with FBG regioisomers. Xbridge phenyl column (100 × 4.6 mm, 3.5 µm). Gradient: 3% ACN, 10 mM phosphate buffer (pH 7–8), 1 mL·min-1, 1 min; linear gradient to 20% ACN, 11 min; 20% ACN, 2 min.

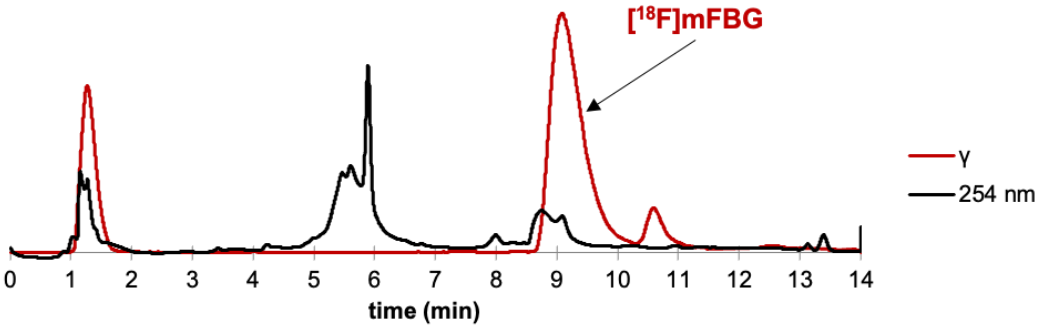

2.11.3.8. Figure S4: Crude radio-HPLC chromatogram following radiosynthesis of [^{18}F]mFBG. Xbridge phenyl column (100 × 4.6 mm, 3.5 µm). Gradient: 3% ACN, 10 mM phosphate buffer (pH 7–8), 1 mL·min-1, 1 min; linear gradient to 20% ACN, 11 min; 20% ACN, 2 min.

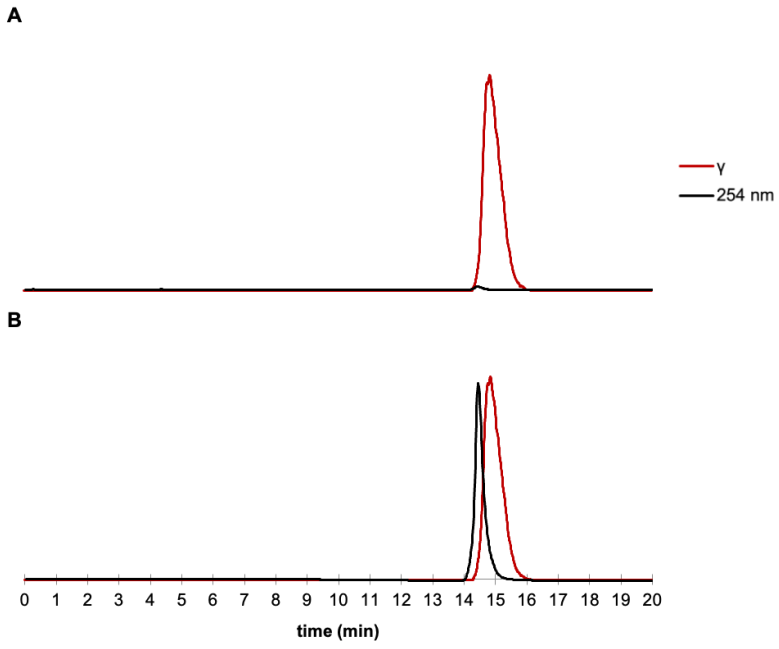

2.11.3.9. **Figure S5. [^{18}F]mFBG purification and quality control.** Radio-HPLC chromatogram following (A) isolation and reformulation of [18F]mFBG and (B) co-injection with non-radioactive standard. Phenomenex Luna column 10 µm C18(2) (100 Å, 250 mm × 4.6 mm). Gradient; 1/99 10 mM PBS/ACN for 1 min, linear gradient to 80/20 over 8 min, isocratic for 7 minutes, then linear gradient back to 1/99 over 3 minutes. Retention time: ~15 min, flow rate = 1 mL/min.

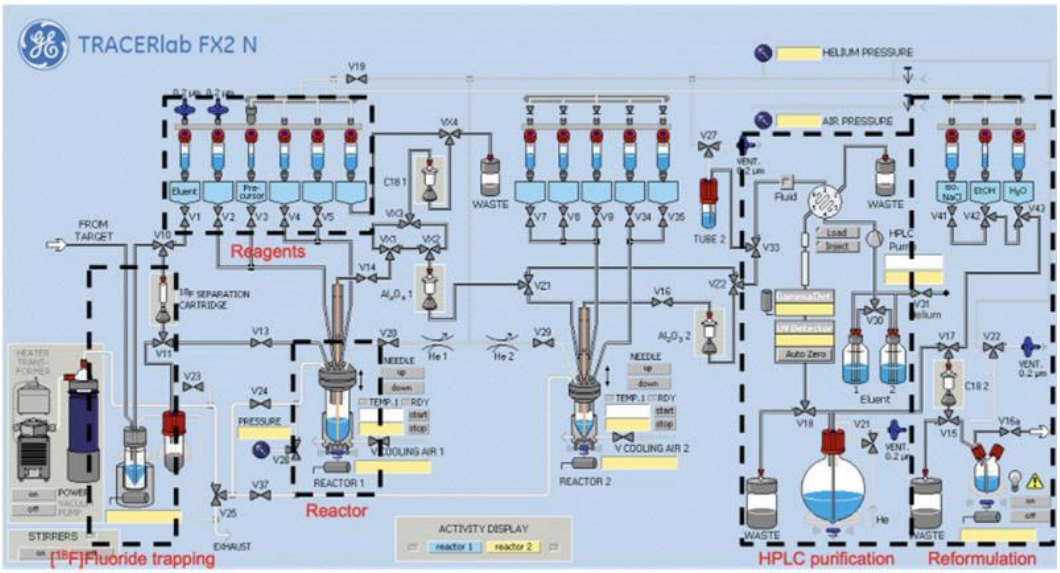

2.11.3.10. **Figure S6.** GE TRACERlab FX2 N automated radiosynthesis schematic.

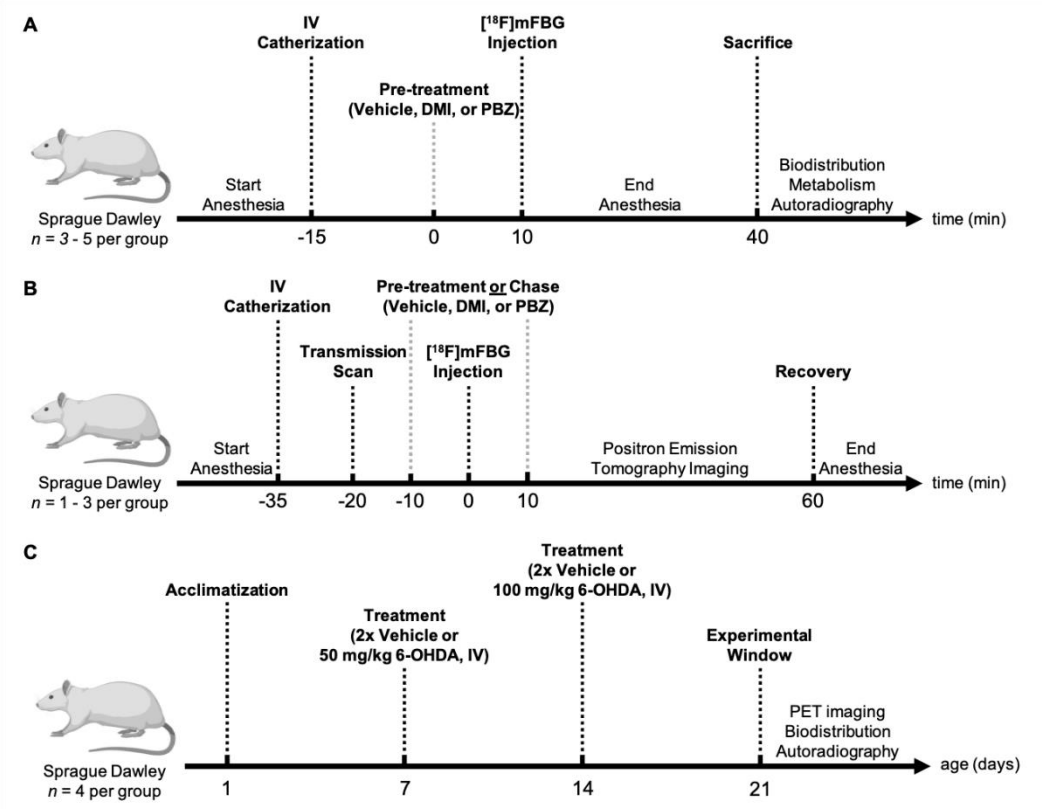

2.11.3.11. **Figure S7.** Timeline of experiments. (A) Pharmacological pre-treatment (B) In vivo PET imaging (C) 6-OHDA treatment cycle

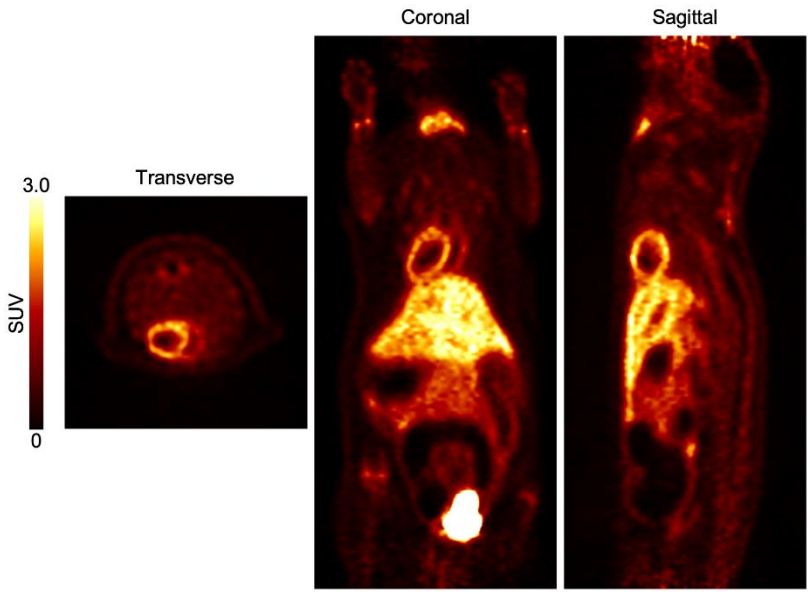

2.11.3.12. Figure S8. Whole body PET. Images are summed from 0-60 min.

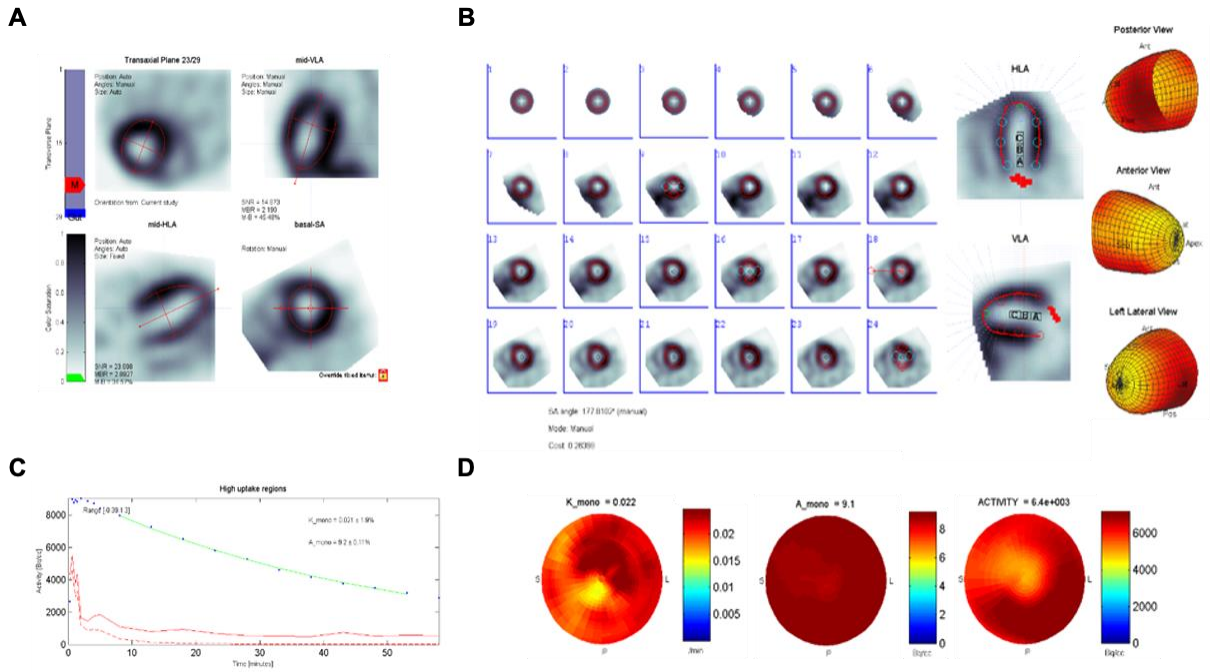

2.11.3.13. **Figure S9.** Flowquant™ workflow. (A) Orientation displaying partial ellipse fitting in orthogonal planes: transaxial plane (top left), mid-ventricular long axis (top right, VLA), mid-horizontal long axis (bottom left, HLA), basal short axis (bottom right, BSA). (B) Registration of reoriented images is confirmed on planar images of the SA (generated by conical sampling). Circles located on the HLA and VLA indicate sampling points used to determine mean tracer activity. Location of sample points are used to develop a 3D model of the LV. (C) Time-activity curve for tissue and blood pool is generated for the duration of the scan and fitted with a mono-exponential trendline from 5.5 to 55.5 minutes. (D) Previously shown sampling points are used to determine the mean activity in the myocardium, presented as polar maps.

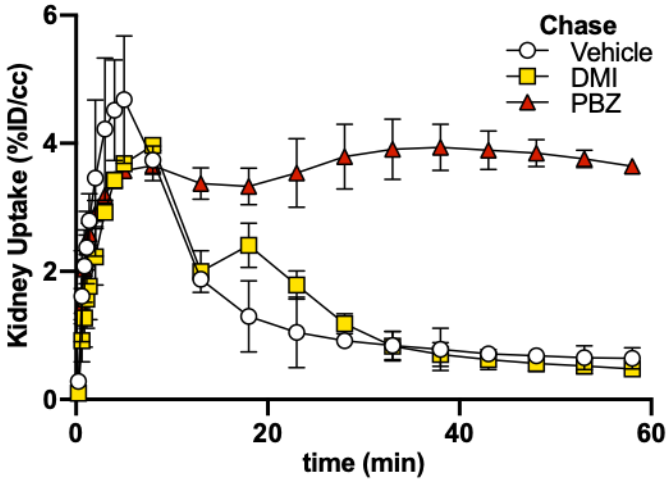

2.11.3.14. Figure S10. Kidney time-activity curves during chase dosing experiments

[PBZ] (mg/mL)	Absorbance (285 nm)
10.5	1606.8
5.3	807.5
2.6	342.7
1.3	175.2

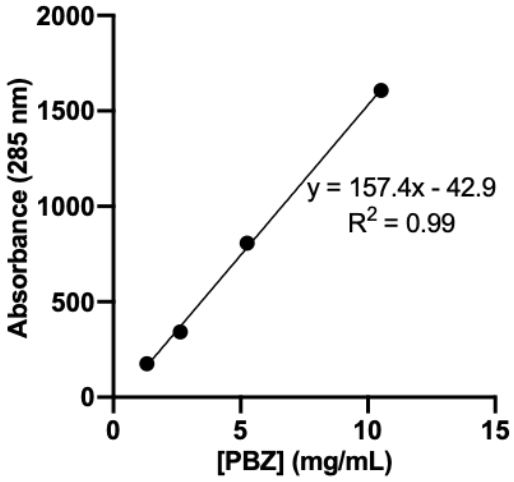

2.11.3.15. Figure S11. Phenoxybenzamine calibration curve

2.11.3.16. **Table S3.** Weight-normalized myocardial uptake in baseline and 6-OHDA vehicle groups

	Baseline	Vehicle
Heart (SUV)	3.90 ± 0.68	4.67 ± 0.28
Age (weeks)	4	8
Animal weight (g)	80 - 110	190 - 270

No significant difference in mean myocardial uptake is observed between groups (n = 4-5 per group, p = 0.08)

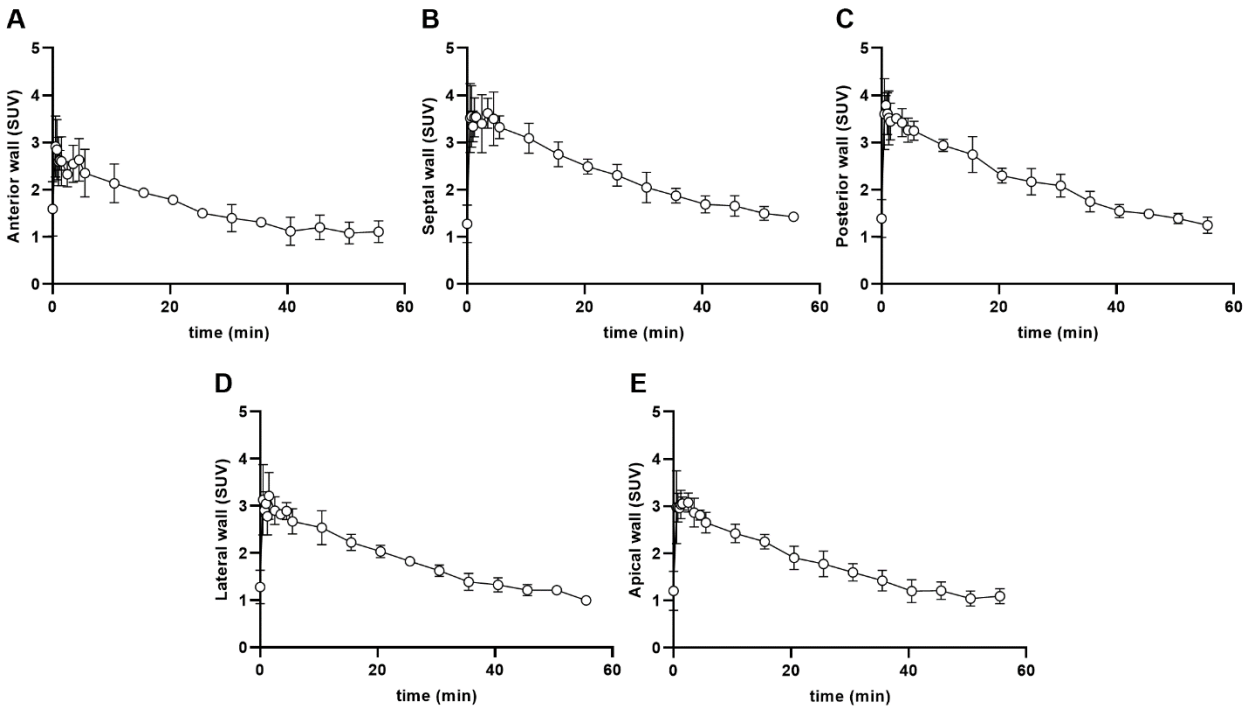

2.11.3.17. **Figure S12.** Regional uptake of [^{18}F]mFBG in the left ventricle. SUV in the (A) anterior (B) septal, (C) posterior (D) lateral and (E) apical wall of the left ventricle

2.11.3.18. **Table S4.** Regional analysis of myocardial K_{mono} values.

Scan #	K_{mono} (min^{-1})				
	Anterior	**Apical**	**Lateral**	**Posterior**	**Septal**
1	0.015	0.033	0.029	0.038	0.032
2	0.067	0.023	0.016	0.010	0.024
3	0.060	0.025	0.022	0.025	0.035
4	0.042	0.021	0.027	0.022	0.021
5	0.010	0.031	0.018	0.025	0.021
mean ± SD	*0.039 ± 0.023*	*0.026 ± 0.005*	*0.022 ± 0.005*	*0.024 ± 0.009*	*0.027 ± 0.006*

2.11.3.19. **Table S5.** Regional analysis of myocardial A_{mono} values.

Scan #	A_{mono} (SUV)				
	Anterior	**Apical**	**Lateral**	**Posterior**	**Septal**
1	1.927	3.093	3.684	3.990	4.170
2	3.899	3.243	3.066	3.718	3.810
3	2.705	3.155	2.685	3.450	3.400
4	2.320	2.880	3.076	3.699	3.740
5	3.369	2.924	2.860	3.557	3.830
mean ± SD	*2.844 ± 0.710**	*3.059 ± 0.137*	*3.074 ± 0.337*	*3.683 ± 0.182*	*3.790 ± 0.245**

* values significantly different by one-way ANOVA followed by Bonferroni correction

2.11.3.20. References

(1) Preshlock, S.; Calderwood, S.; Verhoog, S.; Tredwell, M.; Huiban, M.; Hienzsch, A.; Gruber, S.; Wilson, T. C.; Taylor, N. J.; Cailly, T.; Schedler, M.; Collier, T. L.; Passchier, J.; Smits, R.; Mollitor, J.; Hoepping, A.; Mueller, M.; Genicot, C.; Mercier, J.; Gouverneur, V. Enhanced Copper-Mediated ^{18}F-Fluorination of Aryl Boronic Esters Provides Eight Radiotracers for PET Applications. *Chem. Commun.* **2016**, *52* (54), 8361–8364. https://doi.org/10.1039/C6CC03295H.

(2) Rong, H.J.; Yang, C.F.; Chen, T.; Xu, Z.G.; Su, T.D.; Wang, Y.Q.; Ning, B.K. Iodine-Catalyzed Guanylation of Amines with *N*,*N*′-Di-Boc-Thiourea. *Org. Biomol. Chem.* **2019**, *17* (42), 9280–9283. https://doi.org/10.1039/C9OB02014D.

(3) Garg, P. K.; Garg, S.; Zalutsky, M. R. Synthesis and Preliminary Evaluation of *para*- and *meta*-[^{18}F]Fluorobenzylguanidine. *Nucl. Med. Biol.* **1994**, *21* (1), 97–103. https://doi.org/10.1016/0969-8051(94)90135-X.

3. Chapter III: Imaging Cardiac Sympathetic Nerve Dysfunction in Heart Failure using [^{18}F]*meta*-Fluorobenzylguanidine

The manuscript is currently being drafted and has not yet been submitted to a journal.

Uzair S. Ismailani,[1,2] Ariel Buchler,[2,3], Serena Pulente, Megan Fortier, Jadde De Carvalho Tso, Erin Mulvihill, Robert A. deKemp,[2] and Benjamin H. Rotstein[1,2,3]*

[1] *Department of Biochemistry, Microbiology and Immunology, University of Ottawa, Ottawa, Ontario, Canada*

[2] *University of Ottawa Heart Institute, Ottawa, Ontario, Canada*

[3] *Department of Chemistry and Biomolecular Sciences, University of Ottawa, Ottawa, Ontario, Canada*

Correspondence: Benjamin H. Rotstein, PhD
University of Ottawa Heart Institute
40 Ruskin Street, H-5219
Ottawa, Ontario, Canada
K1Y 4W7
Phone: 613-696-7324
Email: benjamin.rotstein@uottawa.ca

3.1. Statement of the manuscript

The manuscript "**Imaging Cardiac Sympathetic Nerve Dysfunction in Heart Failure using [^{18}F]meta-Flurobenzylguanidine**" is currently in the final phases of drafting and requires follow up experiments such as Western blot of DSS rat hearts and ELISA on blood samples prior to journal submission. The majority of this chapter consists of *in vivo* PET imaging to determine the intraneuronal mechanisms of [^{18}F]mFBG retention and washout. The mechanistic experiments performed in SD rats mentioned in this chapter were completed by me and Ariel Buchler. DSS rat imaging and blood pressure monitoring was a longitudinal study performed by me, Ariel Buchler, and Jadde De Carvalho Tso. Echocardiography of DSS rats was performed by Serena Pulente and Megan Fortier. All data was analyzed by me, and data interpretation was a collaborative effort of myself and Dr. Rotstein. The manuscript was written by me and edited by Dr. Benjamin Rotstein.

3.2. Abstract

Cardiac sympathetic dysfunction is central to the development of cardiovascular diseases such as heart failure (HF). Molecular imaging using positron emission tomography (PET) radiotracers targeting the norepinephrine transporter (NET) has provided adequate contrast of the left ventricle (LV) wall and demonstrated application in assessing sympathetic nerve function and global cardiac sympathetic innervation. The lack of fluorine-18 containing SNS radiotracers demonstrating NET dependency in commonly used small animals such as mice and rats has precluded preclinical investigations in these species, hindering disease research critical for quantitative interpretation. Our previous work demonstrated adequate NET-dependent uptake of [^{18}F]metafluorobenzylguanidine ([^{18}F]mFBG) in the rat myocardium sensitive to neuronal ablation. In this study, we use PET imaging in Sprague Dawley (SD) rats to explore the intraneuronal kinetics and washout mechanisms of [^{18}F]mFBG, and demonstrate its application by imaging Dahl Salt-sensitive (DSS) rats induced with HF using a high salt diet. Intraneuronal vesicular retention of [^{18}F]mFBG was probed using the vesicular monoamine transporter (VMAT) inhibitor reserpine (RSP), and markedly reduced retention in the LV by 35% within 5 minutes (2.07 ± 0.24 vs 3.17 ± 0.41 SUV). Tyramine (TYR) serial chase dosing was performed to supplement neuronal washout following radiotracer accumulation, and increased cardiac washout by 55% (k_{mono} = 0.025 ± 0.009 vs 0.045 ± 0.012 min^{-1}). Changes in cardiac sympathetic tone were induced by chase dosing using sympatholytic and sympathomimetic alpha-2 (α_2) targeting pharmaceuticals dexmedetomidine (DEX) and yohimbine (YH), respectively. DEX chase attenuated washout by 76% (k_{mono} = 0.006 ± 0.008 min^{-1}, p = 0.0037), whereas YH chase increased myocardial washout by 31% (k_{mono} = 0.036 ± 0.007 min^{-1}) with respect to baseline imaging. Imaging performed in C57BL/6 mice, containing intrinsically lower cardiac parasympathetic input, demonstrated a ~5.5 fold increase in cardiac clearance of the tracer (k_{mono} = 0.14 ± 0.008 vs

0.025 ± 0.009 min^{-1}). DSS rats displayed similar cardiac uptake at baseline in comparison to SD rats. However, myocardial uptake in low salt (LS) fed DSS control rats significantly increased in 9-week-old rats (3.14 ± 1.04 vs 6.31 ± 0.92 SUV) and stabilized in 14-week and 21-week-old rats. Declining cardiac function measured by echocardiography and non-invasive blood pressure was observed in rats kept on HS diet for 4-weeks (HS-4) and worsened in HS-16 rats. Concomitant with poor hemodynamic parameters, 32% reduced peak uptake in the LV was noted by [^{18}F]mFBG PET in HS-16 rats (7.26 ± 0.78 vs 4.92 ± 0.48 SUV), consistent with the magnitude of previously established desipramine sensitivity. PET imaging with [^{18}F]mFBG therefore demonstrates sensitivity in an animal model of HF and can be utilized for serial imaging studies to determine SNS function in small animals.

3.3. Introduction

The cardiac autonomic nervous system exists in a state of dynamic equilibrium to maintain functional homeostasis. Balance is achieved through a multilevel complex neural network to control cardiac inotropy, chronotropy, lusitropy, and dromotropy.[1–4] Ischemic events, such as in myocardial infarction (MI), and chronic activation of the sympathetic nervous system (SNS) following insult, such as in heart failure (HF), cause pathology of sympathetic neurons in the left ventricle.[5,6] Increased sympathetic drive following an injury results in hemodynamic changes in cardiovascular, renal, and peripherical vascular systems.[6,7] Aberrant afferent signaling driven by an imbalance in sympathetic-parasympathetic control leads to elevated efflux of inflammatory cytokines and catecholamines, exacerbating cardiac function and leading to congestive HF.[8,9] In late stages, regional adrenergic denervation of the LV is often observed, and excess sympathetic activity measured by NE spillover is a well-known negative prognostic indicator post-MI in

congestive heart failure.[7,10,11] Furthermore, reduced parasympathetic input resulting in increased action potential propagation and rapid repolarization in the ventricles manifests ventricular tachycardia, increasing the risk of sudden death.[1,6,12–14]

On a molecular level, an increased rate of norepinephrine release (NE) from the presynaptic bouton overstimulates postsynaptic adrenoreceptors to increase cardiac contractility and vascular tone, inevitably causing β_1 adrenoreceptor desensitization and downregulation.[15,16] In conjunction, progressive dysfunction or downregulation of the norepinephrine transporter (NET), responsible for recycling synaptic NE in the presynaptic neuron, contributes heavily to overall disease progression.[10,17] As such, assessing NET activity has become a point of emphasis in evaluating sympathetic nerve function.

Molecular imaging has been at the forefront of both diagnosis and risk stratification of autonomic dysfunction for several decades, most notably with the development of ligands targeting NET such as *meta*-[^{123}I]iodobenzylguanidine ([^{123}I]mIBG), used in planar scintigraphy and single photon emission tomography (SPECT) imaging.[18] [^{123}I]mIBG has displayed prognostic power in independently predicting the risk of cardiac events in patients with heart failure (HF) and significant left ventricular dysfunction using the early and late timepoint heart-to-mediastinum ratio (H/M) as a global indicator of myocardial neuronal uptake and washout, respectively.[19] Recent studies using [^{123}I]mIBG scintigraphy have also detected extrinsic cardiac sympathetic dysfunction in Parkinson's syndromes.[20,21]

Limitations in the spatial resolution and absolute quantification of [^{123}I]mIBG imaging have precipitated the development of analogous positron emission tomography (PET) radioligands containing amphetamine, benzylguanidine, and phenethylguanidine (PHEG) cores such as [^{11}C]hydroxyephedrine ([^{11}C]HED), [^{18}F]flubrobenguane ([^{18}F]FBBG), and 4-[^{18}F]fluoro-*meta*-

hydroxyphenethylguandine ([^{18}F]4F-MHPG), respectively, for more accurate assessments of cardiac sympathetic nerve density using NET as a proxy.[18,22] The utility of [^{11}C]HED for quantifying sympathetic innervation was exemplified in the Prediction of Arrhythmic Events with Positron Emission Tomography (PAREPET) clinical trial, providing evidence of low denervation scores for those at high risk of arrhythmic death, independent of left ventricular ejection fraction (LVEF).[23] Due to the short half-life of carbon-11, a fluorinated analogue of [^{123}I]mIBG, [^{18}F]FBBG was developed, and provided similar regional innervation data as [^{11}C]HED.[24] First in-human trials of [^{18}F]4F-MHPG and its regioisomer [^{18}F]3F-PHPG displayed high contrast in the myocardium, and analogous baseline innervation scores to both [^{11}C]HED and [^{18}F]FBBG.[25]

[^{11}C]HED uptake into the neuron depends on NET, whereas neuronal retention is governed by vesicular storage and synaptic release.[26,27] Due to high NET affinity, [^{11}C]HED re-enters the neuron via NET and thus displays minimal myocardial clearance in higher species limiting its use to the quantification of sympathetic innervation.[26,28] [^{18}F]FBBG and ^{18}F-PHEG analogues also display irreversible kinetics.[25,26,29] However, these fluorinated analogues are shown to be trapped within the presynaptic vesicle irreversibly rather than released into the synaptic cleft and recycled by NET.[26,29,30] In small animal imaging, [^{11}C]HED uptake and retention is dependent on NET, yet neither of the fluorinated analogs display any NET dependence due to differential non-neuronal catecholamine handling, hindering preclinical investigations of cardiac neuronal nerve density in the most common species for cardiovascular research, rats and mice.[31]

Our recent evaluation of *meta*-[^{18}F]fluorobenzylguanidine ([^{18}F]mFBG) in rats revealed appreciable NET-dependent uptake and monoexponential myocardial washout insensitive to selective NET inhibition by desipramine (DMI) chase dosing.[32] Consequently, [^{18}F]mFBG displays preferential clearance into plasma, and is unlikely to remain trapped within presynaptic

vesicles. The unique myocardial kinetics of [^{18}F]mFBG prompted us to investigate the intraneuronal mechanisms responsible for [^{18}F]mFBG retention and washout in the absence of NET reuptake. Given that the [^{123}I]mIBG washout rate is a meaningful imaging parameter in humans and rats, we further hypothesized that [^{18}F]mFBG cardiac clearance is also a function of sympathetic tone, a criteria that cannot be measured with the current generation of PET SNS radioligands.[20,33,34] Furthermore, a recent study that included absolute kinetic quantification of [^{18}F]mFBG in the LV of neuroblastoma patients revealed a slow but measurable washout rate from the myocardium, consistent with a decrease in sympathetic tone expected moving from rats to higher species.[35]

To assess intraneuronal mechanisms of [^{18}F]mFBG handling in SD rats, we performed *in vivo* PET imaging and employed various pharmacological agents. The vesicular monoamine transporter (VMAT2) inhibitor reserpine (RSP) was used to determine the contribution of [^{18}F]mFBG vesicular storage on neuronal retention, as was the biogenic catecholamine depleting agent tyramine (TYR). Alterations in sympathetic tone were performed by targeting the presynaptic alpha-2 adrenergic receptor (α_2R) with dexmedetomidine (DEX) and yohimbine (YH) to decrease and increase presynaptic neuronal firing rate, respectively. PET imaging was also performed in mice to support increased tracer washout in species naturally exhibiting higher sympathetic tone. We also aimed to abolish extraneuronal uptake in the myocardium using corticosterone to selectivity visualize sympathetic nerves. Lastly, [^{18}F]mFBG imaging was performed in Dahl-salt sensitive (DSS) rats induced with HF following a high salt (HS) diet to determine its application in imaging cardiac neuronal dysfunction.

3.4. Results and discussion

[^{18}F]mFBG retention is dependent on vesicular storage. To determine the neuronal retention mechanism of [^{18}F]mFBG, animals were treated with the VMAT2 inhibitor RSP (4 mg/kg, ip) 4 hours prior to administering the radiotracer. Dynamic PET scans were performed for 60 minutes from the time of tracer injection and baseline imaging data were obtained in age-matched controls. Time-activity curves (TAC) obtained from the left ventricle (LV) were fitted to a monoexponential function to obtain quantitative parameters for cardiac uptake (A_0) and washout (k_{mono}). Baseline imaging revealed clear uptake in the LV that peaks at ~3.4 standardized uptake value (SUV) from 2.5–5 min post-injection. Cardiac activity decreased monoexponentially (r^2 = 0.99, 10.5–55.5 min) following peak uptake with an observed k_{mono} of 0.025 ± 0.009 min^{-1} and A_0 of 2.87 ± 0.44 SUV.

Reserpinized rats displayed rapid initial uptake of [^{18}F]mFBG in the LV within 0.5 min, followed by considerable early-phase washout from the myocardium sustained from 0.5–5 min resulting in a maximal 35% depletion of myocardial retention at 5 min (2.07 ± 0.24 vs 3.17 ± 0.41 SUV, p = 0.0001). Monoexponential fitting revealed a similar myocardial clearance rate to baseline imaging during the second washout phase (10.5–55.5 min, 0.026 ± 0.016 min^{-1}), and a proportional 35% reduction in A_{mono} (1.87 ± 0.32 SUV, p = 0.0007).

RSP is a well-established pharmaceutical used clinically to treat hypertension. Preclinical investigations with this compound have determined the mechanism of action of this drug in small animals. Inhibition of VMAT2 in the presynaptic neuron eliminates stable storage of catecholamines within vesicles.[36] Extravesicular neurotransmitters are subject to metabolism and likely expelled from the neuron by facilitated diffusion, consequently reducing the long-term action of NE in the synapse and ameliorating hypertension.[37,38] Baseline animals and those treated

with RSP displayed similar peak myocardial retention within the first minute, likely due to NET-dependent influx of [^{18}F]mFBG and tissue perfusion. The initial clearance phase of the tracer is thus representative of tracer washout from the presynaptic neuron. Notably, our initial evaluation with this tracer revealed a 31–36% NET dependency of [^{18}F]mFBG uptake, and is consistent with the magnitude of reduction observed with RSP pretreatment.[32] RSP pretreatment in rabbits with [^{11}C]HED revealed similar findings of minor changes in peak uptake but considerable washout over the duration of the scan.[27] Moreover, [^{123}I]mIBG retention was not observed to be significantly different by 40 minutes in rabbits, but has displayed RSP dependency at late time-points in the rat heart.[27,39] In contrast, [^{18}F]mFBG neuronal retention appears to rely on vesicular storage immediately upon entry into the neuron.[40] Further evidence for vesicular/neuronal storage mechanisms were probed using a chase dosing protocol for the biogenic catecholamine releaser TYR to induce neuronal efflux of [^{18}F]mFBG.[41]

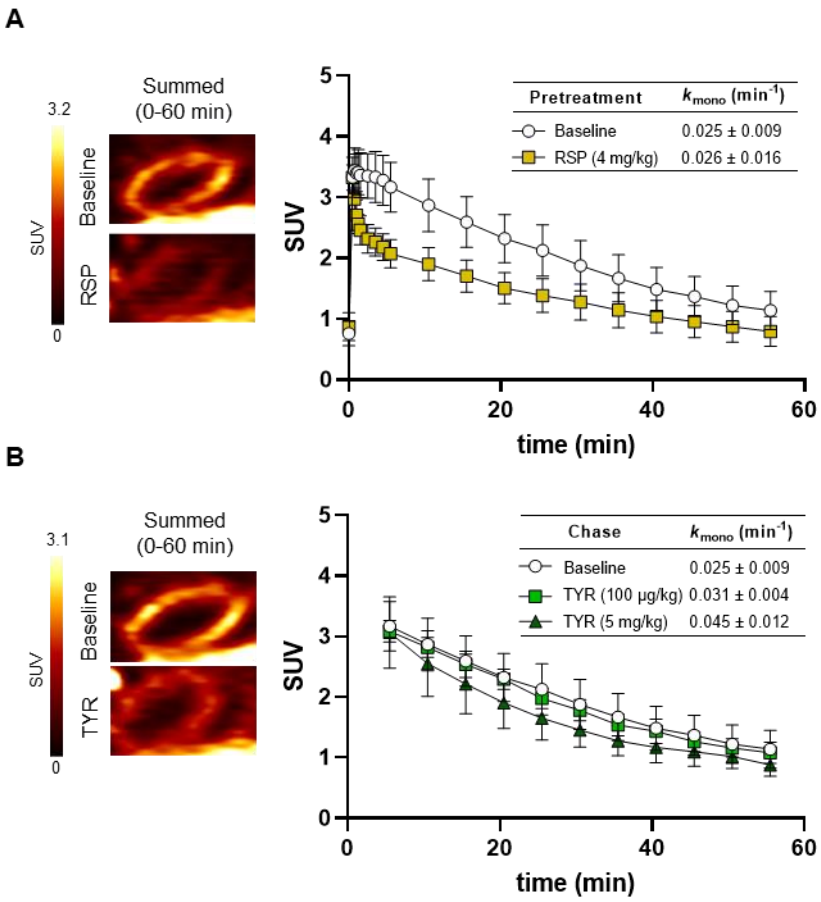

3.4.1. **Figure 1**. Time-activity curves and representative images for baseline, RSP, and TYR treatments. Baseline, *n* = 7; RSP, *n* = 6; TYR (100 µg/kg), *n* = 4; TYR (5 mg/kg), *n* = 4.

Due to the high susceptibility of TYR to monoamine oxidase (MAO) metabolism in the myocardium ($t_{1/2}$ = ~5 min), TYR is administered in repeated doses to achieve an adequate response.[42] Chase dosing was performed with TYR (100 µg/kg, 5 mg/kg, iv) at 10 minutes and was readministered every ten minutes for a total of five injections. Low dose tyramine injections (100 µg/kg) led to a moderate but insignificant increase in the washout rate of [^{18}F]mFBG (k_{mono} = 0.031 ± 0.004 min^{-1}). However, high dose tyramine injections (5 mg/kg) significantly accelerated myocardial tracer efflux (k_{mono} = 0.045 ± 0.012 min^{-1}, p = 0.013) by ~55% in comparison to

baseline. Mechanistically, TYR exerts its pressor activity by release of NE from storage granules in adrenergic neurons.[41,43–46] Furthermore, TYR stoichiometrically displaces NE from isolated storage granules and saturates MAO binding sites with successive injections to reduce the rate of NE replenishment.[47] Excessive accumulation of neurotransmitters in the axoplasm is hypothesized to energetically drive reverse NET transport of displaced molecules back into the synapse, similar to the action of amphetamines.[48,49] Given the dependency of [^{18}F]mFBG retention on vesicular storage, accelerated tracer clearance from the neuron is likely to be a product of both vesicular efflux and neuronal release. Similar results were obtained with [^{18}F]AF78, a PHEG analogue displaying irreversible kinetics via vesicular trapping. Upon administration of TYR (1 mg/kg, 5 doses), significant tracer washout was observed from the myocardium of non-human primates (NHP).[50]

[^{18}F]mFBG washout is dependent on sympathetic tone. Next, we investigated whether changes in [^{18}F]mFBG myocardial washout rate were dependent on sympathetic tone by administering the selective sympatholytic and sympathomimetic α_2 agonist DEX and antagonist YH, respectively, using a chase-dosing protocol (pharmacological treatment administered 10 min after tracer injection). Chase dosing with DEX attenuated the washout rate (k_{mono} = 0.006 ± 0.008 min^{-1}, p = 0.0037) by 76% with respect to baseline imaging. In contrast, YH chase accelerated myocardial clearance by ~31% (k_{mono} = 0.036 ± 0.007 min^{-1}, p = 0.04).

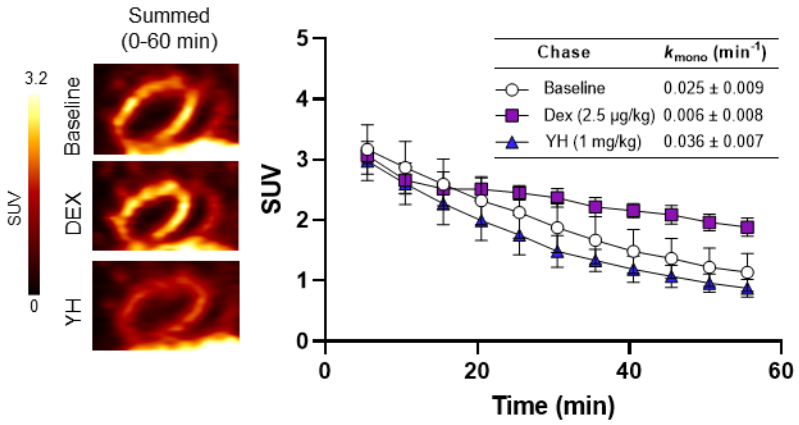

3.4.2. **Figure 2.** Time-activity curves and representative images for baseline, DEX, and YH treatments. Baseline, *n* = 7; DEX (2.5 µg/kg), *n* = 6; YH (1 mg/kg), *n* = 5.

Neurohormonal homeostasis is maintained by negative feedback mediated by presynaptic α_2R. Under physiological conditions, increased sympathetic outflow can lead to agonism of presynaptic α_2Rs by NE, initiating downstream signal transduction pathways.[51] Inhibition of adenylyl cyclase induces hyperpolarization of the neuron, inevitably preventing calcium ions from entering the nerve terminal, thereby suppressing the neuronal firing rate and attenuating the release of NE from storage vesicles.[51,52] Systemic decrease in sympathetic tone by DEX is attributed to the stimulation of α_{2A}R in the locus coeruleus of the brain stem, whereas peripheral α_{2B}R activation in vascular smooth muscle induces vasoconstriction, resulting in a short-lived hypertensive response concomitant with a decreased heart rate presumably mediated by enhanced baroreceptor reflexes due to its short-lived nature.[52–58] In contrast, increased cardiac sympathetic tone and hemodynamic changes of the α_2-antagonist YH may be due to receptor occupancy in the CNS and by direct action on α_2R present on cardiac presynaptic nerve terminals.[59–64] Regardless, marked reduction in sympathetic activity following DEX chase dosing is attributed to prolonged retention

of [^{18}F]mFBG within presynaptic vesicles due to hyperpolarization and reduced action potential propagation. Given that the opposite effect is observed following YH-chase, [^{18}F]mFBG washout is therefore influenced by alterations in sympathetic signaling induced by activation or blockade of central and/or peripheral α_2Rs.

Additional evidence for [^{18}F]mFBG clearance and sympathetic tone was obtained in healthy C57BL/6 mice. Mice exhibit a far greater conscious resting heart rate (HR) of ~500–700 beats per minute (BPM) in comparison to rats averaging 300–500 BPM.[65,66] We hypothesized that this smaller species exhibiting a lower intrinsic HR due to reduced parasympathetic input and higher sympathetic nerve activity demonstrates greater myocardial washout.[67,68] Animals were pre-treated with vehicle, NET inhibitor desipramine (DMI) or the neural and extraneural inhibitor phenoxybenzamine (PBZ) ten minutes prior to administering [^{18}F]mFBG. Exponential fitting was performed to obtain quantitative metrics.

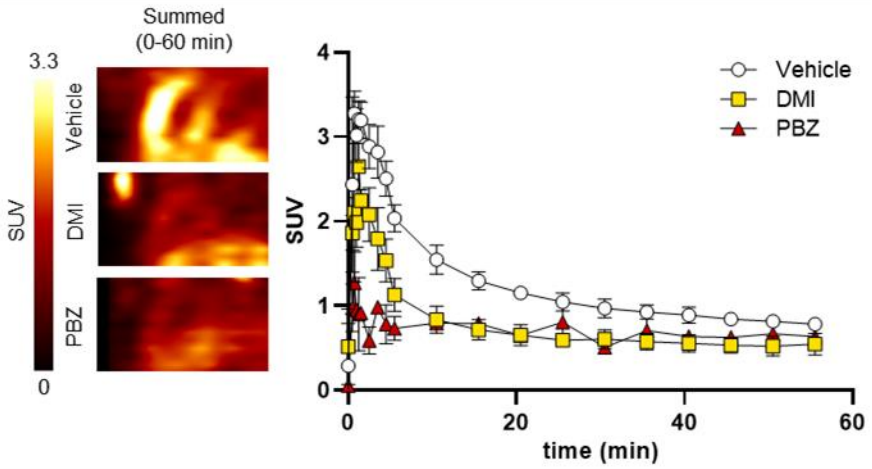

3.4.3. Figure 3. Representative *in vivo* myocardial PET imaging in C57BL/6 mice following pretreatment. Vehicle, *n* = 4; DMI, *n* = 3; PBZ, *n* = 2.

Animals pre-treated with vehicle displayed myocardial uptake peaking at ~3.2 SUV at 1.5 min (A_0 = 2.90 ± 0.3 SUV), followed by a rapid exponential washout (r^2 = 0.96, 2–60 min k_{mono} = 0.14 ± 0.008 min^{-1}) for the remainder of the scan. Desipramine pre-treated mice displayed ~31% reduced peak uptake noted at 2 minutes (2.2 ± 0.12 SUV, p = 0.0009), reduced A_0 (2.3 ± 0.2 SUV, p = 0.0312) and increased clearance from the myocardium (k_{mono} = 0.26 ± 0.005 min^{-1} p < 0.0001) in comparison to animals treated with vehicle. Pre-treatment with PBZ further diminished myocardial uptake by 72% at 2 min (0.91 ± 0.05 SUV, p < 0.0001). [^{18}F]mFBG imaging in mice provided similar NET-dependency as observed in rat imaging, with approximately 30% contribution of myocardial retention by NET, and 40% contribution to extraneural transport.

Interestingly, myocardial washout under baseline conditions was observed to be approximately 5.5 times faster in mice than in rats (k_{mono} = 0.14 ± 0.008 vs 0.025 ± 0.009 min^{-1}, p < 0.0001). Given the inverse relationship of body weight and heart rate, the myocardium of smaller animals such as mice are required to contract and relax at a faster rate to maintain cardiac output.[69] Studies conducted in "β-less" and muscarinic M_2 receptors (M_2R) knockout mice have demonstrated cardiac sympathetic tone to be a major contributor of HR regulation in mice at ambient temperatures, whereas vagal tone predominates fluctuations in HR at thermoneutrality (30 °C).[70] While it is understood that direct measurements of sympathetic tone by microneurography were not performed in this study, the relative differences in basal levels of sympathetic and parasympathetic activation in the heart of smaller to larger species are known.[67] Humans, displaying greater input from parasympathetic control at rest are expected to have lower sympathetic tone in comparison to rats, and mice, respectively. The observation that [^{18}F]mFBG washout is progressively slower from mice to humans therefore supports the hypothesis that [^{18}F]mFBG washout may be a function of sympathetic tone.

Pilot studies were then performed to diminish the contribution of extraneuronal uptake in rats by pre-treating animals with the uptake-2 inhibitor corticosterone (CTC, iv 5 mg/kg, ip 20 mg/kg).

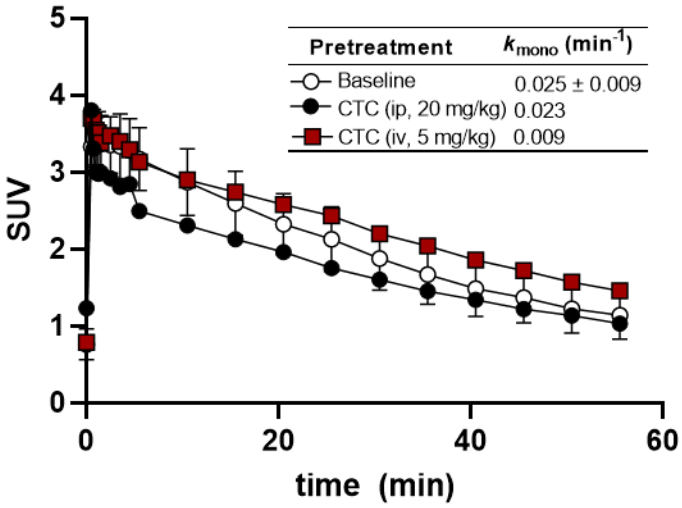

3.4.4. Figure 4. *in vivo* myocardial PET imaging in SD rats following pretreatment with CTC. Baseline, n = 7; CTC ip, n = 1; CTC iv, n = 1.

Pretreatment with CTC (20 mg/kg, ip) 45 minutes prior to administering [^{18}F]mFBG revealed moderately lower uptake in the LV at 5.5 min (2.49 SUV), with no change in tracer washout (k_{mono}_0.023 min^{-1}). In contrast, pretreatment with CTC (5 mg/kg, iv) led to similar myocardial uptake (3.13 SUV) with a slower washout rate (0.009 min^{-1}). CTC is a well-established *in vitro* inhibitor of the uptake-2 transporter (OCT3), and has demonstrated selective inhibition in isolated perfused rat hearts.[71,72] In our pilot study, the expected magnitude of reduction in the LV was ~40%. However, CTC treatment resulted in ~25% reduced uptake. While iv treatment of CTC displayed the expected reduced washout rate, the uptake remained the same. Further studies may

be warranted with CTC or analogous inhibitors which have displayed reductions in myocardial activity.[73]

[^{18}F]mFBG imaging detects NET dysfunction in HF. [^{18}F]mFBG imaging was performed in DSS rats fed low salt (LS, 0.2%) and high-salt (HS, 8%) diets to demonstrate its application in imaging HF. DSS rats developed by Dahl *et* al exhibit hypertension and left ventricular hypertrophy when fed high salt diet for 5 weeks, and display left ventricular dilation, cardiac failure, and death within 10-15 weeks after initiating the diet.[74–77] PET images were obtained using a Bruker Si78 PET-CT, and time-activity curves were generated using PMOD. Both cohorts (4-weeks old) were initially placed on LS chow diet for one week to establish baseline imaging parameters and underwent non-invasive blood pressure monitoring under isoflurane via tail cuff. After one week of chow diet (5-weeks old), one cohort was switched to HS diet for the remainder of the study. Echocardiography and non-invasive BP monitoring was performed within 1-week of PET imaging to determine cardiac function at each imaging time point. All data were collected in age-matched LS controls to distinguish between differences in organ uptake. Baseline imaging of rats fed LS diet revealed favorable peak uptake in the LV (3.14 ± 1.04 SUV) within 5 min, and similar A_0 as previously determined in SD rats (3.15 ± 1.03 SUV), followed by a monoexponential washout phase (r^2 = 0.99, k_{mono} = 0.034 ± 0.0094 min^{-1}). Hemodynamic parameters and measurements obtained from echocardiography are summarized in **table 3** for LS and HS rats.

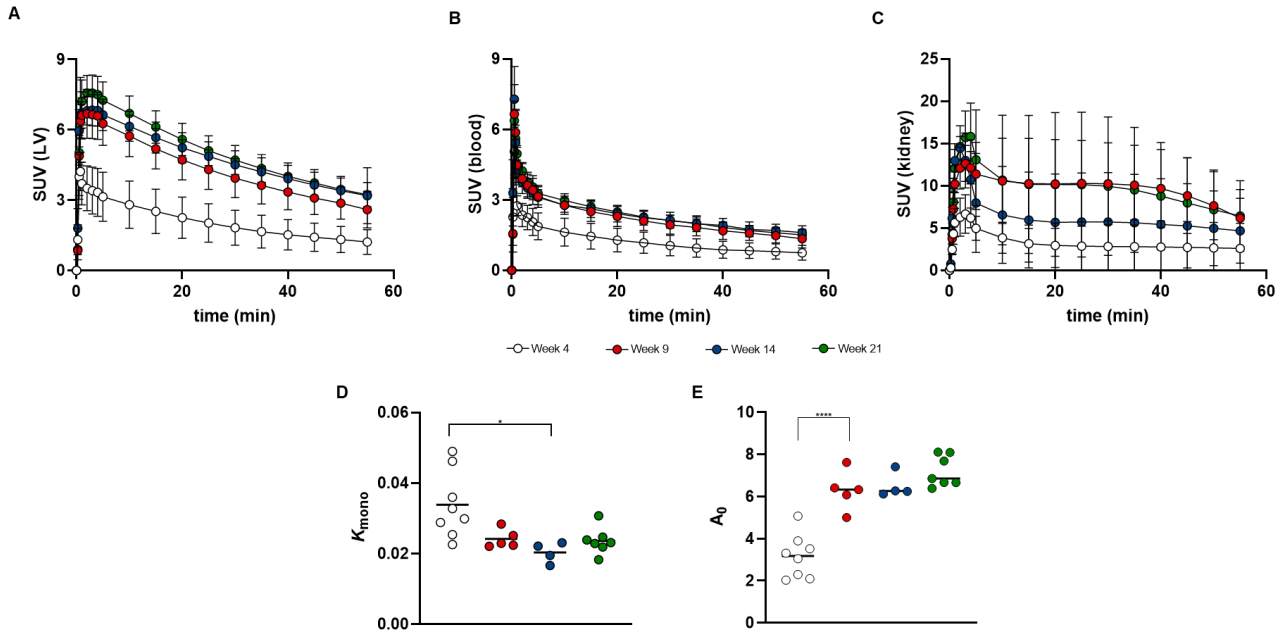

3.4.5. **Figure 5.** PET time-activity curves of LS DSS rats for (**A**) LV (**B**) blood (**C**) kidney and corresponding quantitative LV exponential parameters (**D**) K_{mono} and (**E**) A_{mono} . Week 4, n = 8; Week 9, n = 5; Week 14, n = 4; Week 21, n = 7.

Significant age-dependent changes were observed in LS controls. PET imaging of 4-week-old LS DSS control rats displayed significantly lower peak uptake in the myocardium in comparison to 9-week-old (6.31 ± 0.92 SUV, $p < 0.0001$), 14-week-old (6.62 ± 0.66 SUV, $p = 0.0003$) and 21-week-old rats (7.26 ± 0.78 SUV, $p < 0.0001$). Consequently, A_0 was also observed to be significantly lower in 4-week-old LS rats in comparison to all older cohorts. Reduced uptake was also observed for peak kidney retention (6.20 ± 1.16 vs 12.14 ± 1.9 SUV, $p < 0.0001$) and blood activity (5.06 ± 1.13 vs 6.65 ± 0.6 SUV, $p = 0.0152$), whereas K_{mono} was found to be significantly higher (0.034 ± 0.0094 vs 0.024 ± 0.0026 min^{-1}, $p = 0.043$) in 4-week-old rats in comparison to 9-week-olds and all other ages. Furthermore, significant age-related differences were observed in almost all parameters of cardiac function measured by echocardiography in early

timepoints of LS rats and are likely a consequence of dynamic physiological changes occurring as the animals reach maturity (Table 1). To provide more reliable comparisons of HS diet-induced changes, comparative analyses between cohorts were limited to animals 9-weeks and older.

3.4.6. Table 1. Echocardiography performed in LS controls.

LS controls	Week 4	Week 9	Week 14	Week 21
Area (mm^2)	42.5 ± 18.5	87.6 ± 28.6*	69.5 ± 30.1	68.6 ± 22.9
EDA (mm^2)	64.4 ± 7.4	110.7 ± 11.9*	93.5 ± 17.2	92.6 ± 7.1
ESA (mm^2)	32.9 ± 4.0	66.7 ± 7.9*	60.2 ± 13.7	54.4 ± 6.3
Volume (µL)	150.3 ± 117.2	462.3 ± 284.0*	325.6 ± 240.2	299.7 ± 169.1
ESV (µL)	190.4 ± 35.1	256.0 ± 49.2*	241.3 ± 86.6	185.4 ± 38.8
EDV (µL)	295.4 ± 43.1	642.3 ± 93.4*	525.6 ± 137.8	493.5 ± 44.3
SV (µL)	208.4 ± 36.1	387.1 ± 76.4*	284.3 ± 61.8	303.1 ± 27.1
HR (bpm)	437.8 ± 23.7	407.0 ± 23.5	387.8 ± 10.7	379.9 ± 33.3
EF (%)	70.5 ± 5.3	60.0 ± 6.6*	54.8 ± 6.2	62.0 ± 5.1
FS (%)	12.2 ± 2.2	9.6 ± 2.7	9.7 ± 1.6	10.9 ± 3.1
CO (mL/min)	90.9 ± 14.0	158.0 ± 35.1*	110.4 ± 24.4	115.2 ± 14.8

*Statistical significance ($p < 0.05$) reached using one-way ANOVA. Week 4, $n = 7$; Week 9, $n = 7$; Week 14, $n = 4$; Week 21, $n = 6$.

Age-matched LS controls and rats switched to HS diet for 4-weeks (LS-4, HS-4), 9-weeks (LS-9, HS-9), and 16-weeks (LS-16, HS-16) underwent PET imaging and hemodynamic monitoring to assess cardiac function at each imaging timepoint (**figure 6, table 2**). LV uptake and washout remained consistent in HS-4 and HS-9 relative to LS controls (**figure 6A,B)**. HS-4 rats were found to have significantly higher systolic (138 ± 3.3 vs 114 ± 5 mmHg, $p = 0.0003$) and diastolic (112 ± 12 vs 85 ± 13 mmHg, $p = 0.0260$) blood pressure in comparison to LS-4 rats, in addition to increased MAP (120 ± 8.5 vs 95 ± 9.6 mmHg, $p = 0.0072$). Blood pressure parameters remained elevated in HS-9 rats in comparison to LS-9 controls, with minimal deviation from the previous time-point (HS-4).

3.4.7. Table 2. Summary of non-invasive blood pressure measurements.

	LS-4	HS-4	LS-9	HS-9	LS-16	HS-16
Systolic (mmHg)	114 ± 5	138 ± 3*	118 ± 7	129 ± 11*	111 ± 3	164 ± 4*
Diastolic (mmHg)	85 ± 13	112 ± 12*	90 ± 13	100 ± 12*	90 ± 3	142 ± 1*
MAP (mmHg)	95 ± 10	120 ± 8*	99 ± 11	110 ± 11*	97 ± 2	149 ± 2*
HR (bpm)	378 ± 16	343 ± 11*	369 ± 13	334 ± 15*	371 ± 3	349 ± 5*

*Statistical significance ($p < 0.05$) reached using a two-sample t-test for groups kept on LS and HS diet for an equivalent period. LS-4, $n = 7$; HS-4, $n = 8$, LS-9, $n = 4$; HS-9, $n = 4$, LS-16, $n = 2$; HS-16, $n = 2$.

HS-16 rats demonstrated significantly increased systolic (164 ± 4 vs 111 ± 3 mmHg, p = 0.0041), diastolic (142 ± 1 vs 90 ± 3 mmHg, p = 0.0015), and MAP (149 ± 2 vs 97 ± 2 mmHg, p = 0.0014) readings in comparison to LS-16 rats. All parameters were significantly elevated at HS-16 in comparison to HS-4 and HS-9. HS-16 rats also demonstrated significantly increased end-systolic area (ESA, 54.4 ± 6.3 vs 62.2 mm^2, p = 0.044), end-systolic volume (ESV, 185.4 ± 38.8 vs 244.5 ± 34.4 µL, p = 0.027), reduced ejection fraction (EF, 62.0 ± 5.1 vs 52.8 ± 3.4%, p =0.009), and diminished cardiac output (CO, 115.2 ± 14.8 vs 93.5 ± 11.5 mL/min, p = 0.025).

3.4.8. Table 3. Echocardiography data for LS and HS rats.

	LS-4	HS-4	LS-9	HS-9	LS-16	HS-16
Area (mm^2)	87.6 ± 28.6	88.6 ± 23.2	69.5 ± 30.1	89.1 ± 31.0	68.6 ± 22.9	82.3 ± 17.1*
EDA (mm^2)	110.7 ± 11.9	109.2 ± 14.1	93.5 ± 17.2	102.0 ± 12.8	92.6 ± 7.1	94.6 ± 5.4
ESA (mm^2)	66.7 ± 7.9	73.0 ± 13.2	60.2 ± 13.7	73.9 ± 9.5	54.4 ± 6.3	62.2 ± 4.4*
Volume (µL)	462.3 ± 284.0	432.1 ± 183.9	325.6 ± 240.2	479.6 ± 254.8	299.7 ± 169.1	410.8 ± 147.1*
ESV (µL)	256.0 ± 49.2	299.9 ± 95.6	241.3 ± 86.6	345.8 ± 65.7	185.4 ± 38.8	244.5 ± 34.4*
EDV (µL)	642.3 ± 93.4	618.6 ± 114.5	525.6 ± 137.8	594.7 ± 92.0	493.5 ± 44.3	516.5 ± 53.2
SV (µL)	387.1 ± 76.4	318.7 ± 59.2	284.3 ± 61.8	248.9 ± 26.3	303.1 ± 27.1	272.1 ± 26.8
HR (bpm)	407.0 ± 23.5	399.4 ±21.0	387.8 ± 10.7	373.1 ± 11.0	379.9 ± 33.3	343.5 ± 19.2
EF (%)	60.0 ± 6.6	52.1 ± 42.0	54.8 ± 6.2	42.0 ± 2.1	62.0 ± 5.1	52.8 ± 3.4*
FS (%)	9.6 ± 2.7	7.6 ± 2.1	9.7 ± 1.6	9.8 ± 2.6	10.9 ± 3.1	9.5 ± 2.2
CO (mL/min)	158.0 ± 35.1*	123.1 ± 24.3*	110.4 ± 24.4	92.7 ± 7.1	115.2 ± 14.8	93.5 ± 11.2*

*Statistical significance ($p < 0.05$) reached using a two-sample t-test for groups kept on LS and HS diet for an equivalent period. LS-4, $n = 7$; HS-4, $n = 8$; LS-9, $n = 4$; HS-9, $n = 3$; LS-16, $n = 6$; HS-16, n = 5.

Concomitant with these haemodynamic measurements, PET imaging in HS-16 rats revealed 32% reduced peak uptake (7.26 ± 0.78 vs 4.92 ± 0.48 SUV, $p = 0.0004$) and A_0 (7.21 ± 0.73 vs 4.82 ± 0.44 SUV, $p = 0.0002$) in the LV, consistent with the magnitude of NET dependence displayed by [^{18}F]mFBG rat imaging.

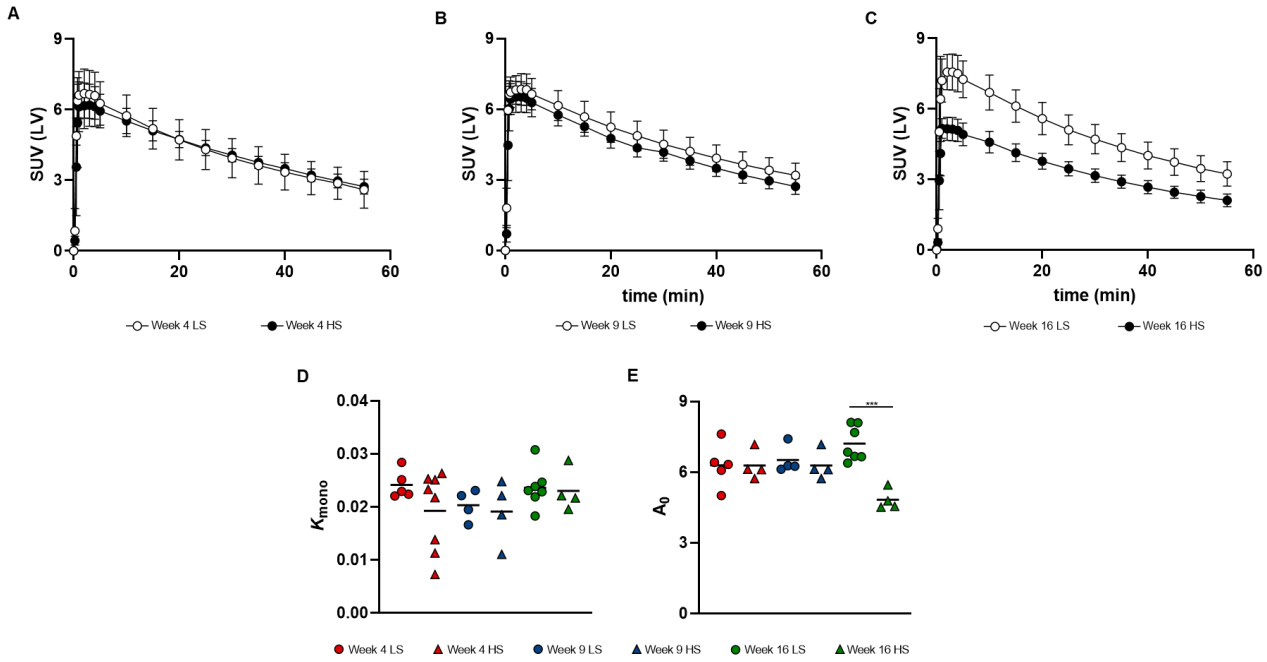

3.4.9. **Figure 6.** Left ventricular PET time-activity curves of DSS rats for (**A**) LS-4 and HS-4 (**B**) LS-9 and HS-9 (**C**) LS-16 and HS-16 (**D**) corresponding quantitative LV exponential parameters K_{mono} and (**E**) A_{mono} . LS-4, n = 5; HS-4, n = 8; LS-9, n = 4; HS-9, n = 4; LS-16, n = 7; HS-16, n = 4. ***P = 0.0002

Renal uptake of [^{18}F]mFBG (figure 7) evaluated at 3-minutes post injection was also observed to be reduced by 34% in HS-20 rats (15.69 ± 3.15 vs 10.27 ± 2.32 SUV, p = 0.0154) in comparison to LS-20. No other significant differences in renal uptake were noted at any earlier timepoint

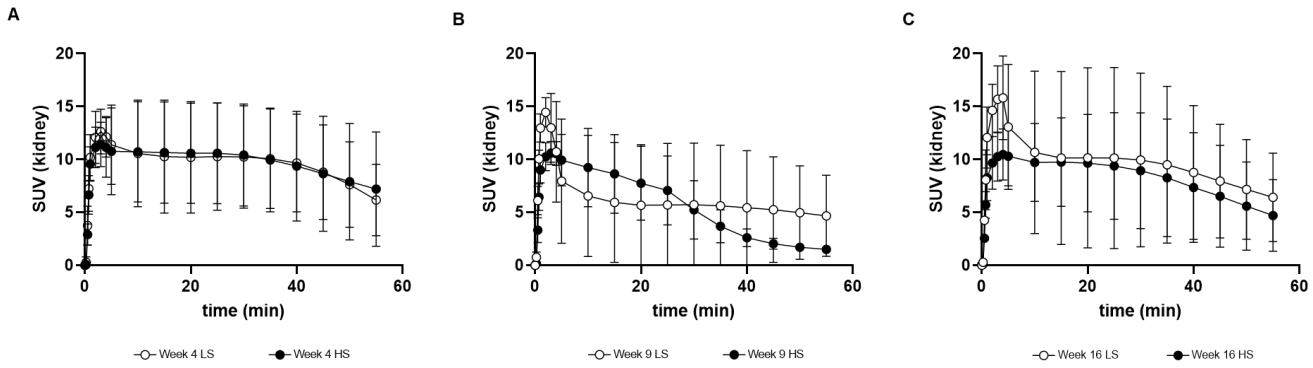

3.4.10. **Figure 7.** Kidney time-activity curves of DSS rats at (**A**) LS-4 and HS-4 (**B**) LS-9 and HS-9 (**C**) LS-16 and HS-16. LS-4, *n* = 5; HS-4, *n* = 8; LS-9, *n* = 4; HS-9, *n* = 4; LS-16, *n* = 7; HS-16, *n* = 4.

Imaging was performed again at HS-20, but no differences were observed in LV retention in comparison to HS-16 (data not shown). BP measurements revealed sustained systolic, diastolic, and MAP readings to HS-16 rats (data not shown). Animals were sacrificed one week later, and blood was collected via cardiac puncture. The heart and lungs were weighed. Hearts were perfused, flash-frozen, and stored at -80 °C for further analysis.

3.4.11. Table 4. Wet mass of heart and lungs

Organ	LS-20	HS-20
	Weight (g)	
Lung	1.53 ± 0.04	1.63 ± 0.11
Heart	1.28 ± 0.06	1.59 ± 0.09*
Kidney	2.61 ± 0.09	4.05 ± 0.44*
Lung/BW	3.65 ± 0.19	3.83 ± 0.18
Heart/BW	3.05 ± 0.21	3.75 ± 0.11*
Kidney/BW	6.27 ± 0.48	9.24 ± 0.52*
Animal bodyweight (kg)	0.42 ± 0.02	0.42 ± 0.03

*Statistical significance ($p < 0.05$) reached using an unpaired t-test. LS-20, $n = 6$; HS-20, $n = 5$; Kidney, $n = 3$/group

Due to variations in animal weight, organ mass was corrected for bodyweight. HS-20 rats had ~1.25-fold higher HW/BW ratio (3.83 ± 0.056 vs 3.07 ± 0.31 g/kg, $p = 0.0464$), and ~1.6 fold higher kidney/BW ratio (9.24 ± 0.52 vs 6.27 ± 0.48, $p = 0.0019$), whereas the lung/BW ratio was unchanged. The significantly higher heart/BW and kidney/BW coincident with systolic dysfunction (measured by echo) are suggestive towards the development of cardiac hypertrophy and kidney dysfunction, consistent with an HF phenotype, and in agreement with, previous reports using this animal model.[78]

Cardiac SNS imaging tracers have demonstrated good application in clinical trials for risk stratification and providing detailed molecular information that can be used as a parameter for sympathetic function. The development of an SNS radioligand capable of assessing sympathetic denervation along with changes in sympathetic tone is thus pivotal to the functional assessment of cardiovascular diseases. One major limitation in the evaluation of preclinical SNS radioligands is the absence of a NET-dependent fluorine-18 SNS radiotracer in small animals (rats, mice),

consequently hindering preclinical investigations in more widely available species. In our previous work, we demonstrated DMI and 6-hydroxydopamine-dependent [^{18}F]mFBG uptake in SD rats. However, the subcellular kinetics and washout mechanism of this tracer were not explored. In this study, we investigated the behavior of [^{18}F]mFBG following NET transport into the neuron using a variety of pharmacological inhibitors and demonstrated the application of [^{18}F]mFBG in imaging HF using DSS rats.

RSP is a commonly used VMAT2 inhibitor that has been used to explore the dependency of intravesicular storage using [^{11}C]HED and [^{123}I]mIBG.[27,39] Studies with RSP are typically conducted in higher species, but have been performed in isolated rat hearts with [^{11}C]epinephrine[79] and *in vivo* using [^{123}I]mIBG.[39] Due to selective non-neuronal uptake of [^{18}F]FBBG in rodents[31], RSP has only been used in cell-lines and isolated perfused rabbit hearts to provide evidence for dependency of vesicular storage on tracer retention.[30,80] The results from RSP pre-treatment demonstrated that [^{18}F]mFBG rapidly enters the neuron after injection, and is washed out of the neuron until 5 minutes, resulting in a maximal 35% reduction in uptake and A_0. As the contribution of NET-dependency of [^{18}F]mFBG is ~30-35%, these findings are consistent with a complete loss of radiotracer from the nerve terminal in the absence of storage granules. The resulting depletion of [^{18}F]mFBG in the neuron within 5 minutes in conjunction with the absent change in K_{mono} also further demonstrates the lack of [^{18}F]mFBG reuptake by NET following release from the presynaptic terminal, since [^{11}C]HED washout in reserpinized rats occurs for ~30 minutes.[27] Interestingly, [$^{123/131}$I]mIBG intravesicular accumulation appears to be a prolonged process, requiring 4 h to reach maximum vesicular retention.[39] [^{18}F]mFBG thus demonstrates more rapid entry into the vesicle, perhaps due to enhanced binding and transport via VMAT2. Attempts to increase the neuronal/vesicular clearance of [^{18}F]mFBG were performed by serial chase dosing

animals with TYR, 10 minutes after administering the tracer. Our results demonstrate an increase in [^{18}F]mFBG washout, inducing an ~2-fold increase in K_{mono} at the highest TYR dose (5 mg/kg). The unique ability of TYR to release catecholamines and presumably radiotracer from vesicles back into the axoplasm, and occupy MAO, are thought to drive amphetamine-like reverse transport by NET. Increased tracer washout following preloading of the myocardium with [^{18}F]mFBG further demonstrates the dependency of vesicular storage on tracer retention and implicates the physiological importance of evaluating K_{mono} as a relevant parameter for [^{18}F]mFBG myocardial efflux. The distinct target affinities of TYR for other receptors such as the trace amine associated receptor (TAAR) and post-synaptic receptors must be considered when drawing conclusions for this study.[81,82] However, the results obtained by Chen *et al.* demonstrating similarly increased neuronal washout of [^{18}F]AF78 following chase dosing support our findings.[50]

Due to the irreversible kinetics displayed by currently used SNS radiotracers, measurements of sympathetic tone are not feasible under baseline conditions. Based on our results, we hypothesize that [^{18}F]mFBG rapidly enters the presynaptic vesicle and is released back into the synapse over time via vesicular fusion with the presynaptic membrane. Pharmacological methods to alter the rate of vesicular release and action potential propagation using the presynaptic α_2R agonist DEX and antagonist YH demonstrated a remarkable 76% attenuation and 31% increase in tracer washout following chase dosing, respectively. The dependency of [^{18}F]mFBG washout on peripheral and/or central α_2 receptor modulation, and consequently on systemic sympathetic tone highlights the utility of measuring [^{18}F]mFBG washout as a function sympathetic drive. Alterations in tracer washout are therefore unlikely to be attributed to diffusion and are rather influenced by changes in neurohormonal signaling. Moreover, the expected changes in plasma NE spillover following administration of TYR, DEX, and YH are consistent with the observed attenuation or

acceleration in K_{mono}.[62,64,83–85] Furthermore, Grkovski *et al* performed the absolute quantification of myocardial time-activity curves in humans by reversible Logan graphical analyses, and noted significantly slower [^{18}F]mFBG efflux in the myocardium over 4 h (5.1 ± 2.2 to 3.4 ± 1.0 SUV) in comparison to the relatively rapid washout of [^{18}F]mFBG observed in mouse and rat imaging showed in this study.[35] [^{18}F]mFBG washout may therefore be altered in diseases that affect myocardial SNS tone such as in obstructive sleep apnea, obesity, hypertension, HF, and arrhythmias, necessitating its quantification as a valuable preclinical and clinical metric for assessing disease severity.[86]

Cardiac imaging with [^{18}F]mFBG was conducted in DSS rats to evaluate its preclinical utility in detecting HF. The results depicted an age-dependent increase in the SUV and A_0 in the LV by ~50% in 9-week-old to 21-week-old LS rats, concomitant with ~25% increase in blood activity, 33% increase in peak kidney retention, and a ~30% reduction in K_{mono} in comparison to 4-week-old LS rats. Age-related changes in SUV were observed to stabilize in 9-week-old rats and onward. The associated increase in myocardial extraction may be attributed to increased expression of NET and/or extraneural transporters, increased myocardial tissue permeability, increased plasma free fraction of tracer, and lower NE concentrations resulting in reduced competition with substrate influx by NET. Rats switched to HS diet displayed significant differences in comparison to those kept on LS diet. Results obtained from non-invasive BP monitoring depicted maximal increases in systolic, diastolic, and MAP, whereas diastolic dysfunction and reduced cardiac output were observed by echocardiography in HS-16 rats, concomitant with ~32% reduction in myocardial activity when compared to LS-16 rats. In addition, reduced renal uptake of [^{18}F]mFBG was observed by PET imaging, consistent with reports of renal tubular damage, inflammation, and interstitial fibrosis.[87,88] Cardiac hypertrophy was evident with an observed ~20% increase in

LV/BW ratio in HS-16 rats, with no evidence of pulmonary edema, consistent with the development of an early stage HF phenotype in this animal model.[78] Reduced LV uptake in HS-16 rats is consistent with the observed reduction in cardiac function and suggests cardiac sympathetic denervation or downregulated/dysfunctional NET to be the main contributor of this observation. These results are consistent with other assessments of [^{3}H]NE tissue uptake in hearts[89] and [^{131}I]mIBG heart uptake in DSS rats fed HS diet.[90]

3.5. Conclusion

In this study, [^{18}F]mFBG intraneuronal mechanisms were investigated, and DSS rats were used to evaluate the feasibility of imaging HF using this tracer. VMAT2 inhibition displayed marked decrease in [^{18}F]mFBG neuronal uptake, implicating intact storage granules as a necessity for neuronal retention. TYR chase dosing further supported this finding and caused increased tracer washout over the duration of the scan. Changes in sympathetic tone were assessed using the α_2 agonist DEX and antagonist YH to significantly reduce or accelerate cardiac neuronal washout. DSS rat imaging with [^{18}F]mFBG displayed ~32% reduction in myocardial uptake in rats kept on HS diet for 16 weeks in comparison to respective controls, concomitant with impaired cardiac function, elevated systolic, diastolic, and MAP, LV hypertrophy, and impaired [^{18}F]mFBG renal uptake. Cardiac PET imaging using [^{18}F]mFBG therefore demonstrates sensitivity in measuring changes in sympathetic function in an animal model for HF. This work represents the first reversible neurohumoral PET tracer showing sensitivity in preclinical disease models, and enables the use of [^{18}F]mFBG imaging for large scale animal studies to evaluate SNS function in disease.

3.6. Materials and Methods

Automated Radiosynthesis. The radiosynthesis of [^{18}F]mFBG was performed as previously described. [^{18}F]fluoride (10-11 Gbq) was trapped from a [^{18}O]H_2O target solution onto a Sep-pak Accel Plus QMA Plus Light cartridge (equilibrated with 10 mL EtOH, 10 mL H_2O, 10 mL of 0.1 M $NaHCO_3$, and 10 mL H_2O) and eluted into the reactor. 1 mL of acetronitrile was added to the reactor and heated to 80 °C for 5 min followed by 120 °C for 3 min under a nitrogen stream to yield dried [^{18}F]TEAF. The reactor was cooled to 40 °C using compressed air prior to the addition of a solution of precursor (12 mg) in DMSO (0.6 mL). Radiofluorination was performed by heating the reactor to 120 °C for 10 min and subsequently cooled to 50 °C. 12M HCl (0.6 mL) was then added to the reactor to facilitate Boc-deprotection at 120 °C for 5 min. The reactor was cooled with compressed air and quenched with a mixture of 30/70 mixture of acetonitrile: water. The crude reaction was purified by reversed-phase prep-HPLC (Phenomenex Luna 10 µm C18(2), 250 × 10 mm column, 15/75 ACN/H_2O + 0.1% TFA, flow rate of 5 mL/min). The product was collected from 12-15 min into a bulk vessel containing 40 mL of sterile water. The solution was passed through a carboxy-methyl (CM) ion exchange cartridge at a flow rate of 2.0-2.5 mL/min and rinsed with 10 mL of H_2O. [^{18}F]mFBG was eluted from the cartridge using 4-4.5 mL of physiological saline and passed through an Sep-Pak Alumina N Plus Light cartridge (equilibrated with 10 mL of H_2O) followed by a sterile filter into a crimped vial fitted with a vent needle. RCY was determined by correcting the quantity of initial activity to the end of synthesis (EoS). Molar activity was determined using UV absorbance of a known amount of radioactivity under identical HPLC conditions used to generate a calibration curve for the nonradioactive standard. The ratio of

radioactivity (GBq) to moles (μmol) yielded molar activity (GBq/μmol), the value was decay-corrected to EoS.

Animal care. Male SD rats (80-110 g) and DSS rats (100-110 g) were purchased from Charles River Laboratories (Senneville, Quebec) and housed in environmentally enriched cages with free access to water and food. Housing, handling, and experimental procedures were performed in strict accordance with the guidelines of the Canadian Council on Animal Care and with the approval of the University of Ottawa Animal Care Committee. SD rats used in this study were 5-6 weeks old. DSS rats used in this study were 4-21 weeks old.

PET Imaging. SD rats (4-6 weeks old, 100-200 g) were anesthetized with 2% isoflurane and placed in the PET scanner. Following a ten-minute transmission scan, animals were injected with [^{18}F]mFBG as a bolus over 30 s via the lateral tail vein and kept on isoflurane for the duration of the imaging protocol. Dynamic PET imaging was performed for 60 min (4 × 15 s frames; 4 × 1 min frames; 10 × 5 min frames) using a Siemens DPET scanner. DSS rats (4 – 20 weeks old, 110-450 g) were imaged using a Bruker SI78 PET-CT scanner, and attenuation correction was performed by CT acquisition prior to initiation of a PET scan. The collected emission data from the Siemens DPET scanner were corrected for attenuation and scatter and reconstructed using the 3-dimensional ordered subsets expectation maximization/maximum a posteriori (3D-OSEM/MAP) algorithm. Emission data obtained from the Bruker SI78 PET/CT was reconstructed using maximum-likelihood expectation-maximization (MLEM) algorithm. For data obtained from imaging SD rats, volumes of interest (VOI) were drawn for the LV and cardiac blood pool using Flowquant. Blood pool time-activity curves were generated using mean values of three ROI samples located in the LV cavity, LV base, and left atrium. Imaging data obtained from the Bruker SI-78 PET-CT scanner for DSS rats were analyzed using PMOD. LV TACs were generated by

using the 3D masking tool and masking all liver activity. Several masking iterations are performed to ensure adequate removal of liver spillover on the LV wall. ROIs of the LV were then generated by 3D-isocountour. Kidney TACs were generated by 3D-isocountour, and blood-activity was estimated by drawing a VOI in the LV cavity. Uptake values from the Siemens DPET scanner were obtained in nCi/cc, whereas data from the Bruker SI78 PET/CT were obtained in kBq/cc. The data was converted to SUV using the total injected dose and animal bodyweight, as shown in the time-activity curves

Pharmacological blocking studies. Male SD and DSS rats were anesthetized using 2% isoflurane and received lateral tail vein injections of 4-18 MBq of [^{18}F]mFBG in 0.1-0.4 mL of sterile saline (0.9% sodium chloride). VMAT2 inhibition was performed by administering RSP (4 mg/kg, ip) 4 hours prior to administering [^{18}F]mFBG and initiating a PET scan. Extraneuronal blockade was performed by pretreating animals with CTC (20 mg/kg, ip) 45-minutes prior to initiating a scan or 10 minutes (iv, 5 mg/kg) prior to initiating PET. Chase dosing with TYR (5 mg/kg, 5x) was administered 10 minutes after initiating [^{18}F]mFBG imaging and re-administered every 10 minutes up to 50 minutes (5 total injections). Chase dosing with α_2R ligands YH (1 mg/kg) and DEX (2.5 µg/kg) was performed 10 minutes after initiating a [^{18}F]mFBG scan. Baseline and blockade studies performed in C57/BL6 mice were performed by either pre-treating animals with saline, DMI (1 mg/kg), or PBZ (25 mg/kg) 10 minutes prior to initiating a scan. Formulations for each pharmaceutical are as follows: RSP (10% acetic acid in sterile H_2O, pH adjusted to 5.5-6 with Na_2CO_3), TYR (10% DMSO in saline), DEX (0.9% saline), YH (sterile H_2O), CTC (40% PEG400, 15% DMSO, 35% sterile H_2O), DMI (0.9% saline), PBZ (0.9% saline).

Echocardiography. Echocardiographic images were acquired using the Vevo 3100 high-frequency small animal ultrasound system (FUJIFILM VisualSonics, Toronto, Canada), using the

MX250 linear array transducer. Rats were anesthetized with 1.0-1.5% isoflurane with 1.5 l/min 100% oxygen and images of the LV were taken before administration of HS diet, and 4, 9, and 16 weeks after initiating HS diet] using parasternal long axis (PLAX) view in B-mode. PLAX B-mode images were analyzed in a dedicated quantification software (Vevo LAB version 5.6.1), where tracings of the endocardium at end-diastole and end-systole were manually completed using Vevo LAB's operator defined LV trace function.

Non-invasive blood pressure. Animals were anesthetized with 2% isoflurane and placed in a prone position on a heated plate. Blood pressure was acquired using a non-invasive IITC Life Science MRBP rat blood pressure tail cuff. Three independent measurements were taken for one animal and averaged to obtain a mean value. Mean values for each animal were then combined to obtain average ± standard deviation for each cohort.

Tissue collection. Animals were anesthetized with 2% isoflurane and placed supine on a heated plate. The heart, lung, and kidney were excised and weighed. Hearts were perfused with 10 mM PBS and immediately flash frozen and stored at -80 °C for further analysis. The organ weight for each animal was corrected for animal bodyweight by taking the ratio of g (tissue weight)/kg (animal weight).

Statistical analysis. Statistical analysis was performed using GraphPad Prism 9.0.0. Significance was set at 0.05. The data are presented as mean ± standard deviation. Differences between two groups were determined using a two-tailed unpaired Student's t-test. Differences between three or more groups were tested using one-way ANOVA.

3.7. References

(1) Goldberger, J. J.; Arora, R.; Buckley, U.; Shivkumar, K. Autonomic Nervous System Dysfunction. *J. Am. Coll. Cardiol.* **2019**, *73* (10), 1189–1206. https://doi.org/10.1016/j.jacc.2018.12.064.

(2) Burnstock, G. Autonomic Neurotransmission: 60 Years Since Sir Henry Dale. *Annu. Rev. Pharmacol. Toxicol.* **2009**, *49* (1), 1–30. https://doi.org/10.1146/annurev.pharmtox.052808.102215.

(3) Gabella, G. Autonomic Nervous System. In *eLS*; John Wiley & Sons, Ltd, 2001. https://doi.org/10.1038/npg.els.0000081.

(4) Low, P. A. Autonomic Nervous System Function. *J. Clin. Neurophysiol.* **1993**, *10* (1), 14–27.

(5) Graham, L. N.; Smith, P. A.; Huggett, R. J.; Stoker, J. B.; Mackintosh, A. F.; Mary, D. A. S. G. Sympathetic Drive in Anterior and Inferior Uncomplicated Acute Myocardial Infarction. *Circulation* **2004**, *109* (19), 2285–2289. https://doi.org/10.1161/01.CIR.0000129252.96341.8B.

(6) Zhang, D. Y.; Anderson, A. S. The Sympathetic Nervous System and Heart Failure. *Cardiol. Clin.* **2014**, *32* (1), 33–vii. https://doi.org/10.1016/j.ccl.2013.09.010.

(7) Borovac, J. A.; D'Amario, D.; Bozic, J.; Glavas, D. Sympathetic Nervous System Activation and Heart Failure: Current State of Evidence and the Pathophysiology in the Light of Novel Biomarkers. *World J. Cardiol.* **2020**, *12* (8), 373–408. https://doi.org/10.4330/wjc.v12.i8.373.

(8) Schwinger, R. H. G. Pathophysiology of Heart Failure. *Cardiovasc. Diagn. Ther.* **2021**, *11* (1), 26376–26276. https://doi.org/10.21037/cdt-20-302.

(9) Van Linthout, S.; Tschöpe, C. Inflammation – Cause or Consequence of Heart Failure or Both? *Curr. Heart Fail. Rep.* **2017**, *14* (4), 251–265. https://doi.org/10.1007/s11897-017-0337-9.

(10) Lymperopoulos, A.; Rengo, G.; Koch, W. J. The Adrenergic Nervous System in Heart Failure: Pathophysiology and Therapy. *Circ. Res.* **2013**, *113* (6). https://doi.org/10.1161/CIRCRESAHA.113.300308.

(11) White, I. A. Cardiac Sympathetic Denervation in the Failing Heart. *Circ. Res.* **2016**, *118* (8), 1189–1191. https://doi.org/10.1161/CIRCRESAHA.116.308621.

(12) Floras, J. S.; Ponikowski, P. The Sympathetic/Parasympathetic Imbalance in Heart Failure with Reduced Ejection Fraction. *Eur. Heart J.* **2015**, *36* (30), 1974–1982. https://doi.org/10.1093/eurheartj/ehv087.

(13) Xiao, Y.-F. Cardiac Arrhythmia and Heart Failure: From Bench to Bedside. *J. Geriatr. Cardiol.* **2011**, *8* (3), 131–132. https://doi.org/10.3724/SP.J.1263.2011.00131.

(14) Wu, P.; Vaseghi, M. The Autonomic Nervous System and Ventricular Arrhythmias in Myocardial Infarction and Heart Failure. *Pacing Clin. Electrophysiol. PACE* **2020**, *43* (2), 172–180. https://doi.org/10.1111/pace.13856.

(15) Bernstein, D.; Fajardo, G.; Zhao, M. THE ROLE OF β-ADRENERGIC RECEPTORS IN HEART FAILURE: DIFFERENTIAL REGULATION OF CARDIOTOXICITY AND CARDIOPROTECTION. *Prog. Pediatr. Cardiol.* **2011**, *31* (1), 35–38. https://doi.org/10.1016/j.ppedcard.2010.11.007.

(16) Lohse, M. J.; Engelhardt, S.; Eschenhagen, T. What Is the Role of β-Adrenergic Signaling in Heart Failure? *Circ. Res.* **2003**, *93* (10), 896–906. https://doi.org/10.1161/01.RES.0000102042.83024.CA.

(17) Kreusser, M. M.; Lehmann, L. H.; Haass, M.; Buss, S. J.; Katus, H. A.; Lossnitzer, D. Depletion of Cardiac Catecholamine Stores Impairs Cardiac Norepinephrine Re-Uptake by Downregulation of the Norepinephrine Transporter. *PLOS ONE* **2017**, *12* (3), e0172070. https://doi.org/10.1371/journal.pone.0172070.

(18) Chen, X.; Kudo, T.; Lapa, C.; Buck, A.; Higuchi, T. Recent Advances in Radiotracers Targeting Norepinephrine Transporter: Structural Development and Radiolabeling Improvements. *J. Neural Transm.* **2020**, *127* (6), 851–873. https://doi.org/10.1007/s00702-020-02180-4.

(19) Jacobson, A. F.; Senior, R.; Cerqueira, M. D.; Wong, N. D.; Thomas, G. S.; Lopez, V. A.; Agostini, D.; Weiland, F.; Chandna, H.; Narula, J.; ADMIRE-HF Investigators. Myocardial Iodine-123 Meta-Iodobenzylguanidine Imaging and Cardiac Events in Heart Failure. Results of the Prospective ADMIRE-HF (AdreView Myocardial Imaging for Risk Evaluation in Heart Failure) Study. *J. Am. Coll. Cardiol.* **2010**, *55* (20), 2212–2221. https://doi.org/10.1016/j.jacc.2010.01.014.

(20) Jeong, Y. J.; Jeong, J.-E.; Cheon, S.-M.; Yoon, B.-A.; Kim, J. W.; Kang, D.-Y. Relationship between the Washout Rate of I-123 MIBG Scans and Autonomic Function in Parkinson's Disease. *PLOS ONE* **2020**, *15* (3), e0229860. https://doi.org/10.1371/journal.pone.0229860.

(21) Joers, V.; Emborg, M. E. Modeling and Imaging Cardiac Sympathetic Neurodegeneration in Parkinson's Disease. *Am. J. Nucl. Med. Mol. Imaging* **2014**, *4* (2), 125–159.

(22) Langer, O.; Halldin, C. PET and SPET Tracers for Mapping the Cardiac Nervous System. *Eur. J. Nucl. Med. Mol. Imaging* **2002**, *29* (3), 416–434. https://doi.org/10.1007/s002590100640.

(23) Fallavollita, J. A.; Heavey, B. M.; Luisi, A. J.; Michalek, S. M.; Baldwa, S.; Mashtare, T. L.; Hutson, A. D.; Dekemp, R. A.; Haka, M. S.; Sajjad, M.; Cimato, T. R.; Curtis, A. B.; Cain, M. E.; Canty, J. M. Regional Myocardial Sympathetic Denervation Predicts the Risk of Sudden Cardiac Arrest in Ischemic Cardiomyopathy. *J. Am. Coll. Cardiol.* **2014**, *63* (2), 141–149. https://doi.org/10.1016/j.jacc.2013.07.096.

(24) Zelt, J. G. E.; Britt, D.; Mair, B. A.; Rotstein, B. H.; Quigley, S.; Walter, O.; Garrard, L.; Robinson, S.; Mielniczuk, L. M.; deKemp, R. A.; Beanlands, R. S. Regional Distribution of Fluorine-18-Flubrobenguane and Carbon-11-Hydroxyephedrine for Cardiac PET Imaging of Sympathetic Innervation. *JACC Cardiovasc. Imaging* **2020**. https://doi.org/10.1016/j.jcmg.2020.09.026.

(25) Raffel David M.; Jung Yong-Woon; Koeppe Robert A.; Jang Keun Sam; Gu Guie; Scott Peter J.H.; Murthy Venkatesh L.; Rothley Jill; Frey Kirk A. First-in-Human Studies of [18F] Fluorohydroxyphenethylguanidines. *Circ. Cardiovasc. Imaging* **2018**, *11* (12), e007965. https://doi.org/10.1161/CIRCIMAGING.118.007965.

(26) Werner, R. A.; Rischpler, C.; Onthank, D.; Lapa, C.; Robinson, S.; Samnick, S.; Javadi, M.; Schwaiger, M.; Nekolla, S. G.; Higuchi, T. Retention Kinetics of the 18F-Labeled Sympathetic Nerve PET Tracer LMI1195: Comparison with 11C-Hydroxyephedrine and 123I-MIBG. *J. Nucl. Med. Off. Publ. Soc. Nucl. Med.* **2015**, *56* (9), 1429–1433. https://doi.org/10.2967/jnumed.115.158493.

(27) Nomura, Y.; Matsunari, I.; Takamatsu, H.; Murakami, Y.; Matsuya, T.; Taki, J.; Nakajima, K.; Nekolla, S. G.; Chen, W.-P.; Kajinami, K. Quantitation of Cardiac Sympathetic Innervation in Rabbits Using 11C-Hydroxyephedrine PET: Relation to 123I-MIBG Uptake. *Eur. J. Nucl. Med. Mol. Imaging* **2006**, *33* (8), 871–878. https://doi.org/10.1007/s00259-006-0105-7.

(28) Harms, H. J.; de Haan, S.; Knaapen, P.; Allaart, C. P.; Rijnierse, M. T.; Schuit, R. C.; Windhorst, A. D.; Lammertsma, A. A.; Huisman, M. C.; Lubberink, M. Quantification of [11C]-Meta-Hydroxyephedrine Uptake in Human Myocardium. *EJNMMI Res.* **2014**, *4* (1), 52. https://doi.org/10.1186/s13550-014-0052-4.

(29) Jung, Y.-W.; Jang, K. S.; Gu, G.; Koeppe, R. A.; Sherman, P. S.; Quesada, C. A.; Raffel, D. M. [18F]Fluoro-Hydroxyphenethylguanidines: Efficient Synthesis and Comparison of Two Structural Isomers as Radiotracers of Cardiac Sympathetic Innervation. *ACS Chem. Neurosci.* **2017**, *8* (7), 1530–1542. https://doi.org/10.1021/acschemneuro.7b00051.

(30) Chen, X.; Werner, R. A.; Lapa, C.; Nose, N.; Hirano, M.; Javadi, M. S.; Robinson, S.; Higuchi, T. Subcellular Storage and Release Mode of the Novel 18F-Labeled Sympathetic Nerve PET Tracer LMI1195. *EJNMMI Res.* **2018**, *8* (1), 12. https://doi.org/10.1186/s13550-018-0365-9.

(31) Mu, L.; Krämer, S. D.; Warnock, G. I.; Haider, A.; Bengs, S.; Cartolano, G.; Bräm, D. S.; Keller, C.; Schibli, R.; Ametamey, S. M.; Kaufmann, P. A.; Gebhard, C. [11C]MHED PET Follows a Two-Tissue Compartment Model in Mouse Myocardium with Norepinephrine Transporter (NET)-Dependent Uptake, While [18F]LMI1195 Uptake Is NET-Independent. *EJNMMI Res.* **2020**, *10* (1), 114. https://doi.org/10.1186/s13550-020-00700-7.

(32) Ismailani, U. S.; Buchler, A.; Farber, G.; Pekošak, A.; Farber, E.; MacMullin, N.; Suuronen, E. J.; Vasdev, N.; Beanlands, R. S. B.; de Kemp, R. A.; Rotstein, B. H. Cardiac Sympathetic Positron Emission Tomography Imaging with Meta-[18F]Fluorobenzylguanidine Is Sensitive to Uptake-1 in Rats. *ACS Chem. Neurosci.* **2021**. https://doi.org/10.1021/acschemneuro.1c00575.

(33) Verschure, D. O.; Nakajima, K.; Verberne, H. J. Cardiac 123I-MIBG Imaging in Heart Failure. *Pharmaceuticals* **2022**, *15* (6), 656. https://doi.org/10.3390/ph15060656.

(34) Takatsu, H.; Noda, T.; Arai, M.; Kunishima, A.; Inoue, M.; Tazawa, S.; Kurosawa, H.; Nishigaki, K.; Fujiwara, H. Washout of I-123 Meta-Iodobenzylguanidine for Assessing Cardiac Sympathetic Activity with Progression of Hypertension in Dahl Salt-Sensitive Rats. *J. Nucl. Cardiol.* **1999**, *6* (2), 204–210. https://doi.org/10.1016/S1071-3581(99)90081-8.

(35) Grkovski, M.; Zanzonico, P. B.; Modak, S.; Humm, J. L.; Narula, J.; Pandit-Taskar, N. F-18 Meta-Fluorobenzylguanidine PET Imaging of Myocardial Sympathetic Innervation. *J. Nucl. Cardiol.* **2022**. https://doi.org/10.1007/s12350-021-02813-5.

(36) Paton, D. M.; Golko, D. S. Effect of Reserpine on the Structure–Activity Relationships for the Inhibition of Noradrenaline Uptake in Adrenergic Nerves in Rat and Rabbit Ventricle by Phenethylamines. *Can. J. Physiol. Pharmacol.* **1977**, *55* (2), 196–205. https://doi.org/10.1139/y77-029.

(37) Iversen, L. L.; Glowinski, J.; Axelrod, J. The Uptake and Storage of H3-Norepinephrine in the Reserpine-Pretreated Rat Heart. *J. Pharmacol. Exp. Ther.* **1965**, *150* (2), 173–183.

(38) Shore, P. A. C. the Mechanism of Norepinephrine Depletion by Reserpine, Metaraminol and Related Agents. the Role of Monoamine Oxidase. *Pharmacol. Rev.* **1966**, *18* (1), 561–568.

(39) Nakajo, M.; Shimabukuro, K.; Yoshimura, H.; Yonekura, R.; Nakabeppu, Y.; Tanoue, P.; Shinohara, S. Iodine-131 Metaiodobenzylguanidine Intra- and Extravesicular Accumulation in the Rat Heart. *J. Nucl. Med.* **1986**, *27* (1), 84–89.

(40) Mangner, T. J.; Tobes, M. C.; Wieland, D. W.; Sisson, J. C.; Shapiro, B. Metabolism of Iodine-131 Metaiodobenzylguanidine in Patients with Metastatic Pheochromocytoma. *J. Nucl. Med. Off. Publ. Soc. Nucl. Med.* **1986**, *27* (1), 37–44.

(41) Bhagat, B. Amphetamine and Stores of Noradrenaline. *J. Pharm. Pharmacol.* **1965**, *17* (3), 191–192. https://doi.org/10.1111/j.2042-7158.1965.tb07644.x.

(42) Brodie, B. B.; Costa, E.; Groppetti, A.; Matsumoto, C. Interaction between Desipramine, Tyramine, and Amphetamine at Adrenergic Neurones. *Br. J. Pharmacol.* **1968**, *34* (3), 648–658. https://doi.org/10.1111/j.1476-5381.1968.tb08494.x.

(43) Burn, J. H.; Rand, M. J. The Action of Sympathomimetic Amines in Animals Treated with Reserpine. *J. Physiol.* **1958**, *144* (2), 314–336.

(44) Lockett, M. F.; Eakins, K. E. Chromatographic Studies of the Effect of Intravenous Injections of Tyramine on the Concentrations of Adrenaline and Noradrenaline in Plasma. *J. Pharm. Pharmacol.* **1960**, *12* (1), 513–517. https://doi.org/10.1111/j.2042-7158.1960.tb12702.x.

(45) Hertting, G.; Axelrod, J.; Patrick, R. W. Actions of Cocaine and Tyramine on the Uptake and Release of H3-Norepinephrine in the Heart. *Biochem. Pharmacol.* **1961**, *8* (2), 246–248. https://doi.org/10.1016/0006-2952(61)90009-0.

(46) Axelrod, J.; Gordon, E.; Hertting, G.; Kopin, I. J.; Potter, L. T. On the Mechanism of Tachyphylaxis to Tyramine in the Isolated Rat Heart. *Br. J. Pharmacol. Chemother.* **1962**, *19*, 56–63. https://doi.org/10.1111/j.1476-5381.1962.tb01426.x.

(47) Schümann, H. J.; Phiuppu, A. The Mechanism of Catecholamine Release by Tyramine. *Int. J. Neuropharmacol.* **1962**, *1* (1), 179–182. https://doi.org/10.1016/0028-3908(62)90030-8.

(48) Robertson, S. D.; Matthies, H. J.; Galli, A. A Closer Look at Amphetamine Induced Reverse Transport and Trafficking of the Dopamine and Norepinephrine Transporters. *Mol. Neurobiol.* **2009**, *39* (2), 73–80. https://doi.org/10.1007/s12035-009-8053-4.

(49) Sitte, H. H.; Huck, S.; Reither, H.; Boehm, S.; Singer, E. A.; Pifl, C. Carrier-Mediated Release, Transport Rates, and Charge Transfer Induced by Amphetamine, Tyramine, and Dopamine in Mammalian Cells Transfected with the Human Dopamine Transporter. *J. Neurochem.* **1998**, *71* (3), 1289–1297. https://doi.org/10.1046/j.1471-4159.1998.71031289.x.

(50) Chen, X.; Werner, R. A.; Koshino, K.; Nose, N.; Mühlig, S.; Rowe, S. P.; Pomper, M. G.; Lapa, C.; Decker, M.; Higuchi, T. Molecular Imaging-Derived Biomarker of Cardiac Nerve Integrity — Introducing High NET Affinity PET Probe ^{18}F-AF78. *Theranostics* **2022**, *12* (9), 4446–4458. https://doi.org/10.7150/thno.63205.

(51) Giovannitti, J. A.; Thoms, S. M.; Crawford, J. J. Alpha-2 Adrenergic Receptor Agonists: A Review of Current Clinical Applications. *Anesth. Prog.* **2015**, *62* (1), 31–38. https://doi.org/10.2344/0003-3006-62.1.31.

(52) Gertler, R.; Brown, H. C.; Mitchell, D. H.; Silvius, E. N. Dexmedetomidine: A Novel Sedative-Analgesic Agent. *Proc. Bayl. Univ. Med. Cent.* **2001**, *14* (1), 13–21.

(53) Bloor, B. C.; Ward, D. S.; Belleville, J. P.; Maze, M. Effects of Intravenous Dexmedetomidine in Humans: II. Hemodynamic Changes. *Anesthesiology* **1992**, *77* (6), 1134–1142. https://doi.org/10.1097/00000542-199212000-00014.

(54) Kallio, A.; Scheinin, M.; Koulu, M.; Ponkilainen, R.; Ruskoaho, H.; Viinamäki, O.; Scheinin, H. Effects of Dexmedetomidine, a Selective A2-Adrenoceptor Agonist, on Hemodynamic Control Mechanisms. *Clin. Pharmacol. Ther.* **1989**, *46* (1), 33–42. https://doi.org/10.1038/clpt.1989.103.

(55) Hammer, G. B.; Drover, D. R.; Cao, H.; Jackson, E.; Williams, G. D.; Ramamoorthy, C.; Van Hare, G. F.; Niksch, A.; Dubin, A. M. The Effects of Dexmedetomidine on Cardiac Electrophysiology in Children. *Anesth. Analg.* **2008**, *106* (1), 79–83. https://doi.org/10.1213/01.ane.0000297421.92857.4e.

(56) Hogue, C. W.; Talke, P.; Stein, P. K.; Richardson, C.; Domitrovich, P. P.; Sessler, D. I. Autonomic Nervous System Responses during Sedative Infusions of Dexmedetomidine. *Anesthesiology* **2002**, *97* (3), 592–598. https://doi.org/10.1097/00000542-200209000-00012.

(57) Kaur, M.; Singh, P. M. Current Role of Dexmedetomidine in Clinical Anesthesia and Intensive Care. *Anesth. Essays Res.* **2011**, *5* (2), 128–133. https://doi.org/10.4103/0259-1162.94750.

(58) Housmans, P. R. Effects of Dexmedetomidine on Contractility, Relaxation, and Intracellular Calcium Transients of Isolated Ventricular Myocardium. *Anesthesiology* **1990**, *73* (5), 919–922. https://doi.org/10.1097/00000542-199011000-00020.

(59) Nahimi, A.; Jakobsen, S.; Munk, O. L.; Vang, K.; Phan, J. A.; Rodell, A.; Gjedde, A. Mapping A2 Adrenoceptors of the Human Brain with 11C-Yohimbine. *J. Nucl. Med.* **2015**, *56* (3), 392–398. https://doi.org/10.2967/jnumed.114.145565.

(60) Tank, J.; Heusser, K.; Diedrich, A.; Brychta, R. J.; Luft, F. C.; Jordan, J. Yohimbine Attenuates Baroreflex-Mediated Bradycardia in Humans. *Hypertension* **2007**, *50* (5), 899–903. https://doi.org/10.1161/HYPERTENSIONAHA.107.095984.

(61) Wang, Y.; Yu, X.; Wang, F.; Wang, Y.; Wang, Y.; Li, H.; Lv, X.; Lu, D.; Wang, H. Yohimbine Promotes Cardiac NE Release and Prevents LPS-Induced Cardiac Dysfunction via Blockade of Presynaptic A2A-Adrenergic Receptor. *PLOS ONE* **2013**, *8* (5), e63622. https://doi.org/10.1371/journal.pone.0063622.

(62) Grossman, E.; Rea, R. F.; Hoffman, A.; Goldstein, D. S. Yohimbine Increases Sympathetic Nerve Activity and Norepinephrine Spillover in Normal Volunteers. *Am. J. Physiol.-Regul. Integr. Comp. Physiol.* **1991**, *260* (1), R142–R147. https://doi.org/10.1152/ajpregu.1991.260.1.R142.

(63) Biaggioni, I.; Robertson, R. M.; Robertson, D. Manipulation of Norepinephrine Metabolism with Yohimbine in the Treatment of Autonomic Failure. *J. Clin. Pharmacol.* **1994**, *34* (5), 418–423. https://doi.org/10.1002/j.1552-4604.1994.tb04981.x.

(64) Goldberg, M. R.; Hollister, A. S.; Robertson, D. Influence of Yohimbine on Blood Pressure, Autonomic Reflexes, and Plasma Catecholamines in Humans. *Hypertension* **1983**, *5* (5), 772–778. https://doi.org/10.1161/01.HYP.5.5.772.

(65) Wekstein, D. R. Heart Rate of the Preweanling Rat and Its Autonomic Control. *Am. J. Physiol.-Leg. Content* **1965**, *208* (6), 1259–1262. https://doi.org/10.1152/ajplegacy.1965.208.6.1259.

(66) Janssen, P. M. L.; Biesiadecki, B. J.; Ziolo, M. T.; Davis, J. P. The Need for Speed; Mice, Men, and Myocardial Kinetic Reserve. *Circ. Res.* **2016**, *119* (3), 418–421. https://doi.org/10.1161/CIRCRESAHA.116.309126.

(67) Rowan, W. H.; Campen, M. J.; Wichers, L. B.; Watkinson, W. P. Heart Rate Variability in Rodents: Uses and Caveats in Toxicological Studies. *Cardiovasc. Toxicol.* **2007**, *7* (1), 28–51. https://doi.org/10.1007/s12012-007-0004-6.

(68) Lakin, R.; Guzman, C.; Izaddoustdar, F.; Polidovitch, N.; Goodman, J. M.; Backx, P. H. Changes in Heart Rate and Its Regulation by the Autonomic Nervous System Do Not Differ Between Forced and Voluntary Exercise in Mice. *Front. Physiol.* **2018**, *9*.

(69) Milani-Nejad, N.; Janssen, P. M. L. Small and Large Animal Models in Cardiac Contraction Research: Advantages and Disadvantages. *Pharmacol. Ther.* **2014**, *141* (3), 235–249. https://doi.org/10.1016/j.pharmthera.2013.10.007.

(70) Swoap, S. J.; Li, C.; Wess, J.; Parsons, A. D.; Williams, T. D.; Overton, J. M. Vagal Tone Dominates Autonomic Control of Mouse Heart Rate at Thermoneutrality. *Am. J. Physiol.-Heart Circ. Physiol.* **2008**, *294* (4), H1581–H1588. https://doi.org/10.1152/ajpheart.01000.2007.

(71) Martel, F.; Ribeiro, L.; Calhau, C.; Azevedo, I. Comparison between Uptake2 and ROCT1: Effects of Catecholamines, Metanephrines and Corticosterone. *Naunyn. Schmiedebergs Arch. Pharmacol.* **1999**, *359* (4), 303–309. https://doi.org/10.1007/PL00005356.

(72) Inhibition of Noradrenaline Uptake2 in the Isolated Rat Heart by Steroids, Clonidine and Methoxylated Phenylethylamines. *Eur. J. Pharmacol.* **1972**, *20* (3), 329–340. https://doi.org/10.1016/0014-2999(72)90194-X.

(73) Ohshima, Y.; Sasaki, I.; Watanabe, S.; Sakashita, T.; Higashi, T.; Ishioka, N. S. Organic Cation Transporter 3 Mediates the Non-Norepinephrine Transporter Driven Uptake of Meta-[211At]Astato-Benzylguanidine. *Nucl. Med. Biol.* **2022**, *112–113*, 44–51. https://doi.org/10.1016/j.nucmedbio.2022.06.005.

(74) Dahl, L. K.; Heine, M.; Tassinari, L. EFFECTS OF CHRONIC EXCESS SALT INGESTION : EVIDENCE THAT GENETIC FACTORS PLAY AN IMPORTANT ROLE

IN SUSCEPTIBILITY TO EXPERIMENTAL HYPERTENSION. *J. Exp. Med.* **1962**, *115* (6), 1173–1190. https://doi.org/10.1084/jem.115.6.1173.

(75) Dahl, L. K.; Heine, M.; Tassinari, L. Role of Genetic Factors in Susceptibility to Experimental Hypertension Due to Chronic Excess Salt Ingestion. *Nature* **1962**, *194* (4827), 480–482. https://doi.org/10.1038/194480b0.

(76) Inoko, M.; Kihara, Y.; Morii, I.; Fujiwara, H.; Sasayama, S. Transition from Compensatory Hypertrophy to Dilated, Failing Left Ventricles in Dahl Salt-Sensitive Rats. *Am. J. Physiol.-Heart Circ. Physiol.* **1994**, *267* (6), H2471–H2482. https://doi.org/10.1152/ajpheart.1994.267.6.H2471.

(77) Anderson, P. G.; Bishop, S. P.; Peterson, J. T. Chapter 26 - Cardiovascular Research. In *The Laboratory Rat (Second Edition)*; Suckow, M. A., Weisbroth, S. H., Franklin, C. L., Eds.; American College of Laboratory Animal Medicine; Academic Press: Burlington, 2006; pp 773–802. https://doi.org/10.1016/B978-012074903-4/50029-7.

(78) Klotz, S.; Hay, I.; Zhang, G.; Maurer, M.; Wang, J.; Burkhoff, D. Development of Heart Failure in Chronic Hypertensive Dahl Rats. *Hypertension* **2006**, *47* (5), 901–911. https://doi.org/10.1161/01.HYP.0000215579.81408.8e.

(79) Nguyen, N. T. B.; DeGrado, T. R.; Chakraborty, P.; Wieland, D. M.; Schwaiger, M. Myocardial Kinetics of Carbon-11-Epinephrine in the Isolated Working Rat Heart. *J. Nucl. Med.* **1997**, *38* (5), 780–785.

(80) Higuchi, T.; Yousefi, B. H.; Reder, S.; Beschorner, M.; Laitinen, I.; Yu, M.; Robinson, S.; Wester, H. J.; Schwaiger, M.; Nekolla, S. G. Myocardial Kinetics of a Novel [18F]-Labeled Sympathetic Nerve PET Tracer LMI1195 in the Isolated Perfused Rabbit Heart. *JACC Cardiovasc. Imaging* **2015**, *8* (10), 1229–1231. https://doi.org/10.1016/j.jcmg.2014.11.013.

(81) Rutigliano, G.; Accorroni, A.; Zucchi, R. The Case for TAAR1 as a Modulator of Central Nervous System Function. *Front. Pharmacol.* **2018**, *8*, 987. https://doi.org/10.3389/fphar.2017.00987.

(82) Koh, A. H. W.; Chess-Williams, R.; Lohning, A. E. Differential Mechanisms of Action of the Trace Amines Octopamine, Synephrine and Tyramine on the Porcine Coronary and Mesenteric Artery. *Sci. Rep.* **2019**, *9* (1), 10925. https://doi.org/10.1038/s41598-019-46627-5.

(83) Berg, T.; Jensen, J. Tyramine Reveals Failing A2-Adrenoceptor Control of Catecholamine Release and Total Peripheral Vascular Resistance in Hypertensive Rats. *Front. Neurol.* **2013**, *4*.

(84) Ebert, T. J.; Hall, J. E.; Barney, J. A.; Uhrich, T. D.; Colinco, M. D. The Effects of Increasing Plasma Concentrations of Dexmedetomidine in Humans. *Anesthesiology* **2000**, *93* (2), 382–394. https://doi.org/10.1097/00000542-200008000-00016.

(85) Taoda, M.; Adachi, Y. U.; Uchihashi, Y.; Watanabe, K.; Satoh, T.; Vizi, E. S. Effect of Dexmedetomidine on the Release of [3H]-Noradrenaline from Rat Kidney Cortex Slices: Characterization of A2-Adrenoceptor. *Neurochem. Int.* **2001**, *38* (4), 317–322. https://doi.org/10.1016/S0197-0186(00)00096-6.

(86) Charkoudian, N.; Rabbitts, J. A. Sympathetic Neural Mechanisms in Human Cardiovascular Health and Disease. *Mayo Clin. Proc.* **2009**, *84* (9), 822–830.

(87) Tanada, Y.; Okuda, J.; Kato, T.; Minamino-Muta, E.; Murata, I.; Soga, T.; Shioi, T.; Kimura, T. The Metabolic Profile of a Rat Model of Chronic Kidney Disease. *PeerJ* **2017**, *5*, e3352. https://doi.org/10.7717/peerj.3352.

(88) Shea, C. M.; Price, G. M.; Liu, G.; Sarno, R.; Buys, E. S.; Currie, M. G.; Masferrer, J. L. Soluble Guanylate Cyclase Stimulator Praliciguat Attenuates Inflammation, Fibrosis, and End-Organ Damage in the Dahl Model of Cardiorenal Failure. *Am. J. Physiol.-Ren. Physiol.* **2020**, *318* (1), F148–F159. https://doi.org/10.1152/ajprenal.00247.2019.

(89) Buss, S. J.; Backs, J.; Kreusser, M. M.; Hardt, S. E.; Maser-Gluth, C.; Katus, H. A.; Haass, M. Spironolactone Preserves Cardiac Norepinephrine Reuptake in Salt-Sensitive Dahl Rats. *Endocrinology* **2006**, *147* (5), 2526–2534. https://doi.org/10.1210/en.2005-1167.

(90) Nozawa, T.; Igawa, A.; Yoshida, N.; Maeda, M.; Inoue, M.; Yamamura, Y.; Asanoi, H.; Inoue, H. Dual-Tracer Assessment of Coupling Between Cardiac Sympathetic Neuronal Function and Downregulation of β-Receptors During Development of Hypertensive Heart Failure of Rats. *Circulation* **1998**, *97* (23), 2359–2367. https://doi.org/10.1161/01.CIR.97.23.2359.

4. Chapter IV: Evaluation of [^{18}F]FEOBV for imaging the cardiac non-neuronal cholinergic system.

The manuscript is in the editing process and will be submitted to a journal upon approval of all authors

Uzair S. Ismailani,[1,2±] **Ariel Buchler**,[2,3±], and Benjamin H. Rotstein[1,2,3*]

[1] *Department of Biochemistry, Microbiology and Immunology, University of Ottawa, Ottawa, Ontario, Canada*

[2] *University of Ottawa Heart Institute, Ottawa, Ontario, Canada*

[3] *Department of Chemistry and Biomolecular Sciences, University of Ottawa, Ottawa, Ontario, Canada*

[±] Both authors declare equal contribution

Correspondence: Benjamin H. Rotstein, PhD
University of Ottawa Heart Institute
40 Ruskin Street, H-5219
Ottawa, Ontario, Canada
K1Y 4W7
Phone: 613-696-7324
Email: benjamin.rotstein@uottawa.ca

4.1. Statement of the manuscript

The manuscript "**Evaluation of [^{18}F]FEOBV for imaging the cardiac non-neuronal cholinergic system**" details mechanistic work aimed at determining whether myocardial uptake of [^{18}F]FEOBV is a saturable process. This manuscript is currently being drafted and awaiting edits prior to journal submission. All experiments have been completed by me and Ariel Buchler. Both of us declare equal contribution in performing the experiments mentioned in this chapter. Data interpretation was a collaborative effort of myself, Dr. Rotstein, and Ariel Buchler. The manuscript was written by me and edited by Dr. Benjamin Rotstein and Ariel Buchler.

4.2. Significance

To date, there are no PNS radiotracers available for cardiac imaging. Imaging the cardiac NNCS enables researchers and clinicians to visualize and quantify changes occurring in the myocardium at the onset of PNS dysfunction in cardiac disease. This can further our understanding of molecular changes that occur in disease states and serve as a useful tool for patient management.

4.3. Abstract

Dysfunction of the parasympathetic nervous system (PNS) has been implicated in the worsening of conditions such as heart failure and diabetes mellitus. Acetylcholine (ACh) signaling in the myocardium predominantly occurs in the atria, where dense PNS nerve fibers synapse with cardiac tissue. While the ventricles are diffusely innervated by cholinergic neurons, cardiomyocytes have been shown to possess intrinsic acetylcholine transmission machinery that also contributes to overall myocardial health that is subject to dysfunction at the onset of disease. Therefore, molecular imaging of the non-neuronal cholinergic system (NNCS) can be vital in assessing the function of cardiomyocyte derived ACh signaling mechanisms in cardiovascular

disease. In this study, we used the vesicular acetylcholine transporter (VAChT) radioligand [^{18}F]FEOBV in CD-1 mice to validate its use in imaging the NNCS. We performed *ex vivo* biodistribution at 30 minutes under baseline and blocking conditions using vesamicol and non-radioactive FEOBV to demonstrate target dependence and determined the role of isoflurane in tracer retention. We discovered no changes in the uptake of [^{18}F]FEOBV in the ventricles, indicative of a lack of specific binding. Metabolism was determined in plasma and myocardial samples, revealing 20% and 57% of intact parent, respectively. PET imaging was performed in C57BL/6 mice and demonstrates rapid uptake in the LV that peaked within 2 min followed by a rapid 10-minute washout phase. PET imaging in mice containing myocardial specific VAChT knockouts (VAChT$^{Myh6\text{-}Cre\text{-}flox/flox}$) and upregulated VAChT (VAChT^{Hyp}) showed no differences in LV or blood uptake of [^{18}F]FEOBV in comparison to their respective controls. In summary, [^{18}F]FEOBV does not display any target dependence in the ventricles and therefore does not appear to accurately report on the NNCS in mice.

4.4. Introduction

The cardiac autonomic nervous system (ANS) is composed of sympathetic and parasympathetic nervous systems (SNS, PNS) primarily regulated by two neurotransmitters with opposing functions, namely, norepinephrine (NE) and acetylcholine (ACh), respectively.[1] Basal cardiac function is thus dependent on a net balance of these opposing interactions to maintain homeostasis. The myocardium is observed to be densely innervated by SNS efferents in both ventricles, whereas parasympathetic nerve fibres are primarily localized in the atria and sparsely innervate the ventricles.[2–4] While dysfunction or loss of myocardial sympathetic neurons has been implicated in the development of a multitude of conditions such as myocardial infarction (MI),

heart failure (HF) and arrhythmias, accumulating evidence has shown disruptions in ACh signalling to also heavily contribute to the declining myocardial health observed in these disease states.[4–7]

With the rapid development of catecholamine and benzylguanidine based positron emission tomography (PET) radiotracers targeting the norepinephrine transporter (NET) for SNS imaging, significant advances have been made in non-invasively determining cardiac sympathetic function, consequently aiding in the risk stratification and treatment management of patients with cardiovascular diseases.[8,9] In contrast, cardiac imaging of the PNS has proven to be more difficult due to the low density of parasympathetic nerve fibres in the ventricles in addition to challenges associated with quantifying the anatomically smaller and thinner atrial wall densely innervated by the PNS. To date, the most promising radioligand for imaging the cardiac PNS is [^{11}C]donepezil.[10–12] This radioligand is a reversible inhibitor for acetylcholinesterases (AChE), an enzyme primarily located in the synaptic cleft of cholinergic synapses, and responsible for the metabolic degradation of ACh to terminate cholinergic transmission.[10] [^{11}C]Donepezil has demonstrated considerable specific binding in the myocardium, but displays comparable binding affinity towards sigma-1 receptors (S1R) abundantly expressed in the heart.[11,12] Given the low density of AChE in the LV, it is hypothesized that myocardial uptake is likely due to the nonneuronal cardiomyocyte derived cholinergic system (NNCS), however the relative contribution of [^{11}C]donepezil uptake in the myocardium to S1R and AChE is unknown.

Mouse and rat cardiomyocytes independently express ACh transmission machinery such as choline acetyltransferase (ChAT), choline transporter (CHT1), VAChT, and AChE.[13,14] Accumulating evidence suggests NNCS-mediated cardiac ACh transmission is crucial for cardiac cell survival, angiogenesis, metabolism, and diabetes-associated cardiovascular complications.[13,15]

Studies in cardiac-specific VAChT knockouts have also shown significantly reduced heart rate (HR) recovery following exercise and exacerbated cardiac hypertrophy and LV remodelling.[16] Given the emerging role of aberrant NNCS signaling in the development or progressive worsening of cardiac diseases, molecular imaging of the NNCS can reveal unique biochemical changes occurring at the onset of disease and provide a quantifiable metric for NNCS function.

The radioligand exhibiting high selectivity (low S1R affinity) for imaging presynaptic cholinergic nerve terminals is (-)-5-[^{18}F]fluoroethoxybenzovesamical ([^{18}F]FEOBV).[17] [^{18}F]FEOBV is a substrate for the vesicular acetylcholine transporter (VAChT), responsible for the transport of ACh into secretory vesicles.[18] Molecular imaging of VAChT with [^{18}F]FEOBV has demonstrated immense application in visualizing changes in cholinergic innervation in neurodegenerative diseases such as in Alzheimer's and Parkinson's disease.[19,20] Recent work aimed at quantifying the myocardial uptake of [^{18}F]FEOBV in healthy participants demonstrated peak uptake within 5 minutes followed by slow monophasic washout.[21] However, due to the toxicity of vesamicol and its derivatives (FEOBV) blocking studies were not performed. In a separate study, 15 healthy subjects were subjected to [^{18}F]FEOBV PET. In analyzing the myocardial uptake, the authors noted ~4x higher distribution volume (V_D) in comparison to a previous study by Saint-Georges *et al.* (using similar methods of quantification), suggesting a dramatic age influence as the mean age of the study was 72 years instead of 37 years.[22]

In order to provide evidence for target-dependent uptake of [^{18}F]FEOBV in the myocardium, we performed *ex* vivo biodistribution under baseline and blocking conditions in the presence and absence of isoflurane, supplemented with plasma and myocardial metabolism in healthy CD-1 mice. *In vivo* PET imaging was performed in C57BL/6 mice to obtain LV and blood

time-activity curves (TAC), and mutant mice containing both downregulated and upregulated VAChT were assessed to demonstrate this tracer's application in imaging the NNCS.

4.5. Results and discussion

Synthesis. [^{18}F]FEOBV was synthesized in high yield and molar activity using an automated procedure as previously described.[23] *Ex vivo* biodistribution and metabolism was performed in CD-1 mice.

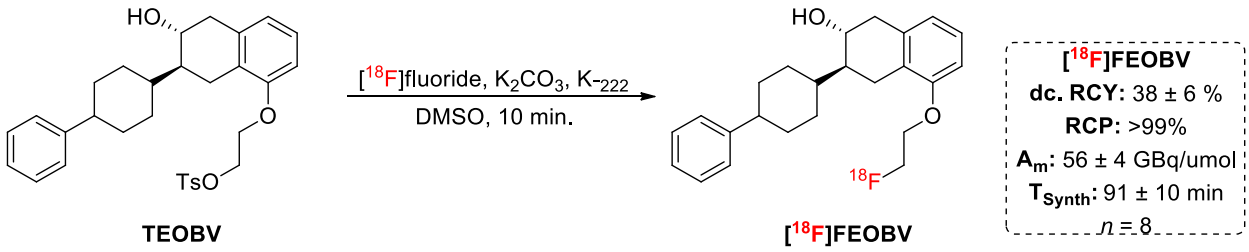

4.5.1. Scheme 1. Automated radiosynthesis of [^{18}F]FEOBV.

Metabolism. Significant metabolism was noted in plasma and myocardium samples at 30 minutes with 17–24% and ~56% intact parent, respectively (table 1). No differences were observed in [^{18}F]FEOBV metabolism in anesthetized and conscious mice, and one major polar metabolite was observed but not identified. Tracer instability in the myocardium is usually a significant concern when quantifying LV activity. However, given the rapid kinetic profile (0-2.5 min uptake, 10-15 min washout) of [^{18}F]FEOBV in the myocardium of humans, quantitative parameters can be established for early timepoints which likely reduces the contribution of metabolite dependent myocardial activity.[21]

4.5.2. **Table 1.** Plasma and myocardial metabolism of [^{18}F]FEOBV in CD-1 mice at 30 minutes.[a]

Fraction	Isoflurane				Conscious			
	Plasma		Myocardium		Plasma		Myocardium	
	Baseline	Vesamicol | Block	Baseline	Vesamicol | Block	Baseline	Vesamicol Block	Baseline	Vesamicol Block
Parent Radiotracer (%)	17	-	57	61	24	-	56	-
Polar Metabolites (%)	82	-	46	39	74	-	41	-
Nonpolar Metabolites (%)	1	-	2	1	1	-	2	-
Extraction Efficiency (%)	91	93	83	95	92	-	90	-

[a] Percent parent compound obtained for pooled samples following tracer administration (n = 3/group)

Ex vivo biodistribution was performed in male CD-1 mice 30 minutes after injecting [^{18}F]FEOBV in the lateral tail vein. Baseline uptake studies revealed retention of [^{18}F]FEOBV in the ventricles (2.38 ± 0.54 %ID/g), pancreas (6.52 ± 0.42 %ID/g), lung (5.54 ± 2.41 %ID/g) and whole brain (7.11 ± 1.52 %ID/g). Renal retention (7.56 ± 2.25 %ID/g) predominated over hepatic retention (2.76 ± 0.28 %ID/g) and minimal *in vivo* defluorination (0.83 ± 0.19 %ID/g) of the tracer was observed after 30 minutes. Pretreatment with the well-characterized non-competitive and reversible VAChT inhibitor vesamicol did not alter the uptake of [^{18}F]FEOBV in the ventricles

(2.38 ± 0.46 %ID/g). However, reduced uptake following vesamicol blockade was noted in select organs such as the pancreas (6.52 ± 0.42 vs 4.91 ± 1.19 %ID/g, p = 0.092), intestine (3.11 ± 0.31 vs 2.41 ± 0.44 %ID/g, p = 0.087), lung (5.54 ± 2.41vs 3.75 ± 0.37 %ID/g), and brain (7.11 ± 1.52 vs 5.55 ± 1.44 %ID/g), but not found to be statistically significant due to limited sample size and moderate blocking magnitudes. Regardless, specific binding is likely observed in these organs as they are densely innervated by the PNS, and likely representative of VAChT specific uptake.[22,24] Brain uptake of [^{18}F]FEOBV is well characterized and found to have high specific uptake in selective regions such as the striatum.[18,25] As such, collecting whole brain and whole organ samples in our experiment reduced the sensitivity of specific radiotracer retention following VAChT blockade. In addition, administering enough cold mass of VAChT inhibitors to occupy all sites in the body is a well known confound for these studies due to peripheral toxicity at low doses.[18]

4.5.3. **Table 2**. *Ex* vivo Biodistribution of CD-1 mice at 30 min.

Organ	%ID/g				
	Isoflurane Vehicle	Isoflurane Vesamicol	Isoflurane FEOBV	Conscious Vehicle	Conscious Vesamicol
Blood	2.18 ± 0.32	1.74 ± 0.41	2.50 ± 0.66	1.99 ± 0.47	2.43 ± 0.36
Ventricle	2.38 ± 0.54	2.38 ± 0.46	2.77 ± 0.20	2.05 ± 0.35	2.19 ± 0.35
Pancreas	6.52 ± 0.42	4.91 ± 1.19	7.39 ± 0.17	5.39 ± 0.90	4.91 ± 1.11
Intestine	3.11 ± 0.31	2.41 ± 0.44	6.52 ± 3.07	2.89 ± 0.72	3.48 ± 0.78
Stomach	1.91 ± 0.83	1.44 ± 1.13	2.42 ± 1.58	3.27 ± 0.55	2.38 ± 1.21
Liver	2.76 ± 0.28[a]	2.83 ± 0.31	4.80 ± 0.61[a]	2.29 ± 0.44	3.29 ± 0.54
Kidney	7.56 ± 2.25[a]	8.38 ± 2.82	6.12 ± 2.11	4.27 ± 1.63[a]	5.11 ± 0.28
Lung	5.54 ± 2.41	3.75 ± 0.37	4.61 ± 1.05	3.92 ± 0.91	2.93 ± 0.06
Bone	0.83 ± 0.19	0	1.35 ± 1.16	1.29 ± 0.34	1.27 ± 0.34
Brain	7.11 ± 1.52[a]	5.55 ± 1.44	5.77 ± 1.70	3.77 ± 1.45[a]	3.64 ± 0.47

[a]Statistical significance ($p < 0.05$) reached using an unpaired t-test. Isoflurane vehicle ($n = 3$), Isoflurane Vesamicol (150 µg/kg, $n = 3$), Isoflurane FEOBV (10 µg/kg, $n = 3$), Conscious Vehicle ($n = 5$-6), Conscious Vesamicol (150 µg/kg, $n = 3$-5)

Next, animals were pretreated with nonradioactive FEOBV to determine whether myocardial uptake was influenced selectively by this vesamicol derivative. However, retention of the tracer in the ventricles remained unaltered (2.77 ± 0.20 %ID/g). Accelerated clearance of the tracer was evident in this cohort due the increasing trend of intestinal (3.11 ± 0.31 vs 6.52 ± 3.07) and hepatic (2.76 ± 0.28 vs 4.80 ±0.61 %ID/g, $p = 0.0062$) retention compared to vehicle treated controls. Brain uptake was found to be reduced to a similar extent (3.77 ± 1.45 %ID/g) as vesamicol pre-treated mice.

Since the uptake of [^{18}F]FEOBV in the ventricles remained unchanged after pretreatment with both pharmaceuticals, we hypothesized isoflurane-induced reductions in specific binding may contribute to the apparent lack of myocardial selectivity observed in anesthetized mice. Thus, animals were then administered [^{18}F]FEOBV while conscious to determine any significant isoflurane induced effects under baseline and vesamicol blocking conditions. Baseline uptake of [^{18}F]FEOBV in conscious mice displayed similar uptake in the ventricles (2.05 ± 0.35 %ID/g) in

comparison to baseline anesthetized mice. Radiotracer clearance was evident in this cohort due to accelerated renal clearance (7.56 ± 2.2 vs 4.27 ± 1.6 %ID/g, $p = 0.049$). Surprisingly, whole brain uptake of [^{18}F]FEOBV was observed to be ~47% lower in conscious CD-1 mice (7.11 ± 1.52 vs 3.77 ± 1.45, $p = 0.021$) than those that were anesthetized. Conscious animals pretreated with vesamicol displayed minor decreases in pancreatic and lung uptake, and moderately higher liver and kidney retention. Brain uptake was found to be unaltered in conscious mice pretreated with vesamicol in comparison to conscious vehicle-treated controls (3.64 ± 0.47 vs 3.77 ± 1.45). Low uptake and lack of specific binding in the brain of conscious mice may be due to increased clearance of specifically bound [^{18}F]FEOBV, however further studies would be needed to determine whether specific binding in the brain is dependent on isoflurane anesthesia. In general, isoflurane anesthesia and other common anesthetics used to immobilize animals are considered as confounding variables as they interact with dopaminergic, cholinergic, and serotonergic neurotransmitter systems.[26] In addition, pharmacological effects such as altered cerebral blood flow and body temperature have been observed.[26] Indeed, the use of restrainers to immobilize animals has also been shown to induce neurological changes such as a stress-induced reduction of brain AChE activity.[26,27]

Collectively, the biodistribution data suggest that uptake of [^{18}F]FEOBV in the LV is not target dependent. Rather, the evidence indicates that cardiac uptake of this tracer is driven by tissue perfusion, limiting the utility of [^{18}F]FEOBV imaging in mice to cholinergic nerves in the brain and periphery. While it is plausible that species-dependent accumulation of [^{18}F]FEOBV in the myocardium can occur, further studies in higher species would be required to validate this hypothesis.

PET imaging was performed in healthy C57BL/6 mice to obtain LV time-activity curves. Quantification of LV activity was performed using Flowquant. Blood activity was estimated from cardiac blood pool. [^{18}F]FEOBV imaging in mice displayed more rapid peak uptake (1-2 min) and washout (2-10 min) in comparison to human imaging.

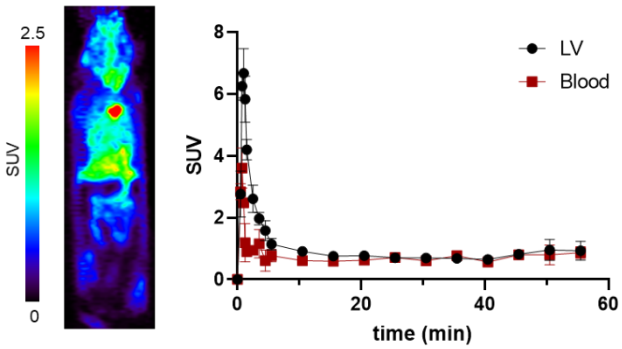

4.5.4. Figure 1. [^{18}F]FEOBV full body coronal PET image and LV time-activity curve. *n* =2

As part of a collaboration with researchers at Western University (Ontario, Canada), PET images of transgenic mouse models containing myocardium-specific VAChT knockouts (VAChT$^{Myh6\text{-}Cre\text{-}flox/flox}$) and upregulated myocardial VAChT (VAChT^{Hyp}) were provided to our group to determine differences in LV activity. Upon analysis of LV and blood TACs, no significant differences were noted in these animals in comparison to their respective controls (data not shown).

4.6. Conclusion

In conclusion, we performed *ex vivo* biodistribution with [^{18}F]FEOBV in CD-1 mice to determine whether any specific binding occurs in the myocardium. Heterologous blockade with vesamicol, and homologous blockade with nonraactive FEOBV revealed no differences in the retention of [^{18}F]FEOBV in the ventricles. Baseline and vesamicol pretreatment were also performed in the absence of anesthesia but did not reveal any differences in myocardial uptake. Plasma metabolism revealed only 20% of the parent tracer intact in after 30 minutes, and 57%

intact parent in the myocardium. PET imaging under baseline conditions revealed rapid uptake and washout kinetics in the LV and blood that reached dynamic equilibrium by 15 minutes. PET imaging in myocardial VAChT knockout mice did not display reduced uptake in the LV. Similarly, mice containing upregulated myocardial VAChT displayed similar uptake to genetic control mice. Based on the data obtained in our study, [^{18}F]FEOBV does not serve as a useful probe for imaging the myocardial cholinergic system in mice, limiting its utility for imaging parasympathetic nerves in the brain and other peripheral organs.

4.7. Materials and methods

Automated Radiosynthesis. The radiosynthesis of [^{18}F]FEOBV was performed as previously described.[23] [^{18}F]fluoride (9 - 10 GBq) was captured onto a Sep-pak Accel Plus QMA Plus Light cartridge from a [^{18}O]H_2O target solution and eluted into the reactor using K_2CO_3 (3.5 mg in 0.5 mL H_2O). 1 mL of ACN containing 15 mg of Kryptofix 2.2.2 (K_{222}) was added to the reactor and heated for 4 minutes at 80 °C, followed by an additional 4 minutes at 60 °C, followed by cooling to 40 °C prior to the addition of the tosylated precursor (TEOBV, 0.5 mg in 0.5 mL DMSO). The radiofluorination was performed at 120 °C for 10 min then cooled to 50 °C prior to the addition of 3.5 mL of a 45% ACN:H_2O solution. The diluted reaction mixture was passed through a Sep-Pak Light Alumina-N cartridge and loaded onto a semi-preparative HPLC column (Synergi Hydro-RP 80, 250 x 10.00 mm 10 µm; mobile phase: 45% ACN: 55% aqueous 50 mM ammonium acetate, flow rate = 4 mL/min). The peak corresponding to [^{18}F]FEOBV eluted between 30-45 minutes. The product fraction was collected into a bulk vessel prefilled with 40 mL of sterile water and passed through a C-18 Sep-Pak cartridge. The cartridge was washed with 10 mL of sterile water, and the product was eluted with 1 mL of ethanol and diluted with 9 mL of saline. The final product was run through a 0.22 µm sterile filter and dispensed into a septum sealed vial fitted with a vent

needle. QC was performed using a Waters 2695 Alliance HPLC equipped with a Phenomenex Luna 10 µm C18(2) (100 Å, 250 mm × 4.6 mm) column, a 996-photodiode array detector (Waters) and a Carroll & Ramsey Associates 105-S high-sensitivity radiation detector. Gradient: 50/50 50 mM ammonium acetate:water, 20 min, flow rate = 1 mL/min). Molar activity was determined using UV absorbance of a known amount of radioactivity under identical analytical HPLC conditions to generate a calibration curve for the nonradioactive standard. The ratio if radioactivity (GBq) to moles (µmol) yielded molar activity (GBq/µmol), the value was decay-corrected to EoS. Radiochemical yield was also decay corrected to EoS.

Animal care. Male CD-1 mice (35-45 g) and C56BL/6 (25-35 g) were purchased from Charles River Laboratories (Senneville, Quebec) and housed in environmentally enriched cages with free access to water and food. Housing, handling, and experimental procedures were performed in strict accordance with the guidelines of the Canadian Council on Animal Care and with the approval of the University of Ottawa Animal Care Committee. CD-1 mice used in this study were 6-8 weeks old.

Ex vivo biodistribution and blocking studies. Male CD-1 mice were anesthetized using 2% isoflurane and received lateral tail vein injections of 3-15 MBq of [^{18}F]FEOBV in 0.1 mL of 10% ethanol in saline. Conscious animals were placed in a restrainer and similarly injected with tracer. For animals requiring pharmacological challenge, vesamicol (150 µg/kg) or FEOBV (10 µg/kg) were injected via the lateral tail vein 10 minutes prior to radiotracer injection. Animals were sacrificed by CO_2 asphyxiation followed by cervical dislocation. All organs were harvested (blood collected by cardiac puncture, atria removed from myocardium), weighted, and counted for radiation in a gamma counter (Hidex Automatic Gamma Counter, Energy window: 480 – 558 keV). Counts per minute (CPM) were converted to nanocurie (nCi) using calibrated standards with

known activities. Percent injected dose (%ID) was calculated by dividing the decay corrected organ activity by the injected dose, and further normalized by sample mass to obtain the percentage injected dose per gram tissue (%ID/g).

Parent fraction in plasma and myocardium. Male CD-1 mice were injected with [^{18}F]FEOBV under baseline and blocking conditions. Blood samples were obtained via cardiac puncture at the 30-minute timepoint and placed in 1 mL heparinized tubes. Blood samples were centrifuged at 4 °C for 7 min at 4000 rpm to obtain plasma. Protein-free plasma (PFP) was then obtained by the addition of an equal volume of ice-cold ACN, followed by centrifugation at 4 °C for 5 min at 4000 rpm. PFP samples from each animal cohort were pooled together. Myocardium samples were perfused with 15 mL of 1X PBS and pooled into a tube containing a 50/50 mixture of ACN/H_2O. The tube was placed in an ice bath and homogenized using a Fisher Scientific PowerGen 125 (125 W, 11V, 50/60 Hz) adapted with a sawtooth, 7 × 95 mm generator. Once myocardium tissue appeared sufficiently homogenized, an aliquot of 1 mL of ACN was added to the tube and samples were homogenized for an additional 5 minutes. The samples were then centrifuged at 4 °C for 5 min at 4000 rpm. For both plasma and myocardium preparations, additional extractions were performed to reach an extraction efficiency ≥ 70%, as measured on the gamma counter. The supernatants were filtered through a 0.22 µm filter, and spiked with nonradioactive standard (10 µL, 1 mg/mL), and injected onto the analytical radioHPLC. Fractions were collected every minute for 20 minutes and placed on the gamma counter to determine the total activity in each fraction.

Statistical Analysis. Statistical analysis was performed using GraphPad Prism. Significance was set at the 0.05 level. The data are presented as mean ± standard deviation. Differences between two groups were tested using a two-tailed unpaired Student's t-test.

4.8. References

(1) Low, P. A. Autonomic Nervous System Function. *J. Clin. Neurophysiol.* **1993**, *10* (1), 14–27.

(2) Machhada, A.; Marina, N.; Korsak, A.; Stuckey, D. J.; Lythgoe, M. F.; Gourine, A. V. Origins of the Vagal Drive Controlling Left Ventricular Contractility. *J. Physiol.* **2016**, *594* (14), 4017–4030. https://doi.org/10.1113/JP270984.

(3) Gordan, R.; Gwathmey, J. K.; Xie, L.-H. Autonomic and Endocrine Control of Cardiovascular Function. *World J. Cardiol.* **2015**, *7* (4), 204–214. https://doi.org/10.4330/wjc.v7.i4.204.

(4) Olshansky, B.; Sabbah, H. N.; Hauptman, P. J.; Colucci, W. S. Parasympathetic Nervous System and Heart Failure. *Circulation* **2008**, *118* (8), 863–871. https://doi.org/10.1161/CIRCULATIONAHA.107.760405.

(5) Borovac, J. A.; D'Amario, D.; Bozic, J.; Glavas, D. Sympathetic Nervous System Activation and Heart Failure: Current State of Evidence and the Pathophysiology in the Light of Novel Biomarkers. *World J. Cardiol.* **2020**, *12* (8), 373–408. https://doi.org/10.4330/wjc.v12.i8.373.

(6) Charkoudian, N.; Rabbitts, J. A. Sympathetic Neural Mechanisms in Human Cardiovascular Health and Disease. *Mayo Clin. Proc.* **2009**, *84* (9), 822–830.

(7) Floras, J. S.; Ponikowski, P. The Sympathetic/Parasympathetic Imbalance in Heart Failure with Reduced Ejection Fraction. *Eur. Heart J.* **2015**, *36* (30), 1974–1982. https://doi.org/10.1093/eurheartj/ehv087.

(8) Chen, X.; Kudo, T.; Lapa, C.; Buck, A.; Higuchi, T. Recent Advances in Radiotracers Targeting Norepinephrine Transporter: Structural Development and Radiolabeling Improvements. *J. Neural Transm.* **2020**, *127* (6), 851–873. https://doi.org/10.1007/s00702-020-02180-4.

(9) van der Bijl, P.; Knuuti, J.; Delgado, V.; Bax, J. J. Cardiac Sympathetic Innervation Imaging with PET Radiotracers. *Curr. Cardiol. Rep.* **2021**, *23* (1), 4. https://doi.org/10.1007/s11886-020-01432-9.

(10) Boutagy, N. E.; Sinusas, A. J. Recent Advances and Clinical Applications of PET Cardiac Autonomic Nervous System Imaging. *Curr. Cardiol. Rep.* **2017**, *19* (4), 33. https://doi.org/10.1007/s11886-017-0843-0.

(11) Gjerløff, T.; Jakobsen, S.; Nahimi, A.; Munk, O. L.; Bender, D.; Alstrup, A. K. O.; Vase, K. H.; Hansen, S. B.; Brooks, D. J.; Borghammer, P. In Vivo Imaging of Human Acetylcholinesterase Density in Peripheral Organs Using 11C-Donepezil: Dosimetry, Biodistribution, and Kinetic Analyses. *J. Nucl. Med.* **2014**, *55* (11), 1818–1824. https://doi.org/10.2967/jnumed.114.143859.

(12) Horsager, J.; Fedorova, T. D.; Berge, N. V. D.; Klinge, M. W.; Knudsen, K.; Hansen, A. K.; Alstrup, A. K. O.; Krogh, K.; Gormsen, L.; Borghammer, P. Cardiac 11C-Donepezil Binding Increases With Age in Healthy Humans: Potentially Signifying Sigma-1 Receptor Upregulation. *J. Cardiovasc. Pharmacol. Ther.* **2019**, *24* (4), 365–370. https://doi.org/10.1177/1074248419838509.

(13) Saw, E. L.; Pearson, J. T.; Schwenke, D. O.; Munasinghe, P. E.; Tsuchimochi, H.; Rawal, S.; Coffey, S.; Davis, P.; Bunton, R.; Van Hout, I.; Kai, Y.; Williams, M. J. A.; Kakinuma, Y.; Fronius, M.; Katare, R. Activation of the Cardiac Non-Neuronal Cholinergic System Prevents the Development of Diabetes-Associated Cardiovascular Complications. *Cardiovasc. Diabetol.* **2021**, *20* (1), 50. https://doi.org/10.1186/s12933-021-01231-8.

(14) Kakinuma, Y.; Akiyama, T.; Sato, T. Cholinoceptive and Cholinergic Properties of Cardiomyocytes Involving an Amplification Mechanism for Vagal Efferent Effects in Sparsely Innervated Ventricular Myocardium. *FEBS J.* **2009**, *276* (18), 5111–5125. https://doi.org/10.1111/j.1742-4658.2009.07208.x.

(15) Oikawa, S.; Kai, Y.; Mano, A.; Ohata, H.; Kurabayashi, A.; Tsuda, M.; Kakinuma, Y. Non-Neuronal Cardiac Acetylcholine System Playing Indispensable Roles in Cardiac Homeostasis Confers Resiliency to the Heart. *J. Physiol. Sci.* **2021**, *71* (1), 2. https://doi.org/10.1186/s12576-020-00787-6.

(16) Roy, A.; Dakroub, M.; Tezini, G. C. S. V.; Liu, Y.; Guatimosim, S.; Feng, Q.; Salgado, H. C.; Prado, V. F.; Prado, M. A. M.; Gros, R. Cardiac Acetylcholine Inhibits Ventricular Remodeling and

Dysfunction under Pathologic Conditions. *FASEB J.* **2016**, *30* (2), 688–701. https://doi.org/10.1096/fj.15-277046.

(17) Ogawa, K.; Shiba, K. In Vivo and In Vitro Characteristics of Radiolabeled Vesamicol Analogs as the Vesicular Acetylcholine Transporter Imaging Agents. *Contrast Media Mol. Imaging* **2018**, *2018*, e4535476. https://doi.org/10.1155/2018/4535476.

(18) Kilbourn, M. R.; Hockley, B.; Lee, L.; Sherman, P.; Quesada, C.; Frey, K. A.; Koeppe, R. A. PET Imaging of (2R,3R)-5-[18F]Fluoroethoxybenzovesamicol ((-)-FEOBV) in Rat and Monkey Brain: A Radioligand for the Vesicular Acetylcholine Transporter. *Nucl. Med. Biol.* **2009**, *36* (5), 489–493. https://doi.org/10.1016/j.nucmedbio.2009.02.007.

(19) Aghourian, M.; Legault-Denis, C.; Soucy, J.-P.; Rosa-Neto, P.; Gauthier, S.; Kostikov, A.; Gravel, P.; Bédard, M.-A. Quantification of Brain Cholinergic Denervation in Alzheimer's Disease Using PET Imaging with [18F]-FEOBV. *Mol. Psychiatry* **2017**, *22* (11), 1531–1538. https://doi.org/10.1038/mp.2017.183.

(20) van der Zee, S.; Kanel, P.; Gerritsen, M. J. J.; Boertien, J. M.; Slomp, A. C.; Müller, M. L. T. M.; Bohnen, N. I.; Spikman, J. M.; van Laar, T. Altered Cholinergic Innervation in De Novo Parkinson's Disease with and Without Cognitive Impairment. *Mov. Disord.* **2022**, *37* (4), 713–723. https://doi.org/10.1002/mds.28913.

(21) Saint-Georges, Z.; Zayed, V. K.; Dinelle, K.; Cassidy, C.; Soucy, J.-P.; Massarweh, G.; Rotstein, B.; Nery, P. B.; Guimond, S.; deKemp, R.; Tuominen, L. First-in-Human Imaging and Kinetic Analysis of Vesicular Acetylcholine Transporter Density in the Heart Using [18F]FEOBV PET. *J. Nucl. Cardiol.* **2021**, *28* (1), 50–54. https://doi.org/10.1007/s12350-020-02323-w.

(22) Horsager, J.; Okkels, N.; Van Den Berge, N.; Jacobsen, J.; Schact, A.; Munk, O. L.; Vang, K.; Bender, D.; Brooks, D. J.; Borghammer, P. In Vivo Vesicular Acetylcholine Transporter Density in Human Peripheral Organs: An [18F]FEOBV PET/CT Study. *EJNMMI Res.* **2022**, *12* (1), 17. https://doi.org/10.1186/s13550-022-00889-9.

(23) Shao, X.; Hoareau, R.; Hockley, B. G.; Tluczek, L. J. M.; Henderson, B. D.; Padgett, H. C.; Scott, P. J. H. Highlighting the Versatility of the Tracerlab Synthesis Modules. Part 1: Fully Automated Production of [F]Labelled Radiopharmaceuticals Using a Tracerlab FX(FN). *J. Label. Compd. Radiopharm.* **2011**, *54* (6), 292–307. https://doi.org/10.1002/jlcr.1865.

(24) Vaillancourt, M.; Chia, P.; Sarji, S.; Nguyen, J.; Hoftman, N.; Ruffenach, G.; Eghbali, M.; Mahajan, A.; Umar, S. Autonomic Nervous System Involvement in Pulmonary Arterial Hypertension. *Respir. Res.* **2017**, *18* (1), 201. https://doi.org/10.1186/s12931-017-0679-6.

(25) Mulholland, G. K.; Wieland, D. M.; Kilbourn, M. R.; Frey, K. A.; Sherman, P. S.; Carey, J. E.; Kuhl, D. E. [18F]Fluoroethoxy-Benzovesamicol, a PET Radiotracer for the Vesicular Acetylcholine Transporter and Cholinergic Synapses. *Synapse* **1998**, *30* (3), 263–274. https://doi.org/10.1002/(SICI)1098-2396(199811)30:3<263::AID-SYN4>3.0.CO;2-9.

(26) Miranda, A.; Bertoglio, D.; Stroobants, S.; Staelens, S.; Verhaeghe, J. Translation of Preclinical PET Imaging Findings: Challenges and Motion Correction to Overcome the Confounding Effect of Anesthetics. *Front. Med.* **2021**, *8*.

(27) Das, A.; Kapoor, K.; Sayeepriyadarshini, A. T.; Dikshit, M.; Palit, G.; Nath, C. Immobilization Stress-Induced Changes in Brain Acetylcholinesterase Activity and Cognitive Function in Mice. *Pharmacol. Res.* **2000**, *42* (3), 213–217. https://doi.org/10.1006/phrs.2000.0678.

5. Chapter V: Interrupted aza-Wittig reaction using iminophosphoranes to synthesize ^{11}C-carbonyls

The manuscript can be accessed at: https://doi.org/10.1039/D1CC01016F.

Uzair S. Ismailani,[1,2] Maxime Munch,[1,2] Braeden A. Mair,[2,3] and Benjamin H. Rotstein[1,2,3]*

[1] *Department of Biochemistry, Microbiology and Immunology, University of Ottawa*

[2] *University of Ottawa Heart Institute*

[3] *Department of Chemistry and Biomolecular Sciences, University of Ottawa*

Correspondence: Benjamin H. Rotstein, PhD
University of Ottawa Heart Institute
40 Ruskin Street, H-5219
Ottawa, Ontario, Canada
K1Y 4W7
Phone: 613-696-7324
Email: benjamin.rotstein@uottawa.ca

5.1. Statement of Manuscript

The manuscript "**Interrupted aza-Wittig reactions using iminophosphoranes to synthesize ^{11}C-carbonyls**" was accepted into *Chemical Communications* on April 26th 2021. In this chapter, I developed the optimization of reaction conditions, cold substrate scope, and performed radiochemistry. Maxime Munch assisted in optimizing the protocol to isolate aryl iminophosphoranes, Maxime Munch and Braeden Mair aided in the completion of ^{11}C-labeled substrates. The synthesis of all radiopharmaceuticals, their isolation, and optimized reaction conditions was performed by me. Maxime Munch, Braeden Mair, and I assembled the supplementary info and analyzed NMR spectra as a joint effort. I wrote the manuscript with Dr. Benjamin Rotstein and all authors edited and approved the final version.

5.2. Abstract

A direct CO_2-fixation methodology couples structurally diverse iminophosphoranes with various nucleophiles to synthesize ureas, carbamates, thiocarbamates, and amides, and is amenable for ^{11}C radiolabeling. This methodology is practical, as demonstrated by the synthesis of >35 products and isolation of the molecular imaging radiopharmaceuticals [^{11}C]URB694 and [^{11}C]glibenclamide.

5.3. Introduction

Positron emission tomography (PET) is a non-invasive molecular imaging modality used to evaluate biological processes *in vivo* with short-lived radionuclides. PET radiopharmaceuticals are used to diagnose metastatic and cardiovascular diseases, to detect biomarkers of neurodegeneration, and to probe molecular and functional mechanisms in living systems. Carbon-11 (^{11}C, $t_{1/2}$ = 20.4 min) is prized for isotopic labeling of biomolecules, and is routinely incorporated into PET imaging agents for both research and clinical applications.[1] Currently, a lack of diverse methods for directly incorporating [^{11}C]CO_2 into complex molecules has limited its use.[2] Consequently, [^{11}C]CO_2 is most often converted into reactive secondary precursors such as [^{11}C]CH_3I or [^{11}C]CH_3OTf, which are accompanied by elongated processing times and significant reductions in radiochemical yield due to sub-quantitative conversions.[3–6]

Isocyanates are valuable synthetic intermediates that can be readily converted into pharmaceutically-relevant functional groups such as carbamates, ureas, and amides.[7,8] Current approaches to synthesizing ^{11}C-isocyanates rely on stepwise trapping of [^{11}C]CO_2 with amines, followed by dehydration using $POCl_3$ or Mitsunobu-type conditions.[2,9,10]

Importantly, the former strategy displays poor tolerance towards anilines and the highly acidic conditions pose challenges for maintaining efficient trapping of [^{11}C]CO_2 in solution. The latter technique has displayed improved utility for synthesizing asymmetrical ureas[10] and also amides using either Grignard reagents[11] or organozinc coupling reactions,[12] though high mass loading of azo reagents and phosphines may complicate radiotracer purification. Each strategy requires careful control of temperature and reagent concentrations during sequential reaction steps in order to prevent formation of complex mixtures of symmetrical byproducts and heterocycles.[9,13] Iminophosphoranes have been shown to undergo the aza-Wittig reaction directly with CO_2 to produce isocyanates in high yields.[14] In the context of ^{11}C, the commercially available precursor *N*-(triphenylphosphoranylidene)aniline (**1a**) was previously reported to prepare acyclic ^{11}C-ureas from [^{11}C]CO_2 in moderate radiochemical yields (RCYs).[15] Del Vecchio *et al*. deployed *o*-azidoanilines and azido alcohols with dimethylphenylphosphine to synthesize cyclic ureas and carbamates in useful yields through a proposed intramolecular Staudinger aza-Wittig sequence (SAW, Scheme 1a) upon heating to 70 °C.[16,17] An intermolecular variant of this reaction produced a linear carbamate in low RCY at much higher temperature.

We aimed to develop conditions that are high yielding and selective for C–O, C–N, C–C, and C–S bond formation and would be amenable for one-pot [^{11}C]CO_2-fixation to prepare radiopharmaceuticals and novel tracer candidates. Through the synthesis of functionalized iminophosphorane precursors, this approach would obviate the need for highly acidic $POCl_3$, Mitsunobu reagents, explosive azide precursors, and toxic phosphines used in current methodologies, enhancing the substrate versatility and practicality of this method for good manufacturing practices (GMP) environments (Scheme 1b).

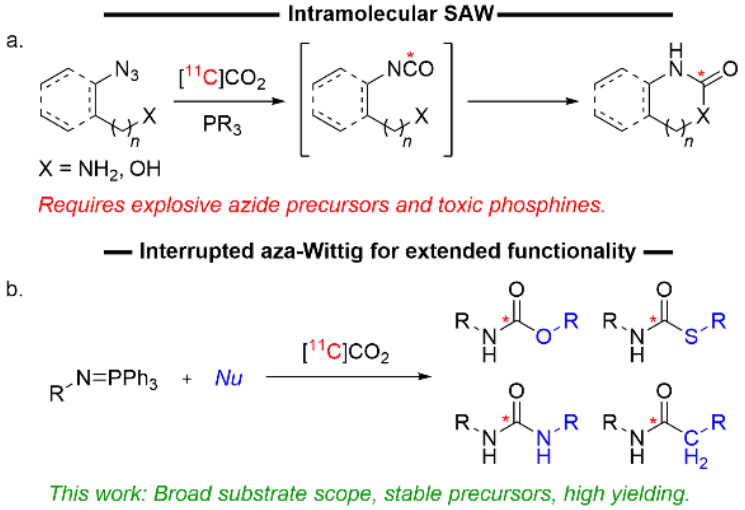

5.3.1. **Scheme 1.** Synthetic approaches to iminophosphorane [^{11}C]CO_2-fixation.

Herein, we describe a versatile and efficient approach to carbonyl ligation using iminophosphorane-CO_2-fixation coupled with intermolecular nucleophilic addition. This method is effective for synthesizing acyclic products with stable isotopes under mild conditions and is suitable for automated synthesis and ^{11}C radiolabeling.

5.4. Results and Discussion

At the outset, we focused on developing a nucleophilic coupling strategy to iminophosphorane-CO_2 fixation conditions using stable isotopes, since no such straightforward high yielding procedure for this coupling has been reported.[14]

5.4.1. **Table 1.** Optimization of reaction conditions.

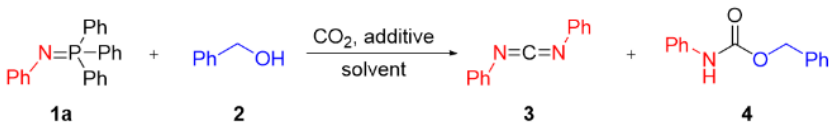

1a 2 3 4

Entry	Solvent	[**2**] (mM)	**3** Yield (%)	**4** Yield (%)
1[a,b]	toluene	100	77	6
2[a,b]	toluene	150	77	6
3[a,c]	toluene	100	42	36
4[a,c]	toluene	250	0	84
5[d]	toluene	250	0	70
6[d]	1,4-dioxane	250	0	72
7[d]	DMF	250	0	75
8[d]	ACN	250	0	78
9[d,e]	ACN	250	0	84
10[d,f]	ACN	250	0	70

[a] UPLC/MS yields; reactions in toluene at 110 °C. [b] Nucleophile added after iminophosphorane consumption. [c] Nucleophile added at t = 0. [d] Conditions: **2** (0.652 mmol), solvent (2.5 mL), 85 °C; then **1** (100 mM, 2.5 mL) added over 1 h. Reaction time: 2h. isolated yields. [e] DBU (2.6 equiv). [f] BEMP (2.6 equiv).

First, CO_2 was bubbled into a heated toluene solution containing (**1a**) until complete consumption of the iminophosphorane, followed by the addition of benzyl alcohol (**2**)**.** Low yield of the desired product **4** (6%) was observed using stepwise addition (Table 1, entry 1). The observed major product was the symmetrical *N*,*N*′-diphenylcarbodiimide (**3**), likely formed by a second aza-Wittig coupling reaction to the isocyanate intermediate. The ratio of **4**:**3** increased to 0.9:1 when the nucleophile was present from the beginning of the reaction (entry 3). Increasing the concentration of **2** led to exclusive formation of **4** in 84% yield (entry 4). This suggests that short-lived free isocyanates are formed in the presence of iminophosphoranes, subject to two competing reaction pathways: aza-Wittig carbodiimide formation and carbamate formation. Thus, at high concentrations of an intercepting nucleophile, it is possible to selectively divert the reaction

towards intermolecular ligation. Carbamate **4** could be prepared and isolated in good yields from hydrocarbon, ethereal, and polar solvents using similar conditions (entries 5–8). With our primary focus on establishing easily translatable conditions to ^{11}C radiochemistry, we were delighted to find that two common CO_2 trapping bases, amidine DBU and phosphazene BEMP (2.6 equiv.), significantly increased the rate of formation of **4**, concomitant with moderate impacts in yield (entries 9–10, table S1). These effects are likely due to the increased availability of soluble activated CO_2 complexes.[18,19]

We assessed the compatibility of the iminophosphorane-CO_2-fixation method with a diverse scope of nucleophiles (Scheme 2a). Under our developed conditions, carbamates derived from benzyl, isopropyl, 4-methoxyphenethyl, and *tert*-butyl alcohol were isolated in 83–94% yields (**4**-**7**). In contrast, phenyl carbamates and thiocarbamates (**8**-**10**) required higher nucleophile concentrations to achieve yields >70%, likely due to their propensity for elimination. Benzyl mercaptan also proved to be a compatible nucleophile, forming the corresponding thiocarbamate **11** in 86% yield. Sterically hindered nucleophiles gave carbamate **7** (83%) and urea **12** (78%). We were gratified to find that amides such as **13** (82%) could be accessed directly by carbon-carbon bond formation using diethyl malonate. Despite this success, some nucleophiles were found to be incompatible with the interrupted aza-Wittig conditions, including Grignard reagents, and phenylacetylene. However, several of our synthesized products (**7**-**10**, **12**) stand in as blocked isocyanates, and facilitate indirect nucleophilic substitution (Scheme 2b).[20] *In situ* formed *O*-phenylcarbamate **8** was transformed to amides **14**-**16** in moderate-to-good yields based on iminophosphorane **1a**. Both direct and indirect nucleophilic substitutions are robust, and further open the door to selective C-C bond formation using iminophosphoranes.

We next investigated the scope of functionalized aryl iminophosphoranes synthesized by the Kirsanov reaction and isolated by our modified general procedure (Scheme 2c, see ESI for details). First, CBz-protected products (**17-21**) were isolated to determine sensitivity to electronic and steric features of iminophosphoranes under the optimized conditions. Electron-rich arenes, aryl bromides, and *ortho*-substitution (**17-18**, **21**) were all well-tolerated in comparison with electron-deficient arenes (**19**-**20**). Alkyl iminophophosphoranes afforded products such as carbamate **22** (82%) and blocked isocyanates **23**-**24** in good yields. The utility of this method for biopharmaceuticals was assessed by targeting the fatty acid amide hydrolase inhibitor URB694 (**25**), melatonin (**26**), and the oral multi-kinase inhibitor regorafenib (**29**). Hydroquinone carbamate **25** was isolated as a mixture of regioisomers in 60% yield.[9] Indirect substitution using phenol-blocked isocyanates yielded melatonin **26** (72%), phenylalanine derivative **27** (84%), and electron-deficient amide **28** (73%). Finally, the urea regorafenib **29** was synthesized first by direct nucleophilic coupling, though indirect substitution using an *N-tert*-butylmethylamine blocked isocyanate intermediate better facilitated purification of **29** in 71% overall yield.[21]

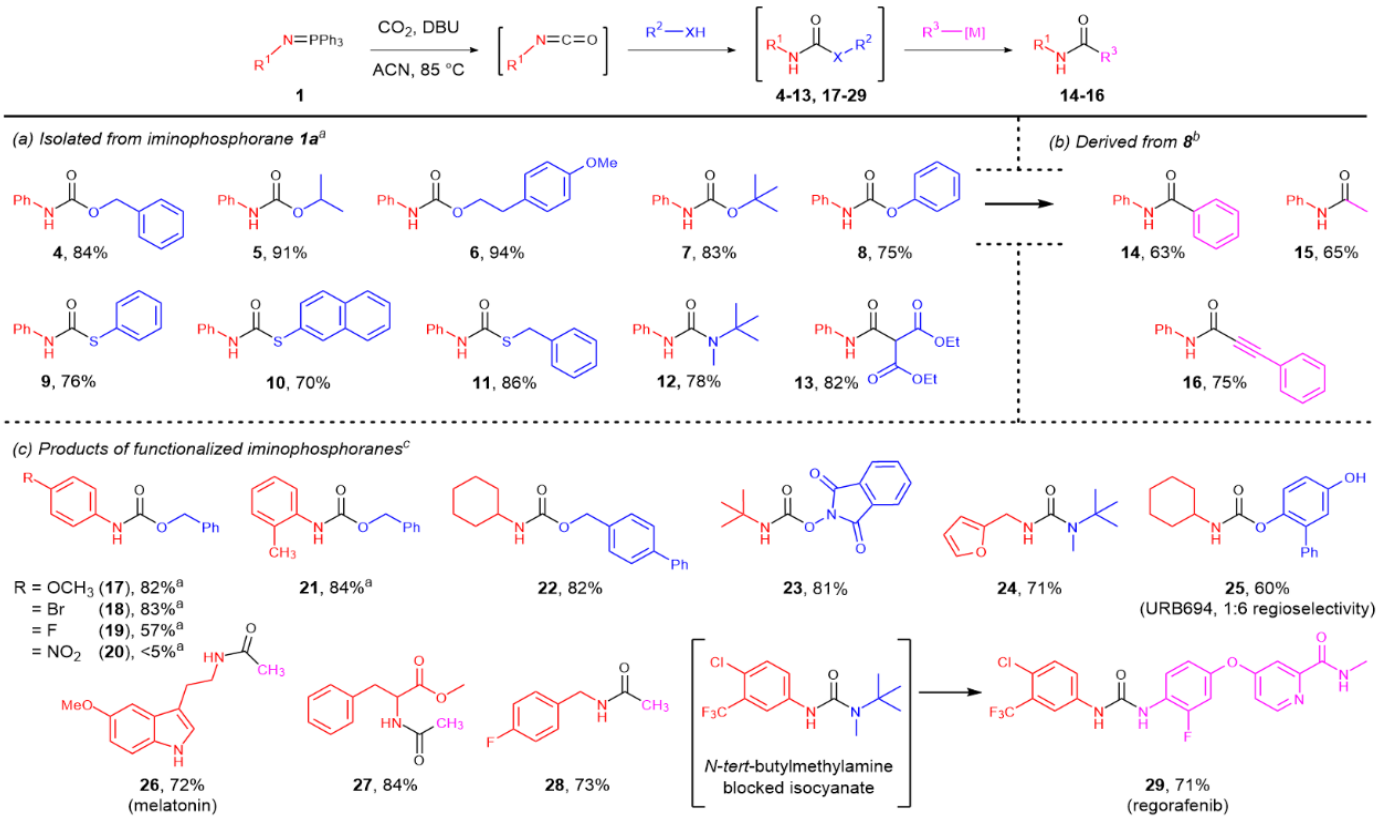

5.4.2. **Scheme 2**. Interrupted aza-Wittig for extended functionality – Reaction scope. [a] Conditions: 1 (0.25 mmol), R^2-XH (2.5 equiv.), DBU (2.6 equiv.), ACN (2.5 mL), reflux; isolated yields. [b] PhOH (10 equiv.), R^3-MgX (20 equiv.) or R^3-SH (2.5 equiv.) or PhCCH (12 equiv.), THF. [c] R^2-XH (10 equiv.), LHMDS (0.99 equiv.), THF. See ESI for detailed procedure.

Satisfied with the iminophosphorane-CO_2 nucleophilic coupling methodology using stable isotopes, we were determined to apply this method to ^{11}C radiochemistry. Since [^{11}C]CO_2 is the limiting reagent in these processes (typically <1 µmol), reconsideration of reaction conditions to produce [^{11}C]**4** was required (Table 2). First, we focused on the influence of the concentration of **1a** on product yield using high concentrations of DBU and benzyl alcohol in ACN (entry 1). We noted a low 13% RCY with these initial conditions, mainly due to a large excess of unreacted [^{11}C]CO_2. Increasing the

concentration of **1a** (entries2–3) led to maximum 32% RCY and reducing the concentration of DBU to 100 mM enhanced the selectivity toward [^{11}C]**4** (entry 4–5). Increasing the reaction temperature in DMF to 100 °C resulted in 65% RCY (entries 6–7). Finally, increasing the concentration of nucleophile **2** further improved the selectivity of [^{11}C]**4**, leading to a 91% RCY (entries 7–9). Trapping efficiencies (TE) of [^{11}C]CO_2 during the optimization of [^{11}C]**4** were all greater than 90%.

5.4.3. Table 2. Radiochemical optimization

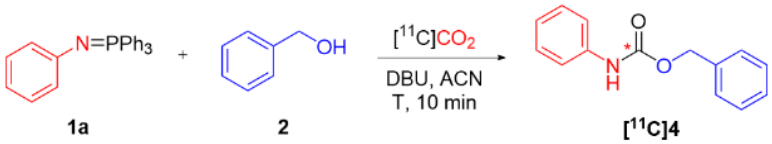

Entry	T (°C)	[**1a**] (mM)	[**2**] (mM)	[DBU] (mM)	RCY[a] (%)
1	65	7	200	200	13
2	65	70	200	200	32
3	65	100	200	200	29
4	65	70	200	150	39
5	65	70	200	100	56
6[b]	65	70	200	100	62
7[b]	100	70	200	100	65
8[b]	100	70	600	100	78
9[b]	100	70	1200	100	91

[a] Radiochemical yield calculated by relative integration of radioHPLC chromatograms, see ESI for details; average of n ≥ 2 except entry 9 which is n = 6; trapping efficiency ≥ 90%. [b] Reaction performed in DMF

Structurally diverse iminophosphoranes were also used to radiolabel compounds using this procedure (Scheme 3). Aniline derived products of **1a** include labeled urea [^{11}C]**30** in 88% RCY, and blocked isocyanate [^{11}C]**12** in 32% RCY. Using benzyl iminophosphorane, *O*-benzyl carbamate [^{11}C]**31** was formed in 64% yield. By substituting DABCO for DBU, *O*-aryl carbamate [^{11}C]**32** (26%), 5-methoxytryptamine carbamate [^{11}C]**33** (84%), and thiocarbamate [^{11}C]**34** (93%)

could be radiolabeled, with TE ranging from 53–83%. We suspect that mildly basic conditions and higher nucleophile concentrations improve the yields of **32-34** due to their sensitivity towards low temperature elimination.[22] From *tert*-butyl iminophosphorane, *N*-hydroxysuccinimide-derived [^{11}C]**23** (99%) was also efficiently radiolabeled.

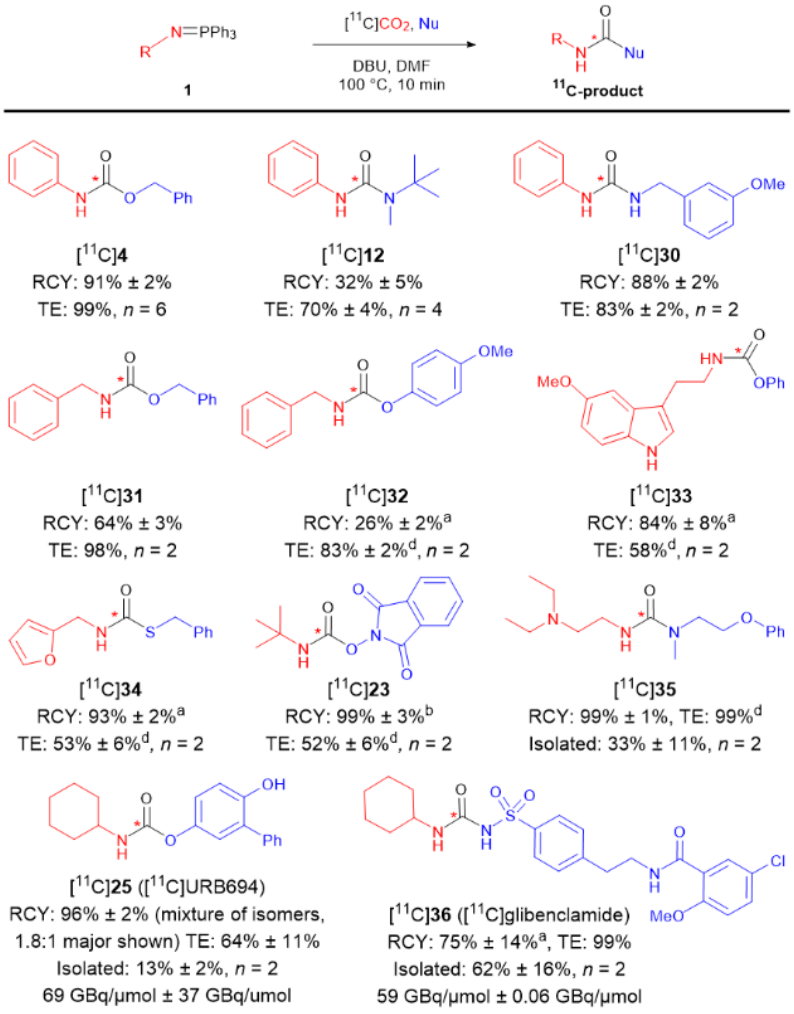

[a] DBU replaced with DABCO. [b] DBU replaced with LHMDS. [c] KO^{t}Bu [d] [^{11}C]CO_2 trapped at -60 °C. See ESI for detailed procedures. * indicates position of ^{11}C. TE = trapping efficiency; isolated RCY decay-corrected to end-of-synthesis

5.4.4. Scheme 3. Carbon-11 substrate scope.

To further demonstrate the practicality of this technique, [^{11}C]**35**, an experimental antiarrhythmic compound containing the β-glucocerebrosidase activating moiety *N*-methyl-*N*-(2-phenoxyethyl)amine, was isolated using a fully automated method (see ESI).[23,24] [^{11}C]**35** was labeled with 99% RCY starting from 15.7 GBq of [^{11}C]CO_2, and obtained in an isolated yield of 33% ± 10.6% (2.7 ± 0.4 GBq) within 22 min of [^{11}C]CO_2 delivery. The fatty acid amide hydrolase inhibitor [^{11}C]URB694 ([^{11}C]**25**, [^{11}C]CURB), used in clinical research to investigate psychiatric illnesses and alcohol use disorder, was prepared from cyclohexyliminophosphorane in 96% ± 2% RCY (2:3 regioselectivity).[25,26] From 25.9 GBq of [^{11}C]CO_2, 1.9 ± 0.7 GBq of [^{11}C]CURB was obtained as the major isomer in 99% radiochemical purity, with an isolated yield of 13% ± 2%, and molar activity of 69 ± 37 GBq·μmol^{-1} within 17 min from [^{11}C]CO_2 delivery. Lastly, the clinically approved sulfonylurea glibenclamide, currently used in the treatment of diabetes mellitus type 2 and shown to reduce tissue damage in preclinical models of CNS injuries, was synthesized with 75% ± 14% RCY.[27] [^{11}C]Glibenclamide ([^{11}C]**36**) is a substrate for organic anion-transporting polypeptide (OATP) transporter and can be used to study the integrity of the blood-brain barrier by non-invasive PET imaging.[28] This radiopharmaceutical, which has been synthesized in two-steps using [^{11}C]CH_3OTf,[29] was efficiently labeled using an iminophosphorane precursor directly from [^{11}C]CO_2. Following purification, 7.4 ± 1.9 GBq of [^{11}C]glibenclamide was obtained with an isolated yield of 62% ± 16% from 25.9 GBq of [^{11}C]CO_2, and a molar activity of 59 ± 0.06 GBq·μmol^{-1} within 21 minutes from the beginning of synthesis.

5.5. Conclusions

In conclusion, we have developed a methodology to synthesize several stable and radiolabeled functional groups using the interrupted aza-Wittig approach. The advantages of this method include direct [^{11}C]CO_2-fixation using stable iminophosphorane precursors prepared from available amines, diverse functional group selectivity, and applicability to PET imaging agents. Radiopharmaceuticals are synthesized under mild reaction conditions with rapid synthesis times and using automated procedures. We anticipate this method contributing to the accessibility of in-demand radiopharmaceuticals such as [^{11}C]CURB and [^{11}C]glibenclamide, among others.

5.6. Funding

Financial and infrastructure support for this work were provided by the University of Ottawa Heart Institute, NSERC (RGPIN-2017-06167), CFI (36848), and the Ontario Ministry for Research, Innovation and Science (ER17-13-119).

5.7. Acknowledgements

The authors are grateful to Marcelo Muñoz and Gapisha Karunakaran for the isolation of chemical standards and preparation of precursors.

5.8. References

1) Antoni, G. J. Labelled Compd. Radiopharm. **2015**, 58 (3), 65–72.

2) Rotstein, B.H.; Liang, S.H.; Placzek, M.S.; Hooker, J.M.; Gee, A.D.; Dollé, F.; Wilson, A.A.; Vasdev, N. *Chem. Soc. Rev.* **2016**, *45* (17), 4708–4726.

3) Långström, B.; Antoni, G.; Gullberg, P.; Halldin, C.; Malmborg, P.; Någren, K.; Rimland, A.; Svärd, H. *J. Nucl. Med.* **1987**, *28* (6), 1037–1040.

4) Larsen, P.; Ulin, J.; Dahlstrøm, K.; Jensen, M. *Appl. Radiat. and Isot.* **1997**, *48* (2), 153–157.

5) Link, J. M.; Krohn, K. A.; Clark, J. C. *Nucl. Med. Biol.* **1997**, *24* (1), 93–97.

6) Jewett, D.M. *Int. J. Rad. Appl. Instrum. A.* **1992**, *43* (11), 1383–1385.

7) Delebecq, E.; Pascault, J.-P.; Boutevin, B.; Ganachaud, F. *Chem. Rev.* **2013**, *113* (1), 80–118.

8) Ghosh, A. K.; Brindisi, M.; Sarkar, A. *ChemMedChem* **2018**, *13* (22), 2351–2373.

9) Wilson, A.A.; Garcia, A.; Houle, S.; Sadovski, O.; Vasdev, N. *Chem. Eur. J.* **2011**, *17* (1), 259–264.

10) Haji Dheere, A.K.; Yusuf, N.; Gee, A. *Chem. Commun.* **2013**, *49* (74), 8193–8195.

11) Bongarzone, S.; Runser, A.; Taddei, C.; Haji Dheere, A.K.; Gee, A.D. *Chem. Commun.* **2017**, *53* (38), 5334–5337.

12) Mair, B.A.; Fouad, M.H.; Ismailani, U.S.; Munch, M.; Rotstein, B.H. *Org. Lett.* **2020**, *22* (7), 2746–2750.

13) Saylik, D.; Horvath, M.J.; Elmes, P.S.; Jackson, W.R.; Lovel, C.G.; Moody, K. *J. Org. Chem.* **1999**, *64* (11), 3940–3946.

14) Molina, P.I.; Alajarin, M.; Arques, A. *Synthesis* **1982**, *1982* (7), 596–597.

15) van Tilburg, E.W.; Windhorst, A.D.; van der Mey, M.; Herscheid, J.D.M. *J. Labelled Compd. Radiopharm.* **2006**, *49* (4), 321–330.

16) Del Vecchio, A.; Caillé, F.; Chevalier, A.; Loreau, O.; Horkka, K.; Halldin, C.; Schou, M.; Camus, N.; Kessler, P.; Kuhnast, B.; Taran, F.; Audisio, D. *Angew. Chem. Int. Ed.* **2018**, *57* (31), 9744–9748.

17) Del Vecchio, A.; Talbot, A.; Caillé, F.; Chevalier, A.; Sallustrau, A.; Loreau, O.; Destro, G.; Taran, F.; Audisio, D. *Chem. Commun.* **2020**, *56* (78), 11677–11680.

18) Villiers, C.; Dognon, J.-P.; Pollet, R.; Thuéry, P.; Ephritikhine, M. *Angew. Chem. Int. Ed.* **2010**, *49* (20), 3465–3468.

19) Hulla, M.; Dyson, P.J. *Angew. Chem. Int. Ed.* **2020**, *59* (3), 1002–1017.

20) Rolph, M.S.; Markowska, A.L.J.; Warriner, C.N.; O'Reilly, R.K. *Polym. Chem.* **2016**, *7* (48), 7351–7364.

21) Hutchby, M.; Houlden, C.E.; Ford, J.G.; Tyler, S.N.G.; Gagné, M.R.; Lloyd-Jones, G.C.; Booker-Milburn, K.I. *Angew. Chem. Int. Ed. Engl.* **2009**, *48* (46), 8721–8724.

22) Derasp, J.S.; Beauchemin, A.M. *ACS Catal.* **2019**, *9* (9), 8104–8109.

23) Zheng, J.; Jeon, S.; Jiang, W.; Burbulla, L.F.; Ysselstein, D.; Oevel, K.; Krainc, D.; Silverman, R.B. *J. Med. Chem.* **2019**, *62* (3), 1218–1230.

24) Shanklin, Jr., J.R.; Johnson, III, C.P. US4500529A, February 19, 1985.

25) Wilson, A.A.; Garcia, A.; Parkes, J.; Houle, S.; Tong, J.; Vasdev, N. *Nucl. Med. Biol.* **2011**, *38* (2), 247–253.

26) Best, L.M.; Williams, B.; Le Foll, B.; Mansouri, E.; Bazinet, R.P.; Lin, L.; De Luca, V.; Lagzdins, D.; Rusjan, P.; Tyndale, R.F.; Wilson, A.A.; Hendershot, C.S.; Heilig, M.; Houle, S.; Tong, J.; Kish, S.J.; Boileau, I. *Neuropsychopharmacology* **2020**, 1–8.

27) Kurland, D.B.; Tosun, C.; Pampori, A.; Karimy, J.K.; Caffes, N.M.; Gerzanich, V.; Simard, J.M. *Pharmaceuticals* **2013**, *6* (10), 1287–1303.

28) Tournier, N.; Saba, W.; Cisternino, S.; Peyronneau, M.-A.; Damont, A.; Goutal, S.; Dubois, A.; Dollé, F.; Scherrmann, J.-M.; Valette, H.; Kuhnast, B.; Bottlaender, M. *AAPS J.* **2013**, *15* (4), 1082–1090.

29) Caillé, F.; Gervais, P.; Auvity, S.; Coulon, C.; Marie, S.; Tournier, N.; Kuhnast, B. *Nucl. Med. Biol.* **2020**, *84–85*, 20–27.

5.9. Supplementary information

5.9.1. Section 1: General Information

All chemicals and solvents used were purchased and were not further purified unless indicated otherwise. All CO_2 fixation reactions were carried out by bubbling CO_2 (balloon) through the solution. CO_2 was passed through a tube filled with Drierite to obtain anhydrous CO_2. All other reactions were routinely carried out under inert (argon or nitrogen) atmosphere. All solvents used were anhydrous. Anhydrous 1,8-diazabicyclo[5.4.0]undec-7-ene (DBU) was obtained by reflux over KOH pellets, and distillation under reduced pressure. Reaction products were confirmed using ^{1}H-NMR, ^{13}C-NMR, and mass spectrometry. Purification of reaction products was carried out by flash column chromatography using silica gel unless stated otherwise. Analytical thin layer chromatography (TLC) was performed on aluminum or glass backing. ^{1}H-NMR spectra were obtained using a Bruker AVANCE 300 or a Bruker AVANCE 400. Spectral data are reported in ppm using solvent as the reference (for ^{1}H NMR $CHCl_3$ at 7.26 ppm and DMSO at 2.50 ppm). ^{1}H NMR data was reported as: multiplicity (ap = apparent, br = broad, s = singlet, d = doublet, t = triplet, q = quartet, m = multiplet), integration, and coupling constant(s) in Hz. Low resolution mass spectrometry was performed using Waters Xevo TQD with an Acquity UPLC H-Class Plus system. High resolution mass spectrometry was performed using a Kratos Concept – Magnetic Sector Electron Impact Mass Spectrometer. Radiochemical chromatograms were acquired using a Waters 2695 Alliance HPLC equipped with a Phenomenex Luna 10 μm C18(2) 100 Å column (250 x 4.6 mm, 10 μm), a Waters 996 photodiode array detector, and a Carroll & Ramsey Associates 105-S high-sensitivity radiation detector equipped with a 1 cm^3

CsI(Tl) scintillating crystal. Radiolabeled products were synthesized using Synthra MeIplus Research module. Known products generated were characterized in accordance with the literature.

Sigma-Aldrich: *N*-(triphenylphosphoranylidene)aniline; triphenylphosphine dibromide; benzyl alcohol; 2-tert-butylimino-2-diethylamino-1.3-dimethylperhydro-1,3,2-diazaphosphorine; 2-propanol; thiophenol; phenol; diethyl malonate; 4-bromoaniline; 4-fluoroaniline; furfurylamine; methylmagnesium bromide solution (3.0 M in diethyl ether); phenylmagnesium bromide solution (3.0 M in diethyl ether); benzylamine; *N*-methyl-2-phenoxyethanamine; phenylacetylene; 2-phenyl hydroquinone; phenylisocyanate; 5-chloro-2-methoxy-*N*-[2-(4-sulfamoylphenyl)ethyl]benzamide; *N*-butyllithium solution (1.6 M) in hexanes

Oakwood Chemical: 1,8-diazabicyclo[5.4.0]undec-7-ene; 2-(4-methoxyphenyl)ethanol; 4-nitroaniline; cyclohexylamine; *tert*-butylamine; triethylamine; 3-methoxybenzylamine; 1,2,4-triazole-3-thiol

Alfa Aesar: benzyl mercaptan; *tert*-butyl alcohol; *N*-*tert*-butylmethylamine; *p*-anisidine; *o*-toluidine; 4-fluorobenzylamine; 3-chloro-4-(trifluoromethyl)aniline; 4-(4-amine-3-fluorophenoxy)-*N*-methylpicolinamide; *N*-hydroxypthalamide

Acros Organics: 5-methoxytryptamine; L-phenylalanine methyl ester hydrochloride; *N*,*N*-diethylethylenediamine; 2-naphthalenethiol

Tokyo Chemical Company: glibenclamide

5.9.2. Section 2: Synthetic Procedures

5.9.2.1. Synthesis of iminophosphoranes

A flame dried flask was equipped with a magnetic stir bar and charged with triphenylphosphine dibromide (0.6 mmol) dissolved in DCM (2.0 mL) under inert atmosphere. The flask was placed in an ice bath, and a solution containing the corresponding amine (0.6 mmol) and triethylamine (0.6 mmol) in DCM (2 mL) was added to the reactor in a dropwise manner over 10 minutes. The reaction was stirred at room temperature for 4 hours. The solvent was removed under reduced pressure, and anhydrous THF (10 mL) was added to the residue. The solution was filtered through a Celite plug, and the concentrated under reduced pressure. A sufficient volume of chloroform was added to solubilize the residue, and hexane was added to precipitate the product. The product was re-precipitated five or more times to remove unwanted triphenylphosphine oxide (TPPO).

Note: Amine hydrochlorides (0.6 mmol) were first dissolved in DCM (2.0 mL) and 1.1 equiv. of triethylamine was added. After stirring the reaction medium at room temperature for 30 min, ammonium salts were removed by adding Et_2O followed by filtration over a celite pad. Solvents were removed by rotary evaporation under reduced pressure and the afforded free amines were used without further purification.

5.9.2.2. Synthesis of carbamate and thiocarbamate products.

A flame dried flask was charged with the corresponding nucleophile (0.25 mmol), DBU (0.65 mmol), and ACN (2.5 mL). The mixture was brought to reflux, and CO_2 was bubbled through the solution for 10 minutes, prior to the addition of iminophosphorane (IMP). A solution containing IMP (0.25 mmol) in ACN (2 mL) was added dropwise over one hour to the reaction mixture. CO_2 was bubbled continuously throughout the reaction until completion. The contents of

the flask were concentrated under reduced pressure and re-suspended in 5 mL of DCM. The solution was extracted with saturated aqueous NH_4Cl (3 × 10 mL) and dried over magnesium sulfate. The solvent was removed under reduced pressure and purified by flash column chromatography using a 0-25% hexane/ethyl acetate gradient.

Note: Blocked isocyanate products (**7–9, 11–12**) and products of alkyl iminophosphoranes (**22–23, 25**) use 2.5 mmol of nucleophile (10 equiv.) and are not subjected to solvent-solvent extraction unless mentioned otherwise. The concentrated residue is immediately purified by flash column chromatography using a 0-25% hexane/ethyl acetate gradient.

5.9.2.3. Synthesis of urea products

A flame dried flask was charged with an amine nucleophile (0.50 mmol), DBU (0.25 mmol), and ACN (2.5 mL). CO_2 was bubbled through this solution for 10 minutes, followed by the addition of a solution containing iminophosphorane (0.25 mmol) in ACN (2 mL), added dropwise over 20 minutes at room temperature. The contents of the flask were concentrated under reduced pressure and purified by flash chromatography using a 0-25% hexane/ethyl acetate gradient.

5.9.2.4. Synthesis of amides using Grignard reagents via blocked isocyanate intermediates.

A flame dried round bottom flask was charged with the corresponding blocking nucleophile (2.5 mmol), DBU (0.65 mmol), and THF (2.5 mL). The mixture was brought to reflux, and CO_2 was bubbled through the solution for 10 minutes. A solution containing IMP (0.25 mmol) in THF (2 mL) was added dropwise over one hour to the reaction mixture. CO_2 was bubbled continuously throughout the reaction until completion. The reaction solution was sparged with argon for five minutes and added dropwise to a cooled flask containing Grignard (5 mmol) dissolved in THF (2 mL). The reaction was left to stir overnight and quenched with methanol (15 mL). The contents of

the flask were concentrated under reduced pressure, re-suspended in DCM, and extracted with saturated aqueous NH_4Cl (3 × 20 mL), water (3 × 15 mL) and brine (3 × 15 mL) and dried over magnesium sulfate. The solvent was removed under reduced pressure and purified by flash column chromatography using a 0-25% hexane/ethyl acetate gradient.

5.9.2.5. Synthesis of amides using phenylacetylene

A flame dried round bottom flask was charged with phenylacetylene (2.5 mmol) dissolved in THF (5 mL) and cooled to -78 °C. n-Butyllithium (2.45 mmol) was added dropwise to the solution. The solution was left to stir for 2 hrs. The reaction was brought to room temperature, and the contents of this flask were added dropwise to a separate flask containing the prepared blocked isocyanate using procedure **4**. The reaction was left to stir at room temperature for 2 hours. The contents of the flask were concentrated under reduced pressure, resuspended in DCM (5 mL), and extracted with saturated aqueous ammonium chloride (3 × 15mL), water (3 × 15 mL), brine (1 × 15 mL) and dried over magnesium sulfate. The product was purified by flash chromatography using a hexane/ethyl acetate gradient.

5.9.2.6. Synthesis of amides using diethyl malonate

A flame dried round bottom flask was charged with diethylmalonate (10 mmol) and dissolved in THF (5 mL). The flask was cooled to -78 °C, and LHMDS (2.45 mmol) was added dropwise. The reaction was left to stir for 2 h. The solution was brought to room temperature, and 1.25 mL of the solution was added to a separate flask that was charged with DBU (0.65 mmol) and THF (1.25 mL). The reaction was heated to reflux, and CO_2 was bubbled into the reaction for 5 minutes. A solution of IMP (0.25 mmol) in THF (2 mL) was added dropwise to the reaction mixture over 1 hr. CO_2 was bubbled continuously into the reaction until completion. The contents of the flask

were concentrated under reduced pressure and purified by flash column chromatography using a 0-25% hexane/ethyl acetate gradient.

5.9.2.7. Deprotonation of alkyl iminophosphorane salts

The iminophosphorane salt (0.25 mmol) was added to a 5-mL flame dried round bottom flask and dissolved in THF (2.5 mL). The flask was cooled to 0 °C using an ice-water bath, and KHMDS was added to the solution (0.245 mmol). The reaction was left to stir for 5 minutes and brought to room temperature for use.

5.9.2.8. Synthesis of carbon-11 radiolabeled products

Using the Synthra MeIplus Research module (Figure S1), 400 µL of a DMF solution containing iminophosphorane (28.29 µmol), DBU (40 µmol), and nucleophile (483 µmol) were loaded into reactor 1. DMF or ACN (1 mL) was loaded into vial A1. Carbon-11 (CO_2) ($[^{11}C]CO_2$), generated by the bombardment of a gas target filled with pressurized N_2/O_2 mixture using a Siemens 11 MeV cyclotron, at 55 µA for 2 minutes, and was directed to a steel coil cooled at -180 °C. The coil was briefly flushed with $He_{(g)}$ prior to heating to 25 °C. $[^{11}C]CO_2$ was bubbled into the reactor (at room temperature unless otherwise stated) at 5 mL/min. The reactor was then heated to 100 °C for 10 minutes, and solvent from vial A1 was added to the reactor to dilute the mixture. The solution was transferred to a glass vial and analyzed by radioHPLC. Integration of radiation detector chromatograms on analytical HPLC informed radiochemical yields, and products were identified by co-injection of nonradioactive standards. Isolated yields were determined by decay correcting the activity to the end of synthesis (EoS). Analytical HPLC conditions for radiolabeled products (unless otherwise stated): flowrate of 1 mL/min; 50% ACN / 50% 0.1 M AMF for 2 minutes, then gradient to 95% ACN / 5% 0.1 M AMF until 10 minutes, 95% ACN / 5% 0.1 M AMF until 12

minutes, return to 50% ACN / 50% 0.1 M AMF until 13 minutes, then 2 minutes at 50% ACN / 50% 0.1 M AMF.

5.9.2.9. Radiosynthesis of [^{11}C]35

A solution of iminophosphorane **1o** (2.19 µmol in 200 µL of DMF) was prepared, and DBU (2.18 µmol) was added ten minutes prior to end-of-bombardment. The solution of iminophosphorane and a solution of *N*-methyl-2-phenoxyethanamine (0.12 mmol in 200 µmL of DMF) were loaded into the reaction vessel and tightly sealed two minutes prior to end-of-bombardment. [^{11}C]CO_2 was trapped at -180 ˚C. The trap was heated to 25 ˚C, and [^{11}C]CO_2 was released under a stream of helium at 3 mL/min to bubble into the reaction vessel until peak activity. The reactor was heated to 100 ˚C for 1 min and quenched with 800 µL of H_2O. The solution was injected onto an HPLC column for purification. HPLC conditions: Nucleodur C18 Pyramid 7 µm, 250 × 10 mm eluted with 30% ACN/70% 0.1 M AMF at 5 mL/min. The product was collected, and the identity was established by co-injection with the non-radioactive standard using an analytical HPLC.

5.9.2.10. Radiosynthesis of [^{11}C]25b ([^{11}C]URB694)

DMF was degassed using five freeze-thaw cycles prior to use. 2-Phenyl-1,4-dihydroquinone was purified by flash column chromatography (0-25% hexanes/ethyl acetate) on the day of use. A solution of iminophosphorane **1g** (2.27 µmol in 100 µL of DMF, 0.01 mg/µL) was prepared, and DBU (2.27 µmol) was added two minutes prior to end-of-bombardment. The solution was mixed under argon for one minute, and 25 µL of this solution was added to a vial containing 2-phenyl-1,4-dihydroquinone (80.5 µmol) in 125 µL of DMF. This precursor solution was loaded into the reaction vessel and tightly sealed. A stream of helium was swept through the reaction vessel after loading. [^{11}C]CO_2 was trapped at -180 ˚C. The trap was heated to 25 ˚C, and [^{11}C]CO_2 was released

under a stream of helium at 3 mL/min to bubble into the reaction vessel until peak activity. The reactor was heated to 100 ˚C for 2 min and quenched with 800 µL of mobile phase. The solution was injected onto an HPLC column for purification. HPLC conditions: Nucleodur C18 Pyramid 7 µm, 250 × 10 mm eluted with 70% MeOH/30% H_2O containing 1% formic acid at 7 mL/min. The product was collected, and the identity was established by co-injection with the cold standard using an analytical HPLC.

5.9.2.11. Radiosynthesis pf [^{11}C]36 ([^{11}C]Glibenclamide)

DMF was degassed using five freeze-thaw cycles prior to use. A solution of iminophosphorane **1g** (2.27 µmol in 100 µL of DMF) was prepared, and 27.5 µL of DABCO (1.22 µmol, 0.02 mg/µl solution in DMF) was added two minutes prior to the end-of-bombardment. The solution was stirred for 30 seconds, and 25 µL of this solution was added to the reactor. 5-Chloro-2-methoxy-*N*-[2-(4-sulfamoylphenyl)ethyl]benzamide (40.66 µmol) was dissolved in 125 µL of DMF and added to a Teflon sealed vial under inert atmosphere containing potassium *tert*-butoxide (40 µmol), also mixed 2 minutes prior to the end-of-bombardment. The solution was loaded into the reaction vessel and tightly sealed. A stream of helium was swept through the reaction vessel after loading. [^{11}C]CO_2 was trapped at -180 ˚C. The trap was heated to 25 ˚C, and [^{11}C]CO_2 was released under a stream of helium at 3 mL/min to bubble into the reaction vessel until peak activity. The reactor was heated to 100 ˚C for 2 min and quenched with 800 µL of mobile phase. The solution was injected onto an HPLC column for purification. HPLC conditions: Nucleodur C18 Pyramid 7 µm, 250 × 10 mm eluted with 55% ACN/45% H_2O containing 0.1% TFA at 5 mL/min for 10 minutes, then switched to 75% ACN/25% H_2O + 0.1% TFA for 3 minutes. The product was collected, and the identity was established by co-injection with the cold standard using an analytical HPLC.

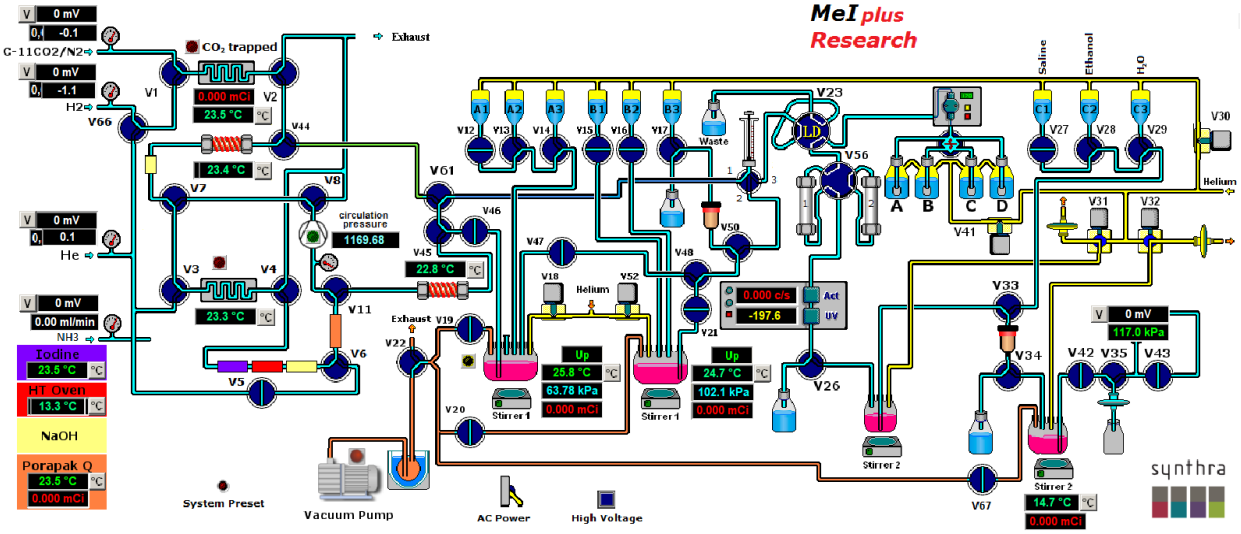

5.9.2.12. Figure S1. Synthra MeIplus Research apparatus scheme.

5.9.3. Section 3: Experimental Data

5.9.3.1. 1b. 4-methoxy-*N*-(triphenylphosphanylidene)anilinium bromide

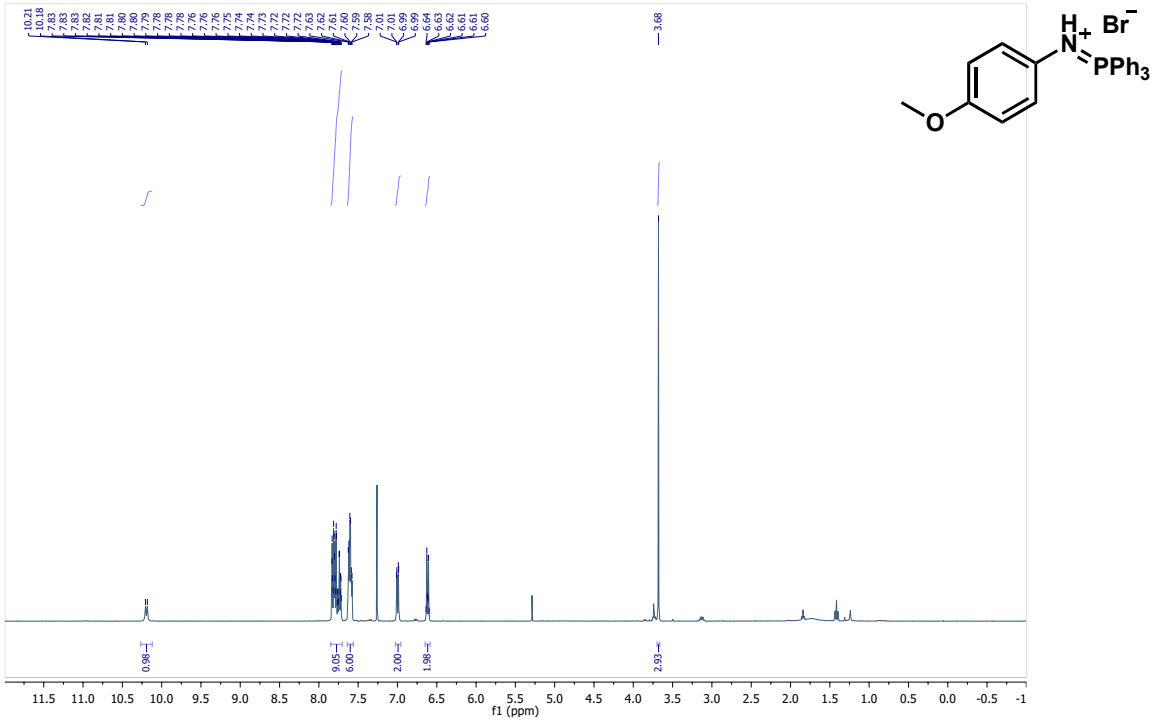

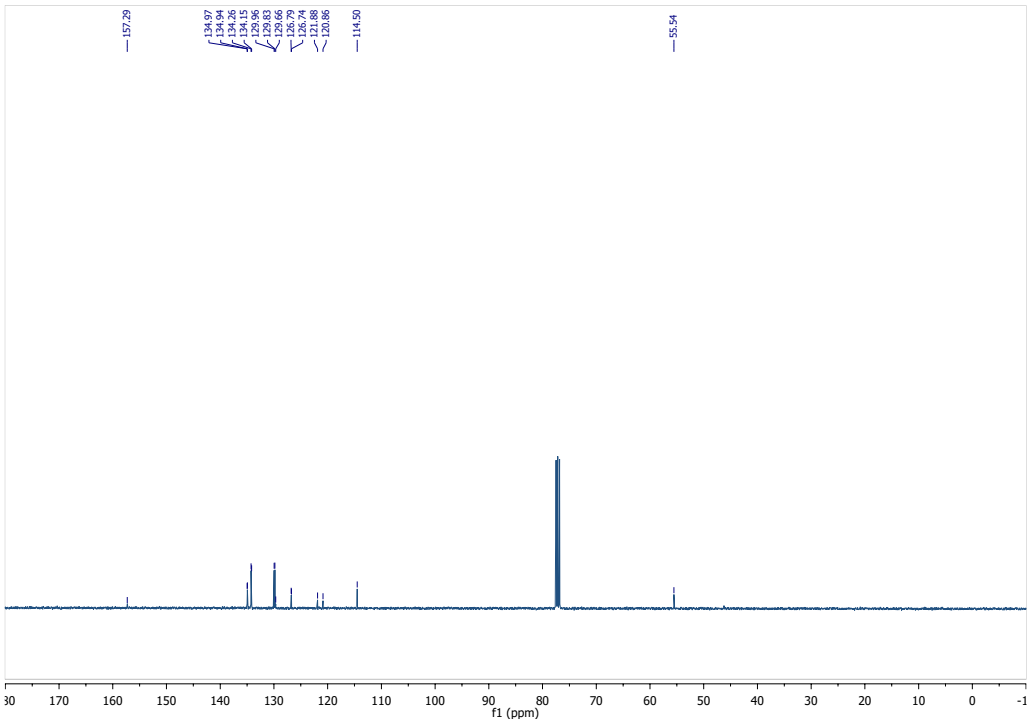
157.29
134.97
134.94
134.26
134.15
129.96
129.83
129.66
126.79
126.74
121.88
120.86
114.50
55.54
170
160
150
140
130
120
110
100
90
80
70
60
50
40
30
20
10
0
f1 (ppm)

5.9.3.2. 1c. 4-bromo-*N*-(triphenylphosphanylidene)anilinium bromide

Followed the general procedure (**1**), product obtained as a white solid (209 mg, yield 68%). ^{1}H-NMR (400 MHz, $CDCl_3$): δ 10.65 (d, *J* = 8.5 Hz, 1H), 7.86–7.75 (m, 9H), 7.66–7.61 (m, 6 H), 7.20 (d, *J* = 8 Hz, 2H), 7.06 (d, *J* = 8 Hz, 2H). ^{13}C-NMR (100 MHz, $CDCl_3$): 137.3, 135.3 (d, *J* = 3 Hz), 134.1 (d, *J* = 11 Hz), 132.2, 130.1 (d, *J* = 14 Hz), 124.8 (d, *J* = 7 Hz), 120.5 (d, *J* = 103 Hz), 117.7. ^{31}P-NMR (162 MHz, $CDCl_3$): δ 32.99 (s, 1P), 29.24 (s, 1P, TPPO). MS (ESI+): Calculated $C_{24}H_{20}NBrP$ as 432.0517, [M+H] found as 432.0504.

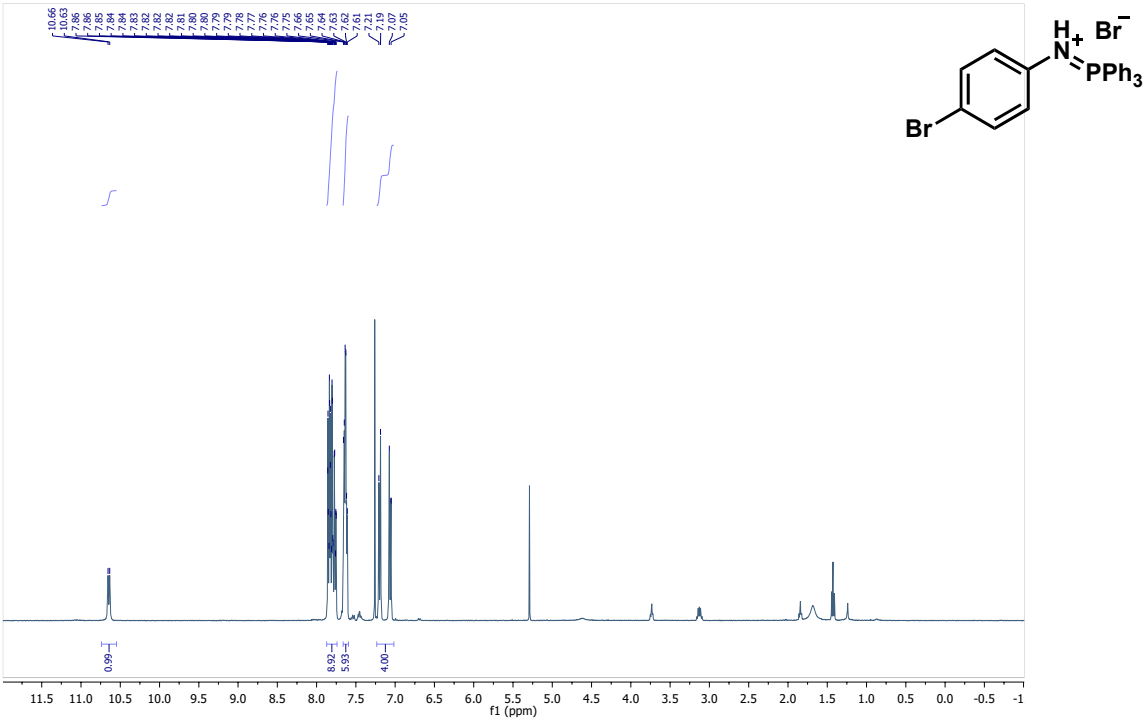

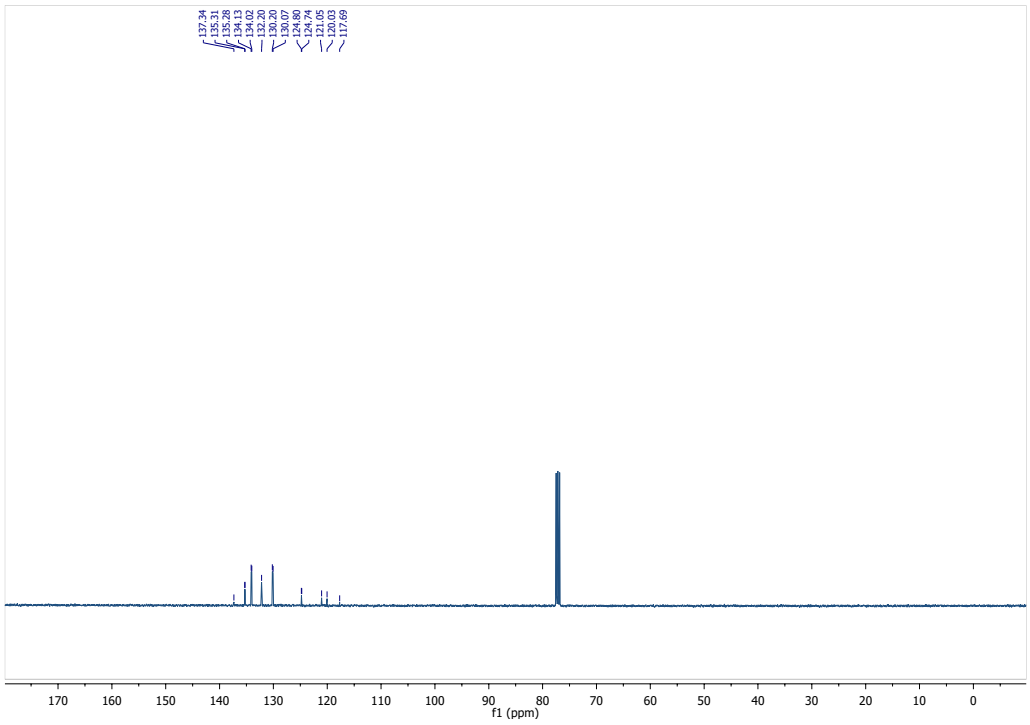
137.34
135.31
135.28
134.13
134.02
132.20
130.70
130.07
124.80
124.74
121.05
120.03
117.69
170 160 150 140 130 120 110 100 90 80 70 60 50 40 30 20 10 0
f1 (ppm)

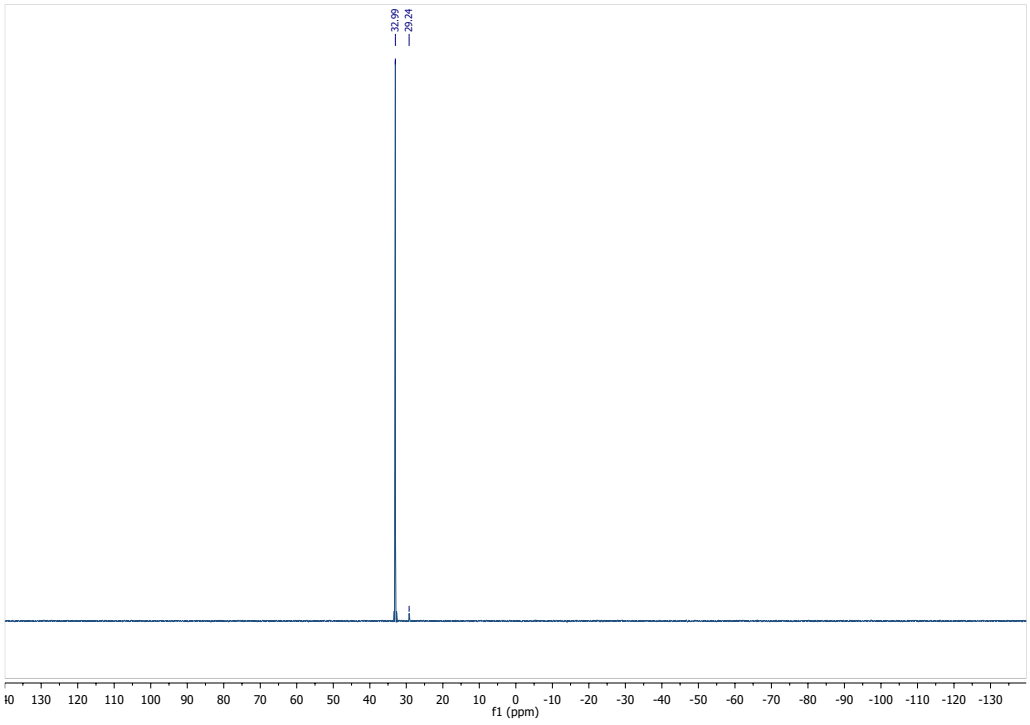
32.99
29.24
130 120 110 100 90 80 70 60 50 40 30 20 10 0 -10 -20 -30 -40 -50 -60 -70 -80 -90 -100 -110 -120 -130
f1 (ppm)

5.9.3.3. 1d. 4-fluoro-*N*-(triphenylphoshanylidene)anilinium bromide

Followed the general procedure (**1**), product obtained as an off-white solid (44 mg, yield 17%). ^{1}H-NMR (400 MHz, $CDCl_3$): δ 7.79 (m, 6H), 7.69 (m, 3H), 7.57 (m, 6H), 6.97 (m, 2H), 6.75 (m, 2H). ^{13}C-NMR (100 MHz, $CDCl_3$): 159.0 (d, *J* = 242 Hz), 134.3 (d, *J* = 3 Hz), 133.7 (d, *J* = 11 Hz), 132.2 (d, *J* = 10 Hz), 129.7 (d, *J* = 13 Hz), 125.5 (dd, *J* = 9, 8 Hz), 123.6 (d, *J* = 101 Hz), 115.7 (d, *J* = 22 Hz). ^{31}P-NMR (162 MHz, $CDCl_3$): δ 34.32 (s, 1P). ^{19}F-NMR (376 MHz, $CDCl_3$): -113.46 (s, 1F, amine), -117.38 (s, 1F). MS (ESI+): Calculated $C_{24}H_{20}NFP$ as 372.1317, [M+H] found as 372.1307.

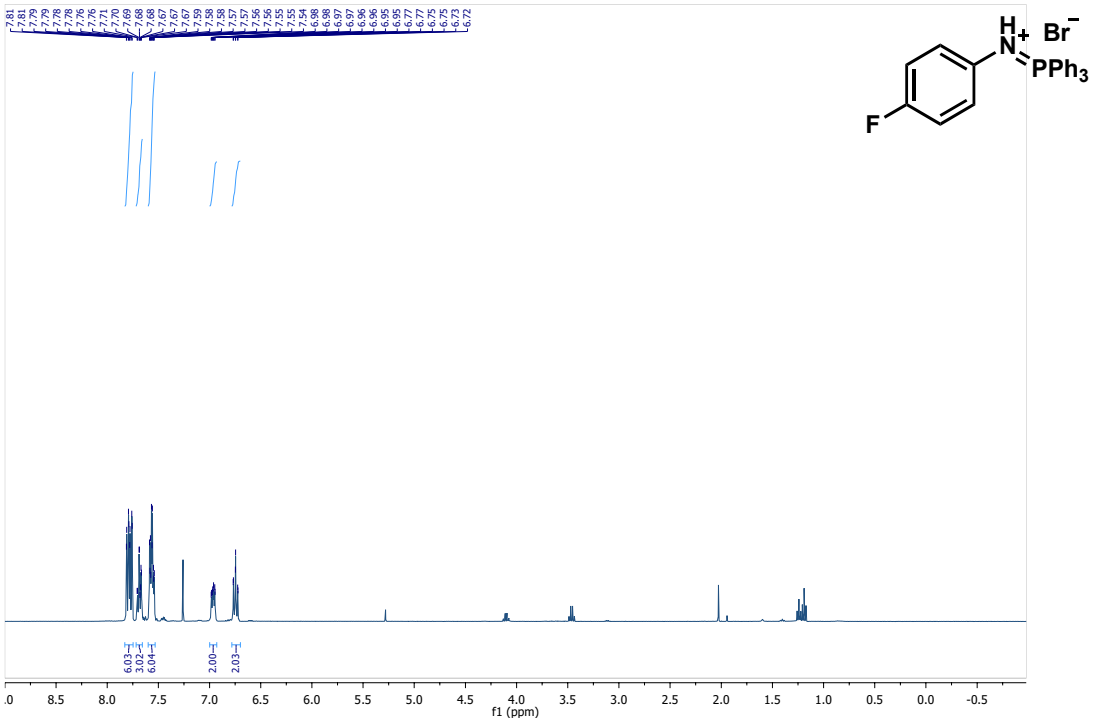

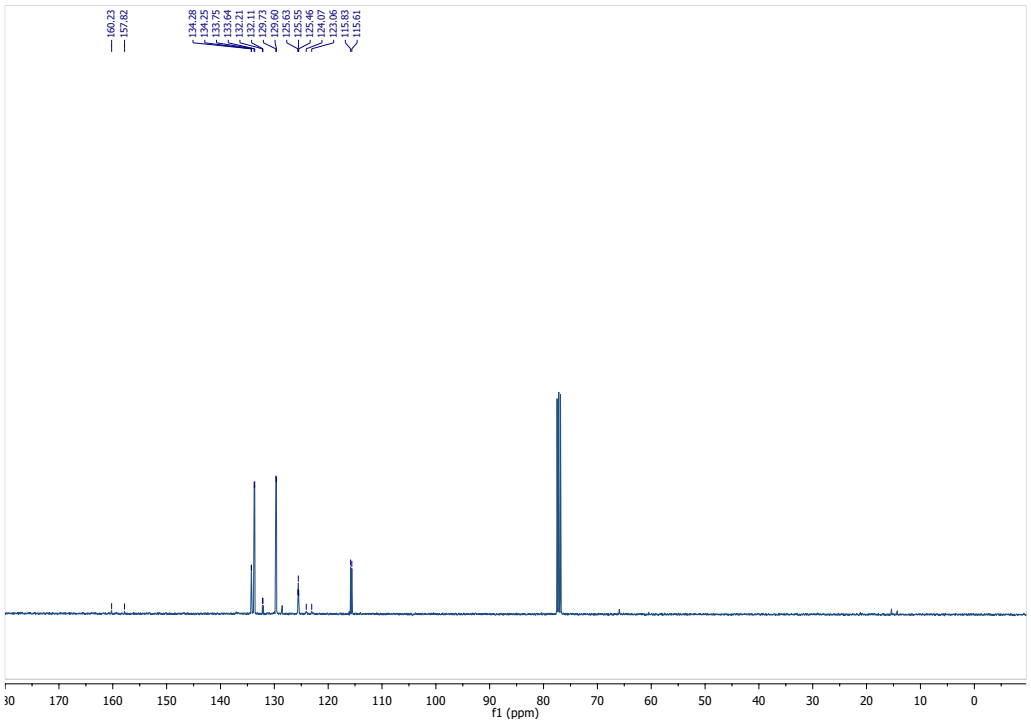
160.23
157.82
134.28
134.25
133.75
133.64
132.21
132.11
129.73
129.60
125.63
125.55
125.46
124.07
123.06
115.83
115.61
f1 (ppm)

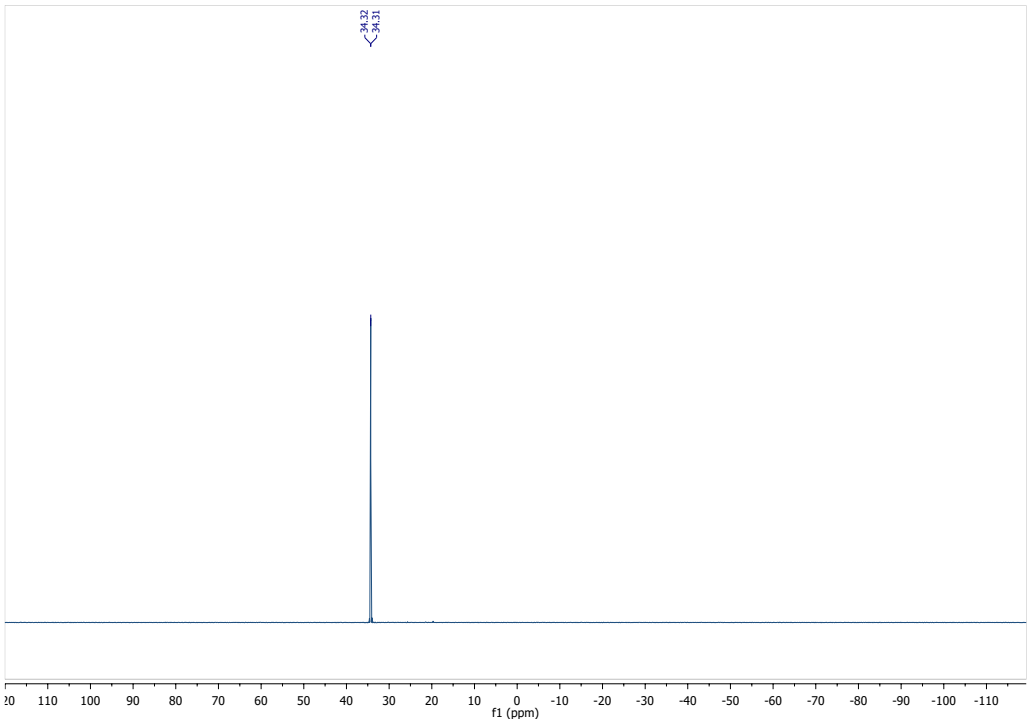
34.32
34.31
f1 (ppm)

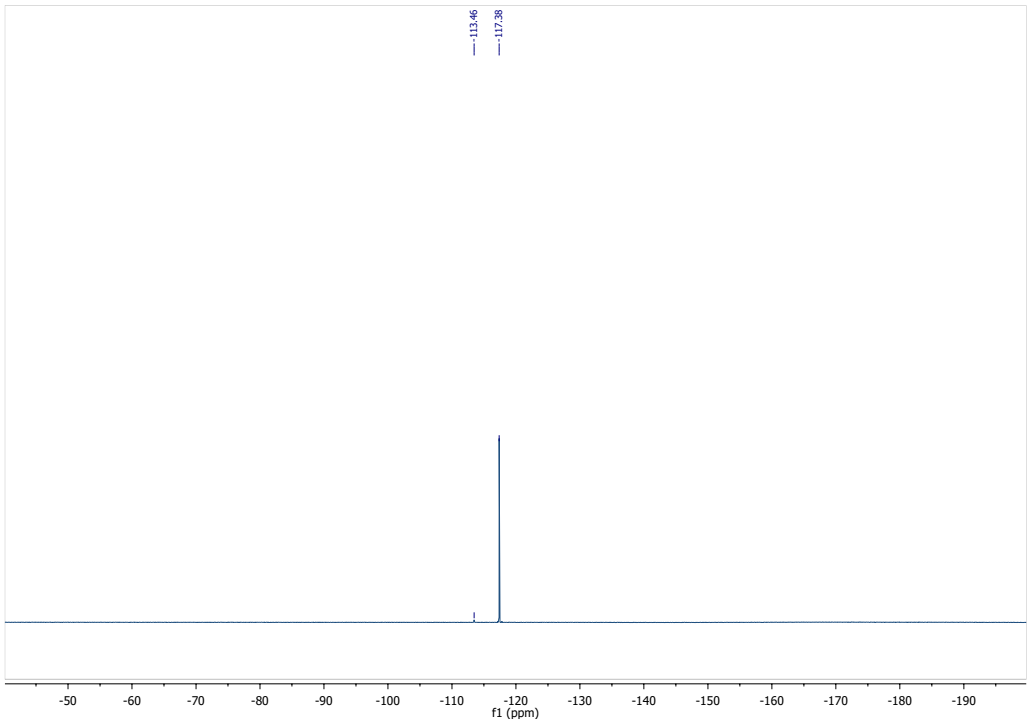
113.46
117.38
-50
-60
-70
-80
-90
-100
-110
-120
-130
-140
-150
-160
-170
-180
-190
f1 (ppm)

5.9.3.4. 1e. 4-nitro-*N*-(triphenylphosphanylidene)anilinium bromide

Followed the general procedure (**1**), product obtained as a yellow solid (230 mg, yield 80%). ^{1}H-NMR (400 MHz, $CDCl_3$): δ 7.95 (d, *J* = 12 Hz, 2H), 7.85–7.74 (m, 9H), 7.63 (m, 6H), 7.23 (s, 2H). ^{13}C-NMR (100 MHz, $CDCl_3$): 135.0, 133.6 (d, *J* = 11 Hz), 132.2 (d, *J* = 10 Hz), 132.1 (d, *J* = 3 Hz), 130.1 (d, *J* = 13 Hz), 128.6 (d, *J* = 12 Hz), 125.1, 121.4 (d, *J* = 10 Hz). ^{31}P-NMR (162 MHz, $CDCl_3$): δ 30.38 (s, 1P), 29.21 (s, 1P, TPPO). MS (ESI+): Calculated $C_{24}H_{20}N_2O_2P$ as 399.1262, [M+H] found as 399.1248.

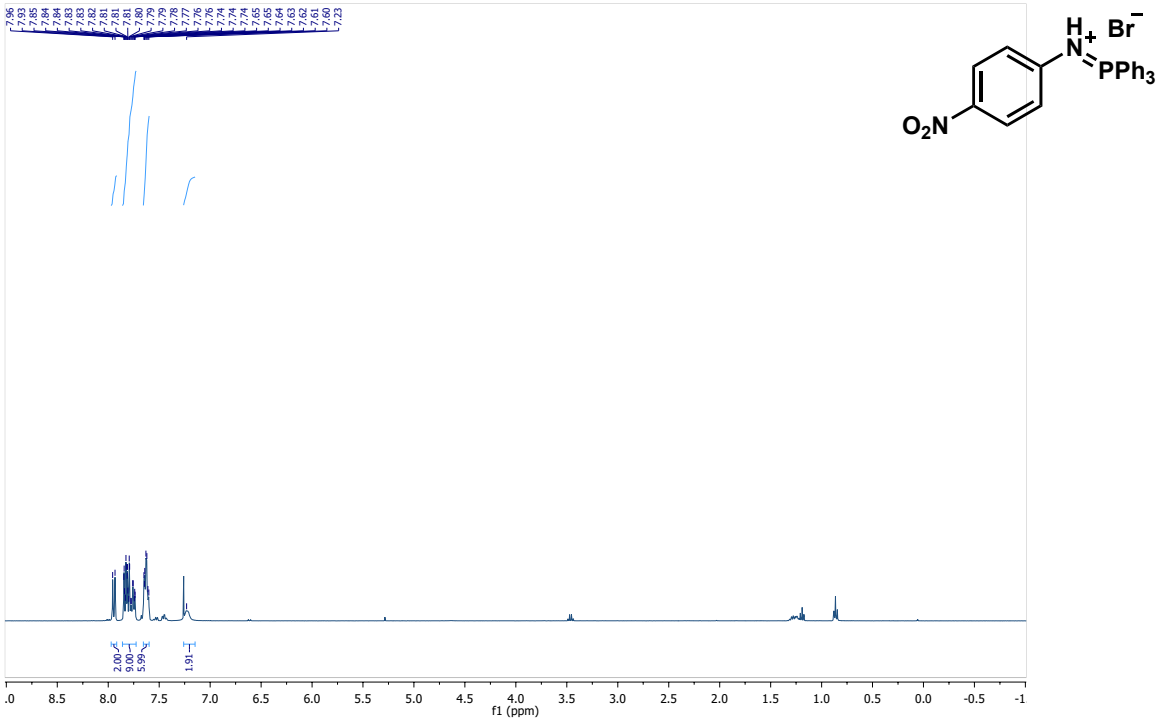

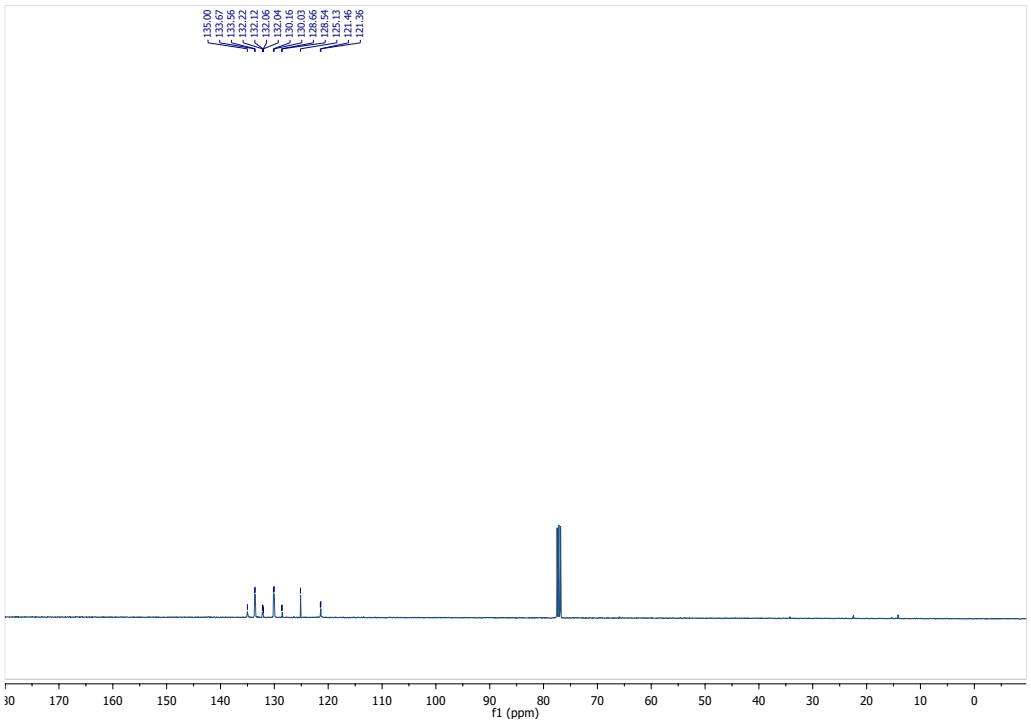
135.00
133.67
133.55
132.22
132.12
132.06
132.04
130.16
130.03
128.66
128.54
125.13
121.46
121.36
f1 (ppm)

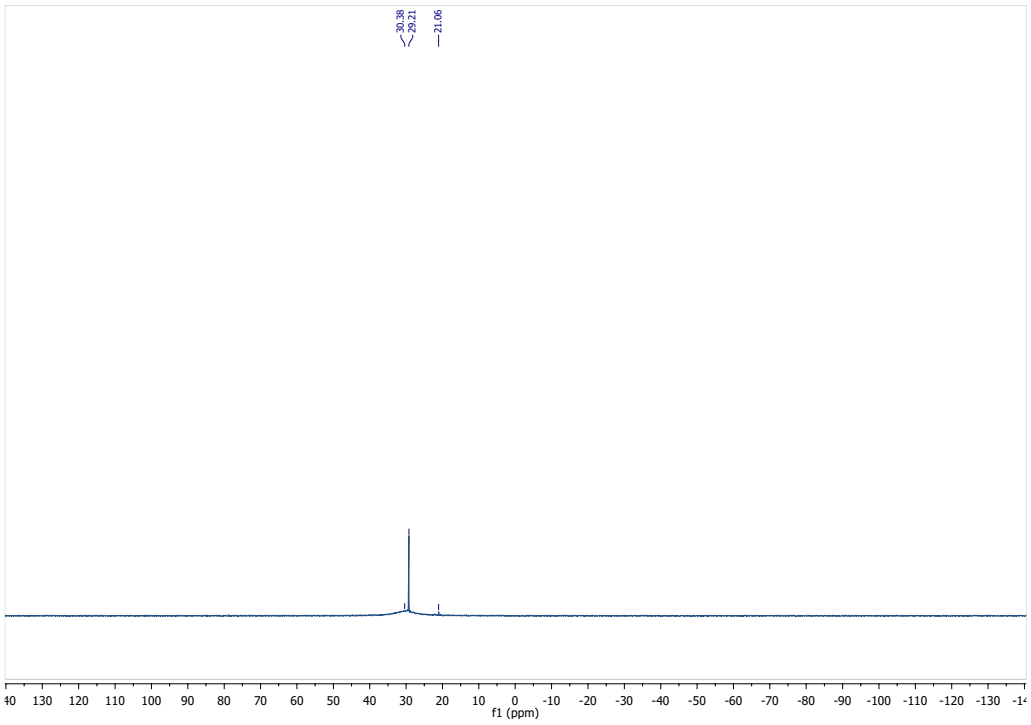
30.38
29.21
21.06
f1 (ppm)

5.9.3.5. 1f. 2-methyl-*N*-(triphenylphosphanylidene)anilinium bromide

Followed the general procedure (**1**), product obtained as a white solid (76 mg, yield 28%). ^{1}H-NMR (400 MHz, $CDCl_3$): δ 10.11 (s, 1H), 7.80–7.58 (m, 9H), 7.59–7.54 (m, 6H), 7.04–6.98 (m, 2H), 6.89 (d, *J* = 1.5 Hz, 1H), 6.88 (d, J = 1.5 Hz, 1H), 2.18 (s, 3H). ^{13}C-NMR (100 MHz, $CDCl_3$): 137.4 (d, *J* = 6 Hz), 134.8 (d, *J* = 3 Hz), 134.1 (d, *J* = 11 Hz), 131.3, 129.7 (d, *J* = 13 Hz), 127.7 (d, *J* = 138 Hz), 126.5, 122.1 (d, *J* = 104 Hz), 19.2. ^{31}P-NMR (162 MHz, $CDCl_3$): δ 34.87 (s, 1P), 29.24 (s, 1P, TPPO). MS (ESI+): Calculated $C_{25}H_{23}NP$ as 368.1568, [M+H] found as 368.1555.

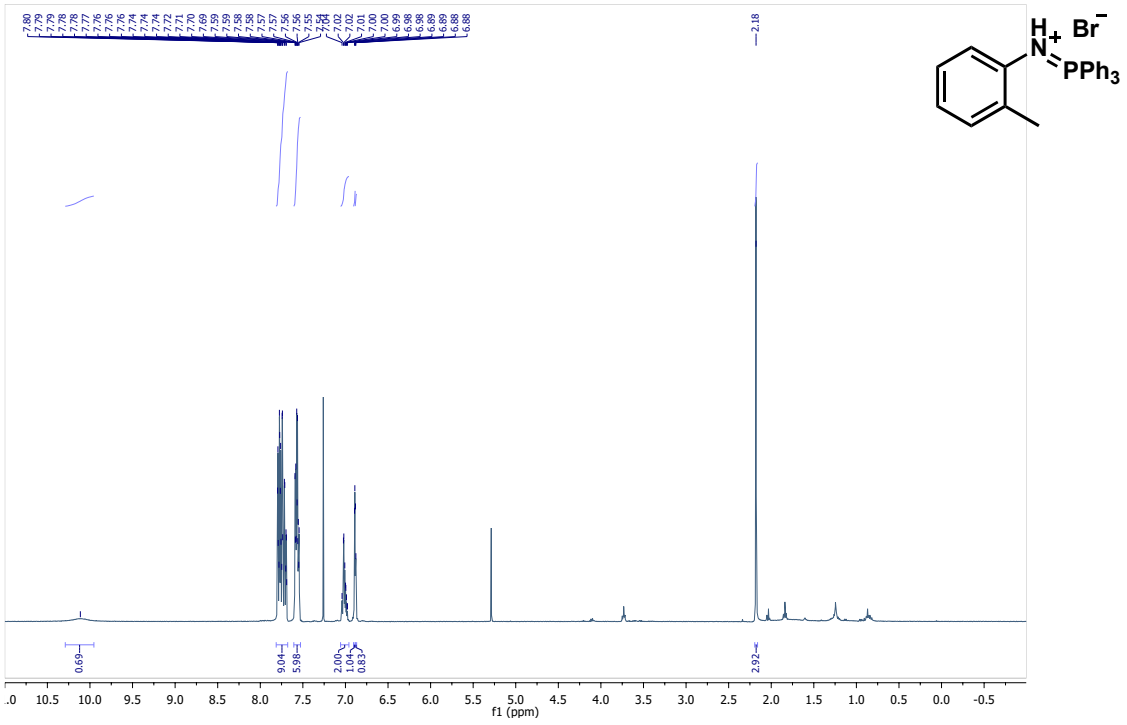

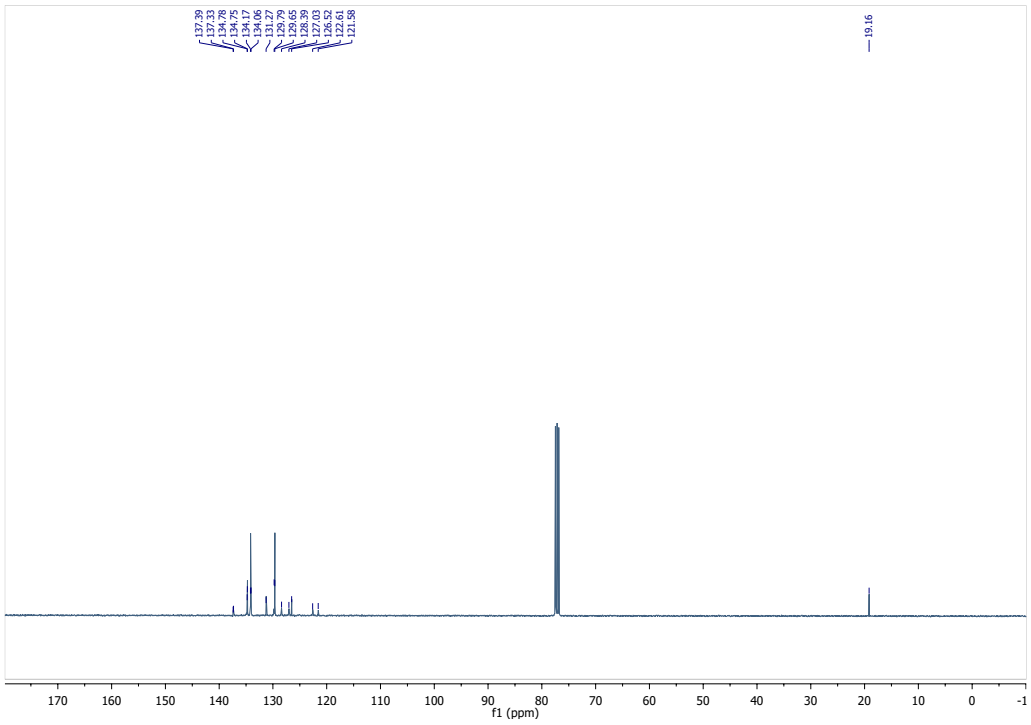
137.39
137.33
134.78
134.75
134.17
134.06
131.27
129.79
129.65
128.39
127.03
126.52
122.61
121.58
19.16
170 160 150 140 130 120 110 100 90 80 70 60 50 40 30 20 10 0 -1
f1 (ppm)

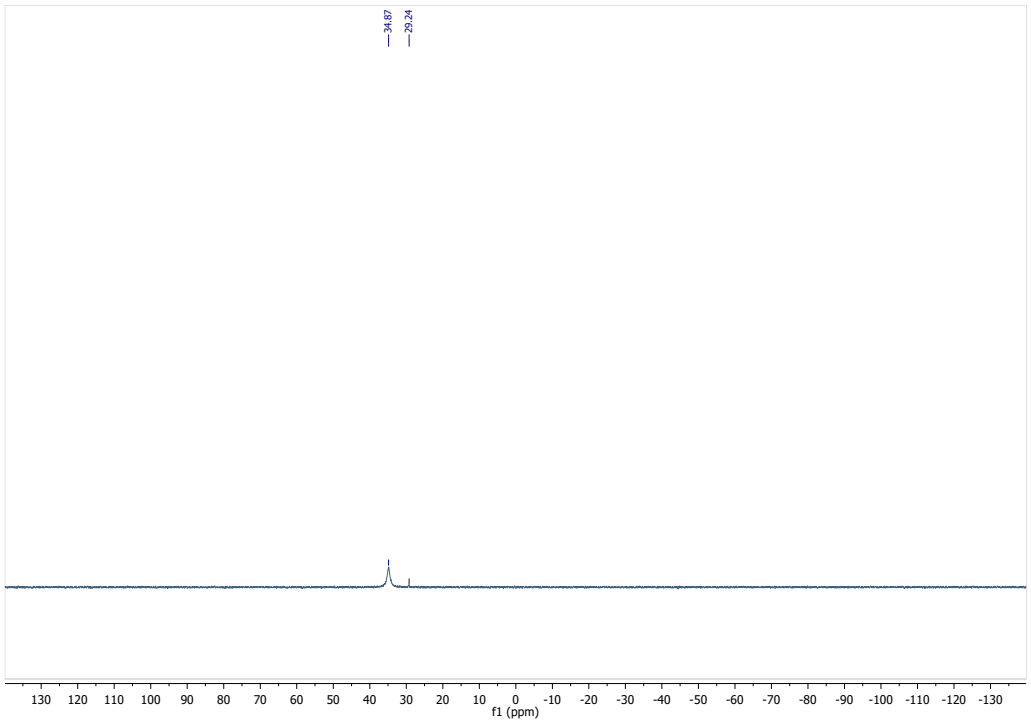
34.87
29.24
130 120 110 100 90 80 70 60 50 40 30 20 10 0 -10 -20 -30 -40 -50 -60 -70 -80 -90 -100 -110 -120 -130
f1 (ppm)

5.9.3.6. 1g. *N*-(triphenylphosphanylidene)cyclohexanaminium bromide

Followed the general procedure (**1**), product obtained as a white solid (147 mg, yield 56%). ^{1}H-NMR (400 MHz, $CDCl_3$): δ 7.88–7.82 (m, 6H), 7.75–7.70 (m, 3H), 7.64–7.59 (m, 6H), 2.69 (m, 1H), 2.12–2.03 (m, 2H), 1.67 (d, *J* = 10.9 Hz, 4H), 1.42 (m, 1H), 1.18 (m, 1H), 0.92 (m, 2H). ^{13}C-NMR (100 MHz, $CDCl_3$): 134.6 (d, *J* = 3 Hz), 133.8 (d, *J* = 11 Hz), 129.8 (d, *J* = 13 Hz), 122.5 (d, *J* = 103 Hz), 54.5, 35.2 (d, *J* = 4 Hz), 25.9, 24.7. ^{31}P-NMR (162 MHz, $CDCl_3$): δ 35.60 (s, 1P). MS (ESI+): Calculated $C_{24}H_{27}NP$ as 360.1881, [M+H] found as 360.1879.

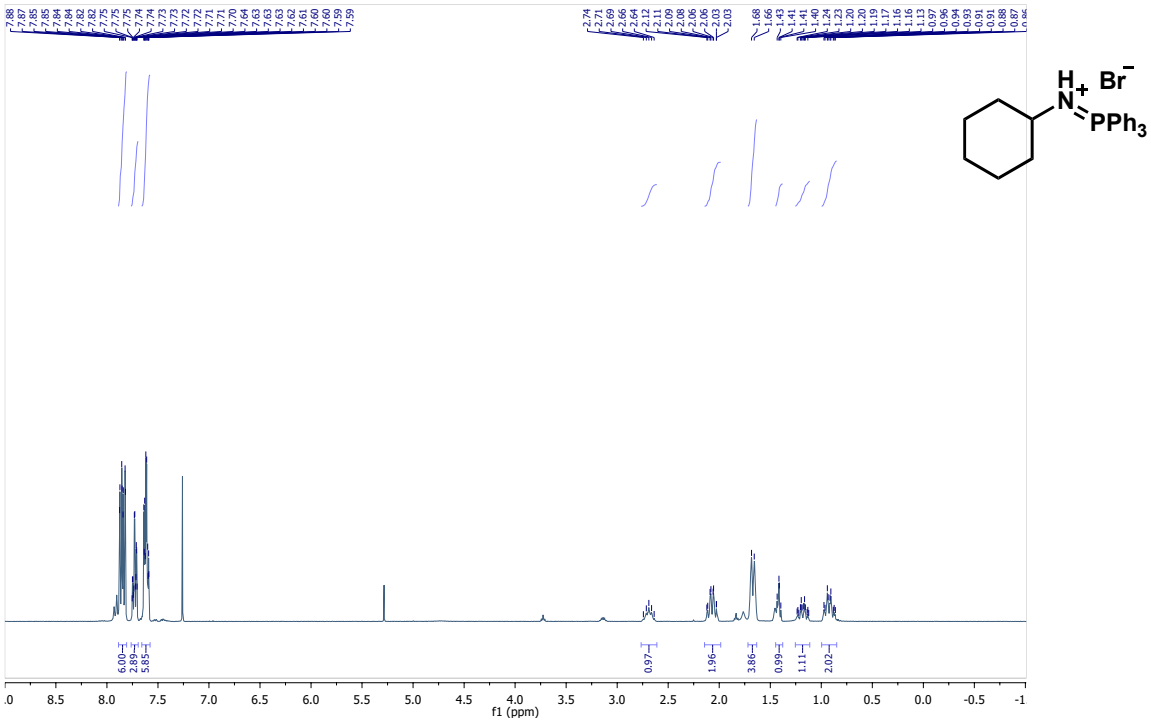

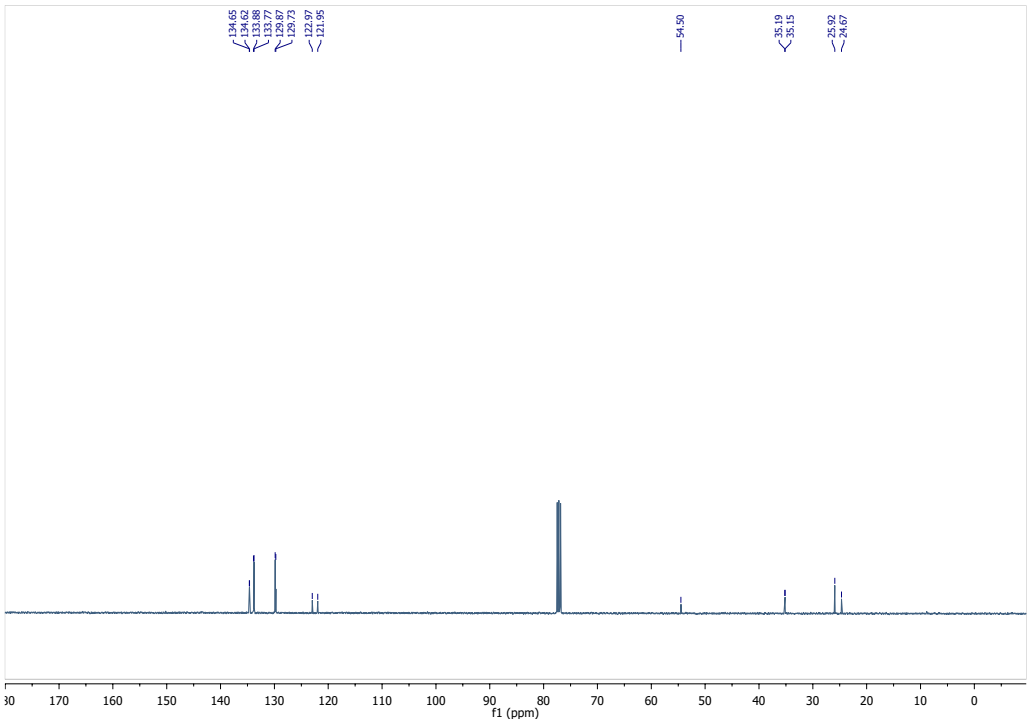
134.65
134.62
133.88
133.77
129.87
129.73
122.97
121.95
54.50
35.19
35.15
25.92
24.67
f1 (ppm)

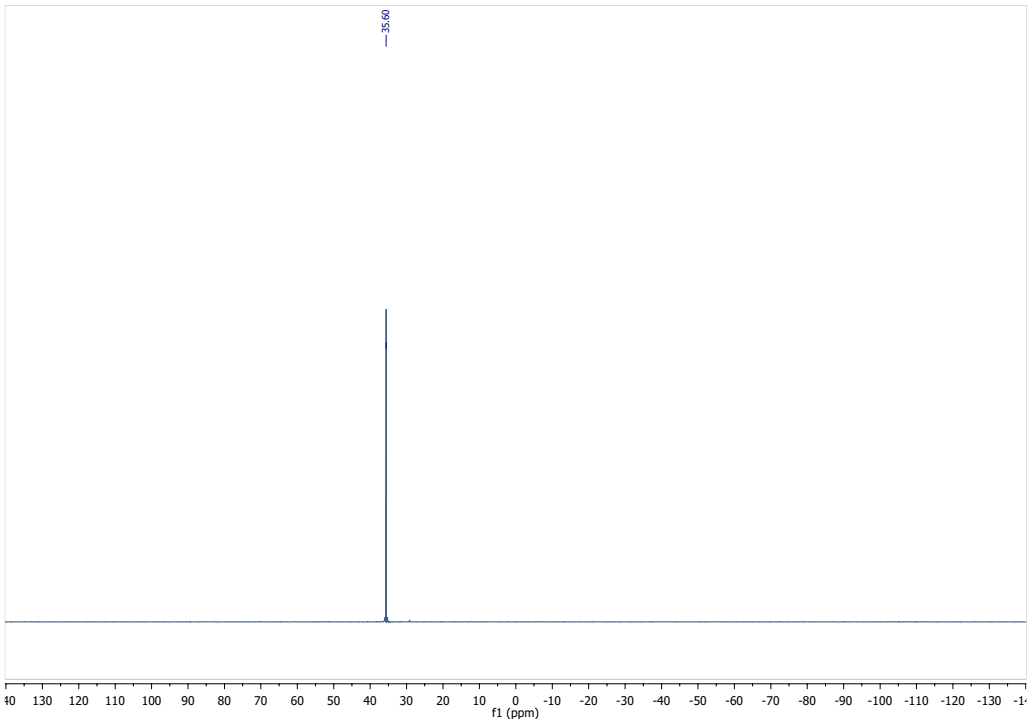
35.60
f1 (ppm)

5.9.3.7. 1h. *tert*-butyl(triphenylphosphanylidene)azanium bromide

Followed the general procedure (**1**), product obtained as a white solid (47 mg, yield 19%). ^{1}H-NMR (400 MHz, $CDCl_3$): δ 7.94–7.89 (m, 6H), 7.71–7.67 (m, 3H), 7.62–7.58 (m, 6H), 7.17 (d, *J* = 6.9 Hz, 1H), 1.29 (s, 9H). ^{13}C-NMR (100 MHz, $CDCl_3$): 134.5 (d, *J* = 3 Hz), 134.0 (d, *J* = 11 Hz), 129.7 (d, *J* = 13 Hz), 123.1 (d, *J* = 102 Hz), 56.6, 32.3. ^{31}P-NMR (162 MHz, $CDCl_3$): δ 31.44 (s, 1P). MS (ESI+): Calculated $C_{22}H_{25}NP$ as 334.1725, [M+H] found as 334.1703.

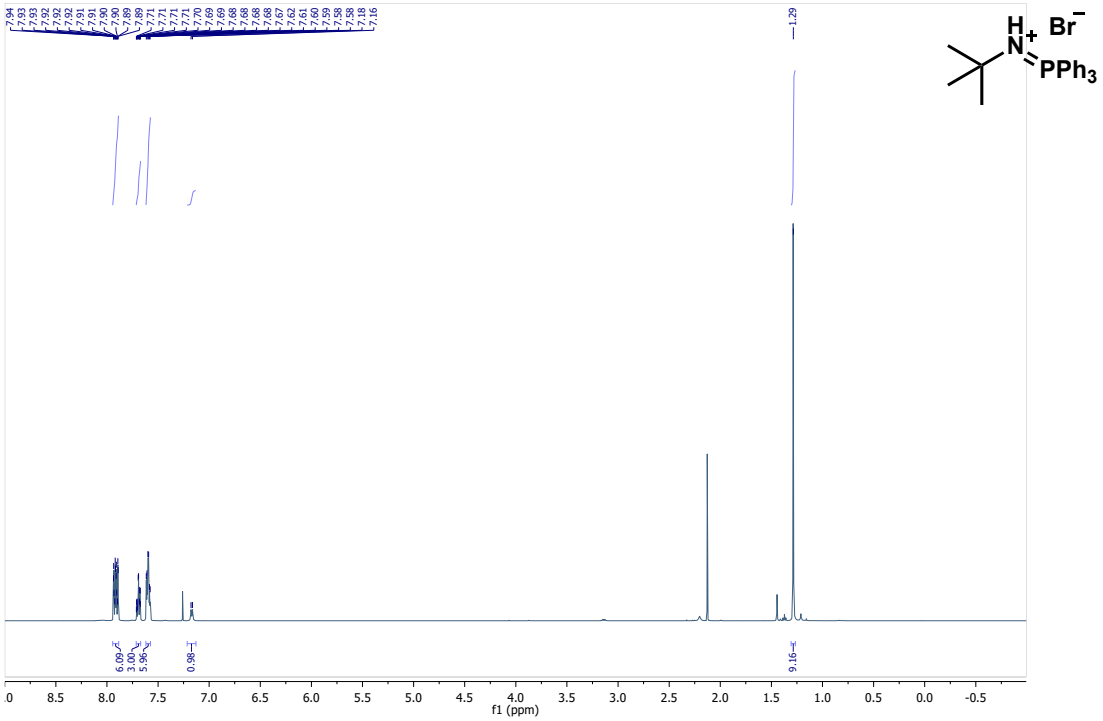

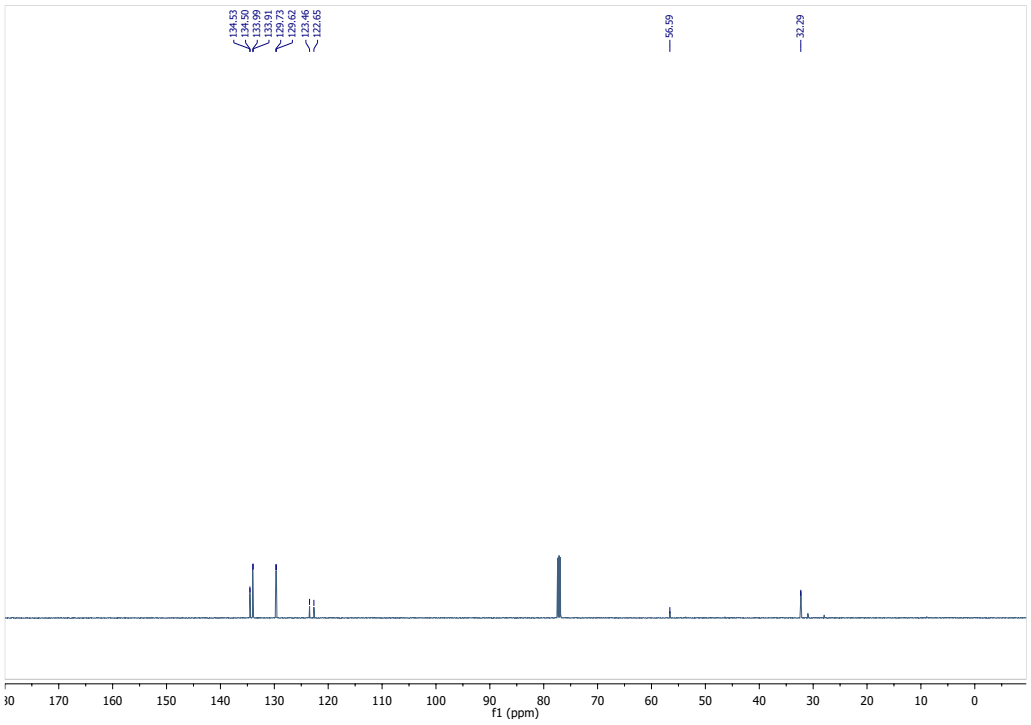
134.53
134.50
133.99
133.91
129.73
129.62
123.46
122.65
56.59
32.29
f1 (ppm)

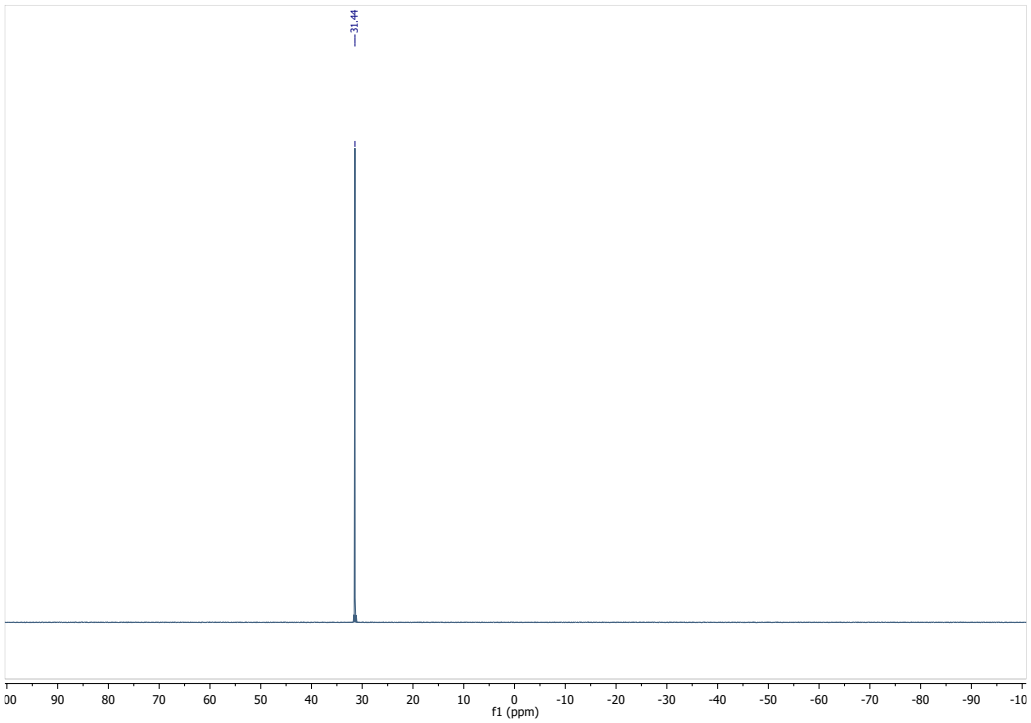
31.44
f1 (ppm)

5.9.3.8. 1i. [(furan-2-yl)methyl](triphenylphosphanylidene)azanium bromide

Followed the general procedure (**1**), product obtained as a white solid (142 mg, yield 54%). ^{1}H-NMR (400 MHz, $CDCl_3$): δ 8.61 (m, 1H), 7.82–7.76 (m, 6H), 7.74–7.69 (m, 3H), 7.61–7.57 (m, 6H), 7.00 (dd, *J* = 1.9, 0.8 Hz, 1H), 6.36 (dd, *J* = 3.3, 0.8 Hz, 1H), 6.17 (dd, *J* = 3.3, 1.8 Hz, 1H), 4.24 (dd, *J* = 16.2, 6.8 Hz, 2H). ^{13}C-NMR (100 MHz, $CDCl_3$): 151.5, 141.6, 134.7 (d, *J* = 3 Hz), 133.8 (d, *J* = 11 Hz), 129.8 (d, *J* = 13 Hz), 121.6 (d, *J* = 103 Hz), 111.0, 109.7, 38.3. ^{31}P-NMR (162 MHz, $CDCl_3$): δ 38.42 (s, 1P). MS (ESI+): Calculated $C_{23}H_{21}NPO$ as 358.1361, [M+H] found as 358.1364.

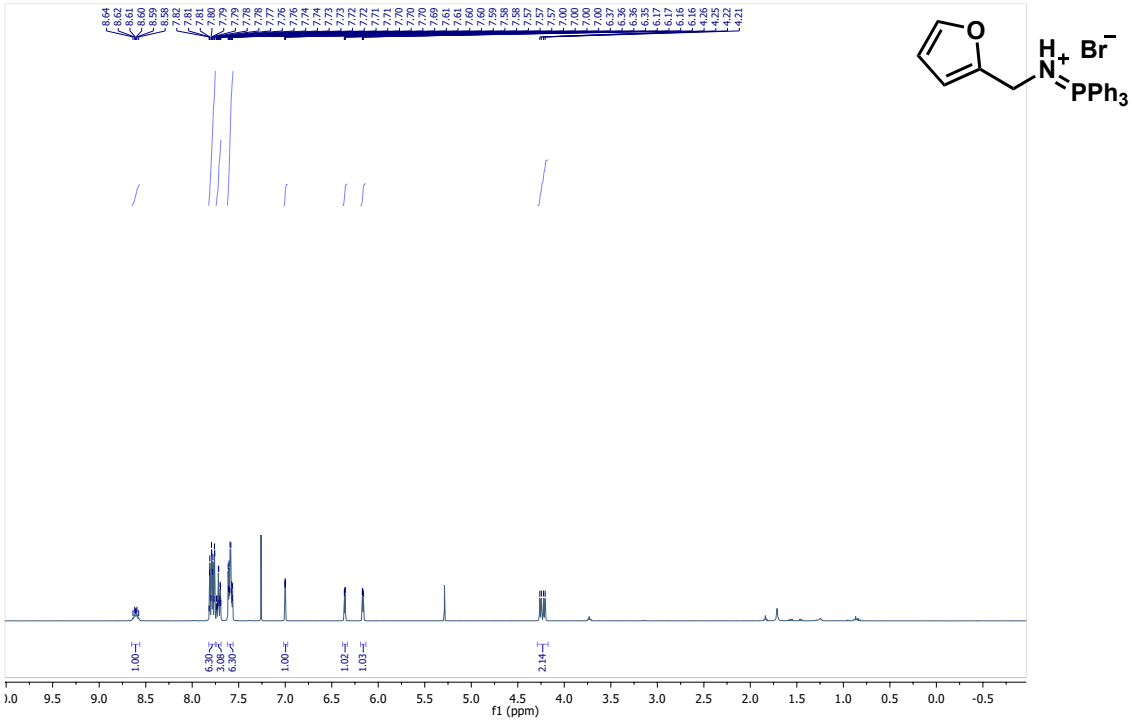

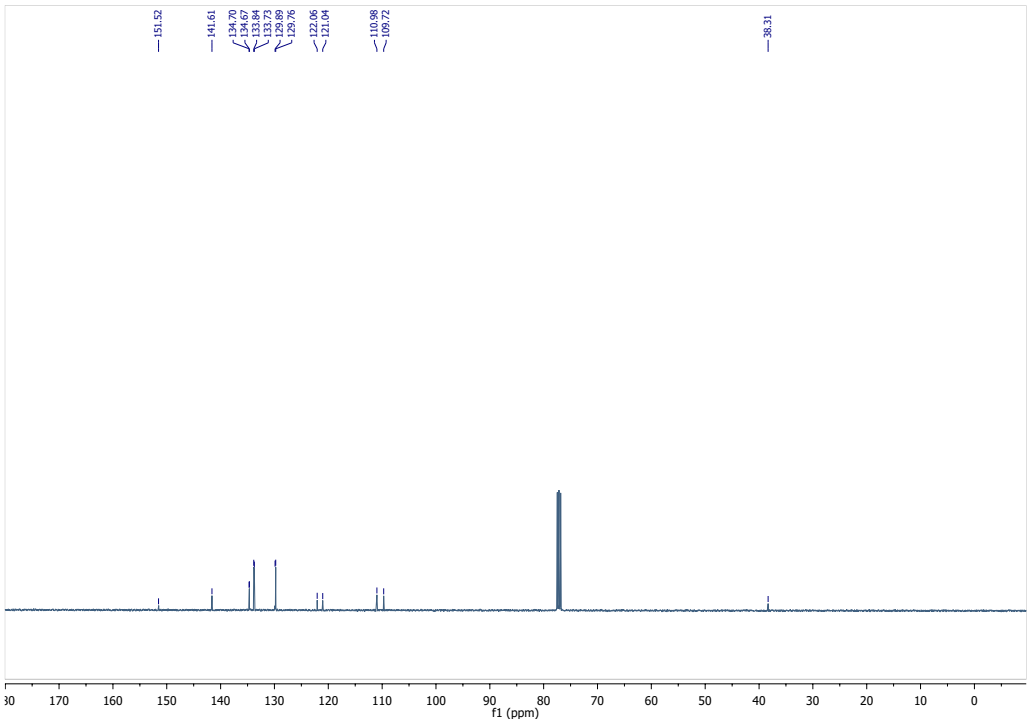
151.52
141.61
134.70
134.67
133.84
133.73
129.89
129.76
122.06
121.04
110.98
109.72
38.31
f1 (ppm)

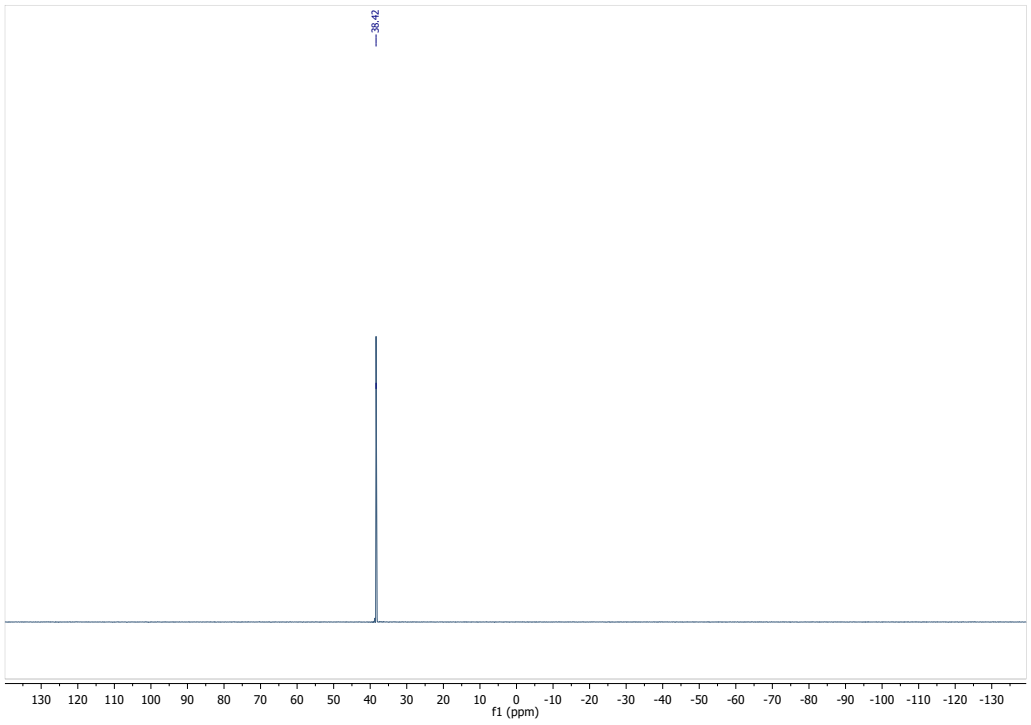
38.42
f1 (ppm)

5.9.3.9. 1j. [2-(5-methoxy-1H-indol-3-yl)ethyl](triphenylphosphanylidene)azanium bromide

Followed the general procedure (**1**), product obtained as a white solid (143 mg, yield 45%). ^{1}H-NMR (400 MHz, $CDCl_3$): δ 8.98 (d, *J* = 2.5 Hz, 1H), 7.70 (m, 1H), 7.63–7.53 (m, 9H), 7.46–7.41 (m, 6H), 7.27 (m, 1H), 7.00 (dd, *J* = 2.4 Hz, 1H), 6.74 (s, 1H), 3.74 (s, 3H), 3.27 (m, 2H), 3.13 (t, *J* = 6.5 Hz, 2H). ^{13}C-NMR (100 MHz, $CDCl_3$): 153.8, 134.6 (d, *J* = 3 Hz), 133.5 (d, *J* = 11 Hz), 131.5, 129.7 (d, *J* = 13 Hz), 127.8, 124.4, 121.5 (d, *J* = 103 Hz), 112.4, 111.7, 111.5, 100.5, 56.2, 43.3, 27.1 (d, *J* = 7 Hz). ^{31}P-NMR (162 MHz, $CDCl_3$): δ 37.61 (s, 1P). MS (ESI+): Calculated $C_{29}H_{28}N_2PO$ as 451.1939, [M+H] found as 451.1922.

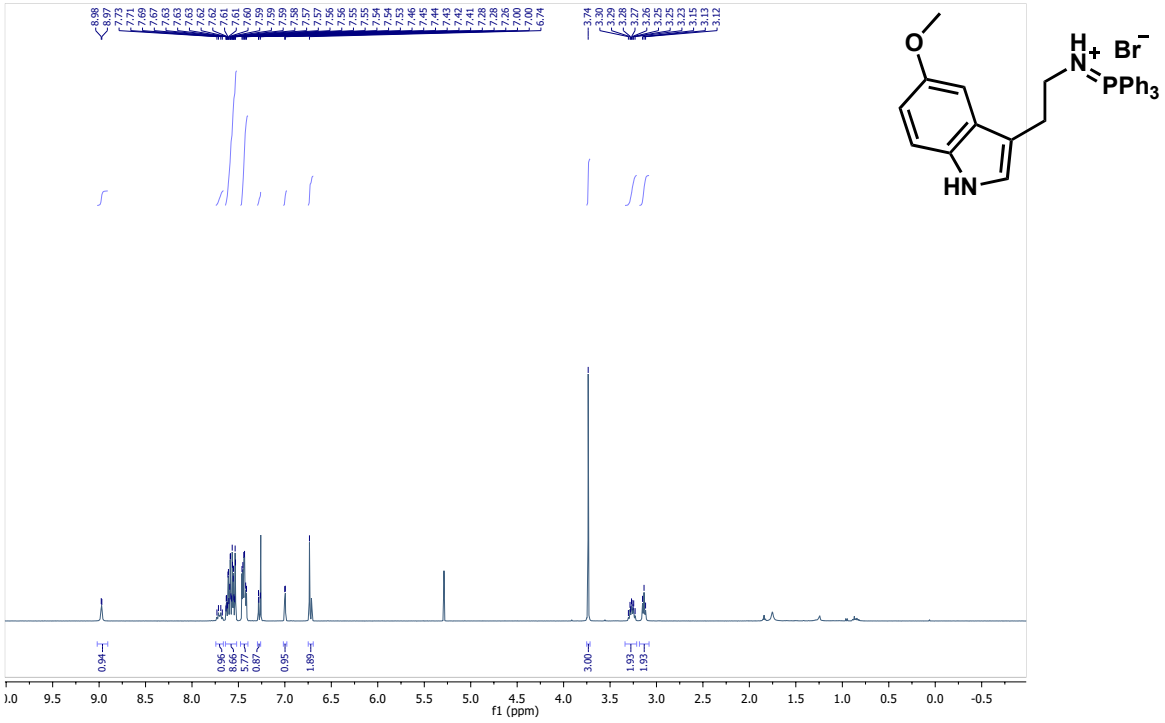

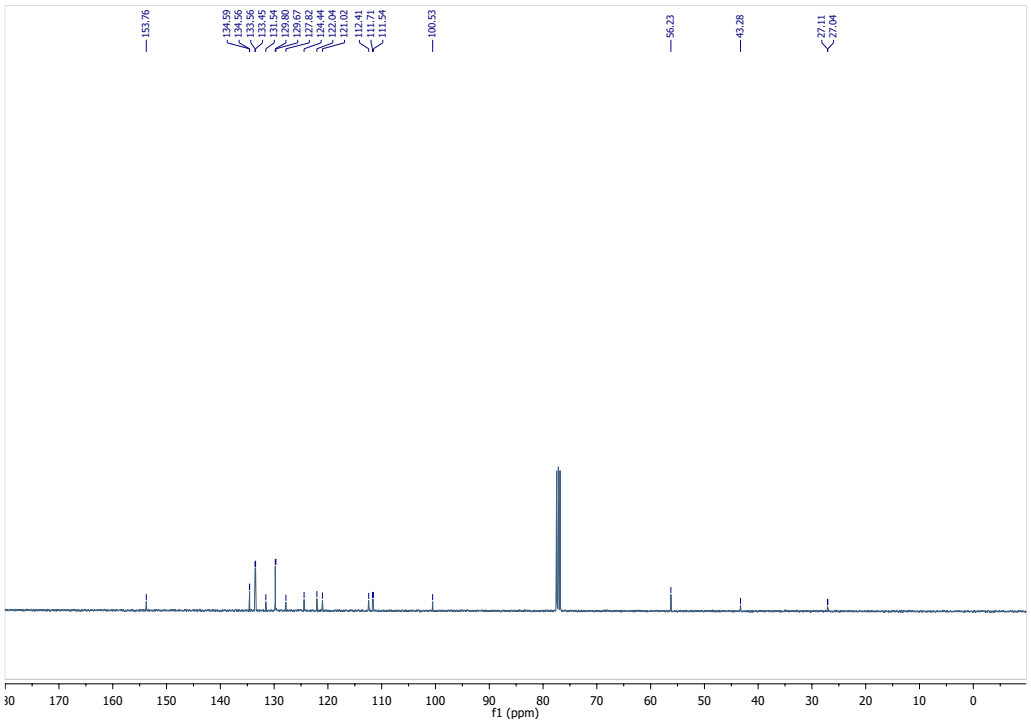
153.76
134.59
134.56
133.56
133.45
131.54
130.80
129.67
127.82
124.44
122.04
121.02
112.41
111.71
111.54
100.53
56.23
43.28
27.11
27.04
f1 (ppm)

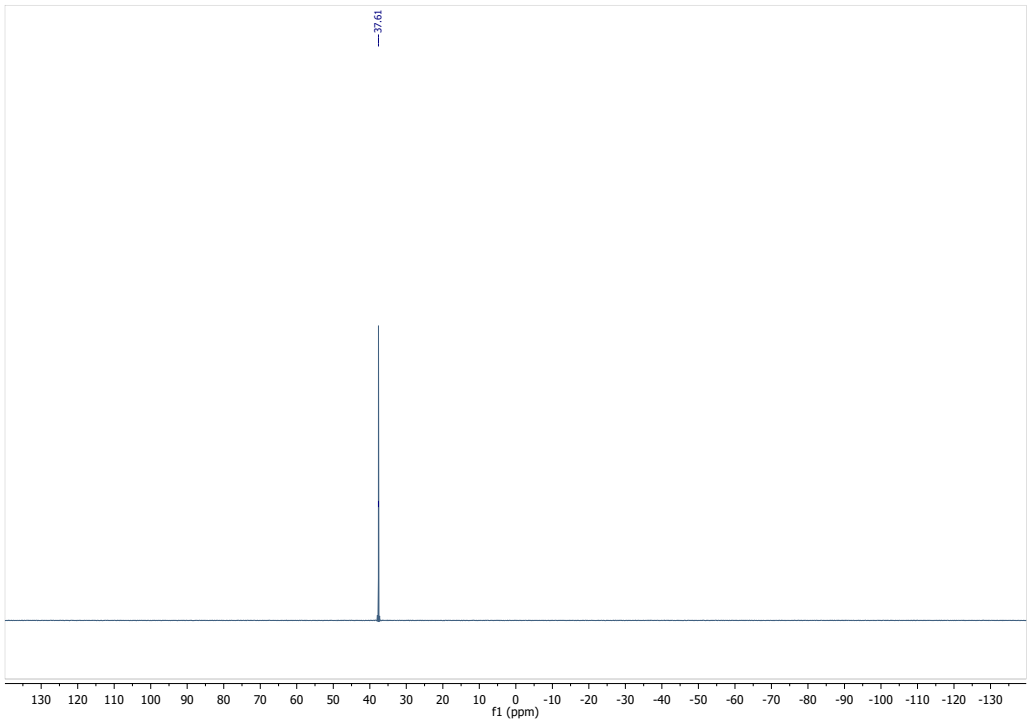
37.61
f1 (ppm)

5.9.3.10. 1k. (1-methoxy-1-oxo-3-phenylpropan-2-yl)(triphenylphosphanylidene)azanium bromide

Followed the general procedure (**1**), product obtained as a white solid (78 mg, yield 25%). ^{1}H-NMR (400 MHz, $CDCl_3$): δ 8.61 (s, 1H), 7.66 (m, 3H), 7.51 (m, 12H), 7.31 (m, 2H), 7.22 (m, 3H), 3.75 (m, 1H), 3.55 (s, 3H), 3.46 (m, 1H), 3.24 (m, 1H). ^{13}C-NMR (100 MHz, $CDCl_3$): 171.8, 137.9, 134.7 (d, *J* = 3 Hz), 134.1 (d, *J* = 11 Hz), 130.2, 129.6 (d, *J* = 13 Hz), 128.6, 126.9, 121.2 (d, *J* = 104 Hz), 58.8 (d, *J* = 3 Hz), 52.6, 37.8 (d, *J* = 8 Hz). ^{31}P-NMR (162 MHz, $CDCl_3$): δ 39.06 (s, 1P), 22.21 (s, 1P, TPPO). MS (ESI+): Calculated $C_{28}H_{27}NPO_2$ as 440.1779, [M+H] found as 440.1785.

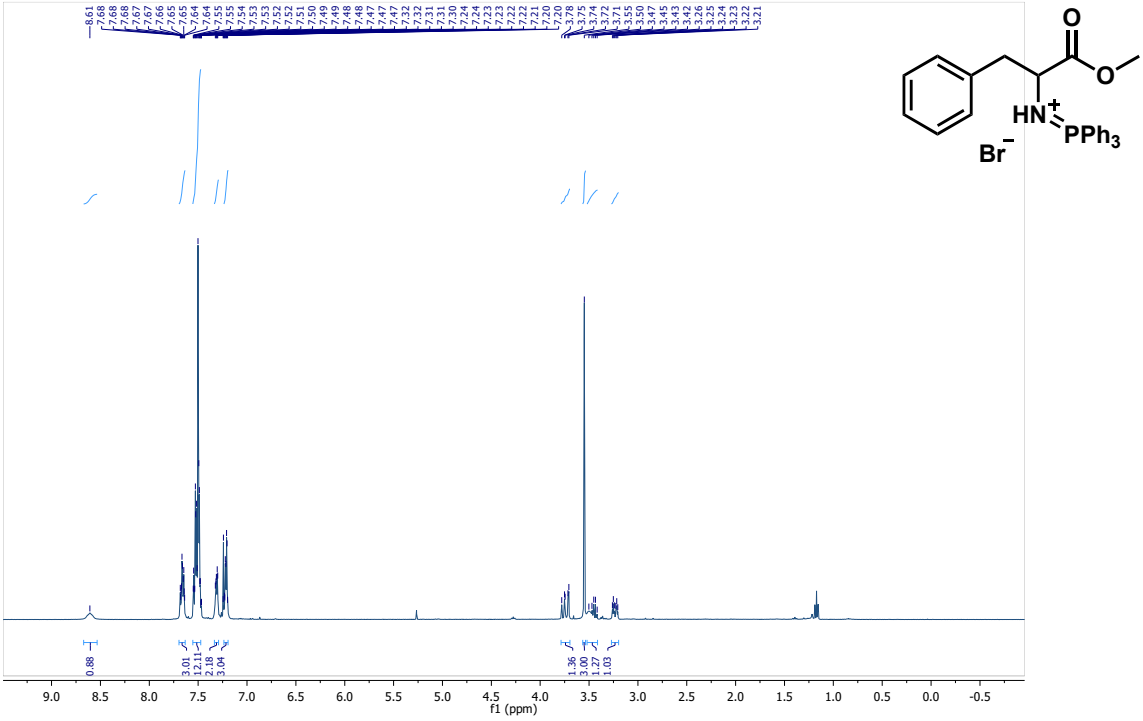

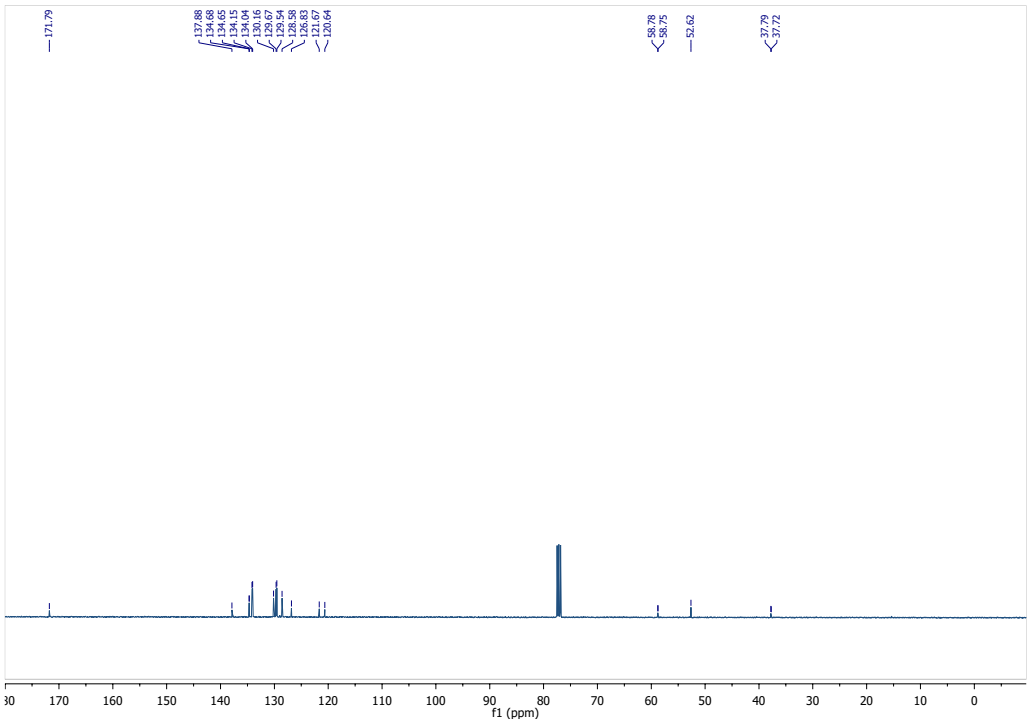
171.79
137.88
134.68
134.65
134.15
134.04
130.16
129.67
129.54
128.58
126.83
121.67
120.64
58.78
58.75
52.62
37.79
37.72
f1 (ppm)

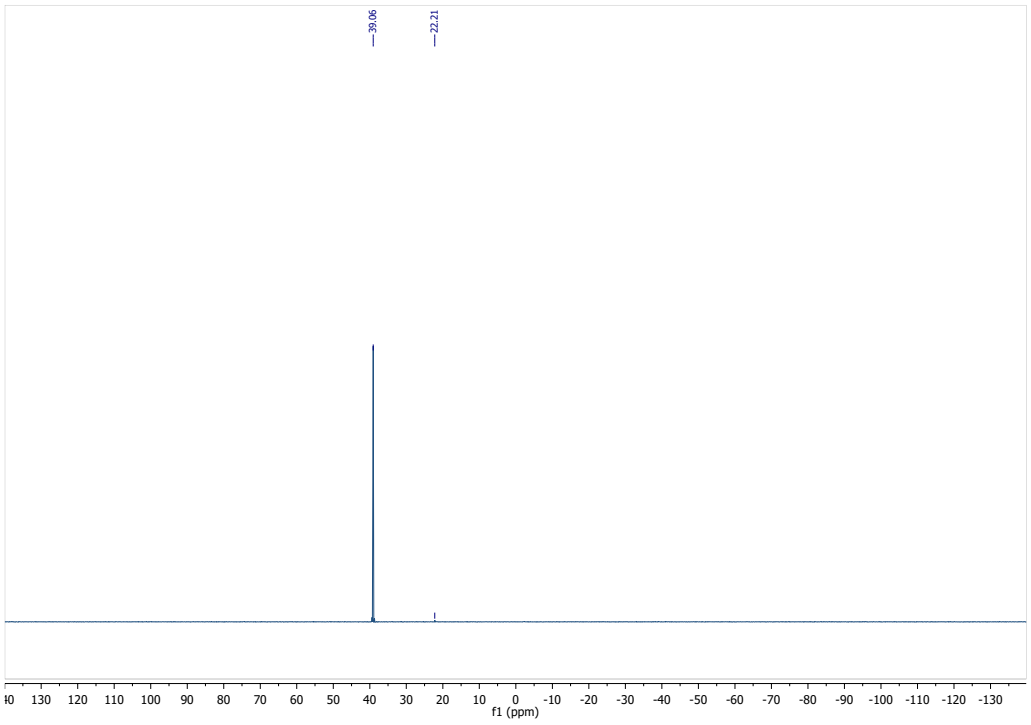
39.06
22.21
f1 (ppm)

5.9.3.11. 1l. [(4-fluorophenyl)methyl](triphenylphosphanylidene)azanium bromide

Followed the general procedure (**1**), product obtained as a white solid (100 mg, yield 36%). ^{1}H-NMR (400 MHz, $CDCl_3$): δ 8.79 (m, 1H), 7.79–7.70 (m, 9H), 7.60–7.56 (m, 6H), 7.18–7.13 (m, 2H), 6.84–6.78 (m, 2H), 4.25 (dd, *J* = 15.8, 7.3 Hz, 2H). ^{13}C-NMR (100 MHz, $CDCl_3$): 162.1 (d, *J* = 246 Hz), 134.8 (d, *J* = 3 Hz), 134.4 (dd, *J* = 3, 3), 133.7 (d, *J* = 11 Hz), 130.1, 129.9 (d, *J* = 13 Hz), 121.6 (d, *J* = 102 Hz), 115.2 (d, *J* = 21 Hz), 45.0. ^{31}P-NMR (162 MHz, $CDCl_3$): δ 38.40 (s, 1P). ^{19}F-NMR (376 MHz, $CDCl_3$): -115.02 (s, 1F). MS (ESI+): Calculated $C_{25}H_{22}NPF$ as 386.1474 [M+H] found as 386.1492.

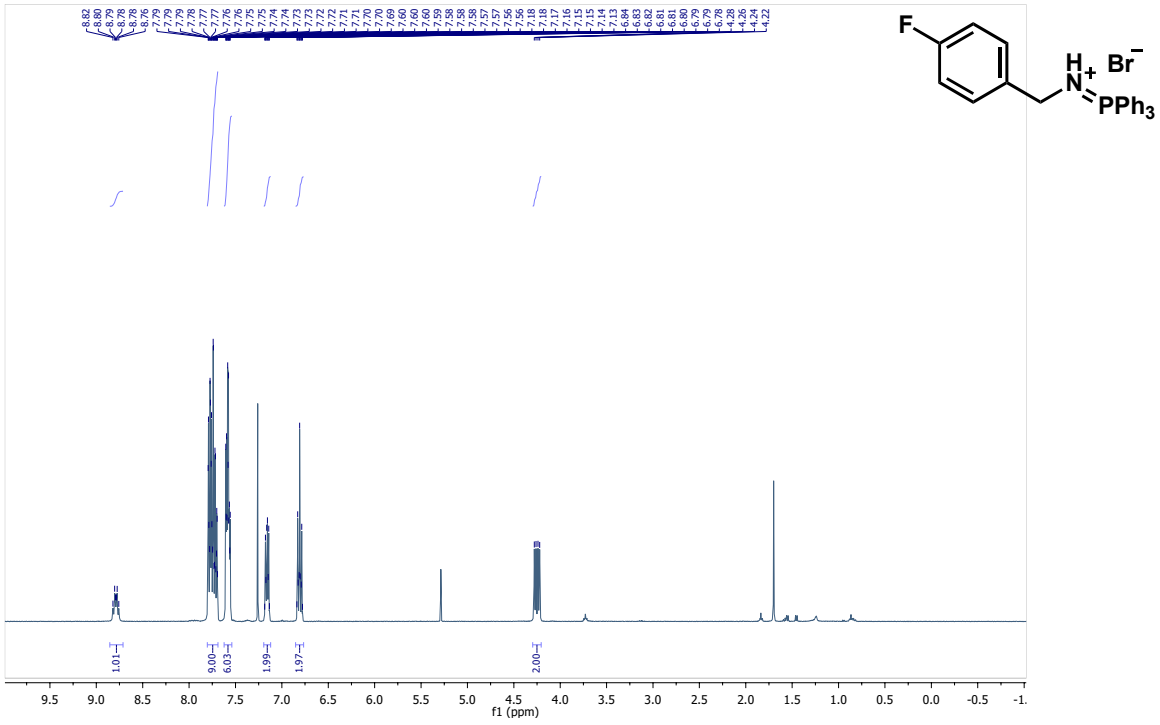

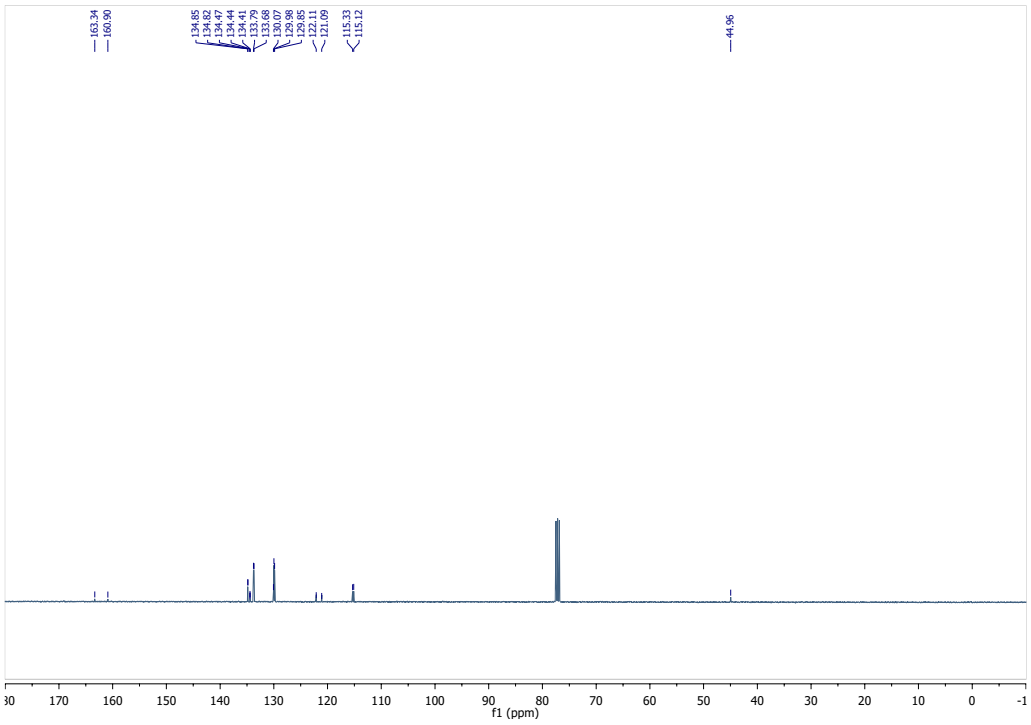
163.34
160.90
134.85
134.62
134.47
134.44
134.41
133.79
133.68
130.07
129.98
129.85
122.11
121.09
115.33
115.12
44.96
170
160
150
140
130
120
110
100
90
80
70
60
50
40
30
20
10
0
f1 (ppm)

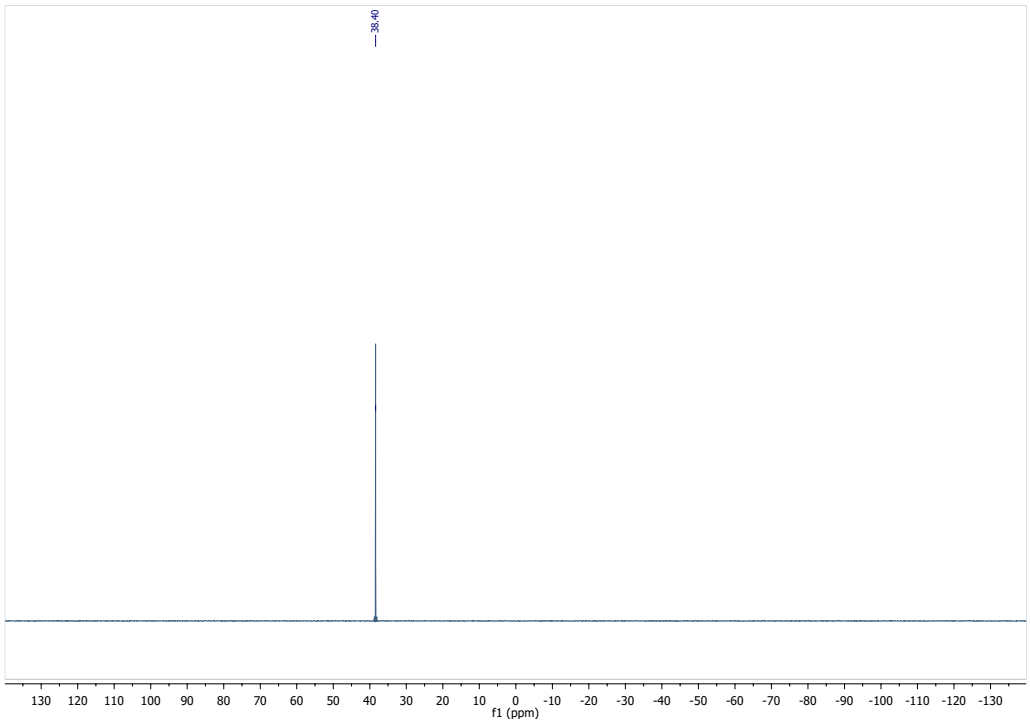
38.40
130 120 110 100 90 80 70 60 50 40 30 20 10 0 -10 -20 -30 -40 -50 -60 -70 -80 -90 -100 -110 -120 -130
f1 (ppm)

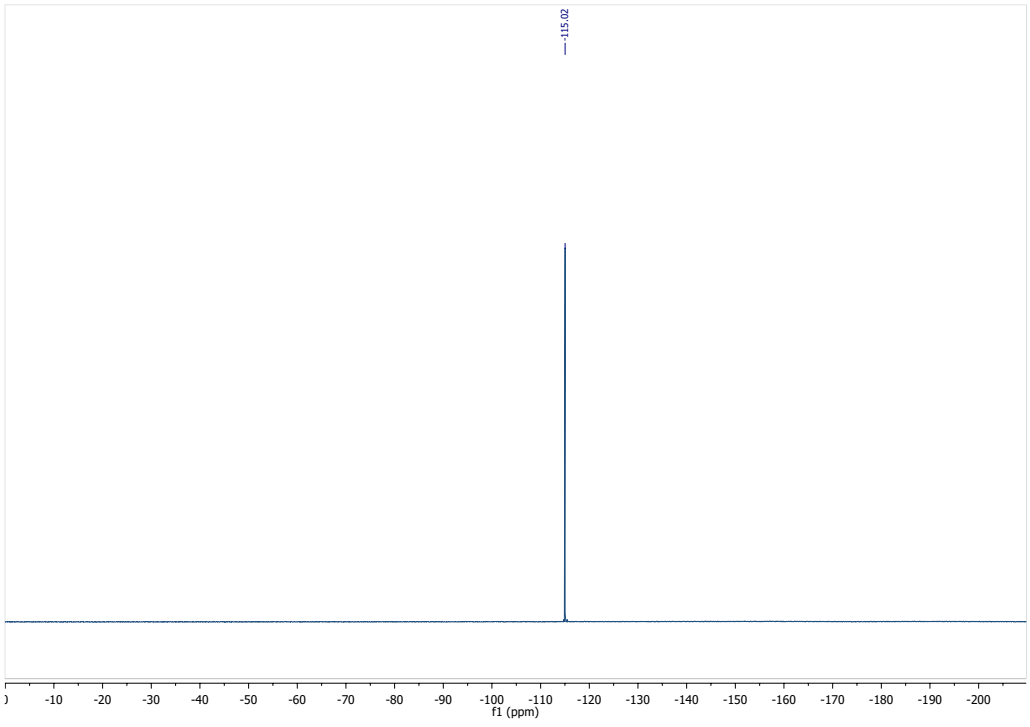
-115.02
-10 -20 -30 -40 -50 -60 -70 -80 -90 -100 -110 -120 -130 -140 -150 -160 -170 -180 -190 -200
f1 (ppm)

5.9.3.12. 1m. 4-chloro-3-(trifluoromethyl)-*N*-(triphenylphosphanylidene)anilinium bromide

Followed the general procedure (**1**), product obtained as a white solid (171 mg, yield 53%). ^{1}H-NMR (400 MHz, $CDCl_3$): δ 10.86 (d, *J* = 7.8 Hz, 1H), 7.83–7.74 (m, 9H), 7.64–7.59 (m, 6H), 7.54 (dd, *J* = 8.7, 2.6 Hz, 1H), 7.22 (d, *J* = 8.5 Hz, 1H), 7.12 (d, *J* = 2.4 Hz, 1H). ^{13}C-NMR (100 MHz, $CDCl_3$): 137.0 (d, *J* = 2 Hz), 135.5 (d, *J* = 3 Hz), 133.9 (d, *J* = 11 Hz), 132.2, 130.2 (d, *J* = 13 Hz), 128.4 (m), 127.9 (d, *J* = 7 Hz), 127.7 (d, *J* = 6 Hz), 122.1 (q, *J* = 274 Hz), 121.7 (quin, *J* = 6 Hz), 119.8 (d, *J* = 102 Hz). ^{31}P-NMR (162 MHz, $CDCl_3$): δ 34.35 (s, 1P), 30.59 (s, 1P, TPPO). ^{19}F-NMR (376 MHz, $CDCl_3$): -63.11 (s, 3F). MS (ESI+): Calculated $C_{25}H_{19}NF_3PCl$ as 456.0896, [M+H] found as 456.0886.

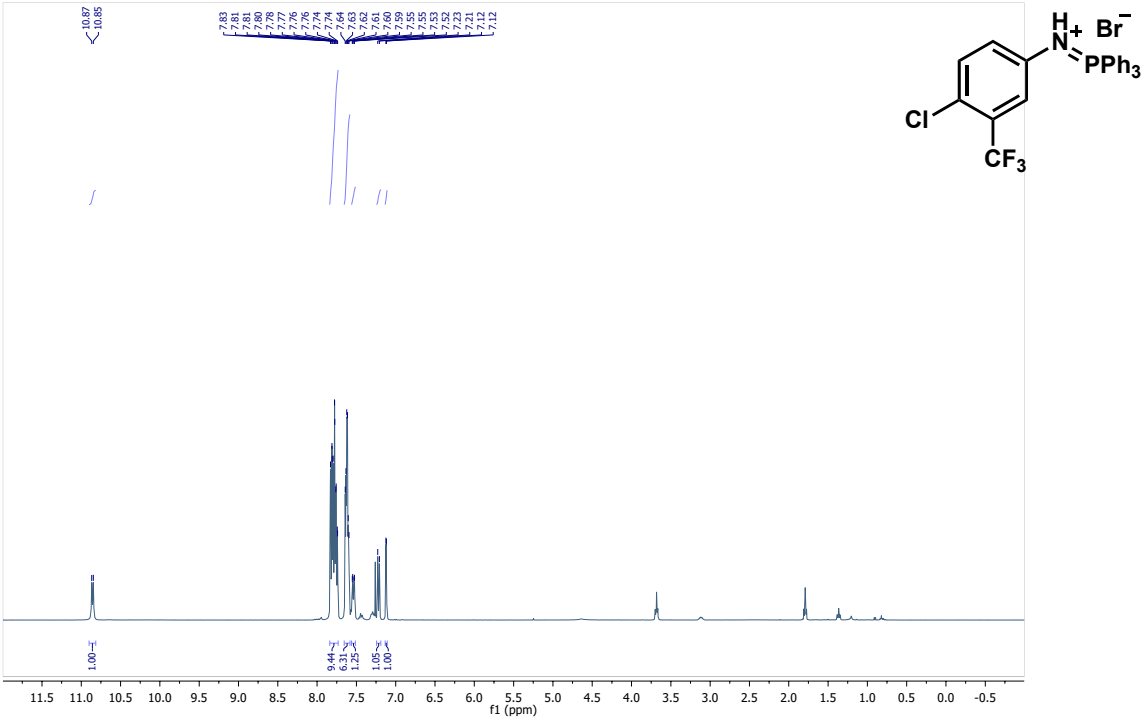

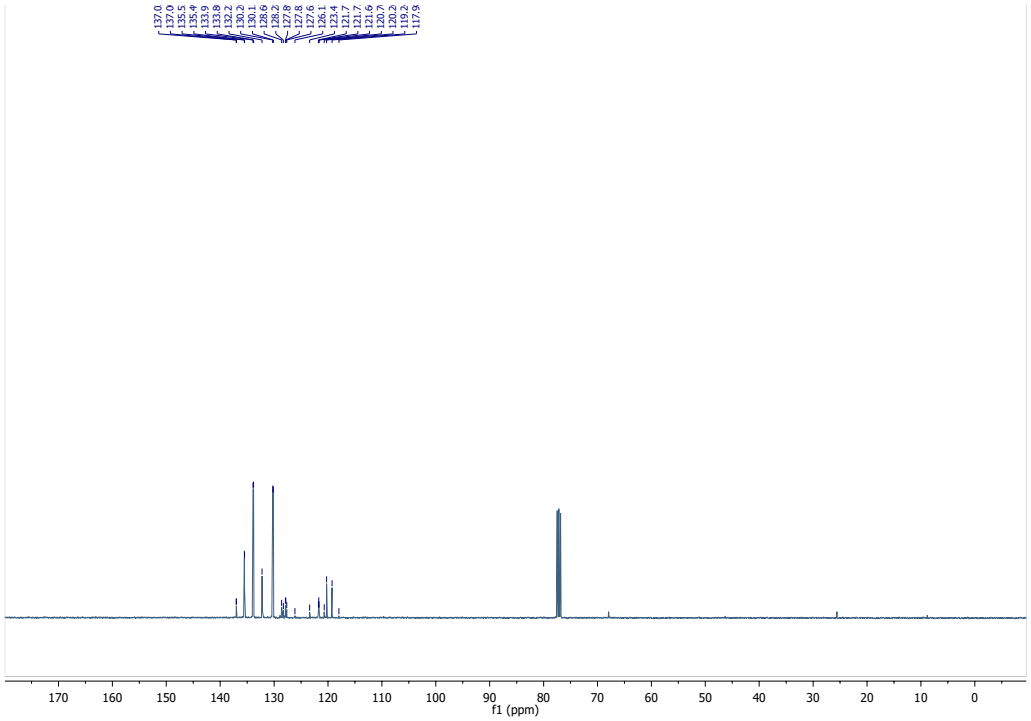
137.0
137.0
135.5
135.4
133.9
133.9
132.7
130.2
130.1
128.6
128.2
127.8
127.8
127.6
126.1
123.4
121.7
121.7
121.6
120.7
120.2
119.2
117.9
170
160
150
140
130
120
110
100
90
80
70
60
50
40
30
20
10
0
f1 (ppm)

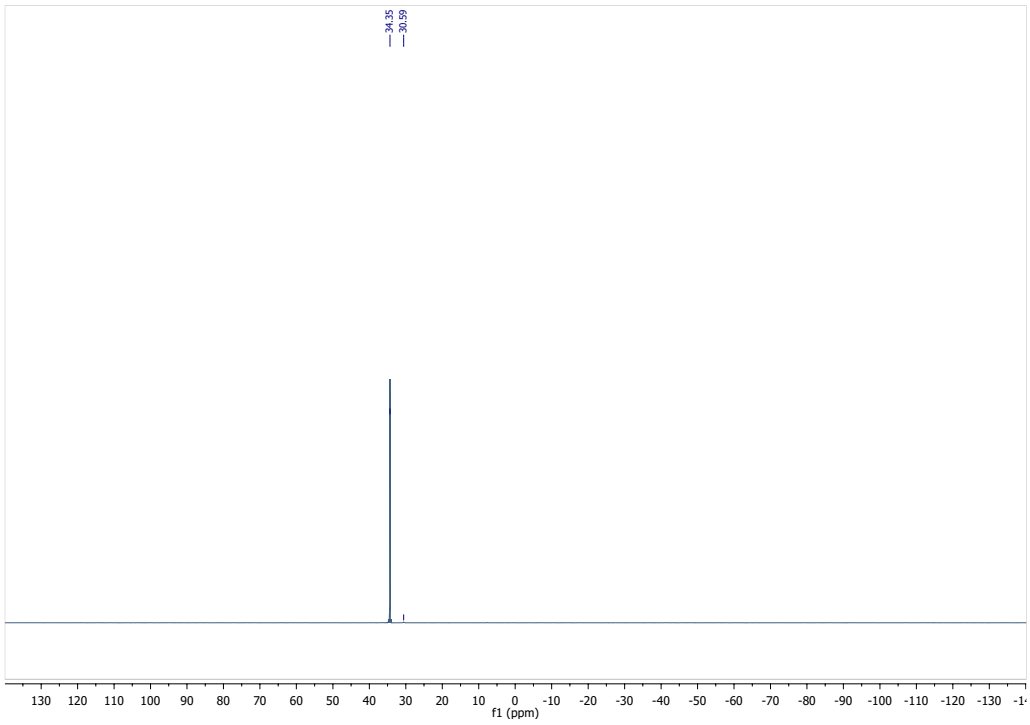
34.35
30.59
130 120 110 100 90 80 70 60 50 40 30 20 10 0 -10 -20 -30 -40 -50 -60 -70 -80 -90 -100 -110 -120 -130
f1 (ppm)

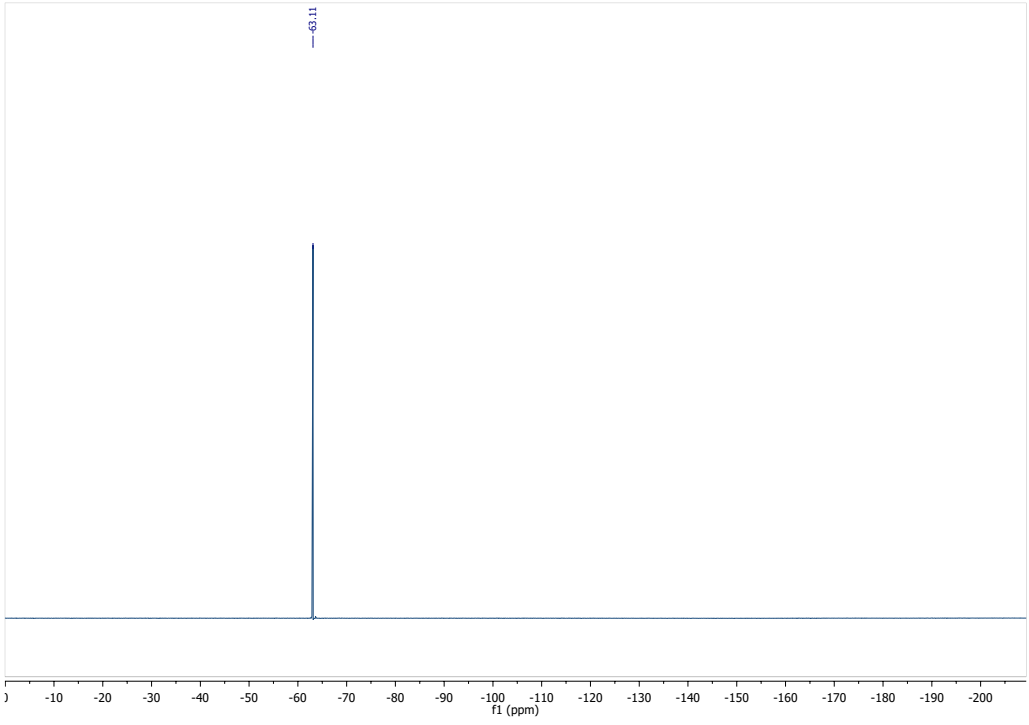
-63.11
-10 -20 -30 -40 -50 -60 -70 -80 -90 -100 -110 -120 -130 -140 -150 -160 -170 -180 -190 -200
f1 (ppm)

5.9.3.13. 1n. benzyl(triphenylphosphanylidene)azanium bromide

Followed the general procedure (**1**), product obtained as a white solid (199 mg, yield 74%). ^{1}H-NMR (400 MHz, $CDCl_3$): δ 8.72 (m, 1H), 7.74 (m, 9H), 7.57 (m, 6H), 7.18 (m, 2H), 7.13 (m, 3H), 4.28 (dd, *J* = 15.9, 7.3 Hz, 2H). ^{13}C-NMR (100 MHz, $CDCl_3$): 138.5 (d, *J* = 3 Hz), 134.7 (d, *J* = 3 Hz), 133.8 (d, *J* = 11 Hz), 129.9 (d, *J* = 13 Hz), 128.4, 128.3, 127.4, 121.7 (d, *J* = 103 Hz), 45.7. ^{31}P-NMR (162 MHz, $CDCl_3$): δ 38.56 (s, 1P), 29.15 (s, 1P, TPPO). MS (ESI+): Calculated $C_{25}H_{23}NP$ as 368.1568, [M+H] found as 368.1574.

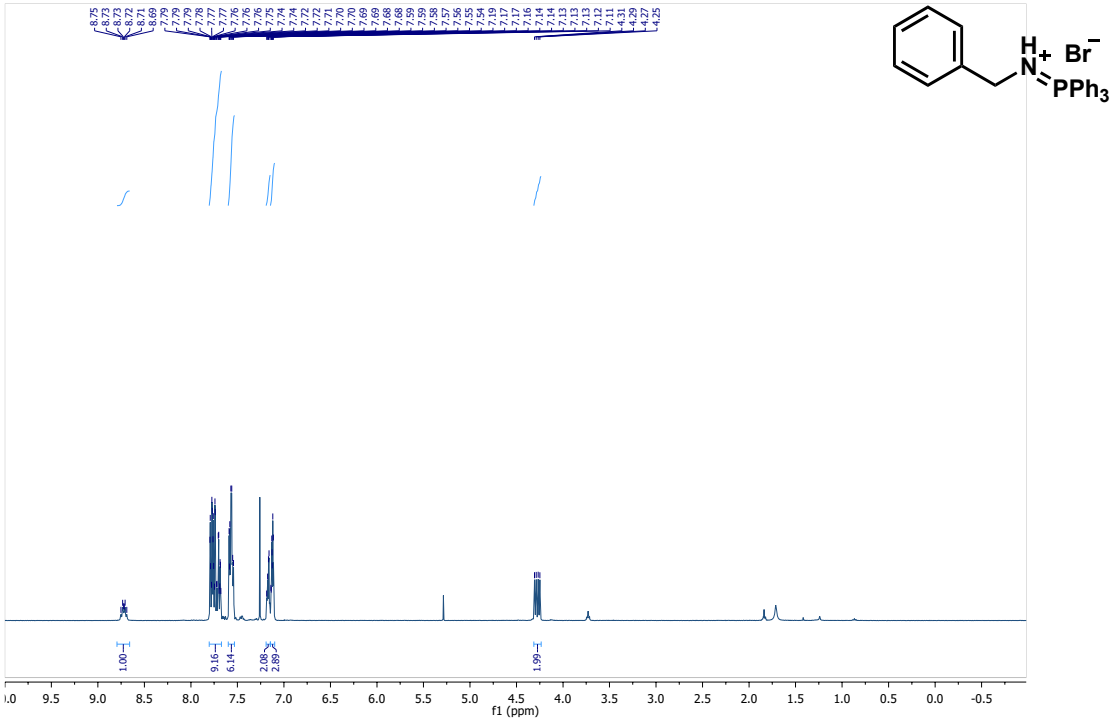

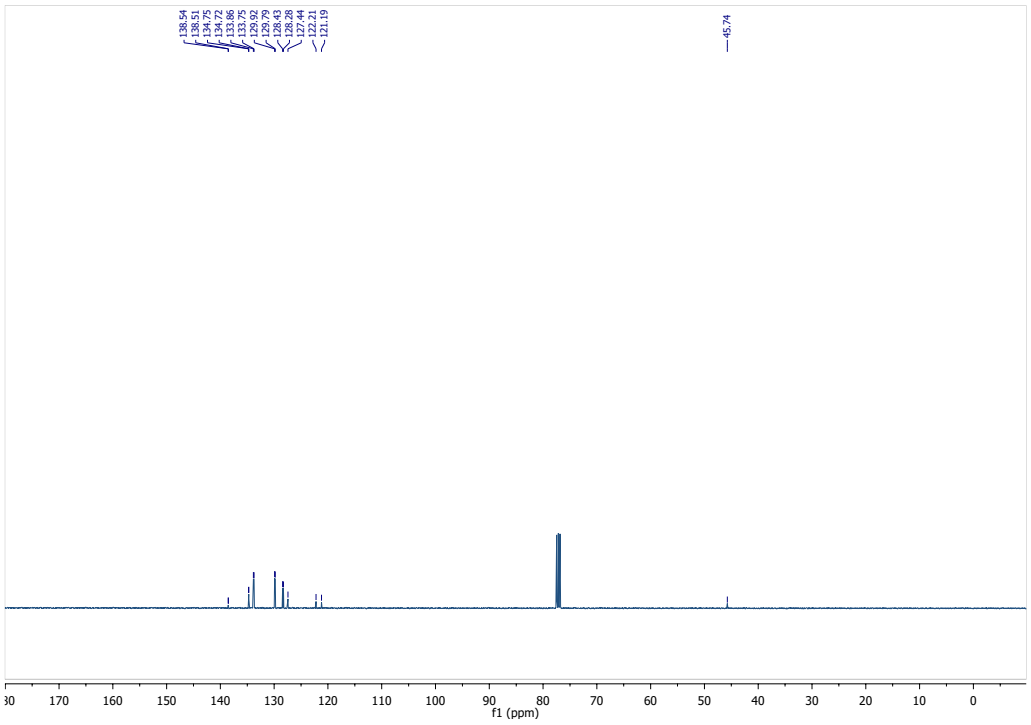
138.54
138.51
134.75
134.72
133.86
133.75
129.92
129.79
128.43
128.28
127.44
122.21
121.19
45.74
170 160 150 140 130 120 110 100 90 80 70 60 50 40 30 20 10 0
f1 (ppm)

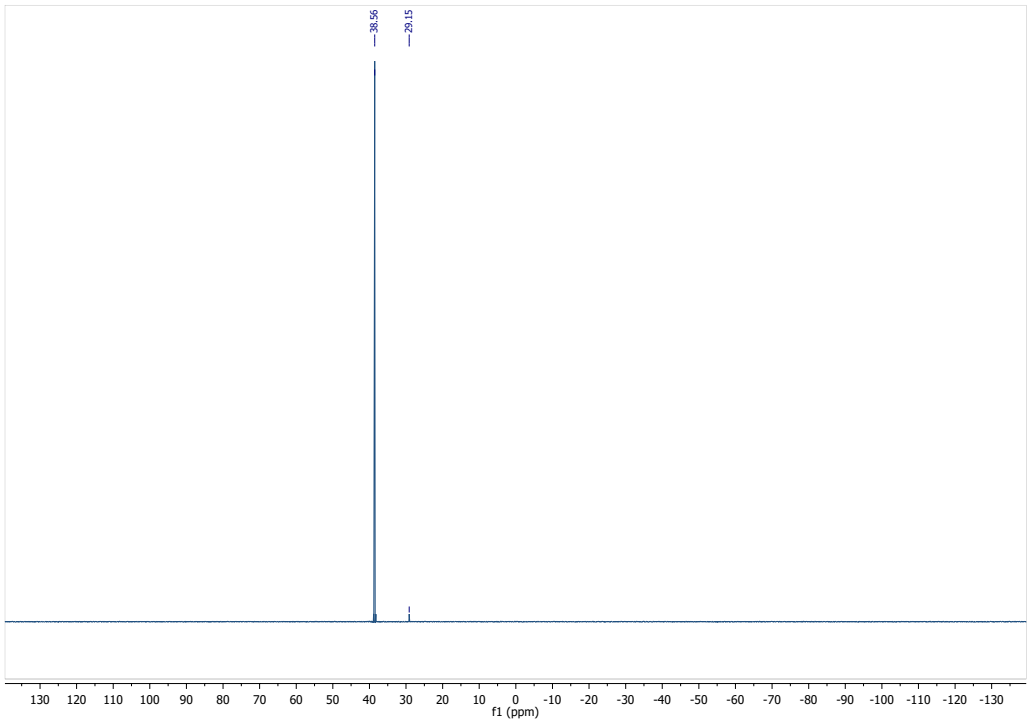
38.56
29.15
130 120 110 100 90 80 70 60 50 40 30 20 10 0 -10 -20 -30 -40 -50 -60 -70 -80 -90 -100 -110 -120 -130
f1 (ppm)

5.9.3.14. 1o. [2-(diethylamino)ethyl](triphenylphosphanylidene)azanium bromide

Followed the general procedure (**1**), product obtained as a sticky yellow solid (113 mg, yield 41%). ^{1}H-NMR (400 MHz, $CDCl_3$): δ 7.83–7.71 (m, 9H), 7.65–7.60 (m, 6H), 3.29 (q, *J* = 8.0, 7.1 Hz, 2H), 2.91 (t, *J* = 7.1 Hz, 2H), 2.60 (q, *J* = 7.4 Hz, 4H), 0.99 (t, *J* = 7.2 Hz, 6H). ^{13}C-NMR (100 MHz, $CDCl_3$): 134.9 (d, *J* = 3 Hz), 133.6 (d, *J* = 11 Hz), 130.0 (d, *J* = 13 Hz), 121.3 (d, *J* = 103 Hz), 53.1, 47.4, 39.8, 10.8. ^{31}P-NMR (162 MHz, $CDCl_3$): δ 38.27 (s, 1P), 29.14 (s, 1P, TPPO). MS (ESI+): Calculated $C_{24}H_{30}N_2P$ as 377.2147, [M+H] found as 377.2166.

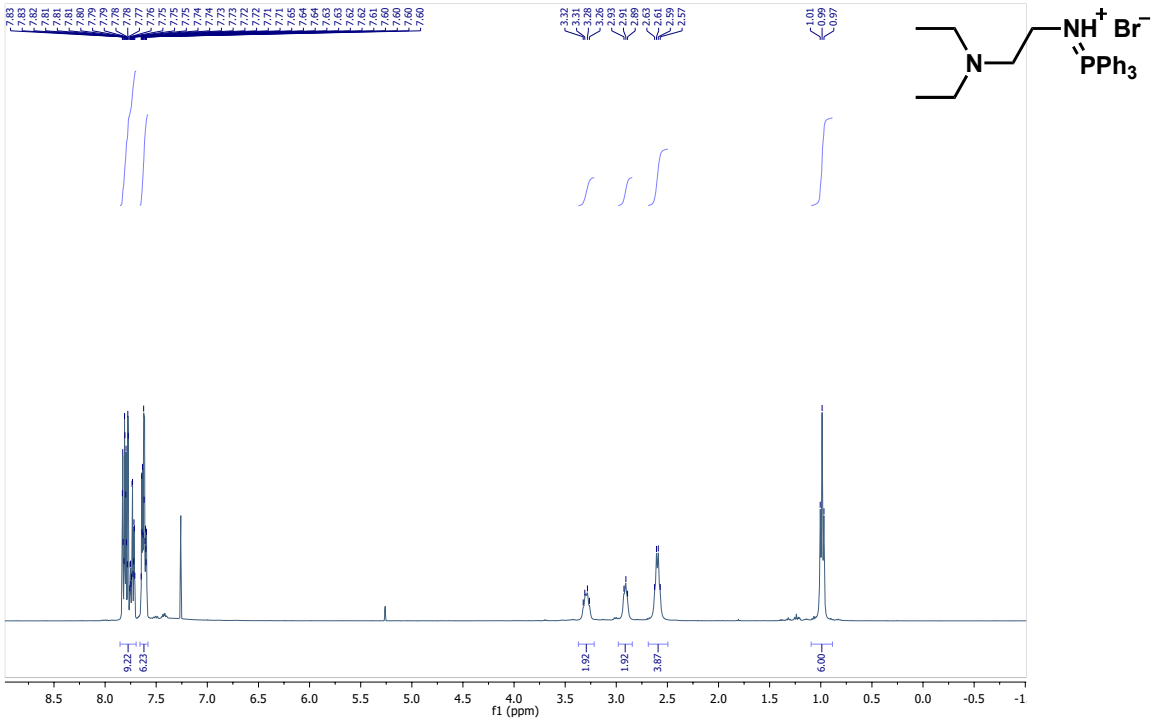

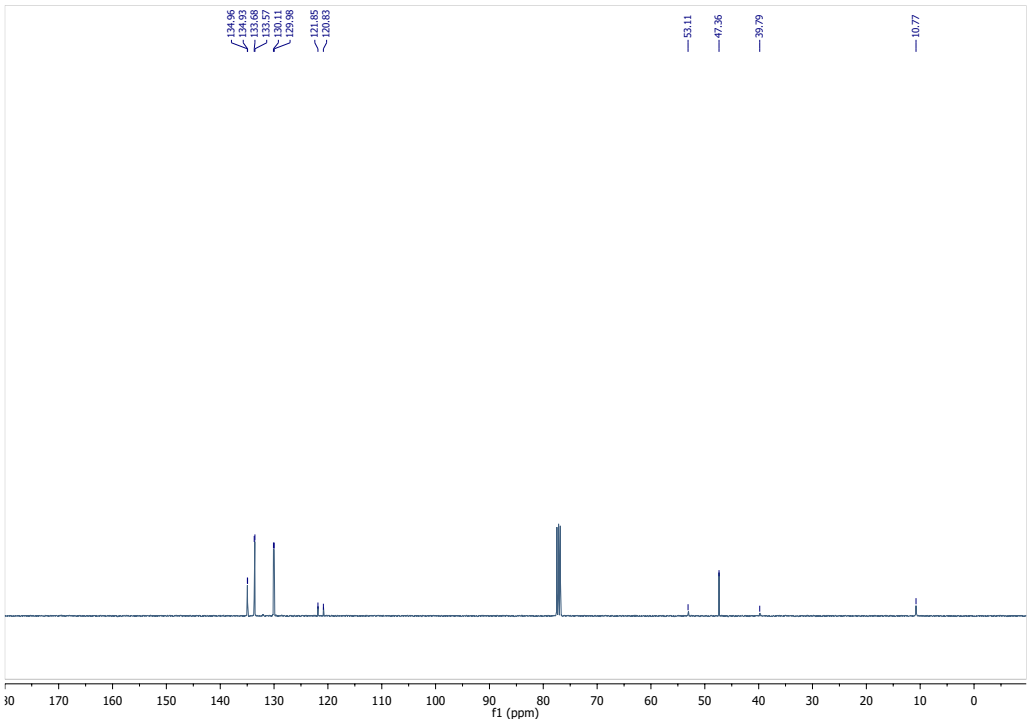
134.96
134.93
133.68
133.57
130.11
129.98
121.85
120.83
53.11
47.36
39.79
10.77
f1 (ppm)

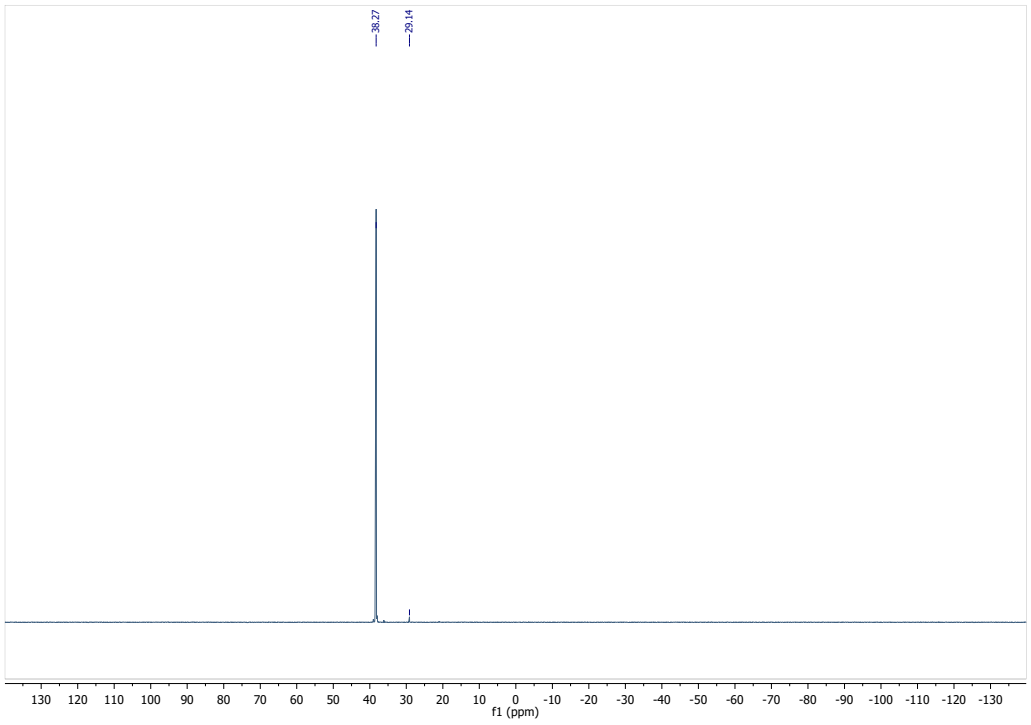
38.27
29.14
f1 (ppm)

5.9.3.15. 4. benzyl *N*-phenylcarbamate

Followed the general procedure (**2**), product obtained as a white powder (23 mg, yield 84%). ^{1}H-NMR (400 MHz, $CDCl_3$): δ 7.43–7.29 (m, 9H), 7.07 (m, 1H), 6.66 (s, 1H), 5.21 (s, 2H). MS (ESI+): Calculated $C_{14}H_{13}NO_2$ as 227.09, [M+H] found as 228.02. Characterized in accordance with the literature.[1]

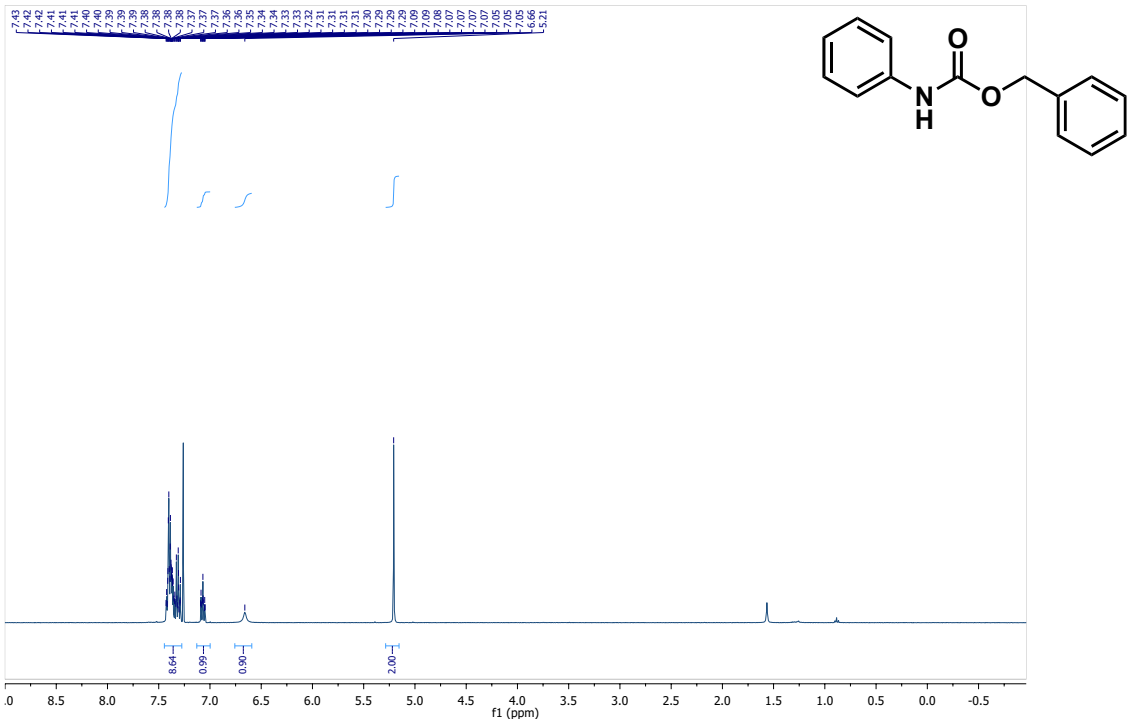

5.9.3.16. 5. propan-2-yl *N*-phenylcarbamate

Followed the general procedure (**2**), product obtained as a white powder (41 mg, yield 91%). ^{1}H-NMR (400 MHz, $CDCl_3$): δ 7.36 (d, 2H), 7.28 (m, 2H), 7.03 (m, 1H), 6.51 (s, 1H), 5.00 (sept, *J* = 6.4 Hz, 1H), 1.28 (d, *J* = 6.3 Hz, 6H). MS (ESI+): Calculated $C_{10}H_{13}NO_2$ as 179.09, [M+H] found as 180.08. Characterized in accordance with the literature.[2]

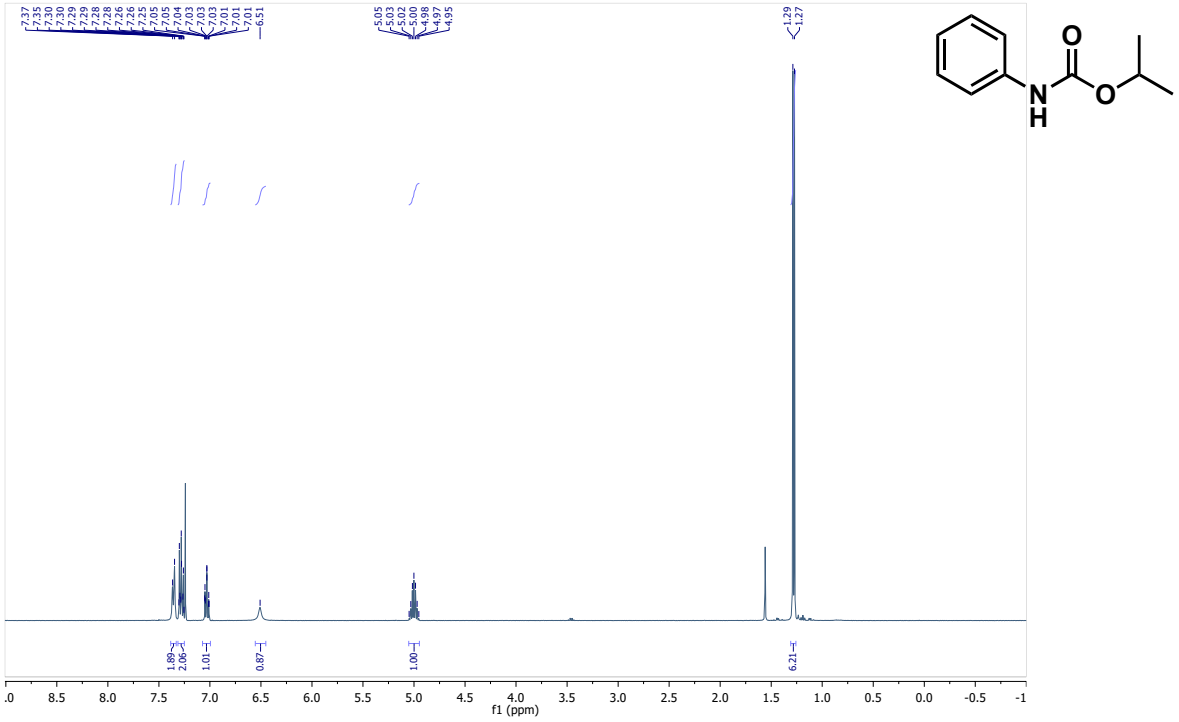

5.9.3.17. 6. 2-(4-methoxyphenyl)ethyl *N*-phenylcarbamate

Followed the general procedure (**2**), product obtained as a white powder (64 mg, yield 94%). ^{1}H-NMR (400 MHz, $CDCl_3$): δ 7.36 (d, 2H), 7.30 (m, 2H), 7.17 (m, 2H), 7.06 (m, 1H), 6.86 (m, 2H), 6.59 (s, 1H), 3.36 (dd, 2H), 3.80 (s, 3H), 2.94 (dd, 2H). ^{13}C-NMR (100 MHz, $CDCl_3$): 158.5, 137.9, 130.0, 129.9, 129.2, 123.6, 118.8, 114.1, 66.0, 55.4, 34.7. MS (ESI+): Calculated $C_{16}H_{17}NO_3Na$ as 294.1106, [M+H] found as 294.1088.

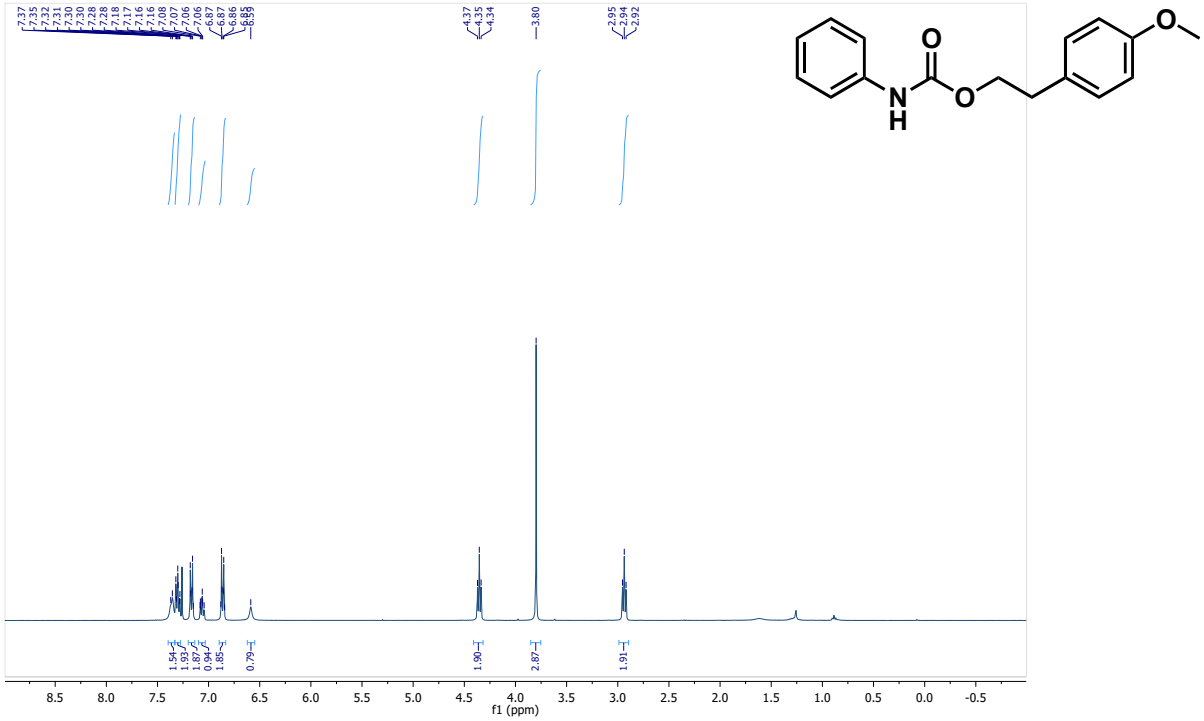

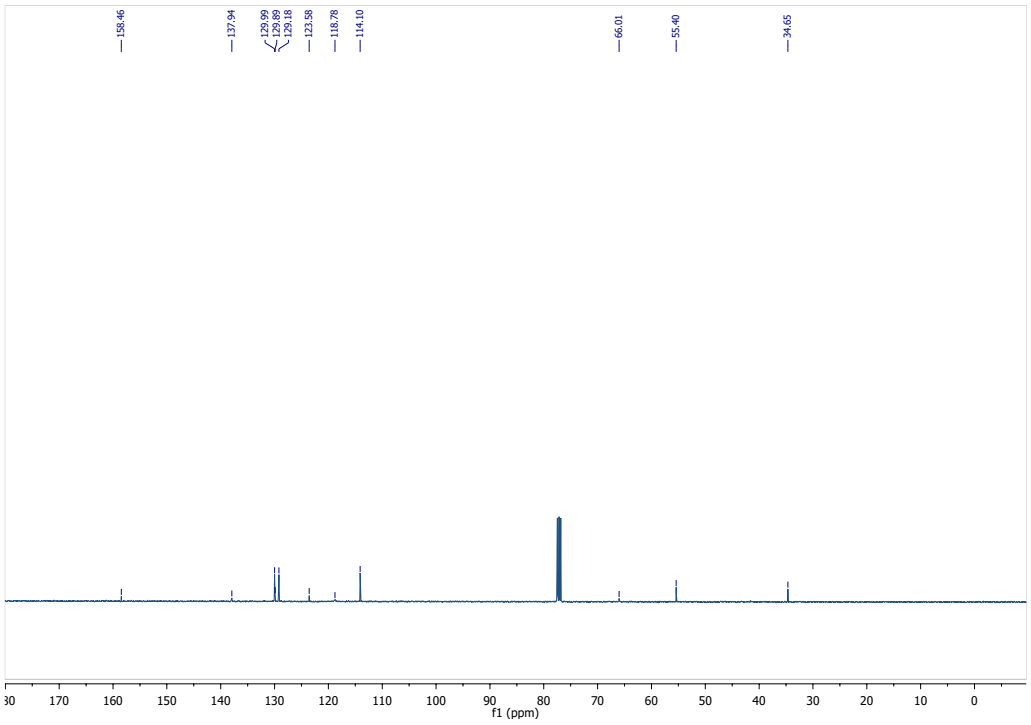
158.46
137.94
129.99
129.89
129.18
123.58
118.78
114.10
66.01
55.40
34.65
170
160
150
140
130
120
110
100
90
80
70
60
50
40
30
20
10
0
f1 (ppm)

5.9.3.18. 7. *tert*-butyl *N*-phenylcarbamate

Followed the general procedure (**2**), using 10 equiv. of *tert*-butyl alcohol. Product obtained as a white powder (40 mg, yield 83%). ^{1}H-NMR (400 MHz, $CDCl_3$): δ 7.36 (m, 2H), 7.29 (m, 2H), 7.03 (dt, *J* = 7.5, 1.2 Hz, 1H), 6.45 (s, 1H), 1.52 (s, 9H). MS (ESI+): Calculated $C_{11}H_{15}NO_2$ as 193.11, [M+H] found as 194.14. Characterized in accordance with the literature.[3]

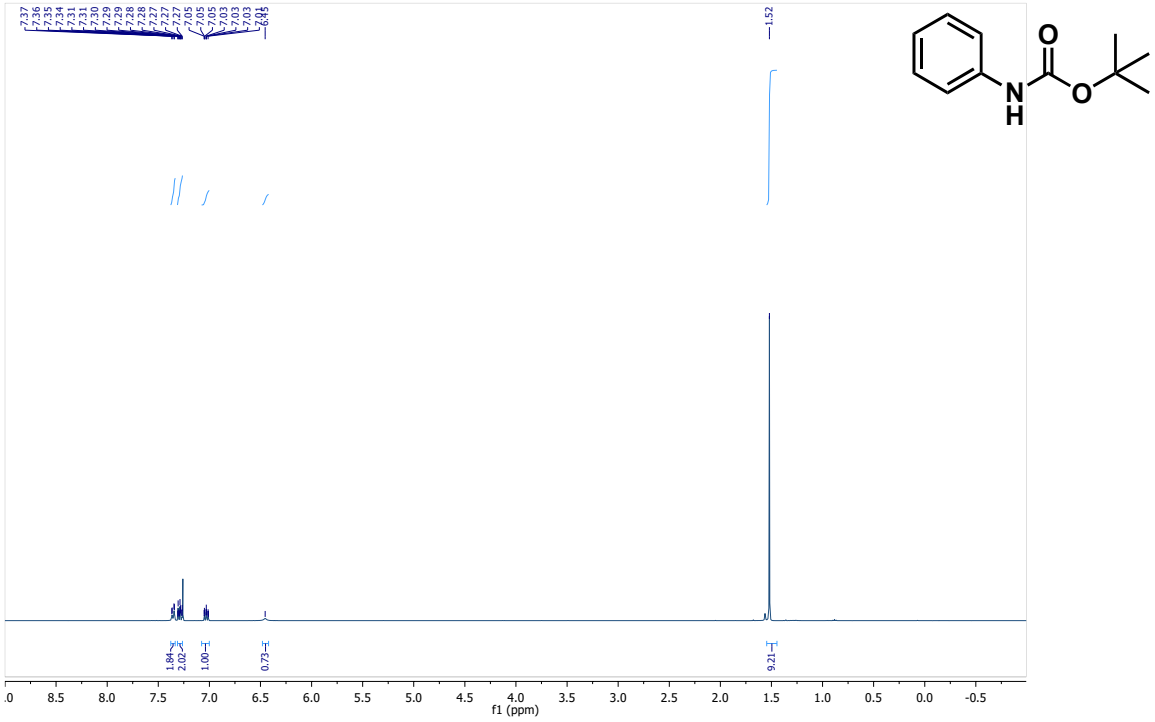

5.9.3.19. 8. phenyl *N*-phenylcarbamate

Followed the general procedure (**2**), using 10 equiv. of phenol. Product obtained as a white powder (40 mg, yield 75%). ^{1}H-NMR (400 MHz, $CDCl_3$): δ 7.45 (d, *J* = 7.8 Hz, 2H), 7.41 (m, 2H), 7.35 (m, 2H), 7.25 (m, 1H), 7.21 (m, 1H), 7.20 (m, 1H), 7.12 (dt, *J* = 7.2, 1.3 Hz, 1H), 6.96 (s, 1H). MS (ESI+): Calculated $C_{13}H_{11}NO_2$ as 213.08, [M+H] found as 214.26. Characterized in accordance with the literature.[4]

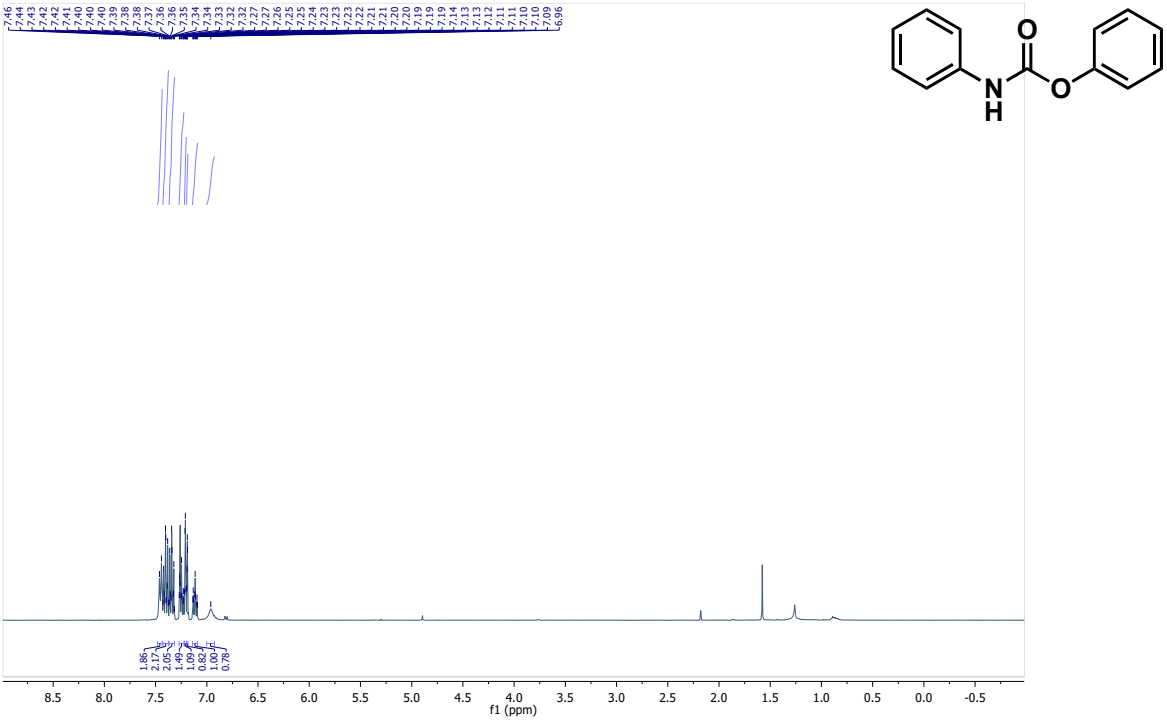

5.9.3.20. 9. *N*-phenyl-1-(phenylsulfanyl)formamide

Followed the general procedure (**2**), using 10 eqv. of thiophenol. Product obtained as a white powder (43.5 mg, yield 76%). ^{1}H-NMR (400 MHz, $CDCl_3$): δ 7.62 (m, 2H), 7.46 (m, 3H), 7.37 (dd, *J* = 8.7, 1.3 Hz, 2H), 7.30 (dd, *J* = 8.7, 7.2 Hz, 2H), 7.11 (m, 1H), 7.05 (s, 1H). MS (ESI+): Calculated $C_{13}H_{11}NOS$ as 229.06, [M+H] found as 230.11. Characterized in accordance with the literature.[5]

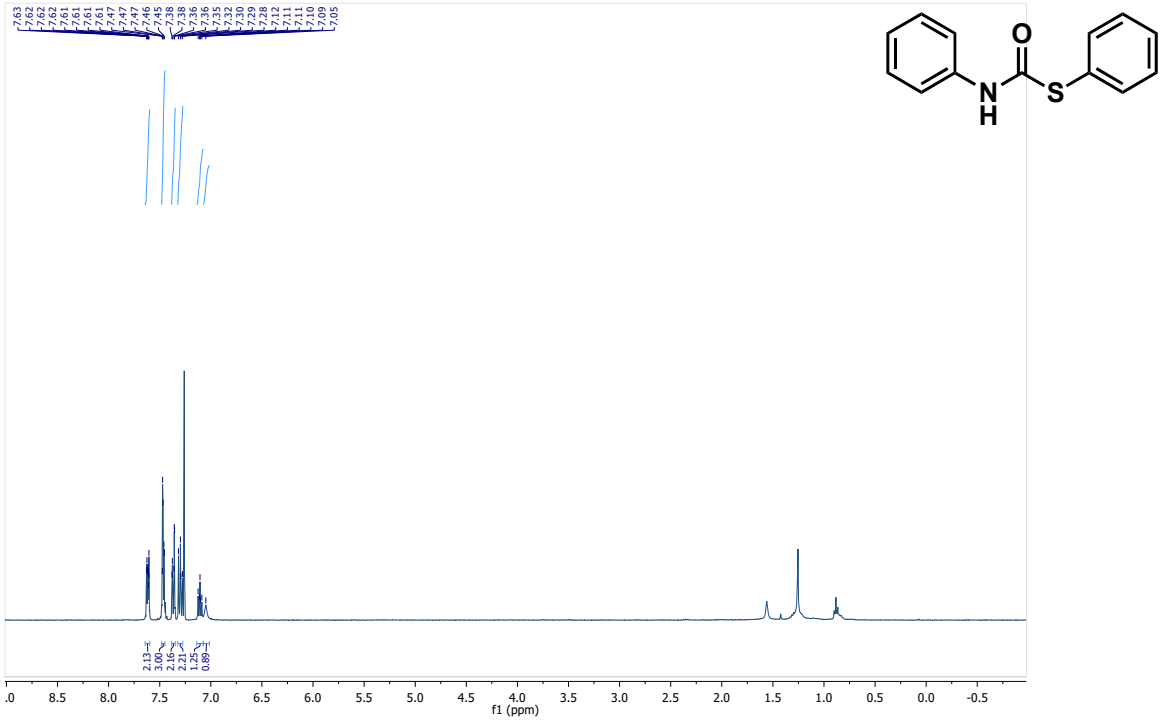

5.9.3.21. 10. 1-(naphthalen-2-ylsulfanyl)-*N*-phenylformamide

Followed the general procedure (**2**), using 10 equiv. of 2-napthalenethiol product obtained as a white powder (49 mg, yield 70%). ^{1}H-NMR (400 MHz, DMSO): δ 10.63 (s, 1H), 8.19 (dd, *J* = 13.6, 1.9 Hz, 1H), 8.02 (m, 3H), 7.63 (m, 3H), 7.56 (m, 2H), 7.36 (m, 2H), 7.11 (m, 1H). ^{13}C-NMR (100 MHz, DMSO): 162.9, 138.8, 134.7, 133.0, 132.7, 132.0, 128.9, 128.3, 127.8, 127.6, 127.2, 126.7, 125.6, 123.6, 119.1. MS (ESI+): Calculated $C_{17}H_{13}NOS$ as 279.07, [M+H] found as 280.26. Characterized in accordance with the literature.[5]

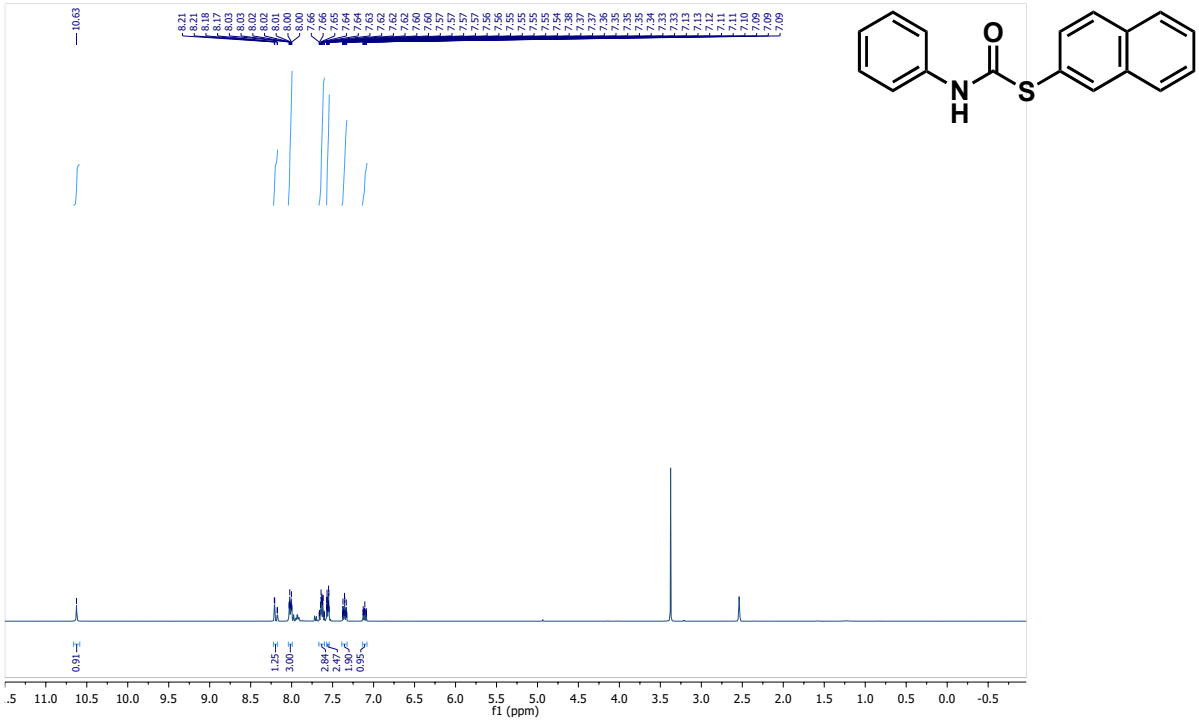

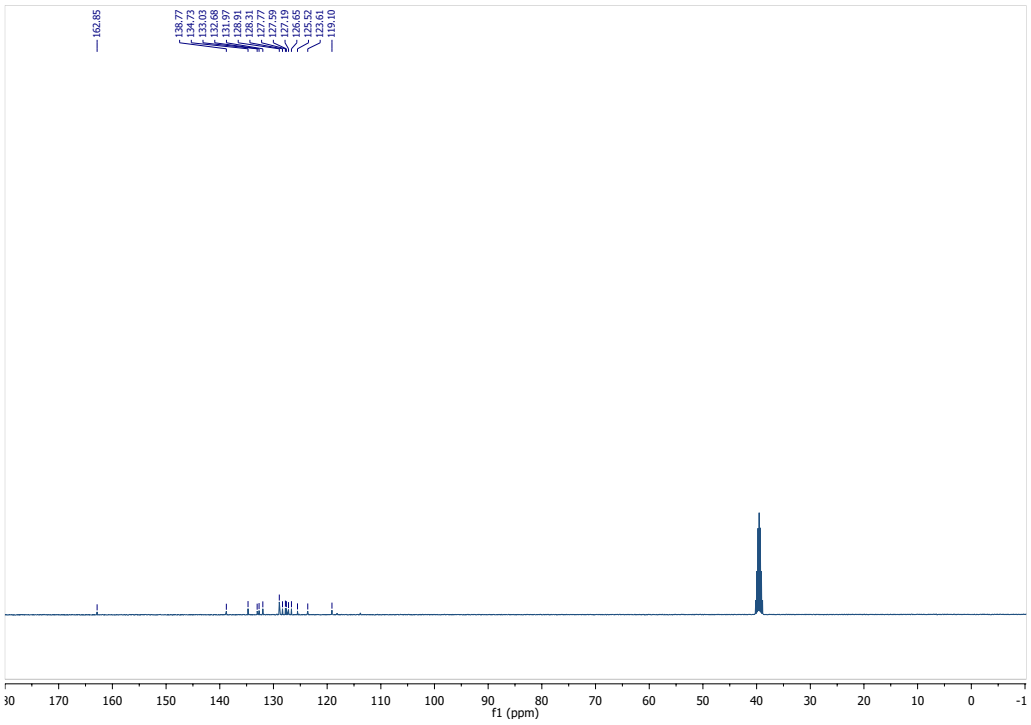
162.85
138.77
134.73
133.03
132.68
131.97
128.91
128.31
127.77
127.59
127.19
126.65
125.52
123.61
119.10
170
160
150
140
130
120
110
100
90
80
70
60
50
40
30
20
10
0
f1 (ppm)

5.9.3.22. 11. *N*-phenyl(benzylsulfanyl)formamide

Followed the general procedure (**2**), product obtained as a white powder (66.5 mg, yield 86%). ^{1}H-NMR (400 MHz, $CDCl_3$): δ 7.40 (m, 3H), 7.35 (m, 2H), 7.31 (m, 3H), 7.26 (m, 1H), 7.12 (m, 1H), 7.06 (s, 1H), 4.23 (s, 2H). ^{13}C-NMR (100 MHz, $CDCl_3$): 165.5, 138.1, 137.8, 129.3, 129.0, 128.8, 127.5, 124.7, 120.0, 34.6. MS (ESI+): Calculated $C_{14}H_{13}NOS$ as 243.07, [M+H] found as 244.13. Characterized in accordance with the literature.[5]

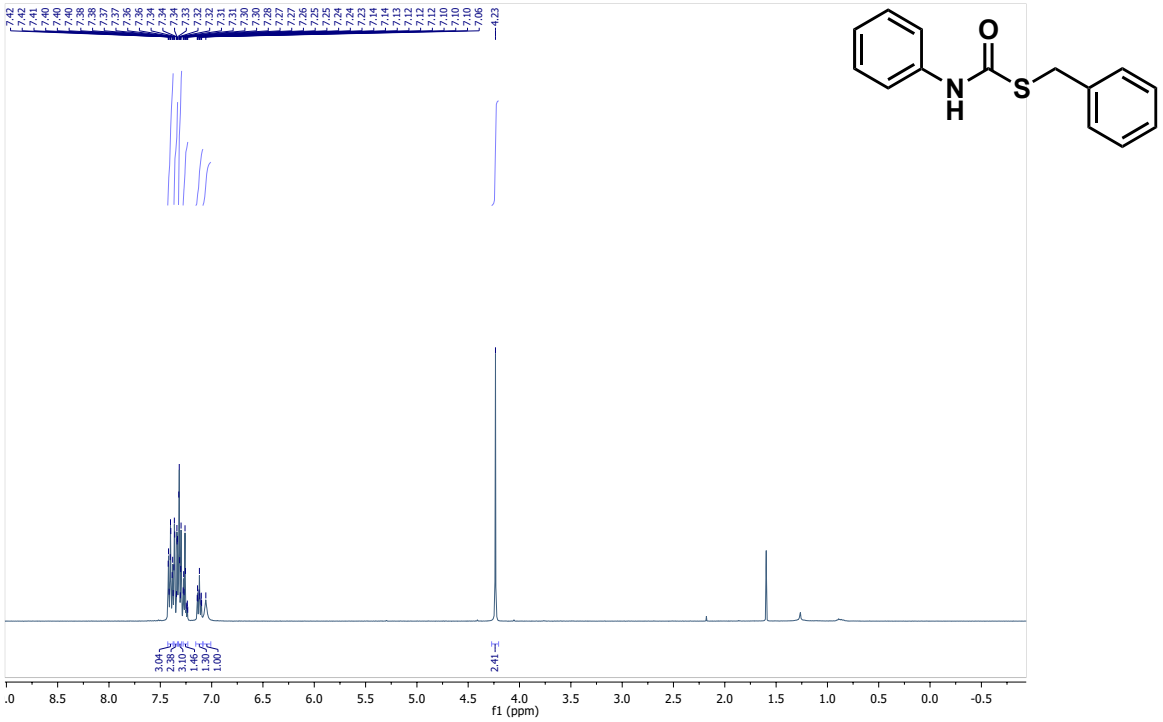

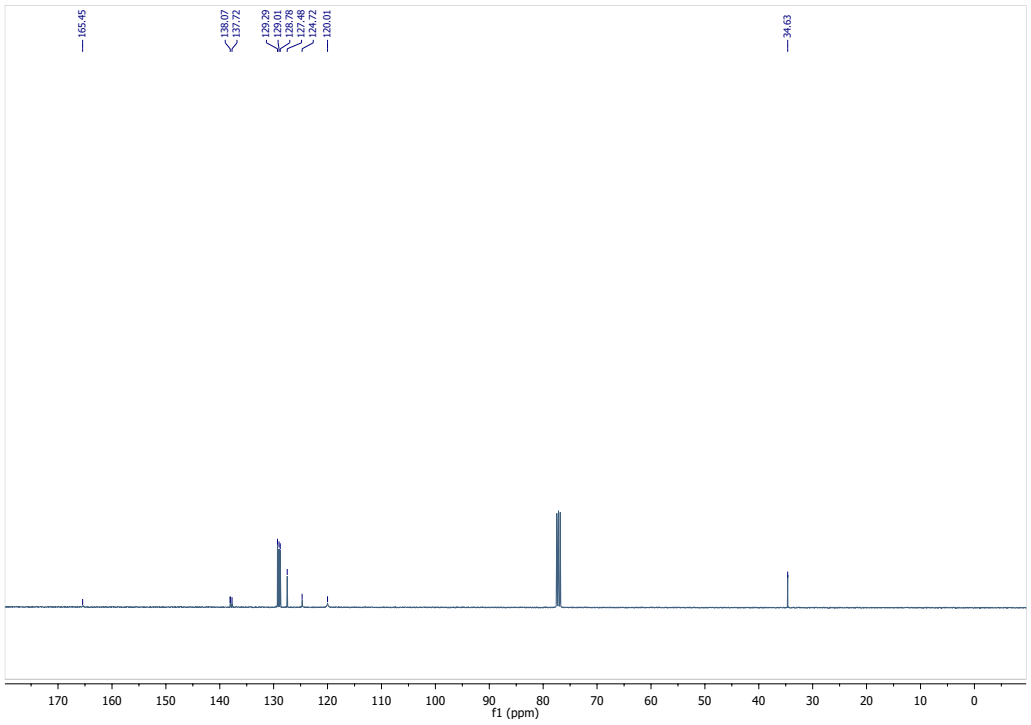
165.45
138.07
137.72
129.29
129.01
128.78
127.48
124.72
120.01
34.63
170
160
150
140
130
120
110
100
90
80
70
60
50
40
30
20
10
0
f1 (ppm)

5.9.3.23. 12. 3-*tert*-butyl-3-methyl-1-phenylurea

Followed the general procedure (**3**), product obtained as a white powder (40 mg, yield 78%). ^{1}H-NMR (400 MHz, $CDCl_3$): δ 7.29 (m, 4H), 7.00 (m, 1H), 6.19 (s, 1H), 2.97 (s, 3H), 1.45 (s, 9H). MS (ESI+): Calculated $C_{12}H_{18}N_2O$ as 206.14, [M+H] found as 207.14. Characterized in accordance with the literature.[6]

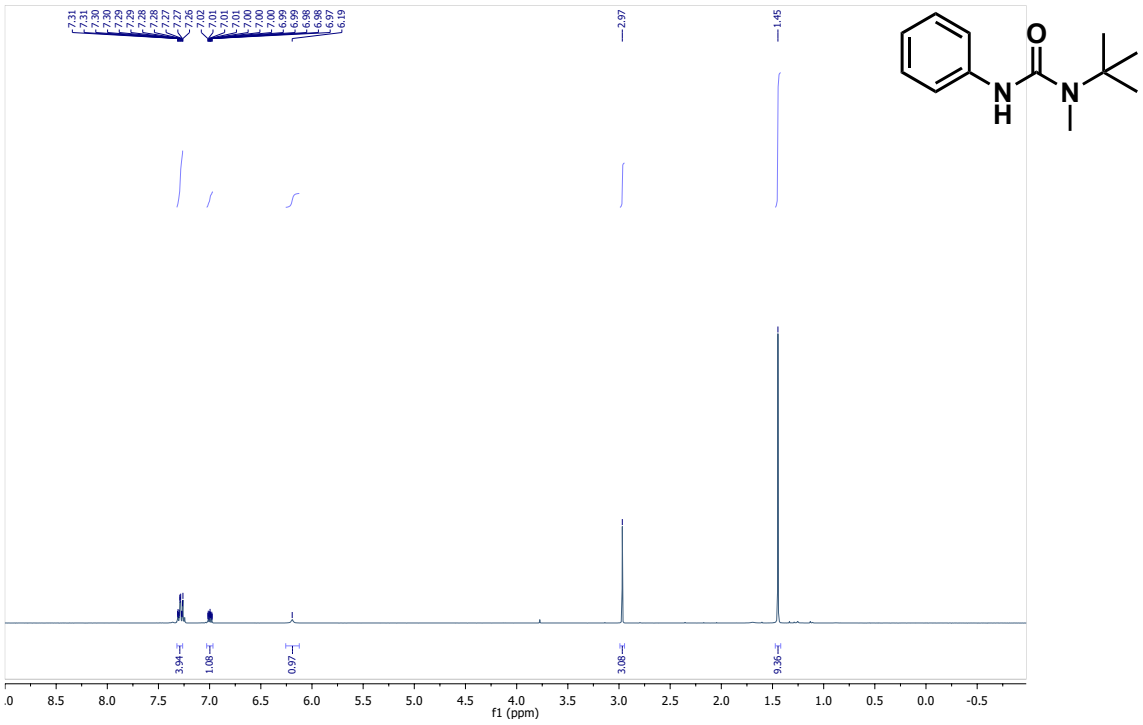

5.9.3.24. 13. 1,3-diethyl 2-(phenylcarbamoyl)propanedioate

Followed the general procedure (**6**), product obtained as a white powder (57 mg, yield 82%). ^{1}H-NMR (400 MHz, $CDCl_3$): δ 9.31 (s, 1H), 7.57 (dd, *J* = 8.7, 1.7 Hz, 2H), 7.34 (m, 2H), 7.14 (m, 1H), 4.45 (s, 1H), 4.31 (dq, *J* = 7.1, 1.3 Hz, 4H), 1.32 (t, *J* = 7.1 Hz, 6H). ^{13}C-NMR (100 MHz, $CDCl_3$): 166.12, 160.17, 137.51, 129.36, 125.20, 120.50, 63.31, 59.95, 14.29. MS (ESI+): Calculated $C_{14}H_{17}NO_5Na$ as 302.1004, [M+H] found as 302.0982. Characterized in accordance with the literature.[7]

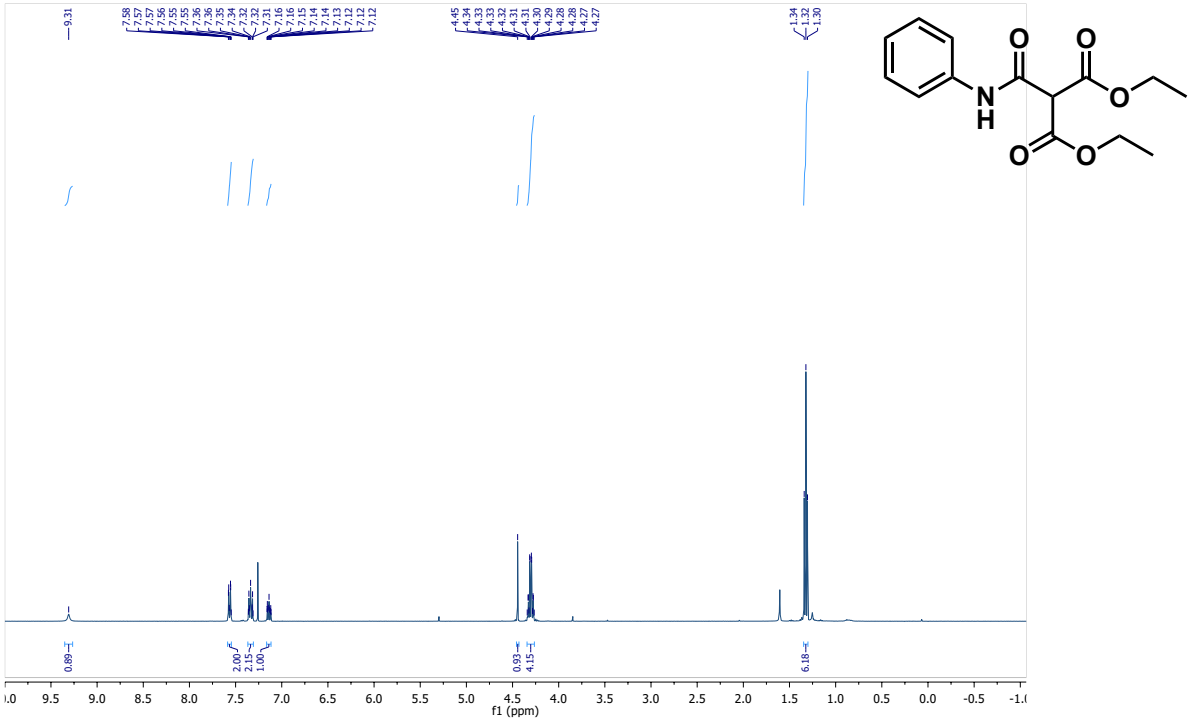

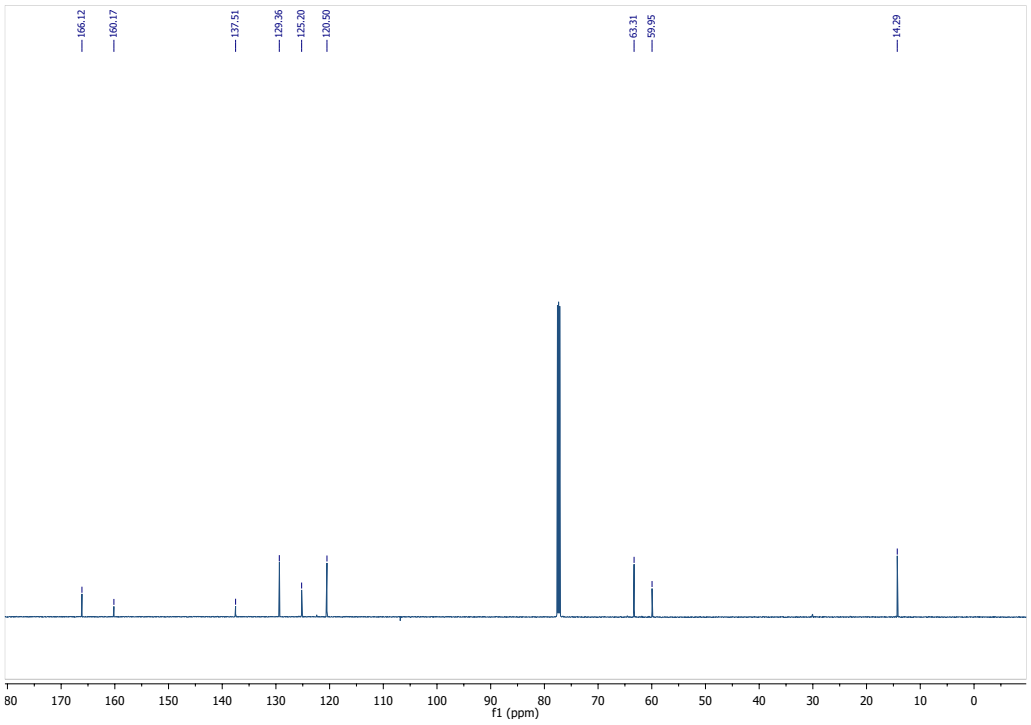
166.12
160.17
137.51
129.36
125.20
120.50
63.31
59.95
14.29
80
170
160
150
140
130
120
110
100
90
80
70
60
50
40
30
20
10
0
f1 (ppm)

5.9.3.25. 14. *N*-phenylbenzamide

Followed the general procedure (**4**), product obtained as a white powder (31 mg, yield 63%). ^{1}H-NMR (400 MHz, $CDCl_3$): δ 7.87 (m, 3H), 7.65 (m, 2H), 7.55 (m, 1H), 7.48 (m, 2H), 7.38 (m, 2H), 7.16 (dt, *J* = 7.1, 1.2 Hz, 1H). MS (ESI+): Calculated $C_{13}H_{11}NO$ as 197.08, [M+H] found as 198.16. Characterized in accordance with the literature.[8]

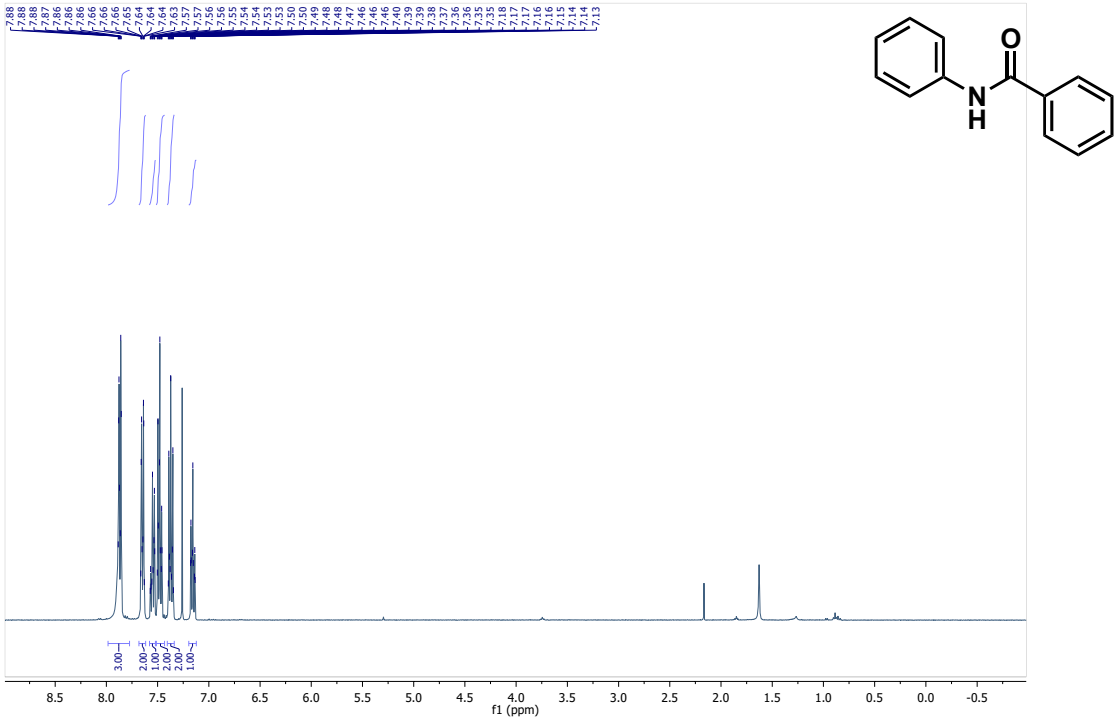

5.9.3.26. 15. *N*-phenylacetamide

Followed the general procedure (**4**), product obtained as a white solid (32 mg, yield 65%). ^{1}H-NMR (400 MHz, $CDCl_3$): δ 8.61 (s, 1H), 7.41 (dd, *J* = 8.6, 1.2 Hz, 2H), 7.24 (dd, *J* = 8.6, 7.3 Hz, 2H), 6.93 (dt, *J* = 7.3, 1.2 Hz, 1H), 3.31 (s, 3H). MS (ESI+): Calculated C_8H_9NO as 135.07, [M+H] found as 136.14. Characterized in accordance with the literature.[9]

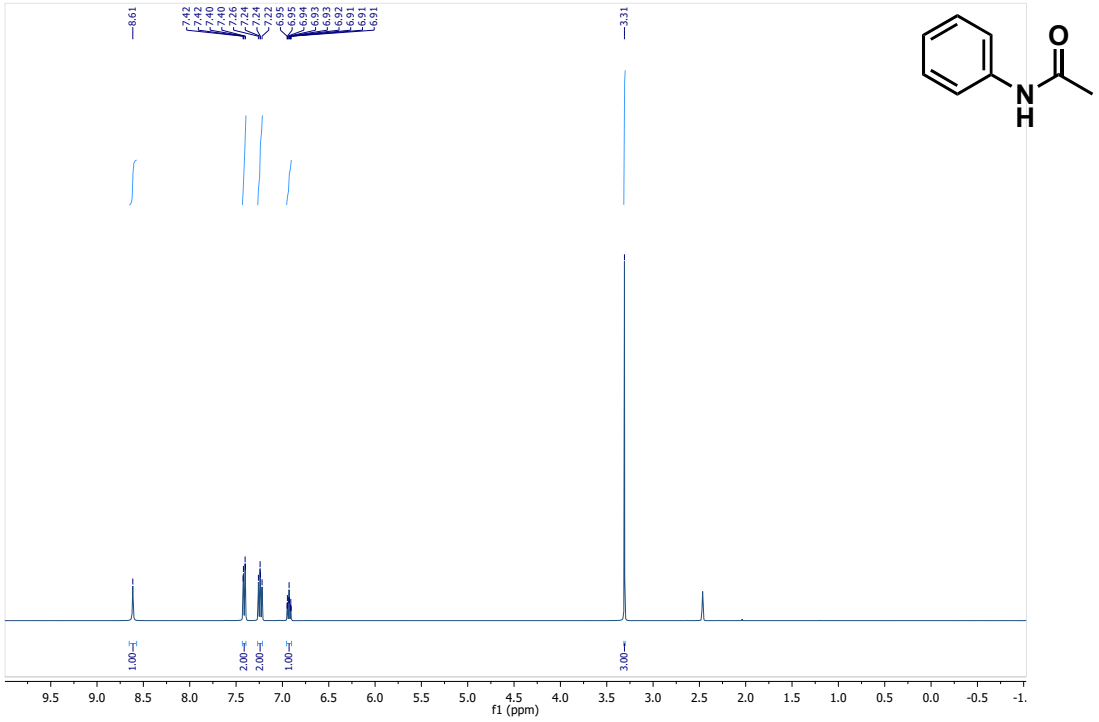

5.9.3.27. 16. *N*,3-diphenylprop-2-ynamide

Followed the general procedure (**5**), product obtained as a brown solid (41.5 mg, yield 75%). ^{1}H-NMR (400 MHz, $CDCl_3$): δ 7.58 (m, 4H), 7.45 (m, 1H), 7.38 (m, 4H), 7.15 (t, *J* = 7.4 Hz, 1H). MS (ESI+): Calculated $C_{15}H_{11}NO$ as 221.08, [M+H] found as 222.09. Characterized in accordance with the literature.[10]

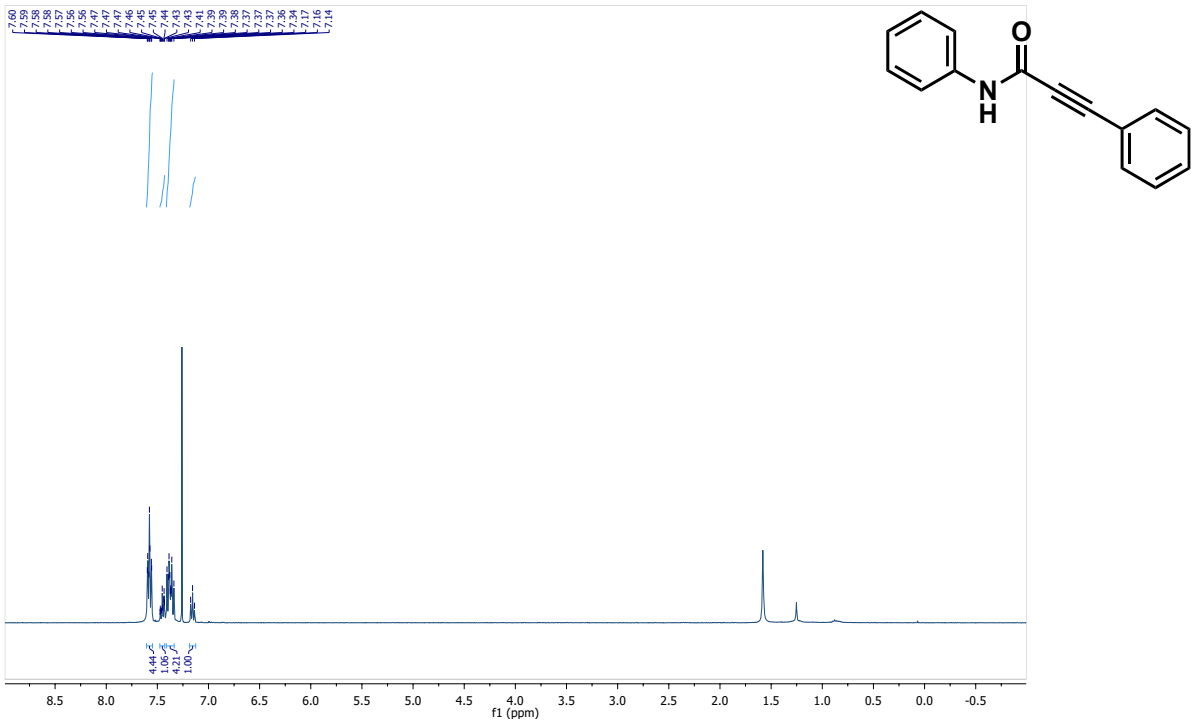

5.9.3.28. 17. benzyl *N*-(4-methoxyphenyl)carbamate

Followed the general procedure (**2**), product obtained as a white powder (53 mg, yield 82%). ^{1}H-NMR (400 MHz, $CDCl_3$): δ 7.40–7.32 (m, 5H), 7.30–7.26 (m, 2H), 6.83 (m, 2H), 6.51 (s, 1H), 5.17 (s, 2H), 3.76 (s, 3H). MS (ESI+): Calculated $C_{15}H_{15}NO_3$ as 257.11, [M+H] found as 258.20. Characterized in accordance with the literature.[1]

5.9.3.29. 18. benzyl *N*-(4-bromophenyl)carbamate

Followed the general procedure (**2**), product obtained as a white powder (64 mg, yield 83%). ^{1}H-NMR (400 MHz, $CDCl_3$): δ 7.42 (m, 1H), 7.39 (m, 5H), 7.35 (m, 1H), 7.28 (d, *J* = 8.5 Hz, 2H), 6.65 (s, 1H), 5.20 (s, 2H). MS (ESI+): Calculated $C_{14}H_{12}BrNO_2$ as 305.01, [M+H] found as 306.19. Characterized in accordance with the literature.[1]

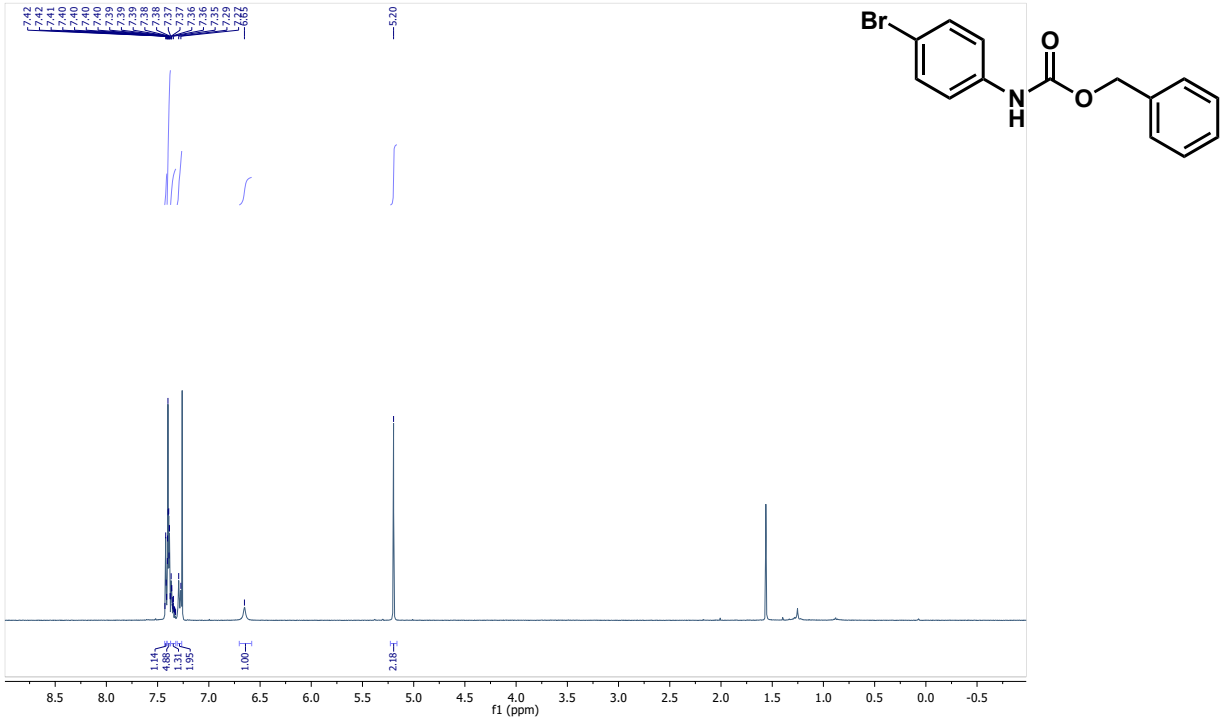

5.9.3.30. 19. benzyl *N*-(4-fluorophenyl)carbamate

Followed the general procedure (**2**), product obtained as a white powder (35 mg, yield 57%). ^{1}H-NMR (400 MHz, $CDCl_3$): δ 7.41–7.32 (m, 7H), 7.00 (m, 2H), 6.70 (s, 1H), 5.20 (s, 2H). ^{19}F-NMR (376 MHz, $CDCl_3$): -119.42 (s, 1F). MS (ESI+): Calculated $C_{14}H_{12}FNO_2$ as 245.09, [M+H] found as 246.06. Characterized in accordance with the literature.[1]

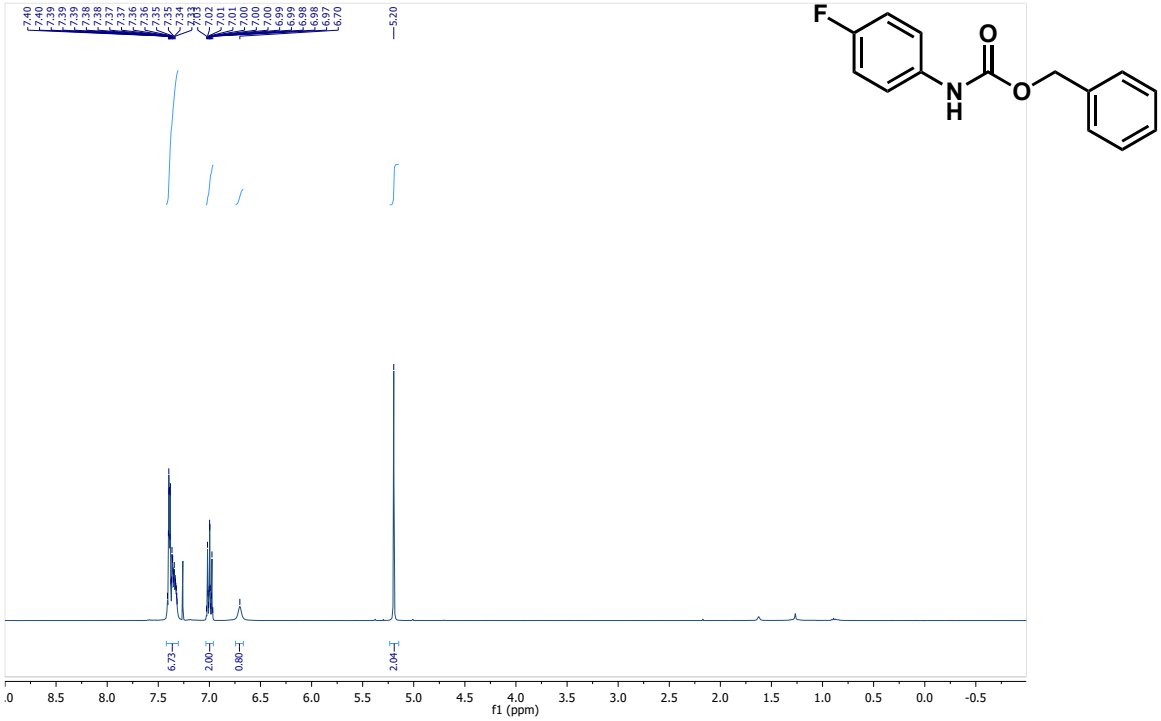

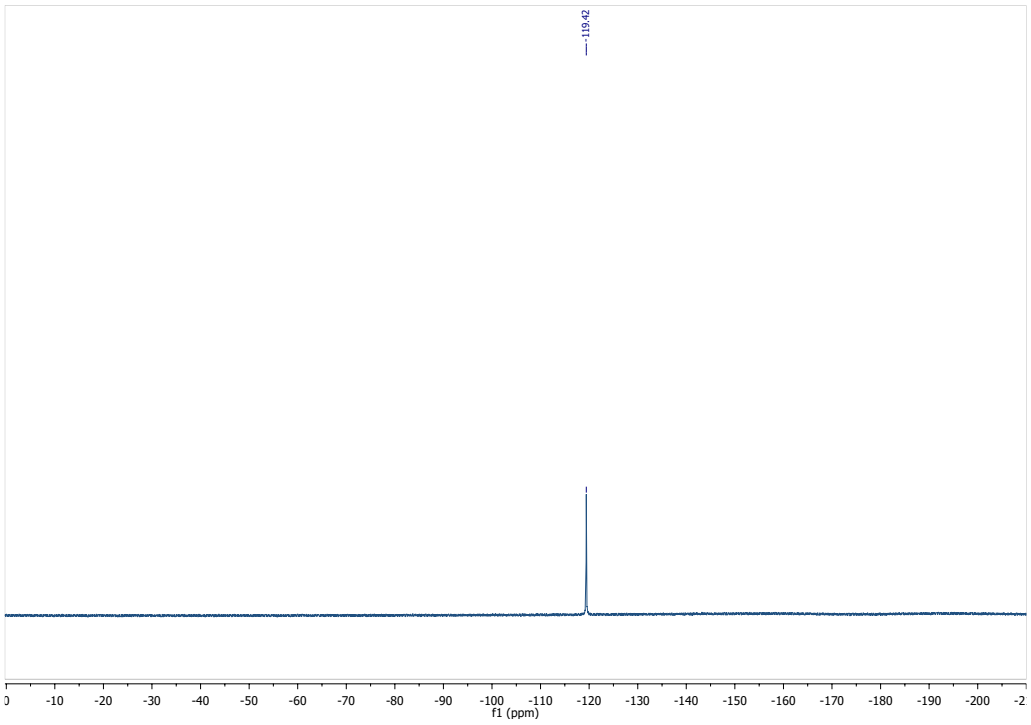
-119.42
0
-10
-20
-30
-40
-50
-60
-70
-80
-90
-100
-110
-120
-130
-140
-150
-160
-170
-180
-190
-200
-2
f1 (ppm)

5.9.3.31. 21. benzyl *N*-(2-methylphenyl)carbamate

Followed the general procedure (**2**), product obtained as a white powder (51 mg, yield 84%). ^{1}H-NMR (400 MHz, $CDCl_3$): δ 7.83 (s, 1H), 7.44–7.34 (m, 5H), 7.22 (m, 1H), 7.16 (d, *J* = 7.5 Hz, 1H), 7.03 (dt, *J* = 7.4, 1.3 Hz, 1H), 6.46 (s, 1H), 5.22 (s, 2H), 2.24 (s, 3H). ^{13}C-NMR (100 MHz, $CDCl_3$): 153.8, 136.2, 135.9, 130.5, 128.8, 128.5, 128.5, 127.1, 124.3, 121.1, 67.3, 17.8. MS (ESI+): Calculated $C_{15}H_{15}NO_2$ as 241.11, [M+H] found as 242.17. Characterized in accordance with the literature.[2]

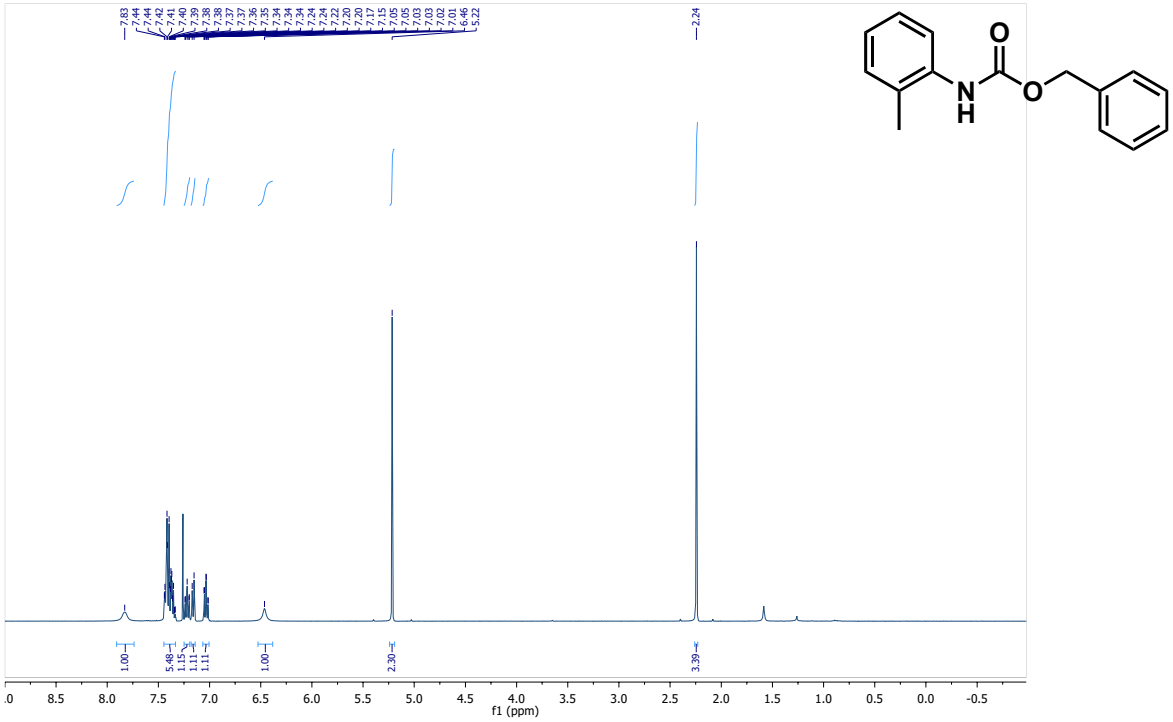

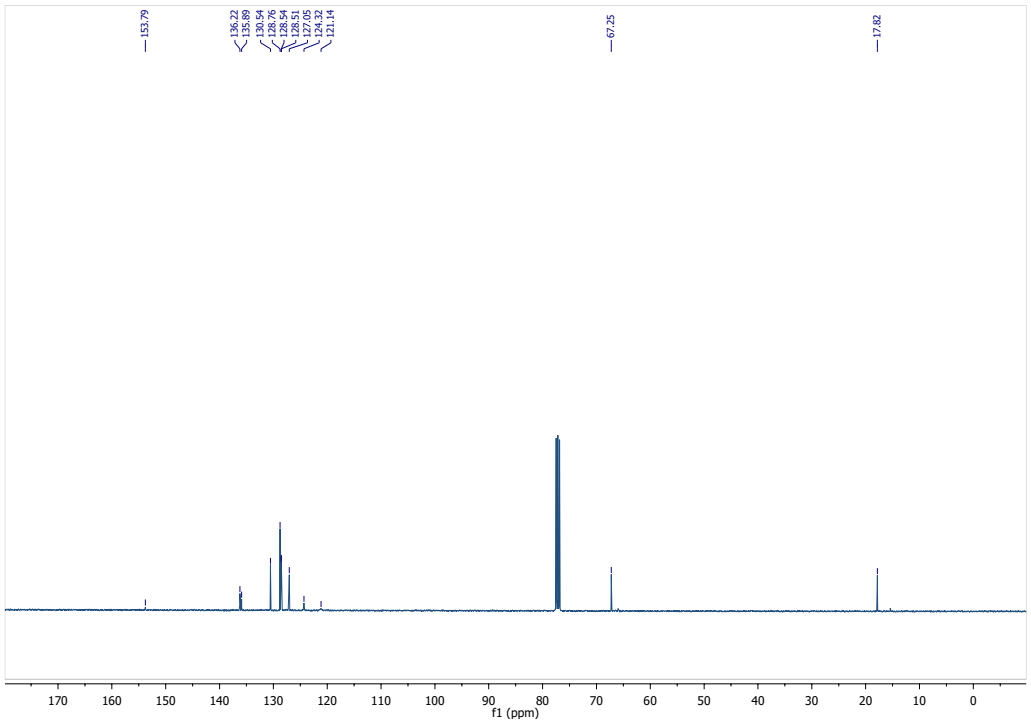
153.79
136.22
135.89
130.54
129.76
128.54
128.51
127.05
124.32
121.14
67.25
17.82
170
160
150
140
130
120
110
100
90
80
70
60
50
40
30
20
10
0
f1 (ppm)

5.9.3.32. 22. [(1,1′-biphenyl)-4-yl]methyl *N*-cyclohexylcarbamate

Followed the general procedure **7**, then procedure **2,** using 10 equiv. of 4-biphenylmethanol**.** The reaction was performed at reflux temperature in THF (2.5 mL). DBU was not used. Product obtained as a white powder (64 mg, yield 82%). ^{1}H-NMR (400 MHz, $CDCl_3$): δ 7.59 (d, *J* = 8.4 Hz, 4H), 7.44 (m, 4H), 7.35 (m, 1H), 5.13 (s, 2H), 4.66 (s, 1H), 3.52 (s, 1H), 1.95 (m, 2H), 1.71 (dt, *J* = 13.5, 3.9 Hz, 2H), 1.61 (m, 2H), 1.36 (m, 2H), 1.15 (m, 2H). ^{13}C-NMR (100 MHz, $CDCl_3$): 155.7, 141.2, 140.9, 135.9, 128.9, 128.8, 127.5, 127.4, 127.3, 66.4, 50.1, 33.6, 25.6, 24.9. MS (ESI+): Calculated $C_{20}H_{23}NO_2Na$ as 332.1626, [M+H] found as 332.1635.

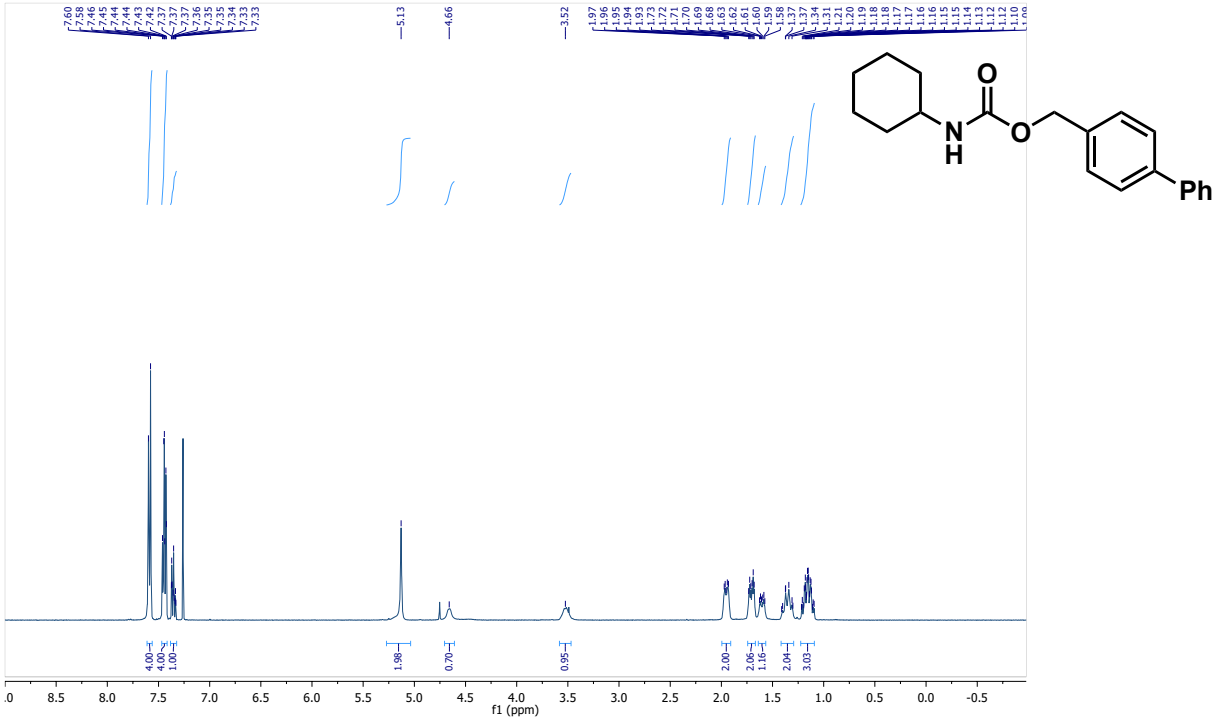

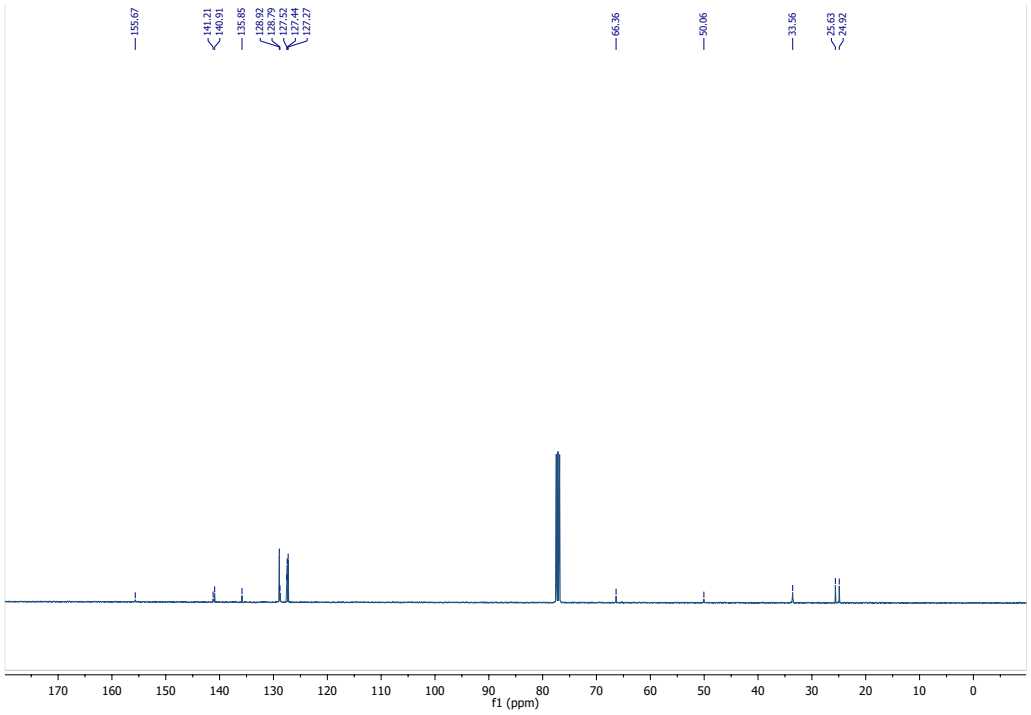
155.67
141.21
140.91
135.85
128.92
128.79
127.52
127.44
127.27
66.36
50.06
33.56
25.63
24.92
170
160
150
140
130
120
110
100
90
80
70
60
50
40
30
20
10
0
f1 (ppm)

5.9.3.33. 23. 1,3-dioxo-2,3-dihydro-1H-isoindol-2-yl *N*-tert-butylcarbamate

Followed the general procedure **7**, then procedure **2** using 10 equiv. of *N*-hydroxypthalimide (NHP). NHP was dissolved in THF (2.5) mL, and 10 equiv. of NEt_3 was added. The reaction was performed at reflux temperature in THF (2.5 mL). DBU was not used. The solvent was removed under reduced pressure, and the residue was dissolved in 10 mL of DCM. Solvent extraction was performed, and the organic layer was extracting using saturated aqueous NH_4Cl (3 × 5 mL), 10% Na_2CO_3 (2 × 5 mL), and water (2 × 5 mL). The solvent was removed under reduced pressure, and the product was purified by flash chromatography using silica gel (0-25% hexane/ethyl acetate). Product obtained as a white powder (54 mg, yield 81%). ^{1}H-NMR (400 MHz, $CDCl_3$): δ 7.88 (dd, *J* = 5.4, 3.1 Hz, 2H), 7.77 (dd, *J* = 5.5, 3.1 Hz, 2H), 5.22 (s, 1H), 1.39 (s, 9H). ^{13}C-NMR (100 MHz, $CDCl_3$): 162.9, 150.1, 134.8, 129.1, 124.0, 52.4, 28.7. MS (ESI+): Calculated $C_{13}H_{14}N_2O_4$ as 262.10, [M+H] found as 263.11.

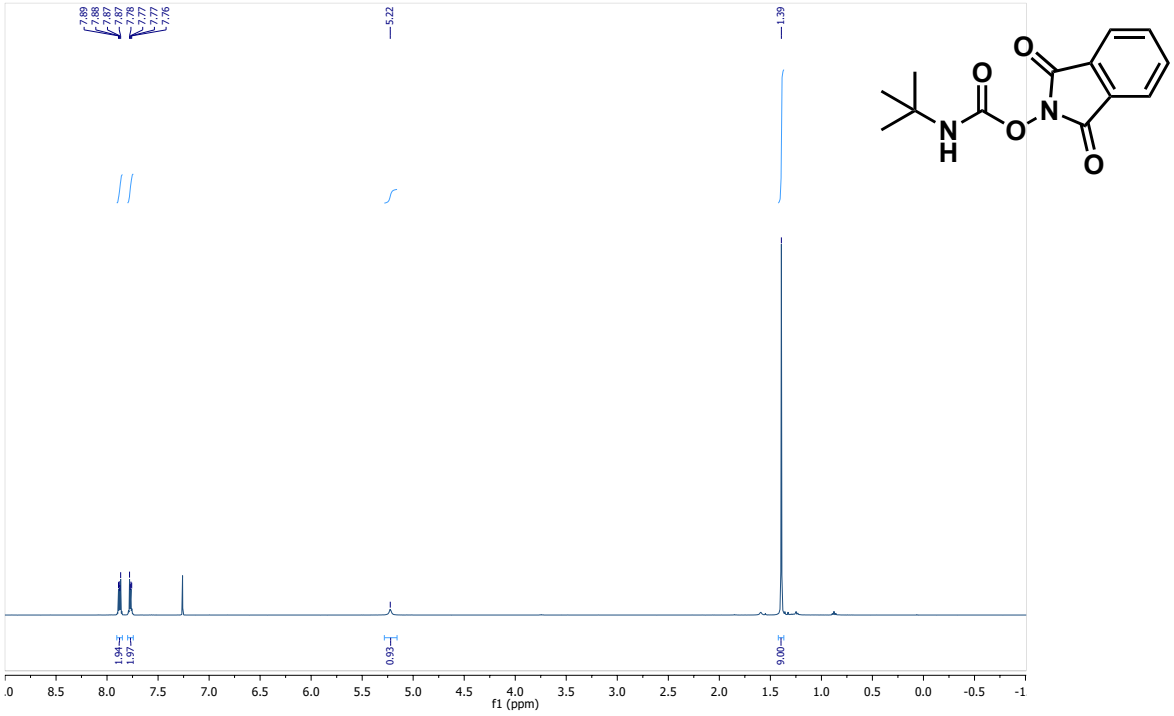

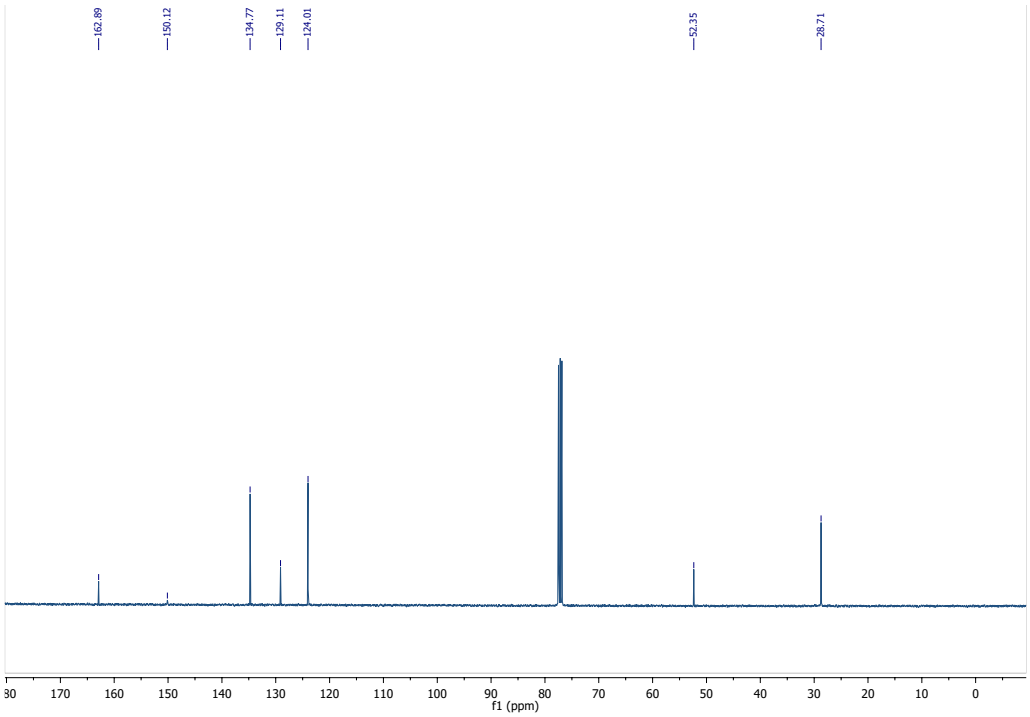
162.89
150.12
134.77
129.11
124.01
52.35
28.71
f1 (ppm)

5.9.3.34. 24. 3-*tert*-butyl-1-[(furan-2-yl)methyl]-3-methylurea

Followed the general procedure (**3**), product obtained as a white powder (37.5 mg, yield 71%). ^{1}H-NMR (400 MHz, $CDCl_3$): δ 7.35 (dd, *J* = 1.9, 0.9 Hz, 1H), 6.31 (dd, *J* = 3.2, 1.9 Hz, 1H), 6.21 (dd, *J* = 3.2, 0.8 Hz, 1H), 4.56 (s, 1H), 4.37 (dd, *J* = 5.3, 0.7 Hz, 2H), 2.82 (s, 3H), 1.40 (s, 9H). ^{13}C-NMR (100 MHz, $CDCl_3$): 158.9, 153.1, 142.0, 110.5, 106.9, 55.9, 38.0, 31.9, 29.1. MS (ESI+): Calculated $C_{11}H_{18}N_2O_2Na$ as 233.1266, [M+H] found as 233.1261.

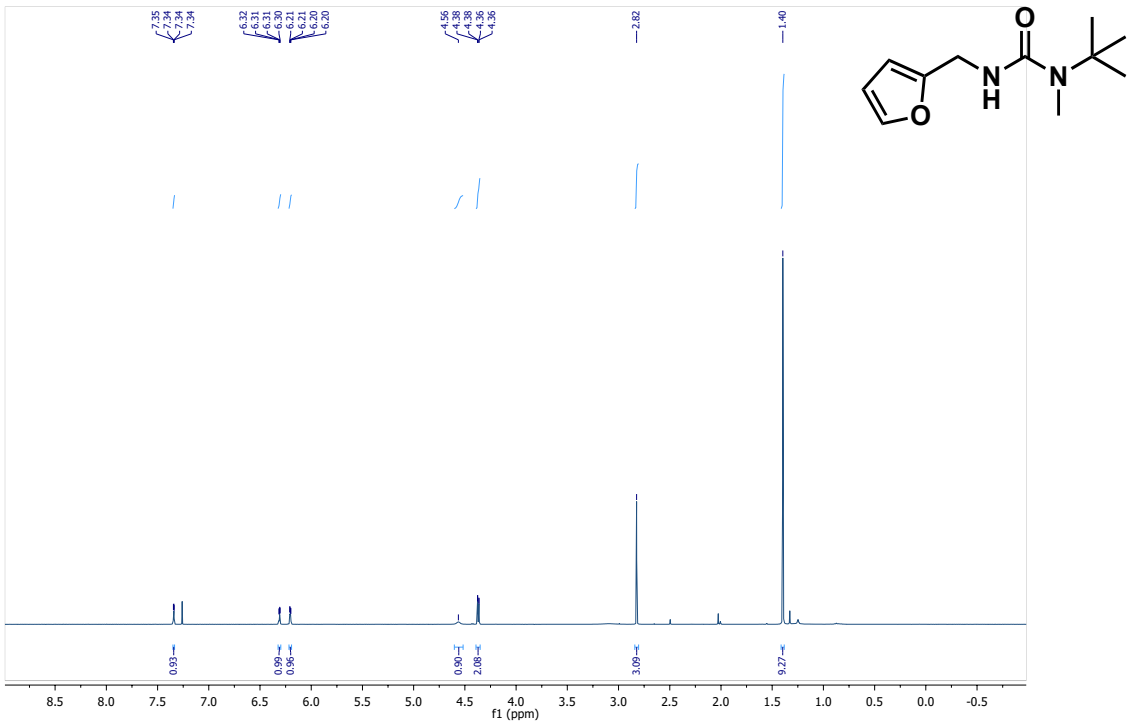

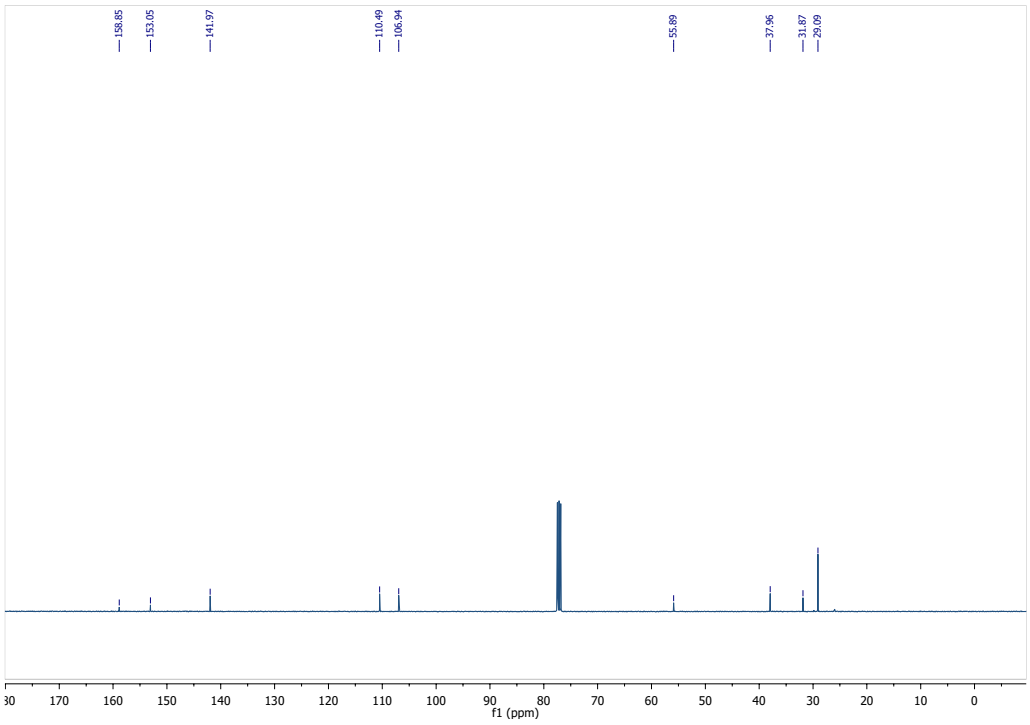
158.85
153.05
141.97
110.49
106.94
55.89
37.96
31.87
29.09
170
160
150
140
130
120
110
100
90
80
70
60
50
40
30
20
10
0
f1 (ppm)

5.9.3.35. 25. 5-hydroxy-(1,1′-biphenyl)-2-yl *N*-cyclohexylcarbamate

Followed the general procedure **7**, then procedure **2** using 10 equiv. of 2-phenyl-1,4-dihydroquinone. The reaction was performed at reflux temperature in THF (2.5 mL). DBU was not used. The obtained product was hydrolyzed in accordance with the literature, and a mixture of isomers was obtained (186 mg, yield 60%). Isomers were separated by prep-HPLC using a Phenomenex C18, 10 μM, 250 × 10 column with 70:30 MeOH/H_2O + 1% formic acid at 10 mL/min. Obtained isomer 1 (*N*-5-hydroxy-[1,1′-biphenyl]-2-yl cyclohexylcarbamate) as a white powder (160 mg, 85%), obtained isomer 2 (*N*-6-hydroxy-[1,1′-biphenyl]-3-yl cyclohexylcarbamate; URB694) as a white powder (26.5 mg, 14%). Isomer 1 ^{1}H-NMR (400 MHz, $CDCl_3$): δ 7.36 (m, 4H), 7.31 (m, 1H), 6.93 (d, *J* = 8.7 Hz, 1H), 6.71 (d, *J* = 3.0 Hz, 1H), 6.60 (dd, *J* = 8.7, 3.0 Hz, 1H), 6.19 (s, 1H), 4.78 (d, *J* = 8.4 Hz, 1H), 3.44 (m, 1H), 1.83 (dd, *J* = 12.6, 4.1 Hz, 2H), 1.68–1.56 (m, 4H), 1.31 (m, 2H), 1.10 (m, 2H). MS (ESI+): Calculated $C_{19}H_{21}NO_3$ as 311.15, [M+H] found as 312.20. Isomer 2 ^{1}H-NMR (400 MHz, $CDCl_3$): δ 7.45 (d, *J* = 4.3 Hz, 4H), 7.37 (m, 1H), 6.98 (m, 2H), 6.89 (d, *J* = 8.5 Hz, 1H), 4.87 (d, *J* = 8.2 Hz, 1H), 3.53 (m, 1H), 1.99 (d, *J* = 12.3 Hz, 2H), 1.72 (m, 2H), 1.69 (m, 2H), 1.35 (m, 2H), 1.20 (m, 2H)**.** MS (ESI+): Calculated $C_{19}H_{21}NO_3$ as 311.15, [M+H] found as 312.18. Characterized in accordance with the literature.[11]

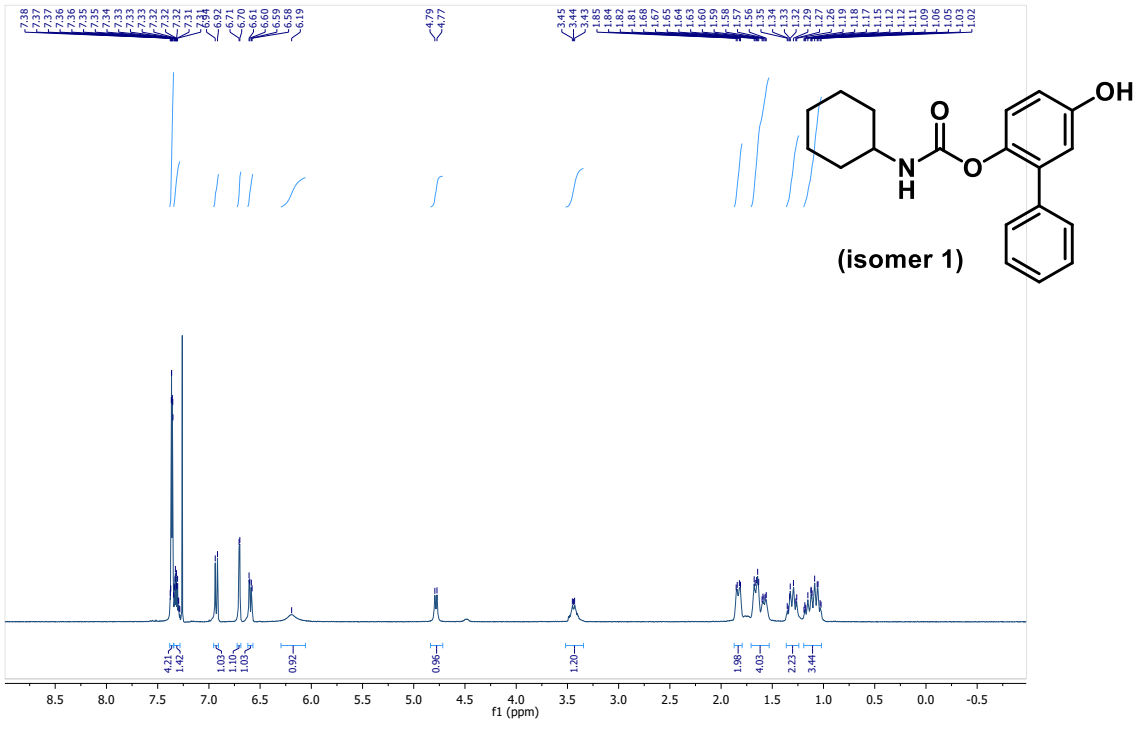

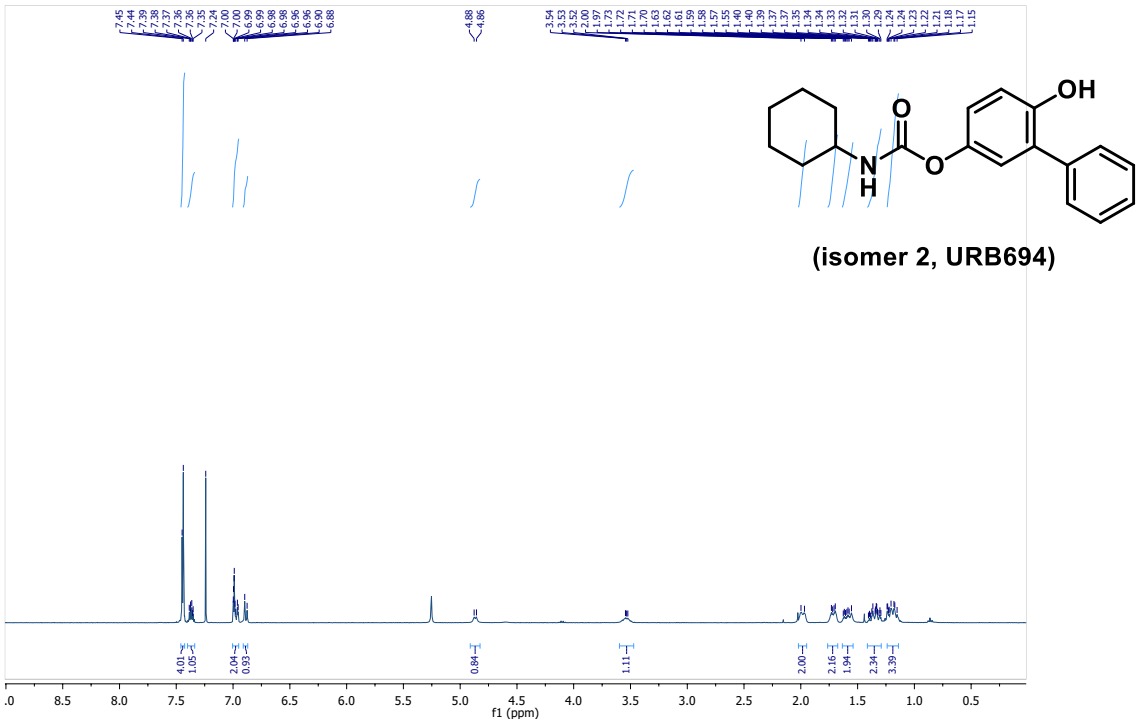
OH
O
N
H
O
(isomer 2, URB694)
f1 (ppm)

5.9.3.36. 26. *N*-[2-(5-methoxy-1H-indol-3-yl)ethyl]acetamide

Followed the general procedure **7**, then procedure **4.** Flash column chromatography at 0–80% hexanes/ethyl acetate. Product obtained as a brown oil (42 mg, yield 72%). ^{1}H-NMR (400 MHz, $CDCl_3$): δ 8.32 (s, 1H), 7.23 (d, *J* = 8.8 Hz, 1H), 6.99 (dd, *J* = 17.0, 2.4 Hz, 2H), 6.85 (dd, *J* = 8.8, 2.5 Hz, 1H), 5.67 (s, 1H), 3.83 (s, 3H), 3.56 (dt, *J* = 6.5 Hz, 2H), 2.91 (t, *J* = 6.8 Hz, 2H), 1.90 (s, 3H). MS (ESI+): Calculated $C_{13}H_{16}N_2O_2$ as 232.12, [M+H] found as 233.15. Characterized in accordance with the literature.[12]

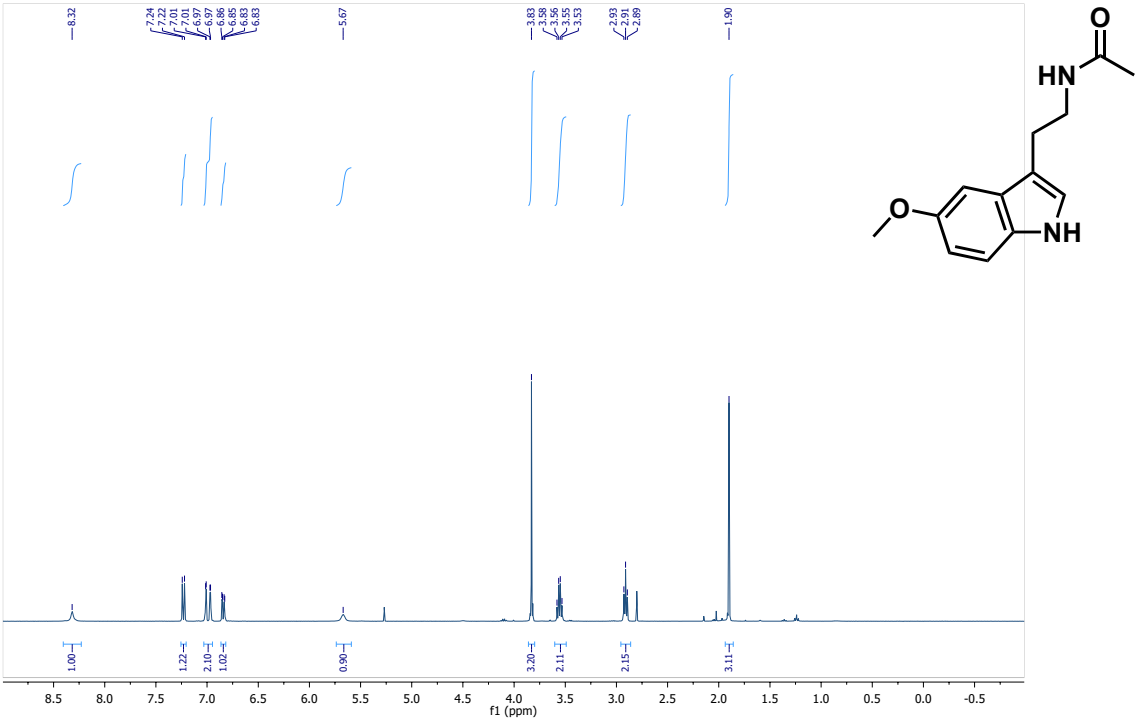

5.9.3.37. 27. methyl 2-acetamido-3-phenylpropanoate

Followed the general procedure **7**, then procedure **4**. Product obtained as a white powder (46.5 mg, yield 84%). ^{1}H-NMR (400 MHz, $CDCl_3$): δ 7.32–7.23 (m, 3H), 7.09 (m, 2H), 5.89 (d, *J* = 7.8 Hz, 1H), 4.90 (dt, *J* = 7.8, 5.7 Hz, 1H), 3.73 (s, 3H), 3.13 (m, 2H), 1.99 (s, 3H). MS (ESI+): Calculated $C_{12}H_{15}NO_3$ as 221.11, [M+H] found as 222.09. Characterized in accordance with the literature.[13]

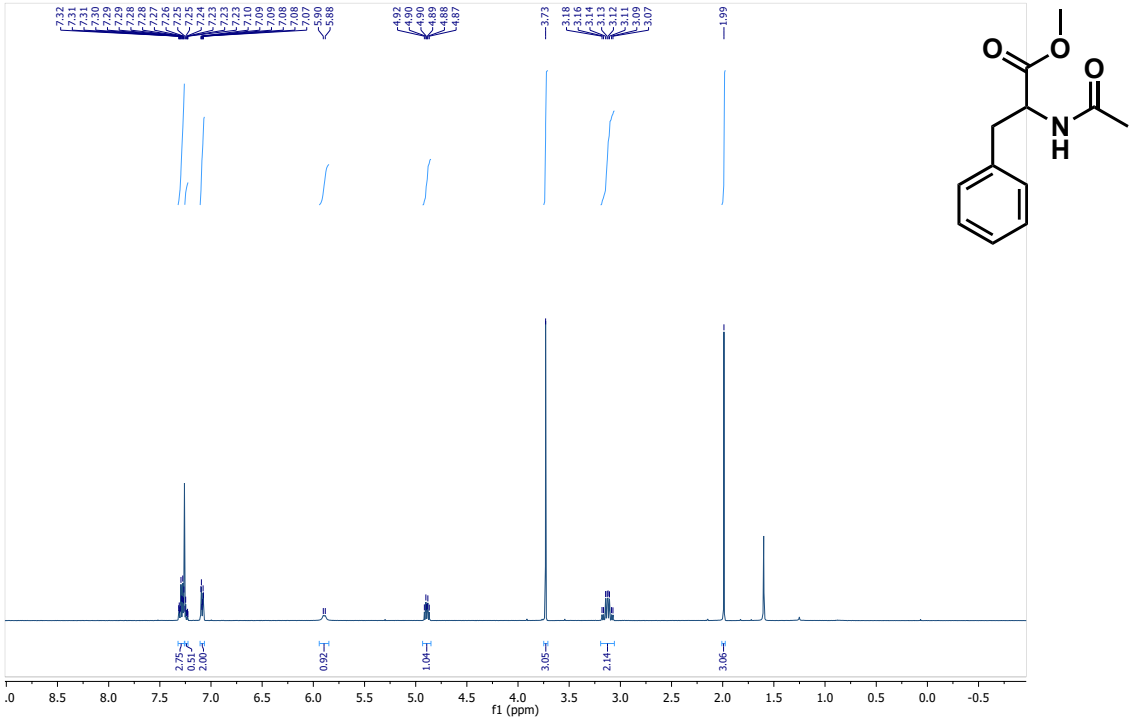

5.9.3.38. 28. *N*-[(4-fluorophenyl)methyl]acetamide

Followed the general procedure **7**, then procedure **4**. Product obtained as a white powder (30.5 mg, yield 73%). ^{1}H-NMR (400 MHz, $CDCl_3$): δ 7.25 (m, 2H), 7.02 (m, 2H), 5.75 (s, 1H), 4.40 (d, *J* = 5.8 Hz, 2H), 2.03 (s, 3H). ^{13}C-NMR (100 MHz, $CDCl_3$): 170.0, 162.3 (d, *J* = 246 Hz), 134.2 (d, *J* = 3 Hz), 129.6 (d, *J* = 8 Hz), 115.7 (d, *J* = 21 Hz), 43.1, 23.4. ^{19}F-NMR (376 MHz, $CDCl_3$): -115.00 (s, 1F). MS (ESI+): Calculated $C_9H_{10}FNO$ as 167.07, [M+H] found as 167.94. Characterized in accordance with the literature.[14]

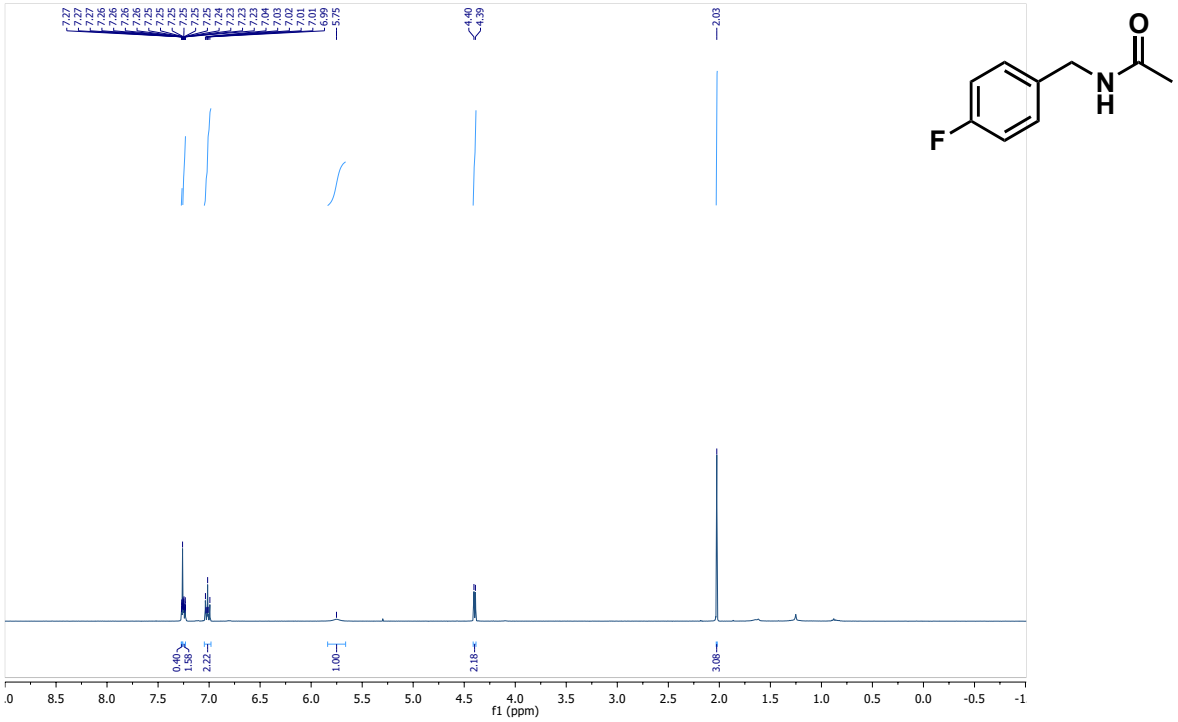

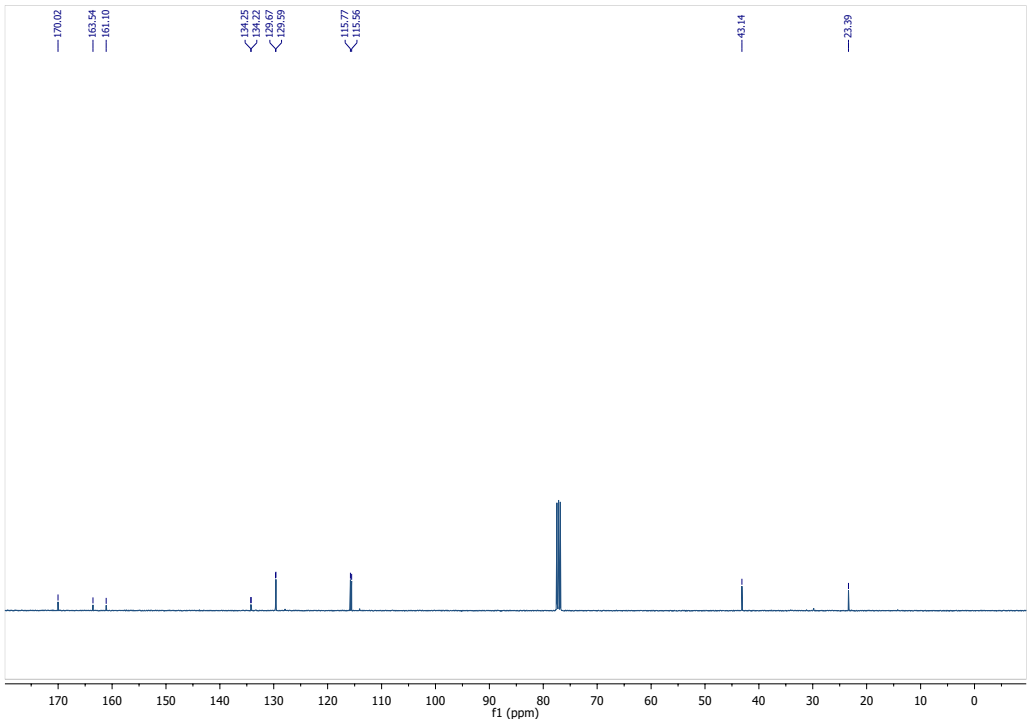
170.02
163.54
161.10
134.25
134.22
129.67
129.59
115.77
115.56
43.14
23.39
170 160 150 140 130 120 110 100 90 80 70 60 50 40 30 20 10 0
f1 (ppm)

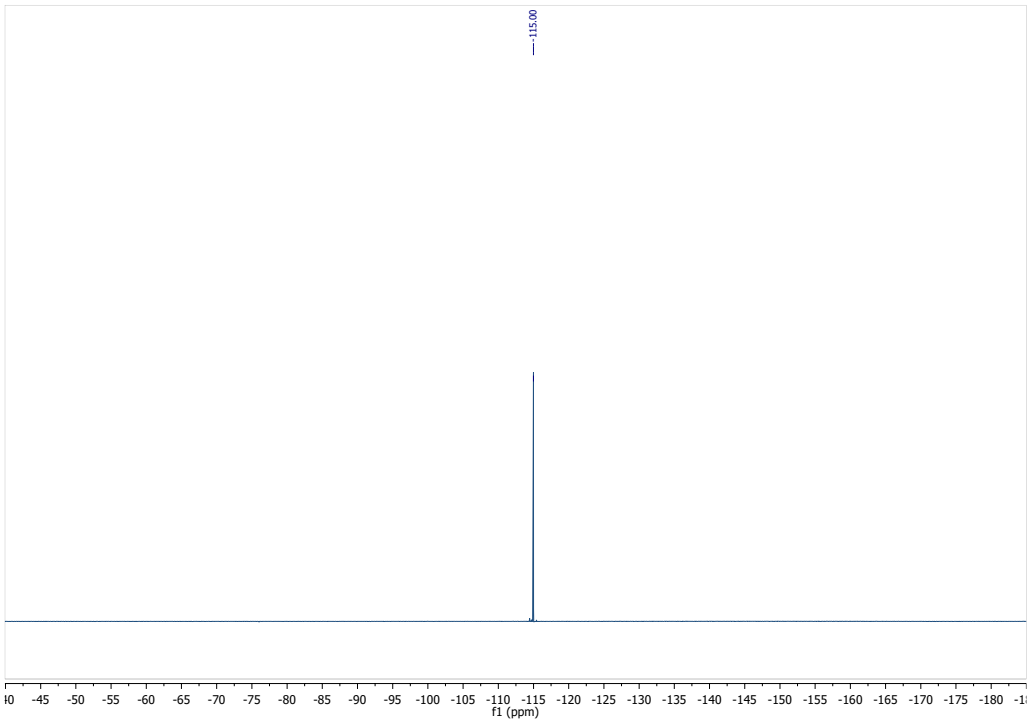
-115.00
-45 -50 -55 -60 -65 -70 -75 -80 -85 -90 -95 -100 -105 -110 -115 -120 -125 -130 -135 -140 -145 -150 -155 -160 -165 -170 -175 -180
f1 (ppm)

5.9.3.39. 29. 4-[4-({[4-chloro-3-(trifluoromethyl)phenyl]carbamoyl}amino)-3-fluorophenoxy]-*N*-methylpyridine-2-carboxamide

Followed the general procedure (**3**) to obtain the urea derived from *N*-*tert*-butylmethylamine. The intermediate was dissolved in toluene (0.25 M), and 1.5 equiv. of 4-(4-amine-3-fluorophenoxy)-*N*-methylpicolinamide was added. The reaction was heated to reflux until completion. Flash column chromatography performed using a gradient of 0–10% DCM/MeOH. The product was obtained as a white powder (85 mg, yield 71%). ^{1}H-NMR (400 MHz, $CDCl_3$): δ 9.54 (s, 1H), 8.80 (m, 1H), 8.76 (s, 1H), 8.53 (dd, 1H), 8.16 (m, 2H), 7.63 (m, 2H), 7.42 (dd, *J* = 2.7, 0.5 Hz, 1H), 7.35 (dd, *J* = 11.6, 2.7 Hz, 1H), 7.19 (dd, *J* = 5.6, 2.6 Hz, 1H), 7.08 (ddd, *J* = 8.9, 2.7, 1.3 Hz, 1H), 2.79 (d, *J* = 4.8 Hz, 3H). ^{19}F-NMR (376 MHz, $CDCl_3$): -61.50 (s, 3F), -124.38 (s, 1F). MS (ESI+): Calculated $C_{21}H_{15}ClF_4N_4O_3$ as 482.08, [M+H] found as 483.14. Characterized in accordance with the literature.[15]

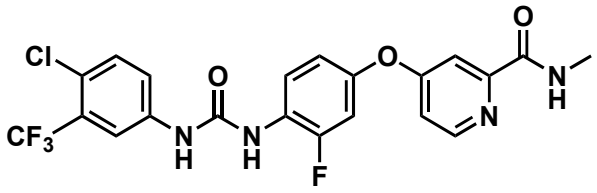

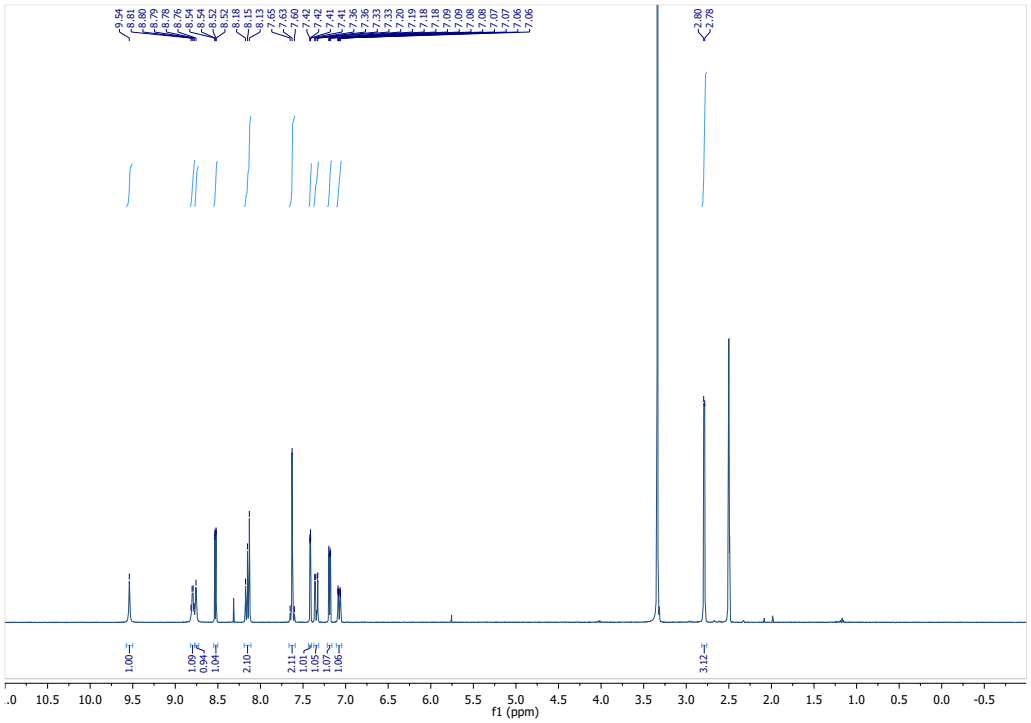

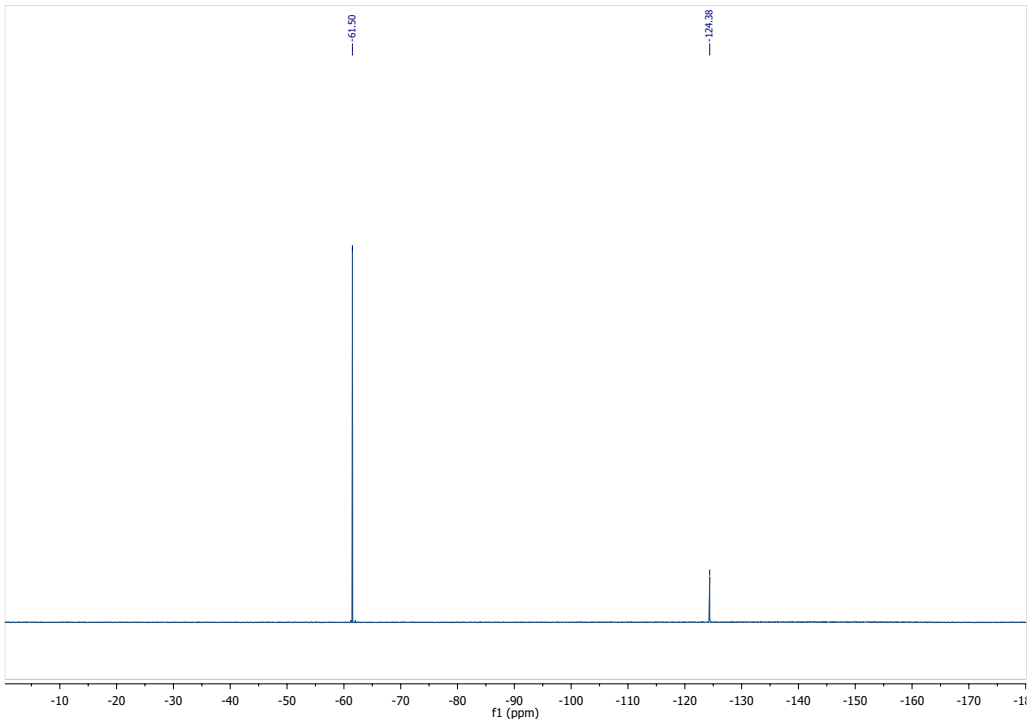
-61.50
-124.38
-10
-20
-30
-40
-50
-60
-70
-80
-90
-100
-110
-120
-130
-140
-150
-160
-170
f1 (ppm)

5.9.3.40. 30. 1-[(3-methoxyphenyl)methyl]-3-phenylurea

Followed the procedure described by Murray et al.,[16] product obtained as a white powder (56 mg, yield 88%). ^{1}H-NMR (400 MHz, $CDCl_3$): δ 7.29 (m, 4H), 7.22 (t, *J* = 7.8 Hz, 1H), 7.07 (m, 1H), 6.82 (m, 3H), 6.66 (s, 1H), 5.31 (s, 1H), 4.37 (s, 2H), 3.76 (s, 3H). ^{13}C-NMR (100 MHz, $CDCl_3$): 159.9, 156.8, 140.8, 138.9, 129.7, 129.1, 123.2, 120.4, 119.4, 112.7, 112.7, 55.2, 43.9. MS (ESI+): Calculated $C_{15}H_{16}N_2O_2Na$ as 279.1109, [M+H] found as 279.1128.

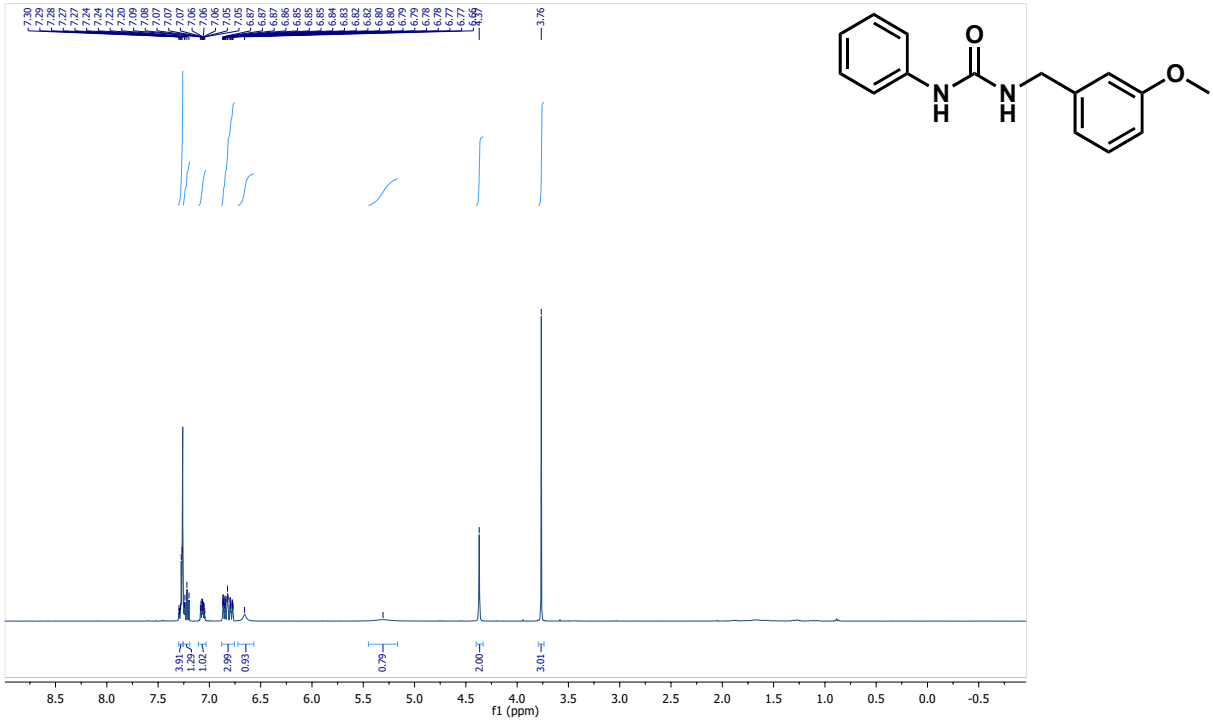

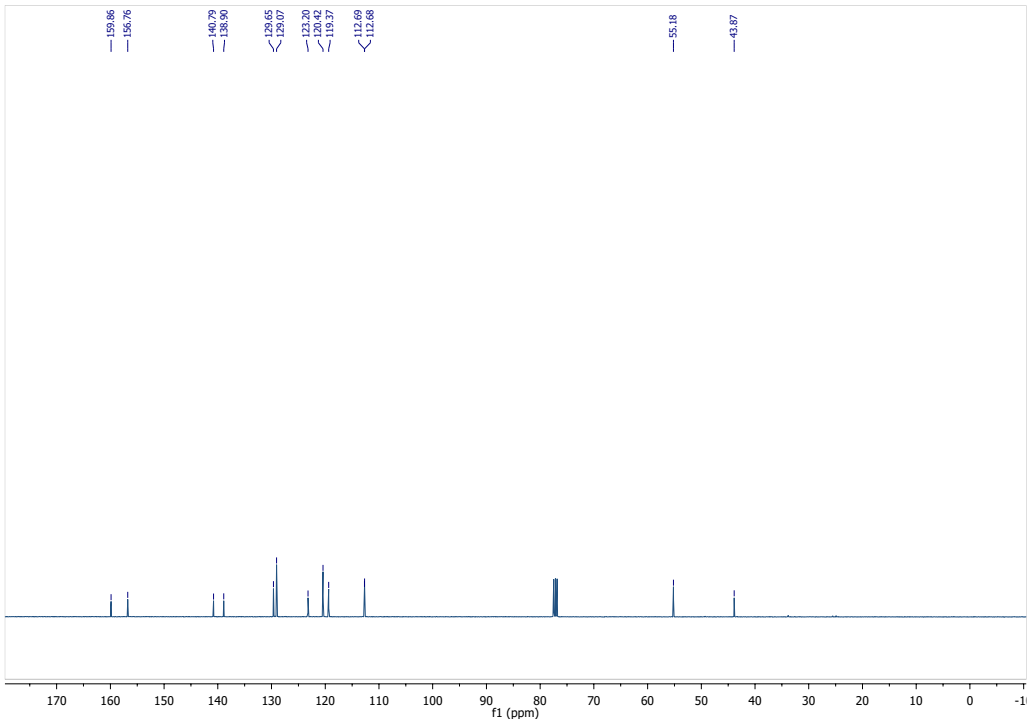
159.86
156.76
140.79
138.90
129.65
129.07
123.20
120.42
119.37
112.69
112.68
55.18
43.87
170
160
150
140
130
120
110
100
90
80
70
60
50
40
30
20
10
0
f1 (ppm)

5.9.3.41. 31. benzyl *N*-benzylcarbamate

Followed the general procedure (**2**), product obtained as a white powder (43 mg, yield 72%). ^{1}H-NMR (400 MHz, $CDCl_3$): δ 7.33 (m, 10H), 5.14 (s, 2H), 5.09 (s, 1H), 4.40 (d, *J* = 6.0 Hz, 2H). MS (ESI+): Calculated $C_{15}H_{15}NO_2$ as 241.11, [M+H] found as 242.17. Characterized in accordance with the literature.[1]

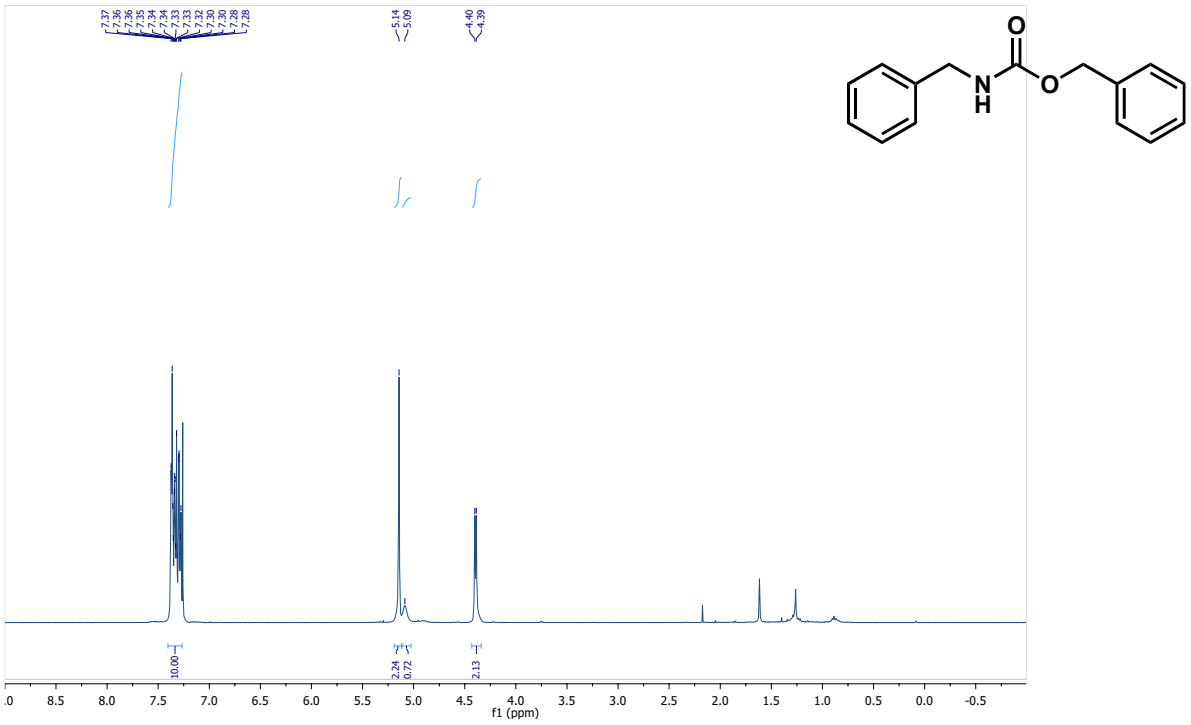

5.9.3.42. 32. 4-methoxyphenyl *N*-benzylcarbamate

Followed the procedure described by Krátký M. et al.,[17] product obtained as a white powder (81 mg, yield 92%). ^{1}H-NMR (400 MHz, $CDCl_3$): δ 7.34 (m, 5H), 7.06 (m, 2H), 6.87 (m, 2H), 5.29 (s, 1H), 4.46 (d, *J* = 6.0 Hz, 2H), 3.79 (s, 3H). MS (ESI+): Calculated $C_{15}H_{15}NO_3$ as 257.11, [M+H] found as 258.16. Characterized in accordance with the literature.[18]

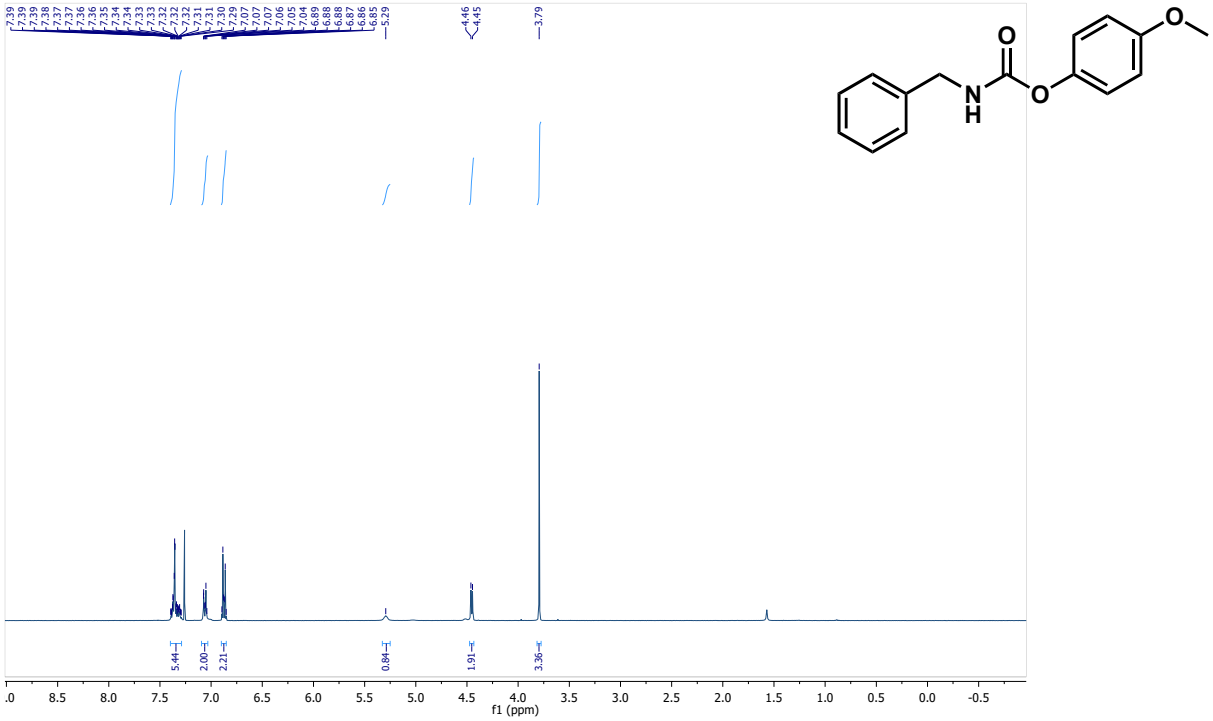

5.9.3.43. 33. phenyl *N*-[2-(5-methoxy-1H-indol-3-yl)ethyl]carbamate

Followed the procedure described by Zhou Y. et al.,[19] product obtained as a light yellow solid (60 mg, yield 74%). ^{1}H-NMR (400 MHz, $CDCl_3$): δ 7.98 (s, 1H), 7.35 (dd, *J* = 8.5, 7.3 Hz, 2H), 7.26 (d, *J* = 9.0 Hz, 1H), 7.19 (m, 1H), 7.09 (m, 4H), 6.89 (dd, *J* = 8.8, 2.4 Hz, 1H), 5.12 (s, 1H), 3.87 (s, 3H), 3.62 (dt, *J* = 6.5 Hz, 2H), 3.03 (m, 2H). ^{13}C-NMR (100 MHz, $CDCl_3$): 154.8, 154.3, 151.2, 131.7, 129.4, 127.8, 125.4, 123.0, 121.7, 112.7, 112.6, 112.2, 100.6, 56.1, 41.5, 25.7. MS (ESI+): Calculated $C_{18}H_{18}N_2O_3Na$ as 333.1215, [M+H] found as 333.1205.

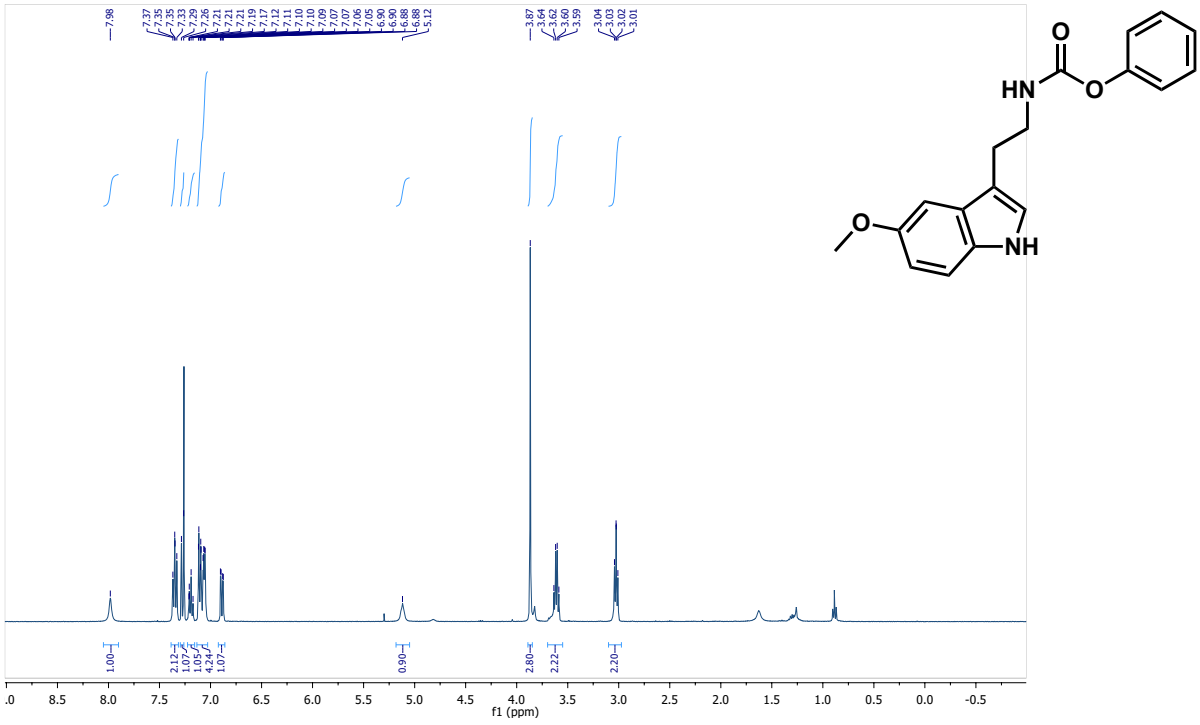

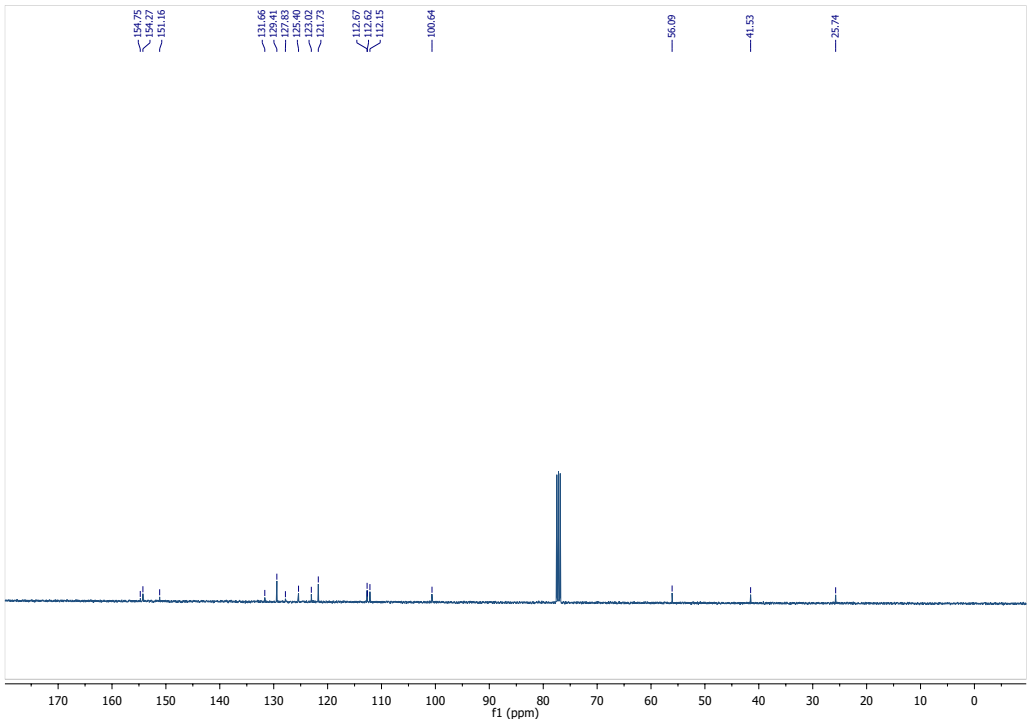
154.75
154.27
151.16
131.66
129.41
127.83
125.40
123.02
121.73
112.67
112.62
112.15
100.64
56.09
41.53
25.74
170
160
150
140
130
120
110
100
90
80
70
60
50
40
30
20
10
0
f1 (ppm)

5.9.3.44. 34. *N*-[(furan-2-yl)methyl](benzylsulfanyll)formamide

Followed the procedure described by Zhou et al.,[19] product obtained as a white powder (63 mg, yield 25%). ^{1}H-NMR (400 MHz, $CDCl_3$): δ 7.32 (m, 5H), 7.24 (m, 1H), 6.32 (dd, *J* = 3.2, 1.9 Hz, 1H), 6.24 (m, 1H), 5.62 (s, 1H), 4.48 (d, *J* = 5.6 Hz, 2H), 4.18 (s, 2H). ^{13}C-NMR (100 MHz, $CDCl_3$): 150.7, 142.6, 138.3, 129.0, 128.7, 127.4, 110.6, 108.0, 38.3, 34.4. MS (ESI+): Calculated $C_{13}H_{13}NO_2SNa$ as 270.0565, [M+H] found as 270.0571.

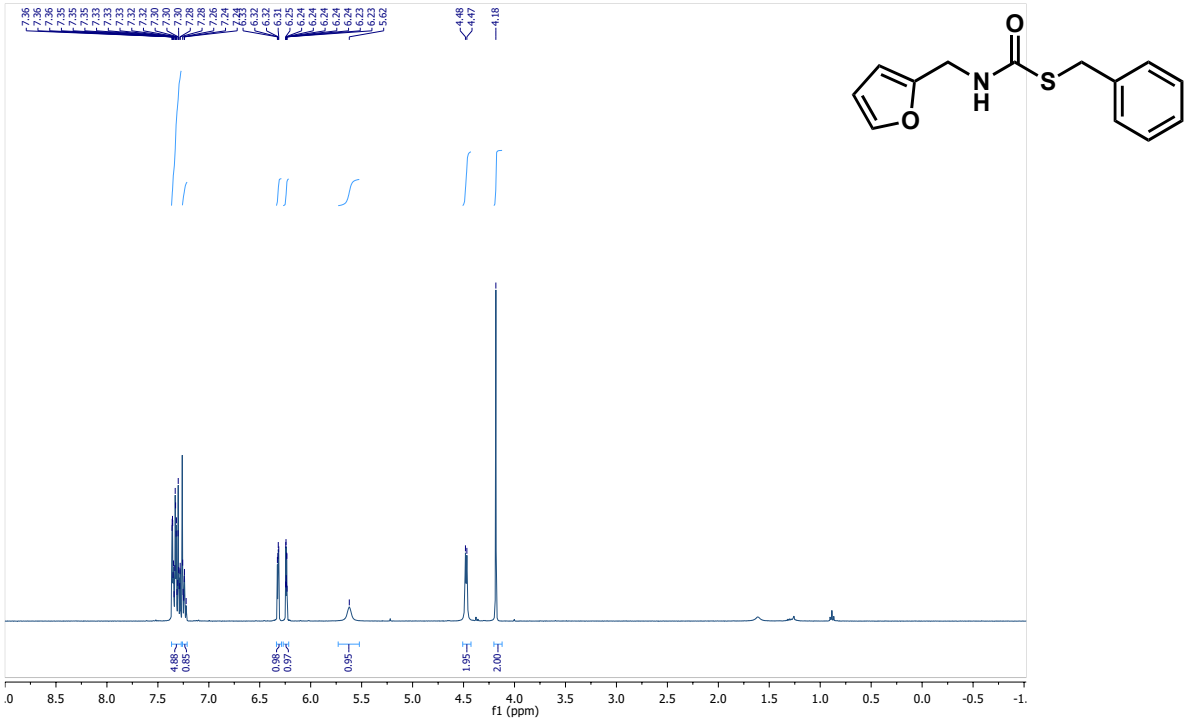

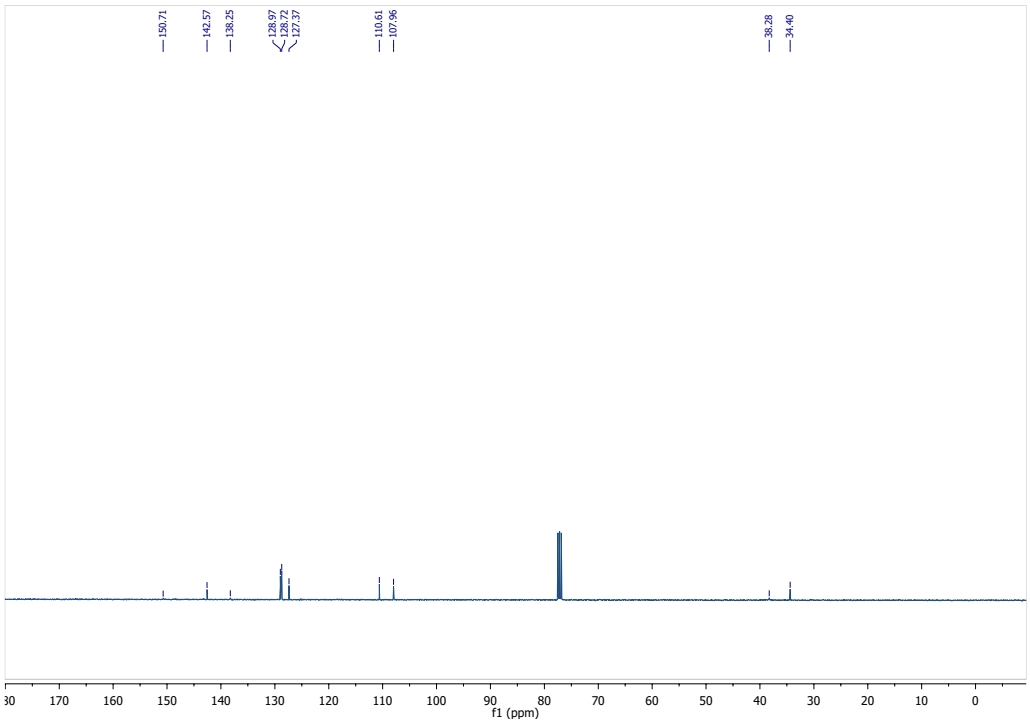
150.71
142.57
138.25
128.97
128.72
127.37
110.61
107.96
38.28
34.40
170
160
150
140
130
120
110
100
90
80
70
60
50
40
30
20
10
0
f1 (ppm)

5.9.3.45. 35. 3-[2-(diethylamino)ethyl]-1-methyl-1-(2-phenoxyethyl)urea

Followed the procedure described by Zhou et al.,[19] product obtained as an oil (42 mg, yield 27%). ^{1}H-NMR (400 MHz, $CDCl_3$): δ 7.27 (m, 2H), 6.92 (m, 3H), 5.40 (s, 1H), 4.10 (t, *J* = 5.3 Hz, 2H), 3.67 (t, *J* = 5.3 Hz, 2H), 3.27 (m, 2H), 2.99 (s, 3H), 2.56 (m, 2H), 2.52 (m, 4H), 1.00 (t, *J* = 7.1 Hz, 6H). MS (ESI+): Calculated $C_{16}H_{27}N_3O_2$ as 293.21, [M+H] found as 294.24. Characterized in accordance with the literature.[20]

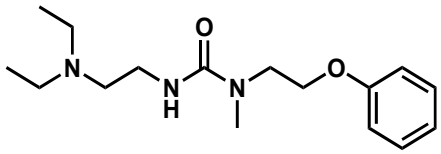

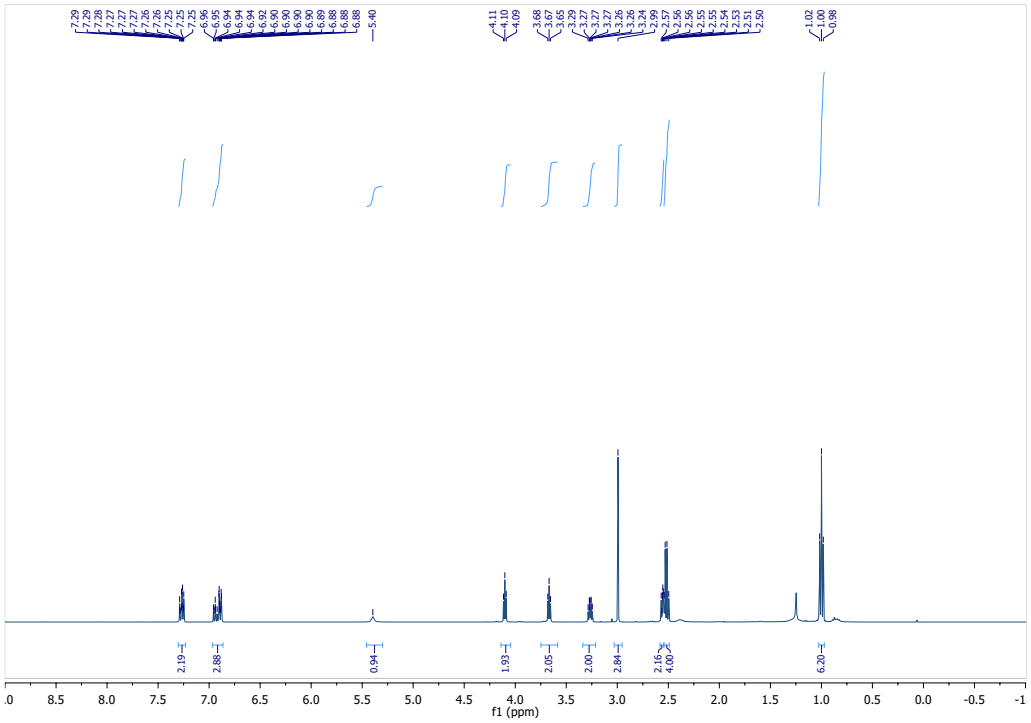

5.9.4. Section 4: Radiochemistry

The peaks indicated by solid arrows are present in the chromatograms following co-injection of products with additional nonradioactive standard. The differences in elution times are due to UV-Vis and radiation detectors placed in series, and in all cases were consistent with delays observed at the time of acquisition. Due to modifications of the radioHPLC system, these delays have varied over the course of this project.

Example calculations:

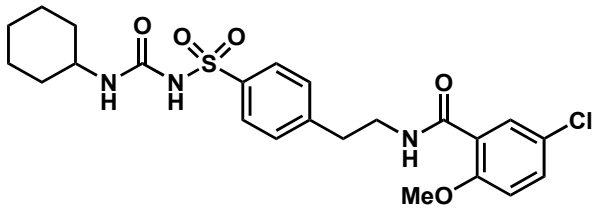

RCY: 75 ± 14%, **TE:** 99%
***n* =** 2

Radiochemical Yield (RCY) determined based on integration of the peaks by radioHPLC.

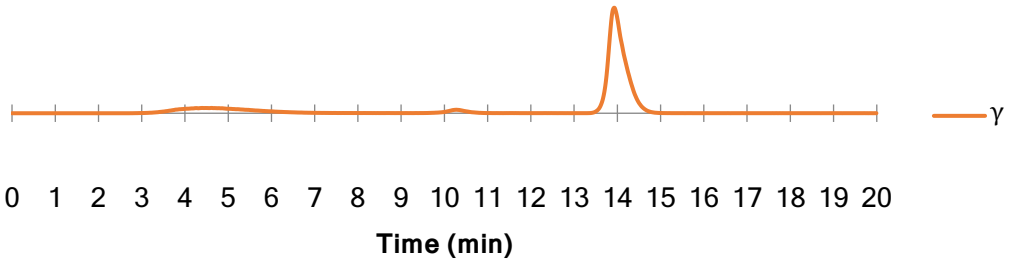

Retention Time (min)	**Area** (μV*sec)	**% Area**	**d.c. Area**	**d.c. % Area**
4.614	5,426,465	15.60%	6,350,537	12%
10.275	905,203	2.60%	1,284,783	2%

13.927	28,444,819	81.79%	45,723,732	86%

Trapping Efficiency (TE) determined based on the activity readings collected at the reactor and the CO_2 trap.

$$TE = \frac{d.c\ A_{\text{reactor}}}{A_{\text{trap}}} x100\% = \frac{640\ mCi \text{ at } 18{:}01}{690\ mCi \text{ at } 17{:}59} x100\% = \frac{685\ mCi \text{ at } 17{:}59}{690\ mCi \text{ at } 17{:}59} x100\% = 99\%$$

Molar Activity (A_M) determined according to the activity concentration at end of synthesis.

$Area_{UV}$ = 48,108

n = $Area_{UV}$ / 298165700.87 μmol^{-1} (according to calib. curve of glibencamide, see Section 5)

= 48108 / 298165700.87 μmol^{-1}

= 0.0001613 μmol

Activity concentration:	19.14 mCi/mL	@	18:36
Injection volume:	10 μL		
Activity injected:	0.19 mCi	@	18:36
Decay-corrected activity injected:	0.26 mCi/mL	@	18:27

A_M = activity injected / n

= 0.26 x 10^{-3} Ci / 1.61 x 10^{-4} μmol

= 1.61 Ci·μmol^{-1}

= 59.57 GBq·μmol^{-1} at end of synthesis

5.9.4.1. [^{11}C]4 (benzyl *N*-phenylcarbamate)

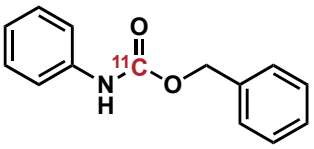

RCY: 91 ± 2%, **TE:** 99%
n **=** 6

Compound was synthesized according to the general procedure (**8**).

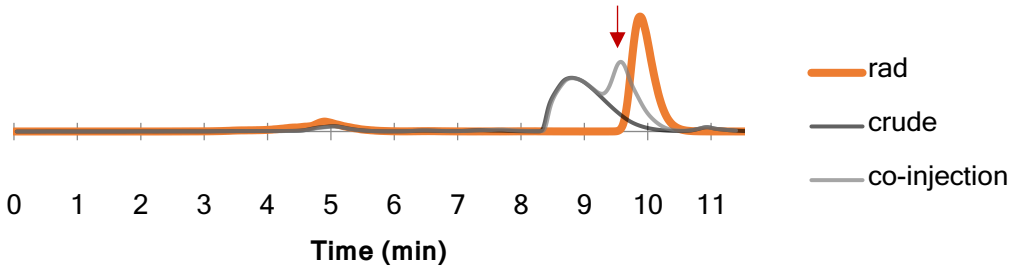

5.9.4.2. [^{11}C]30 (1-[(3-methoxyphenyl)methyl]-3-phenylurea)

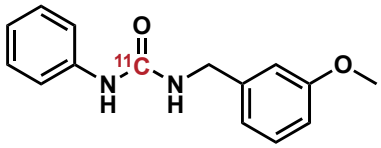

RCY: 88 ± 2%, **TE:** 83 ± 2%
n **=** 2

Compound was synthesized according to the general procedure (**8**).

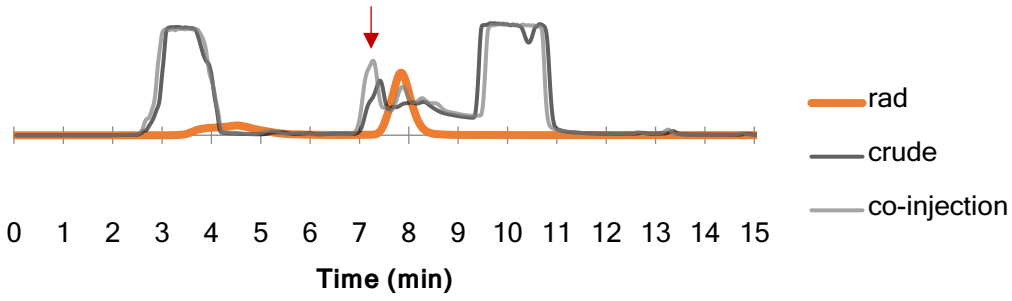

5.9.4.3. [^{11}C]12 (3-tert-butyl-3-methyl-1-phenylurea)

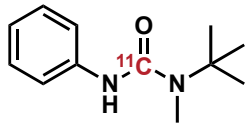

Compound was synthesized according to the general procedure (**8**)

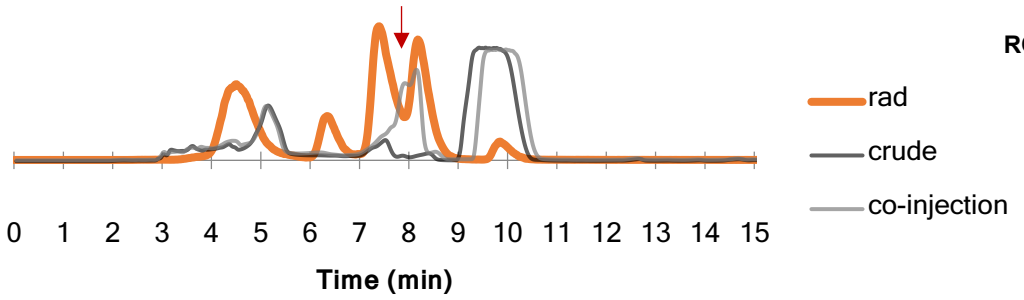

RCY: 32 ± 5%, **TE:** 70 ± 4%
n **=** 2

5.9.4.4. [^{11}C]31 (benzyl *N*-benzylcarbamate)

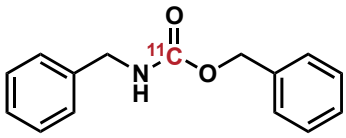

RCY: 64 ± 3%, **TE:** 98 ± 3%
***n* =** 2

Compound was synthesized according to the general procedure (**8**).

Exceptional conditions: Iminophosphorane **1o** (7.83 µmol).

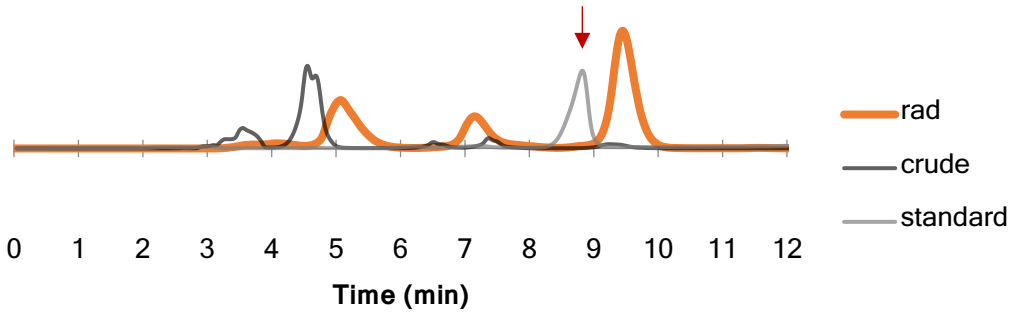

5.9.4.5. [^{11}C]32 (4-methoxyphenyl *N*-benzylcarbamate)

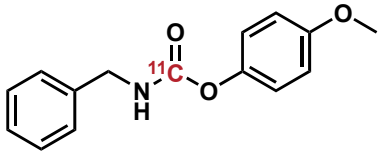

RCY: 26 ± 2%, **TE:** 83 ± 2%
***n* =** 2

Compound was synthesized according to the general procedure (**8**).

Exceptional conditions: Iminophosphorane **1o** (7.83 µmol), phenol (560 µmol), DABCO (160 µmol), no DBU. CO_2 trapped at -60 °C.

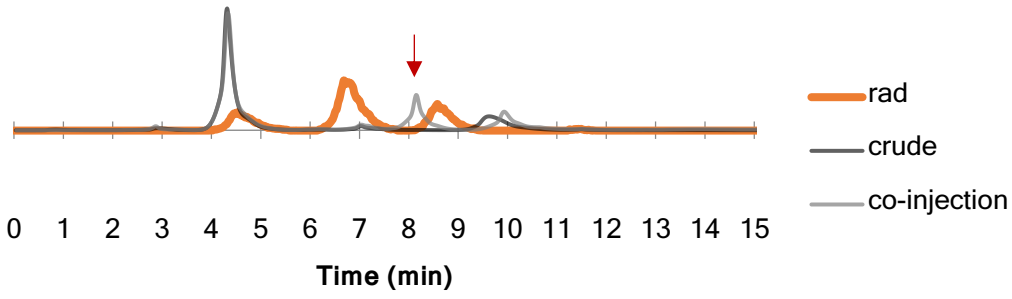

5.9.4.6. [^{11}C]33 (phenyl-*N*-[2-(5-methoxy-1H-indol-3-yl)ethyl]carbamate)

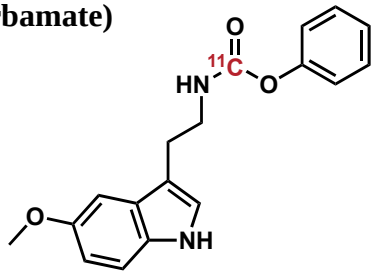

RCY: 84 ± 8%, **TE:** 58%
***n* =** 2

Compound was synthesized according to the general procedure (**8**).

Exceptional conditions: Iminophosphorane **1j** (7.53 µmol), phenol (1300 µmol), DABCO (16.04 µmol), no DBU. Reaction run for 2 min. CO_2 trapped at -60 °C.

Analytical HPLC Conditions: 0-2 mins at 20% ACN / 80% 0.1 M AMF. 2-10 mins gradient to 80% ACN / 20% 0.1 M AMF. 10-12 mins at 80% ACN / 20% 0.1 M AMF. 12-13 mins return to initial conditions.

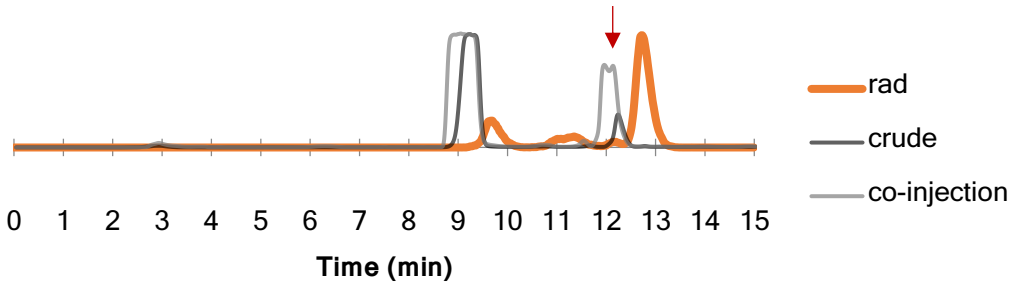

5.9.4.7. [^{11}C]34 (*N*-[(furan-2-yl)methyl](benzylsufanyl)formamide)

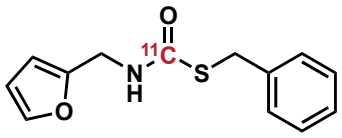

RCY: 93 ± 2%, **TE:** 53 ± 6%
***n* =** 2

Compound was synthesized according to the general procedure (**8**).

Exceptional conditions: Iminophosphorane **1j** (9.13 µmol), benzyl mercaptan (510 µmol), DABCO (16.04 µmol), no DBU. CO_2 trapped at -60 °C.

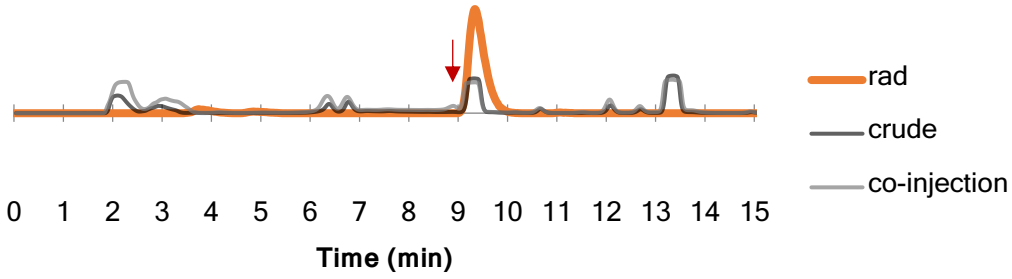

5.9.4.8. [^{11}C]23 (1,3-dioxo-2,3-dihydro-1H-isoindol-2-yl *N*-*tert*-butylcarbamate)

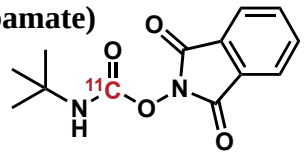

Compound was synthesized according to the general procedure (**8**).

Exceptional conditions: Iminophosphorane **1h** (11.9 µmol), LHMDS (11.7 µmol), *N*-hydroxypthalamide (510 µmol), NEt_3 (510 µmol), no DBU). CO_2 trapped at -60 °C.

RCY: 99 ± 3%, **TE:** 52 ± 6%
n **=** 2

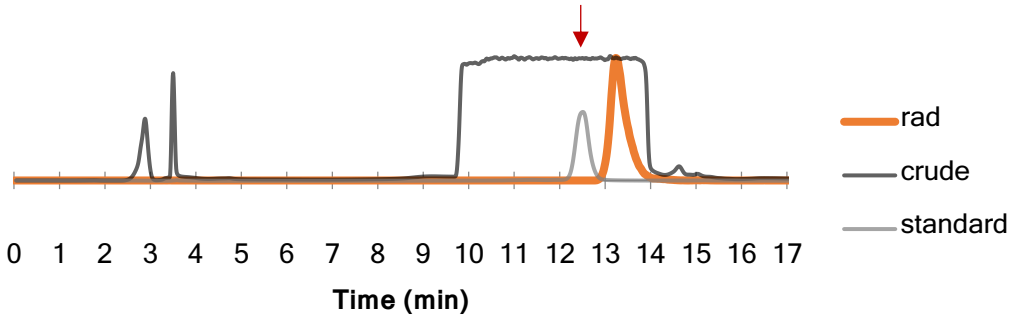

5.9.4.9. [^{11}C]35 (3-[2-(diethylamino)ethyl]-1-methyl-1-(2-phenoxyethyl)urea)

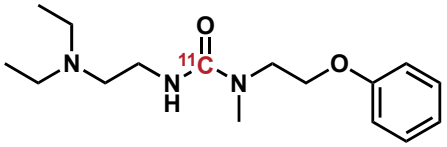

Compound was synthesized using procedure **9**.

Exceptional conditions: Iminophosphorane **1p** (8.75 µmol), *N*-methyl-2-phenoxyethanamine (87.5 µmol), DBU (8.71 µmol). CO_2 trapped at -60 °C.

Analytical HPLC Conditions: 0-2 mins at 20% ACN / 80% 0.1 M AMF. 2-10 min gradient to 65% ACN / 35% 0.1 M AMF. 10-12 min 65% ACN / 35% 0.1 M AMF. 12-13 min return to initial conditions.

RCY: 99 ± 1%, **TE:** 99%
n **=** 2

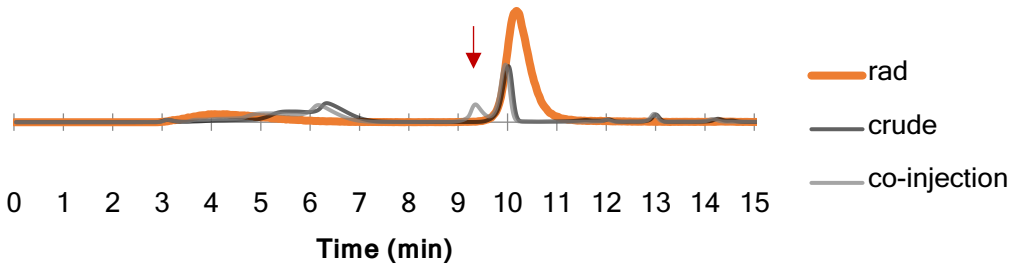

Isolated RCY: 33 ± 11%

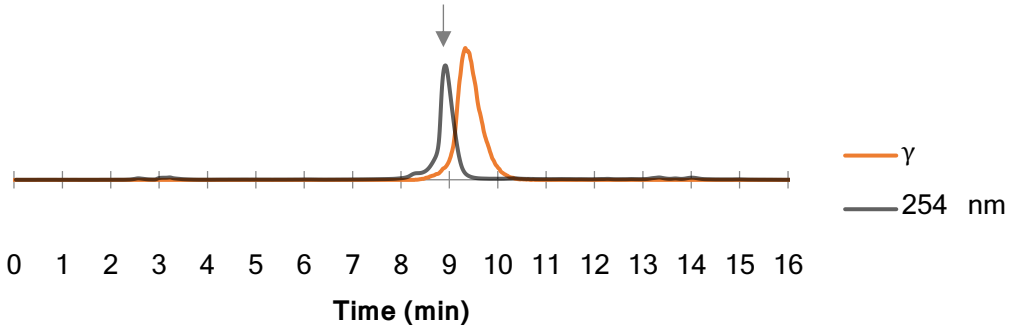
γ
254 nm
0 1 2 3 4 5 6 7 8 9 10 11 12 13 14 15 16
Time (min)

5.9.4.10. [^{11}C]25 (5-hydroxy-(1,1'-biphenyl)-2-yl-*N*-cyclohexylcarbamate)

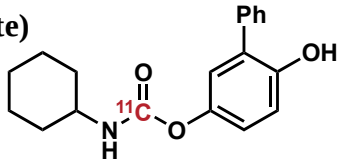

Compound was synthesized using procedure **10**.

RCY: 96 ± 1%, **TE:** 64 ± 11%
(as a mixture of isomers)
n **=** 2

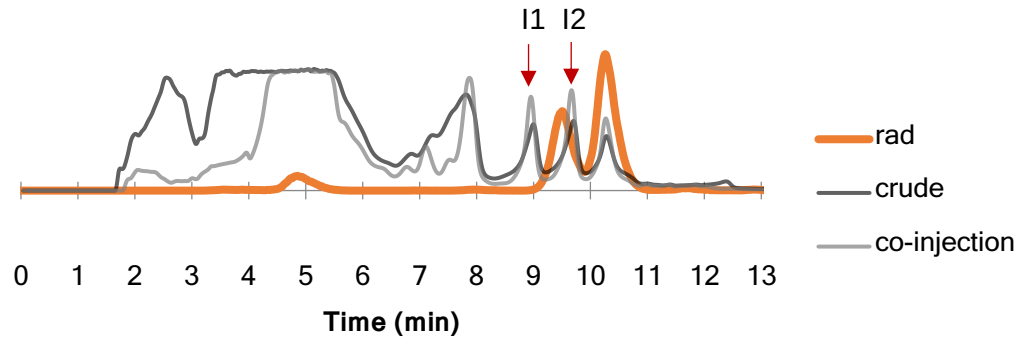

Isomer 1 → 36% area ([^{11}C]*N*-5-hydroxy-[1,1'-biphenyl]-2-yl cyclohexylcarbamate)

Isomer 2 → 64% area ([^{11}C]*N*-6-hydroxy-[1,1'-biphenyl]-3-yl cyclohexylcarbamate; [^{11}C]URB694)

[^{11}C]**URB694**:

Isolated RCY: 13 ± 2%, **Molar Activity:** 69 ± 37 GBq/μmol (*n* = 2)

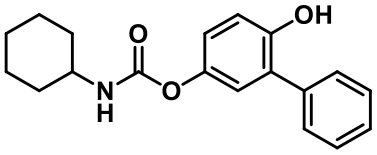

(isomer 2, URB694)

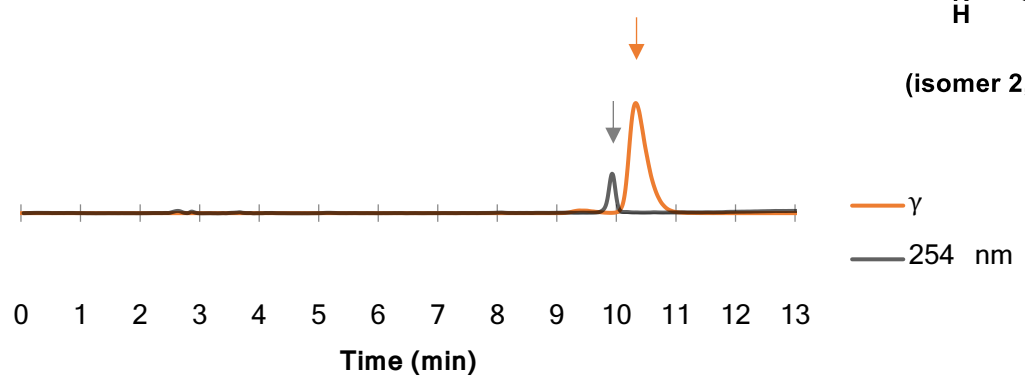

5.9.4.11. [^{11}C]36 (5-chloro-N-[2-4-{[(cyclohexylcarbamoyl)amino]sulfonyl}phenyl)ethyl]-2-methoxybenzamide)

Compound was synthesized using procedure **11**.

Analytical HPLC Conditions: 0-2 mins at 20% ACN / 80% 0.1 M AMF. 2-10 min gradient to 65% ACN / 35% 0.1 M AMF. 10-12 min 65% ACN / 35% 0.1 M AMF. 12-13 min return to initial conditions.

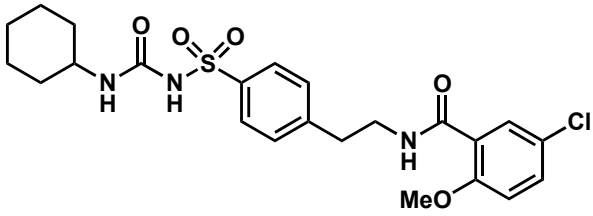

RCY: 75 ± 14%, **TE:** 99%
***n* =** 2

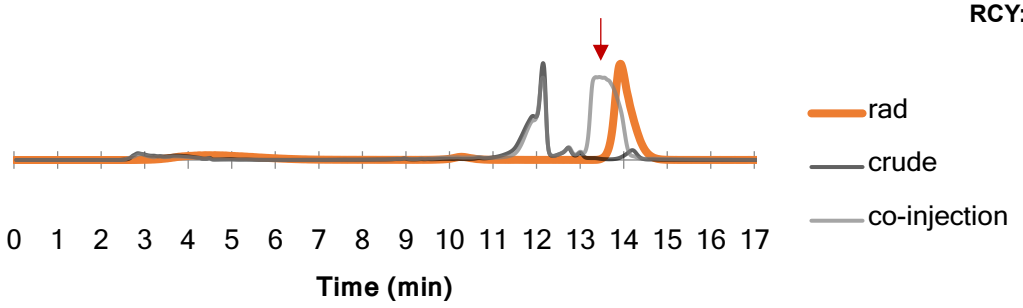

[^{11}C]**Glibenclamide**:

Isolated RCY: 62 ± 16%, **Molar Activity:** 59 ± 0.06 GBq/μmol (*n* = 2)

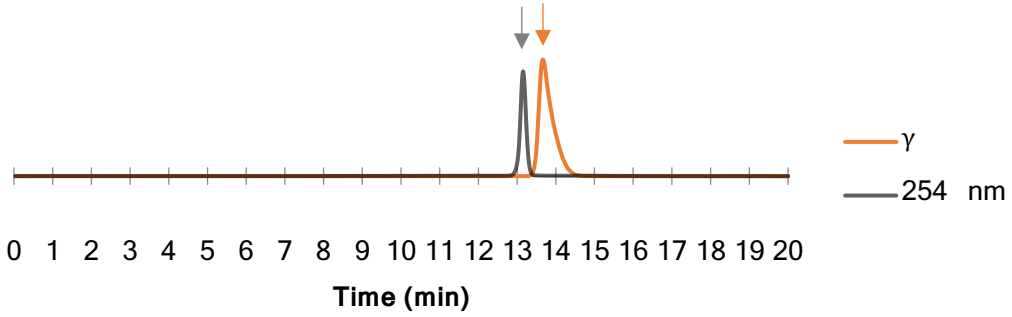

5.9.5. Section 5. Standard Curves

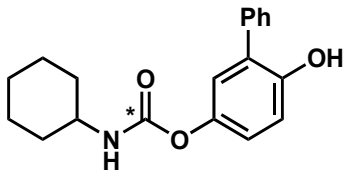

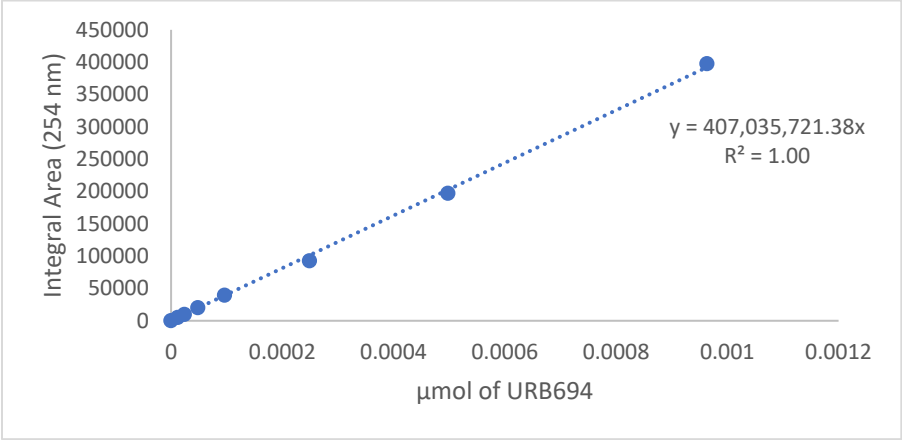

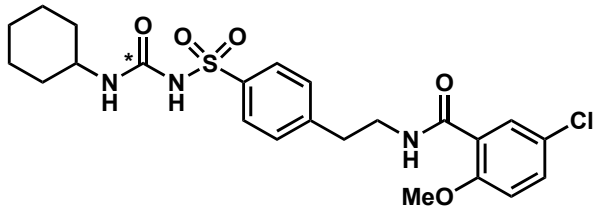

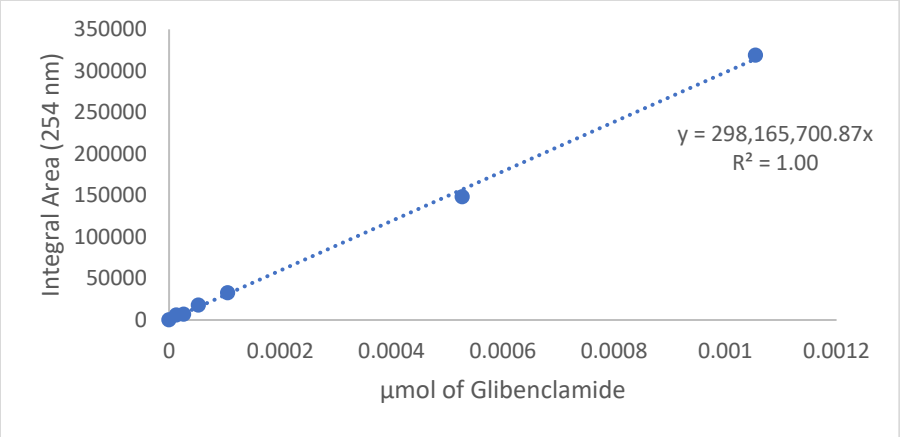
Integral Area (254 nm)
350000
300000
250000
200000
150000
100000
50000
0
0
0.0002
0.0004
0.0006
0.0008
0.001
0.0012
µmol of Glibenclamide
y = 298,165,700.87x
R² = 1.00

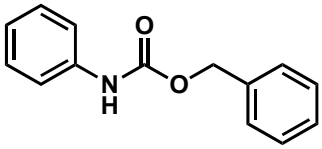
O
N
H
O

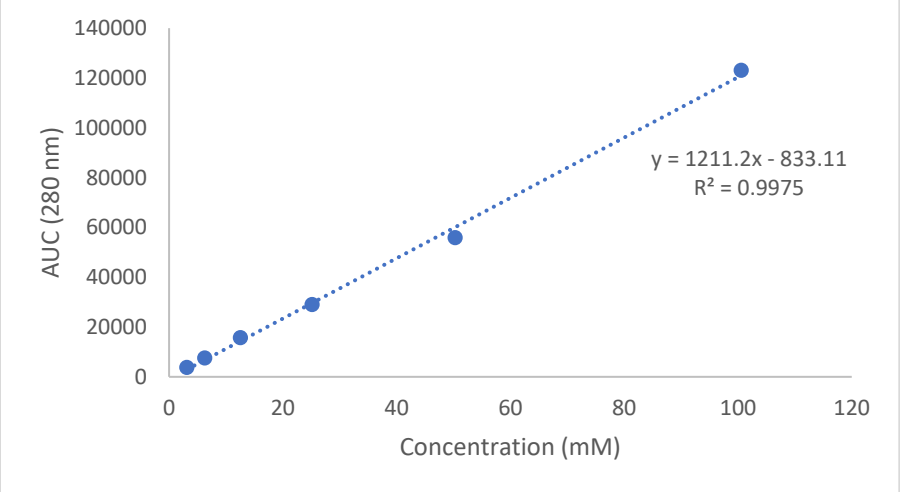
AUC (280 nm)
140000
120000
100000
80000
60000
40000
20000
0
0
20
40
60
80
100
120
Concentration (mM)
y = 1211.2x - 833.11
R² = 0.9975

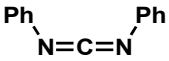

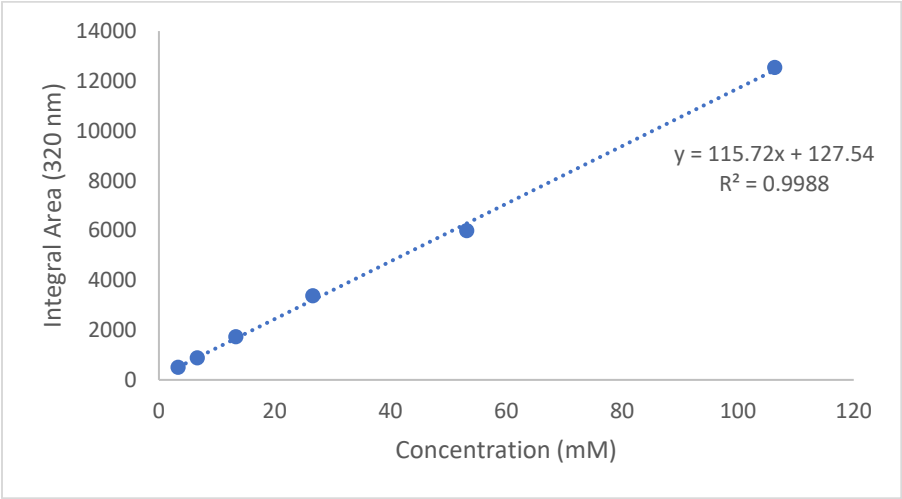

5.9.6. Section 6: Optimization Table

5.9.6.1. Table S1. Solvent and additive screening[a]

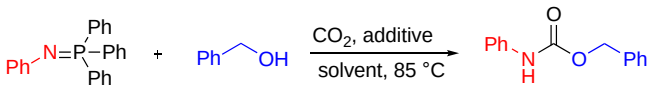

1a **2** **4**

Entry	Solvent	Additive	Rxn time [b]	Yield
1	Toluene	-	2h	70%
2	Dioxane	-	2h	72%
3	DMF	-	2h	75%
4	DMSO	-	2h	64%
5	THF	-	2h	72%
6	**ACN**	**-**	**2h**	**78%**
7	**ACN**	**DBU**	**1h**	**84%**
8	ACN	BEMP	1h	70%
9	ACN	DMAP	2h	65%
10	ACN	Pyridine	2h	72%
11	ACN	K_2CO_3	2h	75%

[a]Reaction conditions: **1** (0.25mmol), **2** (1.25mmol), additives (0.55mmol), dry solvent (2.5mL). Isolated yield.

5.10. References

(1) Li, S.; Khan, R.; Zhang, X.; Yang, Y.; Wang, Z.; Zhan, Y.; Dai, Y.; Liu, Y.; Fan, B. One Stone Two Birds: Cobalt-Catalyzed in Situ Generation of Isocyanates and Benzyl Alcohols for the Synthesis of N-Aryl Carbamates. Org. Biomol. Chem. 2019, 17 (24), 5891–5896. https://doi.org/10.1039/C9OB00924H.

(2) Guo, J.Y.; Zhong, C.H.; He, Z.Y.; Tian, S.K. Benzyne-Promoted Curtius-Type Rearrangement of Acyl Hydrazides in the Presence of Nucleophiles. Asian J. Org. Chem. 2018, 7 (1), 119–122. https://doi.org/10.1002/ajoc.201700598.

(3) Chen, A.; Wang, D.; Samankumara, L. P.; Wang, G. Synthesis of Sterically Congested Carbamates of Carbohydrates through Organic Base Catalysis. Synthesis 2019, 51 (15), 2897–2908. https://doi.org/10.1055/s-0037-1612425.

(4) Huang, H.; Wang, W.; Xu, X.; Zhu, C.; Wang, Y.; Liu, J.; Li, W.; Fu, W. Discovery of 3-((Dimethylamino)Methyl)-4-Hydroxy-4-(3-Methoxyphenyl)-N-Phenylpiperidine-1-Carboxamide as Novel Potent Analgesic. Eur. J. Med. Chem. 2020, 189, 112070. https://doi.org/10.1016/j.ejmech.2020.112070.

(5) Hosseinzadeh, R.; Tajbakhsh, M.; Aghili, N. Synthesis of Unsymmetrical Ureas and S-Thiocarbamates under Catalyst-Free Conditions in a [BMIM]BF_4 Ionic Liquid. Heteroat. Chem. 2015, 26 (2), 175–182. https://doi.org/10.1002/hc.21244.

(6) Hutchby, M.; Houlden, C.E.; Ford, J.G.; Tyler, S.N.G.; Gagné, M.R.; Lloyd-Jones, G.C.; Booker-Milburn, K.I. Hindered Ureas as Masked Isocyanates: Facile Carbamoylation of Nucleophiles under Neutral Conditions. Angew. Chem. Int. Ed. 2009, 48 (46), 8721–8724. https://doi.org/10.1002/anie.200904435.

(7) Ang, K.H., Prager, R.H. The chemistry of 5-oxodihydroisoxazoles V: The photolysis of 2-phenylisoxazol-5(2H)-one 1n alcohols. Tetrahedron, 1992, 48, 9073-9084. https://doi.org/10.1016/S0040-4020(01)82002-0.

(8) Samanta, S.; Ray, S.; Bhaduri, S.N.; Samanta, P.K.; Biswas, P. 3,6-Di(Pyridin-2-Yl)-1,2,4,5-Tetrazine (Pytz) Catalysed Metal-Free Amide Bond Formation from Thioacids and Amines at Room Temperature. Tetrahedron Lett. 2020, 61 (35), 152272. https://doi.org/10.1016/j.tetlet.2020.152272.

(9) Tsukamoto, H.; Suzuki, R.; Kondo, Y. Revisiting Benzenesulfonyl Linker for the Deoxygenation and Multifunctionalization of Phenols. J. Comb. Chem. 2006, 8 (3), 289–292. https://doi.org/10.1021/cc0600066.

(10) Pramanik, M.; Choudhuri, K.; Chakraborty, S.; Ghosh, A.; Mal, P. (Z)-Selective Anti-Markovnikov or Markovnikov Thiol–Yne-Click Reactions of an Internal Alkyne by Amide Hydrogen Bond Control. Chem. Commun. 2020, 56 (20), 2991–2994. https://doi.org/10.1039/D0CC00702A.

(11) Wilson, A.A.; Garcia, A.; Houle, S.; Sadovski, O.; Vasdev, N. Synthesis and Application of Isocyanates Radiolabeled with Carbon-11. Chem. Eur. J. 2011, 17, 259–264. https://doi.org/10.1002/chem.201002345.

(12) Thomson, D.W.; Commeureuc, A.G.J.; Berlin, S.; Murphy, J.A. Efficient Route to the Pineal Hormone Melatonin by Radical-Based Indole Synthesis. Synth. Commun. 2003, 33 (20), 3631–3641. https://doi.org/10.1081/SCC-120024751.

(13) Ticconi, B.; Colcerasa, A.; Stefano, S.D.; Lanzalunga, O.; Lapi, A.; Mazzonna, M.; Olivo, G. Oxidative Functionalization of Aliphatic and Aromatic Amino Acid Derivatives with H2O2 Catalyzed by a Nonheme Imine Based Iron Complex. RSC Adv. 2018, 8 (34), 19144–19151. https://doi.org/10.1039/C8RA02879F.

(14) Tsygankov, A.A.; Makarov, M.; Afanasyev, O.I.; Kashin, A.S.; Naumkin, A.V.; Loginov, D.A.; C. D. Reductive amidation without an external hydrogen source using rhodium on carbon matrix as a catalyst. ChemCatChem. 2020, 12, 112–117. https://doi.org/10.1002/cctc.201901465.

(15) Du, F.; Zhou, Q.; Shi, Y.; Yu, M.; Sun, W.; Chen, G. A New Pathway via Intermediate 4-Amino-3-Fluorophenol for the Synthesis of Regorafenib. Synth. Commun. 2019, 49 (4), 576–586. https://doi.org/10.1080/00397911.2018.1564832.

(16) Murray, C.W.; Berdini, V.; Buck, I.M.; Carr, M.E.; Cleasby, A.; Coyle, J.E.; Curry, J.E.; Day, J.E.H.; Day, P.J.; Hearn, K.; Iqbal, A.; Lee, L.Y.W.; Martins, V.; Mortenson, P.N.; Munck, J.M.; Page, L.W.; Patel, S.; Roomans, S.; Smith, K.; Tamanini, E.; Saxty, G. Fragment-Based Discovery of Potent and Selective DDR1/2 Inhibitors. ACS Med. Chem. Lett. 2015, 6 (7), 798–803. https://doi.org/10.1021/acsmedchemlett.5b00143.

(17) Krátký, M.; Štěpánková, Š.; Vorčáková, K.; Vinšová, J. Investigation of Salicylanilide and 4-Chlorophenol-Based N-Monosubstituted Carbamates as Potential Inhibitors of Acetyl- and Butyrylcholinesterase. Bioorganic Chem. 2018, 80, 668–673. https://doi.org/10.1016/j.bioorg.2018.07.017.

(18) Stephens, M.D.; Yodsanit, N.; Melander, C. Evaluation of Ethyl N-(2-Phenethyl) Carbamate Analogues as Biofilm Inhibitors of Methicillin Resistant Staphylococcus Aureus. Org. Biomol. Chem. 2016, 14 (28), 6853–6856. https://doi.org/10.1039/C6OB00706F.

(19) Zhou, Y.; Ting, K.Y.; Lam, C.M.C.; Kwong, A.K.Y.; Xia, J.; Jin, H.; Liu, Z.; Zhang, L.; Cheung Lee, H.; Zhang, L. Design, Synthesis and Biological Evaluation of Noncovalent Inhibitors of Human CD38 NADase. ChemMedChem 2012, 7 (2), 223–228. https://doi.org/10.1002/cmdc.201100487.

(20) US4500529A - Method of treating cardiac disorders with N-(aryloxyalkyl)-N'-(aminoalkyl)ureas - Google Patents https://patents.google.com/patent/US4500529 (accessed Nov 2, 2020).

6. Chapter VI: Synthesis and evaluation of [^{11}C]MCC950 for imaging NLRP3-mediated inflammation in atherosclerosis

The manuscript can be accessed at: https://doi.org/10.1021/acs.molpharmaceut.2c00915

Uzair S. Ismailani,[1,2] Ariel Buchler,[2,3] Nicole MacMullin,[2] Faduma Abdirahman,[2,3] Myriam Adi,[2,3] Benjamin H. Rotstein[1,2,3]*

[1] Department of Biochemistry, Microbiology and Immunology, University of Ottawa, Ottawa, Ontario, Canada

[2] University of Ottawa Heart Institute, Ottawa, Ontario, Canada

[3] Department of Chemistry and Biomolecular Sciences, University of Ottawa, Ottawa, Ontario, Canada.

Correspondence: Benjamin H. Rotstein, PhD
University of Ottawa Heart Institute
40 Ruskin Street, H-5219
Ottawa, Ontario, Canada
K1Y 4W7
Phone: 613-696-7324
Email: benjamin.rotstein@uottawa.ca

6.1. Statement of the manuscript

The manuscript "**Synthesis and evaluation of [^{11}C]MCC950 for imaging NLRP3-mediated inflammation in atherosclerosis**" was submitted to *ACS Molecular Pharmaceutics* on November 02th 2022. In this chapter, I developed the optimization of reaction conditions and automated the radiosynthesis of [^{11}C]MCC950. *Ex vivo* and *in vivo* imaging experiments were performed in ApoE$^{-/-}$ and C57BL/6 mice with the aid of Ariel Buchler, Nicole MacMullin and Myriam Adi. Metabolism was performed by Faduma Abdirahman. The project was conceived by myself and Dr. Benjamin Rotstein. All data collected was analyzed by me. The manuscript was written by me and edited by all authors. All authors approved the final version.

6.2. Abstract

Overexpression of the NLRP3 inflammasome has been attributed to the progressive worsening of a multitude of cardiovascular inflammatory diseases such as myocardial infarction, pulmonary arterial hypertension, and atherosclerosis. The recently discovered potent and selective NLRP3 inhibitor MCC950 has shown promise in hindering disease progression but NLRP3-selective cardiovascular positron emission tomography imaging has not yet been demonstrated. We synthesized [^{11}C]MCC950 with no-carrier-added [^{11}C]CO_2 fixation chemistry using an iminophosphorane precursor (RCY 45 ± 4 %, >99% RCP, 27 ± 2 GBq/μmol, 23 ± 3 min, n = 6) and determined its distribution both *in vivo* and *ex vivo* in C57BL/6 and atherogenic *ApoE*$^{-/-}$ mice. Small animal PET imaging was performed in both strains following intravenous administration via the lateral tail vein and revealed considerable uptake in the liver that stabilized by 20 minutes (7–8.5 SUV), coincident with secondary renal excretion. Plasma metabolite analysis uncovered excellent *in vivo* stability of [^{11}C]MCC950 (94% intact). *Ex vivo* autoradiography performed on excised aortas revealed heterogenous uptake in atherosclerotic plaques of *ApoE*$^{-/-}$ mice in comparison to C57BL/6 controls (48 ± 17 %ID/m^2 vs 18 ± 8 %ID/m^2, p = 0.002, n = 4-5). Treatment of *ApoE*$^{-/-}$ mice with nonradioactive MCC950 (5 mg/kg, iv) 10 minutes prior to radiotracer administration increased uptake in intestines (5.3 ± 1.8 %ID/g vs 11.0 ± 3.7 %ID/g, p = 0.04, n = 4-6) and in aortic lesions (48 ± 17 %ID/m^2 vs 104 ± 15 %ID/m^2, p = 0.0002, n = 5) by 108% and 117%, respectively, without significantly increasing plasma free fraction (f_p, 1.3 ± 0.4% vs 1.7 ± 0.8%, n = 2). These results suggest that [^{11}C]MCC950 uptake demonstrates specific binding and may prove useful for *in vivo* NLRP3 imaging in atherosclerosis.

Keywords: NOD-like receptor pyrin domain-containing protein 3 (NLRP3); atherosclerosis; molecular imaging; autoradiography; positron emission tomography; MCC950; carbon-11; CO_2-fixation

6.3. Introduction

Atherosclerosis is a chronic inflammatory disease that is characterized by the thickening and hardening of arterial walls due to the deposition of lipids, infiltration of leukocytes, and proliferation of vascular smooth muscle cells.[1,2] The resulting lesions are generally asymptomatic in early stages, but continual growth and inflammation result in the formation of unstable plaques that are prone to ruptures and consequent angina, myocardial infarction, and sudden cardiac death.[1,3] Increasing evidence suggests that the progression of atherosclerosis is driven by the aberrant activation of the innate immune system and upregulation of inflammasomes.[4–6]

Inflammasomes are cytoplasmic multi-protein complexes found in macrophages and microglia. They comprise oligomers of NOD-like receptor (NLR) protein, apoptosis-associated speck-like protein containing a caspase recruitment domain (ASC), and caspase-1, a cysteine protease that processes proinflammatory cytokines. Specifically, cytokines such as IL-1β and IL-18 are matured by caspase-1 and are markedly upregulated in atherosclerosis due to increased expression of the NLRP3 inflammasome.[4,6] Extracellular danger-associated molecular patterns (DAMPs), such as free fatty acids, activate toll-like receptor 4 (TLR4) on the surface of macrophages and induce NF-κB-dependent transcription of pro-IL-1β and monomeric NLRP3.[4,7] Additionally, receptor-mediated phagocytosis of cholesterol crystals or oxidized low-density lipoprotein (LDL) destabilizes phagolysosomes, releasing cathepsin B and amplifying NLRP3 inflammasome assembly.[4,6,7] Chronic stimulation of this pathway promotes sterile inflammation

and the development of atheromas. However, NLRP3 inflammasome inhibitors have shown considerable promise in attenuating disease progression.[8–14]

The diaryl sulfonylurea MCC950 is a first-in-class potent and selective NLRP3 inhibitor (IC_{50} = 8 nM) shown to have excellent anti-inflammatory activity *in vivo*.[15] MCC950 has demonstrated the considerable potential of NLRP3 inhibition against a multitude of inflammatory disease models including neurodegenerative disorders, autoimmune conditions, and cardiovascular diseases, among others.[16] While current literature suggests that MCC950 accesses the central nervous system (CNS) at therapeutic doses,[16] its recent *in vivo* evaluation as a positron emission tomography (PET) radiotracer revealed poor blood brain barrier (BBB) penetration at microdoses, limiting its use for brain imaging.[17]

Carbon-11 is revered for isotopic labeling of biologically relevant molecules but its use is limited by the synthetic methods available for incorporating it into diverse functional groups.[18,19] Radiolabeled sulfonylureas can be synthesized by rhodium-mediated [^{11}C]CO carbonylation of a sulfonyl azide and an amine (Scheme 1).[20–22] However, the availability of [^{11}C]CO is constrained to a small number of PET research facilities as it requires specialized infrastructure and equipment to produce. These drawbacks are indicative of the growing need for inexpensive and efficient strategies to label sulfonylureas directly from [^{11}C]CO_2. Cyclotron-produced [^{11}C]CO_2 can be converted into more reactive intermediates following stepwise trapping and dehydration using phosphorous oxychloride ($POCl_3$) or Mitsunobu reagents to yield ^{11}C-isocyanates.[19,23,24] Indeed, Mitsunobu conditions were used to prepare [^{11}C]MCC950 from carrier-added [^{11}C]CO_2 in low radiochemical yield (RCY) and low molar activity.[17] The challenge lies in the condensation of the sterically hindered aromatic 4-amino-1,2,3,5,6,7-hexahydro-s-indacene (**1**) with [^{11}C]CO_2 and addition of the weakly nucleophilic furyl sulfonamide (**2**) to the ^{11}C-isocyanate intermediate.

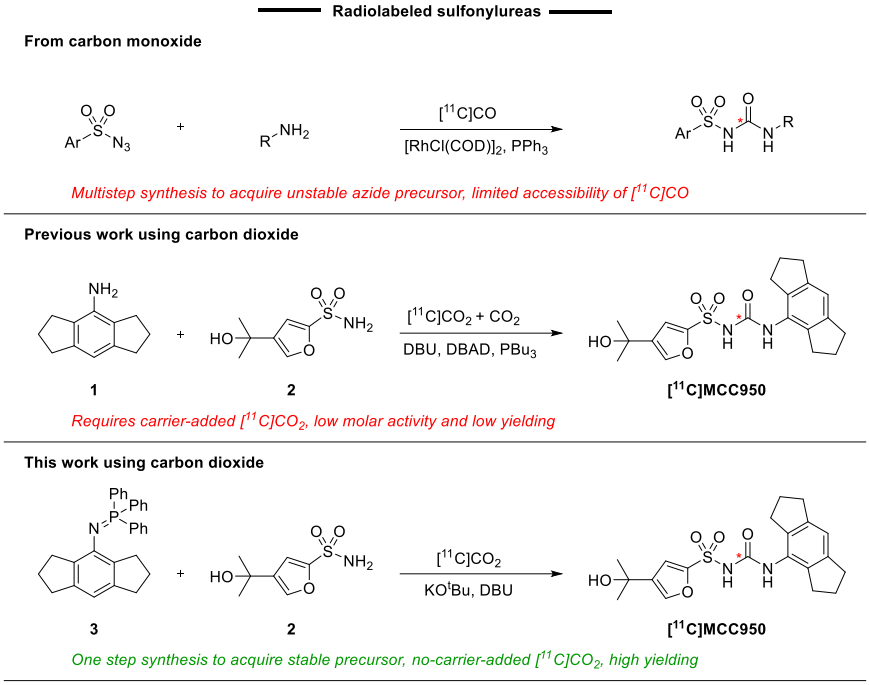

6.3.1. **Scheme 1**. Radiosynthetic methods to label ^{11}C-sulfonylureas

Our goal was to develop a high-yielding reliable synthesis of [^{11}C]MCC950 using our previously developed iminophosphorane [^{11}C]CO_2-fixation methods,[25] and to evaluate this probe for detecting atheromas in *ApoE*$^{-/-}$ mice. Our *in vivo* and *ex vivo* evaluation includes small animal PET imaging and biodistribution to determine tracer kinetics, metabolite analysis to assess tracer stability, and autoradiography under baseline and homologous blockade conditions to detect probe specificity towards NLRP3-mediated inflammation in atheromas.

6.4. Materials and methods

Male C57BL/6J (strain #000664) and *ApoE*$^{-/-}$ (strain #002052) mice were purchased from Jackson Laboratory and acclimated upon arrival for 1 week. Animals were housed in groups of four and monitored periodically until 12–14 weeks of age. C57BL/6 mice were kept on normal chow diet whereas *ApoE*$^{-/-}$ mice were fed western atherogenic diet (TD.88137, Envigo) from 6 weeks of age. Both animal strains were provided with free access to food and water and housed in environmentally enriched cages. Animal handling, housing, and experimental procedures were conducted in strict accordance with the guidelines of Canadian Council on Animal Care and received approval of the University of Ottawa Animal Care Committee.

Synthesis of N-(triphenylphosphoranylidene)-1,2,3,5,6,7-hexahydro-s-indacen-4-amine (3)

A flame dried flask was equipped with a magnetic stir bar and charged with triphenylphosphine dibromide (0.60 mmol) under inert atmosphere and dissolved in DCM (5.0 mL). The flask was placed in an ice bath, and a solution containing 4-amino-1,2,3,5,6,7-hexahydro-s-indacene (**1**, 0.57 mmol) and triethylamine (1.73 mmol) in DCM (5 mL) was added to the reactor in a dropwise manner over 10 minutes. The flask was placed under reflux for 4 hours. The solvent was removed under reduced pressure, and the product was purified by flash column chromatography on silica gel using a 0-25% hexane/ethyl acetate gradient to give **3** as an off-white solid (247 mg, 61%). ^{1}H-NMR (400 MHz $CDCl_3$): δ 7.68-7.62 (m, 6H), 7.52-7.47 (m, 3H), 7.43-7.39 (m, 6H), 6.60 (s, 1H), 2.79-2.76 (t, 4H), 2.51-2.47 (t, 4H), 1.85-1.78 (m, 4H) ppm. ^{13}C-NMR (100 MHz, $CDCl_3$): δ 142.8 (d, J = 2 Hz), 136.4 (d, J = 8 Hz), 134.2, ,133.2, 132.5 (d, J = 10 Hz), 131.2 (d, J = 3 Hz), 128.2 (d, J = 12 Hz), 111.1, 33.5, 32.2, 25.5 ppm. ^{31}P-NMR (162 MHz, $CDCl_3$): 6.09 (s, 1P) ppm. HRMS (ESI) calculated for $C_{30}H_{20}NP$ $[M + H]^+$ 434.2038. Found $[M + H]^+$ 434.2043.

Radiochemistry

DMF and DBU were degassed using five freeze-thaw cycles prior to use. Precursor **3** (3.06 mg, 7.07 μmol) was loaded directly into the reactor. 4-(2-hydroxypropan-2-yl)furan-2-sulfonamide **2** (5.86 mg, 28.57 μmol) and KO^{t}Bu (3.14 mg, 27.9 μmol) were weighed in Teflon sealed vials and kept under inert atmosphere. Two minutes prior to the end-of-bombardment, **2**was dissolved in 100 μL of DMF and added to the vial containing KO^{t}Bu. After mixing for 30 seconds, the solution was loaded into the reactor, followed by the addition of DBU (7.46 μL of a 10 μL/mL solution in DMF, 9.97 μmol). The reaction vessel was tightly sealed, and a stream of helium was swept through the reactor after loading. [^{11}C]CO_2 was trapped in a steel coil at -180 ˚C, which was subsequently heated to 25 ˚C under a stream of helium at 3 mL/min to release [^{11}C]CO_2 into the reaction solution until peak activity. The reactor was then heated to 120 ˚C for 3 min prior to addition of 800 μL of mobile phase. The crude reaction mixture was purified by HPLC: Nucleodur C18 Pyramid 7 μm, 250 × 10 mm eluted with 30% ACN/50mM NH_4OAc at 5 mL/min (retention time 6–9 min). The product was collected in a bulk vessel loaded with 25 mL of H_2O and passed through a Sep-Pak C18 Plus Light cartridge. The cartridge was washed with 10 mL of H_2O and eluted with 1.5 mL of EtOH. 13.5 mL of saline was added to the vessel and the contents were passed through a 0.22 μm sterile filter. The identity was established by co-injection with the cold standard using a Waters 2695 Alliance HPLC equipped with a Phenomenex Luna 10 μm C18(2) (100 Å, 250 mm × 4.6 mm) column, a 996-photodiode array detector (Waters), and a Carroll & Ramsey Associates 105-S high-sensitivity radiation detector. Gradient: 80/20 H_2O/ACN for 2 min, linear gradient to 35/65 over 8 min, 35/65 for 2 min, linear gradient to 80/20 for 1 min, 80/20 for 7 min.

PET imaging

C57BL/6 and *ApoE*$^{-/-}$ mice (12–14 weeks old, 30–45 g) were anesthetized with isoflurane (3%) and placed on the bed of a PET scanner. Following a 10-minute transmission scan, animals were injected with [^{11}C]MCC950 (13 MBq) as a bolus via the lateral vein and maintained under isoflurane during the acquisition. Whole body PET scans were performed for 60 minutes (4 × 15 s frames; 4 × 1 min frames; 10 × 5 min frames) using a Siemens Inveon DPET scanner. The collected emission data were corrected for scatter and attenuation, and reconstructed using the 3-dimensional ordered subsets expectation-maximization/maximum a posteriori (3D-OSEM/MAP) algorithm. Volumes of interest (VOI) were drawn in AMIDE to obtain time-activity curves. Uptake values were obtained in nCi/cc and converted to SUV using total injected dose and animal bodyweight.

Ex vivo biodistribution and autoradiography

C57BL/6 and *ApoE*$^{-/-}$ mice (12–14 weeks old, 30–45 g) were anesthetized with isoflurane (3%) and received lateral tail vein injections of 37–44 MBq of [^{11}C]MCC950 in 0.1–0.2 mL ethanolic saline (10% ethanol in 0.9% sodium chloride). For animals requiring pharmacological challenge, nonradioactive MCC950 (5 mg/kg, 0.9% sodium chloride) was injected via the lateral tail vein 10 minutes prior to radiotracer injection. Fifteen minutes after tracer injection, blood was collected via cardiac puncture and mice were sacrificed by myocardial perfusion. Organs of interest were excised, rinsed in water, weighed, and counted for radioactivity using a Hidex Automatic Gamma counter (energy window: 350–650 keV). Counts per minute (cpm) were converted to activity (nCi) using calibration standards of known activities. Percent injected dose (%ID) was calculated by dividing organ counts (nCi) by the injected dose and further normalized by organ weight to obtain percent injected dose per gram tissue %ID/g. In parallel, aortas harvested

from biodistribution were exposed to a super-resolution Storage Phosphor Screen (BAS-IP SR 2025E) in an electrophoresis Systems Autoradiography Cassette (FBXC 810) for 5 h. The screen was scanned with a Cyclone Plus Storage Phosphor System and images were analyzed using OptiQuant software by drawing aortic arch regions of interest (ROI) that were ORO positive. Digital light units (DLU) were converted to activity (nCi) using calibration standards of known activity. %ID was determined by dividing lesion activity by the injected dose and further normalized by area to obtain activity density in units of %ID/m^2.

Plasma metabolite analysis

Blood samples collected from cardiac puncture at 15 minutes after tracer injection were placed in heparinized tubes and centrifuged at 4 °C for 7 minutes at 4000 rpm to obtain plasma samples. Protein-free plasma (PFP) was obtained by adding an equal volume of ice-cold ACN, followed by centrifugation at 4 °C for 5 min at 4000 rpm. The supernatants were collected, pooled together, and then filtered through a 0.22 μm filter, spiked with nonradioactive standard (10 μL, 1 mg/mL), and injected onto the analytical radioHPLC. Fractions were collected every minute for 20 minutes and the total activity in each fraction was determined by gamma counting.

Plasma free fraction

ApoE$^{-/-}$ mice (12–14 weeks old, 30–45 g) were anesthetized with isoflurane (3%) and received lateral tail vein injections of either cold MCC950 or saline. After 25 minutes, blood was collected via cardiac puncture and the animals were sacrificed. Blood samples were placed in heparinized tubes and centrifuged at 4 °C for 7 minutes at 4000 rpm to obtain plasma samples. Samples were stored at -20 °C prior to use. [^{11}C]MCC950 (3.7 MBq) was added to each sample plus an additional sample containing only PBS and incubated at 37 °C for 10 minutes. The total

radioactivity of each sample was measured on a gamma counter. Following incubation, samples were passed through a cellulose centrifugal filter unit with a 30,000 MW cut-off (Centrifree®, Millipore). The filtrate containing plasma free fraction was collected into a vessel and measured on a gamma counter. The decay-corrected ratio of activity that passed through the filter was calculated and converted into a percentage.

Statistical analysis

Statistical analysis was performed using GraphPad Prism. Data are presented as mean ± standard deviation. Differences between multiple groups were tested using 1-way or 2-way ANOVA with Tukey's multiple comparison test. Significance was set at the 0.05 level.

6.5. Results

Radiochemistry

Our recent work highlighted the versatility of iminophosphoranes in synthesizing ^{11}C-labeled compounds, including the sulfonylurea [^{11}C]glyburide in high yield and molar activity, and prompted us to target [^{11}C]MCC950 using this methodology. Indeed, the precursor iminophosphorane (**3**) was easily prepared from commercially available 4-amino-1,2,3,5,6,7-hexahydro-s-indacene (**1**) and triphenylphosphine dibromide in 63% yield using the Kirsanov reaction (see ESI). After combining **3** with furyl sulfonamide **2** and [^{11}C]CO_2 under our previously optimized conditions, we observed an appreciable 42 ± 3% radiochemical yield of [^{11}C]MCC950 with excellent trapping efficiency (Table 1, entry 1). Increasing the reaction temperature to 120 °C improved the RCY to 72 ± 2% and lowering the concentration of iminophosphorane led to a reduced yield of 52 ± 4% (entries 2-3). Higher temperatures facilitated product formation under low precursor loading conditions (entry 4). Reducing the concentration of DBU depressed RCY

to 56 ± 2% while retaining the TE. However, the weaker base DABCO diminished the RCY to 9 ± 2% and TE to 52 ± 4% (entry 6), in-line with our previously obtained results using aryl iminophosphoranes. RCY, but not TE, could be restored in the absence of base (entries 7-9). Due to both milder reaction conditions and quantitative TE, entry 2 was chosen as the optimal conditions for radiotracer production.

6.5.1. Table 1. Optimization of reaction conditions

Entry	Deviation from original conditions[a]	RCY (%)	TE (%)
1	none	42 ± 3	99 ± 2
2	**120 °C**	**72 ± 2**	**99 ± 1**
3	35 mM **3**	52 ± 4	99 ± 3
4	45 mM **3**, 150 °C	63 ± 3	99 ± 0
5	50 mM DBU	56 ± 2	99 ± 2
6	DABCO	9 ± 2	54 ± 1
7	no base, 120 °C	42 ± 3	52 ± 2
8	no base, 150 °C	56 ± 2	58 ± 1
9	no base, 88 mM **3**, 150 °C	82 ± 3	58 ± 2

[a]Original conditions: 70 mM **3**, 285 mM **2**, 100 mM DBU, KO^{t}Bu 280 mM, 100 µL DMF, 100 °C. *n* = 2 per entry.

The radiosynthesis of [^{11}C]MCC950 was then performed using a fully automated method on a Synthra MeIplus Research module. From 25.9 GBq of [^{11}C]CO_2, we obtained an isolated RCY of 45 ± 4% (5.18 ± 0.5 GBq) and molar activity (A_m) of 27 ± 2 GBq/µmol within 23 min (Scheme 2), which is suitable for preclinical evaluation. [^{11}C]MCC950 identity was confirmed by coelution with a nonradioactive standard on analytical HPLC, and radiochemical purity was observed to be >99%.

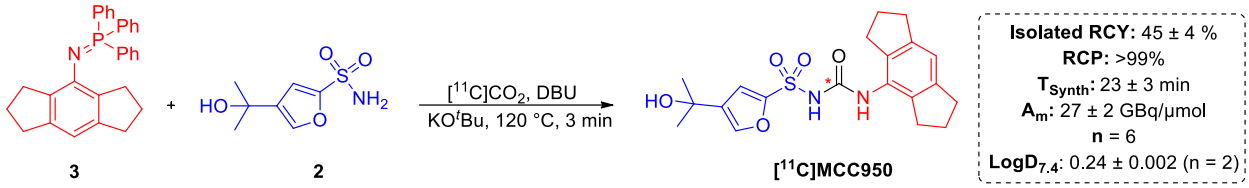

3 2 [11C]MCC950

6.5.2. Scheme 2. Automated radiosynthesis of [^{11}C]MCC950

LogD

Radiotracer lipophilicity was measured by the shake-flask method[26] to uncover the physicochemical properties of the tracer. At physiological pH, [^{11}C]MCC950 bears an anionic charge, and was thus observed to have low lipophilicity ($LogD_{7.4}$ = 0.24 ± 0.002), despite its hydrophobic hexahydro-s-indacene and furan ring systems.

PET imaging and biodistribution

Dynamic PET scans were performed to assess the distribution of [^{11}C]MCC950 in C57BL/6 controls fed normal chow diet, and *ApoE*$^{-/-}$ mice fed Western diet from 6 weeks of age (Figure 1). Blood radioactivity was estimated by VOI placed over the left ventricular cavity. In both strains of mice, blood activity rapidly declined and stabilized at 0.3–0.4 SUV by 10 min**.** In addition, [^{11}C]MCC950 rapidly accumulated in the liver and stabilized by 20 min (7–8.5 SUV). No significant differences in tracer kinetics were observed between C57BL/6 and *ApoE*$^{-/-}$ mice. As previously observed, [^{11}C]MCC950 exhibits no uptake in the brain, and this finding appears to be independent of molar activity.[17] Indeed, other radiotracers containing sulfonylureas have also been shown to have low BBB penetration in animals and humans, likely due to their unfavorable physicochemical properties.[27,28]

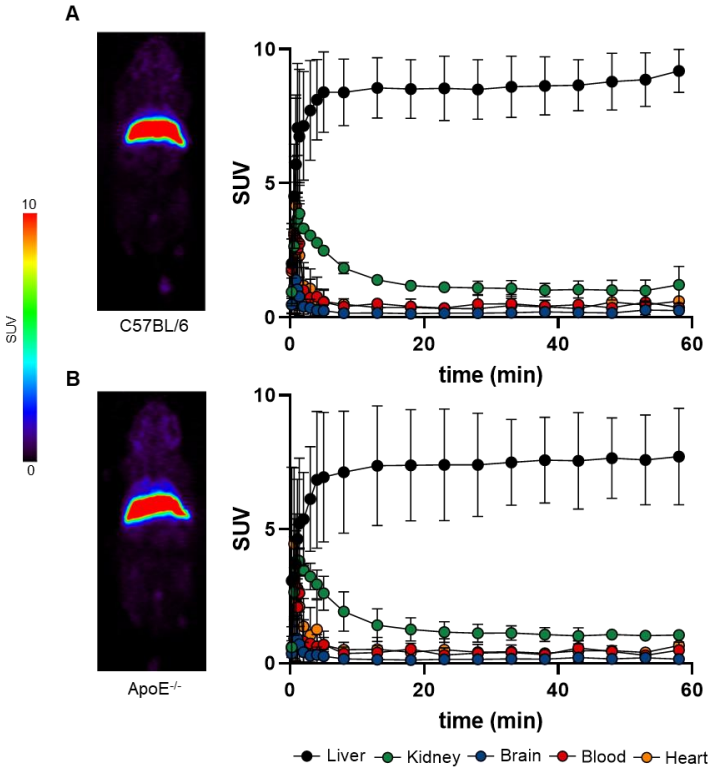

6.5.3. **Figure 1.** Dynamic PET imaging of [^{11}C]MCC950 in mice. Summed PET images and time-activity curves for (A) C57BL/6 and (B) *ApoE*$^{-/-}$ mice (n = 2 per group).

To determine tracer uptake and the extent of specific binding in lesions, we performed *ex vivo* biodistribution 15 minutes after radiotracer iv tail vein injection, followed by autoradiography of aortas under baseline and blocking conditions. At baseline, C57BL/6 and *ApoE*$^{-/-}$ mice predominantly exhibited hepatic (52.7 ± 16.6 %ID/g vs 24.9 ± 10.3 %ID/g, $p < 0.05$), renal (4.0 ± 0.3 %ID/g vs 8.2 ± 4.3 %ID/g), and intestinal (3.7 ± 0.6 %ID/g vs 5.3 ± 1.8 %ID/g) clearance (Figure 2). Blood radioactivity concentration was similar in C57BL/6 (5.5 ± 3.9 %ID/g) and *ApoE*$^{-/-}$ mice (4.2 ± 1.3 %ID/g). Consistent with our *in vivo* findings, limited uptake of the tracer (<2 %ID/g) was observed in the myocardium, brain, and remaining organs.

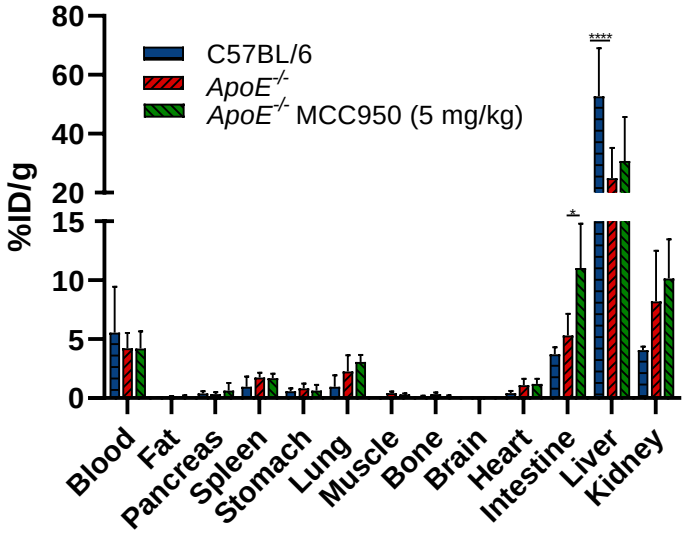

6.5.4. **Figure 2.** *Ex vivo* biodistribution of [^{11}C]MCC950 15 minutes after radiotracer injection. Two-way ANOVA: *P = 0.04, *n* = 4-5 per group

Homologous blockade was performed in *ApoE*$^{-/-}$ mice using nonradioactive MCC950 (5 mg/kg, iv) 10 minutes prior to administering the radiotracer (Figure 2). Intestinal uptake was increased by two-fold in MCC950 treated mice (11.0 ± 3.7, $p < 0.05$). Otherwise, minimal differences were observed between organs under blocking conditions.

Autoradiography

Following *ex vivo* biodistribution, aortic arch uptake of [^{11}C]MCC950 was visualized by autoradiography and displayed regional uptake in lipid rich Oil red O (ORO) positive atherosclerotic lesions (Figure 3). [^{11}C]MCC950 was found to have 2.7-fold higher uptake in *ApoE*$^{-/-}$ mice compared to C57BL/6 controls (48 ± 17 %ID/m^2 vs 18 ± 8 %ID/m^2, $p = 0.016$). Increased uptake in the lesion aligns with expected findings, as mice kept on Western diet overexpress NLRP3 and its respective inflammasome components.[13,29] In order to determine if

tracer uptake within the lesion is specific, homologous blocking was performed as previously described. Animals pretreated with MCC950 displayed a further 2.2-fold increase in plaque uptake in comparison to untreated animals (104 ± 15 %ID/m^2 vs 48 ± 17 %ID/m^2, p = 0.0002).

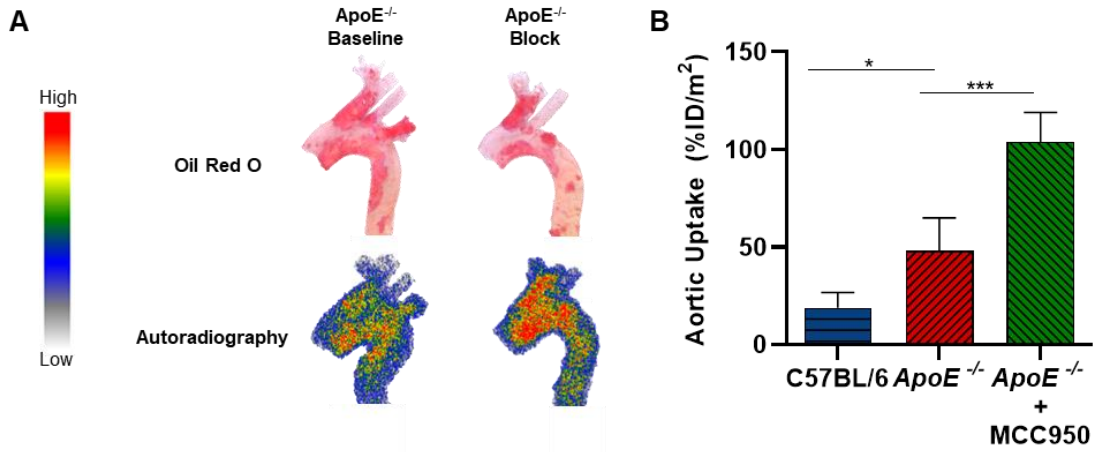

6.5.5. **Figure 3.** *Ex vivo* aortic autoradiography of [^{11}C]MCC950. (A) Representative ORO brightfield images and autoradiograms after intravenous injection of 37 MBq [^{11}C]MCC950 in *ApoE*$^{-/-}$ mice. Homologous blockade was performed with nonradioactive MCC950 (5 mg/kg, iv) 10 minutes prior to tracer administration. (B) [^{11}C]MCC950 aortic lesion uptake in C57BL/6 and ApoE$^{-/-}$ mice. One-way ANOVA: ***P = 0.0002, *P = 0.002, n = 4-5 per group.

6.5.6. **Table 2. [**^{11}C]MCC950 plasma stability[a]

Fraction	C57BL/6	*ApoE*$^{-/-}$ baseline	*ApoE*$^{-/-}$ block
Parent radiotracer	92%	94%	93%
Polar metabolites	6%	4%	5%
Non-polar metabolites	2%	2%	2%
Extraction efficiency	92%	91%	92%
Plasma free fraction[b]	n.d.	1.3 ± 0.4%	1.7 ± 0.8%

[a]Percent parent compound of total radioactivity obtained for pooled samples following intravenous tracer administration (n = 5 per group).
[b]Determined *in vitro* (n = 2 per group).

Plasma metabolite Analysis

Whole-blood samples collected from *ex vivo* biodistribution at 15 minutes post-injection were pooled for plasma metabolite analysis using fractional radio-HPLC followed by gamma counting. In C57BL/6 and *ApoE*$^{-/-}$mice, 92–94% of the plasma radioactivity corresponded to intact [^{11}C]MCC950, and blocking conditions were observed to have no effect on the metabolic stability of the parent tracer (Table 2). The major metabolite under all conditions was observed to be polar, consistent with previously reported stereospecific ring hydroxylation on the hexahydro-s-indacene moiety.[30] Plasma free fraction (f_p) was then measured for *ApoE*$^{-/-}$ mice under baseline and blocking conditions (Table 2). Under baseline conditions, 1.3 ± 0.4% of the tracer was unbound, and blockade with cold MCC950 (5 mg/kg, iv) led to a moderate but not statistically significant increase of f_p to 1.7 ± 0.8%.

6.6. Discussion

MCC950 is a first-in-class NLRP3 inhibitor which has demonstrated considerable promise in resolving inflammation in conditions as diverse as neurodegenerative disorders, myocarditis, and atherosclerosis.[11,12,15,31–35] To evaluate the brain uptake of this inhibitor and to develop a tool for measuring target engagement, Hill *et al.* radiolabeled [^{11}C]MCC950 at low molar activity for PET imaging in several species and found poor brain uptake.[17] Xu *et al.* labeled NLRP3 inhibitors lacking the sulfonylurea moiety, which were observed to have moderate brain uptake (≤1.5 SUV).[36] Despite its lack of CNS penetration, [^{11}C]MCC950 and its derivatives could have profound applications in imaging NLRP3 mediated-inflammation in the periphery.

In atherosclerosis, MCC950 has displayed remarkable use as a therapeutic in significantly reducing plaque area, diminishing the concentration of pro-inflammatory cytokines and macrophages, and improving the lipid profile in *ApoE*$^{-/-}$ mice.[12,37] Previous reports have identified cholesterol crystals in early stages of lesion development to trigger NLRP3-mediated inflammation that is sustained and worsens with greater plaque progression.[38] Furthermore, NLRP3 expression is observed to be significantly higher in unstable plaques in comparison to stable lesions and has been significantly correlated with atherosclerosis severity scores in humans.[39] As an imaging probe, MCC950 may prove useful in discriminating stages of lesion development and determining plaque stability.

In this work, we prepared high molar activity [^{11}C]MCC950 using an operationally simple iminophosphorane precursor for [^{11}C]CO_2-fixation and evaluated it in a widely used mouse model of atherosclerosis. [^{11}C]MCC950 shows predominant distribution to the liver in both atherosclerotic and control animals, with no accumulation within the brain and fast clearance from other organs. It is highly stable in circulation and is taken up into lipid-rich inflammatory lesions in the aorta. Pretreatment with nonradioactive MCC950 has minimal effect on tissue distribution but augments atherosclerotic lesion uptake by more than two-fold.

Increased uptake in target organs following receptor blockade has been described in the development of CNS radiotracers. This phenomenon may occur due to an increase in radiotracer f_p as a result of plasma protein occupancy by the homologous blocking agent.[40] Consequently, organ activity must be normalized by metabolite-corrected plasma radiotracer levels for accurate estimation of target binding parameters. For example, homologous blockade of the α_2-adrenoceptor antagonist [^{11}C]yohimbine in the rat brain with 0.3 mg/kg of the reference standard decreases binding potentials by 50–60%, but the effect on activity uptake is masked by increased

f_p due to saturation of plasma protein binding sites.[41] In addition to plasma normalization, biochemical mechanisms may also explain increased uptake following blockade. Treatment of non-human primates with 4-aminopyridines prior to imaging with the K^+ channel blocker [^{18}F]3F4AP increases volumes of distribution in the brain.[42] An increase in neuronal firing and open, bindable channels is proposed to account for the unanticipated observation. Self-blockade of certain radiolabeled mGluR2 positive allosteric modulators decreases activity uptake across brain regions yet increases volumes of distribution in these same regions. Yuan *et al.* suggest receptor potentiation towards binding, nonspecific binding, and ligand cooperativity as possible explanations.[43,44] Indeed, similar mechanisms may be at play when observing increased tracer uptake following blockade with MCC950.

We surmised that increased plaque uptake of [^{11}C]MCC950 following homologous blockade may be due to drug-induced inflammasome deactivation. The active NLRP3 inflammasome has been reported to undergo disaggregation upon incubation with MCC950, theoretically increasing the number of NLRP3 monomers available for radiotracer binding.[45] Non-specific binding of the tracer is unlikely to contribute to the higher signal observed following blockade based on a moderate 1.3-fold increase in f_p at this dose, compared to 2.2-fold higher tracer uptake in lesions. Accordingly, the more probable hypothesis to explain the observed increased uptake following pretreatment remains an increase in specific binding in plaques.

Conclusions

In this study, a high-yielding radiosynthesis for the lead sulfonylurea NLRP3 inhibitor [^{11}C]MCC950 was developed, enabling preclinical evaluation of this compound for imaging atherosclerotic plaques. Radiotracer kinetics were determined by *in vivo* dynamic PET imaging and revealed rapid uptake in the liver and prominent renal excretion. *Ex vivo* biodistribution was

also performed at 15 minutes and corroborated these findings. [^{11}C]MCC950 stability studies displayed >90% of the parent tracer intact in plasma, with no differences observed between animal strains. Measurements of f_p demonstrated 1.3 ± 0.4% of the parent unbound to plasma proteins, and a minor increase to 1.7 ± 0.8% unbound following homologous blockade. Last, *ex vivo* autoradiography displayed heterogeneity of lesions within the aortae of *ApoE*$^{-/-}$ mice, and blockade with cold MCC950 increased plaque uptake by 2.2-fold. Increased retention of the tracer within the lesion following attempted homologous blockade is likely due to a biochemical disaggregation of NLRP3 oligomers, consequently increasing the available monomeric binding sites for [^{11}C]MCC950. This tracer successfully visualized aortic atherosclerotic lesions *ex vivo* and represents the first ^{11}C-labelled sulfonylurea to be evaluated for cardiovascular plaque imaging. Further studies are warranted to explore these findings. The availability of a readily accessible method to synthesize labeled sulfonylureas directly from [^{11}C]CO_2 could enable *in vivo* assessment of novel NLRP3 inhibitors and assist in the development of inflammasome-targeted therapies for inflammatory diseases.

6.7. Acknowledgements

The authors thank the staff of the University of Ottawa Heart Institute (UOHI) PET Radiochemistry Laboratory, Biomedical Engineering, and Animal Care and Veterinary Services for cyclotron, small animal PET scanner, and animal care support. The authors acknowledge financial support from CFI (JELF 36848 & 39358), CIHR (PJT 148968), NSERC (RGPIN-2017-06167), and the Ontario Ministry for Research Innovation and Science (ER17-13-119). U.S.I. was supported by Ontario QEII-GSST and the UOHI Endowed Fellowship. A.B. was supported by Ontario OGS, QEII-GSST, and UOHI Endowed Research Scholarship. M.A. was supported by NSERC USRA and University of Ottawa UROP.

6.8. Supporting information

Experimental methods, synthetic procedures, NMR spectra, radiochemistry automation procedures, HPLC chromatograms and calibration curve

6.9. Declaration of Competing Interest

The authors declare no conflicts of interest

6.10. References

(1) Libby, P.; Buring, J. E.; Badimon, L.; Hansson, G. K.; Deanfield, J.; Bittencourt, M. S.; Tokgözoğlu, L.; Lewis, E. F. Atherosclerosis. *Nat. Rev. Dis. Primer* **2019**, *5* (1), 1–18. https://doi.org/10.1038/s41572-019-0106-z.

(2) Lusis, A. J. Atherosclerosis. *Nature* **2000**, *407* (6801), 233–241. https://doi.org/10.1038/35025203.

(3) Shah, P.; Bajaj, S.; Virk, H.; Bikkina, M.; Shamoon, F. Rapid Progression of Coronary Atherosclerosis: A Review. *Thrombosis* **2015**, *2015*, e634983. https://doi.org/10.1155/2015/634983.

(4) Karasawa, T.; Takahashi, M. Role of NLRP3 Inflammasomes in Atherosclerosis. *J. Atheroscler. Thromb.* **2017**, *24* (5), 443–451. https://doi.org/10.5551/jat.RV17001.

(5) Stitham, J.; Rodriguez-Velez, A.; Zhang, X.; Jeong, S.-J.; Razani, B. Inflammasomes: A Preclinical Assessment of Targeting in Atherosclerosis. *Expert Opin. Ther. Targets* **2020**, *24* (9), 825–844. https://doi.org/10.1080/14728222.2020.1795831.

(6) Jin, Y.; Fu, J. Novel Insights Into the NLRP3 Inflammasome in Atherosclerosis. *J. Am. Heart Assoc.* **2019**, *8* (12), e012219. https://doi.org/10.1161/JAHA.119.012219.

(7) Grebe, A.; Hoss, F.; Latz, E. NLRP3 Inflammasome and the IL-1 Pathway in Atherosclerosis. *Circ. Res.* **2018**, *122* (12), 1722–1740. https://doi.org/10.1161/CIRCRESAHA.118.311362.

(8) Duewell, P.; Kono, H.; Rayner, K. J.; Sirois, C. M.; Vladimer, G.; Bauernfeind, F. G.; Abela, G. S.; Franchi, L.; Nuñez, G.; Schnurr, M.; Espevik, T.; Lien, E.; Fitzgerald, K. A.; Rock, K. L.; Moore, K. J.; Wright, S. D.; Hornung, V.; Latz, E. NLRP3 Inflammasomes Are Required for Atherogenesis and Activated by Cholesterol Crystals. *Nature* **2010**, *464* (7293), 1357–1361. https://doi.org/10.1038/nature08938.

(9) Usui, F.; Shirasuna, K.; Kimura, H.; Tatsumi, K.; Kawashima, A.; Karasawa, T.; Hida, S.; Sagara, J.; Taniguchi, S.; Takahashi, M. Critical Role of Caspase-1 in Vascular Inflammation and Development of Atherosclerosis in Western Diet-Fed Apolipoprotein E-Deficient Mice. *Biochem. Biophys. Res. Commun.* **2012**, *425* (2), 162–168. https://doi.org/10.1016/j.bbrc.2012.07.058.

(10) Gage, J.; Hasu, M.; Thabet, M.; Whitman, S. C. Caspase-1 Deficiency Decreases Atherosclerosis in Apolipoprotein E-Null Mice. *Can. J. Cardiol.* **2012**, *28* (2), 222–229. https://doi.org/10.1016/j.cjca.2011.10.013.

(11) van der Heijden, T.; Kritikou, E.; Venema, W.; van Duijn, J.; van Santbrink, P. J.; Slütter, B.; Foks, A. C.; Bot, I.; Kuiper, J. NLRP3 Inflammasome Inhibition by MCC950 Reduces Atherosclerotic Lesion Development in Apolipoprotein E–Deficient Mice—Brief Report. *Arterioscler. Thromb. Vasc. Biol.* **2017**, *37* (8), 1457–1461. https://doi.org/10.1161/ATVBAHA.117.309575.

(12) Sharma, A.; Choi, J. S. Y.; Stefanovic, N.; Al-Sharea, A.; Simpson, D. S.; Mukhamedova, N.; Jandeleit-Dahm, K.; Murphy, A. J.; Sviridov, D.; Vince, J. E.; Ritchie, R. H.; de Haan, J. B. Specific NLRP3 Inhibition Protects Against Diabetes-Associated Atherosclerosis. *Diabetes* **2020**, *70* (3), 772–787. https://doi.org/10.2337/db20-0357.

(13) Zeng, W.; Wu, D.; Sun, Y.; Suo, Y.; Yu, Q.; Zeng, M.; Gao, Q.; Yu, B.; Jiang, X.; Wang, Y. The Selective NLRP3 Inhibitor MCC950 Hinders Atherosclerosis Development by Attenuating Inflammation and Pyroptosis in Macrophages. *Sci. Rep.* **2021**, *11* (1), 19305. https://doi.org/10.1038/s41598-021-98437-3.

(14) Hettwer, J.; Hinterdobler, J.; Miritsch, B.; Deutsch, M.-A.; Li, X.; Mauersberger, C.; Moggio, A.; Braster, Q.; Gram, H.; Robertson, A. A. B.; Cooper, M. A.; Groß, O.; Krane,

M.; Weber, C.; Koenig, W.; Soehnlein, O.; Adamstein, N. H.; Ridker, P.; Schunkert, H.; Libby, P.; Kessler, T.; Sager, H. B. Interleukin-1β Suppression Dampens Inflammatory Leucocyte Production and Uptake in Atherosclerosis. *Cardiovasc. Res.* **2021**, cvab337. https://doi.org/10.1093/cvr/cvab337.

(15) Coll, R. C.; Robertson, A. A. B.; Chae, J. J.; Higgins, S. C.; Muñoz-Planillo, R.; Inserra, M. C.; Vetter, I.; Dungan, L. S.; Monks, B. G.; Stutz, A.; Croker, D. E.; Butler, M. S.; Haneklaus, M.; Sutton, C. E.; Núñez, G.; Latz, E.; Kastner, D. L.; Mills, K. H. G.; Masters, S. L.; Schroder, K.; Cooper, M. A.; O'Neill, L. A. J. A Small-Molecule Inhibitor of the NLRP3 Inflammasome for the Treatment of Inflammatory Diseases. *Nat. Med.* **2015**, *21* (3), 248–255. https://doi.org/10.1038/nm.3806.

(16) Li, H.; Guan, Y.; Liang, B.; Ding, P.; Hou, X.; Wei, W.; Ma, Y. Therapeutic Potential of MCC950, a Specific Inhibitor of NLRP3 Inflammasome. *Eur. J. Pharmacol.* **2022**, *928*, 175091. https://doi.org/10.1016/j.ejphar.2022.175091.

(17) Hill, J. R.; Shao, X.; Massey, N. L.; Stauff, J.; Sherman, P. S.; Robertson, A. A. B.; Scott, P. J. H. Synthesis and Evaluation of NLRP3-Inhibitory Sulfonylurea [11C]MCC950 in Healthy Animals. *Bioorg. Med. Chem. Lett.* **2020**, *30* (12), 127186. https://doi.org/10.1016/j.bmcl.2020.127186.

(18) Nerella, S. G.; Singh, P.; Tulja, S. Carbon-11 Patents (2012–2022): Synthetic Methodologies and Novel Radiotracers for PET Imaging. *Expert Opin. Ther. Pat.* **2022**, *32* (7), 817–831. https://doi.org/10.1080/13543776.2022.2070003.

(19) Rotstein, B. H.; Liang, S. H.; Placzek, M. S.; Hooker, J. M.; Gee, A. D.; Dollé, F.; Wilson, A. A.; Vasdev, N. 11CO Bonds Made Easily for Positron Emission Tomography

Radiopharmaceuticals. *Chem. Soc. Rev.* **2016**, *45* (17), 4708–4726. https://doi.org/10.1039/C6CS00310A.

(20) Taddei, C.; Pike, V. W. [11C]Carbon Monoxide: Advances in Production and Application to PET Radiotracer Development over the Past 15 Years. *EJNMMI Radiopharm. Chem.* **2019**, *4* (1), 25. https://doi.org/10.1186/s41181-019-0073-4.

(21) Villa, A.; Klein, B.; Janssen, B.; Pedragosa, J.; Pepe, G.; Zinnhardt, B.; Vugts, D. J.; Gelosa, P.; Sironi, L.; Beaino, W.; Damont, A.; Dollé, F.; Jego, B.; Winkeler, A.; Ory, D.; Solin, O.; Vercouillie, J.; Funke, U.; Laner-Plamberger, S.; Blomster, L. V.; Christophersen, P.; Vegeto, E.; Aigner, L.; Jacobs, A.; Planas, A. M.; Maggi, A.; Windhorst, A. D. Identification of New Molecular Targets for PET Imaging of the Microglial Anti-Inflammatory Activation State. *Theranostics* **2018**, *8* (19), 5400–5418. https://doi.org/10.7150/thno.25572.

(22) Åberg, O.; Långström, B. Synthesis of Substituted [11C]Ureas and [11C]Sulphonylureas by Rh(I)-Mediated Carbonylation. *J. Label. Compd. Radiopharm.* **2011**, *54* (1), 38–42. https://doi.org/10.1002/jlcr.1803.

(23) Wilson, A. A.; Garcia, A.; Houle, S.; Sadovski, O.; Vasdev, N. Synthesis and Application of Isocyanates Radiolabeled with Carbon-11. *Chem. – Eur. J.* **2011**, *17* (1), 259–264. https://doi.org/10.1002/chem.201002345.

(24) Dheere, A. K. H.; Yusuf, N.; Gee, A. Rapid and Efficient Synthesis of [11C]Ureas via the Incorporation of [11C]CO2 into Aliphatic and Aromatic Amines. *Chem. Commun.* **2013**, *49* (74), 8193–8195. https://doi.org/10.1039/C3CC44046J.

(25) Ismailani, U. S.; Munch, M.; Mair, B. A.; Rotstein, B. H. Interrupted Aza-Wittig Reactions Using Iminophosphoranes to Synthesize ^{11}C–Carbonyls. *Chem. Commun.* **2021**, 10.1039.D1CC01016F. https://doi.org/10.1039/D1CC01016F.

(26) Wilson, A. A.; Jin, L.; Garcia, A.; DaSilva, J. N.; Houle, S. An Admonition When Measuring the Lipophilicity of Radiotracers Using Counting Techniques. *Appl. Radiat. Isot.* **2001**, *54* (2), 203–208. https://doi.org/10.1016/S0969-8043(00)00269-4.

(27) van der Wildt, B.; Janssen, B.; Pekošak, A.; Stéen, E. J. L.; Schuit, R. C.; Kooijman, E. J. M.; Beaino, W.; Vugts, D. J.; Windhorst, A. D. Novel Thienopyrimidine-Based PET Tracers for P2Y12 Receptor Imaging in the Brain. *ACS Chem. Neurosci.* **2021**, *12* (23), 4465–4474. https://doi.org/10.1021/acschemneuro.1c00641.

(28) Marie, S.; Comtat, C.; Caillé, F.; Becquemont, L.; Bottlaender, M.; Tournier, N. 11C-Glyburide PET Imaging Unveils the Negligible Brain Penetration of Glyburide in Humans. *Neurology* **2019**, *92* (17), 813–814. https://doi.org/10.1212/WNL.0000000000007378.

(29) Wang, R.; Wang, Y.; Mu, N.; Lou, X.; Li, W.; Chen, Y.; Fan, D.; Tan, H. Activation of NLRP3 Inflammasomes Contributes to Hyperhomocysteinemia-Aggravated Inflammation and Atherosclerosis in ApoE-Deficient Mice. *Lab. Invest.* **2017**, *97* (8), 922–934. https://doi.org/10.1038/labinvest.2017.30.

(30) Salla, M.; Butler, M. S.; Pelingon, R.; Kaeslin, G.; Croker, D. E.; Reid, J. C.; Baek, J. M.; Bernhardt, P. V.; Gillam, E. M. J.; Cooper, M. A.; Robertson, A. A. B. Identification, Synthesis, and Biological Evaluation of the Major Human Metabolite of NLRP3 Inflammasome Inhibitor MCC950. *ACS Med. Chem. Lett.* **2016**, *7* (12), 1034–1038. https://doi.org/10.1021/acsmedchemlett.6b00198.

(31) Hull, C.; Dekeryte, R.; Buchanan, H.; Kamli-Salino, S.; Robertson, A.; Delibegovic, M.; Platt, B. NLRP3 Inflammasome Inhibition with MCC950 Improves Insulin Sensitivity and Inflammation in a Mouse Model of Frontotemporal Dementia. *Neuropharmacology* **2020**, *180*, 108305. https://doi.org/10.1016/j.neuropharm.2020.108305.

(32) Gordon, R.; Albornoz, E. A.; Christie, D. C.; Langley, M. R.; Kumar, V.; Mantovani, S.; Robertson, A. A. B.; Butler, M. S.; Rowe, D. B.; O'Neill, L. A.; Kanthasamy, A. G.; Schroder, K.; Cooper, M. A.; Woodruff, T. M. Inflammasome Inhibition Prevents α-Synuclein Pathology and Dopaminergic Neurodegeneration in Mice. *Sci. Transl. Med.* **2018**, *10* (465), eaah4066. https://doi.org/10.1126/scitranslmed.aah4066.

(33) Chen, K.-P.; Hua, K.-F.; Tsai, F.-T.; Lin, T.-Y.; Cheng, C.-Y.; Yang, D.-I.; Hsu, H.-T.; Ju, T.-C. A Selective Inhibitor of the NLRP3 Inflammasome as a Potential Therapeutic Approach for Neuroprotection in a Transgenic Mouse Model of Huntington's Disease. *J. Neuroinflammation* **2022**, *19* (1), 56. https://doi.org/10.1186/s12974-022-02419-9.

(34) Ren, P.; Wu, D.; Appel, R.; Zhang, L.; Zhang, C.; Luo, W.; Robertson, A. A. B.; Cooper, M. A.; Coselli, J. S.; Milewicz, D. M.; Shen, Y. H.; LeMaire, S. A. Targeting the NLRP3 Inflammasome With Inhibitor MCC950 Prevents Aortic Aneurysms and Dissections in Mice. *J. Am. Heart Assoc.* **2020**, *9* (7), e014044. https://doi.org/10.1161/JAHA.119.014044.

(35) Li, X.; Yang, W.; Ma, W.; Zhou, X.; Quan, Z.; Li, G.; Liu, D.; Zhang, Q.; Han, D.; Gao, B.; Li, C.; Wang, J.; Kang, F. 18F-FDG PET Imaging-Monitored Anti-Inflammatory Therapy for Acute Myocardial Infarction: Exploring the Role of MCC950 in Murine Model. *J. Nucl. Cardiol.* **2021**, *28* (5), 2346–2357. https://doi.org/10.1007/s12350-020-02044-0.

(36) Xu, Y.; Xu, Y.; Blevins, H.; Lan, Y.; Liu, Y.; Yuan, G.; Striar, R.; Zagaroli, J. S.; Tocci, D. R.; Langan, A. G.; Zhang, C.; Zhang, S.; Wang, C. Discovery of Carbon-11 Labeled Sulfonamide Derivative: A PET Tracer for Imaging Brain NLRP3 Inflammasome. *Bioorg. Med. Chem. Lett.* **2021**, *34*, 127777. https://doi.org/10.1016/j.bmcl.2021.127777.

(37) Ma, Q.; Fan, Q.; Han, X.; Dong, Z.; Xu, J.; Bai, J.; Tao, W.; Sun, D.; Wang, C. Platelet-Derived Extracellular Vesicles to Target Plaque Inflammation for Effective Anti-

Atherosclerotic Therapy. *J. Controlled Release* **2021**, *329*, 445–453. https://doi.org/10.1016/j.jconrel.2020.11.064.

(38) Baldrighi, M.; Mallat, Z.; Li, X. NLRP3 Inflammasome Pathways in Atherosclerosis. *Atherosclerosis* **2017**, *267*, 127–138. https://doi.org/10.1016/j.atherosclerosis.2017.10.027.

(39) Liu, Y.; Li, C.; Yin, H.; Zhang, X.; Li, Y. NLRP3 Inflammasome: A Potential Alternative Therapy Target for Atherosclerosis. *Evid.-Based Complement. Altern. Med. ECAM* **2020**, *2020*, 1561342. https://doi.org/10.1155/2020/1561342.

(40) Van de Bittner, G. C.; Ricq, E. L.; Hooker, J. M. A Philosophy for CNS Radiotracer Design. *Acc. Chem. Res.* **2014**, *47* (10), 3127–3134. https://doi.org/10.1021/ar500233s.

(41) Phan, J.-A.; Landau, A. M.; Jakobsen, S.; Wong, D. F.; Gjedde, A. Radioligand Binding Analysis of A2 Adrenoceptors with [11C]Yohimbine in Brain in Vivo: Extended Inhibition Plot Correction for Plasma Protein Binding. *Sci. Rep.* **2017**, *7* (1), 15979. https://doi.org/10.1038/s41598-017-16020-1.

(42) Guehl, N. J.; Ramos-Torres, K. M.; Linnman, C.; Moon, S.-H.; Dhaynaut, M.; Wilks, M. Q.; Han, P. K.; Ma, C.; Neelamegam, R.; Zhou, Y.-P.; Popko, B.; Correia, J. A.; Reich, D. S.; Fakhri, G. E.; Herscovitch, P.; Normandin, M. D.; Brugarolas, P. Evaluation of the Potassium Channel Tracer [18F]3F4AP in Rhesus Macaques. *J. Cereb. Blood Flow Metab.* **2021**, *41* (7), 1721–1733. https://doi.org/10.1177/0271678X20963404.

(43) Yuan, G.; Guehl, N. J.; Zheng, B.; Qu, X.; Moon, S.-H.; Dhaynaut, M.; Shoup, T. M.; Afshar, S.; Kang, H. J.; Zhang, Z.; El Fakhri, G.; Normandin, M. D.; Brownell, A.-L. Synthesis and Characterization of [18F]JNJ-46356479 as the First 18F-Labeled PET Imaging Ligand for Metabotropic Glutamate Receptor 2. *Mol. Imaging Biol.* **2021**, *23* (4), 527–536. https://doi.org/10.1007/s11307-021-01586-0.

(44) Yuan, G.; Dhaynaut, M.; Guehl, N. J.; Afshar, S.; Huynh, D.; Moon, S.-H.; Iyengar, S. M.; Jain, M. K.; Pickett, J. E.; Kang, H. J.; Ondrechen, M. J.; El Fakhri, G.; Normandin, M. D.; Brownell, A.-L. Design, Synthesis, and Characterization of [18F]MG2P026 as a High-Contrast PET Imaging Ligand for Metabotropic Glutamate Receptor 2. *J. Med. Chem.* **2022**, *65* (14), 9939–9954. https://doi.org/10.1021/acs.jmedchem.2c00593.

(45) Tapia-Abellán, A.; Angosto-Bazarra, D.; Martínez-Banaclocha, H.; de Torre-Minguela, C.; Cerón-Carrasco, J. P.; Pérez-Sánchez, H.; Arostegui, J. I.; Pelegrin, P. MCC950 Closes the Active Conformation of NLRP3 to an Inactive State. *Nat. Chem. Biol.* **2019**, *15* (6), 560–564. https://doi.org/10.1038/s41589-019-0278-6.

6.11. Supporting information

6.11.1. General information

All reagents and solvents purchased were not further purified unless stated otherwise. All reactions were carried out under inert (argon) atmosphere. All solvents used were anhydrous. Anhydrous 1,8-diazabicyclo[5.4.0]undec-7-ene (DBU) was obtained by refluxing over CaH_2 followed by distillation under reduced pressured. Reaction products were confirmed using ^{1}H-NMR, ^{13}C-NMR, and mass spectrometry. ^{1}H-NMR spectra were obtained using a Bruker AVANCE 400 spectrometer. Spectral data are reported in ppm using solvent as a reference (^{1}H NMR $CHCl_3$ at 7.26 ppm). ^{1}H NMR data was reported as: multiplicity (ap = apparent, br = broad, s = singlet, d = doublet, t = triplet, q = quartet, m = multiplet), integration, and coupling constant(s) in Hz. Low resolution mass spectrometry was performed using a Waters Xevo TQD with an Acquity UPLC-H-Class Plus system. High resolution mass spectrometry was performed using a Kratos Concept – Magnetic Sector Electron Impact Mass Spectrometer. Radiochemical chromatograms were obtained using a Waters 2695 Alliance HPLC equipped with a Phenomenex Luna 10 µm C18(2) 100 Å column (250 × 4.6, 10 µmm), a Waters 996 photodiode array detector, and a Carroll & Ramsey Associates 105-S high-sensitivity radiation detector equipped with a 1 cm^3 CsI(Tl) scintillating crystal. Radiolabeled products were synthesized using a Synthra MeIplus Research module.

Sigma-Aldrich: triphenylphosphine dibromide

AstaTech: 2-Furansulfonamide, 4-(1-hydroxy-1-methylethyl)-, 1,2,3,5,6,7-Hexahydro-S-5-indacen-4yl-amine, MCC950 (sodium salt).

6.11.2. Synthetic procedures

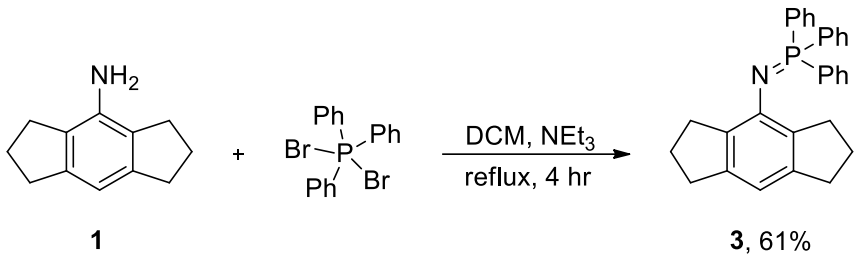

1 **3**, 61%

6.11.2.1. Scheme S1. Synthesis of iminophosphorane precursor

A flame dried flask was equipped with a magnetic stir bar and charged with triphenylphosphine dibromide (0.60 mmol) under inert atmosphere and dissolved in DCM (5.0 mL). The flask was placed in an ice bath, and a solution containing 4-amino-1,2,3,5,6,7-hexahydro-s-indacene (**1**, 0.57 mmol) and triethylamine (1.73 mmol) in DCM (5 mL) was added to the reactor in a dropwise manner over 10 minutes. The flask was placed under reflux for 4 hours. The solvent was removed under reduced pressure, and the product was purified by flash column chromatography on silica gel using a 0-25% hexane/ethyl acetate gradient to give **3** as an off-white solid (247 mg, 61%). ^{1}H-NMR (400 MHz $CDCl_3$): δ 7.68-7.62 (m, 6H), 7.52-7.47 (m, 3H), 7.43-7.39 (m, 6H), 6.60 (s, 1H), 2.79-2.76 (t, 4H), 2.51-2.47 (t, 4H), 1.85-1.78 (m, 4H) ppm. ^{13}C-NMR (100 MHz, $CDCl_3$): δ 142.8 (d, J = 2 Hz), 136.4 (d, J = 8 Hz), 134.2, ,133.2, 132.5 (d, J = 10 Hz), 131.2 (d, J = 3 Hz), 128.2 (d, J = 12 Hz), 111.1, 33.5, 32.2, 25.5 ppm. ^{31}P-NMR (162 MHz, $CDCl_3$): 6.09 (s, 1P), 29.04 (s, 1P, TPPO) ppm. HRMS (ESI) calculated for $C_{30}H_{20}NP$ $[M + H]^+$ 434.2038. Found $[M + H]^+$ 434.2043.

6.11.3. Experimental Data

6.11.3.1. 3. *N*-(triphenylphosphoranylidene)-1,2,3,5,6,7-hexahydro-s-indacen-4-amine

^{1}H NMR:

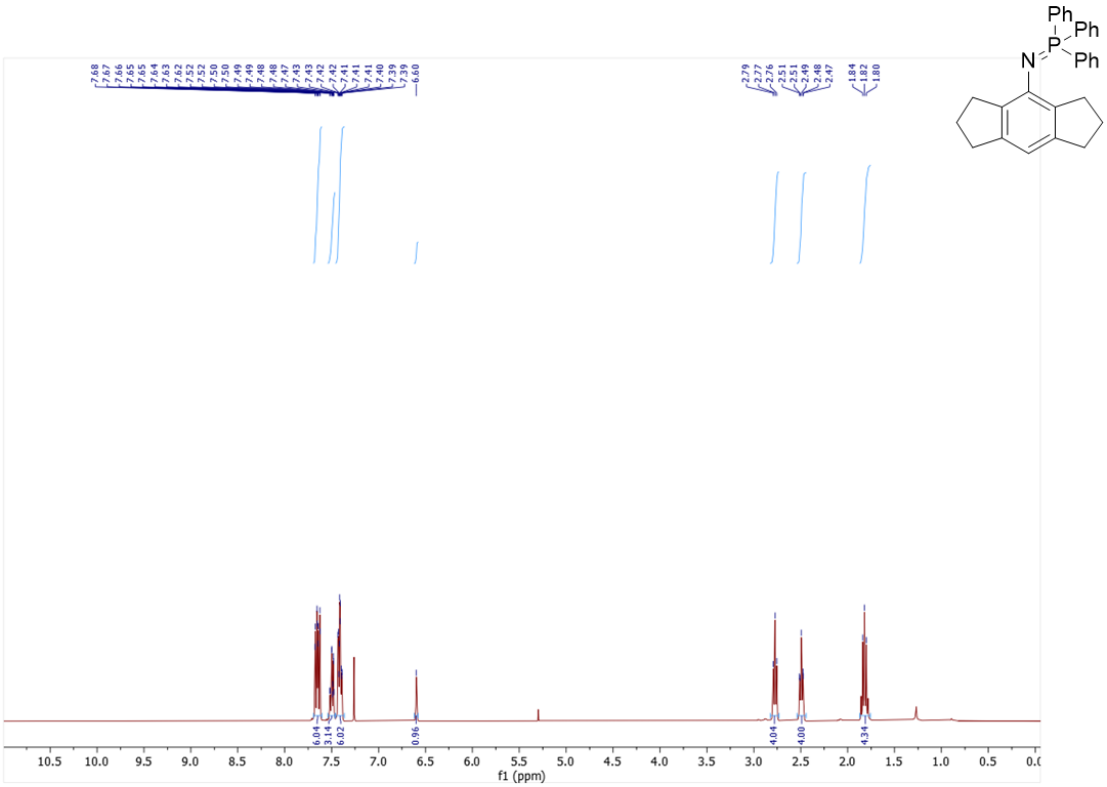

^{13}C NMR:

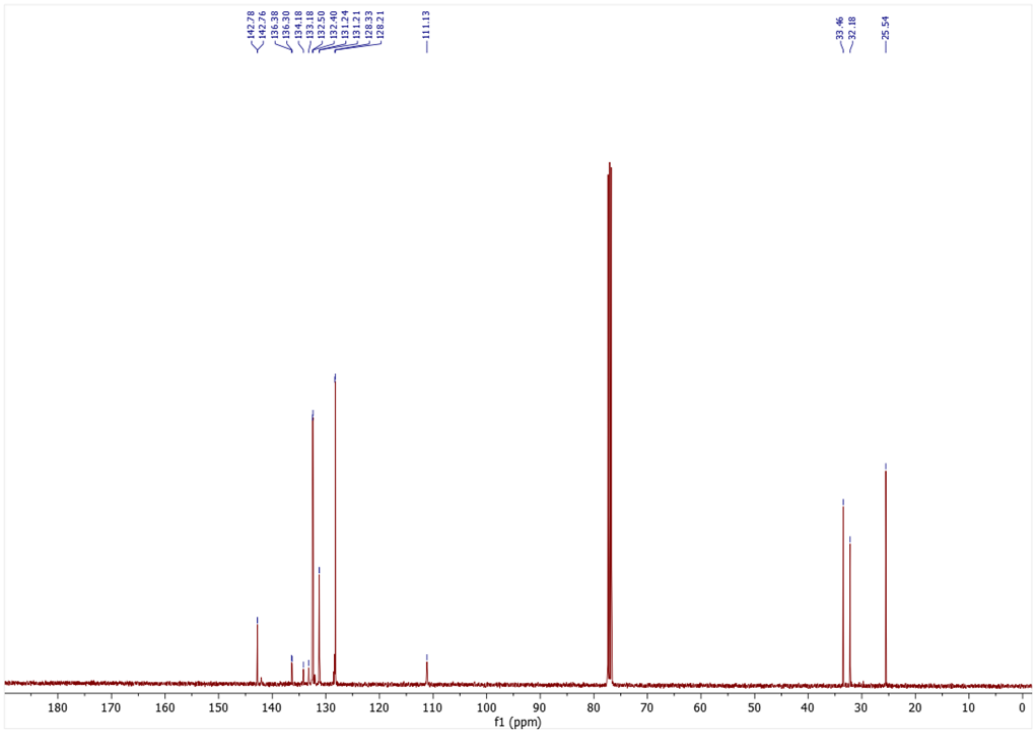

^{31}P NMR:

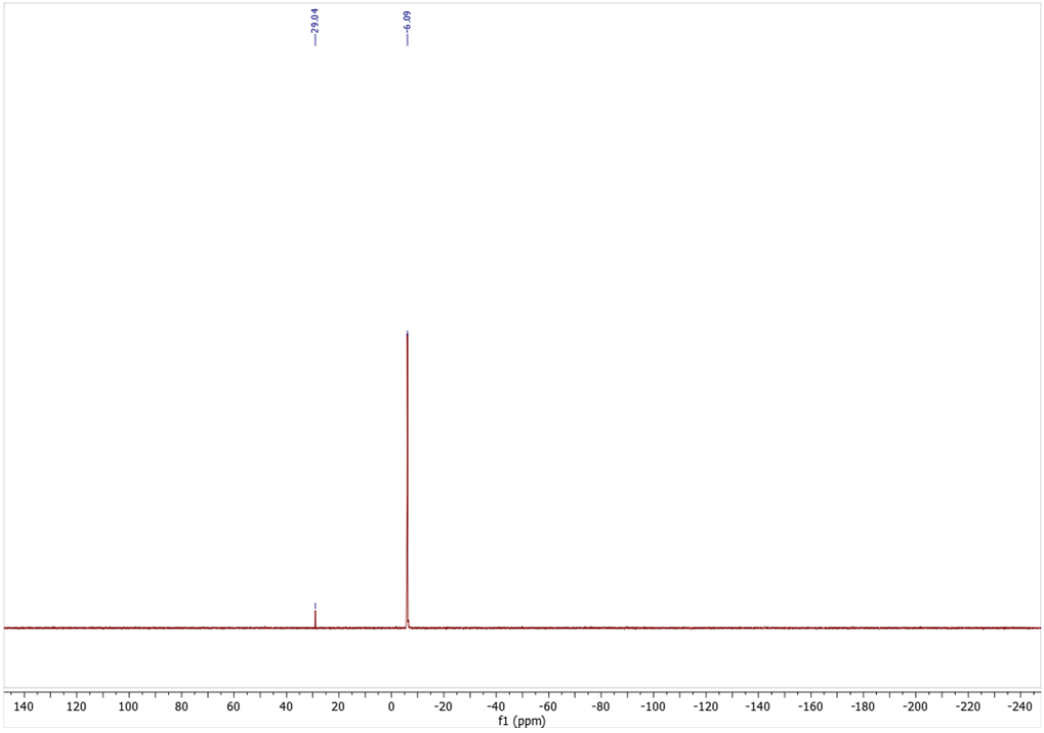

6.11.4. Radiosynthesis

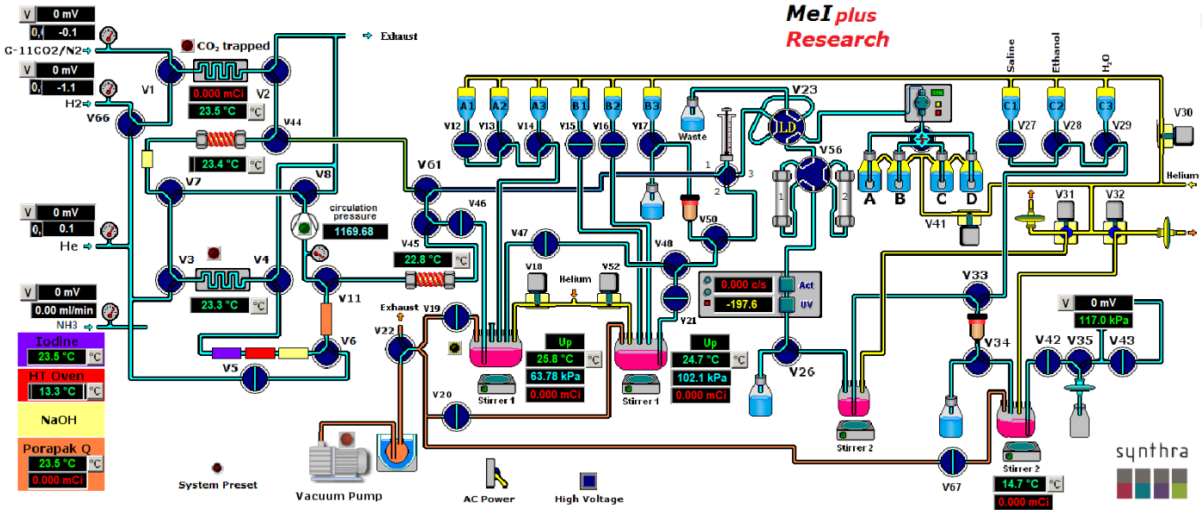

6.11.4.1. Figure S1. Syntha MeIplus Research Apparatus scheme.

Automated radiosynthesis of [^{11}C]MCC950

HPLC mobile phase (0.8 mL, 30% ACN/50 mM NH_4OAc) was loaded into V2. DMF and DBU were degassed using five freeze-thaw cycles prior to use. Precursor **3** (3.06 mg, 7.07 µmol) was loaded directly into the reactor. 4-(2-hydroxypropan-2-yl)furan-2-sulfonamide **2** (5.86 mg, 28.57 µmol) and KO^{t}Bu (3.14 mg, 27.9 µmol) were weighed in Teflon sealed vials and kept under inert atmosphere. Two minutes prior to the end-of-bombardment, **2** was dissolved in 100 µL of DMF and added to the vial containing KO^{t}Bu. After mixing for 30 seconds, the solution was loaded into the reactor, followed by the addition of DBU (7.46 µL of a 10 µL/mL solution in DMF, 9.97 µmol). The reaction vessel was tightly sealed, and a stream of helium was swept through the reactor after loading. Carbon-11 ([^{11}C]CO_2) was generated by the bombardment of a gas target filled with a pressurized N_2/O_2 mixture using a Siemens 11 MeV cyclotron, at 55 µA for 20 minutes, and was directed to a steel coil cooled at -180 ˚C. The coil was briefly flushed with $He_{(g)}$ prior to heating to 25 ˚C under a stream of helium at 3 mL/min to release [^{11}C]CO_2 into the reaction solution until peak activity. The reactor was then heated to 120 ˚C for 3 min prior to addition of 800 µL of mobile phase. The crude reaction mixture was purified by HPLC: Nucleodur C18 Pyramid 7 µm, 250 × 10 mm eluted with 30% ACN/50mM NH_4OAc at 5 mL/min (retention time 6–9 min). The product was collected in a bulk vessel loaded with 25 mL of H_2O and passed through a Sep-Pak C18 Plus Light cartridge. The cartridge was washed with 10 mL of H_2O and eluted with 1.5 mL of EtOH. 13.5 mL of saline was added to the vessel and the contents were passed through a 0.22 µm sterile filter. The identity was established by co-injection with the cold standard using a Waters 2695 Alliance HPLC equipped with a Phenomenex Luna 10 µm C18(2) (100 Å, 250 mm × 4.6 mm) column, a 996-photodiode array detector (Waters), and a Carroll & Ramsey Associates 105-S high-sensitivity radiation detector. Gradient: 80/20 H_2O/ACN for 2 min, linear gradient to 35/65 over 8 min, 35/65 for 2 min, linear gradient to 80/20 for 1 min, 80/20 for 7 min.

6.11.4.2. Radiochemical Identity and Isolation

Peaks indicated by solid arrows in chromatograms following co-injection of products with nonradioactive standard. The differences in elution times are due to UV-Vis and radiation detectors placed in series.

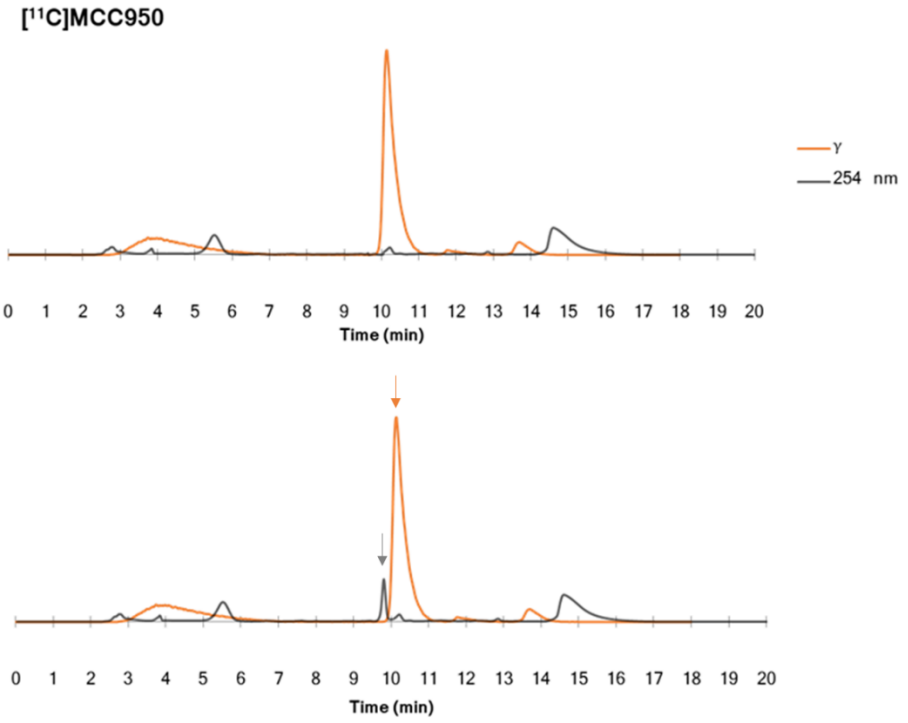

6.11.4.3. **Figure S2.** Chromatogram of crude [^{11}C]MCC950 reaction mixture. Crude reaction mixture with (bottom) and without (top) spiked reference standard.

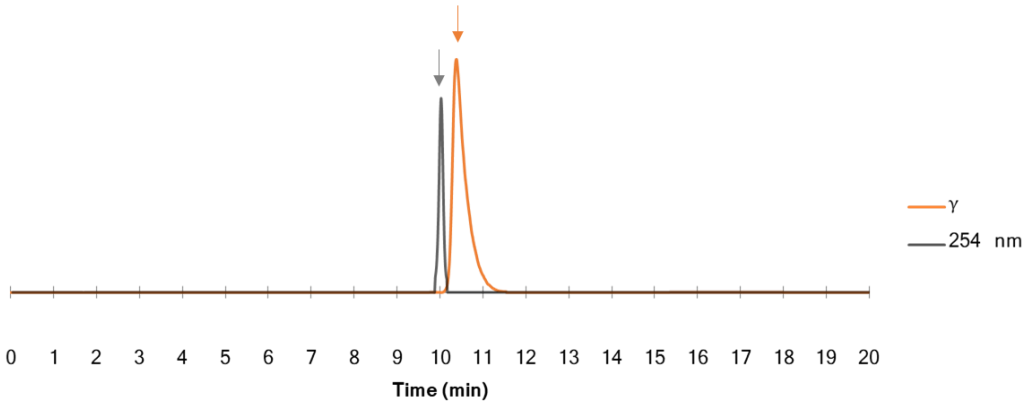

6.11.4.4. **Figure S3.** Chromatogram of isolated [^{11}C]MCC950 spiked with reference standard.

6.11.5. Standard Curve

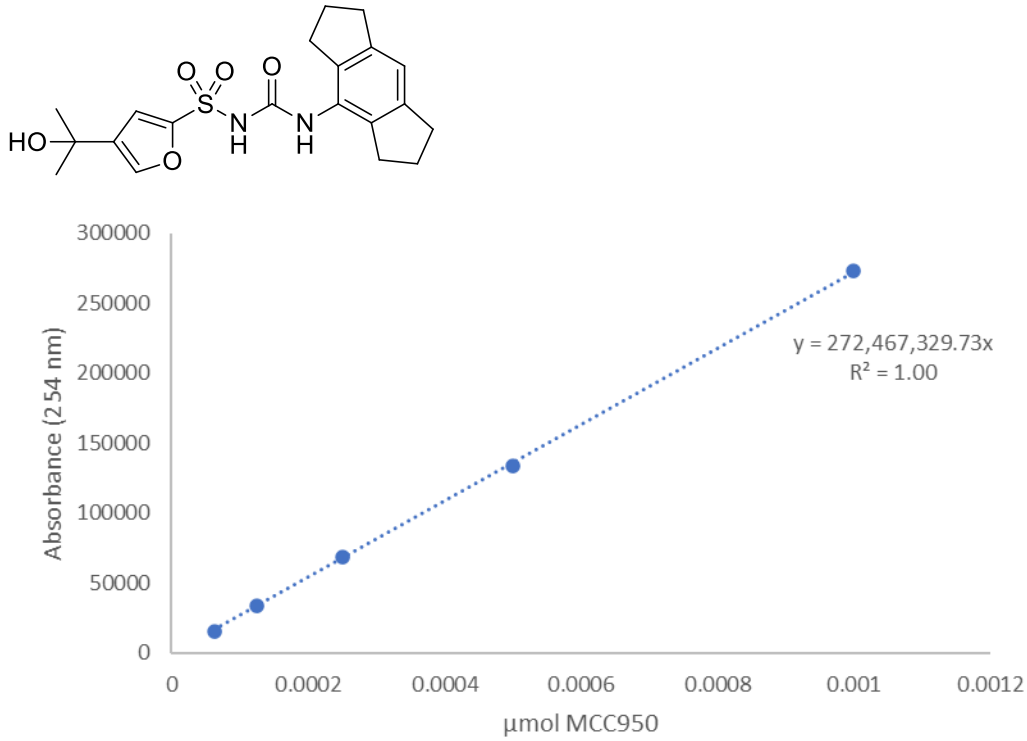

6.11.5.1. Figure S4: Standard curve of MCC950

7. Chapter VII: General Discussion and future directions

NET is one of the most important markers in molecular imaging for detecting cardiac dysfunction in preclinical and clinical research. One of the most important tracers that was never utilized to its full potential for cardiac imaging is [^{18}F]mFBG, owing to its challenging synthesis and complex reformulation, hindering its widescale use until recently. With the development of spirocyclic iodonium ylide (SCIDY) radiofluorination by Rotstein *et al*[1], [^{18}F]mFBG can be synthesized in high yields and molar activity. In this thesis, we report the optimization of [^{18}F]mFBG radiofluorination, deprotection, and CM ion exchange reformulation.[2] Furthermore, we investigated the mechanisms of uptake and myocardial washout in rats and evaluated the utility of this tracer in detecting HF in work that spans two chapters. We also evaluated the PNS tracer [^{18}F]FEOBV for imaging the cardiac NNCS in mice as an extension for ANS imaging. Given the various etiologies that can lead to the development of HF, and the multitude of accompanying molecular changes, developing a tracer for upstream cardiovascular diseases that may inform disease severity was also of importance. Coronary artery disease (CAD) is the most common cause of HF in developed countries, and remains a primary risk factor for HF development.[3] Thus, developing an imaging probe to detect the severity of atherosclerosis can inform patient health and reduce complications that lead to subsequent MI and development of HF pathophysiology. To start, our goal was to develop a novel radiotracer that can detect aortic plaques *ex vivo*, and has the potential to detect myocardial inflammation *in vivo*. The candidate radiotracer we selected was the sulfonylurea containing NLRP3 inhibitor MCC950, however limitations in its radiosynthesis hindered our ability to evaluate this radioligand in animals. We envisioned an alternative synthetic pathway; however, it utilized a radiochemical technique that was not extensively explored. As a result, we performed a comprehensive study on the limitations of the *aza*-Wittig reaction using

iminophosphorane precursors for radiochemistry (chapter V). Finally, with the ability to efficiently label ^{11}C-sulfonylureas using this technology, we extended its application to the synthesis of [^{11}C]MCC950, which we evaluated for imaging atherosclerotic plaques in ApoE$^{-/-}$ mice. With the development and evaluation of the radiotracers mentioned in this body of work, molecular changes in autonomic function and vascular inflammation can provide prognostic value and aide in risk stratification of patients, with the eventual goal of reducing the burden of HF.

7.1. Cardiac imaging using [^{18}F]mFBG in rats

Our *ex vivo* biodistribution studies with [^{18}F]mFBG established NET-dependent myocardial retention via DMI pretreatment and determined the remaining retention to be due to extraneural transport. In contrast, [^{123}I]mIBG and [^{18}F]FBBG show desipramine insensitivity in rats.[4,5] Consequently, developing a NET selective fluorinated probe for SNS imaging in small animals has proven to be even more challenging than in humans due to differential catecholamine handling in these species. To date, only two other radiotracers demonstrated DMI sensitivity in rats, but have yet to be evaluated further to demonstrate their application for PET imaging.[6,7] Regardless, our studies have also shown myocardial retention to be sensitive to chemical sympathectomy by 6-OHDA by *ex vivo* biodistribution, *in vivo* PET, and autoradiography on mid-ventricular slices. One of the most interesting features of [^{18}F]mFBG is its monoexponential cardiac washout and insensitivity to desipramine and phenoxybenzamine chase-dosing. While [^{11}C]HED is continuously recycled into the neuron via vesicular release and NET reuptake as evidence by DMI displacement,[8] [^{18}F]mFBG displays no reuptake and is thus hypothesized to clear to plasma upon exit from the presynaptic neuron. Theoretically, biochemical changes in VMAT2 transport or NET dysfunction would be more readily apparent at early timepoints in a tracer that possesses limited reuptake. The leading fluorinated derivative for SNS imaging, [^{18}F]FBBG,

displays DMI pretreatment sensitivity in rabbits, but is retained within the neuron by a different mechanism than [^{11}C]HED. Rather than continuous release and reuptake, [^{18}F]FBBG appears to be trapped within the neuronal vesicle and unable to be released.[8,9] In mature neuronal preparations, several distinct pools of vesicles have been discovered.[10,11] The readily releasable pool (RRP) is discharged within seconds following stimulation.[10] Following depletion of the RRP, a secondary releasable pool termed the recycling pool (RP) is then released.[10] Interestingly, a third pool known as the resting/reserve pool (R_tP) was identified in hippocampal nerve terminals and is only released following intense stimulus.[10] While the exact transport mechanisms are unclear, irreversible uptake of [^{18}F]FBBG and [^{18}F]PHEG analogues may be due to retention in R_tP vesicles, whereas [^{11}C]HED is transported into RRP vesicles. This may also explain why [^{18}F]FBBG washout is observed to be consistent, whereas [^{11}C]HED washout is increased in patients with ischemic cardiomyopathy (ICM), rendering [^{11}C]HED to be more sensitive to changes in tracer "leakage" from the neuron.[12] On the basis of our RSP pretreatment experiment, it is evident that [^{18}F]mFBG is also a substrate for VMAT2 and must be stored into vesicles in order to maintain neuronal retention. Given this finding, basal myocardial washout is likely composed of a neuronal compartment influenced by active release with endogenous NE in RRP vesicles, since passive diffusion of charged polar molecules is hypothesized to be a minor contributor to tracer efflux from both the axoplasm and acidic cytosol within the vesicle.[13]

Indeed, pretreatment of rats with DMI revealed a significantly faster washout rate from the myocardium in the absence of neural uptake (0.024 ± 0.003 min^{-1} vs 0.058 ± 0.02 min^{-1}), suggesting neural washout to be an inherently slower process. However, studies in diseased DSS HS rats did not significantly affect cardiac washout of the tracer. We hypothesize that the lack of changes observed in myocardial washout in disease state may be a consequence of not generating

the expected late-stage HF phenotype. Furthermore, we do not yet have any supporting evidence to show SNS tone is higher in HS-16 rats and await competitive ELISA results to determine changes in NE plasma spillover. Regardless, we demonstrated that cardiac washout is a parameter that can be influenced by pharmaceuticals that excite or depress sympathetic function via α_2 antagonism or agonism, respectively. Given this finding, it is unlikely that myocardial washout is of no physiological importance in disease assessment. In fact, the leading radioligands currently used including [^{123}I]mIBG, [^{11}C]HED, and [^{18}F]FBBG all report increased washout in the myocardium of individuals presenting with some form or dysautonomia.[12,14–17]

Imaging experiments in humans with [^{18}F]mFBG have also demonstrated significant cardiac washout and reversible kinetics.[18] Since contribution of extraneural uptake in higher species and humans is far less significant[8], we believe neural washout to be a significant contributor to reduced uptake over time. However, the distinct modes of tracer loss from the neurons are not entirely understood, even with years of molecular imaging data obtained using [^{123}I]mIBG in healthy and diseased populations.[19–24] While active exocytotic release is typically considered to be a major contributor, leakage from the neuron by facilitated diffusion and reverse NET transport remain plausible. Nevertheless, our studies have determined important compartments that dictate neuronal retention in rats as shown in figure 1.

In evaluating [^{18}F]mFBG in DSS rats, we uncovered reduced uptake in the LV coincident with declining cardiac function and transition to HF. While tissue studies have not yet been performed to pinpoint the exact cause of reduced uptake, the magnitude of decrease is consistent with the previously determined contribution of NET-dependent myocardial uptake. Thus, the current evidence suggests dysfunctional or downregulated NET is likely the culprit, but Western blotting for NET must be performed to validate this hypothesis. Nevertheless, [^{18}F]mFBG PET

imaging has demonstrated good application in imaging an animal model of HF and is therefore a promising radioligand to noninvasively detect SNS dysfunction in small animals.

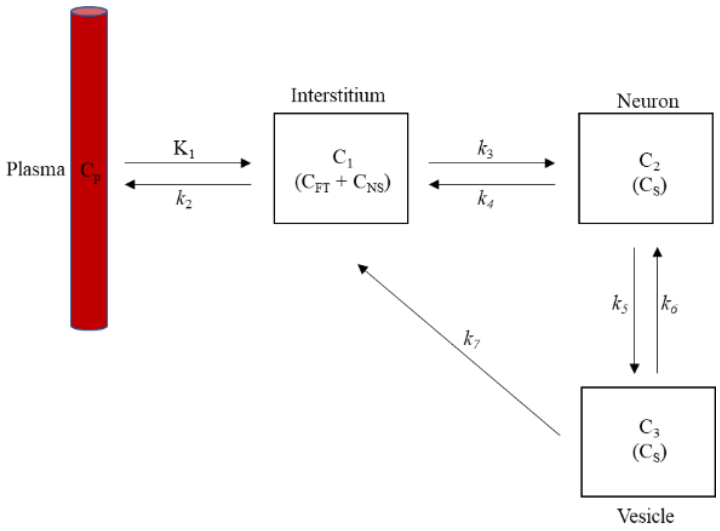

7.1.1. **Figure 1.** Compartmental kinetics of [^{18}F]mFBG. K_1 is the rate constant that describes transport of [^{18}F]mFBG from plasma into the interstitium. Rate constant k_2 represents tracer in the interstitium transported back into plasma. Radiotracer in the interstitium is composed of unbound free tracer and nonspecifically bound tracer. Rate constant k_3 is representative of tracer that is specifically transported into the neuron by NET. Whereas k_4 represents extravesicular transport of [^{18}F]mFBG from the axopasm back into the interstitium. Rate constant k_4 is the summation of mechanisms contributing to loss of tracer from the neuron such as reverse NET transport or facilitated diffusion of the tracer. Rate constant k_5 is representative of VMAT2-mediated transport of [^{18}F]mFBG into neuronal storage vesicles, and k_6 describes reverse transport. Lastly, k_7 is representative of exocytotic release of tracer back into the interstitium. Constant k_8 describing the reverse process is not included as exocytotic release of tracer cannot be reversed.

In small animal imaging with SNS radiotracers, rapid delivery of radiotracer from plasma to the interstitium has been hypothesized to contribute to perfusion-dependent uptake into target tissue. This has been postulated for radiotracers with high binding affinity to the target such as [^{11}C]HED. However, compartmental modeling of [^{11}C]HED in mice demonstrates K_1 to be a DMI-dependent parameter that describes uptake of the tracer from plasma to nerve terminal rather than plasma to extracellular space or interstitium.[25] Due to the rapid transport of [^{11}C]HED from plasma to extracellular space, NET uptake was the rate limiting step as demonstrated by homologous blocking dose-dependency studies. However, [^{11}C]HED myocardial uptake in humans is more susceptible to perfusion-dependent retention due to significantly slower transport of plasma at 1 ml/min/g (humans) in comparison to 9ml/min/cm^3 (mice).[26,27] The estimated K_1 parameter has been measured to be 0.6 mL/min/g for [^{11}C]HED, and approaches maximal plasma flow, potentially influencing regionally reduced uptake due to perfusion defects.[28] Human imaging of [^{18}F]mFBG in neuroblastoma patients has determined K_1 to be 1.11 ml/min/g.[18] Thus, SNS imaging may also require obtaining MBF data to quantify NET function prior to [^{18}F]mFBG PET.

Based on our studies in rats, [^{18}F]mFBG myocardial kinetics have been uncovered to be NET dependent (k_3) as demonstrated by DMI blockade. Sensitivity to RSP pretreatment provides evidence of vesicular transport (k_5). Washout parameters are influenced by exocytotic release (k_7) evidenced by adrenoreceptor chase, and neuronal leakage via diffusion, facilitated transport, or reverse NET transport may occur (k_4). Lastly, extraneural washout of the tracer is observed in rodents and should be considered as a major compartment when interpreting [^{18}F]mFBG imaging data.

7.1.2. Future directions

First, cardiac tissue studies should be performed on the hearts of DSS rats to determine the origin of reduced uptake. Western blot for NET of HS and LS fed rats should provide evidence for changes in NET expression. Immunofluorescence can also be performed by utilizing tyrosine hydroxylase (TH) staining to visualize whether loss of sympathetic nerve density explains the results obtained by PET and Western blotting. Blood samples have also been collected for several of these rats and norepinephrine (NE) enzyme-linked immunosorbent assay (ELISA) can be performed to observe changes in plasma NE spillover over the duration of the study.

Second, coronary artery ligation (CAL) animal models should be used since the multiple etiologies can contribute to HF. To this end, cardiac function can be monitored by echo, and PET imaging can be performed at several stages (early to late-stage HF). Flow imaging can be performed to determine whether changes in perfusion influence regions of reduced cardiac uptake. At the endpoint, tissue studies can be performed to determine changes in NET expression over the course of HF.

7.2. Cardiac cholinergic system

PNS imaging performed with [^{18}F]FEOBV did not enable us to selectively determine NNCS function due to a lack of specific binding. We attempted to block the uptake in the myocardium by treating animals with the nonreversible VAChT inhibitor (-)-vesamicol, which also displays moderate sigma-1 receptor binding affinity.[29] While we observed reduced uptake in organs highly innervated by the PNS such as in the brain and pancreas, myocardial uptake remained unchanged. Isoflurane was not observed to have any effect on cardiac uptake, and mice expressing reduced or increased cardiac VAChT displayed minimal differences in uptake. In this event, the most probable hypothesis is that cardiac uptake of [^{18}F]FEOBV in mice is driven by perfusion and nonspecific interactions in tissue. It has been previously hypothesized in isolated rat hearts that due to high lipophilicity [^{18}F]FEOBV undergoes passive diffusion and is distributed to lipid rich sites, with washout also being driven by freely diffusible tracer.[30] In addition, VAChT receptor density is hypothesized to be low given the effective blocking doses of 10-150 μg/kg for VAChT inhibitors. While it is unlikely that receptor density is too low to be imaged even with high molar activity [^{18}F]FEOBV, nonspecific myocardial retention may also be a consequence of imaging small animals such as mice and rats. As recent data has demonstrated some evidence of age-dependent retention of [^{18}F]FEOBV in the human myocardium, advancing studies to higher species such as rabbits or pigs may provide supporting evidence for specific binding with this tracer.

7.2.1. Future directions

Future studies with [^{18}F]FEOBV are unlikely to lead to novel findings in small animals. While larger animals are harder to obtain, PET imaging can be performed in pigs or non-human primates. The images can be quantified and corrected for plasma metabolism and blocking studies can be performed at low doses to ensure adequate safety and avoid toxicity. Blocking studies in higher species will identify if any specific binding occurs. While it is unlikely that [^{18}F]FEOBV myocardial retention in humans is dependent on sigma-1 receptors given this ligands improved selectivity over (-)vesamicol[31,32], pretreatment with sigma-1 receptor antagonists can rule out this possibility. Cardiovascular diseases such as HF can also be induced in pig models, and quantification of LV activity can be determined as cardiac function declines.[33] Absolute quantification can be performed to observe whether perfusion-independent changes in LV activity occur as the disease progresses. Alternatively, other tracers can be evaluated for cardiac NNCS imaging such as ligands for acetylcholine esterase or choline transporter.

7.3. Carbon-11 radiochemistry

Iminophosphoranes have served as important synthetic intermediates for several years, with numerous research groups utilizing the Staudinger reaction in important synthetic pathways. Typically, iminophosphoranes are formed *in situ* due to complications in purification. Namely, these compounds display sensitivity to hydrolysis in water making solvent-solvent extraction difficult, are moisture sensitive and thus display poor bench top stability, have high polarity making column chromatography by silica challenging, and yield triphenylphosphine oxide (TPPO) as a by-product of the Kirsanov reaction complicating high purity isolations.[34] Given these drawbacks, direct isolation of iminophosphosphoranes is typically avoided in synthetic organic chemistry. Regardless, we were able to develop a simple isolation method for these precursors by

utilizing their ability to form hydrobromide salts *in situ* to obtain a stable form of these precursors. While these compounds display good reactivity with CO_2 when reacting them with the natural isotope of carbon (99% carbon-12), difficulties in separating TPPO from polar products were still a major challenge that may hinder its use. However, we were still able to generate a multitude of products with differing polarity, in addition to relevant pharmaceuticals using this chemistry.

Moreover, we successfully synthesized several carbon-11 labelled products in high yield and trapping efficiency with this technology. Most notably, was the automated synthesis of the radiopharmaceutical [^{11}C]glibenclamide. This compound contains a sulfonylurea moiety previously labelled using a two step method with [^{11}C]CH_3OTf in 5% RCY.[35] Alternative methods for labeling sulfonylureas require the use of [^{11}C]carbon monoxide ([^{11}C]CO), a secondary precursor that is not commonly used at many sites. Iminophosphorane chemistry has displayed good substrate tolerance and represents a unique method to synthesize and obtain in-demand radiopharmaceuticals in high yield using an automated method.

7.4. Evaluation of [^{11}C]MCC950

MCC950 is a unique first in-class NLRP3 inhibitor that has shown application as a therapeutic for inflammatory conditions. Given its active role in the progression of atherosclerosis in mice and humans, we performed an *ex vivo* evaluation to determine whether imaging NLRP3-mediated inflammation in atherosclerotic plaques with this tracer is plausible. Using an iminophosphorane precursor, we successfully isolated the radiopharmaceutical in high yield with an automated method. Plaques were visualized by *ex vivo* autoradiography and showed heterogenous uptake within the aortic arch in lipid rich regions, whereas minimal accumulation was noted in C57BL/6 mice. Under blockade conditions with nonradioactive MCC950, we noted a ~2-fold increase in the accumulation of tracer within the plaque. We hypothesized that this

increase in uptake may be nonspecific and likely due to an increase in the plasma free fraction of the tracer, since administering cold MCC950 10 minutes prior to the radioligand could significantly occupy plasma proteins. This phenomenon has been observed in CNS imaging, where higher uptake in the brain may be noted as a result of reduced plasma protein binding and higher BBB penetration.[36] However, when we determined the increase in plasma free fraction, we noted a moderate ~1.2-fold increase in free fraction of this tracer. In these scenarios, normalization of radiotracer uptake by blood activity is typically required to provide a more accurate assessment of changes that occurred in the organ of interest. Given that blood activity concentrations remained consistent following homologous blockade, the ratio of plaque-to-blood uptake will remain high. Thus, normalized uptake values still provide higher aortic arch uptake. Given this finding, the most probable hypothesis is that the uptake within the plaque is target dependent. With this in mind, we suspected that biochemical mechanisms likely explain this phenomena. One study investigating open and closed NLRP3 conformers performed *in vitro* studies with MCC950 and showed inhibitor-dependent disaggregation of NLRP3 oligomers back to NLRP3 monomers.[37] This would theoretically increase the total number of available binding sites and may explain the increase in radiotracer accumulation.

In summary, we successfully synthesized [^{11}C]MCC950 in high yields suitable for its preclinical evaluation. From our *ex vivo* biodistribution and blocking studies, we noted increased aortic arch uptake following homologous blockade, likely explained by biochemical disaggregation of NLRP3 oligomers into monomers. Further work dedicated to imaging NLRP3-mediated inflammation may provide a non-invasive means of detecting atherosclerotic plaques by PET imaging and determine risk factors in populations with high expression of NLRP3.

7.4.1. Future directions

Future studies with this tracer are warranted to further determine the extent of specific binding within the plaque, such as the use of double knockout ApoE$^{-/-}$ NLRP3$^{-/-}$ mice, or RNA silencing techniques to provide more direct evidence that [^{11}C]MCC950 uptake is driven by changes in NLRP3 expression. Furthermore, tracer kinetics can be optimized by synthesizing derivatives that retain high potency and have favorable characteristics for non-invasive *in vivo* imaging of atherosclerotic lesions.

7.4.2. Major findings and conclusions

From the sympathetic imaging project in rats, we determined that: 1) Uptake of [^{18}F]mFBG in rats is NET-sensitive, 2) minimal reuptake of the tracer occurs via neural and extra neural transporters, 3) [^{18}F]mFBG is metabolically stable in the myocardium but significantly less stable in plasma, 4) [^{18}F]mFBG is a VMAT substrate and requires vesicular storage for stable neural retention, 5) [^{18}F]mFBG washout is sensitive to alterations in sympathetic tone, 6) tracer uptake is sensitive in a HS diet induced disease model for HF. In summary, [^{18}F]mFBG is the first tracer to display reversible kinetics and sensitivity to NET expression in rodents, with supporting evidence that indicates tracer washout reflects vesicular efflux/neuronal leakage rates.

Imaging the NNCS with [^{18}F]FEOBV provided us with the following conclusions: 1) Uptake in the myocardium may be driven by perfusion due to insensitivity to pharmacological blockade, 2) isoflurane anesthesia has minimal impact on the myocardial retention of the tracer, 3) [^{18}F]FEOBV has moderate stability in the myocardium and lower stability in plasma after 30 minutes, 4) [^{18}F]FEOBV imaging in rodents is unlikely to be a sensitive imaging agent for detecting molecular changes of VAChT in the NNCS.

The development of iminophosphorane chemistry enabled the: 1) Synthesis and isolation of stable iminophosphorane precursors, 2) synthesis of in-demand pharmacueticals and radiopharmaceuticals in high yield and molar activity, 3) enabled the radiosynthesis of sulfonylureas directly of [^{11}C]CO_2.

From the vascular imaging project with [^{11}C]MCC950, we concluded that: 1) [^{11}C]MCC950 can be synthesized efficiently using iminophosphorane chemistry, 2) [^{11}C]MCC950, distributes primarily to the liver and kidney and demonstrates baseline uptake in aortic plaques of ApoE$^{-/-}$ mice, 3) increased plaque uptake following blockade is unlikely to be due to nonspecific binding due to moderate increases in plasma free fraction, 4) biochemical mechanisms such as oligomer disaggregation after pretreatment with nonradioactive MCC950 is a more probable explanation to increased aortic plaque uptake.

7.5. References

(1) H. Rotstein, B.; Wang, L.; Y. Liu, R.; Patteson, J.; E. Kwan, E.; Vasdev, N.; H. Liang, S. Mechanistic Studies and Radiofluorination of Structurally Diverse Pharmaceuticals with Spirocyclic Iodonium(Iii) Ylides. *Chem. Sci.* **2016**, *7* (7), 4407–4417. https://doi.org/10.1039/C6SC00197A.

(2) Ismailani, U. S.; Buchler, A.; Farber, G.; Pekošak, A.; Farber, E.; MacMullin, N.; Suuronen, E. J.; Vasdev, N.; Beanlands, R. S. B.; de Kemp, R. A.; Rotstein, B. H. Cardiac Sympathetic Positron Emission Tomography Imaging with Meta-[18F]Fluorobenzylguanidine Is Sensitive to Uptake-1 in Rats. *ACS Chem. Neurosci.* **2021**. https://doi.org/10.1021/acschemneuro.1c00575.

(3) Lala, A.; Desai, A. S. The Role of Coronary Artery Disease in Heart Failure. *Heart Fail. Clin.* **2014**, *10* (2), 353–365. https://doi.org/10.1016/j.hfc.2013.10.002.

(4) Rischpler, C.; Fukushima, K.; Isoda, T.; Javadi, M. S.; Dannals, R. F.; Abraham, R.; Wahl, R.; Bengel, F. M.; Higuchi, T. Discrepant Uptake of the Radiolabeled Norepinephrine Analogues Hydroxyephedrine (HED) and Metaiodobenzylguanidine (MIBG) in Rat Hearts. *Eur. J. Nucl. Med. Mol. Imaging* **2013**, *40* (7), 1077–1083. https://doi.org/10.1007/s00259-013-2393-z.

(5) Higuchi, T.; Yousefi, B. H.; Kaiser, F.; Gärtner, F.; Rischpler, C.; Reder, S.; Yu, M.; Robinson, S.; Schwaiger, M.; Nekolla, S. G. Assessment of the 18F-Labeled PET Tracer LMI1195 for Imaging Norepinephrine Handling in Rat Hearts. *J. Nucl. Med. Off. Publ. Soc. Nucl. Med.* **2013**, *54* (7), 1142–1146. https://doi.org/10.2967/jnumed.112.104232.

(6) Li, X.; Shi, S.; Zhou, H.; Zhao, Z.; Lu, J. Novel [18F]-Labeled Meta-Bromobenzylguanidine Derivatives: Potential Positron Emission Tomography Imaging

Probes for the Norepinephrine Transporter. *Mol. Pharm.* **2021**, *18* (10), 3811–3819. https://doi.org/10.1021/acs.molpharmaceut.1c00429.

(7) Woo, S.-K.; Moon, B. S.; Kim, B. S.; Kim, M. H.; Lee, Y. J.; Jung, J. H.; Lee, K. C.; Seo, Y.; Kim, W.; Lim, S. M.; Lee, B. C.; Kim, S. E. Feasibility of Myocardial PET Imaging Using a Benzylguanidine Analog: Meta-(3-[18F]Fluoropropyl)Benzylguanidine ([18F]MFPBG). *Nucl. Med. Biol.* **2018**, *61*, 63–70. https://doi.org/10.1016/j.nucmedbio.2018.04.005.

(8) Werner, R. A.; Rischpler, C.; Onthank, D.; Lapa, C.; Robinson, S.; Samnick, S.; Javadi, M.; Schwaiger, M.; Nekolla, S. G.; Higuchi, T. Retention Kinetics of the 18F-Labeled Sympathetic Nerve PET Tracer LMI1195: Comparison with 11C-Hydroxyephedrine and 123I-MIBG. *J. Nucl. Med. Off. Publ. Soc. Nucl. Med.* **2015**, *56* (9), 1429–1433. https://doi.org/10.2967/jnumed.115.158493.

(9) Sinusas, A. J.; Liu, C. Multi-Tracer Positron Emission Tomography Quantification of Sympathetic Innervation. *JACC Cardiovasc. Imaging* **2021**, *14* (7), 1437–1439. https://doi.org/10.1016/j.jcmg.2020.10.007.

(10) Alabi, A. A.; Tsien, R. W. Synaptic Vesicle Pools and Dynamics. *Cold Spring Harb. Perspect. Biol.* **2012**, *4* (8), a013680. https://doi.org/10.1101/cshperspect.a013680.

(11) Stevens, D.; Schirra, C.; Becherer, U.; Rettig, J. Vesicle Pools: Lessons from Adrenal Chromaffin Cells. *Front. Synaptic Neurosci.* **2011**, *3*.

(12) Zelt, J. G. E.; Britt, D.; Mair, B. A.; Rotstein, B. H.; Quigley, S.; Walter, O.; Garrard, L.; Robinson, S.; Mielniczuk, L. M.; deKemp, R. A.; Beanlands, R. S. Regional Distribution of Fluorine-18-Flubrobenguane and Carbon-11-Hydroxyephedrine for Cardiac PET

Imaging of Sympathetic Innervation. *JACC Cardiovasc. Imaging* **2020**. https://doi.org/10.1016/j.jcmg.2020.09.026.

(13) Ahdut-Hacohen, R.; Duridanova, D.; Meiri, H.; Rahamimoff, R. Hydrogen Ions Control Synaptic Vesicle Ion Channel Activity in Torpedo Electromotor Neurones. *J. Physiol.* **2004**, *556* (Pt 2), 347–352. https://doi.org/10.1113/jphysiol.2003.058818.

(14) AlJaroudi, W. Heart Rate and 123I-MIBG in Heart Failure with Preserved Ejection Fraction: More Variability and Slower Washout—A Secret Recipe for Better Survival. *J. Nucl. Cardiol.* **2020**, *27* (3), 843–848. https://doi.org/10.1007/s12350-018-01514-w.

(15) Jeong, Y. J.; Jeong, J.-E.; Cheon, S.-M.; Yoon, B.-A.; Kim, J. W.; Kang, D.-Y. Relationship between the Washout Rate of I-123 MIBG Scans and Autonomic Function in Parkinson's Disease. *PLOS ONE* **2020**, *15* (3), e0229860. https://doi.org/10.1371/journal.pone.0229860.

(16) Tomiyama, Y.; Yoshinaga, K.; Katoh, C.; Sakakibara, M.; Kasai, K.; Manabe, O.; Naya, M.; Nishijima, K.; Tamaki, N. Increased Cardiac 11C-Hydroxyephedrine (HED) Washout Using Compartment Model Analysis in Patients with Heart Failure. *J. Nucl. Med.* **2015**, *56* (supplement 3), 1764–1764.

(17) Dai, Y.; Zelt, J.; Mielniczuk, L.; Beanlands, R.; de Kemp, R. ACCELERATED TRACER WASHOUT IN REGIONS OF SYMPATHETIC DENERVATION IN HEART FAILURE PATIENTS WITH ISCHEMIC CARDIOMYOPATHY USING FLUBROBENGUANE POSITRON EMISSION TOMOGRAPHY IMAGING. *Can. J. Cardiol.* **2021**, *37* (10, Supplement), S78. https://doi.org/10.1016/j.cjca.2021.07.156.

(18) Grkovski, M.; Zanzonico, P. B.; Modak, S.; Humm, J. L.; Narula, J.; Pandit-Taskar, N. F-18 Meta-Fluorobenzylguanidine PET Imaging of Myocardial Sympathetic Innervation. *J. Nucl. Cardiol.* **2022**. https://doi.org/10.1007/s12350-021-02813-5.

(19) Bengel, F. M.; Barthel, P.; Matsunari, I.; Schmidt, G.; Schwaiger, M. Kinetics of 123I-MIBG After Acute Myocardial Infarction and Reperfusion Therapy. *J. Nucl. Med.* **1999**, *40* (6), 904–910.

(20) Tobes, M. C.; Jaques, S.; Wieland, D. M.; Sisson, J. C. Effect of Uptake-One Inhibitors on the Uptake of Norepinephrine and Metaiodobenzylguanidine. *J. Nucl. Med. Off. Publ. Soc. Nucl. Med.* **1985**, *26* (8), 897–907.

(21) Nakajo, M.; Shimabukuro, K.; Yoshimura, H.; Yonekura, R.; Nakabeppu, Y.; Tanoue, P.; Shinohara, S. Iodine-131 Metaiodobenzylguanidine Intra- and Extravesicular Accumulation in the Rat Heart. *J. Nucl. Med.* **1986**, *27* (1), 84–89.

(22) Henderson E B; Kahn J K; Corbett J R; Jansen D E; Pippin J J; Kulkarni P; Ugolini V; Akers M S; Hansen C; Buja L M. Abnormal I-123 Metaiodobenzylguanidine Myocardial Washout and Distribution May Reflect Myocardial Adrenergic Derangement in Patients with Congestive Cardiomyopathy. *Circulation* **1988**, *78* (5), 1192–1199. https://doi.org/10.1161/01.CIR.78.5.1192.

(23) Wakasugi, S.; Inoue, M.; Tazawa, S. Assessment of Adrenergic Neuron Function Altered with Progression of Heart Failure. *J. Nucl. Med.* **1995**, *36* (11), 2069–2074.

(24) Kurata, C.; Shouda, S.; Mikami, T.; Wakabayashi, Y.; Nakano, T.; Sugiyama, T.; Tawarahara, K.; Sakata, K. Comparison of [123I]Metaiodobenzylguanidine Kinetics with Heart Rate Variability and Plasma Norepinephrine Level. *J. Nucl. Cardiol.* **1997**, *4* (6), 515–523. https://doi.org/10.1016/S1071-3581(97)90010-6.

(25) Mu, L.; Krämer, S. D.; Warnock, G. I.; Haider, A.; Bengs, S.; Cartolano, G.; Bräm, D. S.; Keller, C.; Schibli, R.; Ametamey, S. M.; Kaufmann, P. A.; Gebhard, C. [11C]MHED PET Follows a Two-Tissue Compartment Model in Mouse Myocardium with Norepinephrine Transporter (NET)-Dependent Uptake, While [18F]LMI1195 Uptake Is NET-Independent. *EJNMMI Res.* **2020**, *10* (1), 114. https://doi.org/10.1186/s13550-020-00700-7.

(26) Krämer, S. D. Quantitative Aspects of Drug Permeation across in Vitro and in Vivo Barriers. *Eur. J. Pharm. Sci.* **2016**, *87*, 30–46. https://doi.org/10.1016/j.ejps.2015.10.013.

(27) Rijnierse, M. T.; Allaart, C. P.; de Haan, S.; Harms, H. J.; Huisman, M. C.; Wu, L.; Beek, A. M.; Lammertsma, A. A.; van Rossum, A. C.; Knaapen, P. Sympathetic Denervation Is Associated with Microvascular Dysfunction in Non-Infarcted Myocardium in Patients with Cardiomyopathy. *Eur. Heart J. - Cardiovasc. Imaging* **2015**, *16* (7), 788–798. https://doi.org/10.1093/ehjci/jev013.

(28) Sasano, T.; Abraham, M. R.; Chang, K.-C.; Ashikaga, H.; Mills, K. J.; Holt, D. P.; Hilton, J.; Nekolla, S. G.; Dong, J.; Lardo, A. C.; Halperin, H.; Dannals, R. F.; Marbán, E.; Bengel, F. M. Abnormal Sympathetic Innervation of Viable Myocardium and the Substrate of Ventricular Tachycardia After Myocardial Infarction. *J. Am. Coll. Cardiol.* **2008**, *51* (23), 2266–2275. https://doi.org/10.1016/j.jacc.2008.02.062.

(29) Efange, S. M. N.; Mach, R. H.; Smith, C. R.; Khare, A. B.; Foulon, C.; Akella, S. K.; Childers, S. R.; Parsons, S. M. Vesamicol Analogues as Sigma Ligands: Molecular Determinants of Selectivity at the Vesamicol Receptor. *Biochem. Pharmacol.* **1995**, *49* (6), 791–797. https://doi.org/10.1016/0006-2952(94)00541-S.

(30) Evaluation of (−)[18F]Fluoroethoxybenzovesamicol as a New PET Tracer of Cholinergic Neurons of the Heart. *Nucl. Med. Biol.* **1994**, *21* (2), 189–195. https://doi.org/10.1016/0969-8051(94)90008-6.

(31) Saint-Georges, Z.; Zayed, V. K.; Dinelle, K.; Cassidy, C.; Soucy, J.-P.; Massarweh, G.; Rotstein, B.; Nery, P. B.; Guimond, S.; deKemp, R.; Tuominen, L. First-in-Human Imaging and Kinetic Analysis of Vesicular Acetylcholine Transporter Density in the Heart Using [18F]FEOBV PET. *J. Nucl. Cardiol.* **2021**, *28* (1), 50–54. https://doi.org/10.1007/s12350-020-02323-w.

(32) Horsager, J.; Okkels, N.; Van Den Berge, N.; Jacobsen, J.; Schact, A.; Munk, O. L.; Vang, K.; Bender, D.; Brooks, D. J.; Borghammer, P. In Vivo Vesicular Acetylcholine Transporter Density in Human Peripheral Organs: An [18F]FEOBV PET/CT Study. *EJNMMI Res.* **2022**, *12* (1), 17. https://doi.org/10.1186/s13550-022-00889-9.

(33) Hunter, I.; Terzic, D.; Zois, N. E.; Olsen, L. H.; Goetze, J. P. Pig Models for the Human Heart Failure Syndrome. *Cardiovasc. Endocrinol. Metab.* **2014**, *3* (1), 15. https://doi.org/10.1097/XCE.0000000000000022.

(34) Batesky, D. C.; Goldfogel, M. J.; Weix, D. J. Removal of Triphenylphosphine Oxide by Precipitation with Zinc Chloride in Polar Solvents. *J. Org. Chem.* **2017**, *82* (19), 9931–9936. https://doi.org/10.1021/acs.joc.7b00459.

(35) Caillé, F.; Gervais, P.; Auvity, S.; Coulon, C.; Marie, S.; Tournier, N.; Kuhnast, B. Automated Two-Step Manufacturing of [11C]Glyburide Radiopharmaceutical for PET Imaging in Humans. *Nucl. Med. Biol.* **2020**, *84–85*, 20–27. https://doi.org/10.1016/j.nucmedbio.2019.12.008.

(36) Van de Bittner, G. C.; Ricq, E. L.; Hooker, J. M. A Philosophy for CNS Radiotracer Design. *Acc. Chem. Res.* **2014**, *47* (10), 3127–3134. https://doi.org/10.1021/ar500233s.

(37) Tapia-Abellán, A.; Angosto-Bazarra, D.; Martínez-Banaclocha, H.; de Torre-Minguela, C.; Cerón-Carrasco, J. P.; Pérez-Sánchez, H.; Arostegui, J. I.; Pelegrin, P. MCC950 Closes the Active Conformation of NLRP3 to an Inactive State. *Nat. Chem. Biol.* **2019**, *15* (6), 560–564. https://doi.org/10.1038/s41589-019-0278-6.